


# MID-INFRARED TRANSMITTING Ge-Sb-Se CHALCOGENIDE GLASS FIBRES:

# FOR POTENTIAL USE IN MEDICAL DIAGNOSTICS

JESSICA HELEN BUTTERWORTH, BSc (Hons)

Supervisors: Angela Seddon, Trevor Benson, Emma Barney

Thesis submitted to the University of Nottingham for the degree of Doctor of Philosophy

January 2017

# Abstract

This Project is aimed at developing and fabricating mid-infrared (MIR) transmitting germanium-antimony-selenium (Ge-Sb-Se) chalcogenide glass fibres for passive transmission in MIR sensing and as new high-purity low-loss optical fibres for active MIR supercontinuum generation (SCG). The work reported in this Thesis can be divided into three main categories: (i) a study of four Ge-Sb-Se glass compositions (atomic %): ($Ge_{19}Sb_{15}Se_{66}$), ($Ge_{20}Sb_{10}Se_{70}$), ($Ge_{24}Sb_{4}Se_{72}$) and ($Ge_{22}Sb_{8}Se_{70}$), in terms of their thermal properties, optical properties and cytotoxicity to match potential glass pairs for small-core step-index MIR SCG fibres; (ii) to develop and optimise methods of achieving high-purity chalcogenide glasses and (iii) a preliminary study of the structure of Ge-Sb-Se glasses along the stoichiometric tie-line x($GeSe_2$)-(1-x)( $Sb_2Se_3$), to guide future selection of candidate glass pairs to draw to step-index fibre.

The MIR spectral region covers the wavelengths 3-50 μm and characteristic vibrational absorption spectra unique to each molecular type. Vibrational spectroscopy can detect subtle changes in the specific spectral response within this region. Molecular vibrations are indicative of changes within biological cells relative to normal biological cells, signifying the presence or absence of a disease. This Project contributes to the collaborative MINERVA Project which is developing a remote skin cancer detection system using MIR absorption spectroscopy aiming to carry out disease diagnosis *in vivo*. Providing broadband photons at MIR wavelengths has previously presented difficulties. Conventional MIR blackbody light sources are weak and optical fibres for transmitting MIR light to/from tissue *in vivo* can be limited by strong material absorption such as silica glass > 2.4 μm and tellurite, and heavy metal fluoride, > 4.75

μm. In contrast, chalcogenide glasses have been shown to transmit MIR light out to 25 μm and MIR SCG from ~ 2 – 15.1 μm has recently been demonstrated in chalcogenide glass fibre.

This Thesis reports on the characterisation of four Ge-Sb-Se glass compositions to match potential glass pairs for fabrication of step-index fibres based on particular thermal properties and desired fibre numerical aperture (NA). Three glass pairs are drawn to fibre: Pair I ($Ge_{22}Sb_8Se_{70}$) and ($Ge_{24}Sb_4Se_{72}$), Pair II ($Ge_{19}Sb_{15}Se_{66}$) and ($Ge_{20}Sb_{10}Se_{70}$), and Pair III ($Ge_{20}Sb_{10}Se_{70}$) and ($Ge_{24}Sb_4Se_{72}$). Difficulties emerged and are examined in the extrusion and fibre drawing processes arising from a mismatch in the glass pair's physical properties. Thus, a hierarchy of the order of selection of physical properties is suggested, with matching the glass transition temperature ($T_g$) deemed to be the top priority. The optical properties of the fabricated fibres are characterised in terms of predicted NA, near-field imaging and optical loss measurements. The minimum loss achieved (2.42 dB/m at 6.66 μm wavelength) is for Pair I (Core: $Ge_{22}Sb_8Se_{70}$ and cladding: $Ge_{24}Sb_4Se_{72}$). The effect of heat-treating to purify the precursor elements Sb and Se on subsequent fibre loss is observed and it is established that glass purity was a critical factor affecting the intensity of hydride and oxide impurity absorption bands punctuating the 2.5 – 10 μm wavelength transmission region. Therefore, distillation methods are explored as a means of generating high-purity chalcogenide glasses and a new distillation rig is developed.

Preliminary cytotoxicity tests on a fibre fabricated from Pair I are conducted to provide the foundations of a procedure for future chalcogenide glass fibre cytotoxicity testing. The initial data demonstrated the potential of etching the Ge-Sb-Se chalcogenide glass fibres in propylamine to reduce any cytotoxic response caused by the Ge-Sb-Se fibres.

Neutron diffraction experiments are combined with $T_g$ and density measurements along the stoichiometric tie-line x($GeSe_2$)-(1-x)( $Sb_2Se_3$), to aid in a greater understanding of the structure-property relationship of Ge-Sb-Se glasses for the future selection of candidate glass step-index fibre pairs. The preliminary work established that the stoichiometric glasses are predominantly made up of [$GeSe_4$] and [$SbSe_3$] units. From the neutron diffraction data, it is suggested that the average bond length of a Sb-Se bond was 2.62 ± 0.001 Å and the average bond length of a Ge-Se bond was 2.37 ± 0.001 Å. Extracting the coordination of the Ge and Sb elements is found to be difficult on account of an overlap of the Ge-Se and Sb-Se peaks. Therefore further analysis, using nuclear magnetic resonance (NMR) and X-ray diffraction (XRD) is suggested. It is shown that, as the vitreous structure changes from higher levels of [$SbSe_3$] units to incorporate more [$GeSe_4$] (thus a reduction of Sb), the $T_g$ of the glass increases and the density decreases. A close match in $T_g$ (< 23 °C) is recommended as critical for the successful fabrication of a Ge-Sb-Se chalcogenide glass fibre. Thus, knowledge of the trend in $T_g$, dependent on the ratio of [$SbSe_3$] units to [$GeSe_4$] units, is an initial step in selecting theoretical Ge-Sb-Se compositions with a closer match of thermal properties as candidate glass step-index fibre pairs. Having a more accurate guide to select theoretically Ge-Sb-Se glass compositions to match thermal properties is suggested to save time synthesising and characterising obsolete compositions.

It is concluded that Ge-Sb-Se chalcogenide glass fibres, developed through this Project, are strong candidates towards achieving MIR SCG small-core fibres, with the potential application for the transmission of MIR to and from potentially cancerous skin tissue samples. Therefore, enabling *in vivo* mapping for an immediate diagnostic response.

# List of publications

This list of publications is arising in whole or part of the work described in this thesis.

J. H. Butterworth, D. Jayasuriya, Q.Q. Li, D. Furniss, N.A. Moneim, E. Barney, S. Sujecki, T.M. Benson, J.S. Sanghera and A. B. Seddon. Towards Mid-infrared Supercontinuum Generation: Ge-Sb-Se Mid-Infrared Step-Index Small-Core Optical Fiber. Optical Fibers and Sensors for Medical Diagnostics and Treatment Applications XIV. Proc. of SPIE. San Francisco. USA. Vol. 8938. (2014).

J. H. Butterworth, D. Furniss, E. Barney, T.M. Benson and A. B. Seddon. Towards Mid-IR Supercontinuum Generation: Chalcogenide Glass Optical Fibres to be used for SCG for Mid-IR Medical Diagnostics. Optical Glasses. Proc. of International Symposium on Non Oxide and New Optical Glasses. Jeju-Si. South Korea. (2014).

J. H. Butterworth, D. Furniss, E. Barney, T.M. Benson and A. B. Seddon. Towards Mid-IR Supercontinuum Generation. International Conference on Optical, Optoelectronic and Photonic Materials. Leeds. UK. (2014).

H. Parnell, J. H. Butterworth, H. Sakr, Z. Tang, D. Furniss, T.M. Benson, C. Scotchford and A.B. Seddon. Ge-Sb-Se Glass Fiber-Optics for In-Vivo Mid-Infrared Optical Biopsy. Optical Biopsy XIV: Toward Real-Time Spectroscopic Imaging and Diagnosis. Proc. of SPIE. San Francisco. USA. Vol. 9703. (2016).

T. Arnold, D. Furniss, J. H. Butterworth and E. Barney. Optimsing Core-Clad Ratios in Glass Extrusions for Optical Fibre Applications. M.Eng. MM4MPR Indiviual Research Paper. in Mechanical, Materials and Manufacturing Engineering. The University of Nottingham: UK.(2014).

C.E. Podesta, J. H. Butterworth and A.B. Seddon. Biocompatibility of Sb-Se-Ge Containing Chalcogenide Glass Optical Fibres for Cancer Detection. M.Eng. MM4MPR Indiviual Research Paper. in Mechanical, Materials and Manufacturing Engineering. The University of Nottingham: UK.(2014).

D. Jayasuriya, J.H. Butterworth, D. Furniss and A. B. Seddon. Towards Ge-Sb-Se IR Step Index Monomode Optical Fibre for Mid-Infrared Supercontinuum Generation. MM4MPR Indiviual Research Paper. in Mechanical, Materials and Manufacturing Engineering. The University of Nottingham: UK.(2013).

# Acknowledgements

This PhD Project was carried out in the Mid-Infrared Photonics Group, George Green Institute for Electromagnetics Research, Faculty of Engineering in part support of the EU FP7 MINERVA project. Funding was provided jointly by a DTG EPSRC Scholarship from the University of Nottingham, UK and a Scholarship from the US ONRG (Office of Naval Research Global).

When Professor Angela B. Seddon first mentioned the prospect of doing a PhD at my undergraduate graduation ceremony, it was impossible to imagine how my PhD journey would evolve. Not only have I worked towards one of my proudest achievements, I have been very fortunate to have had many exciting opportunities along the way. I have learnt a variety of skills in and outside of the laboratory which will stay with me forever, such as presenting at three international conferences to poster presentation competitions to national entrepreneur competitions. To complete my PhD would not have been possible without the support and friendship of some amazing people.

Firstly, I will always be indebted to three inspirational professors who were continuously supportive with invaluable guidance. Their advice and direction helped me to achieve more than I ever thought possible, and consequently my confidence in my abilities grew immensely. Therefore, I would like to give my greatest thanks to my supervisors Professor Angela B. Seddon, Professor Trevor M. Benson and Doctor Emma Barney.

I was grateful to be a member of the MIR Photonics Research Group which I believe to have some of the best mentors at the University of Nottingham. Dr Zhuoqi Tang and Dr David Furniss never hesitated to help, and even worked late into the night if required! Their approach to research helped me to tailor and improve my own and their support has been vital to my success. I would like to thank them for every minute of their hard work and their explanations. I am very grateful to have profited from their vast experience and expertise in this field.

My family is my strength and is everything to me. I have been blessed with the most loving, caring and supportive family who are always there whenever I need them. To my Mum, Dad and siblings, Tom and Georgia, you are my closest friends as well as family. I am thankful for you every day! You have always believed in me, encouraged me to follow my dreams, visited me in Nottingham at the drop of a hat and sent me many ‘Happy Boxes’ filled with treats to kept me going.

Daniel, thank you for always knowing the perfect thing to say to make me smile and keeping me laughing. You spent months working alongside me and making ‘a work weekend’ not seem so bad. You did not complain once about my late nights at work. You mean the world to me and I am looking forward to our next chapter!

Finally, I would like to thank my clan/tribe/Nottingham family who have been amazing friends over the years: Sarah, Kate, Sophie, Helen, Harriet and Hesham. We have worked hard together but have had so much fun along the way, creating valuable memories!

# Glossary of symbols and abbreviations

| Abbreviation | Description | Abbreviation | Description |
|---|---|---|---|
| **Glass codes** | | | |
| JBXX | Glass composition code. JB is Jessica Butterworth followed by glass composition number | Pair X | Glass pair code. Pair followed by Roman Numeral indicating either Pair I, II or III |
| MXXXJHB | Glass melt code. M is for melt number given in chronological order with the MIR Photonics Research Group and this Author's initials. | EXXXJHB | Extrusion code.E is for extrusion, followed by the extrusion number given in chronological order with the MIR Photonics Research Group and this Author's initials. |
| FXXXJHB | Fibre code. F is for fibre, followed by the fibre number given in chronological order with the MIR Photonics Research Group and this Author's initials. | FXXXDJJHB | Fibre code. F is for fibre, followed by the fibre number given in chronological order with the MIR Photonics Research Group, DJ is Dinuka Jayasuriya and this Author's initials. |
| **Elemental precursors** | | | |
| As | Arsenic | Sb | Antimony |
| Ga | Gallium | Se | Selenium |
| Ge | Germanium | $SiO_2$ | Silica glass |
| S | Sulfur | Te | Tellurium |
| **General symbols and abbreviations** | | | |
| α | Absorption/ extinction coefficient | I | Light intensity |
| $\alpha_m$ | Acceptance angle | min | Minutes |
| $\alpha_L$ | Linear thermal expansion coefficient | ID | Inner diameter |
| $\theta_{crit}$ | Critical angle | l | Length |
| ø | Diameter | $m$ | Reduced mass |
| ε | Molar extinction coefficient | MIR | Mid- infrared |
| $n_2$ | Nonlinear refractive index | N | Nines purity (*e.g.* 5N = 99.999%) |
| $n$ or $n_0$ | Linear refractive index | NIR | Near-infrared |
| $\mu$ | Micron | NA | Numerical aperture |
| $A$ | Absorbance | OD | Outer diameter |
| c | Velocity of light in free space or concentration of absorbing species | $P_{in}$ | Initial optical power |
| CCR | Critical cooling rate | $P_{out}$ | Measured optical power after transmittance |
| DSC | Differential scanning calorimetry | ppm | Parts per million |
| DTA | Differential thermal analysis | % R | The percentage Fresnel reflection |
| EDX | Energy dispersive X-ray diffraction | s | Seconds |
| E | Energy of particles | SIF | Step index fibre |
| FIR | Far-infrared | SCG | Supercontinuum generation |
| h | Planck's constant or hour | T | Temperature or transmittance |

| Glossary of symbols and abbreviations (continued) | | | |
|---|---|---|---|
| **Abbreviation** | **Description** | **Abbreviation** | **Description** |
| $T_{bp}$ | Boiling temperature | $T_m$ | Melting temperature |
| $T_d$ | Dilatometric softening temperature | TEC | Thermal expansion coefficient |
| $T_c$ | Crystallisation temperature | TMA | Thermomechanical analysis |
| $T_f$ | Fictive temperature | ν | Vibrational frequency |
| $T_g$ | Glass transition temperature | wt. | Weight |
| $T_l$ | Liquidus temperature | XRD | X-ray diffraction |
| **Terminology and abbreviations for Chapter 7** | | | |
| AA/AM | Antibiotics-antimycotics | In vitro | In glass |
| Cytotoxicity | The degree to which it is toxic to cells | In vivo | In body/ organism |
| DMEM | Dulbecco's Modified Eagle's Medium | ISO | International Organisation for Standardisation |
| Ex vivo | Out of body/ organism | NEAA | Non-essential amino acids |
| FBS | Foetal bovine serum | PBS | Phosphate-buffered saline |
| HEPES | 4-(2-hydroxyethyl)-1-piperazineethanesulfonic acid | S.D. | Standard deviation |
| HMDS | Hexamethyldisilazane | | |
| **Terminology and abbreviations for Chapter 8** | | | |
| 2θ, ϕ | Direction of a scattered neutron | $j$ and $k$ | Elements in the sample |
| σ | Total scattering cross-section | $\delta_{jk}$ | Kronecker delta |
| $b$ | Neutron scattering length | MAS | Magic-angle spinning |
| $\bar{b}_j$ | Coherent neutron scattering length for element j | $M(Q)$ | Lorch modification function |
| $c_j$ | The atomic fraction for element j | $n^o$ | Average atomic number density |
| $c_j\bar{b}_j\bar{b}_k$ | Coefficient for the partial correlation coefficients | NMR | Nuclear magnetic resonance |
| $e^{-\mu t}$ | Attenuation | Q | Magnitude of the scattering vector for elastic scattering |
| $\frac{d\sigma}{d\Omega}$ | Differential cross-section | t | Sample thickness |
| $d\Omega$ | Solid angle | $T^0(r)$ | Average density contribution to the correlation function |
| $n$ | Coordination number | $T(r)$ | Total correlation function |
| FSDP | First sharp diffraction peak | r | The distance of the scattered neutron from the scattering atom or the distance between atoms in a glass |
| $I_0$ | Incident neutron flux | R | Number of neutrons |
| i(Q) | Distinct scattering | $R^2$ | Correlation coefficient |
| $I(Q)$ | Total scattering | Δr | Resolution in r space |
| $I^S(Q)$ | Self-scattering | μ | Linear attenuation coefficient |

# Table of contents

**Abstract ..... i**

**List of publications ..... iv**

**Acknowledgements ..... v**

**Glossary of symbols and abbreviations ..... vi**

**Table of contents ..... viii**

**1. Overview ..... 1**

1.1. Introduction ..... 1

1.2. Aims and objectives ..... 3

1.3. Layout of this Thesis ..... 4

**2. Background and literature review ..... 6**

2.1. Glass science fundamentals ..... 6

2.1.1. Structure and properties of chalcogenide glasses determining their application in mid-infrared (MIR) optics ..... 12

2.1.2. Ge-Sb-Se glass system ..... 18

2.2. Neutron diffraction scattering for structure-property relationships ..... 23

2.3. Introductory statements on electromagnetic wave interactions with atoms and molecules ..... 28

2.3.1. Infrared radiation and molecular absorption/ infrared spectroscopy and molecular structure ..... 30

2.4. Prospects for using vibrational spectroscopy for cancer detection ..... 34

2.4.1. MId- to NEaR infrared spectroscopy for improVed medical diAgnostics (MINERVA EU (European Union) Project 2012-2017) ..... 38

2.4.2. Clinical application and considerations ..... 41

2.5. Supercontinuum generation (SCG) fibres ..... 45

2.6. Chalcogenide glass optical fibres ..... 49

2.6.1. Fabricating chalcogenide glass optical fibres for MIR ..... 52

2.6.2. Fabricating high purity chalcogenide glass ..... 55

2.7. Summary ..... 63

**3. Glass preparation and characterisation methods ..... 65**

3.1. Preparation of silica glass ampoules used for chalcogenide glass melting ..... 66

3.1.1. Silica glass ampoule selection ..... 67

3.1.2. Silica glass ampoule preparation: air and vacuum baking ..... 69

3.2. Ge-Sb-Se chalcogenide glass rod synthesis ..... 70

3.2.1. Purification of precursor elements ..... 71
3.2.2. Batching ..... 78
3.2.3. Silica glass ampoule sealing ..... 80
3.2.4. Melting, quenching and annealing ..... 81
3.3. Silica glass ampoule opening, Ge-Sb-Se chalcogenide glass cutting, polishing and grinding ..... 89
3.3.1. Silica glass ampoule opening and chalcogenide glass cutting ..... 89
3.3.2. Chalcogenide glass grinding and polishing ..... 90
3.4. Extrusion ..... 91
3.4.1. Co-extrusion to fabricate a structured core-cladding preform ..... 95
3.4.2. Tube extrusion to fabricate an outer cladding tube ..... 98
3.5. Fibre and cane drawing ..... 100
3.5.1. Drawing core/ cladding cane from a co-extruded core/ cladding preform 100
3.5.2. Rod-in-tube fibre drawing ..... 101
3.6. Ge-Se-Sb chalcogenide glass characterisation ..... 103
3.6.1. X-ray diffraction (XRD) ..... 104
3.6.2. Density ..... 105
3.6.3. Differential scanning calorimetry (DSC) ..... 106
3.6.4. Differential thermal analysis (DTA) ..... 109
3.6.5. Thermomechanical analysis (TMA) ..... 111
3.6.6. Fourier transform infrared spectroscopy (FTIR) ..... 117
3.7. Scanning electron microscopy (SEM) and energy dispersive X-ray (EDX) .. 122
3.7.1. Introduction to scanning electron microscopy (SEM) and energy dispersive X-ray spectroscopy (EDX) ..... 122
3.7.2. SEM Sample preparation ..... 123
3.7.3. Equipment and methodology ..... 124
3.8. Summary ..... 125

**4. Characterisation of the physical and optical properties of Ge-Sb-Se chalcogenide glasses to match potential glass pairs for a high purity small core-cladding MIR SCG fibre ..... 126**

4.1. Determining the success of (JB01) $Ge_{19}Sb_{15}Se_{66}$, (JB02) $Ge_{20}Sb_{10}Se_{70}$ , (JB03) $Ge_{24}Sb_{4}Se_{72}$ and (JB04) $Ge_{22}Sb_{8}Se_{70}$ glass melting ..... 127
4.1.1. Investigation of material amorphicity using X-ray diffraction (XRD) .... 131
4.1.2. Assessment of nominal batched Ge-Sb-Se glass composition using SEM energy-dispersive X-ray microanalysis (EDX) ..... 134
4.1.3. Determining the mid-IR transmission of (JB01) $Ge_{19}Sb_{15}Se_{66}$, (JB02) $Ge_{20}Sb_{10}Se_{70}$ , (JB03) $Ge_{24}Sb_{4}Se_{72}$ and (JB04) $Ge_{22}Sb_{8}Se_{70}$ bulk chalcogenide glasses using Fourier transform infrared spectroscopy (FTIR) ..... 136

4.2. Determining the thermal properties of (JB01) $Ge_{19}Sb_{15}Se_{66}$, (JB02) $Ge_{20}Sb_{10}Se_{70}$ , (JB03) $Ge_{24}Sb_{4}Se_{72}$ and (JB04) $Ge_{22}Sb_{8}Se_{70}$ chalcogenide glasses to develop the optimum glass pair for fabrication of a MIR core-cladding optical fibre 139

4.2.1. Onset $T_g$ of (JB01) $Ge_{19}Sb_{15}Se_{66}$, (JB02) $Ge_{20}Sb_{10}Se_{70}$ , (JB03) $Ge_{24}Sb_{4}Se_{72}$ and (JB04) $Ge_{22}Sb_{8}Se_{70}$chalcogenide glasses..... 140

4.2.2. Differential thermal analysis (DTA) ..... 143

4.2.3. Thermal mechanical analysis (TMA)..... 147

4.3. Development of selecting Ge-Sb-Se chalcogenide glass pairs from extrusion and fibre drawing experience ..... 160

4.4. Discussion..... 167

4.5. Summary..... 171

**5. Fabrication of Ge-Sb-Se chalcogenide glass fibres ..... 172**

5.1. Understanding velocity during extrusion and optimising core/ cladding ratios in co-extrusions for optical fibre applications ..... 173

5.2. Optimising the bore diameter in Ge-Sb-Se chalcogenide glass tube extrusions 178

5.3. Optical fibre dimensions..... 180

5.3.1. Fabricating small core fibres ..... 181

5.3.2. Specification of Ge-Sb-Se fibre small core sizes ..... 182

5.4. Investigation of Pair I (core composition JB04; $Ge_{22}Sb_{8}Se_{70}$ at. % and cladding composition JB03; $Ge_{24}Sb_{4}Se_{72}$) SCG fibre ..... 182

5.4.1. Trial 1: E014JHB (tube extrusion of outer cladding composition JB03) and E015JHB (co-extrusion of core composition JB04 and cladding composition JB03) 183

5.4.2. Trial 1: F018JHB (cane and intermediate fibre produced from co-extrusion E014JHB), F019JHB (small core fibres produced from F018JHB cane and tube extrusion E014JHB)..... 185

5.4.3. Trial 1: Analysis of fibre F018JHB and F019JHB geometry via scanning electron microscopy (SEM) ..... 186

5.4.4. Trial 2: E017JHB and E019JHB (tube extrusion of outer cladding composition JB03, with redesign of pin and die) and E018JHB (co-extrusion of core composition JB04 and cladding composition JB03)..... 189

5.4.5. Trial 2: F021JHB (cane and intermediate fibre produced from co-extrusion E019JHB) for F023JHB (small core fibres produced from F021JHB cane and tube extrusion E018JHB)..... 192

5.4.6. Trial 2: Analysis of fibre F023JHB geometry via SEM..... 193

5.5. Investigation of Pair II (core composition JB01; $Ge_{19}Sb_{15}Se_{66}$ and cladding composition JB02; $Ge_{20}Sb_{10}Se_{70}$ ) SCG fibre ..... 195

5.5.1. E025JHB, E026JHB, E029JHB (tube extrusions of outer cladding composition JB02) and E030JHB (co-extrusion of core composition JB01 and cladding composition JB02) ..... 195

5.5.2. F029JHB (cane produced from co-extrusion E030JHB), F031JHB (cane produced directly from melt M098JHB) for F032JHB (small core fibres produced from F031JHB cane and E028JHB tube extrusion) ..... 199

5.5.3. Analysis of fibre F031JHB and F032JHB geometry via SEM analysis .. 201

5.6. Investigation of Pair III (core composition JB02; $Ge_{20}Sb_{10}Se_{70}$ and cladding composition JB03; $Ge_{24}Sb_4Se_{72}$ ) SCG fibre. ..... 205

5.6.1. E039JHB (tube extrusion of outer cladding composition JB03), E040JHB (co-extrusion of core composition JB02 and cladding composition JB03) and E042JHB (single unstructured extrusion of core composition JB02) ..... 206

5.6.2. F034JHB (produced cane and intermediate fibre from single extrusion E042JHB) and F035JHB (small core fibres from F034JHB cane and tube extrusion E039JHB) ..... 209

5.6.3. Analysis of fibre F034JHB and F035JHB geometry via SEM analysis .. 212

5.7. Investigation of Ge-Sb-Se fibre amorphicity using X-ray diffraction (XRD) 215

5.8. Conclusions ..... 216

5.9. Summary ..... 223

**6. Light guiding and fibre loss measurements of Ge-Sb-Se chalcogenide glass fibres and a new purification method to fabricate high purity SCG MIR glass fibres ..... 224**

6.1. Overview ..... 224

6.2. Near-field Ge-Sb-Se fibre performance ..... 224

6.2.1. Sample preparation, equipment and methodology ..... 226

6.2.2. Near-field imaging at 1463 nm: results ..... 226

6.3. Fibre optical loss ..... 228

6.3.1. Introduction to fibre optical loss ..... 228

6.3.2. Fibre optical loss: methodology ..... 230

6.3.3. Fibre optical loss: results ..... 233

6.4. Distillation ..... 237

6.4.1. Trial of Se distillation with in-house built rig (code D011JHBZQT) ..... 238

6.4.2. Developing the distillation rig design ..... 245

6.4.3. Trial of distillation rig with distillation of $GaI_3$ (code D018MINJHBZQT) 247

6.5. Conclusions ..... 256

6.6. Summary ..... 259

**7. Preliminary cytotoxic evaluation of fibre F018JHB ..... 260**

7.1. Overview ..... 260

7.2. Cell preparation ..... 261
7.2.1. Preparation of the culture medium ..... 262
7.2.2. Defrosting frozen cell lines ..... 262
7.2.3. Cell preparation and obtaining the required cell concentration ..... 264
7.2.4. Cell counting ..... 265
7.3. Sample preparation and Alamar Blue assay methodology ..... 266
7.3.1. Step-index fibre F018JHB (core JB04; $Ge_{22}Sb_8Se_{70}$ and cladding JB03; $Ge_{24}Sb_4Se_{72}$) preparation ..... 267
7.3.2. Material control preparation, sample sterilisation and sample preparation in the tissue culture plastic (TCP) well plate ..... 269
7.3.3. Cell seeding into tissue culture plastic (TCP) wells and incubation ..... 270
7.3.4. Alamar Blue assay ..... 271
7.3.5. Scanning electron microscopy (SEM) preparation of the cytotoxicity test sample materials after Alamar Blue testing ..... 273
7.4. Analysis of cell metabolic activity after exposure to fibre F018JHB (core JB04; $Ge_{22}Sb_8Se_{70}$ and cladding JB03; $Ge_{24}Sb_4Se_{72}$) after either being etched in propylamine or non-etched and controls (bioactive glass fibre and polycarbonate membrane) using Alamar Blue assays ..... 275
7.4.1. Trial 1 ..... 277
7.4.2. Trial 2 ..... 278
7.4.3. Discussion ..... 279
7.5. Cell coverage analysis of fibre F018JHB (core JB04; $Ge_{22}Sb_8Se_{70}$ and cladding JB03; $Ge_{24}Sb_4Se_{72}$) and controls (bioactive glass fibre and polycarbonate membrane) using Scanning Electron Microscopy (SEM) ..... 282
7.5.1. Trial 1 ..... 283
7.5.2. Trial 2 ..... 284
7.5.3. Discussion ..... 288
7.6. Conclusions ..... 295
7.6.1. Final remarks ..... 297
7.7. Summary ..... 297
**8. Structure-property relationship of Ge-Sb-Se glasses along the stoichiometric tie-line x($GeSe_2$)-(1-x)($Sb_2Se_3$) ..... 299**
8.1 Overview ..... 299
8.2 Preparation and methodology ..... 300
8.2.1 Ge-Sb-Se glass melting and characterisation ..... 300
8.2.2 Ge-Sb-Se glass rod preparation for neutron diffraction experiments ..... 301
8.2.3 Neutron scattering diffraction: analysis of data to extract T($r$) ..... 303
8.3 Results ..... 308

8.3.1 Onset glass transition temperature ($T_g$) and density results ..... 308
8.3.2 Neutron scattering diffraction results ..... 310
8.4 Discussion ..... 318
8.4.1 Onset glass transition temperature ($T_g$) and density ..... 318
8.4.2 Neutron diffraction data ..... 321
8.5 Conclusions ..... 328
8.6 Summary ..... 330
**9. Conclusions and suggestions for future work ..... 331**
9.1. Conclusions ..... 331
9.1.1. A study of physical, optical and cytotoxic properties of Ge-Sb-Se glass compositions (atomic %): $Ge_{19}Sb_{15}Se_{66}$, $Ge_{20}Sb_{10}Se_{70}$ , $Ge_{24}Sb_{4}Se_{72}$ and $Ge_{22}Sb_{8}Se_{70}$ to match potential glass pairs for small-core step-index MIR SCG fibres. 331
9.1.2. The development of methods to achieve high-purity chalcogenide glasses. 337
9.1.3. A preliminary study of the structure-property relationship of Ge-Sb-Se glasses along the stoichiometric tie-line x($GeSe_2$)-(1-x)( $Sb_2Se_3$) to guide future selection of candidate glass pairs to draw to fibre. ..... 339
9.2. Suggestions for future work ..... 342
9.2.1. Further investigation of physical, optical and cytotoxic properties and cytotoxicity of Ge-Sb-Se glass compositions to match potential glass pairs for small core-cladding MIR SCG fibres. ..... 343
9.2.2. The development of methods to achieve high-purity chalcogenide glasses. 346
9.2.3. Future analysis proposed to help better understanding of the role of Se within the Ge-Sb-Se glasses for greater investigation into the structure-property relationship 347
**References ..... 346**
**Appendix I ..... xiv**
**Appendix II ..... xvi**
**Appendix III ..... xvii**

# 1. Overview

## 1.1. Introduction

The mid-infrared (MIR), spanning the wavelength range 3 – 50 μm [1], is a promising spectral region for direct, remote molecular sensing which has the potential to be exploited for bio-chemical sensing and bio-medical sensing. The vibrational energy levels of organic molecules and their functional groups are spaced corresponding to the energy of MIR radiation. The absorption of MIR radiation sets the molecular bonds into resonant oscillation at the same frequency and is determined by the molecular symmetry of the molecule as this influences which bonds will undergo the net dipole change. For instance the 6 – 15 μm MIR region, known as the "fingerprint region", is particularly useful in the indentification of organic functional groups [2-5]. In addition, the relative position and type of neighbouring intramolecular bonds also influence the vibrational frequency of a molecular bond. In turn, these are completely dependent on the molecular structure and hence provide the potential means for unique molecular identification.

A MIR glass is an amorphous material that can transmit radiation within the 3-50 μm wavelength MIR spectral region [1]. A set of requirements for suitable MIR glasses for passive transmission of MIR light encompasses: a wide transparent spectral range spanning as much of the MIR 3-50 μm wavelength region as possible, stability towards crystallisation and effects of moisture, mechanical degradation and non-toxicity. However, there is no glass yet known, which has a complete set of these desired characteristics.

The pursuit of suitable glass fibre candidates for MIR supercontinuum generation (SCG), has been intensified in recent years. The use of silica glass fibres is limited by strong material absorption above 2.4 μm [6]. Fluoride [7] or tellurite [8, 9] SCG fibres can cover part of the MIR spectral region from 1~ 5 μm and chalcogenide glasses [2, 10-16] have demonstrated MIR SCG from ~ 2 – 15.1 μm.

The chalcogenides glasses based on sulfur (S), selenium (Se) and tellurium (Te) are combined with elements from other Groups in the Periodic Table (*e.g.* arsenic (As), antimony (Sb) or germanium (Ge)) to aid glass stability against devitrification [17, 18]. Glass compositions can be adjusted to control the MIR transmission window, which is bound by the optical band gap at short wavelength and the multiphonon absorption edge at long wavelength. Currently the most established chalcogenide ternary glass systems are based on As-containing glasses [19]. However, As is a well-known toxic element and has been classified in Group 1 as carcinogenic to humans by the International Agency for Research on Cancer (IARC 1987) [20]. Thus there is need to develop a chalcogenide glass system which does not contain As. Here, the suitability of Sb-containing glasses has been investigated.

Numerous fabrication methods have been developed to realise high-purity low-loss chalcogenide glass optical fibres (*e.g.* single or double crucible method, or from a pre-fabricated single-rod, rod-in-tube or more complex rod (preform)) [21-27]. Step-index fibres (SIF) successfully guide light at the interface between two different refractive indices glasses (*e.g.* a high index core surrounded by a low index cladding). However, the fabrication of low-loss chalcogenide glass fibres has remained challenging, mainly due to the following three reasons: (i) the natural tendency of absorption of impurities in raw materials (such as oxides, hydrides, hydroxide and water impurities [22]); (ii) extrinsic scattering caused by discrete submicron inclusions (often inadvertently

brought in during the fibre fabrication process) of different refractive index to the glass matrix and (iii) high vapour pressures of constituent elements at the melting temperatures. Furthermore, to achieve the difference in refractive indices of the glasses requires the core and cladding glass to have different compositions. Thus the fabrication of a robust MIR SCG chalcogenide glass fibre requires an in-depth understanding of the fabrication process and the chalcogenide glass's thermal properties to allow fibre drawing.

### 1.2. Aims and objectives

The aim and objectives (steps taken to achieve the aim) of this Project are listed in Table 1.1.

**Table 1.1: Aims and objectives of this Project.**

| **Aim** |
|---|
| • To fabricate and develop new chalcogenide glass-based optical fibres without containing As for; (1) passive transmission in MIR sensing and (2) as new high-purity low-loss optical fibres for active MIR SCG. |
| **Objectives** |
| • To study four Ge-Sb-Se glass compositions (atomic %): ($Ge_{19}Sb_{15}Se_{66}$); ($Ge_{20}Sb_{10}Se_{70}$); ($Ge_{24}Sb_{4}Se_{72}$) and ($Ge_{22}Sb_{8}Se_{70}$), to achieve the following:<br>  ○ To obtain a greater understanding of the optical and physical properties of candidate Ge-Sb-Se glasses, in order to match potential glass pairs to fabricate small-core step-index MIR SCG fibres.<br>  ○ To fabricate and characterise Ge-Sb-Se glass small-core step-index MIR SCG fibres.<br>  ○ To develop a procedure and provide the foundations for preliminary cytotoxicity evaluation of the Ge-Sb-Se glass fibres.<br>• To investigate and optimise methods of achieving high-purity chalcogenide glasses.<br>• To introduce the structure-property relationship of Ge-Sb-Se glasses along the stoichiometric tie-line x($GeSe_2$)-(1-x)( $Sb_2Se_3$) to guide future selection of candidate glass pairs to draw to step-index fibre. |

### 1.3. Layout of this Thesis

This Thesis is comprised of nine chapters. A brief introduction to the Project has been given in Chapter 1 and the aim and objectives of the Project were highlighted. Chapter 2 will provide the background information required to understand the process of fabricating glasses that can transmit MIR light and potential applications, including: the properties and structure of glasses (focused mainly on Ge-Sb-Se chalcogenide glasses), fabrication techniques, the importance of limiting extrinsic impurities and methods to reduced them, the basics of vibrational spectroscopy and how it has the potential to be exploited for cancer detection, and the medical diagnostic system proposed by Seddon [3, 28]. Chapter 3 will detail the experimental methodology followed in preparing and characterising the Ge-Sb-Se glasses and fibres fabricated in this Project. It should be noted that for the extrusion and fibre drawing processes, only the generic procedure for each process will be presented and pertinent extrusion and fibre drawing parameters for each fabricated fibre will be given in Chapter 5. The characterisation and results deployed in this Project will be reported in Chapters 4-8, as outlined in Figure 1.1. Chapter 4 will provide a study of the physical and optical properties of four different Ge-Sb-Se glass compositions: ($Ge_{19}Sb_{15}Se_{66}$), ($Ge_{20}Sb_{10}Se_{70}$), ($Ge_{24}Sb_{4}Se_{72}$) and ($Ge_{22}Sb_{8}Se_{70}$). Pairs of these four compositions were matched based on particular thermal properties and were fabricated into MIR fibres. The extrusion and fibre drawing process of these fabricated MIR fibres, the issues faced whilst fabricating the fibre preforms and the development of the extrusion technique as a result of this Project, will be reported in Chapter 5. In Chapter 6 the characterisation of the optical properties of the fabricated MIR fibres via near-field imaging and fibre loss measurements will be discussed. A new purification technique will also be described in Chapter 6 and results will be given.

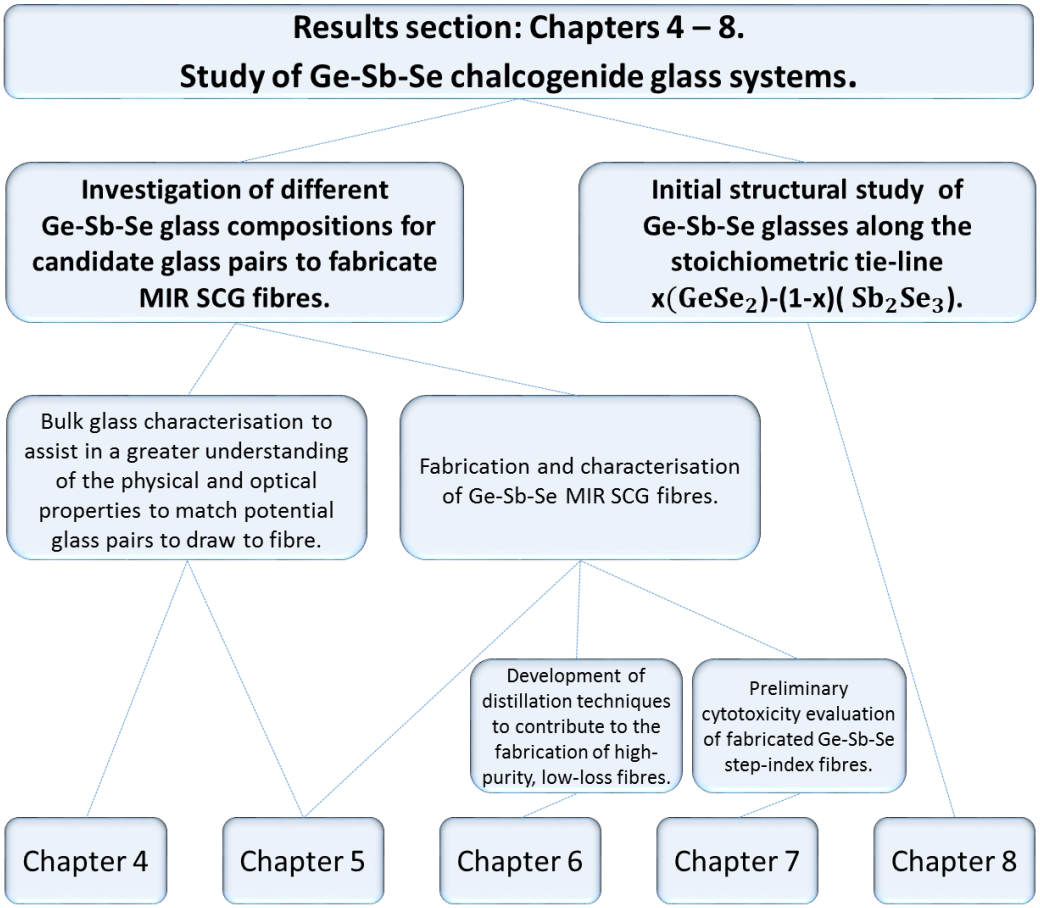



**Figure 1.1 Outline of the results section of this Thesis: Chapters 4-8.**

The preliminary cytotoxicity results of a fabricated step-index Ge-Sb-Se chalcogenide glass fibre will be presented in Chapter 7. In Chapter 8 results from a study of the structure-property relationship of Ge-Sb-Se glasses along the stoichiometric tie-line $x(GeSe_2)$-$(1-x)(Sb_2Se_3)$ using a combination of glass transition temperature ($T_g$), density and neutron diffraction measurements will be reported and discussed. The conclusions reached throughout this Project and suggestions for further work to be conducted will be given in Chapter 9.

# 2. Background and literature review

Currently there is great research interest in glasses that can transmit mid-infrared (MIR) light. This chapter provides the background information required to understand the process of fabricating such glass. The chapter is split into six sections: starting with a description of the general properties of inorganic compound glasses, section 2.1; then discussing how the structure of glasses can be analysed using neutron diffraction, section 2.2. One of the aims of this Project was to produce low optical loss chalcogenide glass optical fibres for MIR sensing. A simple introduction to electromagnetic wave interactions with atoms and molecules and how MIR radiation is absorbed is given in section 2.3. Vibrational spectroscopy for cancer detection is explained in section 2.4 and the potential of chalcogenide glass optical fibres for a medical diagnostics system is presented. The fibres fabricated in this Project were intended for supercontinuum generation (SCG) and a brief summary of the current status of SCG is provided in section 2.5. Optical fibre properties, glass fibre fabrication methods and fabricating high purity glasses are discussed in section 2.6. This chapter is summarised in section 2.7.

## 2.1. Glass science fundamentals

Glass has been used by humans since our earliest origins. A naturally occuring glass, obsidian, was used as tips for spears and archaeologists have found man-made glass, in the form of a glazes for pottery coatings dating back to 4000 BC [29]. With advancing technology and greater understanding of the glass forming process (see Figure 2.1) a wide range of glasses has been developed with properties suited to a wide variety of applications.

It is important to understand what is meant by the term ‘glass’ in terms of both molecular structure and chemical composition. Under first inspection glasses have some characteristics of a normal solid, for example fracture stress and hardness [30-32]. However, further examination shows a molecular structure comparable to that of a liquid at low temperature.

In 1976, the U.S. National Research Council defined glass as:

'An X-ray amorphous material which exhibits the glass transition, this being defined as that phenomenon in which a solid amorphous phase exhibits with changing temperature a more or less sudden change in the derivative thermodynamic properties, such as heat capacity and expansion coefficient, from crystal-like to liquid-like values' [33, 34].

Thus the glass-like, or vitreous state, is a state of matter rather than a particular substance and can be described as that of a solid with only short-range order, similar to that of a liquid, frozen in its structure. There are many different types of glass forming substances, which can be classified into main groups of: oxide systems; halide systems; chalcogenide systems; ionic salts; aqueous solutions; metallic systems and organic polymers [30-34]. These glasses have different properties arising from their different molecular structures and can be tailored for specific applications. Glasses are considered as isotropic materials, they have the same properties in all directions.

Theoretically, most inorganic materials can form a glass if the rate of cooling is fast enough. However, this is limited by the quantity of the material being quenched and how energetically favourable it is. A good glass former is one which can form glass with a moderate cooling rate, for instance < 0.5 °C $min^{-1}$. One of the first advances in understanding glass structure was made by Zachariasen in his publication: 'The atomic arrangement in glass' [35] in 1932. His treatise was specifically on silica, silicate and

metal oxide types of glass. He proposed the random network theory where: 'the atomic or molecular arrangement in the glasslike state is an extended network which lacks symmetry and periodicity'. He introduced the idea that the requirements of a good glass former are; small cations, low co-ordination number (co-ordination number of 3 or 4) and corner sharing of units. He also suggested that an open structure is necessary to accommodate disorder without significantly increasing lattice energy. Thus glass will form if the disordered state has lower lattice energy than its corresponding crystal state. The resulting random network structure has long chains which are cross-linked at intervals and where large cations with a low charge can exist in holes within the network. Therefore the physical properties of a glass depend on the ratio of the number of anions to cations in the network as they determine the length of the chains. This is discussed further in section 2.1.1 in regards to a chalcogenide glass.

Nonetheless, there are a few faults with Zachariasen's model where some glass forming systems are exceptions to his rules. It has been found that some basic oxides can be incorporated into the network with only local disturbance. In other glass systems, basic cations are distributed uniformly throughout the structure. Atoms will satisfy their own local structural requirements which is reflected in the way glass properties differ with composition.

It is helpful to consider the state of glass in relation to the crystalline state. In addition, the glass transition can be explained with help from the volume/ temperature diagram and an understanding of the term fictive temperature, see Figure 2.1.

The most informative characteristics of the glass-crystal transition are the nucleation rate of the crystalline phase, the rate of crystal growth and the temperature dependence of these parameters.

Most solids are crystalline with a repeated molecular structure. However, glass is an amorphous solid and does not have a repeated molecular structure.

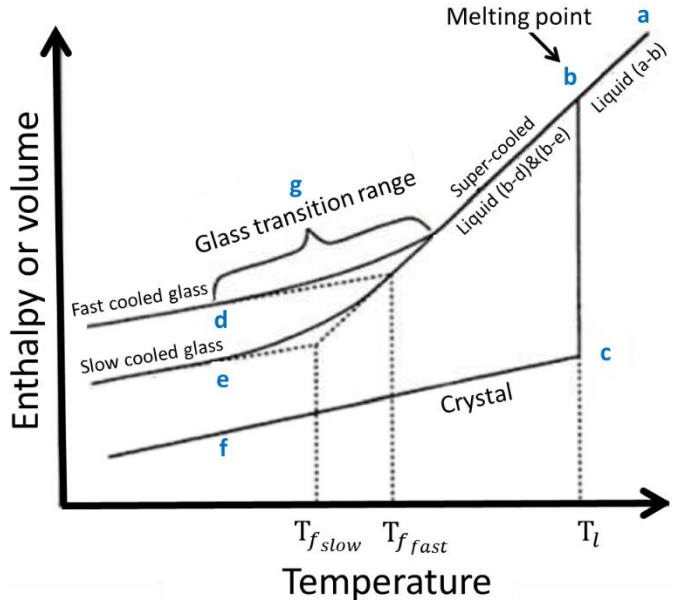



**Figure 2.1 Schematic diagram of the relationship between glassy, liquid and crystalline solid states. The fictive temperature ($T_f$) is defined in the figure for fast and slow cooling rates. The glass transition range ($T_g$) and the liquidus temperature ($T_l$) are also shown [36]. Glasses with a low tendency to crystallise are promising for fibre optics.**

When a glass melt is cooled from above to its liquidus $T_l$ there is a gradual decrease in enthalpy, Figure 2.1 line (a-b), which causes a reduction in the amplitude of atomic vibrations and the density of the melt tends to increase. Many materials when molten above $T_l$ (true liquid above liquidus) have a viscosity close to that of water, $10^{-2}$ Pa.s. With continued cooling from the liquidus $T_l$ one of two routes can be taken. If the liquid is quenched quickly through the liquidus to the glass transition range, ((b-d) or (b-e)), the molecular motions of the melt are considerably reduced.

A supercooled liquid ((b-d) or (b-e)) experiences a decrease in volume per unit mass and increase in viscosity with decreasing temperature to the glass transition range temperature $T_g$, *i.e.* glassy state. Over the $T_g$ range, the supercooled liquid becomes a solid glass where the shear viscosity equals $\sim 10^{12.5}$ Pa.s [37] impeding the movement of atoms and a further decrease in volume due to the decrease in atomic vibration. The

viscosity becomes so great, due to the decrease in system enthalpy with decrease in temperature, that no further changes are possible. $T_g$ can also be defined as the position where the liquid and vitreous enthalpy/ temperature or volume/ temperature lines intersect. $T_{f_{slow}}$ and $T_{f_{fast}}$ [37] represent different quenching rates of a glass. A faster quenching rate, $T_{f_{fast}}$ (b-d), results in a shorter amount of time available for configurational changes. The lower $T_g$ values for a lower quenching rate occur due to the lower temperature to which the supercooled liquid falls from the supercooled liquid-state metastable equilibrium. However, the dependency of $T_g$ on the cooling rate is relatively weak in practise, thus tends to change 3-5 °C for every order of magnitude change in the cooling rate [37].

Non-uniform cooling temperatures during glass formation can generate permanent stresses in the glass. Annealing is an important process to reduce the stresses, where the glass is held at $T_g$ (less than $10^{12.5}$ Pa.s viscosity) for a short time. This is to ensure the temperature is uniform throughout the glass and therefore slowly cooled through the $T_g$ range to ensure all parts of the glass cool at the same rate. The annealing process conducted for the germanium-antinomy-selenium (Ge-Sb-Se) chalcogenide glasses synthesised in this Project will be described in section 3.2.4. Annealing allows the stresses within the glass to relax and obviates retention of permanent stress when cooled to room temperature.

The second route of cooling from above the liquidus Figure 2.1 line (b-c), allows the growth of nuclei and crystals within the melt. Nucleation is the first step in forming a solid from the liquid state. Crystallisation occurs along (b-c) and then the crystalline solid cools to ambient temperature along (c-f), undergoing thermal contraction equal and opposite to the thermal expansion on reheating the crystalline solid from ambient

temperature. Crystallisation generates a dramatic decrease in volume as the solid forms a stable crystal caused by an ordered, compact rearrangement of atoms. The relaxation processes are almost instantaneous and the crystallisation state is the lowest enthalpy state (*e.g.* equilibrium state).

The tendency of glasses to crystallise is determined by a number of factors, including the difference between the temperatures of crystallisation ( $T_c$) and glass transition ( $T_g$), which can be measured under dynamic heating by means of thermal analysis. The critical cooling rate (CCR) of a glass-forming melt is a good indication of the likelihood of crystallisation on melt-cooling. The greater the CCR, the higher the probability of crystallisation at melt solidification (*e.g.* the CCR is higher than the cooling rate). In this Project differential thermal analysis (DTA) was used to study the thermal behaviour (*e.g.* $T_c$ and $T_g$) on reheating the glass and the phase changes of the Ge-Sb-Se glasses ( $T_l$), will be discussed in section 4.2.2.

The fictive temperature may be taken as the temperature at which the property of interest (*e.g.* specific volume or enthalpy) when extrapolated along the glass expansion plot intersects the equilibrium liquid expansion (for Figure 2.1 plotted as volume vs temperature). The fictive temperature provides at best a numerical measure of the structure of the glass as it was frozen in from the supercooled liquid and to what extent the structure has shifted from metastable equilibrium. A good glass former will tend to have a greater viscosity at the liquidus causing the atoms within the liquid to have restricted motion. The rate of crystal growth is dependent on kinetic factors (*e.g.* the thermal energy available to make structural rearrangements and for atoms to diffuse). Therefore a high viscosity indicates a resistance to diffusion and, moreover, a resistance to crystallisation.

It is worth noting that, crystallisation dramatically raises the optical loss due to scattering of a glass or fibre and this is discussed further in section 2.6.2. Throughout the glass synthesis and glass fibre fabrication processes conducted in this Project, regular investigation into whether crystals had formed were made. This was achieved by means of X-ray diffraction (XRD; section 3.6.1) and scanning electron microscopy (SEM; section 3.7).

### 2.1.1. Structure and properties of chalcogenide glasses determining their application in mid-infrared (MIR) optics

A mid-infrared (MIR) glass is an amorphous material that can transmit radiation in the 3-50 µm wavelength MIR spectral region [1]. A set of requirements for suitable MIR glasses encompasses: a wide transparent spectral range spanning as much of the MIR 3-50 µm wavelength region as possible; stability towards crystallisation and effects of moisture, mechanical degradation and non-toxicity. However, there is no glass yet known, which has a complete set of these desired characteristics. The use of silica glass fibres is limited by strong material absorption above 2.9 µm [6]. For this reason, the pursuit of suitable glasses to transmit out to further wavelengths, has been intensified in recent years. Several non-silica glasses have been proposed as candidates for MIR supercontinuum generation (SCG) fibres, see section 2.5. SCG fibres can cover part of the MIR spectral region from 1~ 5 µm when based on fluoride [7] or tellurite [8, 9] fibres and at least 1.4 – 13.3 µm when based on chalcogenide glasses [2]. Note that in section 2.5 the development to date of MIR SCG is briefly discussed.

Chalcogenide glasses have been studied seriously since the 1950s, for application in the electronics industry, imaging and more recently photonics [17, 18]. The chalcogenides form Group 16 of the Periodic Table and consist of the elements oxygen (O), sulfur (S), selenium (Se), tellurium (Te) and radioactive polonium (Po). However,

[O] is considered an impurity in chalcogenide glasses and manifests to spoil MIR transparency, *e.g.* as oxide vibrational absorption mostly present in the 7-14 µm spectral range [22], see section 2.6.2. Po is highly toxic and unstable [38]. Chalcogenide glasses are inorganic glassy materials which are based on one or more of these glass-forming chalcogen elements.

Chalcogenide glasses generally adapt a structure predominantly based on covalent bonded chains of 2-coordinated chalcogen group atoms, *e.g.* [-Se-], with well-defined spatial bonds and a maximum ionic conductivity reaching 9 % [18]. Cross-linking is contributed by 3- and 4-coordinated Group 14 (*e.g.* As and Sb) and Group 15 (*e.g.* Ge) atoms, respectively, with weak Van der Waals forces between atoms [39, 40]. Group 14 and 15 atoms are usually selected for addition as they contribute thermal stability. The electronegativity of cations and anions of chalcogenide glass component elements are comparable (*e.g.* electronegativity value of Se= 2.55, Sb = 2.05, As = 2.18 and Ge= 2.01 [41]) as the elements are close to each other in the Periodic Table, where they are all members of the "p block". Therefore the chemical bonding is relatively weak. Unlike silicate and other oxide glasses, where the oxygen is restricted to bonding only with cations, the constituents of chalcogenide glasses can form homopolar bonds. The chalcogen element acting as an anion or the cations, Ge and Sb, can form homopolar bonds (*e.g.* Se-Se, Ge-Ge or Sb-Sb). Heteropolar bonds are also formed (*e.g.* Ge –Se or Sb-Se). However, abiding to the chemically ordered covalent network model (COCN), chalcogenide systems will favour the formation of heteropolar anion-cation bonds over homopolar anion-anion or cation-cation bonds where possible [42]. There are many compositions which have a satisfactory combination of mechanical properties and MIR transmission, for MIR optical fibres [43-47]. However, chalcogenide glass stability, purity and toxicity remain issues that need further investigation.

To understand chalcogenide glasses forming ability, firstly consider the pure chalcogens. At low temperatures, <160 °C, sulfur (S) melts to form 8-membered rings with non-polar covalent bonding between adjacent S atoms.

When the temperature is increased, the rings re-organise to form long chains, with chain lengths exceeding 106 atoms [48]. Selenium (Se) melts consist of shorter chains. Tellurium (Te) melts form even shorter chains, resulting in greater difficulty to form as a glass on melt-cooling [49]. (For example, amorphous Te has been made by splat-cooling [49] or melt-spinning [50] methods to achieve high cooling rates of the order of $10^3 - 10^6$ $Ks^{-1}$).

The effect of the weaker bonding in chalcogenide glasses can be seen in the mechanical properties of the glass, such as Vickers hardness. Chalcogenide glasses, with Vickers hardness ranging from 0.3 GPa-2.0 GPa, are much softer than oxide glasses, where Vickers hardness is typically between 2-8 GPa [31]. Consequently the elastic modulus of chalcogenide glasses is also lower (Young's modulus from 17 to 18.5 GPa) compared to silica (Young's modulus 72.1 GPa) [21]. This is a direct result of the electronegativity of the bonds in oxides and chalcogenides. Silica, for example, exhibits polar bonds that arise from the difference in electronegativity of Si (2.0 [51]) and O (3.44 [51]) causing the electrons in the bond to be more strongly associated with the O atom. In contrast, the molecular bonds making up chalcogenide glasses are less polar (the electronegativity value of Se, Ge and Sb are similar, being Se= 2.55 Ge=2.01 and Sb = 2.05 [41]) meaning that the bonds are less ionic in nature, with the electrons shared more equally between the bonding atoms. Indeed, in many chalcogen-rich compositions, homopolar bonds are present which approach complete covalency. The mechanical stability of the Ge-Sb-Se chalcogenide fibres fabricated in this Project will be discussed in section 5.7. Due to the fragile and brittle nature of the fibres,

complications in fibre drawing arose and it was suggested that micro-cracks might have limited the light guiding ability of some of the fibres, analysed in section 6.2. To counteract the low Vickers hardness, the robustness of fibres can be increased by using an on-line polymer coating of the fibre, discussed further in section 2.6.1. It is suggested that the calculated limit of mechanical strength estimated as 1/10 of the Young's modulus is 1.8 GPa and is sufficient for optical fibres [22].

One of the main interests of chalcogenide glasses is associated with their phonon energy. A phonon is a quantum of vibrational energy [52] (just as a photon is a quantum of electromagnetic energy, see section 2.3). Hence, a phonon is a quantised value of the energy of the vibrational frequency of a lattice when reacting to an incident radiation wave of the same frequency or multiples thereof. The extinction coefficient (α, also called the absorption coefficient) is a measure of the relative light absorption of a particular vibrational mode [53]. Phonon energy is an intrinsic property of glass and is dependent on bond strength in the glass network, mass and composition. Glasses made up of lighter atoms have high phonon energy as they can form strong bonds and can shift the vibrational frequency, and therefore the resonant absorption, of the glass to shorter wavelengths [54]. Heavier atoms form weaker bonds (due to a reduced electronegativity) resulting in a lower frequency of atomic vibrations. Thus resonant absorption of a glass made up of heavier atoms results in a shift towards longer wavelengths and the glass will have low phonon energy. Accordingly, chalcogenide glasses, with a framework built up of heavy atoms and weaker bonding than the more polar bonding in silica glasses, exhibit low vibrational modes resulting in low phonon energies.

The chalcogen elements differ in relative atomic mass, with Te being the heaviest, then Se and S the lightest. With increase in mass, the elements also increase in size; the

relative atomic mass and atomic radius of S, Se and Te are 32.068/ 88 pm, 78.971/ 103 pm and 127.60/ 123 pm, respectively [55]. Thus with an increased mass down the chalcogen Group, the multi-phonon absorption edge is shifted to longer wavelengths. Sulfide glasses have a phonon energy ranging between ~ 400 – 450 $cm^{-1}$ [56] whereas telluride and selenide glasses have phonon energy ranges between 230-350 $cm^{-1}$ [57]. Short-wave and long-wave absorption edges are shifted to longer wavelengths during substitution of Se for S and to shorter wavelengths during the substitution of Se for Te, see Figure 2.2.

From Figure 2.2, it may be seen that all of the chalcogenide glasses have a short wavelength cut-off absorption edge at wavelengths approximately between < 1- 2.5 µm.

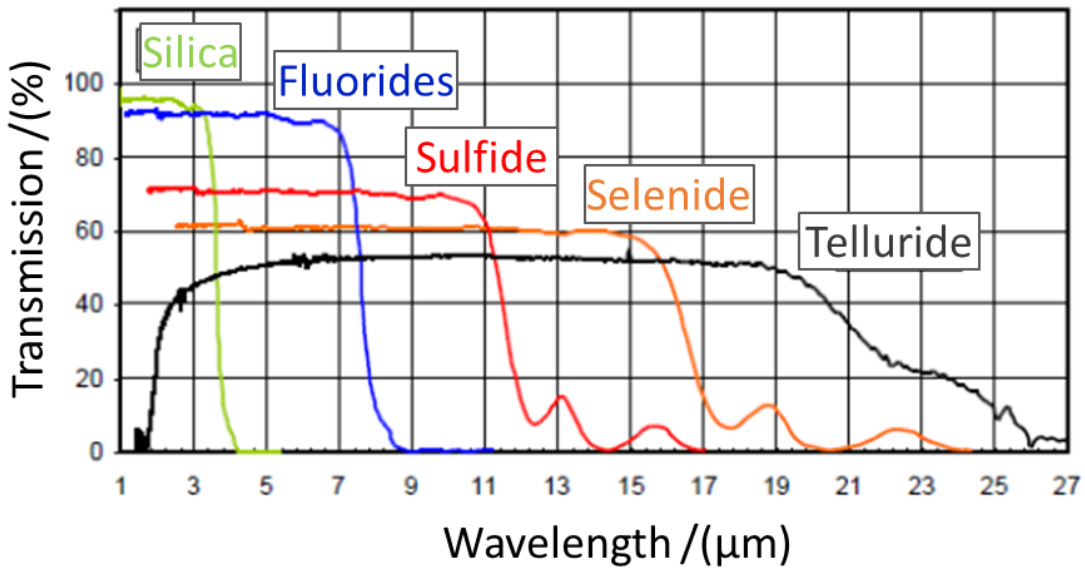



**Figure 2.2 Transmission range of the chalcogenide glasses sulfide, selenide and telluride bulk glasses in the wavelengh range of 1-27 µm. Silica and fluorides are included for reference (Figure from [19]).**

This arises due to the chalcogenide glasses being semi-conductors with a forbidden electronic band-edge > 2 eV, manifesting itself as an optical edge theoretically in the 0.6-2 µm wavelength range. This wavelength cut-off increases with the atomic mass of the chalcogens from S to Te, thus chalcogenide glasses are opaque across much of the

visible region of the spectrum [58]. The long wavelength cut-off absorption edge is a result of the multiphonon absorption due to the overtone and combination vibrations of the fundamental vibrational absorptions of the molecular bonds within the glass, *e.g.* [≡Ge-Se-] or [=Sb-Se] [19, 59]. The MIR transmission of the Ge-Sb-Se glasses synthesised in this Project will be discussed in section 4.1.3 of this Thesis: the absorption band-edge was found to be between 0.71-0.76 µm, as shown in Figure 4.4.

The change in relative atomic mass also affects the chemical bonding of analogous glasses based on S, Se and Te, respectively, becoming weaker with an increase in atomic mass and resulting in a lower $T_g$. Furthermore the addition of heavier atoms result in an increase in the refractive index of a glass [60]. Using the greatly investigated chalcogen (X) binary system $As_2X_3$, a summary of the different effects of the chalcogens is shown in Table 2.1.

There are many steps involved in the synthesis of chalcogenide glass via melting, such as precise batching and melting steps to ensure high purity and homogeneous bulk glasses, see Chapter 3. The Ge-Sb-Se chalcogenide glasses synthesised in this Project exhibited a liquidus between 650- 900 °C, compared to silica which exhibits its liquidus at ~2000 °C [58]. This was one of the factors which enabled fabrication to be carried out in commercially available low $OH^-$ silica ampoules, see section 3.1 for details on chalcogenide glass fabrication.

Several of the components of these glasses are toxic (As, Se and potentially Sb). Contamination of hydroxide and oxide impurities can impair the MIR transmission of the chalcogenide glass, for instance 1 ppm of H-Se causes 1 dB/m loss [22]. It has also been proved to be difficult to remove impurities, which contribute to extrinsic loss, from the glasses as elements are readily oxidised and hydrolysed, see section 2.6.2.

MIR supercontinuum generation fibres based on chalcogenide glasses are further discussed in section 2.5.

**Table 2.1 Summary of how the addition of each chalcogen (X) affects the glass properties of an $As_2X_3$ binary system. It is difficult to form amorphous $As_2Te_3$, where data were unavailable an $As_2Se_2Te$ glass has been included for comparison. Key: α and β are crystalline phases of $As_2Te_3$ and ? means not available to this Author.**

| Properties | $As_2S_3$ [22] | $As_2Se_3$ [22] | $As_2Te_3$ [61, 62] | | $As_2Se_2Te$ [22] |
|---|---|---|---|---|---|
| | | | α | β | |
| Glass forming | Highest tendency to glass formation | Greater tendency to glass formation compared to $As_2Te_3$ | Lowest tendency to glass formation | | |
| Refractive index<br>at λ=3 μm<br>at λ= 5 μm | <br>2.395<br>2.386 | <br>2.8275<br>2.79984 | ? | ? | <br>?<br>? |
| Density / (kg/m³) | 3200 | 4620 | 6343 | 6130 | 5070 |
| Glass transition temperature, $T_g$, /(°C) | 185 | 170 | ? | ? | 148 |
| Short-wavelength absorption edge, μm, at absorption coefficient 1 $cm^{-1}$ | 0.62 | 0.85 | 0.48 | 0.28 | 1.23 |
| Long-wavelength absorption edge, μm, at absorption coefficient 1 $cm^{-1}$ | 11.53 | 17.50 | ? | ? | 18.52 |

### 2.1.2. Ge-Sb-Se glass system

This thesis focuses on the ternary glass system; germanium (Ge), a Group 14 element, antimony (Sb), a Group 15 element, and selenium (Se) chalcogen, a Group 16 element, in a variety of compositions. It has been reported that the binary Ge-Se chalcogenide glasses are useful for MIR applications due to their wide transmission window, e.g. $Ge_{20}Se_{80}$ has a transmission range from 0.9 μm to 12 μm [18]. However, binary glasses have a lower tendency to form glass compared with ternary systems, since the tendency

to crystallise decreases with the increased number of components in the alloy, the so called 'Jamming effect' [63].

### 2.1.2.1. Ge-Sb-Se glass structure

In a stoichiometric glass the 4-coordinated Ge and 3 co-ordinated Sb have a mixed layer 3D (dimensional) structure composed of pseudotrigonal [$SbSe_3$] units and tetrahedral [$GeSe_4$] units [64], as shown in Figure 2.3. Ge-Sb-Se glasses have a structure made up of Ge-Se, Sb-Se and Se-Se bonds in the glass. Each Se anion is bonded to two cations (Sb/Ge) providing the network connectivity. In glasses that are Se rich, these basic structural units remain linked by Se-Se chains of increasing length with higher Se concentrations. Theoretical results of the bond energy values are shown in Table 2.2.

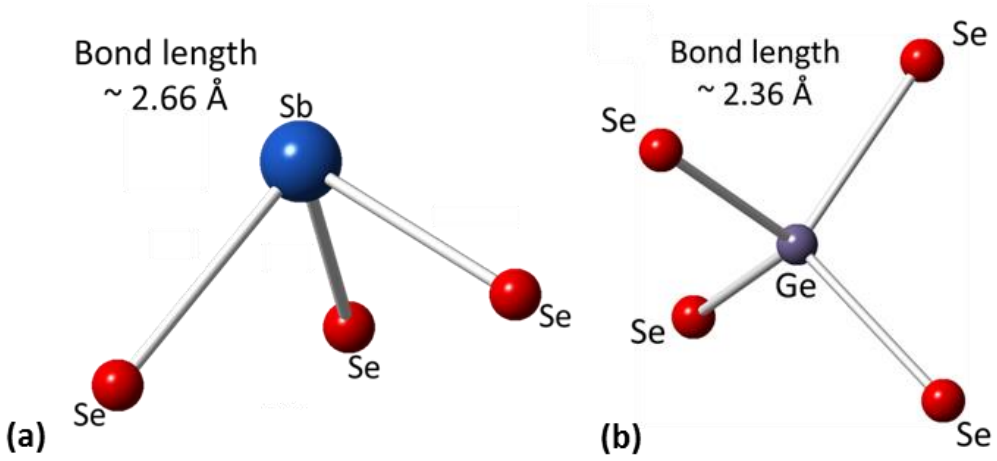



**Figure 2.3. Representation of the basic structural elements found in Ge-Sb-Se glasses. Note that the bond length is related to the coordination number. (a) Sb is a lone pair electron element that can form three bonds to anions, pseudotrigonal [$SbSe_3$] units [65]. (b) Ge can form four bonds to anions, tetrahedral [$GeSe_4$] units [66].**

The structure of Ge-Sb-Se glasses was investigated in this Project of a series of compositions along the stoichiometric tie line, $x(GeSe_2)$-$(1-x)(Sb_2Se_3)$; the stoichiometric tie-line is shown in Figure 2.5 and was chosen to simplify the investigation of the Ge-Sb-Se glass structure, see Chapter 8, as follows. By varying the

composition along the tie line (varying x from 0.4 to 0.9) Sb was substituted for Ge. In contrast to glass compositions selected for study of their optical properties, these compositions contain only enough Se to satisfy the bonding requirements of Sb (1.5 Se atoms per Sb) and Ge (2 Se atoms per Ge). This served to simplify the structure of the glasses, ensuring that they were composed of [$SbSe_3$] and [$GeSe_4$] units only. The theory behind the neutron diffraction technique used to study the structure of the stoichiometric Ge-Sb-Se glasses is discussed in section 2.2 and the results obtained will be analysed in Chapter 8.

**Table 2.2 Values of bond energy in Ge-Sb-Se chalcogenide glass.**

| **Bonds** | **Bond energy /(kJ/mol) [42]** | **Bond energy /(kJ/mol) [67]** |
|---|---|---|
| Ge-Se | 206.77 | 205.61 |
| Se-Se | 184.10 | 184.10 |
| Sb-Se | 183.93 | 183.85 |
| Ge-Ge | 154.81 | 154.81 |
| Ge-Sb | 141.25 | 141.17 |
| Sb-Sb | 126.44 | 126.44 |

### 2.1.2.2. Ge-Sb-Se glass properties

The properties of a $Ge_xSb_{10}Se_{90}$-x glass system, where the composition was varied from Se rich (0 – 24 at. % Ge), through the stoichiometric composition (25 at. % Ge) to Se poor glasses (> 26 at. % Ge) are shown in Figure 2.4 [68]. It can be seen that, with an increase in Ge concentration up to 25 at. % Ge, the $T_g$ increased (Figure 2.4 (a)), while the network density decreased as the length of the Se-Se chains in the glass was reduced (Figure 2.4 (b)). This indicates an increasing glass stability within the

system. Furthermore it was reported that the stoichiometric composition $Sb_{10}Se_{65}Ge_{25}$ provided the lowest density (Figure 2.4(b)) and refractive index at 1550 nm wavelength (Figure 2.4(c)) [68].

Sharma *et al.* studied $Ge_{19}Se_{81-x}Sb_x$ compositions, where x = 0, 4, 8, 12, 16, 17.2 and 20, and found that with the greater addition of Sb, the transmission spectrum moved towards longer wavelength [42]. They reported that the composition $Ge_{19}Sb_{17.2}Se_{63.8}$ had the maximum $T_g$.

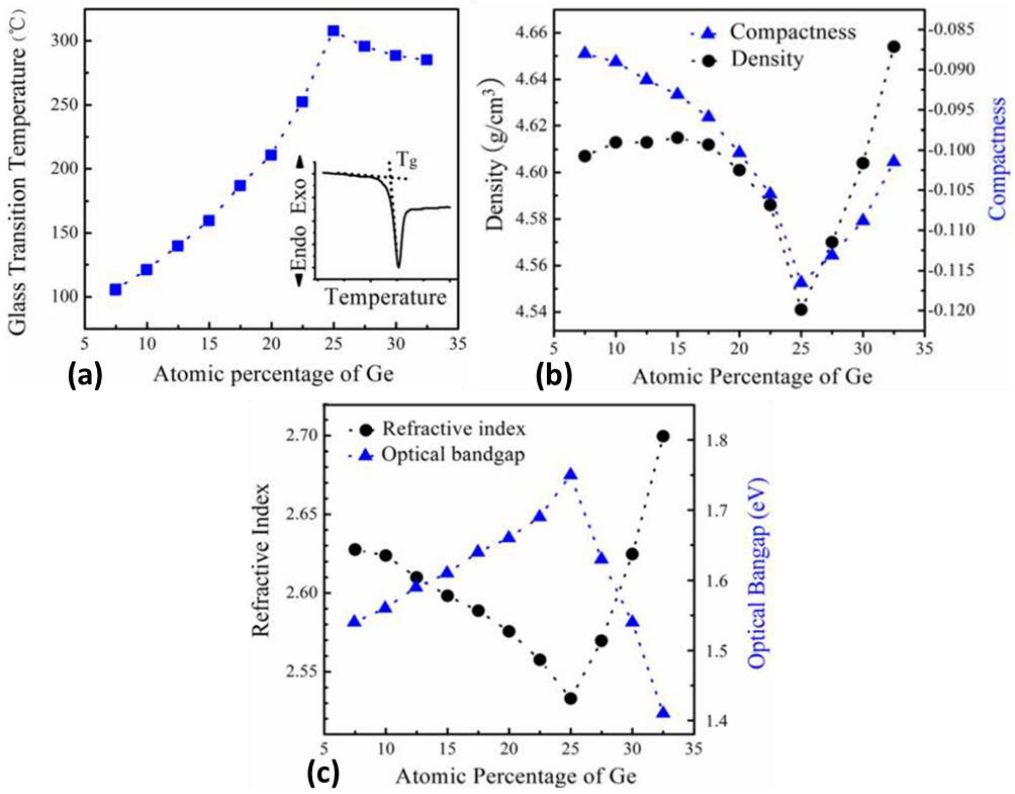



**Figure 2.4 Properties of a $Ge_xSb_{10}Se_{90}$-x glass system [68]. (a) Glass transition temperature ($T_g$) with inset defining the $T_g$. (b) Density and compactness. (c) Refractive index and optical bandgap collected at 1550 nm.**

Currently the most established chalcogenide ternary glass systems are based on arsenic (As) containing glasses [19]. In a Ge-As-Se based glass, the atomic radii of each element are similar sizes, thus their melting combination has the advantage of a large glass forming region and strong stability against crystallisation, see Figure 2.5.

However, As is a well-known toxic element and has been classified in Group 1 as carcinogenic to humans, by the International Agency for Research on Cancer (IARC 1987) [20]. Thus, commercialisation of an As-containing product would prove difficult, especially for medical applications. Sb is potentially a suitable substitute for As due to its similar structural behaviour and it is known to improve the thermal stability of amorphous Se [69]. Like As, Sb is in Group 15 of the Periodic Table and is a lone pair electron element that can form three bonds to anions. A preliminary cytotoxicity evaluation of Ge-Sb-Se glasses will be discussed in Chapter 7.

#### 2.1.2.3. Ge-Sb-Se compositions chosen for this Project

A ternary phase diagram for the Ge-Sb-Se glass system, shown in Figure 2.5, has been reported in the literature [70, 71]. This system has a large glass formation domain. The range of glass formation is bound by 5-35 at. % Ge, 5-40 at. % Sb and 60-90 at. % Se, close to the Se corner. This indicates that Se rich compositions can form glass. The Ge-As-Se glass forming region has been included for comparison [72].

The stoichiometric tie-line, x($GeSe_2$)-(1-x)( $Sb_2Se_3$), used for the structural studies, is indicated along with the four Ge-Sb-Se glass compositions for optical studies; JB01 ($Ge_{19}Sb_{15}Se_{66}$), JB02 ($Ge_{20}Sb_{10}Se_{70}$), JB03 ($Ge_{24}Sb_4Se_{72}$) and JB04 ($Ge_{22}Sb_8Se_{70}$). The compositions for optical studies were selected based on the bulk glass physical properties reported in [1]. The fabrication of Ge-Sb-Se chalcogenide bulk glasses and fibres is further discussed in section 2.6.1. The verification of the reported physical properties in [1] along with the identification as to whether the Ge-Sb-Se chalcogenide glasses have the required stability for optical fibre fabrication will be discussed in Chapter 4. The analysis of the Ge-Sb-Se fibres optical properties will be discussed in Chapter 6.

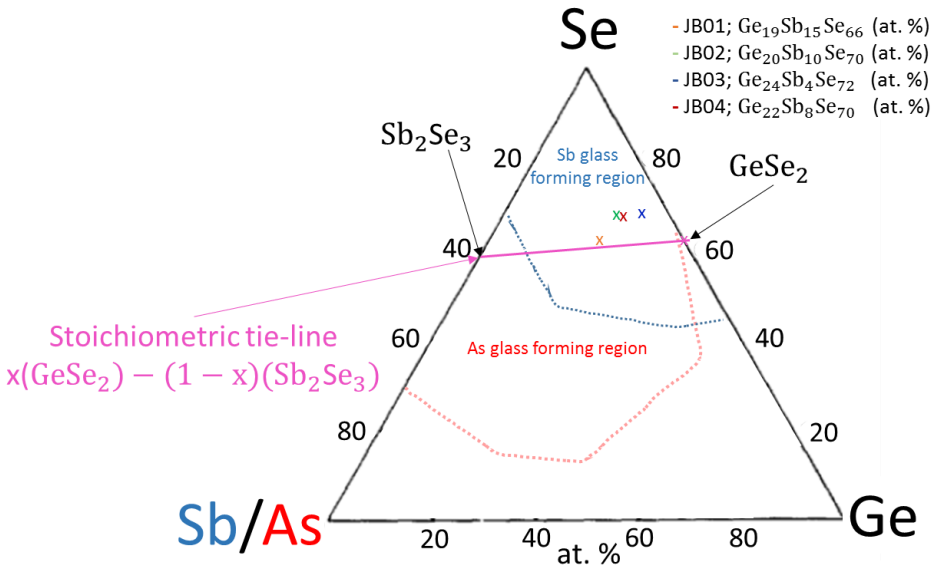



**Figure 2.5 The glass forming region versus atomic % for the Ge-Sb-Se glass system [70, 71] and the Ge-As-Se glass system [72] for comparison. Ge-Sb-Se vitreous phase held is defined by 5-35 at. % Ge, 5-40 at. % Sb and the remainder being Se. The compositions of the Ge-Sb-Se glasses synthesised in this Project are indicated. JB01 ( $Ge_{19}Sb_{15}Se_{66}$; orange), JB02 ( $Ge_{20}Sb_{10}Se_{70}$; green), JB03 ( $Ge_{24}Sb_4Se_{72}$; blue) and JB04 ($Ge_{22}Sb_8Se_{70}$; red). The stoichiometric tie-line, x($GeSe_2$)-(1-x)( $Sb_2Se_3$), used for the structural studies that will be presented in Chapter 8 is drawn in pink.**

## 2.2. Neutron diffraction scattering for structure-property relationships

Structural studies of glass compositions along the stoichiometric tie line, x($GeSe_2$)-(1-x)( $Sb_2Se_3$), where x = 0.9, 0.8, 0.7, 0.6, 0.5 and 0.4, were conducted using neutron diffraction scattering experiments and analysis of the results obtained will be presented in Chapter 8.

Neutron diffraction is a powerful method for analysing the structure of disordered materials [73]. Neutron diffraction allows a material to be analysed at the atomic level and can provide detailed information about the microscopic behaviour. The GEM (GEneral Materials) diffractometer at the ISIS Neutron and Muon Source[1], was used for the experiments described in this Project. ISIS generates a neutron flux using the

[1] ISIS Neutron and Muon Source, Rutherford Appleton Laboratory in Didcot UK, http://www.isis.stfc.ac.uk/

spallation. Spallation is a process where a high-power particle accelerator fires a particle beam into a metal target to release neutrons. More information about the facility and the operation of the neutron and muon source can be found in [73-75].

Here, a brief introduction to the theory of neutron scattering is given, greater detail can be found [76-78]. In a neutron diffraction experiment thermal neutrons interact with the nucleus of an atom and how much the atom scatters the neutrons is detected. A thermal neutron can be defined as a free neutron that is not bound within an atomic nucleus. A free neutron is an unstable particle and will undergo a three-body decay to an electron, an electron anti-neutrino and a proton, with a half-life of ~ 10 minutes [79]. Usually in a neutron scattering experiment, the time taken for a neutron to travel from the source to the detector is far less than the neutron's half-life. Thus the assumption can be made that the finite lifetime of a neutron is of no practical significance in a neutron scattering experiment [73]. Considering neutrons as wavelike particles, they interfere as they scatter through the sample if the wavelength is comparable to the inter-atomic distances present in the sample [80]. Wave interactions with atoms and molecules is discussed further in section 2.3. Thermal neutrons possess a kinetic energy with velocities ~ 2200 $ms^{-1}$ which results in a de Broglie wavelength, λ, of the order of 1.8 Å [73]. This is similar to the inter-atomic distances in the Ge-Sb-Se glasses. Thus thermal neutrons can interact with the nucleus of the atoms within the Ge-Sb-Se glass and how much the atom scatters the neutron is detected. Furthermore thermal neutrons have energies (~ 100 meV) which are of the same order as excitation energies in condensed matter. By measuring the change in the energy of a neutron as it undergoes inelastic scattering the energy of the thermal excitation can be found accurately.

In a neutron diffraction experiment a beam of neutrons with incident flux $I_0$ is incident on a sample, and the experiment measures how the neutrons scatter in a given direction (2θ, ϕ). This is shown schematically in Figure 2.6.

When a beam of neutrons is scattered from a sample, the total scattering cross-section (σ) can be calculated as the total number of neutrons scattered per second (in all directions) divided by $I_0$.

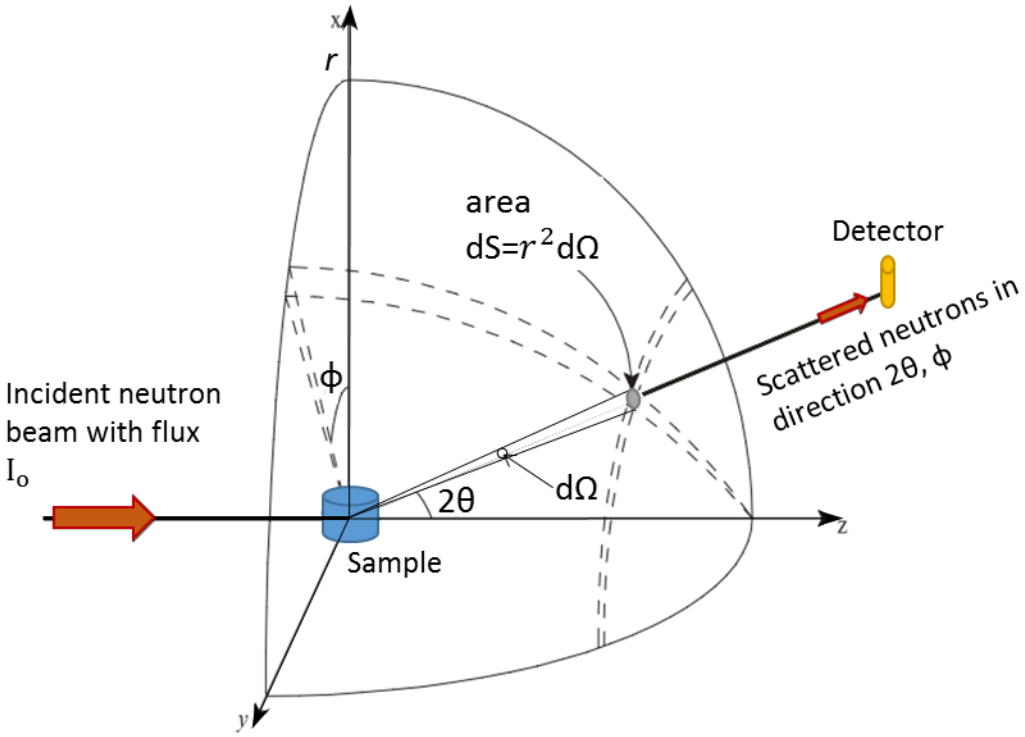



**Figure 2.6 The cross-section of a neutron scattering experiment. r is the distance of the scattered neutron from the scattering atom. $I_0$ is the number of incident neutrons per $cm^2$ per second (neutron flux). dΩ is the number of neutrons scattered into the solid angle. Adapted from [73].**

In a neutron diffraction experiment the differential cross-section $\left(\frac{d\sigma}{d\Omega}\right)$ is measured where neutrons are scattered into a solid angle (dΩ) in a particular direction (2θ, ϕ). Thus, the $\frac{d\sigma}{d\Omega}$ can be defined as [73]:

$$\frac{d\sigma}{d\Omega} = \frac{R}{I_0 d\Omega} \qquad \textbf{Equation 2.1}$$

where R is the number of neutrons of wavelength λ which are scattered into the solid angle $d\Omega$ in the direction 2θ ϕ. The scattering occurs in an elementary cone of solid angle $d\Omega$, shown in Figure 2.6. This is equivalent to the total scattering of neutrons from the sample, I($Q$), where $Q$ is the magnitude of the scattering vector for elastic scattering, as shown in Equation 2.2 [81]:

$$\mathbf{Q} = \frac{\mathbf{4\pi \sin \theta}}{\boldsymbol{\lambda}} \qquad \textbf{Equation 2.2}$$

The interference between scattered waves from the same nucleus in an atom within the sample is known as self-scattering, $I^S(Q)$, whereas the interference between scattered waves from different nuclei of different atoms in the sample is termed distinct scattering, i(Q). The total scattering is the sum of $I^S(Q)$ and i(Q) [74]:

$$\frac{\mathbf{d\sigma}}{\mathbf{d\Omega}} = \mathbf{I(Q)} = \mathbf{I^S(Q)} + \mathbf{i(Q)} \qquad \textbf{Equation 2.3}$$

i(Q) contains the structural information for the scattering system. This pattern is measured in reciprocal space but can be interpreted in terms of correlation functions in real space. i(Q) must first be corrected for inelastic effects but then a Fourier transform of i(Q) can be performed to generate the total correlation function, T($r$). T($r$) measures the frequency of the occurrence of interatomic distances in the sample. The extraction of i(Q) data, inelasticity corrections and the calculation of T($r$) will be discussed further in section 8.2.1. The structural analysis obtained from the neutron diffraction experiments conducted in this Project will be given in section 8.3.2

The relative interactions of neutrons with elements define how strongly the neutrons scatter. Detecting the scattering power of neutrons is advantageous as it is not proportional to the atomic number nor number of electrons in an atom. The strength of

neutron scattering depends on the precise structure of the nucleus and so varies haphazardly across the periodic table. The benefits of this are:

- Distinctions between neighbouring elements in the Periodic Table can be made as they generally have substantially different scattering cross-sections.
- Light atoms can be detected in the presence of heavier atoms.
- Isotopes of the same element can be identified as they present substantially different scattering lengths for neutrons. Thus isotopic substitution can be used to label different parts of a molecule.

After a neutron flux is generated, it is essential that it is in the correct energy range for a particular experiment. The energy spectrum of neutrons depends on the temperature of the moderators surrounding the source, as the neutron 'gas' is in thermal equilibrium with the materials of the moderators [73]. The diffractometer GEM is shown schematically in Figure 2.7. Approximately 2 x $10^{16}$ neutrons arrived per second at the instrument and a liquid methane moderator (100 K) was used to moderate the neutron thermal energies to a velocity of ~2200 $ms^{-1}$ [74]. Rotating disc choppers were used to define the pulse width of the neutron beam.

GEM was selected for the neutron diffraction experiment described in Chapter 8 of this Thesis, based on its 7270 detectors which covered a scattering angle range from 1.1° to 169.3° [74], see Figure 2.7. The detectors were arranged in eight detector banks covering a wide range in scattering angle, 2θ. In GEM the samples were inserted ~17 m from the moderator. This 17 m path length was relatively long (compared to the 11 m of other diffractometers at ISIS such as LOQ) allowing the spread of wavelengths for high resolution, without reducing the flux incident on the sample being measured.

The scattering pattern produced by Bragg peaks do not appear in an amorphous material. Therefore it is necessary to obtain high count rates to achieve a good signal to noise ratio. The wide angular coverage by the detectors facilitated obtaining a high Q by maximising the θ coverage as well as varying wavelength. (Q is the magnitude for the scattering vector for elastic scattering, see Equation 2.3).

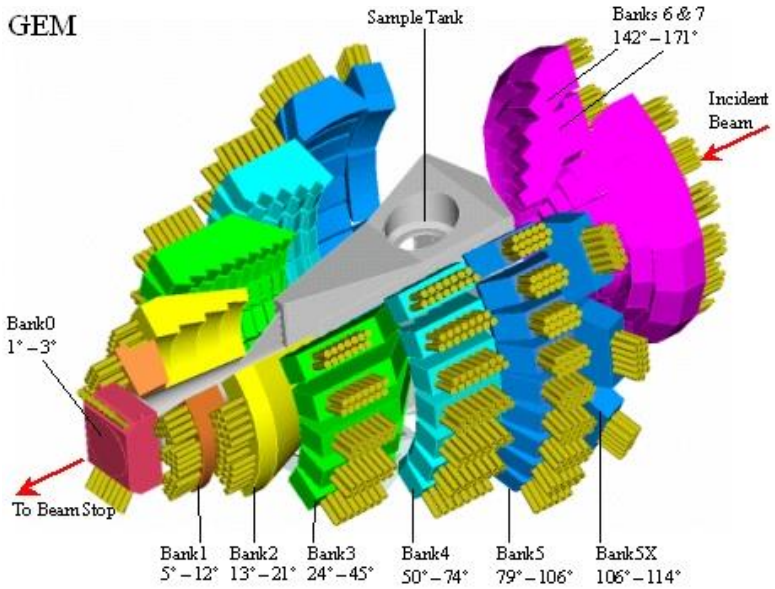



**Figure 2.7. 3D image of GEM diffractometer depicting the layout of the eight detection banks. Data taken from banks 3,4 and 5 were used for the structural analysis in this thesis [74].**

## 2.3. Introductory statements on electromagnetic wave interactions with atoms and molecules

The research in this Project has contributed towards the development of a medical diagnostic system using mid- to near-infrared spectroscopy, as discussed in section 2.4.1. To appreciate how this diagnostic system might work in the future, first it is important to understand electromagnetic wave interactions with atoms and molecules. The electromagnetic spectrum is a continuous range of radiation of different wavelengths, where regions can be categorised according to the frequency (or corresponding wavelength) of the wave, see Figure 2.8. Electromagnetic radiation transfers energy via the interaction of electromagnetic radiation with matter, and the

nature of this interaction depends on the wavelength. Electromagnetic radiation of different wavelengths finds different application, as shown in Figure 2.8.

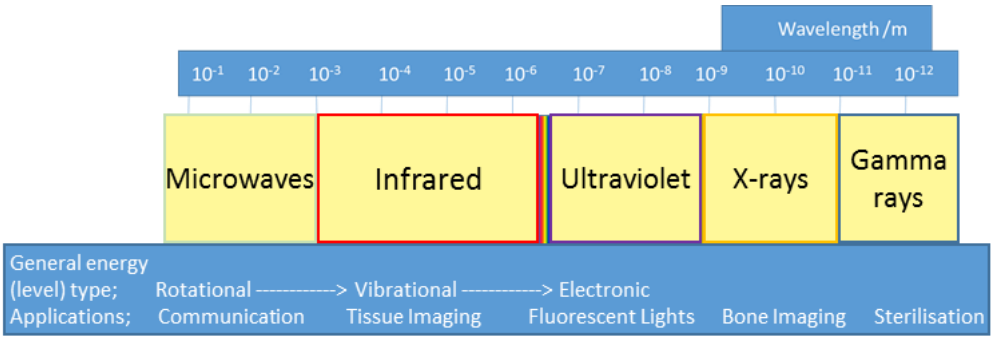



**Figure 2.8 The Electromagnetic Spectrum. The left side shows longer wavelengths with low frequency and the right side shows shorter wavelengths with high frequency. The regions of the Electromagnetic Spectrum are associated with either rotational, vibrational or electronic energy levels in matter. For example; ultraviolet photons which have high frequency induce electronic transitions in atoms, whereas infrared photons with lower frequency generate vibrational motion.**

Electromagnetic radiation in free space can be considered as mutually propagating, electric and magnetic fields, which are perpendicular to one another and oscillate in time. When the electromagnetic wave does not propagate, due to the energy being spatially confined in the vicinity of the source, it is known as an evanescent wave or field. This also occurs at an interface when the incident angle is greater than the critical angle, making the wave undergo total internal reflection. The phenomenon of total internal reflection and how it is promoted in optical fibres is discussed in section 2.6.

The wavelength, frequency and hence energy must be considered in the emission or absorption of an electromagnetic wave by a material:

$$\boldsymbol{\lambda = \frac{c}{\nu}} \qquad \textbf{Equation 2.4}$$

In Equation 2.4, the wavelength of light ($\lambda$) in metres (m), multiplied by the vibrational frequency ($\nu$) of light ($s^{-1}$), equals the velocity (c) of light (in free space c = 2.997925 x $10^8$ $ms^{-1}$). The Bohr equation, Equation 2.5, considers electromagnetic radiation as

a stream of particles (or quanta) where the energy of the particles (E) is equal to ν multiplied by Planck's constant (h) (6.626 x $10^{-34}$ Js) [31].

$$E_1 - E_0 = h\nu \qquad \textbf{Equation 2.5}$$

Infrared (IR) radiation has lower energy and longer wavelength than UV (ultraviolet) rays, X-rays and gamma rays, see Figure 2.8. Single molecules, dimers and compounds in all gases, liquids and solids manifest some of their internal energy through constant molecular vibrational motion. The vibrations involve stretching or bending of molecular bonds at particular frequencies. Each vibrational mode lies in the ground state energy level at normal room temperature. The relationship between frequency and energy stated in the Bohr equation can help to explain how a particular molecular vibrational mode in a molecule is stimulated after exposure to IR radiation.When the molecule is stimulated (*e.g.* when the molecule is exposed to IR radiation) the internal energy increases resulting in more energetic vibrations. This is discussed further in section 2.3.1.

### 2.3.1. Infrared radiation and molecular absorption/ infrared spectroscopy and molecular structure

In 1971 Gerhard Herzberg, from Ottawa, Canada, won the Nobel Prize for his discovery relating IR spectroscopy and molecular structure [82]. This section discusses how molecules absorb IR radiation and applications of this phenomeneon are discussed in section 2.4.

There is much discrepancy amongst scientists in determining the precise wavelength boundaries for the IR region. In accordance with ISO standards the regions are defined as near-infrared (NIR, 12820.51– 4,000 $cm^{-1}$or 0.78-3 µm, MIR (3333-200 $cm^{-1}$ or 3-50 µm) and far-infrared (FIR, 200-10 $cm^{-1}$ or 50 to 1000 µm) [1]. A pragmatic

definition of the MIR spectral region is 3-25 µm because common MIR detectors go out to 25 µm [46, 83].

Molecules can absorb energy from MIR radiation via resonance. Resonance occurs when the incident radiation has the same frequency as that of a transition from the lowest energy form of the atom to an upper level. This causes a fundamental change in the electric dipole movement of the molecule as it induces a particular molecular vibration to vibrate with higher amplitude, but at the same frequency. Molecules are only MIR active if this non-uniform distribution of positive and negative charges of the atoms occurs. This occurs in so-called heteronuclear diatomic molecules. The fluctuations in the dipole moment interact with the alternating electric field of the radiation. Therefore one small part of the molecule has higher vibration motion than the rest of the molecule.

The Szigeti equation [84], Equation 2.6, can be used to calculated the frequency ($v$) of a stretching vibrational mode of a molecular bond. The bond force constant ($f$) related to the strength of the molecular bond is divided by the reduced mass ($m$) of the two vibrating atomic masses: ($m_1 m_2$) [84]:

$$\boldsymbol{v \propto (f/m)^{1/2}} \qquad \textbf{Equation 2.6}$$

$$\boldsymbol{m = \frac{m_1 m_2}{(m_1 + m_2)}} \qquad \textbf{Equation 2.7}$$

From Equation 2.6 it can be calculated that the photon energy of MIR radiation has an associated frequency range, which corresponds with the frequency range of molecular vibrations [84]. In the MIR, the alternating electric field of the incident radiation sets the molecular bonds into resonant oscillation at the same frequency. Resonant

frequencies to stimulate electronic oscillations lie in the UV and the photon energy is too high to stimulate molecular vibrations in the MIR [85].

The positions of atoms in a molecule are not fixed. They are subject to a number of different vibrations, falling into the two main categories of stretching (*i.e.* a change in bond length) and bending (*i.e* .a change in bond angle and bond length): Figure 2.9 illustrates this for methylene ($-CH_2$).

Each of the fundamental modes of vibration shown for ($-CH_2$) in Figure 2.9, would have a particular quantised discrete energy level, depending on the molecule or molecular moiety. Incident radiation is absorbed when it is at the same frequency as one of the vibrational modes of the molecule. Molecular vibration is established by the molecular structure consisting of: molecular shape, atomic mass and bond strengths. Vibrations are generated when the bond lengths between atoms vary and the atoms move relative to one another.

A particular molecule's unique vibrations arise due to the different degrees of translational and rotational freedom. The stiffness of the bonds between atoms and the masses of the atoms at each end also contribute. However, rotational transitions of gaseous or liquid molecules are of little use to MIR spectroscopists as they typically occur at lower frequencies and longer wavelengths (microwave region) than MIR radiation [86]. Although some rotational transitions can occur in the MIR region, due to molecular collisions and interactions, the data is not discrete; the absorption of MIR radiaton by this mechanism produces broad spectra that are difficult to distinguish. For this reason rotational transitions are not considered further in this Thesis.

**Stretching Vibrations**
Change in inter-atomic distance along bond axis. Strong coupling of stretching vibrations occurs when there is a common atom between the two vibrating bonds.

**Bending Vibration**
Change in angle between 2 bonds. Coupling of bending vibrations occurs when there is a common bond between vibrating groups.

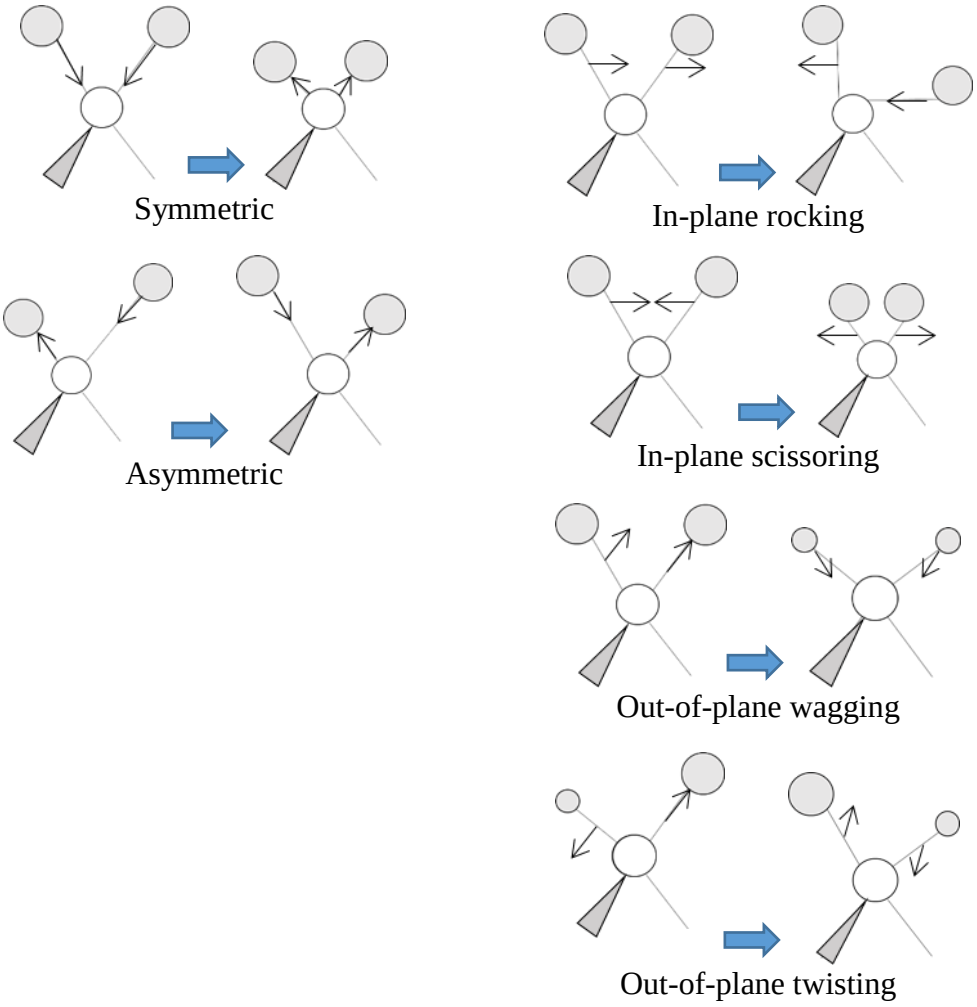



**Figure 2.9 Vibrational modes of methylene (-$CH_2$) functional group. Molecular structure is made up of the molecular shape (bond angles and bond lengths), and therefore atomic masses and bond strengths. Vibrational modes lie in the ground state energy level. However, after a stimulus from a photon of matched frequency to the vibrational frequency, the internal phonon energy increases and vibrational modes vibrating at the same frequency but with increased amplitude are set in motion. Each vibrational mode is quantized and has an energy associated with it and only when the photon is the same frequency as one of the modes of vibration will it be absorbed.**

The vibrational energy levels of organic molecules and their functional groups have spacings corresponding to the energy of MIR radiation. The absorption of MIR

radiation is determined by the molecular symmetry of the molecule as this influences which bonds will undergo the net dipole change. The frequencies of the light absorbed correspond to the characterisic vibrational frequencies of the bonding within functional groups of molecules. In addition, the relative position and type of neighbouring intramolecular bonds also influence the vibrational frequency of a molecular bond. In turn, these are completely dependent on the molecular structure and hence provide the means for, often unique, molecular identification. This is known as the molecular fundamental absorption band and 'fingerprint region' where molecules have large extinction coefficients [3].

The extinction coefficient of a particular vibrational mode of a molecule defines how strongly it absorbs MIR light. This potentially enables the absorption of MIR radiation to give rise to MIR absorption spectra of cells and tissues providing information about the absence or existence of disease. MIR absorption spectra could also provide information about biological cell architecture and composition, metabolic processes and packing of cellular components [4], as discussed in section 2.4. The NIR region is less useful for analysis as they mainly comprise of overtone and combination bands, which have small extinction coefficients.

### 2.4. Prospects for using vibrational spectroscopy for cancer detection

It is estimated that 1 in 2 people born after 1960 in the UK will develop cancer during their lifetime; and approximately 50 % of these will die as a result of the disease within 10 years of diagnosis [87]. An epidemiological study conducted by Maddams *et al*. predicted that the incidence of cancer cases in the over 65s will have trebled by 2040, compared to 2010 where there were 1.3 million new cases [88]. Skin cancers are the most common malignancy of humans, with 2-3 million cases detected worldwide per

year [89-93]. In the UK the rate of incidence of malignant melanoma has quadrupled within the last 35 years [87]. The incidence varies, with very high rates in the Caucasian population [93, 94]. Fair skin has very low levels of eumelanin in the epidermis (a UV-blocking dark pigment). It is well known that high frequency photons in UV radiation cause electronic transitions when exposed to matter. In human skin, this can lead to genetic mutations, immunosuppression and oxidative stress [95, 96]. In the advanced stages of skin cancer in current thinking the cancer can metastasise; this is the spread of the cancer to another organ or location. Identifying the primary tumour as early as possible increases the efficiency of treatment and thus patient survival [97].

Current cancer diagnostic tests are arduous and depend greatly on human judgement. The 'Gold Standard' biopsy and examination for cancer depends entirely on the expertise of the doctor and histologist [98]. Although surgical methods remain the mainstay of treatment, novel research and innovation are vital to reduce morbidity. Therefore it would be beneficial to develop a medical diagnostic system which can analyse and image tissue instantly (such as using vibrational spectroscopy) with accurate diagnostics, removing the margin of human error and with the additional benefit of being minimally invasive.

Vibrational spectroscopy uses the mechanisms of molecular absorption discussed in section 2.3 and detects the absorbance of light at particular wavelengths, due to specific molecular vibrations resonant with the light's frequency. There are two types of vibrational spectroscopy which exploit the wave interaction with atoms and molecules described in section 2.3, Raman spectroscopy and IR spectroscopy.

Raman spectroscopy is a sister analytical technique that utilises the phenomenon of inelastic light scattering which can produce characteristic spectra unique to specific molecules. It measures the shift of frequency of the light as a result of the exchange

between an incident photon and the vibrations in the molecule [99]. The energy lost or gained by the electromagnetic field is matched by a change in the phonon energy of the molecules. The predominant frequencies in the Stokes and anti-Stokes fields are characteristic of the molecule. Unlike MIR absorption, where a change in the molecular dipole must occur, for a molecular vibration to be Raman-active a change in the dipole during the vibrations does not occur [99].

Ramen spectroscopy provides a useful comparator to MIR spectroscopy and can be considered as a complementary technique. As Raman spectroscopy can utilise robust and established silica glass fibres, it has enabled Raman sensing systems to overtake MIR spectroscopy in clinical trials. However, there is an argument, that compared to MIR spectroscopy with large extinction coefficients, the Raman signal is intrinsically weak and artefacts due to the fluorescence of the silica fibre can affect the spectrum [3]. Raman spectroscopy has high molecular specificity. Yet, Raman scattering (Stokes and anti-Stokes scattering) is a relatively low-probability phenomenon (~1 in $10^8$) in comparison to elastic scattering [100]. Therefore low sensitivity can be an issue. Acquisition times are also very long, approximately only 1 in 30 million photons are scattered, transferring energy to the molecule. Highly efficient laser sources, low-noise detectors and effective Rayleigh filters are a few of the technological advances to help increase the sensitivity [101].

In 2001 McIntosh *et al.* reported the first system based on NIR reflection spectroscopy to test for skin cancer executed *in vivo* (in the body) [102, 103]. They made use of readily available silica fibre optics in the NIR reflection probe, which are transparent to NIR radiation. However, as previously stated, the extinction coefficient of the overtone and combination bands occurring in NIR are far weaker than the extinction coefficients of the fundamental vibrational absorption bands occurring in the MIR

spectral region. The visual examination by a consultant dermatologist and histopathology results, proved to be more accurate than the NIR *in vivo* probe spectroscopic analysis (*e.g.* the system was 81.8 % accurate for detecting a basal cell carcinoma whereas a clinician was 94.8 % accurate [102]). In the MIR region (defined in this Project at 3 – 25 μm) the molecular fundamental vibrations absorb much more strongly, with extinction coefficients ($\mathrm{Mcm^{-1}}$) (molecular absorptivity) $10^3 - 10^5$ times larger than in the NIR region [25].

As mentioned in section 2.3.1, functional groups absorb at wavelengths in the MIR spectral region and the frequencies of the light absorbed correspond to the characterisic vibrational frequencies of the chemical bonding. For instance the 6 – 15 μm MIR region known as the "fingerprint region" is particularly useful in the indentification of organic functional groups.

In MIR spectroscopy a polychromatic (rainbow of light) MIR light beam, interacts with the sample and beam is collected after sample interaction. During interaction with the sample some of the MIR frequencies are absorbed (stimulating particular modes of vibrations, see Figure 2.9) reducing the collected beam brightness at those particular frequencies. The collected intensity is expressed as a fraction of the incident radiation intensity. This characteristic nature of the MIR light frequency absorption allows detection, identification and quantification of the molecular makeup of the sample. In research carried out by McIntosh *et al*. MIR spectra of a basal cell carcinoma conducted on a biopsied tissue sample were observed *in vitro* [104]. It was reported that 'discrimination of basal cell carcinoma from the epidermis *ex vivo* classification was 98.7 %' [104]. In 2009, Ly *et al.* also successfully demonstrated differentiation between cancer types from MIR spectroscopy *in vitro* of skin tissues [105]. Highly informative spectra were obtained and it was found that the most reliable results were obtained

within the MIR 'fingerprint' region between 6-15 μm. The research in this Project is contributing to a MIR spectroscopy skin cancer detection system with the intention of progressing the technology to accurate *in vivo* diagnostics, as will be discussed further in section 2.4.1.

### 2.4.1. MId- to NEaR infrared spectroscopy for improVed medical diAgnostics (MINERVA EU (European Union) Project 2012-2017)

MINERVA[2] is a collaborative project working on developing a remote skin cancer detection system using MIR absorption spectroscopy. The involvement of the MIR Photonics Glasses Research Group at the University of Nottingham, UK, (and thus this Author) is to develop bright discrete and broadband MIR fibre optic sources and passive fibre for routeing the MIR light to where it is needed. The Research Group has had successful results reporting a record breaking broadband MIR light source, covering the 6-15 μm 'fingerprint region' [2].

It is well established that early detection of cancer, and therefore instant diagnosis, can have profound impacts, not only for the patient but for the overall population, lowering the economic cost of cancer treatment, estimated at ~$0.3 B per annum to the British health system [106]. Furthermore as mentioned in section 2.4 it would be beneficial to develop a medical diagnostic system which is minimally invasive and removes the margin of human error. These benefits were some of the main driving points for the MINERVA Project.

The diagnostic system proposed by Seddon [3, 28] is shown schematically in Figure 2.10. The bench top system contains a bright MIR supercontinuum source (SC). This would be generated by a rare-earth MIR fibre laser pumped non-linear SC generation

[2] The MINERVA Project (www.minerva-project.eu) supported through the EU Seventh Framework Programme (FP7).

(SCG) MIR fibre (the focus of this Project is fabricating such a SCG MIR fibre). The MIR light would be passed through a FT (Fourier transform)-MIR spectrometer and onto the patient's skin *in vivo* via delivery and collection passive MIR fibre. The skin tissue section spectrum would be collected by a FT-MIR instrument and a MCT (mercury-cadmium-telluride) detector. Statistical analysis of the entire molecular spectrum and mapping of the distribution of molecular species are required to obtain molecular discrimination across the MIR tissue image. It is worth highlighting that the majority of MIR radiation emitted by human skin is in the wavelength range of 5-10 μm and this would interfere with the MIR spectroscopic absorbance [3]. Therefore a background 'noise' would need to be considered and deducted when analysing the spectra.

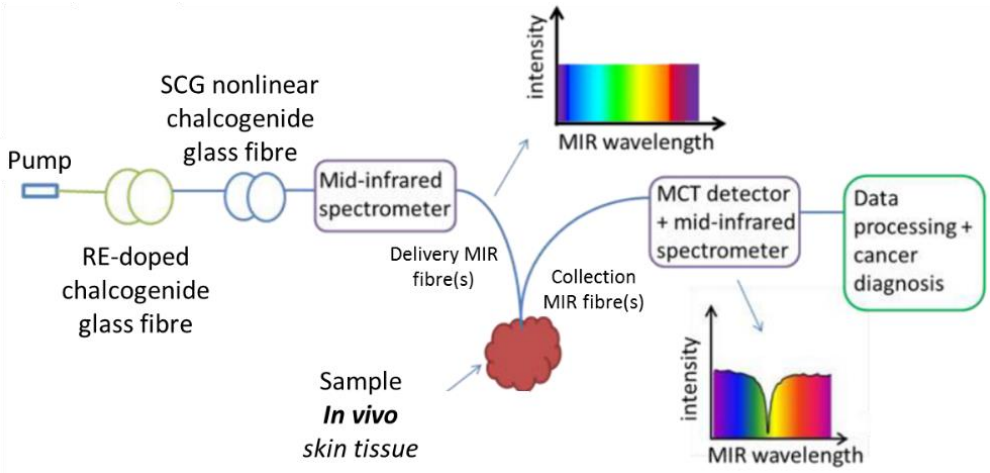



**Figure 2.10 Future, projected systematic methodology by Seddon *et al.* within MINERVA [3, 28]. A MIR spectral imaging system of biological tissue *in vivo*. Statistical analysis of the MIR light tissue interaction would produce characteristic spectral data used to detect molecular discrimination and early cancer diagnosis. The bench-top system consists of a bright MIR supercontinuum (SCG) source (a rare-earth MIR fibre laser pumped non-linear SCG MIR fibre) passed through a FT-MIR spectrometer and onto the patient's skin *in vivo* via delivery and collection passive MIR fibre. The skin tissue spectrum is captured by a MCT (mercury-cadmium-telluride, Hg-Cd-Te) and a FT-MIR spectrometre. Statistical analysis of the spectra is used to obtain molecular discrimination across the MIR tissue image.**

Currently from the literature, the conclusions are being drawn that searching for specific cancer marker absorption peaks are of limited value [107]. For example, the

instrumental changes arising in the MIR spectra when a deregulation mechanism such as tumour or cancer occurs within a cell, are subtle and not easily detected except by careful statistical analysis of MIR absoprtion spectra of malignant verus normal tissue.

In 1999 Boussard-Pledel *et al.* suggested evidence that malignant tissues led to modification of the structural conformation of the proteins which was detectable in the MIR fingerprint in the shape and position of the amide I and II bands [5]. Therefore mathematical algorithms, such as multivariate analysis, are required. Visual representation and maps can be generated after spectroscopic rastering of the tissue with either principal component analysis or clustering techniques applied [3]. More recently, direct imaging using focal plane array MCT (mercury-cadmium-telluride) detectors is possible and faster than rastering.

The non-invasive, MIR remote spectroscopic sensing system initiated by MINERVA, not only has the potential to encourage patients to seek medical advice earlier, it can aid surgery intra-operatively to detect residual cancer tissue immediately and better define the margins of the cancer. Furthermore, it reduces the impact of human error possible during current histopathological methods for detecting disease which relies on scrutiny of dyes. MIR examinations could be performed at local medical centres rather than using hospital resources, reducing patient waiting times, thereby saving cost, patient convenience and suffering.

MIR *in vivo* biopsies could provide remarkably sensitive biological analysis. There is demand for a novel MIR remote spectroscopic sensing system, which does not require direct contact with the patient yet still provides rich MIR spectra. There are several practical hurdles to overcome before this technology can become effective for clinical applications. It is not yet known how deep the MIR radiation will penetrate or how

much MIR radiation is safe to patients; these factors are discussed further in section 2.4.2.

### 2.4.2. Clinical application and considerations

Breaching the gap between laboratory research and theory to clinical application can be difficult and it is important to understand the relationship between the optical and biological properties of tissue. Practical problems need to be considered and well-thought-out. Here, a few of the clinical concerns potentially faced by the Seddon *et al.* medical diagnostic system are deliberated [3, 28].

It is known that exposure to high frequency wavelengths, for example in the UV region of the electromagnetic spectrum, can result in genetic mutations due to DNA molecules absorbing the photons. This results in an excited state which allows for the rearrangement of electrons [108] causing the denaturation of cells. Currently there is no evidence or guidelines to suggest how much exposure to MIR is safe. Although the photon energy is significantly less than ionizing UV radiation, the photon density of the MIR radiation beam must be considered. Human tissue comprises ~ 70% [109] water and if low frequency radiation is absorbed in large enough amounts, it can produce heat. This can lead to burns and tissue damage, advantageously used in medical procedures such as cauterisation [110]. $CO_2$ lasers have a reputation as ‘a laser scalpel’. They operate at a wavelength of 10.6 µm (within the MIR region) with an extremely high irradiance or power density, e.g. on a 100 µm spot, a 3 W $CO_2$ laser will have an irradiance greater than 38 kW/cm$^2$ [111]. $CO_2$ lasers have a limited penetration depth as all of the incident energy is quenched by the water tissue, preventing deeper tissue damage. This is also a consideration for the MIR laser as the actual penetration depth reached is still unknown.

One of the most important determinants of skin cancer prognosis is tumour thickness. Increased tumour thickness or the depth of invasion correlates with metastasis and ultimately poorer prognosis. Breslow's depth [112] was used as a prognostic factor in melanoma of the skin.

Figure 2.11 shows the results of a study of 98 cutaneous malignant melanomas where it was found that both the tumour thickness and the stage of invasion could be used to assess prognosis [112]. More recently this system has been replaced with The American Joint Committee on Cancer (AJCC) and International Union for Cancer Control TNM staging system; this utilises the size of the Tumour (T), whether the cancer has spread to the lymph nodes (N) and whether the tumour has metastases (M) in prognosis [113].

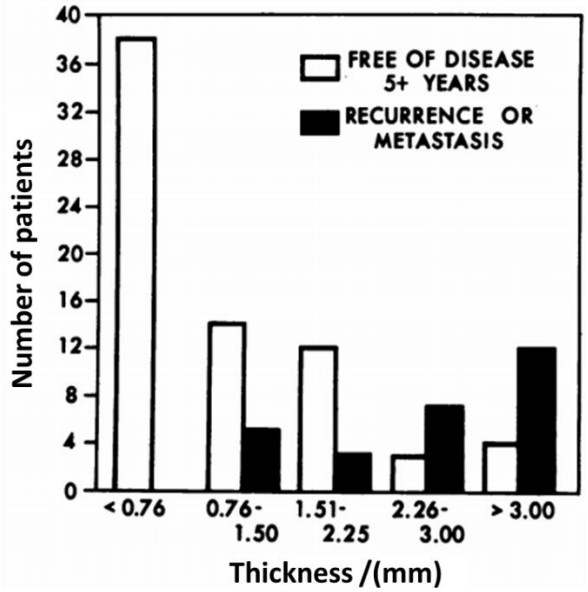



**Figure 2.11 Breslow's results showed the maximum thickness of melanomas. Tumours with thickness less than 0.76 mm did not recur or metastasise [112].**

Demonstrating that MIR light can penetrate into the dermis layer of the skin, thus covering all layers of the epidermis, is an important step for developing an optical sensor for skin cancer detection. This would have to be achieved without significant quenching effects, which occur with the $CO_2$ laser, or large scattering effects. The relative thickness of different strata within the epidermis (layers of the skin), varies

throughout the body from 0.05 mm on the eyelids to 1.5 mm on the palms and soles of feet [114]. The spatial variability of the refractive index of skin tissue also needs to be considered as the scattering properties depend upon particle size, type and density of the skin cells [115]. Refractive index ranges from ~1.41 to 1.49 in epidermal tissues to 1.36 to 1.41 in dermal tissues, over the wavelength range 325 to 1557 nm [116-118]. This difference between the refractive index of tissue layers also generates light scattering within the skin. Mourant *et al.* found that the majority of light scattering from an unpolarised He-Ne laser at 632.8 nm occurred at the organelles (structures within the cell) [115]. Michel *et al.* used both a quantum cascade laser (8.2 – 10.1 μm) and a FTIR spectrometer (1.25 - 16.67 μm) to investigate MIR light interactions with the skin [119]. With the FTIR spectrometer, and ~ 7 mW output power from the FTIR integrated across the full spectral range, they found that light penetrating the skin interacted mainly with the stratum corneum layer of the epidermis. The QCL laser (100 mW peak power and 5 mW average power) offered a higher input power than the FTIR spectrometer. Therefore, using high peak power pulses, light was able to penetrate deeper into the human skin. The results showed scattering centres within the skin, such as collagen fibres and capillaries in the dermis layer.

For remote sensing a high MIR transparency without scattering is the key to achieving high absorption contrast sensitivity. Furthermore the scattering properties of skin components should be considered in terms of light delivery and collection. Part of the research involved for the medical diagnostic system described in section 2.4.1 and Figure 2.10 is to develop high purity chalcogenide glass optical fibres to both deliver and collect the light. The theory behind purification and light transmission in optical fibres is discussed in section 2.6. The small-core MIR supercontinuum generation fibres fabricated in this Project were analysed and the results will be presented in Chapter 5.

The rationale behind the optical fibre dimensions, to increase the power handling capabilities and robustness of the SC source, is briefly explained in section 5.3. The purification techniques for synthesising high purity, low optical loss chalcogenide glasses developed in this Project will be discussed in section 3.2.1 and section 6.4.

Before chalcogenide glasses are used for clinical applications, it is vital to assess their cytotoxicity (the degree to which they are toxic to cells). An initial step was to conduct cytotoxicity tests as an evaluation technique to assess whether the material will have harmful or toxic effects on localised cells. ISO standard 10993-5 specifies test methods used to assess the *in vitro* cytotoxicity of medical devices [120]. To comply with ISO standard 10993-5 a literature review of cytotoxicity tests of chalcogenide glasses is required. However, little research into the cytotoxicity of chalcogenide glasses has been conducted and only chalcogenide glasses containing As have been investigated. Wilhelm *et al.* exposed immortalized human alveolar carcinoma type II epithelial cell lines (A549) to $Te_2As_3Se_5$ chalcogenide glass fibres and discovered that it was the oxide layer that produced a cytotoxic response rather than the glass itself [121]. Lucas *et al.* also coated A549 cell lines on $Te_2As_3Se_5$ chalcogenide fibres [122]. The cells adhered to the fibre surface as a mostly confluent monolayer, forming strong attachment to the fibre and it was proposed that this showed good 'biocompatibility with live biological components'. Keirsse *et al.* also reported that there were no different rates of colonization of *P. mirabilis* biofilm on $Te_2As_3Se_5$ compared to the control (control material not specified), suggesting the chalcogenide fibres were inert towards living organisms [123]. Taga *et al.* investigated the capability of devitrifying $As_{29}Se_{54}Te_{17}$ chalcogenide glass with S-layer proteins and reported a high packing density [124]. Studies have also shown that the hydrophobicity of solid surfaces influences the adhesion of bacteria, eukaryotic cells and proteins [125]. To this Author's knowledge

no cytotoxicity evaluation has been conducted on Sb containing chalcogenide glasses. Therefore, the preliminary evaluation of the cytotoxicity of the Ge-Sb-Se glasses synthesised in this Project are discussed in Chapter 7.

## 2.5. Supercontinuum generation (SCG) fibres

For the MIR remote cancer diagnostic system discussed in section 2.4.1 it was viewed imperative by Seddon [3] that a portable, bright MIR broadband supercontinuum source should be developed. Two requirements are needed of the bright MIR broadband supercontinuum source; a maximum average power output and the maximum width of broadband wavelength output across the MIR spectral region of at least 3 - ≥ 10 μm. Broadband supercontinuum generation relies on anomalous dispersion and strong optical non-linearity in the glass, where monochromatic or narrow-band incident light is converted to light with a very broad spectral bandwidth (white light), generating a rainbow of colours [10, 126, 127]. Spectral broadening can be accomplished by propagating optical pulses through a strongly non-linear device (*e.g.* using a microstructure optical fibre, discussed herein). The result is a spectral continuum. Compared with conventional white-light sources (such as the sun), the resulting light of supercontinua can reach a spectral brightness that is up to a million times brighter [10, 128].

In an optical system, a non-linear optical response (non-linear index of refraction) can occur when there is sufficiently intense illumination. Non-linear refraction can be defined as the change in refractive index as a function of the light intensity (I) travelling through the material. In glasses this can be expressed as $n_2$ (nonlinear refractive index) [129] where:

$$\boldsymbol{n = n_0 + n_2 I} \qquad \textbf{Equation 2.8}$$

where $n_0$ is the linear index of refraction. Thus a high non-linearity is beneficial for SCG as an incident single wavelength can be more greatly dispersed. Chalcogenide glasses possess high non-linear coefficients ($n_2$) (~5 x $n_2^{\text{tellurite}}$, ~ 500 x $n_2^{\text{silica}}$ and ~ 1000 x $n_2^{\text{fluoride}}$) [21, 130-132]. In chalcogenide glass fibres the high non-linear coefficients are accompanied by negligible light absorption, which is extremely important for SCG. In a chalcogenide step-index optical fibre, the tendency to disperse due to high non-linear coefficients can be supplemented with a high difference between refractive index of the core/ cladding glass (on account of composition differences) resulting in better light confinement within the core. The difference in refractive index of the core and cladding glasses is discussed further in section 2.6.

In optical fibres, two approaches for generating SC are most commonly used; pumping a short length of highly non-linear fibre with femtosecond or picosecond pulses [133] or pumping for lengths > 100 m using continuous-wave (CW)/ quasi-CW sources [134]. These supercontinuum sources based on optical fibres are advantageous as they have high brightness broadband outputs with well-defined beam shapes and divergences and spatial coherence.

It is worth mentioning that research within the MIR Photonics Group at the University of Nottingham, UK, (of which this Author is a member) running parallel to this Project has been focussed on developing rare-earth (RE)-doped fibre lasers. A MIR direct emissions fibre laser produced from RE-doped chalcogenide glass could pump MIR supercontinuum generation (SCG) to facilitate wideband, MIR molecular sensing, suggested in the Seddon medical diagnostic system shown in Figure 2.10 [3, 28]. MIR direct emission fibre lasers have advantages for medical application due to their small

size, the appliance is lighter and more compact, they should have good coupling efficiency and are flexible [135-137].

MIR SCG fibres based on chalcogenide glass have been extensively investigated both theoretically and experimentally [10, 11]. It is the combination of wide transmission range, strong nonlinear properties and high optical damage threshold (e.g. > 12 GW/$\mathbf{cm^2}$ for picoseconds pulses at 2.4 μm in $\mathbf{As_2S_3}$) [11] that make chalcogenide fibres an ideal system for fibre based supercontinuum laser sources. Shaw *et al.* demonstrated the first MIR SCG using chalcogenide fibres in 2005 [12]. The supercontinuum source was limited in spectral range (2–3.5 μm) and average power (<10 mW). In 2012 Gattass *et al.* achieved 565 mW broadband SC covering the wavelength range from 1.9-4.8 μm at – 20 dBm, with a step-index core/cladding $\mathbf{As_2S_3}$ fibre (10 μm diameter core, NA ~0.3) [11]. A broad, flat SC occurred from 2.0 – 4.6 μm at -10 dB, as shown in Figure 2.12.

A 40-picosecond pulse duration seed (10-MHz erbium-fibre-based laser) with 200 mW average output power was used. Prior to propagating through the chalcogenide glass fibre, the optical beam was centred at 2.45 μm, had ~ 100 nm bandwidth and ~1.4 W of average power output.

Yu *et al.* accomplished promising SCG results spanning 2.5–7.5 μm using 20 mW peak pump power 150 fs pulses at 5.3 μm [13]. However, 5 mm bulk chalcogenide glass, GeAsS, was used rather than an optical fibre. In 2014, within the MINERVA project (see section 2.4.1), the MIR Photonics Glasses Research Group at the University of Nottingham, UK, in conjunction with the Group of Prof. Bang of DTU, Denmark, demonstrated fibre-based MIR SCG from 1.4-13.3 μm using a core (16 μm diameter) $As_{40}Se_{60}$, cladding $Ge_{10}As_{23.4}Se_{66.6}$ high numerical-aperture optical fibre,

Figure 2.13 [2].

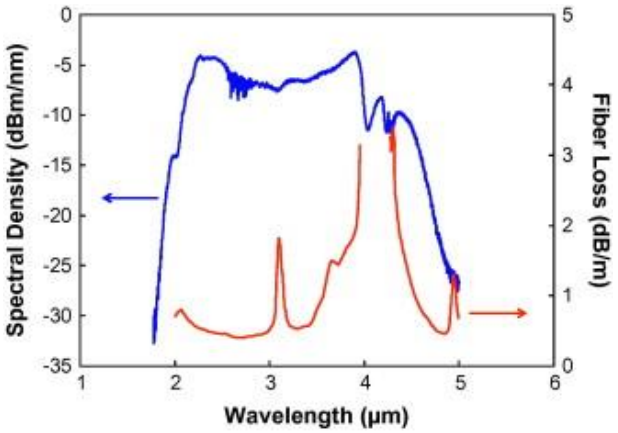



**Figure 2.12 Supercontinuum (SC) spectrum (blue curve) and fibre loss results (red curve) for a step-index core/cladding $As_2S_3$ fibre (10 μm diameter core, NA ~0.3) reported by Gattass *et al.* [11]. A 40-picosecond pulse duration seed (10-MHz erbium-fibre-based laser) with ~ 200 mW output power was used. Prior to propagating through the chalcogenide glass fibre, the optical beam was centred at 2.45 μm, had ~ 100 nm bandwidth and ~1.4 W of average power output. After propagating through the chalcogenide fibre, 565 mW broadband SC was observed. It can be seen that at – 20 dBm the SC spectrum spanned from 1.9 to 4.8 μm and the system provided 10 dB spectral flatness over 2.0 – 4.6 μm wavelength.**

Their record breaking result achieved MIR spectra containing more than 3 octaves in bandwidth making it the widest demonstrated supercontinuum (pumped with 100 fs (full width at half-maximum) pulses at 6.3 μm). –20 dB of spectral flatness occurred from 1.64–11.38 μm. In 2016 Zhao *et al.* [14] demonstrated MIR SCG from ~1.5- 14 μm in a 23 cm long $Ge_{20}As_{20}S_{20}Se_{15}Te_{45}/Ge_{20}As_{20}Se_{17}Te_{43}$ step-index fibre. A 4.5 μm laser was used using a pulse width of 150 fs and 1 kHz. Cheng *et al.* [15] also reported in 2016 the broadest MIR SC covering the 2.0 – 15.1 μm region in a 3 cm long $As_2Se_3/AsSe_2$ fibre pumped in the anomalous dispersion regime (using a pulse width of ~ 170 fs, a repetition rate of ~ 1000 Hz and a wavelength range tuneable from 2.4 to 11 μm). The broadest MIR SCG to date generated in a Ge-Sb-Se fibre was reported by Ou *et al.* spanning from ~1.8 to ~14 μm with a 20 cm long $Ge_{15}Sb_{25}Se_{60}/Ge_{15}Sb_{20}Se_{65}$ fibre pumped with 150 fs pulses at 6.0 μm [16].

This greatly increased luminous intensity of supercontinua is an advantageous gain in sensitivity and wavelength selectivity. MIR broadband SC lasing fibre has the potential to rival and exceed the brightness of MIR light from a synchrotron. The possibility of a portable, bright MIR wideband source is the first step for the MIR remote spectroscopy system for the medical diagnostics (discussed in 2.4.1) to become a reality.

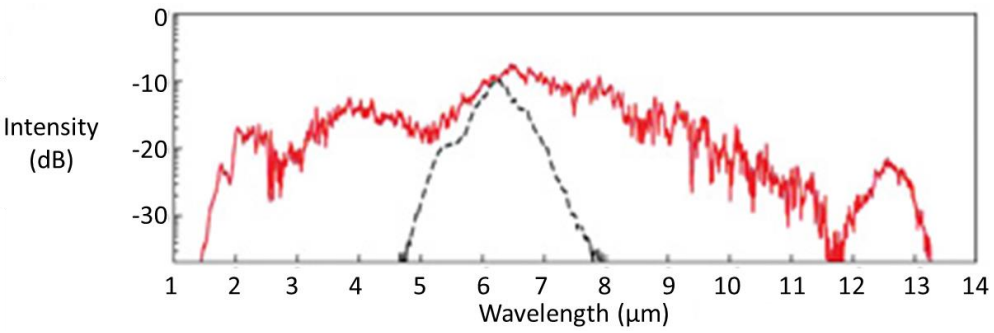



**Figure 2.13 The record breaking MIR SCG by the MINERVA group [2]. A broad, flat SC (1.64–11.38 μm at –20 dB) is shown (solid line is spectral profile at maximum pump power) followed by a strong spectral peak extending the spectrum to 13.3 μm. The dashed line is the input pump spectrum**.

## 2.6. Chalcogenide glass optical fibres

In section 2.1 it was established that the ideal glass for optical fibres provides a combination between a strong resistance towards crystallisation (*e.g.* high viscosity) and a large transparent optical window.

The properties of chalcogenide glasses satisfying the requirements of a MIR glass were discussed in section 2.1.1 and the Ge-Sb-Se chalcogenide glass system used in this Project was described in section 2.1.2. Furthermore, chalcogenide glass fibres have proven themselves to be efficient broadband generators of SCG light, section 2.5. The broad MIR transparency of chalcogenides allows the SC to be extended well into the MIR, and this is now the subject of active research.

Chalcogenide glasses have been known as optical materials for more than 50 years [138]. The first published report on their potental for fibre optic applications using As-S glass, was made in 1965 by Kapany *et al.* [139]. For the last 25 years there has been much active research of chalcogenide glass fibres for fibre optics in the MIR. When transmitting light along a fibre, it is important that the maximum amount of light enters the fibre at the launch end. Excluding reflection loss at the input interface, the greatest amount of light that can be accepted by a fibre (the aceptance angle, $\propto_m$) is determined by a fibre's Numerical Aperture (NA) [140]. For fibre MIR SCG, a large difference is desirable between the refractive indices of the core and cladding to generate as large a NA as possible to control the fibre dispersion. NA characterises the range of angles over which a fibre can accept or emit light, calculated using Equation 2.9.

$$\boldsymbol{NA = (n_{core}^2 - n_{cladding}^2)^{\frac{1}{2}} = sin \propto_m} \qquad \textbf{Equation 2.9}$$

where $n$ is the refractive index (the ratio by how much light will slow in a given material) of the core and cladding.

The first Ge-Sb-Se step-index core/ cladding fibre fabricated in this Project had a core composition $Ge_{22}Sb_8Se_{70}$ atomic (at.) % and a cladding composition $Ge_{24}Sb_4Se_{72}$ at. %. The refractive index from [83] measured at 1463 nm for the core and cladding glasses were, 2.549 ± 0.002 and 2.491 ± 0.003, respectively. Thus the NA was calculated to be 0.54. Table 4.12 collates the NA for all the glass fibres fabricated in this Project.

Total internal reflection (TIR) is the phenonenon which occurs when a propagating wave of light strikes a medium of a lower refractive index than the one it is transmitting through at an angle greater than the critical angle ($\theta_{crit}$), shown in Figure 2.14.

For power delivery applications (*e.g.* the medical diagnostic system discussed in section 2.4.1 and Figure 2.10) it is essential that the greastest amount of light possible is guided along a fibre.

In order for a material to transmit light radiation at a certain wavelength effectively, it must possess a multiphonon absorption cut-off smaller than the photon energy of the light. Photons with energies equal to or less than the mulitphonon absorption edge will be absorbed and promote atomic bond vibration. To access the MIR, standard silica glass fibres cannot be used as they lose their transparency after 2 µm, on account of their high phonon energy see section 2.1.1.

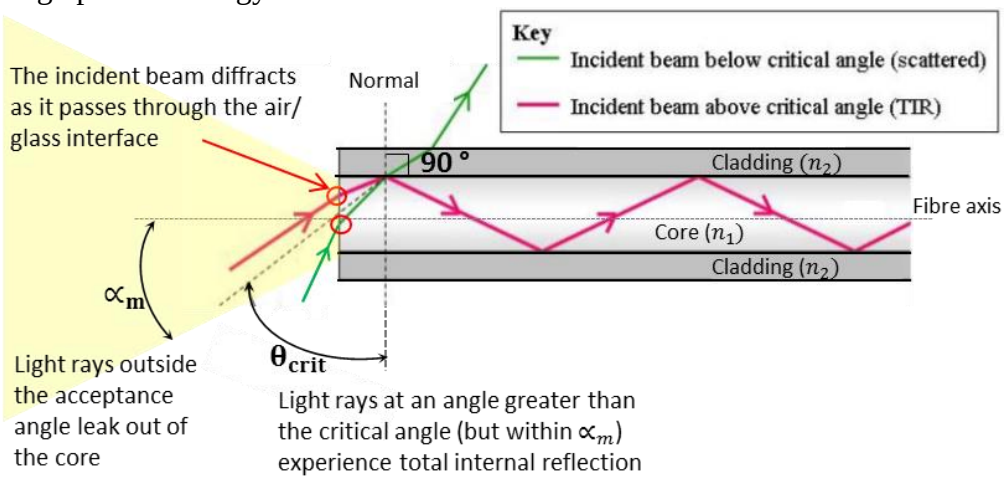



**Figure 2.14 Schematic diagram of light entering a step-index glass optical fibre where the refractive index of the core $(n_1)$ is higher than that of the cladding $(n_2)$. The incident beam diffracts as it passes through the air/ glass interface. The orange cone of light represents the acceptance angle ($\alpha_m$) and any incident beam will be guided by the fibre if it enters the fibre at an angle within the cone of the acceptance. Total internal reflection will occur if the incident beam is greater than the critical angle ($\theta_{crit}$) when it strikes the core/cladding boundary. Figure adapted from [47].**

Important characteristics of optical fibres for their exploitation are optical loss, spectral dependence and mechanical strength. The transmission of MIR in chalcogenide glass step-index fibres (SIF) is somewhat dependent upon the quality of the core/ cladding

surface through which the radiation passes, determined by the fabrication method (discussed in 2.6.1) and the optical loss level (discussed in section 2.6.2).

### 2.6.1. Fabricating chalcogenide glass optical fibres for MIR

There are a number of optical designs and different methods for fabricating core-cladding fibres to maximise MIR transmission. Single-index fibres (unstructured or core-only fibres) are designed with no glass cladding and SIF (structured fibres) have a glass cladding, see Figure 2.15. Both core-only and step-index fibres were fabricated in this Project and their optical properties are characterised in Chapter 6.

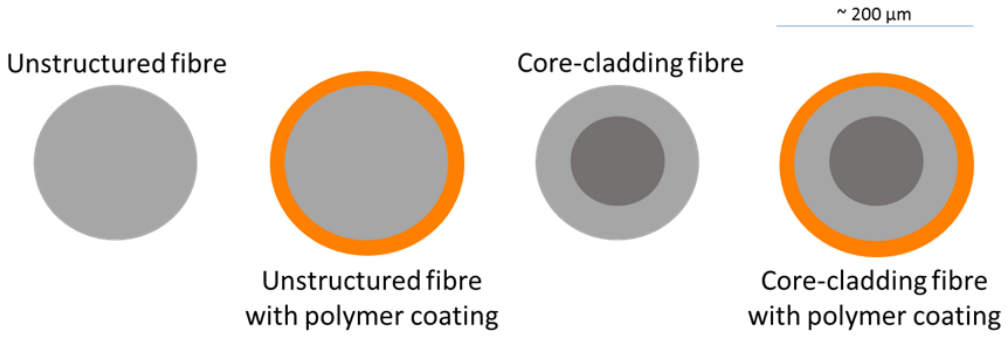



**Figure 2.15 There are a number of optical designs for fibres. Single-index (without the glass cladding or core-only fibres) and step-index (with the glass cladding). Polymer coatings can also be used to improve mechanical strength and resistance to degradation. 200 µm is a typical OD for ≤ 20 mm fibre bend radius.**

In 1953 Heel was the first to suggest the concept of double index fibres made from polymers [141]. As introduced in section 2.6 to enable total internal reflection, the refractive index of the core should be higher than that of the cladding [142]. Heel proposed coating a mono-index polymer fibre of a refractive index of 1.52 (diameter of ~1 mm) with a layer of lower index polymer with a refractive index of 1.47 [141]. He reported that the resulting core/cladding fibres were more efficient than mono-index fibres and could guide light even when bent (non-linear optical path)[141]. For the Ge-Sb-Se chalcogenide glasses synthesised in this Project, the required difference between

the refractive index of the core and cladding glasses was accomplished by having a higher composition of the cation Sb in the core. The Ge-Sb-Se glass system developed in this Project was discussed in section 2.1.2.

There have been several methods used to fabricate chalcogenide optical fibres. Usually fabrication is carried out by either drawing directly from the melt (single or double crucible method) or from a pre-fabricated single-rod, rod-in-tube or more complex rod (preform).

In the double crucible method, crucibles containing the core and cladding glasses are heated to above the liquidus (see Figure 2.1) and directed into a concentric double drawing nozzle [21]. The diameter of the core and clad are determined by the ratio of circular and annular channels of the drawing nozzle and by the volumetric flow rate of the core and cladding melts [21]. A pulling mechanism then draws the double-layered optical fibre and winds it onto a fibre drum. The rotation rate of the pulling mechanism and the pressure of the inert gas over the melt regulates the drawing rate and fibre diameter.

Core/ cladding fibres can also be drawn from pre-fabricated ‘rod-in-tube’ preforms, as performed in this Project. The fibre drawing procedure used in this Project will be given in section 3.5. To draw directly from a fabricated preform, the upper-end of the preform is fixed in a movable holder and lowered so the bottom-end of the preform is in the central hot zone inside a tubular resistance heater. While heating up the lower part of the preform to the glass transition temperature, its thickness decreases under the effect of gravity or drawing force with a formation of a gob (a drawing cone). Similar to the double crucible method, the pulling mechanism then draws the preform and onto a fibre drum. A purified inert gas may be supplied into the drawing zone to preclude oxidation

of the heated chalcogenide glass. The rate of heating and the speed of the rotation of the fibre drum regulates the drawing rate and fibre diameter.

For both the double crucible and drawing directly from a preform methods, optical fibres are produced at a drawing rate from 1-10 m $min^{-1}$, with typically an outer diameter of 0.1-0.8 mm and a core diameter from 3-600 µm [21, 22]. Each of these methods of optical fibre production has its own merits and limitations. The double crucible method is beneficial as it can provide a high-quality surface resulting in high mechanical strength of optical fibres. However, it is preferable to manufacture fibres with a low tendency to crystallise using the crucible method, such as fluoride glasses. Drawing from a preform allows, perhaps, easier control of the ratio of core-cladding diameters. A protective coating (such as F-42 fluoroplasic [21] polyvinylchloride and photocuring polyacrylates [143]) can be applied to the optical fibres. Churbanov *et al.* [144] investigated the stability and mechanical properties of optical chalcogenide glass fibres, *e.g.* $As_2S_3$. They reported that, with a glass cladding and a well-protected surface (such as a polymer coating), the fibre remained stable in terms of mechanical strength and optical loss for three years. Furthermore, they observed degradation of optical and mechanical properties in optical fibres with no protective coating over the three year period. Attempts were made to apply a polymer coating to the Ge-Sb-Se chalcogendide fibres fabricated in this Project. However complications arose due to equipment malfunction whilst applying the polymer coating online, which will be discussed in Chapter 5.

Preforms can be fabricated by several methods such as core drilling, rotational casting or extrusion [23-26] . Special attention must be paid in the ‘rod-in-tube’ method as the internal and external surfaces of the core rod and cladding tube must be optically smooth and chemically pure to maintain a low loss core/ cladding interface in the fibre.

It has been reported that it can be difficult in core drilling to achieve the required surface finish and close fit between the rod and the tube necessary to reduce scattering [23, 24]. Rotational casting is more complex than core drilling, requiring a lathe-mounted mould into which the molten glass is poured and spun during cooling, however it can produce preforms with much smoother internal surfaces. [25, 26]. However, it has been reported that the tube geometry is hard to control and the core's outer surface cools in direct contact with the silica glass ampoule, which can lead to potential defects at the core/ cladding interface [27].

Fibre preforms were fabricated in this Project using the extrusion process. As will be described in section 3.4 two separate extrusions were performed fabricating a co-extruded core/ cladding rod and a outer cladding tube extrusion. It is suggested that this technique produces low interface roughness and therefore lowers scattering losses. The fibre loss measurements conducted for the Ge-Sb-Se glass fibres fabricated using this method are described in Chapter 6. Furthermore it is suggested that a benefit of the extrusion process is the removal of chalcogneide glass that has been in contact with the silica glass ampoule, this will be discussed further in section 5.1.

### 2.6.2. Fabricating high purity chalcogenide glass

The first reports of chalcogenide glass optical fibres by Kapany *et al.* using aresenic-sulfide had exhibited high optical loss > 10 dB/m in the 2-8 µm wavelength range [139]. Optical losses in glasses are observed in the transmission spectra of the optical fibre samples. They are a combination of selective absorption (the position of which is determined by the impurity's nature), the scattering from structural defects, Rayleigh scattering and scattering from the interactions of these impurities and defects [145]. Optical loss still remains a great problem for chalcogenide optical fibres to achieve high

transparancy and has limited their use to relatively short fibre lengths. Recently, light transmission has been proven through 83 m by the MIR Photonic Group, University of Nottingham, UK [146]. Much investigation has been directed at increasing the chemical and phase purity of the glasses.

Loss can be considered as intrinsic loss (the absorption and scattering loss inherent to a material and therefore unavoidable) and extrinsic loss (the loss due to absorption and scattering caused by impurities), Figure 2.16. The major characteristics of intrinsic loss are: the electron and multiphonon absorption; the absorption due to free charge carriers; scattering (predominantly Rayleigh) and the loss due to the "tail of weak absorption" [147]. The intrinsic cut-off absorption edges are at short and long wavelengths and define the transmission window. The short wavelength absoprtion band-edges for the Ge-Sb-Se chalcogenide bulk glasses studied in this Project are shown in Chapter 4, Figure 4.4(a) along with the vibrational absorptions of the impurities in the glass and their respective functional groups, Figure 4.4(b).

Extrinsic optical losses originate from either glass defects or impurities in the glass [147]. Crystallisation (devitrification) of a glass super-cooled melt can dramatically raise the optical loss due to unwanted light scattering of a glass or fibre. Crystallisation is due to phase-separation occurring when a homogenised glass super-cooled melt spontaneously changes into this type of two phase system, see line b-c on the phase diagram in Figure 2.1; such crystals could then scatter the radiation transmitted through the optical glass or fibre.

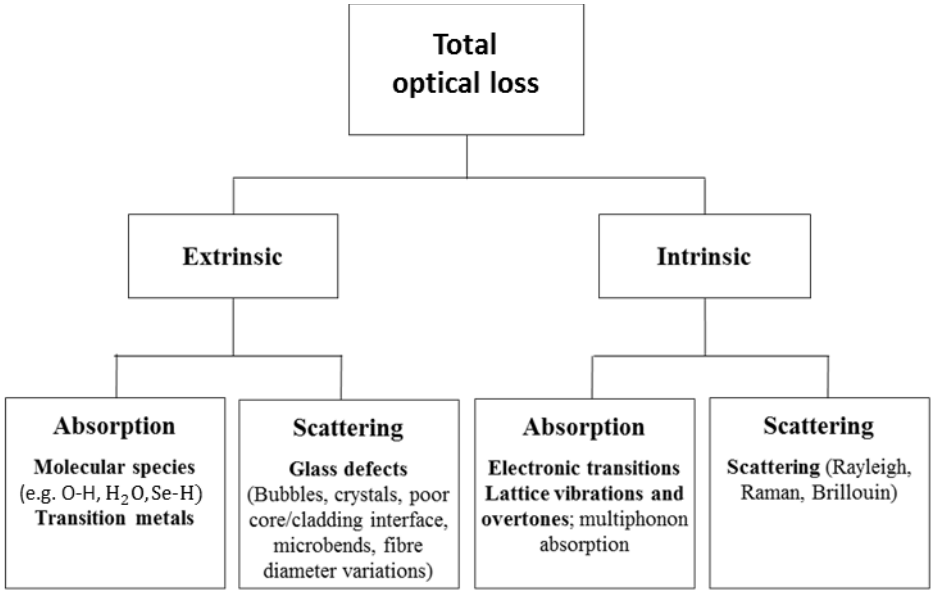



**Figure 2.16 The loss mechanisms contributing to the total optical loss of optical glasses: chalcogenide glasses.**

Thermal processes involved in glass synthesis (*e.g.* cooling of the melt into glass and annealing, see section 3.2.4 for the techniques used in this Project) and optical fibre fabrication (*e.g.* extrusion and fibre drawing, see section 3.4 and section 3.5, respectively) increase the risk of crystallisation if non-optimum time-temperature modes are used. The process of crystallisation involves the rearrangement of atoms, and therefore a high viscosity indicates a resistance to devitrification. Viscosity/ temperature measurements of the Ge-Sb-Se chalcogenide glasses will be discussed in Chapter 4, section 4.2.3.1. The study of the phase-crystallisation behaviour of the as-prepared bulk Ge-Sb-Se chalcogenide glasses will be reported in Chapter 4, section 4.2.2 using DTA analysis.

In this Project it was considered that the three main sources of impurities in the Ge-Sb-Se chalcogenide glasses were;

(i) The silica glass ampoule utilised for the synthesis of glass-forming melt.

(ii) The gaseous environment during synthesis and treatment of the Ge-Sb-Se glasses.

(iii) The initial precursor elements used for synthesis of the Ge-Sb-Se glasses.

These three sources are now considered in more detail:

(i) The pre-treatment of the melt ampoules (*i.e.* annealing, HF-etching, air and vacuum baking) will be described in detail in section 3.1.1. Troles *et al.* found that hydrogen started to enter a $GeSe_4$ chalcogenide glass melt from a silica glass ampoule (with 100 ppm hydrogen content) at 650 °C [148, 149]. Products of the chemical interaction of the chalcogenide glass and the impurities in the silica glass ampoule can form at the chalcogenide glass and silica ampoule interface [150]. These impurity interaction products can enter the melt and form heterophase inclusions. Heterophase inclusions consist of substances which are not readily soluble in chalcogenide glass melts (for example elemental carbon and silicon dioxide). They can be the centres of nucleation (the initial state of crystal formation) and initiate heterogeneous crystallisation (leading to absorption and scattering loss). They can also decrease the mechanical strength and laser damage resistance of optical fibres [150]. Snopatin *et al.* reported that to achieve optical losses at the level of intrinsic losses, the content of impurities of oxygen, carbon and silica should not exceed 0.1-10 ppb wt. [22]. Churbanov *et al.* suggested that the tolerable content of heterophase inclusions is $10^3$-$10^4$ $cm^{-3}$ [21, 22, 145].

(ii) Impurities and glass defects can be reduced by careful fabrication and reducing precursor elements and glass melt exposure to the atmosphere. Chalcogenide glasses are prone to oxidation at high temperatures. Furthermore, elemental Se and Sb oxidise in atmospheric conditions, even at room temperature. Therefore,

strict procedures were implemented in the laboratory to prevent atmospheric exposure, as will be described in Chapter 3, section 3.2.2. For the research in this Project all elements are batched and stored in a glovebox (< 0.1 ppm $H_2O$, < 0.1 ppm $O_2$; MBraun).

(iii) In this Project, the precursor elements Se and Sb were always subjected to an *in-situ* purification step before glass melting by heat-treatment to evolve high vapour pressure contaminants, see section 3.2.1. It has been found in this Project that purifying the Se and Sb had a dramatic effect on reducing the oxide and hydride content in the final Ge-Sb-Se chalcogenide glass fibre, see Figure 6.3 for fibre loss results.

As, Ge, Sb and chalcogens have been extensively investigated and developed for semiconductor applications, with heavy emphasis on reducing electrically active components, such as metal impurities [151-153]. Thus commercially available initial batching elements contain relatively low concentrations of metal impurities (0.1-0.01 ppm wt.), however they contain a high content of hydrogen and oxygen (1-100 ppm wt.) [151-153]. The source and stated purity of the precursor elements used in preparing the Ge-Sb-Se chalcogenide glasses reported in this Project will be given in Table 3.3. The effect of oxygen impurity upon glass transparency is most important in 7-14 µm spectral range and the effect of hydrogen is most significant in the shorter wavelength range 2.5-6.5 µm [154].

The literature reports many different techniques to reduce impurity levels; including heat treatment under vacuum to remove surface oxides [17] (conducted in this Project), chemical distillation with an oxygen getter [155], distillation of high purity starting elements [21], treatment with tellurium halides or reactive chlorine atmospheres [156] and high-temperature oxidation for purifying chalcogenides [157].

Chemical vapour deposition (CVD) has been a successful method in producing high purity silica glass, Equation 2.10.

$$\mathbf{SiCl_{4\ vapour} + O_{2\ gas} \xrightarrow{heat} SiO_{2\ solid} + 2Cl_{2\ exhaust\ gas}} \qquad \textbf{Equation 2.10}$$

The refractive index of the core of a silica optical fibre can be adjusted by reacting a small amount of the dopant $GeO_2$ from $GeCl_4 + O_2$. Silica optical fibres are widely used in telecommunications and have been extensively researched and studied [158]. The technology is now mature and silica glasses are nearly flawless candiates for NIR transmission with field loss of 0.2 dB/ km at 1.55 µm [158].

CVD has the advantage that it allows the glass precursors to distill leaving behind less volatile impurities. The condensed glass 'soot' produced is consolidated by means of viscous flow to form a glass rod preform (thus no above the liquidus is necessarily required) with the desired refractive index profile.

Currently, to this Author's knowledge, to date CVD technologies have not been used in chalcogenide glass fibre fabrication. This is probably due to the their multi-component nature, differing vapour pressures, high volatility and the similar binding energies of the components (*e.g.* homopolar bonds) [159-161]. However, Hewak *et al.* are undertaking the challenge of adapting current chalcogenide fibre manufacturing for CVD proposing that it has the potential to radically improve chalcogenide glass fibre quality and optical transmission [162].

In 1985 Saito *et al.* fabricated a core/ cladding ( $As_2S_3$: $AsS_3$) glass fibre by depositing a thermally evaporated layer of the cladding onto a conventionally melted core rod preform [163]. After drawing to fibre they achieved a minimum optical fibre loss of 0.6 dB/m at wavelengths of 3.3 µm and 4.8 µm. in 1998 Sanghera *et al.* [128] patented a silica glass rig designed to purify homogenised chalcogenide glass. The process

involved melting and homogenising the chalcogenide glass using the method described in section 3.2.4. The glass was then crushed and batched into the distillation ampoule, along with a getter. Chemical getters are introduced into the homogenised glass by heating above the liquidus and holding at high temperature. To remove the oxygen (O) containing impurities from the melt selected metals (such as aluminium (Al) and magnesium (Mg)) may be used that chemically bond preferentially to O to form oxides. These oxides are left behind when the glass is distilled. For example if an Al getter is used, during the melting procedure O is bound with the formation of low-volatile oxide, $Al_2O_3$ [47] (and MgO is formed if a Mg getter is used [47]). For binding to the hydrogen (H) containing impurities, chlorine (Cl) and chlorides of glass forming elements are used. Tellurium chloride [45] ($TeCl_4$) can remove H by binding to form HCl.

Rowe [47], Savage [43] and Sakr [46] of the Mid-Infrared Photonics Research Group at the University of Nottingham,UK, optimised this purification procedure. However, it is worth noting that not all homogenised chalcogenide glasses can be distilled. Sakr reported that a Ge-As-In-Se glass could not be distilled congruently [46]. It was found that the indium (In) had not distilled and had remained in the input chamber.

Chalcogenide glasses can also be synthesised from high purity precursor elements, Figure 2.17 [21, 156, 164]. For the distillation technique, high-purity (usually) elements, (such as Sb, As or Se) may be transferred into a melt-synthesis reactor by evaporation from initial ampoules in an evacuated all-sealed system, in an oil-free high vacuum (*e.g.* $10^{-5}$ Pa). Once distilled, the synthesis reactor maybe sealed off and the melt can then be homogenised in a rocking furnace (*e.g.* at ~ 750 °C for 7 hours for an $As_2Se_3$ melt [21]).

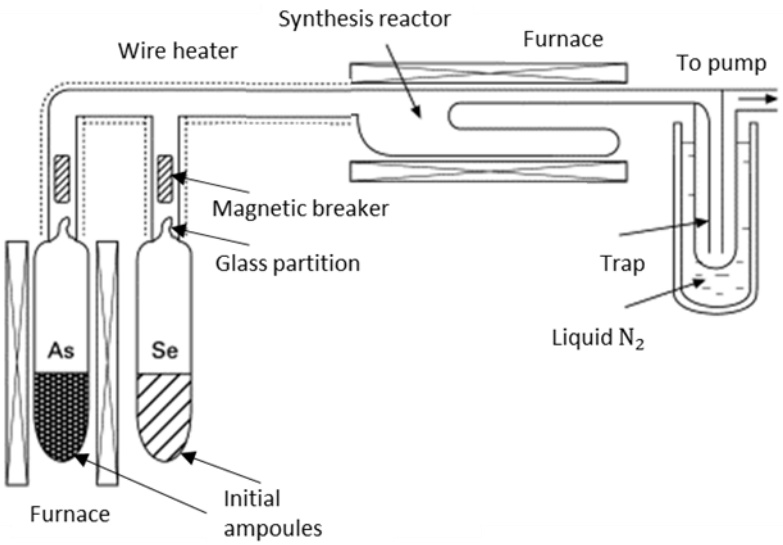



**Figure 2.17 Diagram to illustrate distillation of raw precursor elements from initial ampoules to a synthesis reactor, in a vacuum, for fabrication of high-purity chalcogenide glasses after the Group of Churbanov. Adapted from [21].**

A research group in Russia headed by M. F. Churbanov[3] are the fore-runners in fabricating the highest purity chalcogenide glasses. Their vast experience and knowledge in combining chemical and double distillation methods has led to world-record breaking results [164]. They have achieved losses of 12 dB/km at 3 µm wavelength for a double layered $As_2S_3$ optical glass fibre [22]. More recently in 2015 they reported losses of 70 dB/km at 2.7 and 3.8 µm for an unclad $As_{35}Se_{65}$ optical glass fibre [165] and for a core-cladding $As_{40}Se_{60}/As_{38}Se_{62}$ optical glass fibre, they reported a loss of 67 dB/km at 6-6.6 µm wavelength [165]. They have also achieved low loss of 0.5 dB/m at 1.7-7.5 µm for a $GeS_4$ optical glass fibre [148], however the Se-H absoprtion peak at 4.5 µm dominated and gave rise to a loss of 2.8 dB/m at this wavelength.

Shiryaev[4] and Tang[5] worked in collaboration to produce a world record, executed at the University of Nottingham, for the lowest loss value achieved for an unclad

[3] Professor Mikhael. F. Churbanov, Russian Academy of Science, Moscow, Russia.
[4] Professor Vladamir Shiryaev, Russian Academy of Science, Moscow, Russia.
[5] Dr. Zhuoqi Tang, Mid-Infrared Photonics Glasses Research Group at the University of Nottingham.

$Ge_{10}As_{21}Se_{69}$ optical glass fibre with a loss of 83 dB/km at 6.6 µm [164]. This current Author further optimised new apparatus to fabricate high purity glasses, as will be discussed in Chapter 6, section 6.4.

## 2.7. Summary

Glass science fundamentals were discussed in section 2.1, along with a background study of the properties of chalcogenide glasses in section 2.1.1 and an introduction to the Ge-Sb-Se glasses used in this Project in section 2.1.2. Chalcogenide glass preparation and further characterisation of the bulk Ge-Sb-Se for optical studies is discussed in Chapter 3 and Chapter 4, respectively. The theory behind the neutron diffraction method used to study the structure of a stoichiometric Ge-Sb-Se chalcogenide glass system along the tie-line $x(GeSe_2)$-(1-x)( $Sb_2Se_3$) was explained in section 2.2, and results obtained will be presented and analysed in Chapter 8. The concept of electromagnetic wave interaction with atoms and molecules was introduced in section 2.3, with particular focus on the MIR spectral region in section 2.3.1. An insight into the important role chalcogenide glasses could play for the potential development of a MIR remote spectroscopy system for medical diagnostics and early diagnostics of cancer was given in section 2.4. It was established that exploiting the MIR spectral range, 3- 25 µm, is promising for a novel MIR remote spectroscopic sensing system proposed by Seddon [3, 28] and being worked towards in MINERVA, section 2.4.1. However there are still several hurdles to overcome to reach clinical application as discussed in section 2.4.2. Before chalcogenide glasses are used for clinical applications, it is important to assess the cytotoxicity of the glass. Preliminary cytotoxicity tests of Ge-Sb-Se based glasses and fibres will be presented in Chapter 7. For the diagnostic system being proposed by Seddon, it is important to develop new glass optical fibres to deliver bright, broadband MIR-SCG light. A brief explanation of

SCG was provided in section 2.5 along with the current status of SCG. The fabrication of small-core Ge-Sb-Se MIR-SCG fibres will be described in Chapter 5. The considerations and development of fabricating chalcogenide optical fibres were discussed in section 2.6. Much investigation has been directed at increasing the chemical and phase purity of chalcogenide glasses and developing optical fibres to optimise their transmission efficiency, section 2.6.2. The fabrication of low-loss chalcogenide glass fibres has remained challenging, mainly due to the following two reasons: the natural tendency of absorption of impurities in raw materials and high vapour pressures of constituent elements at temperatures. Methods to optimise MIR optical fibre both in fibre fabrication and producing high purity optical glasses, will be discussed in Chapter 6.

# 3. Glass preparation and characterisation methods

In this Chapter, an overview of the experimental procedures and techniques for Ge-Sb-Se chalcogenide glass preparation, reported in the later Chapters 4-8, are given. Two series of Ge-Sb-Se chalcogenide glasses were synthesised in this Project, both using the melt-quenching method. The as-prepared Ge-Sb-Se glass compositions for optical studies varied and are detailed throughout Chapters 4-7. The as-prepared Ge-Sb-Se glass composition for structural studies, were based on the stoichiometric tie line $x(GeSe_2)$-(1-x)( $Sb_2Se_3$), where x = 0.9, 0.8, 0.7, 0.6, 0.5 and 0.4, as will be discussed further in Chapter 8. All the Ge-Sb-Se chalcogenide glass compositions synthesised for optical studies and the stoichiometric tie-line of the glass series for structural studies were shown in Figure 2.5.

Section 3.1 explains the silica glass ampoule selection and the ampoule pre-treatment, and section 3.2 presents the steps of Ge-Sb-Se chalcogenide glass synthesis from raw materials within these ampoules. Ampoules are described in terms of their outer diameter (OD) and inner diameter (ID) dimensions. All Ge-Sb-Se chalcogenide precursors were stored in a glove-box (MBraun, 150B-G, under $N_2$ atmosphere, < 0.1 ppm $H_2O$, < 0.1 ppm $O_2$) and all batching was conducted within the glove-box. Precursor purification and silica ampoule sealing was conducted under a dynamic high vacuum, $10^{-5}$ Pa (Rotary pump, (to $10^{-2}$ Pa, VRC 200-7.0) and then a diffusion pump (to $10^{-5}$ Pa, Edwards B30207240)). Details of how to open the sealed ampoules to obtain the Ge-Sb-Se chalcogenide glass rods and the preparation of the glass rods are presented in section 3.3. Section 3.4 describes two different extrusion methods: core/ cladding co-extrusion and tube extrusion. Fibre drawing is explained in section 3.4. The full process time in achieving a Ge-Sb-Se chalcogenide glass optical fibre batched from

raw materials was approximately three weeks. Section 3.6 covers the Ge-Sb-Se chalcogenide glass characterisation techniques including: X-ray diffraction (XRD; section 3.6.1); density (section 3.6.2); differential scanning calorimetry (DSC; section 3.6.3); differential thermal analysis (DTA; section 3.6.4); thermal mechanical analysis (TMA; section 3.6.5) including viscosity/ temperature analysis (section 3.6.5.2) and thermal expansion coefficient (TEC; section 3.6.5.3) and Fourier transform infrared spectroscopy (FTIR; section 3.6.6) including bulk transmission (section 3.6.6.2) and fibre characterisation achieved using the fibre loss "cut-back" method (section 3.6.6.3). Compositional and fibre structure analysis from imaging using scanning electron microscopy (SEM) equipped with analytical energy-dispersive X-ray spectroscopy (EDX) is described in section 3.7. Other characterisation techniques including near-field imaging, distillation, biological assays and neutron diffraction experiments are explained elsewhere in this Thesis- in Chapter 6, Chapter 7 and Chapter 8 respectively. The SEM methodology (section 3.7.3) was also used to analyse cell proliferation after biological studies, however the sample preparation is discussed in Chapter 7. All the details for each specific melt, distillation, extrusion and fibre drawing were recorded on their appropriate sheets, typical examples of which are shown in Appendix I.

## 3.1. Preparation of silica glass ampoules used for chalcogenide glass melting

This section details the similar preparation stages that were followed to fabricate all the Ge-Sb-Se chalcogenide bulk glass rods reported throughout this Thesis. Although the intrinsic loss (the loss inherent to a material) cannot be reduced, efforts to minimise extrinsic loss factors (the loss due to absorption and scattering caused by impurities; discussed in section 2.6.2 and analysed further in Chapter 6) were made throughout glass preparation. Materials of high purity were used in the glass preparation in this Project; however chalcogenide glasses are extremely susceptible to hydrolysis and

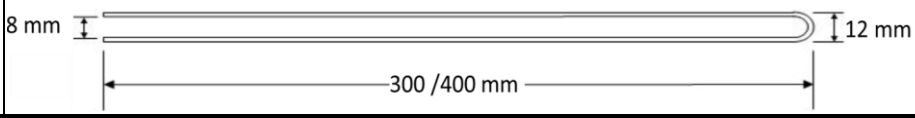
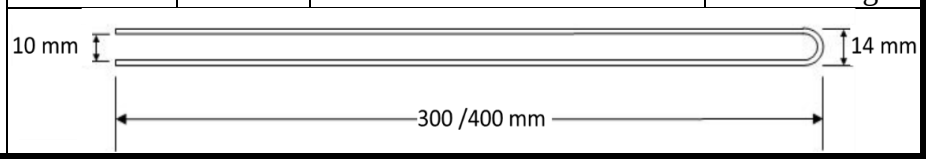
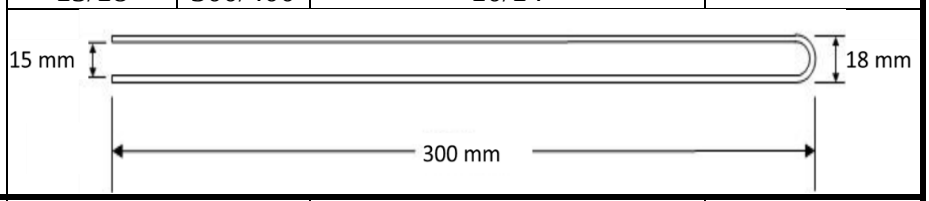
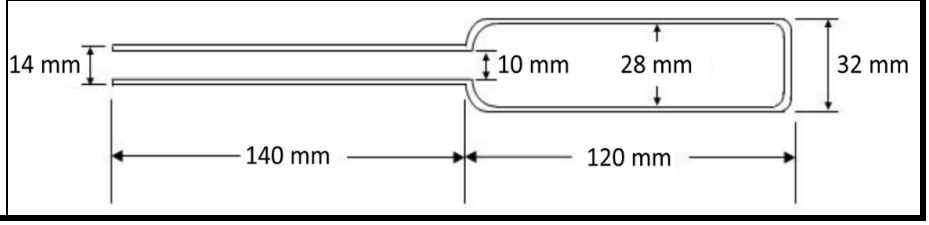
oxidation from the surrounding environment [166]. Thus exposure of the precursor elements to air was minimised viz.: batching in a glove-box, evacuating and sealing silica glass melting ampoules.

### 3.1.1. Silica glass ampoule selection

Silica glass ampoules (H. Baumbach & Co Ltd.; < 1 ppm –[O-H]; received annealed and HF-etched) were used as the containment vessels for the Ge-Sb-Se chalcogenide glass elements. Several ampoule sizes were used for glass rod synthesis, based on the intended application of the glass, see Table 3.1. To make glass rods of the required size for the vanadium cans used in the neutron diffraction experiments (which will be discussed later in Chapter 8) 8/12 mm ID/OD ampoules were used. For general chalcogenide characterisation, where a small batch (~5 to 7 g) was needed, 10/14 mm ID/ OD ampoules were used. For a structured co-extruded core/ cladding chalcogenide glass preform it was necessary to melt two boules separately each in a 15/ 18 mm ID/OD ampoule to create the necessary geometry for the extruder barrel (section 3.4.1). For the outer cladding glass melts for tube extrusion (section 3.4.2) a flat bottom ampoule with a 28 mm ID main body was used to facilitate boule preparation as the flat bottom end did not need to be cut to size. The ampoule selections are summarised in Table 3.1. Each ampoule was inspected and checked for any damage (*e.g.* scratches, chips and cracks) before it was used. If such damage was found the ampoule was discarded. Silica glass has a glass transition temperature ($T_g$) of ~ 1200 °C [58] whereas the melting temperature of the Ge-Sb-Se chalcogenide glasses reported in this thesis is < 900 °C, thus silica glass ampoules were appropriate vessels to contain the chalcogenide glass during melting.

However, although the silica glass ampoules could withstand the melting temperatures of Ge-Sb-Se chalcogenide glasses, it was suspected that the chalcogenide glass could react with $SiO_2$ at elevated temperatures (> 650 °C) [149]. It was thought that the products of this reaction were partially responsible for the O-H and water impurities that presented themselves in the absorption spectra (*e.g.* in the wavelength range 2-10 µm of the finished Ge-Sb-Se chalcogenide glass, see Chapter 6). This was due to the transfer of H, O-H and $H_2O$.

**Table 3.1 Ampoule geometry was chosen based on the intended application of the chalcogenide glass. The size, in terms of inner and outer diameter (ID, OD), length and shape are given.**

| Intended application | Ampoule dimensions (ID / OD, mm) | Length (mm) | Dimensions of silica insert for Se purification (ID / OD, mm). Each 180-280 mm in length | Typical batch weight for ampoule size (g) |
|---|---|---|---|---|
| Structural studies | 8/12 | 300/400 | 5/7 | |
| |  | | | |
| Bulk glass analysis | 10/14 | 300/400 | 7/9 | 15 ± 0.5 g |
| |  | | | |
| Core/ cladding co-extrusion | 15/18 | 300/400 | 10/14 | |
| |  | | | |
| Outer cladding tube extrusion | 28/32 (mm, ID/ OD; L=120 mm) main body.<br>10/14 (mm, ID/OD; L=140 mm) neck. | | 7/9 for neck | 100 ± 0.5 g |
| |  | | | |

The preparation of the Ge-Sb-Se chalcogenide glass rods, is divided into two sections: silica glass ampoule preparation (section 3.1.2) and chalcogenide glass rod fabrication (section 3.2).

### 3.1.2. Silica glass ampoule preparation: air and vacuum baking

The silica glass ampoules (< 1 ppm –[O-H]) were HF-etched (40 % for 10 ± 1 minutes) by the supplier, Baumbach, to reinforce the mechanical strength of the inner surface. Ampoule annealing was also conducted by Baumbach to remove any residual tension. Carbon deposits were extracted in-house by air baking, performed in a vertical furnace (Instron, TF105/4.5/1ZF) tube ID 86 mm, 450 mm in height, with a controller (Eurotherm 2408). The ampoule was placed into the furnace with the unsealed end at the top in an air atmosphere of a 10,000-class clean room. The furnace temperature was gradually increased to 1000 °C, for the air baking schedule see Table 3.2. Air baking at 1000 °C aids the removal of any carbon (*e.g.* dust and grease) on the silica glass ampoule by oxidation to $CO_2$ gas which can then exit the ampoule.

**Table 3.2 Standard air and vacuum baking process for purification of the silica glass ampoules.**

| Stages | Process |
|---|---|
| 1 | Step to 70 °C, dwell 0.1 h |
| 2 | Ramp to 1000 °C at 200 °C/h, dwell 6 h |
| 3 | Ramp to 70 °C at 200 °C/h, dwell until collection |

Vacuum baking was then applied to remove physisorbed and chemisorbed water ($e.g. H_2O$ and –[O-H]) from the inert ampoule surface. An O-ring (Imperial nitrile O-ring, RS Ltd.) was placed around the ampoule, approximately 10 mm from the open

end of the ampoule, to avoid glass-metal contact and to assist in tightly sealing the valve.

A drawing vacuum, ~$10^{-5}$ Pa ($10^{-7}$ mbar), was established using a vacuum valve (Pfeiffer Ltd.) connected to a vacuum turbo-pump (FIFA Turbo-drag Cube, Pfeiffer Ltd.) to evacuate the ampoule. The same furnace and baking schedule was applied as for air baking, Table 3.2. The air and vacuum baked silica glass ampoule was then transferred to a glove-box. The ampoule was either used immediately or stored in a glove-box for a short period (≤ 2 days with the vacuum valve still attached until use) for Ge-Sb-Se chalcogenide glass batching and synthesis, section 3.2.

## 3.2. Ge-Sb-Se chalcogenide glass rod synthesis

This section details the steps required to prepare a Ge-Sb-Se chalcogenide glass rod. The source, state and purity of the chalcogenide glass precursors are listed in Table 3.3.

**Table 3.3 Source and stated purity of precursor elements used in preparing Ge-Sb-Se chalcogenide glasses reported in this thesis including; supplier, nominal purity and description. The solvents used during processing are also listed. Key: N is nine.**

| Component | Description | Source | Product code | Purity |
|---|---|---|---|---|
| **Sb** | 1 -4 mm pieces | Materion | A-1190 | 6N (*i.e.* 99.9999 %) |
| **Ge** | 3-6 mm pieces | Materion | G-1038 | 5N |
| **Se** | 3 mm diameter shot | Materion | S-1037 | 5N |
| **Acetone** | liquid | Sigma Aldrich | 40389 | >99.5 % |
| **De-ionised water** | liquid | Treated in-house with a Triple Red water technology system (Geno DI) | | 1-15 meg ohm |

The 5N purity starting elements, Se and Sb, first underwent an *in-situ* purification step consisting of heat-treatment under vacuum to drive off the higher vapour pressure

contaminants (section 3.2.1). Later, investigation into further purifying Se arose and distillation methods were established to achieve further purification, section 6.4. The development of the distillation apparatus will be described in section 6.4.2. After batching (section 3.2.2) and sealing under vacuum (section 3.2.3), the resulting glass melt was homogenised in a rocking furnace, quenched to form a glass rod and annealed to aid the release of stresses within the glass rod (section 3.2.4).

### 3.2.1. Purification of precursor elements

The attenuation of chalcogenide bulk glasses and fibres is reduced with an increase in the quality of the precursor elements arising from elemental purification [22, 149, 167], as discussed in section 2.6.2. It is important to obtain the highest purity possible for the precursor elements. This ensures good glass formability and limits extrinsic optical loss. Generally, the optical losses in bulk chalcogenide glass can be attributed to: (i) intrinsic loss (arising from the glass matric itself) or (ii) extrinsic loss (*e.g.* impurities present in the glass) [147], which were discussed in section 2.6.2. Ge, Sb and Se have been developed for semiconductor applications, with heavy emphasis on reducing electrically active components, such as metal impurities (0.1-0.01 ppm wt.) [151-153]. Despite the apparent commercialised high purity (*e.g.* > 5n (99.999 %) for Ge) of the chemical precursors used for the synthesis of Ge-Sb-Se chalcogenide glasses, Table 3.3, it is well known that there are hydride (H) and oxide (O) anion impurities present within the commercially supplied elements at unknown levels [168]. These anionic impurities are not stated in the manufacturers' chemical assay. Therefore some of the precursor elements of the chalcogenide glass melt, such as Se and Sb, were treated to an *in-situ* purification step before glass melting by heat treatment of high vapour pressure contaminants. Vacuum purification to remove the impurity volatile oxides from the raw precursor elements could only be achieved if the pure element had higher

melting or boiling point (and therefore lower vapour pressure at temperatures below the boiling point) than the associated oxide species. The difference of vapour pressures between the impurity elemental oxide and the element itself, allowed separation and the impurity volatile oxide to evaporate.

Table 3.4 shows that these criteria were fulfilled for Sb and Se and their respective oxides. For example, the vapour pressure of $SeO_2$ (200.7 mm Hg (26.75 x $10^3$ Pa) at 300 °C) is far higher than that of the pure element Se (0.2 mm Hg (3.99 Pa) at 300 °C) [169].

Prior heat-treatment of the precursor elements Sb and Se, under vacuum, was usually performed during this Project (unless stated otherwise). It has been found in this Project that purifying Se and Sb had a dramatic effect on reducing the oxide content in the final Ge-Sb-Se chalcogenide glass fibre. Evidence of this is shown in the fibre loss spectrum in Figure 6.3. It is expected that this purification step also helped to remove $H_2O$ and $H_2Se$ gases.

For the purification process, the precursor element (Sb or Se) was first batched in a glove-box into a purified silica ampoule (see section 3.1.2) which was capped with a Saunders valve (Edward Saunders) for transfer in the ambient atmosphere to be attached to a vacuum system. A cold trap (to freeze volatiles to protect the pumps) was filled with liquid $N_2$ (BOC) prior to the evacuation procedure. An in-house made furnace (27/ 115 mm ID/ OD) was raised to ensure the hot zone was at the base of the ampoule. A cold-trap, using liquid-nitrogen (boiling point -196 °C [170]), was located between the ampoule and the pump to prevent any carbon or volatiles from reaching the vacuum pump during purification. The precursor element was then heated inside the silica ampoule under a dynamic vacuum of $10^{-5}$ Pa, to the temperature at which

the oxide of higher vapour pressure first vaporised and deposited onto the inside of the ampoule, or in the case of Se on the silica glass insert. The silica glass insert (multilab) was cut to size so that it was suspended (using a silicone O-ring) ~ 10 mm above the Se shots, Figure 3.3, see section 3.2.1.2 for more detail.

**Table 3.4 Properties of selenium (Se) and antimony (Sb) and their oxides. Heat treatment under vacuum helped to reduce oxide impurity levels in the precursor, on account of the elemental vapour pressures being lower than the oxide vapour pressures [171]. Key: - means not available.**

| Element/ Compound | Melting Point ($T_m$) /°C | Boiling Point ($T_{bp}$) / °C | Vapour Pressure /mm Hg | Vapour Pressure / kPa | Ref |
|---|---|---|---|---|---|
| Se | 219 | 685 | 0.2 @ 300 °C | 0.03 @ 300 °C | [169, 172] |
| $SeO_2$ | 340 | 315 sublimes | 200.7 @ 300 °C | 26.8 @ 300 °C | [169] |
| $SeO_3$ | 118 | sublimes | - | | [169] |
| Sb | 630 | 1750 | 1.5 @ 792 °C | 0.2 @ 792 °C | [173, 174] |
| $Sb_2O_3$ | 656 | 1550 | 1.5 @ 519 °C | 0.2 @ 519 °C | [175, 176] |
| $Sb_2O_4$ | 930 | - | - | - | [177] |
| $Sb_2O_5$ | 390* 930** | - | - | - | [177] |
| Ge | 938 | 2830 | - | - | [171] |
| GeO | 700 decomposes | - | - | - | |
| $GeO_2$ | 1115 | - | - | - | |

*At 390 °C: $Sb_2O_5 \rightarrow Sb_2O_4 + \frac{1}{2}O_2 \uparrow$
**At 930 °C: $Sb_2O_5 \rightarrow Sb_2O_3 + O_2 \uparrow$

The purification schedule for both precursor materials is given in Table 3.5.

### 3.2.1.1. Sb purification by heat-treatment

Generally, 10-15 g of as-received raw Sb (6N, Materion) was purified in a silica glass ampoule (10/14 mm ID/OD of 600 mm length), under a vacuum of $10^{-5}$ Pa. The purified Sb maintained its solid form ( Melting point ($T_m$)= 630.5 °C [171]) and was easily removed, after heat-treatment, from the ampoule, shown at point (a) in Figure 3.1.

**Table 3.5 Heat-treatment schedule applied for purification of Se and Sb. All stages were carried out under a vacuum of $10^{-5}$ Pa.**

| Stage | Elemental Precursor | |
|---|---|---|
| | **Se** | **Sb** |
| 1 | Ramp to 210 °C at 200 °C/h | Ramp to 350 °C at 200 °C/h |
| 2 | Dwell 1h | Dwell 1h |
| 3 | Ramp to 260 °C at 100 °C/h | Ramp to 450 °C at 200 °C/h |
| 4 | Dwell 0.5-1 h | Dwell 1 h |
| *Notes* | *The mass of the as-batched Se constrained the dwell periods to ensure that all the Se was melted. E.g. for 10 ± 2 g: 0.5-0.6 h was used and for 40 ± 2 g: 1 h was used. Upon melting the length of Se within the ampoule reduced, thus the furnace was moved gradually down to ensure the Se remained within the hot zone. E.g. the furnace was moved by 40 ± 3 mm to 2 different points to cover the whole length of a 40 ± 2 g batch.* | *Dark fumes were visible and condensed on the inner wall of the ampoule. Silver patterns also condensed.* |
| 5 | Ramp to 30 °C at 300 °C/h | Ramp to 30 °C at 300 °C/h |
| *Notes* | *Melted in ampoule during step 4.* | *Remained solid throughout process. Sb appeared bright and shiny.* |

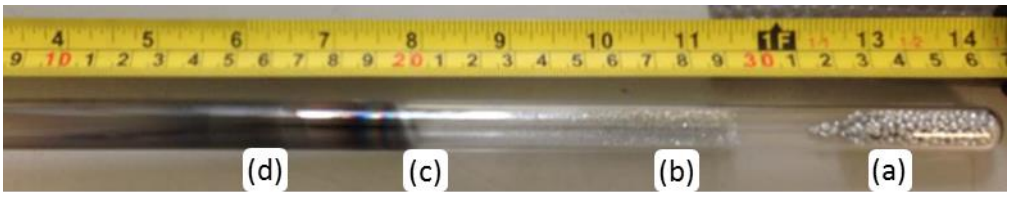



**Figure 3.1 Sb after heat-treatment. (a) The un-melted Sb can be seen at the bottom of the ampoule. After the purification the Sb was bright and shiny, indicating that the surface oxide had been removed. (b) The metallic deposits on the side of the ampoule were considered to be elemental Sb. (c) Oxide deposits can be observed at the top of the ampoule. From their appearance the deposits could either be antimony trioxide or antimony tetraoxide (see Table 3.6). (d) Carbon deposits can be seen at the top of the ampoule.**

After the purification the Sb was bright and shiny, indicating that the surface oxide had been removed. The appearance of the oxides was used to identify the oxide deposits in Figure 3.1 from Table 3.6. The metallic deposits on the side of the ampoule were considered to be elemental Sb. Oxide deposits were observed at the top of the ampoule and from their appearance the deposits were suggested to be either antimony trioxide or antimony tetraoxide. Each batch of Sb was initially weighed to monitor the reduction in mass during purification. The average percentage in weight loss was ~ 0.2 – 0.3 %. After the purification, the Sb was stored in a silica glass bottle (Samco) with a lid (Samco) in a glove-box.

**Table 3.6 Description of antimony compound and its oxides, including; empirical formula; molecular weight; colour; melting point and boiling point [177]. The appearance of the oxides was used to identify the oxide deposits in Figure 3.1.**

| Compound | Empirical formula | Molecular weight | Colour | Melting point ($T_m$) / °C | Boiling point ($T_{bp}$) / °C |
|---|---|---|---|---|---|
| **Antimony** | Sb | 121.75 | Silver-white | 630.5 | 1750 |
| **Antimony Trioxide** | Sb2O3 | 291.50 | White | 656 | 1550 |
| **Antimony Tetraoxide** | Sb2O4 | 307.50 | White | 930 | NA |
| **Antimony Pentoxide** | Sb2O5 | 323.50 | Yellow | 390* 930** | NA |

### 3.2.1.2. Se purification by heat-treatment

Due to the low melting point of Se compared to Sb ($T_m$= 219 °C compared to 630 °C [171]) and temperature at which the Se oxides evaporate (300 °C at 200.7 mm Hg [171]), it was unavoidable that Se melted during purification. A benefit of this was that heat-treating Sb was suggested to reduce oxide levels from the elements surface only, whereas due to Se melting during purification, oxides are suggested to be reduced from

the whole mass. Therefore for all the glass melting described in this Thesis, the Se purification ampoule was used for batching on the other elements and chalcogenide glass melting. Figure 3.2 depicts the steps of glass melting within the Se purification ampoule.

As stated earlier, Table 3.1, the shape of the silica glass ampoule was chosen based on the end application of the Ge-Sb-Se chalcogenide melt. Each ampoule had an insert (Multi-lab, < 4 ppm OH) of a specific size, also given in Table 3.1. Inserts allowed the volatilised contaminants (*e.g.* Se-O) to condense on its surface, rather than the ampoule or for the contaminants to be drawn into the vacuum pump.

Se-O is potentially soluble in vacuum pump oil which could have led to hazardous reactions within the vacuum system or cause cross-contamination for future glass melting. The sacrificial inserts could be removed and were discarded after purification. Before insertion, both ends of the insert were heated gently with an oxy-propane flame (a mixture of $O_2$; BOC and $C_3H_2$; Calor gas) torch (Jensons, Junior Jet 7) to acquire a smooth edge. This eliminated any rough-cut surfaces which could have resulted in silica dust falling into the batched material or scratching the inner surface of the ampoule. The insert was then thoroughly washed, 3 times with acetone and 3 times with de-ionised water. It was then dried in the ante-chamber of the glove-box for 5 minutes under a vacuum of 1 kPa. Approximately 5-16 g of as-received Se (Materion, 5N purity) was batched into an air and vacuum baked ampoule (see section 3.1.2) inside the glove-box.

The insert was positioned inside the ampoule, see Figure 3.3, and suspended using an O-ring (Imperial nitrile O-ring, RS Ltd.). The silica glass ampoule, including the silica glass insert, was evacuated under a high vacuum, $10^{-5}$ Pa.

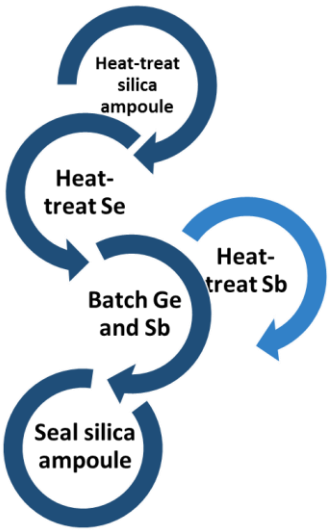



**Figure 3.2 Sequence of events to prepare Ge-Sb-Se chalcogenide glass showing how the antimony was heat-treated in a separate ampoule and then batched, along with Ge, into the pre-treated silica glass ampoule that was used for the purification of Se.**

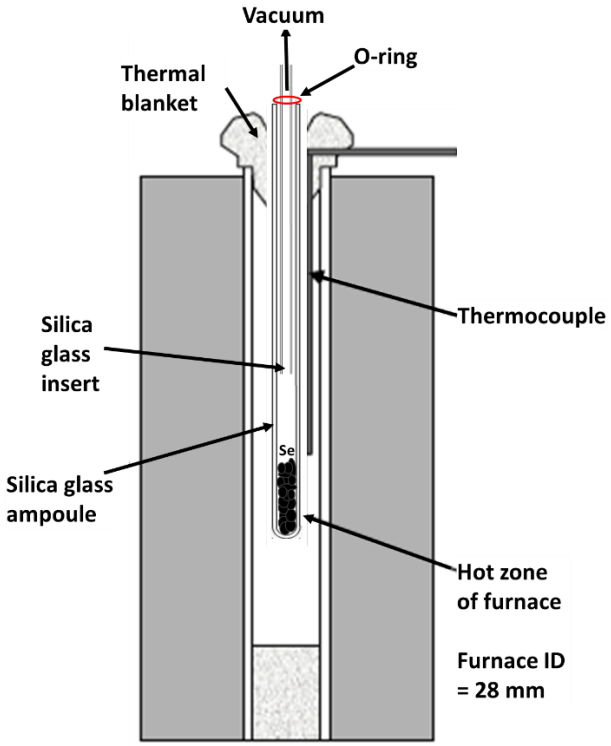



**Figure 3.3 Schematic to show the purification setup of Se by heat treatment of Se held inside a purified silica glass ampoule held under a dynamic high vacuum of $10^{-5}$ Pa with a Rotary pump, (VRC 200-7.0), then a diffusion pump (Edwards B30207240). An in-house made furnace (28 mm ID) was raised over the ampoule assembly to ensure the hot zone was at the base of the ampoule.**

A cold trap (to freeze volatiles to protect the pumps) was filled with $N_2$ (BOC) prior to the evacuation procedure. The ampoule was positioned inside the purification furnace with the heat-treatment schedule applied (Table 3.5). Usually, the dwell time at maximum temperature (260 °C) was adjusted based on the mass of the Se.

As Se has boiling point ($T_{bp}$ = 685 °C [172]) lower than that of the silica ampoule's glass transition temperature ( $T_g \sim$ 1200 °C [178]) it was possible for the Se to be ultra-purified via distillation. This process will be discussed further in Chapter 6, section 6.4.1.

### 3.2.2. Batching

The chemical precursors used for the chalcogenide glass melts are summarised in Table 3.3 including the supplier, nominal purity and description. Large relative surface area of the materials was chosen rather than powder. Furthermore, any remaining powder at the bottom of a chemical bottle was not used. Batching was conducted in a glove-box using a Sartorious balance (model BP221S) accurate to ± 0.1 mg. Before items were placed into the main body of the glove-box, they were first passed into an ante-chamber which was evacuated and refilled with $N_2$ (BOC, 'white-spot') three times. Each chemical precursor was weighed individually in a fresh plastic boat (Fisher, 100 ml, anti-static). The batching error was ± 0.001 g for the precursor elements and, as each chemical was in bulk form rather than powder, a negligible amount of batch remained on the inside of the boat or on the ampoule wall. To avoid cross-contamination, individual stainless steel tweezers were used for each element. Electrostatic fields were generated within the ultra-dry environment of the glove-box. These were overcome by placing the ampoule in an earthed metal anti-static stand. Tweezers were also used to

help remove the static. Compositions discussed in this Thesis are quoted with nominal batch compositions (unless stated otherwise).

As Se melted during the purification procedure, the mass of the remaining Se dictated the calculated weights of the other elements. The as-required quantity of Se (initially calculated based on at. % of Se in the Ge-Sb-Se chalcogenide glass composition and on estimates of the required chalcogenide glass mass) was weighed before and after it was batched inside the ampoule. Additional Se to the original calculated mass was included to compensate for the purification via heat-treatment mass losses (*e.g.* 0.3 g extra for 10 ± 0.5 g). The silica ampoule was also weighed separately and with the batched Se, this was to ensure all the Se was transferred to the ampoule and helped highlight any weighing inconsistencies caused by the electrostatic fields. Individually and with the batched Se, the silica glass ampoule was weighed without the O-ring for consistency. The O-ring on the silica glass insert and the insert itself were inserted after weighing, thus were not included in the measurements. After purification the silica ampoule and purified Se were re-weighed, without the O-ring using the same metal anti-static stand. The mass of the as-purified Se was estimated as the difference between the mass of the silica glass ampoule and Se after purification, and the mass of the empty silica ampoule (weighed before purification). The mass of the as-purified Se was used to calculate the required mass of the remaining Ge and Sb precursors based on the intended mass of the final chalcogenide glass rod. Batching quantities were calculated using a spreadsheet in Excel. The remaining elements were then batched directly into the bottom of the ampoule. The quantities of individual batches (thus the selection of ampoule size) are reported within the relevant Chapters, depending on the end application of the resultant glass see Table 3.1.

### 3.2.3. Silica glass ampoule sealing

Once batching was completed, an O-ring (Imperial nitrile O-ring, RS Ltd.) was attached to the top of the ampoule to reduce glass-metal contact with the valve (Edward Saunders). Once the valve had been fitted and closed, the ampoule was then transferred from the glove-box and connected onto the vacuum rig. The ampoule was evacuated under a dynamic high vacuum, $10^{-5}$ Pa for 30 minutes to ensure removal of any remaining volatiles. The cold trap (to freeze volatiles to protect the pumps) was filled with $N_2$ (BOC, liquid) prior to the evacuation procedure. An oxy-propane (a mixture of $O_2$; BOC and $C_3H_2$; Calor gas) torch (Jensons, Junior Jet 7) was ignited and used to seal the ampoule, Figure 3.4.

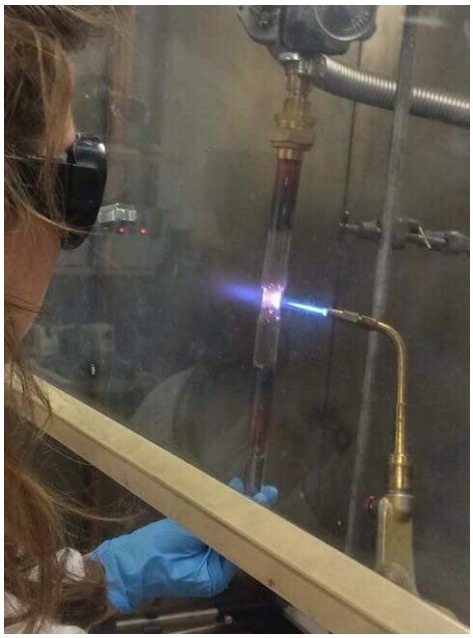


**Figure 3.4 The silica glass ampoule was sealed inside the fume cupboard and attached to the vacuum line, using an oxy-propane flame formed by igniting a mixture of oxygen gas ( $O_2$; BOC) and propane ($C_3H_2$; Calor gas) and handled using a gas torch.**

The outside of the ampoule had been initially cleaned with acetone and then the area that was to be sealed was further cleaned by passing over the oxy-propane flame before the process was started. During the sealing procedure the silica ampoule was heated (≥

50 mm above the batched chemicals to avoid the chemicals being heated) evenly around its circumference using the oxy-propane torch.

As the silica reached ≥ $T_g$ the ampoule walls softened and gradually collapsed inwards due to the low internal pressure of the ampoule ($10^{-5}$ Pa). Once the walls had touched internally to form a small seal, the ampoule was gently pulled from the base to apply a small force to assist its separation from the rest of the vacuum system. It was preferable to seal quickly to avoid dissociating silica ($SiO_2$) into silicon monoxide (Si-O) by heat (at temperatures > 910 °C: $SiO_2 \rightarrow SiO + O_2\uparrow$ [179]) and the deposition of silica fume on the inside of the ampoule wall, thus potentially being incorporated into the Ge-Sb-Se chalcogenide glass melt. Therefore sealing approximately was completed within 2 minutes and the ampoule was rested on a heatproof brick to cool for ~ 5 minutes. Wire (Kanthal 0.65 mm gauge) was twisted around the top end of the ampoule (avoiding the bottom where the chalcogenide melt would form) to assist in manoeuvring the ampoule in and out of the furnace and to allow it to be suspended in the furnace within the hot zone.

### 3.2.4. Melting, quenching and annealing

#### (i) Melting

The Ge-Sb-Se chalcogenide glass composition for optical studies detailed throughout Chapters 4-6, were named 'JB', the initials of this Author, followed by the glass number (*e.g.* JB01). Often, more than one glass was fabricated with the same composition and therefore melt numbers are also recorded (*e.g.* MO30JHB) throughout this Chapter and Thesis. The number represents the experimental number in chronological order of experiments within the Mid-infrared Photonics Group, University of Nottingham, UK.

The main objective of glass melting was to produce a homogeneous mixture, however since the Ge-Sb-Se chalcogenide glass components were sealed within the ampoule it was not possible to mechanically stir the liquid components. Therefore melting was conducted in a resistance furnace (Instron TF105/4.5/1ZF tube ID 86 mm, with a controller Eurotherm 2408) capable of a rocking motion, to aid the homogenisation of the molten components, Figure 3.5. When the rocking motion was applied, the furnace moved through 30 °± 5 ° above and below the horizontal axis. At either extreme of movement the furnace was paused for 2 minutes to ensure the viscous liquid reached the opposite end of the ampoule at that angle. Thermal blanket (Superwool™ 607™ Blanket; classification temperature 1300 °C) was used for thermal insulation and was packed around the ampoule when in the furnace. With the wire suspension and thermal blanket insulation, the centre of the ampoule was thus held in the hot zone of the rocking furnace.

Melting was performed at > 740 °C to avoid growing $GeSe_2$ crystallites [180] (melting temperature 740 °C). The melting schedule was designed to melt Se first so that when the ampoule started rocking the Se liquid would protect the ampoule from scratching by the element solid chunks. The melting temperature selected (850 °C and then 900 °C) had to be greater than or equal to the liquidus temperature ($T_l$) of the Ge-Sb-Se glass in order for the melting to be conducted in the true thermodynamic equilibrium liquid state. $T_l$ can be calculated by the '2/3 rule' [181], Equation 3.1. $T_g$ is expressed in °C. The calculated $T_l$ of the Ge-Sb-Se chalcogenide glasses synthesised for optical studies will be given in Table 4.4.

$$T_l \text{ in } °C = \frac{3(T_g+273)}{2} - 273 \qquad \textbf{Equation 3.1}$$

During melting the furnace was tipped back and forth in a rocking motion on its horizontal axis to ensure a uniform composition of the glass melt, shown in Figure 3.5. The furnace was re-positioned to the vertical 2 h before quenching as a '*refining*' process. Firstly, this was to ensure the melt was collected at the bottom of the ampoule and secondly it was suggested that extra contamination, oxides and any silica-associated particles (~2200 kg/m$^3$ [180]) drifted to the surface of the Ge-Sb-Se chalcogenide liquid-glass forming melt ( 4459-5133 kg/m$^3$ see section 4.3 for density results) on account of their difference in densities.

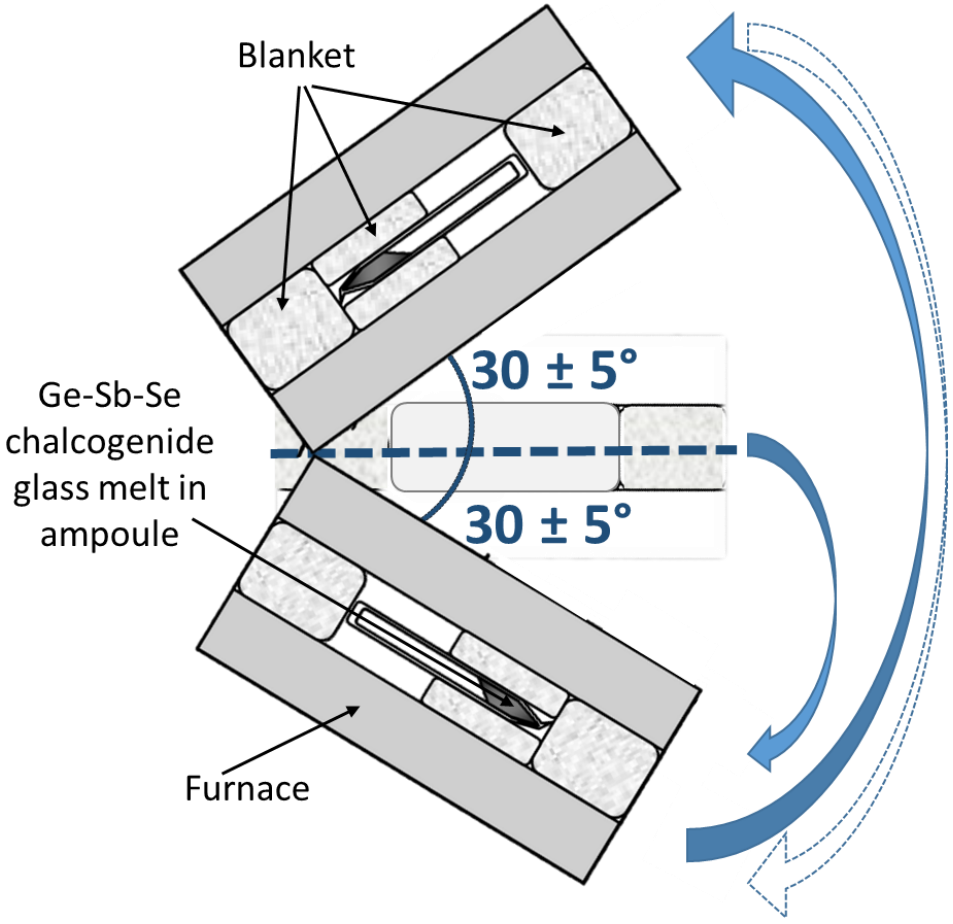



**Figure 3.5 Schematic representation of the movement of the rocking furnace used for melting all of the Ge-Sb-Se chalcogenide glasses here (including the ampoule). Rocking was 30 ± 5 ° about the horizontal axis during melting to assist homogenisation of the viscous molten material. Schematic diagram is not to scale.**

On the first Ge-Sb-Se chalcogenide glass melt (M046JHB with composition $Ge_{24}Sb_4Se_{72}$) a melting schedule based on previous work in the MIR Photonics Group, University of Nottingham, UK, with Ge-As-(In)-Se glasses [45, 46] was followed, Table 3.8. During the first attempt of melting the Ge-Sb-Se glass, it was observed that the Ge-Sb-Se glass-forming melt took a long time to quench (>150 s of the $N_2$ jet applied), compared to the Ge-As-Se glasses previously melted and quenched by the MIR Photonics Group (< 120 s), see section 3.2.4(ii) for quenching method. During this first attempt at Ge-Sb-Se glass melt-quenching the ampoule shattered all of a sudden and the Ge-Sb-Se chalcogenide glass was found to be solid in the remains of the silica ampoule. As was shown in Figure 2.5 the glass forming region for Ge-As-Se is larger than that of Ge-Sb-Se, indicating that As is a better glass former than Sb. Initially, it was thought that higher vapour pressures accumulated in the evacuated ampoule during the melting of the elements to form a Ge-Sb-Se chalcogenide glass, rather than when forming a Ge-As-Se chalcogenide glass. It was suggested that this was potentially the reason behind a pressure build-up. Elemental Se and its oxides have high vapour pressures during heating (Se 0.2 mm Hg (3.99 Pa) at 300 °C and $SeO_2$: 200.7 mm Hg (26.75 x $10^3$ Pa) at 300 °C) [172]. Therefore, in view of this observed shattering of the ampoule during quenching with the $N_2$ jet, an extra step was added to the melting schedule to heat the ampoule slowly and allow it to dwell (2 h at 300 °C) to encourage any reactions (*e.g.* $SeO_2 \rightarrow Se + O_2$ ) to progress to completion by consuming the high volatile constituents before significant melting began. However, a literature survey revealed that As generates a greater vapour pressure than Sb at the 850 °C melting temperature (As: 50 kPa at 849 °C, Sb: 1 kPa at 947 °C [182]), Table 3.7, suggesting that a Ge-Sb-Se melt was unlikely to generate greater vapour pressures during melting.

It was also observed that the silica ampoule pieces did not disperse great distances during the shattering. Therefore, it was then considered that the Ge-Sb-Se melt could have a higher viscosity than the Ge-As-(In)-Se melt, causing a greater drag on the silica ampoule wall during quenching and holding the shattered pieces together. This could put the ampoule wall under a central internal force and subsequently result in an implosion. Until a glass was successfully fabricated it was not possible to prove this hypothesis.

**Table 3.7 Equivalent vapour pressure ranges 0.2 kPa – 5 kPa of arsenic (As) and antimony (Sb) showing that Sb requires much higher temperatures to achieve vapour form [182].**

| Temperature / (°C) | Arsenic vapour pressure / (kPa) | Temperature / (°C) | Antimony vapour pressure / (kPa) |
|---|---|---|---|
| 383 | 0.2 | 792 | 0.2 |
| 428 | 1 | 947 | 1 |
| 450 | 2 | 1022 | 2 |
| 481 | 5 | 1132 | 5 |
| 507 | 10 | 1222 | 10 |
| 535 | 20 | 1322 | 20 |
| 576 | 50 | 1467 | 50 |
| 610 | 101.325 | 1617 | 101.325 |

Building on this work, a new melt schedule was created to melt at a slightly higher temperature (900 °C) and to remove the ampoule from the furnace at a higher temperature where the viscosity should be lower (700 °C) (Table 3.8). This melt schedule resulted in a successful quench, produced a Ge-Sb-Se glass (checked using XRD, section 3.6.1) and was used for all of the successive glass melts. The viscosity/ temperature behaviour of the $Ge_{24}Sb_4Se_{72}$ (at. %) chalcogenide glass will be discussed in Chapter 4. It was found that the viscosity at any particular temperature between $T_g$ and the liquidus, was indeed higher for the Ge-Sb-Se melt (*e.g.* at 360 °C the viscosity of $Ge_{24}Sb_4Se_{72}$ was $10^{5.8}$ Pa.s, compared to $Ge_{15}As_{21}In_1Se_{63}$ which was $10^{4.9}$ Pa.s [46]).

**Table 3.8 The general glass melting schedule for the Ge-Sb-Se chalcogenide glasses fabricated within this Project.**

| Stage | Step | Programme |
|---|---|---|
| 1 | Melting | **Melting programme for M046JHB ( $Ge_{24}Sb_4Se_{72}$)**: Ramp to 300 °C at 60 °C/h (no rocking). |
| | | Ramp from 300 °C to 850 °C at 60 °C/h (rocking*). |
| | | Dwell at 850 °C for 12 h (rocking*). |
| | | Ramp from 850 °C to 650 °C at 65 °C/h (no rocking, furnace put vertical). |
| | | Dwell at 650 °C until quenching (< 30 minutes). |
| | | **Programme for all other glass melting** |
| 2 | | Dwell at 300 °C for 2 h. |
| *Notes* | | *This dwell step was added to melt the Se and to prevent pressure build-up. The reactions were allowed to progress to completion by consuming the high volatile constituents.* |
| 3 | | Ramp from 300 °C to 900 °C at 60 °C/h (rocking*) and dwell at 900 °C for 12 h (rocking*). |
| *Notes* | | *Rocking started above the melting point of Se ($T_m$ of Se is 219 °C [183], however the ampoule was sealed under vacuum thus the melting point might differ) to help reduce scratching of the inner ampoule walls by solid particles. The remaining Sb and Ge solid particles dissolved and rocking helped to homogenise the liquid.* |
| 5 | | Ramp from 900 °C to 700 °C at 65 °C/h (no rocking) and dwell at 700 °C until quenching (< 30 minutes). |
| *Notes* | | *Furnace put vertical for refinement process.* |
| 7 | Quenching | In ambient air; 30 seconds (for 8/12, 10/14 mm ID/OD ampoule), 40 seconds (for 10/14 mm ID/OD ampoule), 45 seconds (for 15/18 mm ID/ OD ampoule) and 1 minute ( for 28/32 mm ID/OD ampoule). |
| 8 | | Ampoule immediately placed in pre-heated furnace at Ge-Sb-Se chalcogenide glass's $T_g$ for same time as quenched in air. |
| 9 | | Ampoule held vertically and was partially removed from furnace presenting ~10 mm of melt above the furnace. $N_2$ jet was focused on one point, perpendicular to the melt, at the top of the contraction cone. Upon solidification of the melt, the surface edge shrank away from the ampoule wall at which point the $N_2$ jet was distributed evenly around the circumference of the ampoule until the entire melt was solidified (therefore shrunken completely away from the wall of the ampoule). |
| 10 | Annealing | Ampoule placed into a 6 h pre-heated furnace (Instron, TF105/4.5/1F, ID tube 86 mm) at the Ge-Sb-Se chalcogenide glass's $T_g \pm 5$ °C ; 0.5 h (for 8/12, 10/14 mm ID/OD ampoule), 0.7 h (for 15/18 mm ID/ OD ampoule) and 1 h (for 28/32 mm ID/OD ampoule). |
| *Notes* | | *Ge-Sb-Se chalcogenide glass held at $T_g$ to allow the molecular structure of the glass to relax and relieve internal stresses.* |
| 11 | | After annealing the Ge-Sb-Se chalcogenide glass was cooled slowly to room temperature by turning the furnace power off. |
| *Notes* | | *Ge-Sb-Se chalcogenide glass is gradually cooled to ensure the temperature profile is homogeneous.* |

* furnace rocked through 30 ° ± 5 ° above and below the horizontal axis, see Figure 3.5.

Please note that a re-melt was required to fabricate Ge-Sb-Se chalcogenide glass test samples to measure the viscosity/ temperature behaviour, see Table 3.9. The viscosity/ temperature behaviour of the four Ge-Sb-Se glass compositions considered for optical fibres will be shown in Figure 4.8.

### (i) Quenching

Quenching was a critical step in glass formation as cooling the glass-forming melt too slowly (< the critical cooling rate (CCR), as was discussed in section 2.1) could result in crystallisation. Nonetheless, it was also important not to quench the glass-forming melt too quickly, as it could have introduced cracks into the as-quenched chalcogenide glass or could have generated tensile stress in the silica ampoule and caused fractures. It has been suggested that the larger the glass melt, the more physically stable a chalcogenide glass is against stresses induced in quenching [47]. This phenomenon can be confirmed by this Author as it was found that smaller glass melts (*e.g.* glass melts fabricated in 8/10 mm ID/OD silica ampoules ~ 10 g, used for structural studies in Chapter 8) had a greater tendency to crack during quenching than larger melts (*e.g.* glass melts fabricated in 28/32 mm ID/OD silica ampoules ~30 g used for outer cladding tube extrusions).

The Ge-Sb-Se glass melts were quenched using the air-furnace-$N_2$ jet quenching method [45] (Table 3.8). The silica glass ampoule was removed from the melting furnace and held suspended in ambient air for 30- 60 s (based on the size of the melt) using the wire support. The ampoule was then placed in a furnace pre-heated to the glass's $T_g$ (measured using DSC section 3.6.3) for the same amount of time that it was cooled in air, to allow thermal equilibrium as the melt surface would have been lower than the melt interior. After this, the ampoule was partially removed from the furnace

presenting ~10 mm of the Ge-Sb-Se chalcogenide melt. A $N_2$ jet was focused on one point on the outside of the ampoule, perpendicular to the melt and just above the contraction cone. Upon solidification of the melt, the surface edge shrank away from the ampoule wall at which point the $N_2$ jet was distributed evenly around the circumference of the ampoule, whilst the ampoule was gradually raised from the furnace, until the entire melt was solidified (therefore shrunken completely away from the wall of the ampoule). The observation was made that during a successful quench the colour of the glass-forming melt changed from a dark grey to a shiny grey-silver, when the solidified glass had detached from the silica wall.

### (ii) Annealing

The physio-chemical properties of glasses are affected by the thermal history induced by the fabrication methods. Quenching, especially, can generate permanent internal stresses that might cause the glass ultimately to fracture. Annealing at $T_g \pm 5$ °C for 0.5 – 1 h (depending upon the size of the melt, see Table 3.8) was conducted in a pre-heated furnace (pre-heated for > 6 h to reach equilibrium before quenching) in order to eliminate the internal stresses yet without glass devitrification and allowing the glass structure to relax to equilibrium structure. After dwelling at $T_g$ the temperature was gradually reduced by turning off the furnace and allowing the ampoule assembly to cool to room temperature.

A glass melt sheet pro forma was used to record the variables and details specific to each glass melt (*e.g.* ampoule size, weight of each chemical, melt date, exact melting, quenching and annealing schedules and any observations or notes). See Appendix I for an example melt sheet.

## 3.3. Silica glass ampoule opening, Ge-Sb-Se chalcogenide glass cutting, polishing and grinding

### 3.3.1. Silica glass ampoule opening and chalcogenide glass cutting

After annealing the Ge-Sb-Se chalcogenide glass rods could be stored in their enclosed silica ampoules, under vacuum and protected from the atmosphere, until required. To open the ampoule first a small slit at the distal end of the ampoule from the glass was made using a diamond coated, circular saw (Isomet saw, Buehler Ltd. with diamond-impregnated blade, LECO Instruments Ltd. 15HC ∅ = 126 mm, thickness = 0.65 mm) to relieve the internal vacuum. Then two stainless steel guides (LECO Instruments Ltd. ∅ = 124 mm, thickness = 3.94 mm) were added either side of the blade to prevent the blade from penetrating through the entire wall of the ampoule, thus scoring the ampoule. Three scores were made at regular intervals from the bottom of the chalcogenide glass rod to ~ 10 mm above the top of the glass rod, around the circumference of the ampoule. The ampoule was then prised open, using a flat head screw driver. This process was very difficult to master to ensure the Ge-Sb-Se chalcogenide glass rod did not become damaged. The risk of chipping or cracking the rod with a too great force being applied by the screw driver was high, shown in Figure 3.6(a). However, towards the end of this Author's PhD the technique was perfected so that only 1 or 2 of the score lines needed to be opened until the Ge-Sb-Se chalcogenide glass became free from the ampoule undamaged, Figure 3.6(b).

Once the Ge-Sb-Se chalcogenide glass rod was free from the ampoule, it was placed on a flat aluminium (Al) block (32 mm by 60 mm, 6.35 mm height) and was heated ~ 50-60 °C on a hot plate (Bibby, Stuart). Wax (Buehler, Crystal Bond LT) was then melted onto the warm Al block to secure the glass rod in place upon cooling. All the components were heated together to reduce thermal shock when the wax was applied

for mounting. The Ge-Sb-Se glass rod samples were cut to size (*e.g.* sliced into discs) using a diamond coated circular saw (Isomet saw, Buehler Ltd. with diamond-impregnated wafering blade, LECO Instruments Ltd. 15HC ∅ = 101 mm, thickness = 0.35 mm). Usually the domed bottom part of the glass rod (shaped by the geometry of the ampoule) and the contraction cone were removed. The contraction cone was where any impurities would gather, see section 3.6.1 for analysis of the contraction cone.

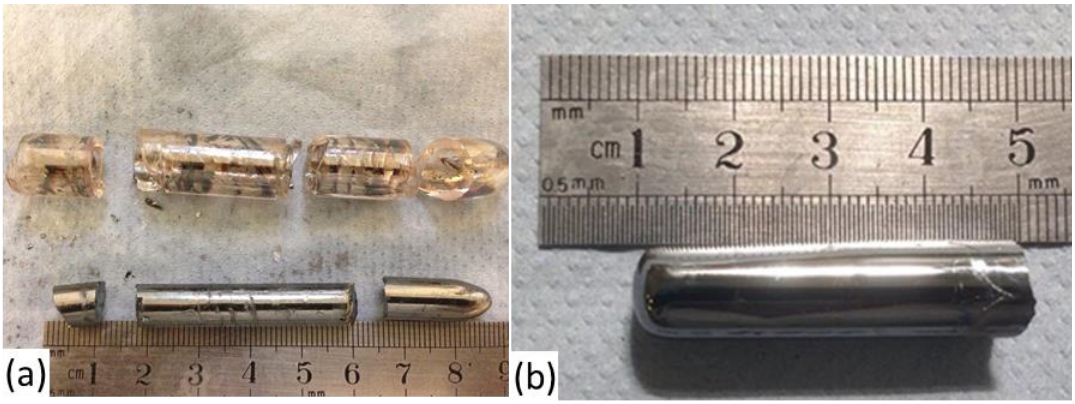



**Figure 3.6 (a) Example of a glass rod (M044JHB, composition $Ge_{19}Sb_{15}Se_{66}$) which was cracked during ampoule opening, due to too much leverage pressure being applied via the screw driver. (b) Example of a good chalcogenide glass forming melt (M052JHB, composition $Ge_{22}Sb_8Se_{70}$) after quenching, annealing and ampoule opening.**

### 3.3.2. Chalcogenide glass grinding and polishing

To attach the glass disc to the grinding/ polishing head the same wax melting procedure was applied as was described in section 3.3.1. The grinding/polishing head was then attached to a rod and inserted into the grinding/ polishing body. On a soda-lime-silica (window glass) sheet ~ 2.5 ml of 1000 grade silicon carbide particle powder (SiC, Buehler) was mixed with a small volume of polishing oil (Buehler). The grinding/polishing jig was then placed onto the sheet such that both the sample and the grinder body face were in contact with the sheet. This helped to ensure that the sample faces would be polished parallel to one another. In a clockwise motion, a full circle was drawn consisting of many smaller circles, rotating the jig 90° with every full circle; a

total of eight full circles were required. The same process was then applied to the other side of the disc.

Polishing media, in the form of impregnated discs, (Buehler) were mounted on magnetic sheets and used with a series of diamond pastes; 6 µm, 3 µm, 1 µm and 0.25 µm (Buehler). Each polishing media was used with only one grade of diamond paste. A polishing machine (Metaser V2000) was operated at 150 rpm (revs per minute), with the grinding/ polishing jig guided in a circular motion in the opposite direction from the polishing disc. The grinding/polishing jig was rotated 90 ° every minute, for a total of 8 minutes or when the successive scratch damage had been removed without rounding the sample edges. Rounding could occur if the sample was polished for too long. Polishing was conducted progressively using finer diamond paste (6 µm, 3 µm, 1µm and ¼ µm). If the ensuing characterisation required it (*e.g.* FTIR) the disc was turned over on the jig and the other side polished using the same method.

The as-polished chalcogenide glass discs were cleaned in acetone (> 99.5 %, Sigma Aldrich), agitated in an ultrasonic bath (Dawe) at 35 °C for 5 minutes and wiped with a lens tissue (Agar Scientific).

### 3.4. Extrusion

All core/ cladding structured fibres have been drawn from co-extruded core/ cladding preforms (unless stated otherwise, if the extrusion failed). Similarly, all tubes were extruded outer cladding tubes. Alternative core/ cladding preform fabrication methods (*e.g.* rod in tube, rotational casting and double crucible) and the potential advantage of using extrusion over these routes were discussed in section 2.6.1. Two extrusion methods were used for this Project. The first was to fabricate a co-extruded core/ cladding preform (section 3.4.1), which was drawn to cane (section 3.5.1) and

suspended in an outer cladding extruded tube (section 3.4.2) for subsequent fibre drawing (section 3.5.2). Not all of the extrusions were successful and this Project particularly investigated why this was and how mismatches in viscosity and/or $T_g$ affected the co-extrusions. The following is a general description of the extrusion method, and a more detailed account including the results, times, temperatures and loads required for each extrusion, will be presented in Chapter 5.

All extrusions were carried out using an extruder designed and built in-house by Dr. David Furniss. An extrusion number (*e.g.* EXXXJHB) was assigned to each extrusion. The number is prefixed by 'E' which stands for extrusion, followed by three numbers which corresponds to the chronological order in which the glass boules (cut from the glass melts) were extruded within the University of Nottingham MIR Photonics Research Group. The initials of this author are given after the number.

The extruder, Figure 3.7(a), could be tilted 90 ° to a horizontal position to aid the insertion of the glass boules. Once in the horizontal position, the piston was withdrawn to allow the insertion of the glass boule(s) and a brass bobbin into the far end of the barrel. The bobbin was closely fitted to the barrel and was designed to prevent the glass melt from escaping upwards during the extrusion process. The bobbin also exerted the force of the punch uniformly across the glass and therefore allowed the punch to not be fitted as closely as would otherwise be the case (a close fit of the punch would have required very accurate alignment from the hydraulic cylinder which would have been difficult to achieve). The piston was lowered to approximately 2 mm from the bobbin to allow the glass and extruder assembly room for expansion during heating. The die base rested onto a polytetrafluoroethylene (PTFE, 12.6 mm bore for 10 mm ID die, 7.6 mm bore for a 5 mm ID die) guide support tube. Through the centre of the support tube

a stainless steel (SS316) shield tube engaged with the base of the die with a silicone 'O' ring to form a seal.

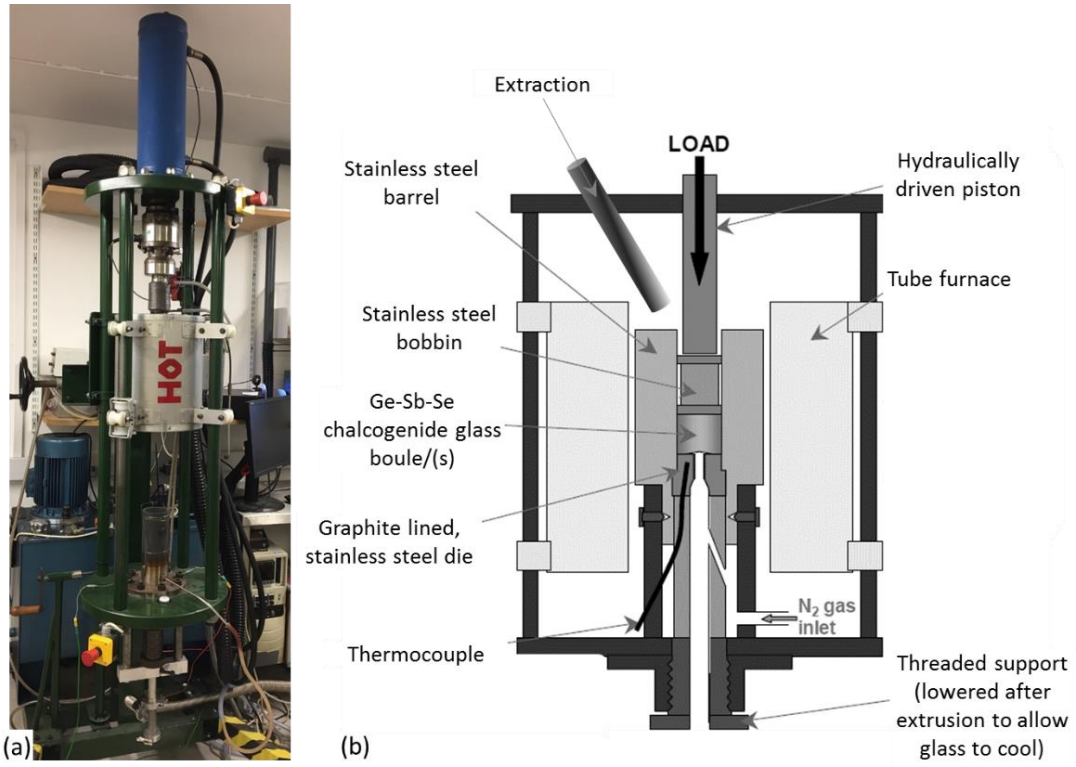



**Figure 3.7 (a) Photograph of in-house built extruder (2.5 m tall). (b) Schematic of inner working of in-house built extruder.**

All extrusions were conducted downwards in a vertical position. For the tube extrusions (section 3.4.2), to reduce glass surface reaction with ambient air, nitrogen (BOC, 'white spot') was used to purge the extrusion chamber (Figure 3.7(b)) and a small over-pressure of $N_2$ (500 ml $min^{-1}$) surrounded the chalcogenide glass feed boule throughout the extrusion process. Extraction was used to remove any toxic volatilised species. However, care had to be taken to ensure the extract was not too powerful and so able to draw out the $N_2$ gas, which entered the chamber below the glass boule. Therefore the extraction tube was placed ~ 20 mm from the extrusion furnace, allowing any escaped volatilised glass components to be withdrawn but without causing low $N_2$ pressure in the chamber. In the case of the co-extrusions a vacuum was supplied to the

shield tube by a two stage oil rotary pump (~ $10^{-2}$ mbar) to ensure no atmosphere was trapped at the core/ cladding interface (section 3.4.2).

Once the minimum load (100 kg) had been applied, and the temperature had been raised slightly above the $T_g$ of the glass, the glass melt expanded to fill the barrel creating a seal. The extrusion chamber was heated using a tube furnace (Figure 3.7). Alterations were made in-house allowing the tube furnace to slide up and down the support frame, which provided access to the extruder set-up. Continuous monitoring of the furnace temperature and the temperature of the die was required, as there was a lag time between raising the furnace temperature before its effect was seen further inside the chamber. A thermocouple was inserted within the die to gauge the glass melt temperature. The temperature at the die was ~ 30 °C lower than that set at the furnace when the extrusion was proceeding at a steady rate. Pico Technology software was used to record the thermocouple temperature (°C), the applied load (kg) and the position of the bobbin (mm) against time (s), Figure 3.8. Usually the load was applied once the temperature had been raised between 40 – 50 °C above the chalcogenide extrudate $T_g$.

As soon as the extrusion had been completed the load was removed and the bobbin, any remaining boule, the die, and the newly formed preform were lowered within the extruder by unscrewing the lower support. This allowed the glass to cool more quickly. For the co-extrusion a slight over pressure of nitrogen (BOC, 'white-spot', 500 ml $min^{-1}$) was supplied which allowed the die support tube to be lowered and provided an inert atmosphere whilst the glass melt cooled (the $N_2$ atmosphere was maintained for the tube extrusion). The extruder was designed to keep the preform encased in the shield tube during cooling, so although the glass was lowered to increase the cooling

rate, the shield tube provided an adequate annealing rate to remove stresses induced by extrusion.

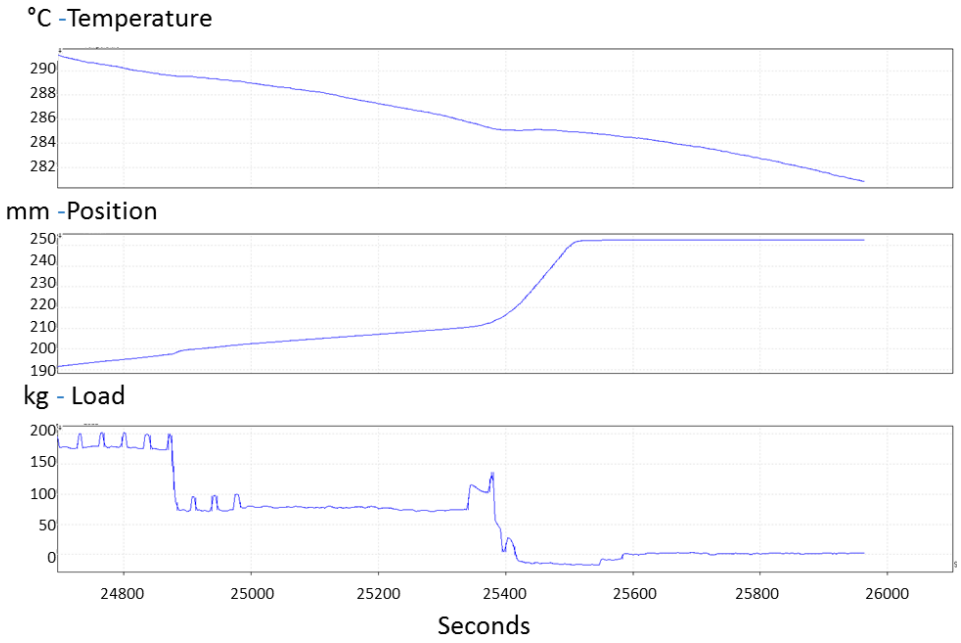



**Figure 3.8 The Pico Technology logging software read out during a co-extrusion (E030JHB, core composition $Ge_{19}Sb_{15}Se_{66}$ and cladding composition $Ge_{19}Sb_{15}Se_{66}$) through a 5 mm inner diameter graphite die. All graphs are plotted against time (seconds). The top curve is temperature ( °C), the middle stepped curve is the position of the bobbin (mm) and the lower curve is the load applied to the bobbin (kg).**

### 3.4.1. Co-extrusion to fabricate a structured core-cladding preform

In order to fabricate a core/ cladding preform via extrusion, firstly two separate Ge-Sb-Se chalcogenide glass rods were melted using 15/ 18 mm ID/OD ampoules (following the method described in section 3.1). The glass rods were cut to ~ 10-15 mm in height (using the cutting method detailed in section 3.3) removing both the contraction cone and the bottom rounded end (shaped by the geometry of the ampoule). Polishing was necessary to obtain the best contact between the two adjoining core and cladding surfaces when placed in the extruder. One cut surface of each glass boule was polished (see 3.3.2 for method). Usually the boules became slightly rounded at the edges during polishing, however it was deemed to be beneficial to have a slightly convex interface between the core and the cladding. This is because the polishing procedure would have

inevitably left damage and possibly debris on the surface of the glass (even after meticulous cleaning with acetone and an ultrasonic bath, see section 3.3.2 ). These defects had the potential to trap gas during co-extrusion (*e.g.* the $N_2$ gas which was passed through the extruder) generating imperfections, such as bubbles at the core/ cladding interface. Nevertheless, in the extrusion process once the glasses had reached above $T_g$ and the load was applied, due to the convex geometry of the surfaces any confined gas should have been expelled preventing any bubble formation at the core/ cladding interface. Due to the highly viscous flow (see section 3.6.5.2 for viscosity/ temperature measurements) of the glasses the mating surfaces then contacted over the whole surface area. Often the tolerance of the inner diameter of the ampoule containment during chalcogenide glass melting caused the glass boule charges to be slightly oversized for the steel barrel. Therefore the sides of the glass boule had to be ground. The boules were thoroughly cleaned (by immersing in acetone agitated in an ultrasonic bath (Dawe) at 35 °C for 5 minutes and wiped with a lens tissue (Agar Scientific)) to avoid impurity inclusions and contaminants, such as carbon from the polishing oil. There was also a risk of residual SiC and diamond particle contamination from the abrasives. The core glass was placed closer to the bobbin so that when the extruder was returned to vertical it was on top. To position the core with the minimal risk of contamination, a lens tissue was placed on the polished cladding surface. The cladding boule was then lowered into the barrel so that just the polished surface was protruding and the lens tissue was placed on top. The polished core surface was then placed on top of this (with the tissue lens still in place between the two). The tissue lens was then removed slowly allowing close, clean, contact between the mating surfaces of the core and cladding boule charges. The bobbin was then inserted on top of the core. The extrusion components for the co-extrusion are shown in Figure 3.9(a). The 5 mm

ID die was graphite lined with a stainless steel (316 SS) bulk body. A schematic of the stages of how the core boule was forced through the centre of the cladding boule during the extrusion is shown in Figure 3.9(b-d). The core and cladding super-cooled melt flow during extrusion is discussed further in section 5.3. Vacuum was applied from a two stage oil rotary pump (there was no gauge fitted to the pump and the vacuum was estimated to be ~ $10^{-2}$ mbar) to help eliminate any voids between the stacked layers.

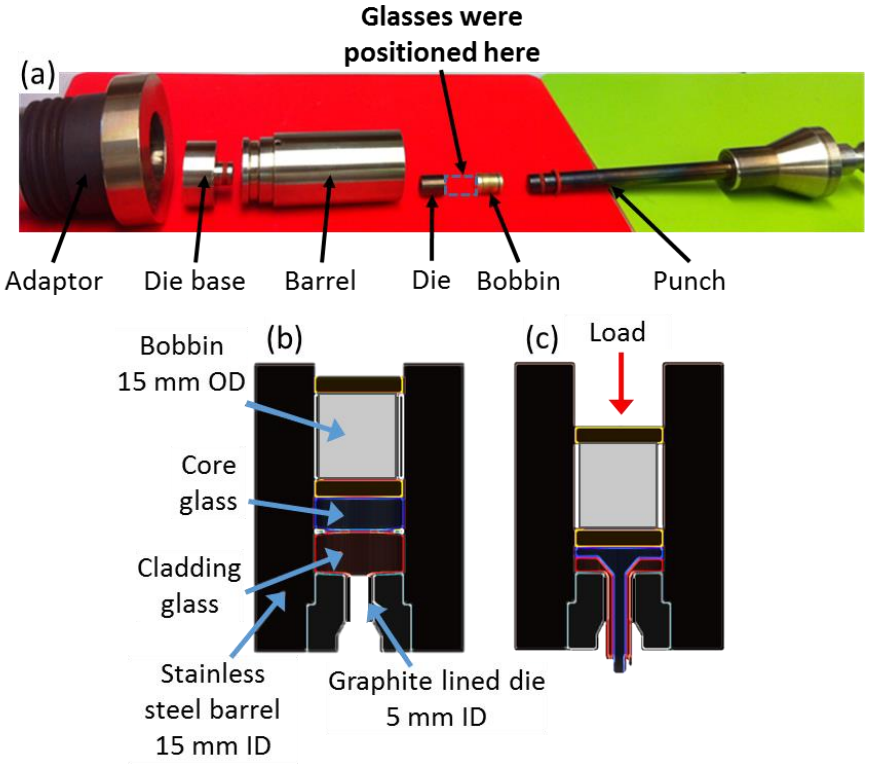



**Figure 3.9. (a) Small extruder barrel (15 mm ID) assembly for co-extrusion, from left to right; adaptor, die base, barrel, die, bobbin and punch. The glasses were positioned between the die and the bobbin, with the saw-cut end of the core glass against the bobbin. The polished cladding surface was then placed abutting the polished core surface, so that when the extruder was vertical the core glass was on top. (b-c) Schematic diagram of co-extruded core and cladding preform. The glasses were heated to above $T_g$ in –situ (b) and the load was applied (c). The core boule was then forced through the centre of the cladding boule.**

Previous studies conducted within the University of Nottingham MIR Photonics Research Group have found that the core/ cladding ratio during a co-extrusion was usually stable to within a few hundred microns for a middle section of a certain axial

length of extruded rod [43]. However, due to the difficulties encountered in extruding the Ge-Sb-Se glasses investigated in this Thesis, further research was conducted by an Undergraduate Mechanical Engineering Student at the University of Nottingham, Mr T. Arnold, using the Ge-Sb-Se glasses extruded by this Author and under the co-supervision of this Author. The results are discussed in Chapter 5, section 5.3.

### 3.4.2. Tube extrusion to fabricate an outer cladding tube

The cladding composition was melted in flat bottomed 28/ 32 mm ID/ OD ampoules as shown in Table 3.1. The boule was cut to ~ 10-15 mm in height, as described in section 3.3. Usually two boules could be made from one 100 g melt (*e.g.* sample M054JHB was cut to a 38.89 g charge boule for extrusion E014JHB, leaving 62.21 g of glass remaining). As mentioned in section 3.3, impurities were likely to congregate in the contraction cone of the chalcogenide melts. Therefore the section of melt used first for extrusion was the one furthest from the contraction cone, shaped flat by the geometry of the ampoule, with the idea that if the extrusion failed, the remaining boule could be used. However, it is worth noting that in this Project new melts were made for every tube extrusion.

The charge boule was loaded into the barrel such that in the vertical position, the saw-cut end was facing down (abutting the die) and the flat bottom end was facing upwards (against the bobbin). As there was only one boule component in the extrusion, no polishing was needed. Thus, the as-annealed boule was removed directly from the ampoule, cut to size, cleaned and loaded into the barrel. Unlike the co-extrusion described in section 3.4.1, which relied on the bobbin pushing the core through the cladding guided by a 5 mm graphite lined die, the die for the tube extrusion was a 10

mm graphite lined die which also required a 3 spoked spider pin (both 1 and 1.5 mm polished NIMONIC alloy 80A[6] (Special Metals) were used in this Project).

Figure 3.10 shows a schematic for the general tube extrusion setup. In the first tube extrusion, E014JHB, the pin extended 8 mm beyond the graphite die to prevent the closure of the bore, after passage through the die and pin, due to swelling. However voids were found at the interface between the core/cladding cane and outer cladding tube in the resultant small core fibres (Figure 5.9); therefore the design of the die and pin were altered for subsequent tube extrusions in this Project. The pin extension beyond the graphite die was increased to 15 mm, as will be discussed in section 5.2.

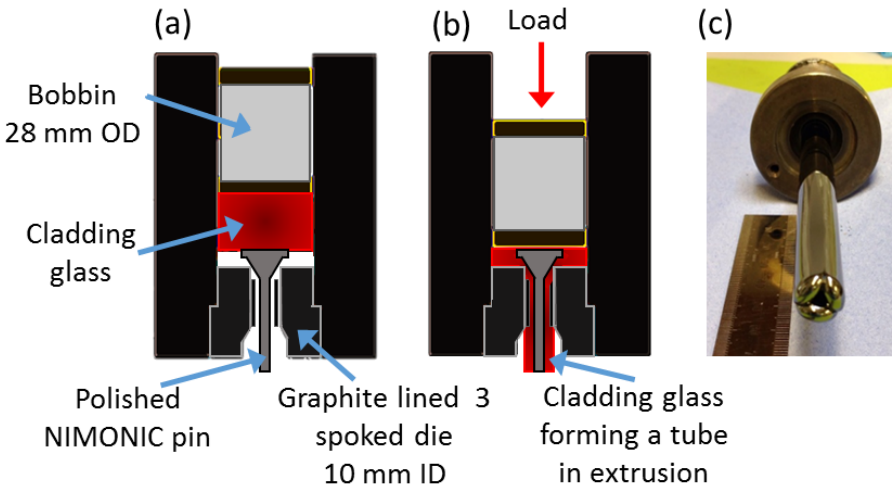



**Figure 3.10 Extrusion of outer cladding tube with a 3 spoked spider pin (NIMONIC, 1 mm for extrusion E014JHB and 1.5 mm for all subsequent extrusions) The 10 mm graphite lined die (bulk material 316 stainless steel) had a lead in angle of 60 °, see Figure 5.2 for re-designed die schematic. (a) Schematic diagram of the first stage of extrusion where the glass boule was heated *in situ* to above $T_g$ before the load was applied. (b) Schematic diagram to show the extrusion process after the load had been applied. The glass boule softened and was extruded through the graphite lined die around the pin. Once the preform was extruded passed the pin the sections join to form a tube. (c) Photograph of outer cladding tube preform E039JHB $Ge_{24}Sb_4Se_{72}$ viewed from the end.**

[6] Nickel-chromium alloy, strengthened by additions of titanium (1.8-2.7 wt. %), aluminium (1-1.8 wt. %), carbon (0.1 wt. %) and other alloying components present only in minimal quantities

## 3.5. Fibre and cane drawing

### 3.5.1. Drawing core/ cladding cane from a co-extruded core/ cladding preform

In this Project, chalcogenide optical fibres were manufactured by drawing from a cane (drawn from a co-extruded core/ cladding preform, section 3.4.1) suspended in an extruded cladding tube (section 3.4.2). It was suggested that a 60 % core/ cladding ratio of the extrudate was optimum for cane drawing and this was thought to occur at a distance of ~ 70 mm measured from the end of the extrudate that exited the die first (see section 5.1). The co-extruded extrudates were broken by scoring with a diamond edge blade and applying hand pressure.

Fibre drawing was conducted using an in-house modified fibre drawing tower (Heathway), Figure 3.11(a). A fibre drawing number (*e.g.* FXXXJHB) was assigned to each fibre draw. The number (represented by a X) is prefixed by 'F' which stands for fibre draw, followed by three numbers which corresponds to the chronological order in which the fibre was drawn within the University of Nottingham MIR Photonics Research Group. The initials of this author are given after the number.

It was vital, at the very least, that the preforms used for fibre drawing were clean and with no imperfections or defects on the fibre surface as this could have resulted in mechanical weakness and crack propagation centres. Thus fibre drawing was conducted in a clean room (Class 10,000). During fibre drawing, the furnace was purged with $N_2$ (BOC, 'white spot') which had been freeze dried by passing the gas through a copper coil immersed in $N_2$ (liquid) to freeze out any residual water. The fibre drawing furnace was RF (radio frequency) heated with water cooling (~ 18 °C) to back off the heating to create a 6 mm hot zone, Figure 3.11(b).

Figure 3.11(c) represents the drawing tower in a basic configuration where the following operations for cane drawing can be identified. A co-extruded core/ cladding glass preform was heated in the RF fibre drawing furnace. The drawn diameter was continuously controlled to produce a cane of typically 500 µm diameter.

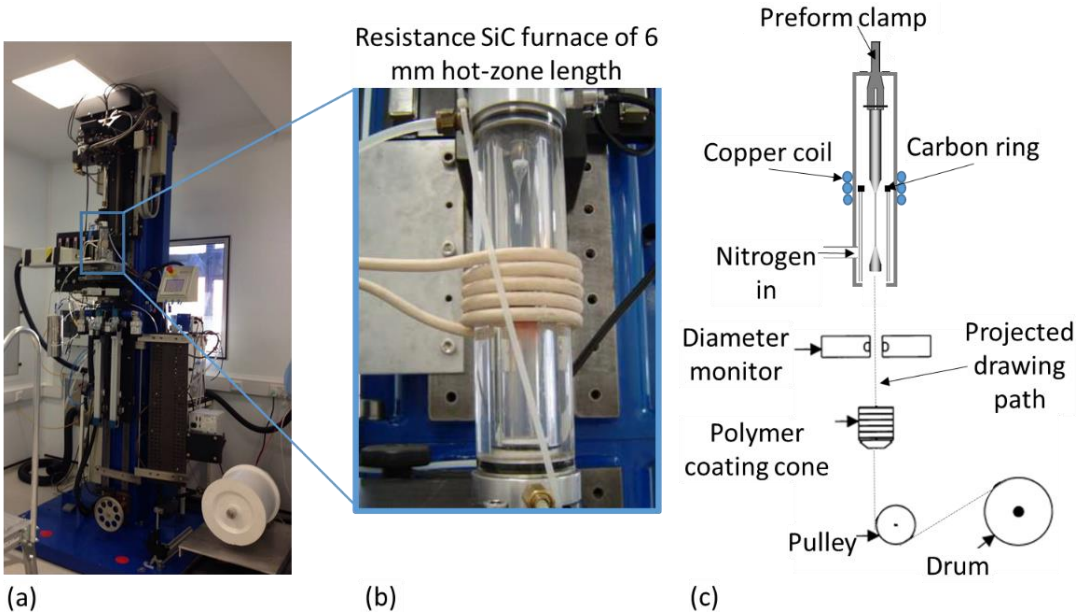



**Figure 3.11 (a) Image of in-house modified fibre drawing tower (3 m tall) with (b) enlarged image of radio-frequency furnace. The coil was operated at 70 kHz. The temperature of the graphite ring was controlled by varying the RF power as a percentage of its maximum. (c) Schematic diagram to represent the fibre drawing setup for cane drawing from a co-extruded core/ cladding preform. For fibre drawing a similar method was used with the cane suspended from a cladding tube extrusion.**

### 3.5.2. Rod-in-tube fibre drawing

An extruded cladding tube (see section 3.4.2) was immersed in a solution of propylamine (98 % Sigma Aldrich) solution at room temperature, within the clean room. Propylamine etching (which can also be considered as chemical polishing) is a process where a small depth (in the range of a few µm) of the chalcogenide glass surface is transformed into soluble complex anions by the strong complexing agents of propylamine. The resultant small reduction in thickness was apparently uniform, with the benefit of producing a visually very clean optical quality surface. The cladding tube

was fixed onto an aluminium ferrule with fast curing glue (Alraldite) at least 24 h before fibre drawing. The freshly drawn cane was suspended within the cladding tube with a blob of UV (ultraviolet) adhesive (3M, curing < 10 seconds when UV light applied) on one end to catch in a loop of wire (Inconel) in the ferrule, Figure 3.12(b), so that it extended ~ 40 mm below the cladding tube. The UV adhesive (dominant spectral peak for curing at 365 nm) was cured using a multispectral UV torch (Ultra fire, WF-501B). Figure 3.12(c) is a schematic diagram of the cross-section of the assembly of the preform for fibre drawing with the cane suspended in an extruded outer cladding tube. A gap can be seen between the ID of the outer cladding tube and the OD of the cane. As will be discussed in section 5.2 alterations to the outer cladding tube extrusion process were made to reduce the size of the bore, thus decreasing the size of the gap. This had the intention of creating a more uniform coalesce of the preform during the collapse down into fibre.

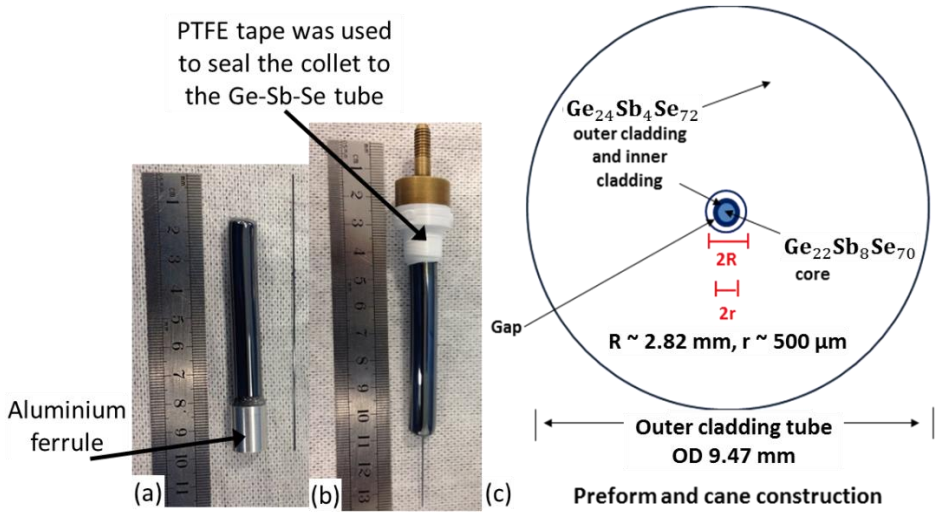



**Figure 3.12 (a) Photograph of drawn cane produced from a co-extruded core/ cladding preform (E015JHB: core composition $Ge_{22}Sb_8Se_{70}$ and cladding composition $Ge_{24}Sb_4Se_{72}$) and outer cladding tube extrusion (E014JHB: cladding composition $Ge_{24}Sb_4Se_{72}$). (b) Construction of the preform for subsequent fibre drawing with the cane suspended in the outer cladding tube extrusion. (c) Schematic diagram of the construction of the preform for fibre drawing with the cane suspended in an outer cladding tube extrusion. The outer diameter (OD) of the tube was 9.47 ± 0.02 mm, the bore radius (R) of the outer cladding tube was 2.82 ± 0.01 mm and the cane diameter (r) was ~ 500 µm.**

The ferrule was fixed in a movable holder so that the lower end (~ 10 mm) of the outer cladding tube and cane preform were placed inside the RF tubular resistance heater. As the preform was heated gradually to the fibre drawing temperature of the glass, its thickness decreased down to fibre thickness as a gob (lump of molten glass) descended under the effect of gravity and drawing force from the formation of drawing the gob. The drawing gob was broken off and the fibre was guided through the pully at the base of the fibre drawing setup, Figure 3.11(c), to the fibre drawing drum. During the drawing process it was intended that the fibre diameter was locally reduced to produce core sizes of ~ 15 µm, ~ 10 µm, and ~ 7 µm for every draw by controlling the feed rate, drawing speed and heating zone of the glass preform. However, as will be discussed in Chapter 5, section 5.7, due to problems of preform geometry and glass melt behaviour these desired core diameters were not achieved. Due to the fibre fragility, a protective 100-150 µm coating PVDF-HFP (poly vinylidene fluoride-*co*-hexafluoropropylene; DSM Desotch) was deposited on-line via the polymer coating cone shown in Figure 3.11(c). After the coating was applied it was cured as it passed through a broad UV mercury arc (Omni Cure S2000, 250 – 400 nm, dominant line for curing was 365 nm). Once again the application of the polymer coating was not always successful, see Chapter 5.7 for further discussion.

## 3.6. Ge-Se-Sb chalcogenide glass characterisation

The majority of the physical and optical techniques used to characterise the as-prepared chalcogenide glass rods and optical fibres in this Project are discussed here. Included are; X-ray diffraction (XRD), section 3.6.1; density, section 3.6.2; differential scanning calorimetry (DSC), section 3.6.3; differential thermal analysis (DTA), section 3.6.4; thermal mechanical analysis (TMA) section 3.6.5, including viscosity/ temperature behaviour, section 3.6.5.2 and thermal expansion coefficient (TEC), section 3.6.5.3 and

Fourier transform infrared spectroscopy (FTIR), section 3.6.6. Further characterisation techniques such as scanning electron microscopy (SEM) and energy dispersive X-ray spectroscopy (SEM-EDX) are explained in section 3.7. Further characterisation techniques in this document are explained in the relevant chapters, including; near-field imaging in Chapter 6, glass distillation in Chapter 6, biological testing in Chapter 7 and neutron diffraction structural analysis in Chapter 8.

### 3.6.1. X-ray diffraction (XRD)

#### 3.6.1.1. Introduction to X-ray diffraction (XRD)

In 1912, Max von Laue, a German physicist, discovered that X-rays were diffracted in an orderly way due to the orderly arrangement of atoms within a crystal [184]. This phenomenon can be exploited to determine the atomic structure of crystals using an X-ray of known wavelength (λ). The directions and intensities of the diffracted X-ray beam are used to deduce the arrangement of the crystal unit cell. The Bragg formulation is a method used for the interpretation of X-ray diffraction, Equation 3.2. When a beam of monochromatic X-rays strikes a crystal, the wavelengths scattered by the atoms in each layer combine to form a reflected wave.

$$n\lambda = 2d \sin\theta \qquad \textbf{Equation 3.2}$$

where the inter-plane spacing between reflecting crystal planes is $d$, $n$ is diffraction order, the diffraction angle is $\theta$ and the path difference for waves reflected by successive planes is $2d \sin\theta$. When the waves combine, a strong reflected beam is produced, shown as a Bragg peak, indicating a crystal. A glass specimen will appear as an ‘amorphous hump’ diffraction pattern with no sharp peaks on account of the lack of long range periodicity.

### 3.6.1.2. Equipment and sample preparation

The Ge-Sb-Se chalcogenide bulk glass sample or fibre was ground into powder to provide an average representation of the glass sample allowing the entire depth of the sample to be analysed rather than just a few nanometres from the bulk surface. For the as-annealed bulk glass, the contraction cone (the cone-shape formed at 10-15 mm of the top of a glass rod) was used; crystallisation was most likely to occur here due to the congregation of any contaminants, if present, offering nucleation sites. Therefore, if the contraction cone was found to be amorphous (non-crystal containing), the remaining glass rod could be deemed to be amorphous. The samples were crushed and ground in an agate pestle and mortar (Fisher) within a fume cupboard. Acetone (Sigma Aldrich, > 99.5 %) was added to avoid heat effects on the crystal structures during grinding.

X-ray diffraction (XRD) was carried out using a diffraction detector (Siemens D500 diffractometer) and an X-ray generator (Krystalloflex 810) working at 40 kV and 20 mA with CuKα radiation emitted from a stationary copper source (0.154 nm wavelength) while the Ge-Sb-Se chalcogenide glass sample was rotated (θ °) at half the speed of the detector (2θ °) so that the sample remained equidistant between the source and detector. All Ge-Sb-Se chalcogenide bulk glass and fibre XRD patterns were measured under the same conditions, 2θ scan; 10 °-70 °, 0.05 ° step and 40 s per step, with a total run time of 13.2 h. It is accepted that XRD measurements made with the source power used can only detect > 3-5 volume % crystals [185].

### 3.6.2. Density

Density measurements were conducted to feed into the structural studies carried out on the Ge-Sb-Se chalcogenide glasses along the stoichiometric tie-line $x(GeSe_2)$-$(1-x)(Sb_2Se_3)$, discussed in Chapter 8. The Ge-Sb-Se chalcogenide glass samples were

weighed (Sartorius balance CP224S; ± 0.1 mg accuracy, 2-3 g comprising of 1 or 2 pieces (~10- 20 mm)) and cleaned using acetone (>99.5%, Sigma Aldrich) and lens tissue (Ross). The density measurements were conducted in a helium (He) gas pycnometer (Micromeritics, AccuPyc 1330) by using the gas displacement method to measure the volume. He atoms can fill pores as small as 1 Å in diameter [186]. The Ge-Sb-Se chalcogenide glass samples were placed into a chamber of known volume. He gas was admitted into the chamber and allowed to reach equilibrium. He gas then flowed into the reference chamber of known internal volume and equilibrium was reached again. The pressure observed upon filling the sample chamber, and then discharging the gas into the reference chamber, allowed calculations of the sample volume as only the Ge-Sb-Se chalcogenide glass sample displaced the He gas. Dividing the volume by the sample weight provided the He gas displacement density.

### 3.6.3. Differential scanning calorimetry (DSC)

In differential scanning calorimetry (DSC), the heat absorbed (an endothermic event) by a material during phase transformation is analysed [187]. DSC was used to determine the onset $T_g$ of the Ge-Sb-Se chalcogenide glasses to assist in the quenching and annealing procedures, section 3.2.4. As will be discussed in Chapter 4, matching the $T_g$ of the Ge-Sb-Se glass pairs was discovered during this work to be the vital parameter in fabricating core-cladding optical chalcogenide glass fibres.

DSC provided an enumerative measure of the electrical energy required to maintain zero-temperature difference between the Ge-Sb-Se chalcogenide glass sample and an inert reference sample. The difference in the energy required for the inert reference and the Ge-Sb-Se chalcogenide glass sample to balance the same temperature is recorded. The chalcogenide glass sample absorbs more electrical energy at $T_g$ (observed as an

endothermic peak on a DSC curve), than the inert reference sample, in order to break bonds and become a supercooled liquid.

An agate pestle and mortar was used to break the Ge-Sb-Se glass into small chunks (~2 – 5 mg). 20 ± 5 mg was placed in an aluminium (Al) pan and lid (Perkin Elmer). The pan and lid were pressure sealed using a presser sealing device (Perkin Elmer) at room temperature and ambient atmosphere. It is worth noting that as the (Al) pans were not hermetically sealed, the Ge-Sb-Se samples were not heated to more than 20 °C above their $T_g$ (the program was stopped manually when it was observed that $T_g$ was reached) to avoid the accumulation of vapour within the pan. Onset Tg measurements were carried out using DSC equipment (Perkin Elmer DSC7 and Pyris 1 DSC analyser) with water circulating chillers and an argon gas flow through the head at the rate of 20 ml $min^{-1}$. DTA (see section 3.6.4) was used to measure the thermal characteristics of the glass > $T_g$ + 50 °C. The DSC was calibrated using indium ($T_m$= 156.60 °C) for the low temperature range and zinc ($T_m$= 419.47 °C) for the high temperature range. A baseline run (where both pans were empty) was carried out initially and subtracted from the curves to remove the effect of any artefacts (*e.g.* noise resulting from the equipment response) unrelated to the Ge-Sb-Se chalcogenide glass. The Ge-Sb-Se chalcogenide glasses were heated at a rate of 10 ºC $min^{-1}$. For each measurement an initial "conditioning" temperature run was carried out to ensure all glasses had the same thermal history. The samples were heated up to the $T_g$ + 50 °C, held isothermally for 1 minute and then cooled to 40 °C at 10 ºC $min^{-1}$. Please note that the initial program temperature was set to 400 °C, however, it was never reached as the program was altered manually to cool after $T_g$ was observed. The samples were reheated at 10 °C $min^{-1}$ to $T_g$ + 50 °C and cooled at 10 °C $min^{-1}$ to 40 °C and the program was repeated

once more. This was so that the second and third run were carried out on a Ge-Sb-Se chalcogenide glass sample with the same thermal history. The first sample reflected the cooling rate during the original glass quenching and annealing process. An average of the second and third run provided the mean $T_g$ and standard deviation.

The "onset temperature" was calculated for $T_g$ using the intersection of two tangents. One was fitted on to the baseline, see Figure 3.13, and the other to the point of maximum gradient in the $T_g$ feature. The values reported for $T_g$ throughout this Thesis were calculated from the second run. This was to ensure a similar thermal history was established for all the Ge-Sb-Se glasses. The varied annealing schedule, see section 3.2.4, for each glass could have affected the as-calculated onset $T_g$ for the first peak, resulting in non-reliable comparisons. A temperature difference in the onset $T_g$ of ± 2 – 4 °C was generally found between the first and second runs, Figure 3.13.

It is worth noting that as the Ge-Sb-Se chalcogenide glass samples were sealed into the Al DSC pans in ambient atmosphere, potentially some oxidation and hydrolysis of the sample could have occurred, especially ≥ $T_g$. However, this was deemed a negligible effect as the onset $T_g$ values from the second and third runs were reproducible (*e.g.* for the $Ge_{19}Sb_{15}Se_{66}$ glass in Figure 3.13 the $T_g$ for the second run was 233.8 °C and for the third run 234.5 °C). Yet, it cannot be ruled out that irreversible oxidation and hydrolysis occurred in the first DSC run and had the potential of contributing to the $T_g$ peak event.

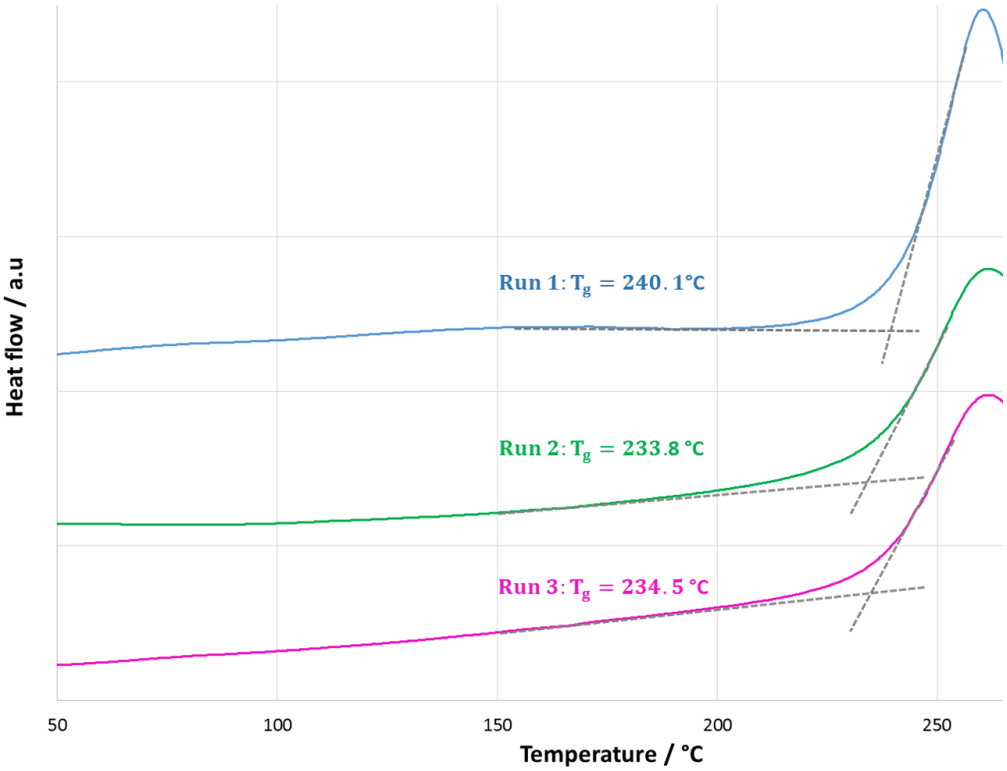



**Figure 3.13 DSC of the glass $Ge_{19}Sb_{15}Se_{66}$ (M081JHB) illustrating the calculation for onset $T_g$ and the repetition of runs to confirm the $T_g$ measurement (vertically shifted for clarity). The $T_g$ calculated from the first run (240.1 °C) was deemed to be incorrect due to the influence of the different thermal history of the glasses. The $T_g$ for the second run was 233.8 °C and for the third run 234.5 °C. A temperature difference in the onset $T_g$ of ± 2 – 4 °C was generally found between the first and the second run due to the different thermal history of the Ge-Sb-Se glasses.**

### 3.6.4. Differential thermal analysis (DTA)

#### 3.6.4.1. Introduction to Differential thermal analysis (DTA)

DTA can be used to study the thermal behaviour to a higher temperature than DSC (*e.g.* glass crystallisation peak temperature ($T_c$) and glass transition temperature ($T_g$) were of interest in this study) and the phase change of a glass. The main reason why the DTA samples were taken to a higher temperature than the DSC samples was because the DTA samples were hermetically sealed, whereas those for DSC were not. The

temperature difference (ΔT) between the sample ampoule and the reference ampoule was measured during the DTA heating process.

It is important to understand the thermal stability of the glass in order to predict the likelihood of crystallisation during fibre drawing. The value of $T_c$ - $T_g$ (the Hruby parameter [188]) is a guide in evaluating the fibre drawing ability of the Ge-Sb-Se chalcogenide glasses. The viscosity-temperature relationship was another significant property affecting fibre drawing that should not be ignored, see section 3.6.5.2.

### 3.6.4.2. Equipment and sample preparation

The as-annealed chalcogenide glass rod was broken into chunks using a pestle and mortar (Agate-Fisher), each chunk weighing ~2-40 mg. Chalcogenide glass reacts with oxygen and water vapour in the atmosphere when heated above its $T_g$. Therefore ~100 mg of sample was weighed (Sartorious scales BP221S accurate +/-1 mg) in ambient atmosphere, batched into a silica glass ampoule (Baumbach 3/4.7 mm ID/OD) and sealed under vacuum ($10^{-5}$ Pa). The reference sample was prepared by sealing an empty silica ampoule which had the same mass (± 20 mg) as the empty sample ampoule, to try to give a flat baseline. The characteristic (silica) $SiO_2$ α↔β transition does not occur in the temperature range of interest. Furthermore $SiO_2$ in the vitreous state does not undergo this glass α →β transformation until after being held at high temperature for some days [189].

DTA measurements were carried out in a Perkin Elmer DTA 7. The DTA was calibrated using indium for the low temperature range ($T_m$ = 156.60 °C) and Al for the high temperature range ($T_m$ = 660.10 °C). The chalcogenide sample and reference were placed in their respective platinum holders within the furnace. All DTA measurements in this Project were obtained at a rate of 10 °C $min^{-1}$ from room temperature 725 °C in a

helium (He) atmosphere. The sample and the reference weight were carefully measured and were equal, within an error of ± 0.01 g. The temperature difference (ΔT) was measured between the sample ampoule and the reference ampoule during isothermal or isochronal heating and a thermal event occurred in the chalcogenide glass (*e.g.* $T_c$ and $T_g$). ΔT between the sample and reference was detected by the thermocouples. Endotherms were plotted against temperature and characteristic temperatures were defined by endothermic ($T_g$ and $T_m$) and the exothermic peaks ($T_c$), discussed in Chapter 4.

It is worth noting that DSC and DTA are very similar characterisation techniques. It is suggested that DSC was the most sensitive technique for finding $T_g$ as there was good thermal contact between the glass sample and the thermocouple due to the samples being pressure sealed in Al pans. DTA samples are sealed under vacuum in silica ampoules which have a wall thickness of ~ 1.7 mm. This meant that the thermal contact between the Ge-Sb-Se chalcogenide glass sample and thermocouple was quite poor. Therefore when $T_g$ is quoted throughout this Thesis it was calculated using the method described in section 3.6.3. Nevertheless DTA was able to cover a greater temperature range compared with DSC thus could potentially show the whole characteristic profile of the Ge-Sb-Se glass from $T_g$ to $T_c$ through to $T_l$, discussed in section 4.2.2.

### 3.6.5. Thermomechanical analysis (TMA)

#### 3.6.5.1. Introduction

Thermomechanical analysis (TMA) measurements can be used to measure the viscosity-temperature characteristics (> $T_g$), section 3.6.5.2, and thermal expansion coefficient (TEC) (< $T_g$), section 3.6.5.3, of the Ge-Sb-Se chalcogenide glasses. The

information gained was importantly used to tailor the fibre drawing procedure. Perkin Elmer TMA 7 thermomechanical equipment was used for both viscosity-temperature and TEC measurements with the relevant probes, Figure 3.15 and Figure 3.16 respectively. For both techniques the sample chamber was purged with He (BOC) flowing at 20 ml $min^{-1}$. A baseline heating run was carried out before the sample run for both techniques to remove any experimental artefacts (*e.g.* thermal expansion of the TMA set-up).

### 3.6.5.2. Viscosity/ temperature analysis

Viscosity maybe defined as a parameter to measure the resistance of a fluid to being deformed by either shear stress or extensional stress (longitudinal stress) [188].The chemical bonds within a melt between atoms affect the viscosity. If the composition of a melt is changed, in such a way as to result in a reduction in the overall average coordination number and hence the number of bonds, then in general, the viscosity is reduced [188].

#### 3.6.5.2.1. Equipment and sample preparation

The as-annealed chalcogenide glass rod was broken into chunks using a pestle and mortar (capacity = 5 x $10^{-5}$ $m^3$, Agate-Fisher). ~2 - 3 g of sample was weighed (Sartorious scales BP221S accurate +/-1 mg) in the ambient atmosphere and inserted into a silica glass ampoule (as-received Baumbach 4/6 mm ID/OD) and sealed under vacuum ($10^{-5}$ Pa). The glass was then re-melted, see Table 3.9. Quenching and annealing were carried out as in previous melts, see section 3.2.4, using 30 s interval times for quenching and 0.5 h for the annealing hold. After annealing, the ampoule was opened and samples were cut, as was described in section 3.3, to yield small cylindrical samples with parallel end faces and at heights of both 1.6 mm and 4.1 mm, for each

glass composition to be measured, shown schematically in Figure 3.14. The two different heights enabled access to two different viscosity regions as will be discussed further in section 4.2.3.1.

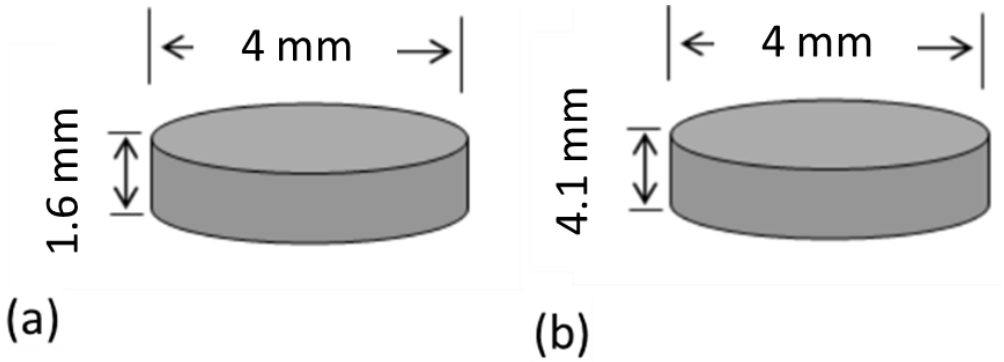



**Figure 3.14. Schematic to show disc height for TMA experiment. (a) Height and diameter parameters for 50 mN load with the intension of accessing for measurement a viscosity of $10^{4.5}$ Pa.s to represent the conditions for fibre drawing. (b) Height parameters for 400 mN load with the intension of accessing a viscosity of $10^{8}$ Pa.s to represent the conditions for extrusion.**

A sample height of 1.6 mm and a load of 50 mN were used for measuring viscosity around $10^{4.5}$ Pa.s which approximately represents the conditions for fibre drawing [45]. A sample height of 4.1 mm and a load of 400 mN were used with the intention of measuring viscosity of $10^{8}$ Pa.s as this approximately represents the conditions for extrusion [45]. However, it was found that the graphical plot results obtained had to be extrapolated to reach a viscosity of $10^{8}$ Pa.s, as will be discussed in section 4.2.3.1.

For viscosity-temperature measurements, the parallel plate method was used. A foot and base plate were attached to the silica glass probe inside the TMA equipment, see Figure 3.15. The Ge-Sb-Se chalcogenide glass cylindrical sample was placed vertically between the foot and the base plate and the foot was lowered to rest on top of the sample with the required load being applied under a helium (BOC) atmosphere. The sample was then heated from room temperature to 200 °C at a rate of 40 °C $min^{-1}$. The

temperature was then held at 200 °C for 1 minute before being heated to 400 °C at a slower rate of either 5 °C $min^{-1}$ or 10 °C $min^{-1}$.

**Table 3.9 Melting schedule of TMA samples used for viscosity/ temperature measurements.**

| Step | | Process |
|---|---|---|
| **1** | Heat Stationary | 15 °C to 600 °C at 60 °C/h |
| **2** | Heat Rocking | 600 °C to 900 °C at 60 °C/h |
| **3** | Dwell | 2 h |
| **4** | Make vertical | |
| **5** | Cool | 900 °C to 600 °C at 80 °C/h |
| **6** | Dwell | 600 °C for ~1 h |
| **7** | Quenching | In ambient air; 30 s. Ampoule was then immediately placed in pre-heated furnace at Ge-Sb-Se chalcogenide glass's $T_g$ for 30 s. Ampoule was then held vertically and was partially removed from furnace presenting ~10 mm of melt above the furnace. $N_2$ jet was focused on one point, 90 ° perpendicular to the melt, at the top of the contraction cone. Upon solidification of the melt, the surface edge shrank away from the ampoule wall at which point the $N_2$ jet was distributed evenly around the circumference of the ampoule until the entire melt was solidified (therefore shrunken completely away from the wall of the ampoule). |
| **8** | Annealing | Ampoule placed into a 6 h pre-heated furnace (Instron, TF105/4.5/1F, ID tube 86 mm) at the Ge-Sb-Se chalcogenide glass's $T_g \pm 5$ °C; 0.5 h. After annealing the Ge-Sb-Se chalcogenide glass was cooled slowly to room temperature by turning the furnace power off. |

The apparatus detected the deformation of the sample by means of a linear variable differential transducer to an accuracy of ± 100 nm. The end height of the sample was calculated prior to heating as the maximum expanded diameter (ø) allowed of the sample was 7.5 mm (defined by the dimensions of the equipment as a greater ø of the sample would touch the thermocouple). For example, for a cylindrical sample of 1.62 mm height and 4.09 mm ø, the end height (h) = $\frac{\pi \text{ x } 2.045^2 \text{ x } 1.62}{\pi \text{ x } 3.75^2}$ . The probe position-temperature curve was monitored in real time. The program was switched to cooling at 10 °C $min^{-1}$ once the sample had reached the lowest acceptable end height before the

sample might flow enough to cause it to touch the thermocouple. For the Ge-Sb-Se chalcogenide glass melts here, this was usually before the program reached 400 °C. The process was repeated twice more to check reproducibility.

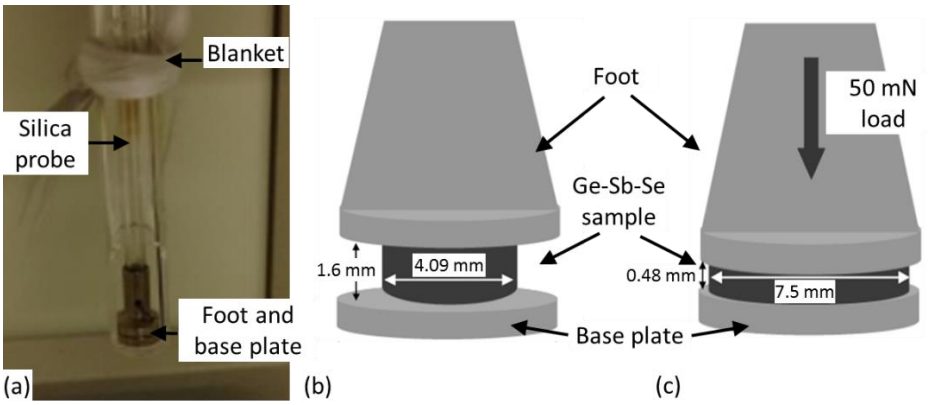



**Figure 3.15 (a) Image to show the foot and base plate attached to the silica glass probe in the Perkin Elmer TMA 7 thermomechanical equipment for viscosity-temperature measurements. (b) Schematic to show the starting position of the foot and base plate with the Ge-Sb-Se glass sample in position. (c) Schematic to show the movement of the foot after a load of 50 mN was applied and the effect on the sample.**

### 3.6.5.3. Thermal expansion coefficient (TEC)

#### 3.6.5.3.1. Introduction to thermal expansion coefficient (TEC)

When a material is heated through a particular temperature range, an endothermic event accompanies the heating where the material takes in energy (in the form of heat) which increases the amplitude of the atomic vibrations. Thus, the distance between atoms within the material is increased and can be recorded as an expansion. Therefore, it follows that during cooling, an equivalent exothermic event occurs, where heat is realised upon contraction of the material. The linear thermal expansion coefficient ($\alpha_L$) is the parameter used to describe this phenomenon of the material's dimensional changes under heat treatment, per degree temperature change, Equation 3.3:

$$\propto_L = \frac{\Delta h}{h_i . \Delta T} \qquad \textbf{Equation 3.3}$$

where $\alpha_L$ is the linear thermal expansion coefficient, $h_i$ the initial height of the material at room temperature and $\Delta h$ the change in height with change in temperature $\Delta T$. Knowledge of $\alpha_L$ of a chalcogenide glass aids in the selection of choosing an appropriate glass pair to coextrude and/ or co-draw to fibre. The importance of $\alpha_L$ will become more apparent in section 4.3 where it was used to select a core/ cladding glass pair in the anticipation that it would help to reduce internal stresses within the fibre.

#### 3.6.5.3.2. Experiment and sample preparation

Unlike for the viscosity-temperature measurements, it was not critical to have perfectly sized or shaped samples for TEC measurements, as long as the top and bottom sample surfaces were near-parallel, thus no re-melt was required to obtain the TEC samples. Samples were cut from discs of the Ge-Sb-Se glass rods, see section 3.3 for cutting method, into rectangular samples where the height (9-10 mm) was greater than the width (4-5 mm by 4- 5 mm). TEC measurements were carried out in the same Perkin Elmer TMA 7 thermomechanical equipment as the viscosity-temperature measurement but with the TEC probe head, Figure 3.16.

The Ge-Sb-Se chalcogenide glass samples were placed under the probe with the longer dimension placed vertically, and the TEC probe was lowered to rest on the top of the sample. A load of 100 mN was applied. The samples were heated from room temperature towards 300 °C at a rate of 5 °C $min^{-1}$. The probe position-temperature curve was monitored manually and the program was switched to isothermal for 1 minute as soon as the sample had reached the $T_g$ and had started to be compressed rather than expanded. This was before the program reached 300 °C, the sample was then cooled at 10 °C $min^{-1}$. Similar to $T_g$ values (see section 3.6.3) $\alpha_L$ is dependent on the

thermal history of the glass sample. Therefore the process was repeated with a second and third run to ensure the same thermal history (*e.g.* cooling at 10 °C $min^{-1}$) and to check reproducibility. A quantitative comparison of $\alpha_L$ for the three runs will be given for a $Ge_{24}Sb_4Se_{72}$ glass in Table 4.10.

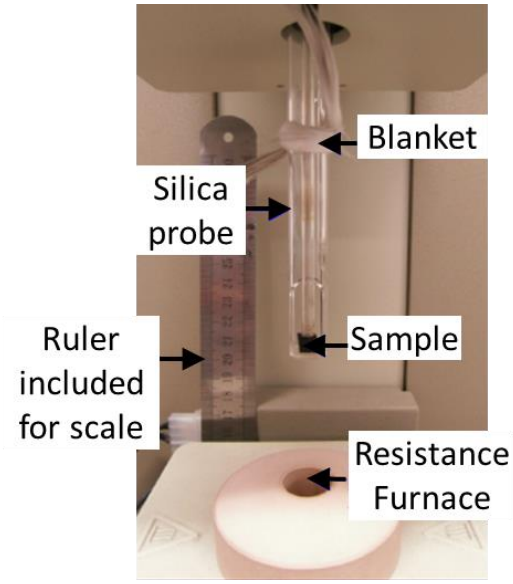



**Figure 3.16 Silica glass probe in the Perkin Elmer TMA 7 thermomechanical equipment for thermal expansion coefficient measurements.**

### 3.6.6. Fourier transform infrared spectroscopy (FTIR)

Fourier transform infrared spectroscopy (FTIR) provides a characteristic 'fingerprint' set of absorption bands comprising the optical absorption response of the Ge-Sb-Se chalcogenide bulk glasses and optical fibres. FTIR loss spectra can be used to gain understanding of the light guiding properties of the Ge-Sb-Se glasses in terms of extrinsic and intrinsic absorption and scattering, see section 2.6.2. The optical absorption is determined by measuring the decrease in the optical intensity of a light beam (from the FTIR source) travelling through the glass. The Beer-Lambert law can be used to relate the transmittance (T) of a material sample to the absorbance (*A*) by:

$$\mathbf{T} = \left(\frac{P_{in}}{P_{out}}\right) = e^{-A} \qquad \textbf{Equation 3.4}$$

where the measured optical power detected after the transmittance is $P_{out}$ and the initial optical power is $P_{in}$. $A$ is related to the concentration of absorbing species in the sample and the path length (l) through which the light is travelling, by [190, 191]:

$$\boldsymbol{A = \varepsilon c l} \qquad \textbf{Equation 3.5}$$

where c is the concentration of absorbing species in the sample and ε is the molar extinction coefficient (absorptivity) of the absorbing species in the sample. In this Thesis absorbance per path length of the sample will be presented in $cm^{-1}$.

It is to be noted that not all of the incident light on the glass surface is absorbed due to light reflection at the glass surface (*e.g.* percentage Fresnel reflection (% R) occurs at the boundary of two surfaces on account of the difference in the refractive indices [140]). The percentage Fresnel reflection at an air/ glass interface for normal incidence can be calculated from Equation 3.6, assuming the refractive index of glass is n and air ≡ in vacuo = 1.

$$\% \boldsymbol{R = 100\left(\frac{n-1}{n+1}\right)^2} \qquad \textbf{Equation 3.6}$$

Due to the Ge-Sb-Se glasses's high refractive index (*e.g.* $Ge_{22}Sb_7Se_{70}$ 2.25 ± 0.05 at 1.064 µm [192]) it can be calculated (from Equation 3.6) that the percentage Fresnel reflection at one interface is 14.8 %. FTIR spectroscopy was used in this Project to investigate the NIR and MIR optical absorbance of the bulk Ge-Sb-Se chalcogenide glass compositions (described in section 3.6.6.2) and also to measure the optical loss of the fabricated Ge-Sb-Se fibres (section 3.6.6.3). The transmission of the bulk glasses is given in section 4.1.2 and for the optical fibres in section 6.3.

### 3.6.6.1. FTIR equipment

For both bulk and fibre FTIR measurements, the FTIR equipment (IFS 66/S, Bruker) was purged with dry air (Parker Filtration, FT-IR purge gas generator, 75-52-12VDC) for 15 minutes to reduce the effect of $CO_2$ (at ~ a wavelength of 4.3 μm [21]) and $H_2O$ (at a wavelength of ~ 6.31 μm [193]) absorption levels when collecting the background signal and all measurements (the level of the $CO_2$ was monitored to ensure its disappearance within the 15 minutes before signal collection). Every spectrum was baseline corrected using Bruker's proprietary software, OPUS.

### 3.6.6.2. Bulk transmission

It was vital that the sample used for bulk absorbance measurement was flat, had parallel faces and was highly polished. The as-annealed Ge-Sb-Se chalcogenide glass rods were cut and polished (using the method as described in section 3.3.2) to a 0.5 μm finish, with a surface finish as clean and scratch-free as possible. The average thickness (*i*.e. optical path length) of the as-prepared samples was 2.5 – 3.5 mm, after polishing. For the bulk glass transmission measurements, the FTIR spectrometer setup included a DTGS detector (Bruker; 0.8 – 27 μm), MIR detector (Bruker; 2-11.7 μm), Globar light source (Bruker; for MIR, 3.3 – 100 μm), tungsten (W) light source (Bruker; for NIR, 0.6 – 3.3 μm) and beam-splitters KBr (Bruker; for MIR) and $CaF_2$ broadband '$CaF_2$-BB' (Bruker; for NIR).

A background spectrum was first collected with an in-house made aluminium sample holder (which prevents light penetration) with a central aperture (5 mm in diameter) in place. The Ge-Sb-Se chalcogenide glass sample was then placed over the central aperture and loaded into the sample chamber of the FTIR spectrometer. The chamber was purged once more. A sample spectrum was taken. The resulting absorbance

spectrum (the Bruker software automatically removed the baseline spectra and applied Fourier transform to provide an interferogram of wavelengths) was divided by the path length of the sample (measured using a Mitutoyo IP54 ± 0.001 mm micrometre) to calculate the absorption coefficient ($P_{out} = P_{In}e^{-\varepsilon c}$). It was not possible to trust the absolute value of the absorbance spectra, on account of the effect of scattering and Fresnel reflections. Nevertheless, the relative absorbance band height, at the corresponding wavelengths of the impurities, was deemed to be reliable. The results presented for the bulk glass composition in section 4.1.3 are reported as absorption coefficient ($cm^{-1}$).

#### 3.6.6.3. Fibre optical loss experiment

Generally ~2 m of Ge-Sb-Se fibre was taken from the fibre drum directly after fibre drawing and positioned between the launch end mirrors and the detection end mirrors. Each end of the fibre was cleaved using a diamond scribe pen (S90R Thorlabs; or 58805-600 Diamond Fibroscribe, Lunzer) and held in place using a clamp. For the glass optical fibre transmission measurements, the FTIR spectrometer setup included a liquid nitrogen cooled InSb detector (Judson; 0.9 – 5.4 μm), MCT detector (Bruker; 2-11.7 μm), Globar light source (Bruker; for MIR, 3.3 – 100 μm), tungsten (W) light source (Bruker; for NIR, 0.6 – 3.3 μm) and beam-splitters KBr (Bruker; for MIR) and $CaF_2$ broadband '$CaF_2$-BB' (Bruker; for NIR).

Fibre loss was determined using the "cut-back" method as described in [164]. At first, the transmission spectrum of a longer piece of optical fibre was registered, which involved measurements of the optical loss spectrum of a fibre of length "*A*" (generally ~ 3 m), with several cleaves over a length of ~ 30 mm referred to as "Group 1", from the distal end of the fibre and the spectrum was collected after each cleave. Cleaving is

a process whereby a diamond blade is used to produce a controlled break in the fibre, with the intention of creating a perfectly smooth cross-section. Several cleaves inevitably had to be made due to the difficulty in producing a high quality cleave, however, the 'group cleave' process enabled identification of the best cleave. Cleaves were assessed optically using GX capture software in conjunction with a Vickers M75 optical microscope and a GX CAM-5 camera. Figure 3.17(a) shows examples images of; (i) a good cleave and (ii) an undesired cleave. In this Project the fibre used for fibre loss measurements usually had ~ 250 µm diameter. Damage is evident in the cleaved edge of the cross-section of both the fibres in Figure 3.17(a). This defect was impossible to completely avoid due to the typical brittle fracture found for all inorganic compound glass fibres. As can be seen in (i) for a core/ cladding fibre, a cleave was deemed to be good if the core guiding region where the light propagates was mostly unaffected by the unavoidable edge defect of the cleaved cross-section of the fibre. In (ii) the impact damage of cleaving propagated too far into the core region of the fibre. Section "*B*" was then cleaved (typically ~ 1.5 m) and again several cleaves were made, referred to as "Group 2" and the spectrum was collected after each cleave, see Figure 3.17.

The length of the cutback after section *A* depended on how low loss the fibre was. For ultralow loss fibre the record in our laboratory is ~ 52 m [164].

The optical losses were calculated using Equation 3.7;

$$\boldsymbol{Loss\ (dB/m) = -(10/L).log_{10}(P_{out}/P_{in})} \qquad \textbf{Equation 3.7}$$

where L is the length of fibre between Group 1 and Group 2 cleaves (section *B*) at which the measured optical power is $P_{out}$ before cutting back and $P_{in}$ after cutting back. The optical attenuation of the Ge-Sb-Se chalcogenide glass fibres presented in section 6.3 are reported in dB/m.

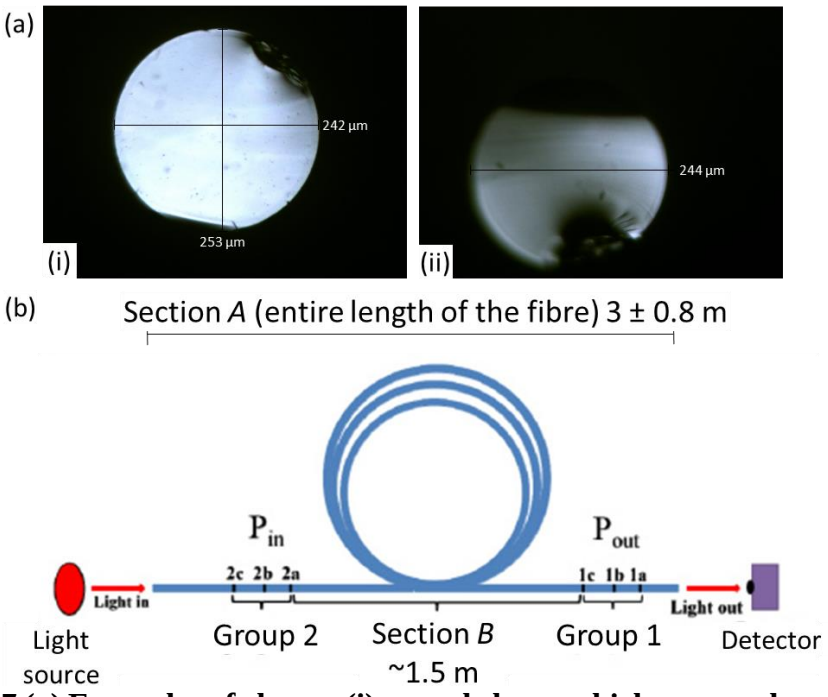



**Figure 3.17 (a) Examples of cleaves (i) a good cleave which was used as the launch end for the fibre loss measurements of the 242 x 253 ± 2 µm fibre F018JHB. (ii) An undesirable cleave during the loss measurements of F018JHB which was discarded. (b) Schematic of the "cut-back" method used for fibre loss measurements. The initial length of the fibre (section *A*) was generally ~3 m with Group 1 (1a, 1b and 1c) cleaves removed from section *A*. Spectrum was collected after each cleave. Section *B* was then cleaved (~1.5 m) with Group 2 (2a, 2b and 2c) cleaves removed. Again the power spectrum was collected after each cleave. Figure adapted from [164].**

## 3.7. Scanning electron microscopy (SEM) and energy dispersive X-ray (EDX)

### 3.7.1. Introduction to scanning electron microscopy (SEM) and energy dispersive X-ray spectroscopy (EDX)

Scanning electron microscopy (SEM) equipped with energy dispersive X-ray spectroscopy (EDX) is a technology applied to obtain information about morphological characteristics and elemental composition of materials. SEM allows images to be viewed at a much higher resolution (up to 100 nm) than an optical microscope [194]. EDX was used to analyse the elemental composition of the core and cladding Ge-Sb-Se glasses (results are discussed in section 4.1.2), the structure of the core/ cladding fibres (discussed throughout Chapter 5) and the biological processes after exposure to 3T3 mammalian cells (section 7.5). Although chalcogenide glasses are considered as

semi-conductors, they do not conduct efficiently enough to avoid electron charging (which prevents the signal electrons from reaching the detector) in the SEM high vacuum mode setting without being carbon or platinum coated. Generally a beam – voltage of 20 kV was used for imaging and 15 kV for compositional analysis, with a 10-15 mm working distance. The accuracy of the analytical SEM-EDX results was estimated to be ± 0.5 at. % (and ± 0.5 wt. %), for elements heavier than oxygen analysed for all the EDX quantification results of elemental composition [185]. The sample preparation of the Ge-Sb-Se bulk glasses and fibres, is discussed in section 3.7.2. The sample preparation and methodology for the F018JHB fibres after incubation with 3T3 mammalian cells is described in Chapter 7, section 7.3.5. The SEM equipment and methodology are discussed in section 3.7.3.

### 3.7.2. SEM Sample preparation

#### 3.7.2.1. Ge-Sb-Se chalcogenide bulk glass samples

The as-prepared Ge-Sb-Se glass rod was sawn (Isomet saw, Buehler Ltd.) to the required shape (variable), as was described in section 3.3. The sawn samples were then polished, cleaned and prepared as was discussed in section 3.3.2. It was important to obtain a flat bottom of the Ge-Sb-Se chalcogenide glass sample to allow it to be mounted on to an aluminium specimen-stub (Agar) using double-sided sticky carbon tabs (Agar). Aluminium tape (Agar) was also added on the Ge-Sb-Se chalcogenide glass sample edges to ensure electronic conduction (see section 3.7.1). Samples were carbon coated (Edwards Coating System, E306A) for 5 s, applied 3-4 times.

#### 3.7.2.2. Fibre samples

The Ge-Sb-Se chalcogenide glass fibres were cleaved into lengths of ~15-20 mm which were directly mounted onto a carbon tab (Agar) stuck on an Al block, as shown

schematically in Figure 3.18. Hand cleaving was accomplished using a diamond scribe pen (S90R Thorlabs; or 58805-600 Diamond Fibroscribe, Lunzer). Any difference in height was accounted for at the bottom of the Al block , as indicated in Figure 3.18, and the fibres were positioned so that the tops were all at the same height. Typically 1- 1.5 mm of the fibre protruded from the top of the Al block. Samples were carbon coated (Edwards Coating System, E306A) for 5 s, applied 3-4 times. Results obtained will be discussed throughout Chapter 5.

### 3.7.3. Equipment and methodology

The SEM equipment (FEG-XL30 ESEM system) comprised; an electron column gun (which emitted a beam of high energy electrons (primary electrons) that propagated through a series of magnetic optical lenses and apertures that converged the beam and accelerated it to focus on the sample); a sample chamber (which was evacuated to 1.3 x $10^{-4}$ . The electron beam was rastered by a scanning coil and focused onto the sample); a detector (as the primary electron beam hit each spot on the sample, secondary electrons (SE, lower-energy electrons) were ejected from the sample surface. SE signals offer the best image resolution [195]. Backscattered electrons (BSE, higher-energy electrons) were released when the primary electrons interacted with the sample's atoms. Therefore this penetration was deeper and could provide information about the sample composition. There was a detector for each type of electron signal, SE or BSE, and a viewing system (the final image of the sample was built up from the number of electrons emitted from each spot on the sample). The quantitative analysis of the presence of the elements in the glass sample was performed using EDX (Oxford Instruments INCA x-sight Si(Li) detector with ATW2 window and INCA Energy software) as described in [195]. Images were taken of any features in the glass (*e.g.* inclusions, bubbles or surface impurities) and analysed by EDXA Phillips XL-30.

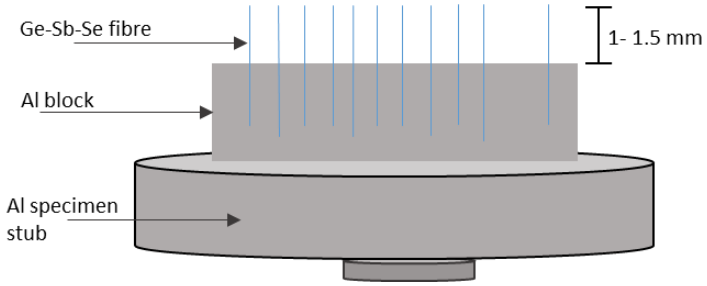



**Figure 3.18 Schematic diagram to show the positioning of the Ge-Sb-Se chalcogenide glass fibre samples on an aluminium (Al) block and Al specimen stub. The samples were between 15 – 20 mm. The fibres were arranged so that any difference in length was only on the Al block ensuring the fibres tops were the same height above the Al block.**

## 3.8. Summary

The pre-treatment of the silica glass ampoules used as a vessel for the Ge-Sb-Se chalcogenide glass melting has been described (section 3.1). The preparation steps of the Ge-Sb-Se chalcogenide glass rods, using the melt-quenching method have been explained (section 3.2). The fibre fabrication processes of extrusion (section 3.4) and fibre drawing (section 1.1) were also detailed. Characterisation techniques including; XRD (section 3.6.1), density (section 3.6.2), DSC (section 3.6.3), DTA (section 3.6.4), TMA (section 3.6.5) and FTIR (section 3.6.6) have been briefly described. SEM and SEM-EDX were also explained (section 3.7). Other Ge-Sb-Se glass characterisation techniques including; near-field imaging, cytotoxicity assays and neutron diffraction experiments are explained elsewhere in section 6.2, section 7.3 and section 8.2, respectively. In chapter 4 the optical and physical properties of the Ge-Sb-Se chalcogenide glasses intended for SCG MIR transmission are characterised.

# 4. Characterisation of the physical and optical properties of Ge-Sb-Se chalcogenide glasses to match potential glass pairs for a high purity small core-cladding MIR SCG fibre

One of the aims of this Project was to establish a core and cladding composition for the generation of broadband supercontinuum (SC) signal in the mid-infrared (MIR; 2-25 μm) for a chalcogenide glass composition not containing toxic arsenic (As). This chapter provides a study of the physical and optical properties of such a chalcogenide system based on germanium (Ge), antimony (Sb) and selenium (Se). The Ge-Sb-Se glass compositions used are given in section 4.1.

In the following sections, each glass characterisation technique is discussed for the individual glass compositions and the as-measured results are provided. X-ray diffraction patterns (XRD) were used to examine the amorphicity of each glass and are presented in section 4.1.1. To determine the accuracy of the batching technique, glass composition was examined by energy-dispersive X-ray microanalysis using a scanning electron microscope equipped with an energy dispersive analyser (EDX) (section 4.1.2). Fourier transform (FT) IR spectroscopy was used to investigate the NIR and MIR absorption of the glass (section 4.1.3). During the fibre fabrication process it was determined that knowledge of various temperature-related physical properties of the glasses, would aid the candidate glass pair selection process. Therefore characterisation techniques were conducted to assess these properties which were; differential scanning calorimetry (DSC; section 4.2.1) which was used to determine the onset $T_g$ value; differential thermal analysis (DTA; section 4.2.2) to confirm onset $T_g$ values from DSC and to investigate the crystallisation temperature of the glass; thermomechanical analysis (TMA; section 4.2.3) to determine the viscosity/ temperature behaviour of the

Ge-Sb-Se chalcogenide glasses (section 4.2.3.1) and thermal expansion coefficient (TEC; section 4.2.3.2). The development of these characterisation techniques and the impact of these thermal properties on fabricating a small core-cladding MIR Ge-Sb-Se SCG fibre, are analysed in section 4.3. There the importance of each characterisation technique is further explained with regards to selection of the candidate glass pairs. Concluding remarks are made as to the importance of the order of selecting particular thermal properties in section 4.4, and an un-fabricated glass pair composition is suggested based on its thermal properties. This chapter is summarised in section 4.5.

## 4.1. Determining the success of (JB01) $Ge_{19}Sb_{15}Se_{66}$, (JB02) $Ge_{20}Sb_{10}Se_{70}$, (JB03) $Ge_{24}Sb_{4}Se_{72}$ and (JB04) $Ge_{22}Sb_{8}Se_{70}$ glass melting

Overall, chalcogenide glass melting is complex. Several of the components of these glasses are toxic and highly volatile. The greatest care was given during glass preparation to reduce factors which could have contributed to crystal nucleation sites (*e.g.* carbon) and optical loss (*e.g.* ppm levels of impurities such as oxide).

To achieve glass solidification the Ge-Sb-Se glasses were prepared by melting in a silica glass ampoule, as-described in section 3.1 (*e.g.* ampoule preparation, precursor purification, batching and melting) and the melting – quenching method, section 3.2 (quenching and annealing). The contraction cone generated in the Ge-Sb-Se glass rods was generally ~10 mm deep due to the effective quenching procedure in air, maintaining temperature at $T_g$ and then applying a $N_2$ jet to the outside of the sealed silica ampoule housing the Ge-Sb-Se chalcogenide glass melt. The as-melted Ge-Sb-Se chalcogenide glass rods, which were used for the characterisation experiments, appeared black and shiny, as shown in Figure 4.1.




**Figure 4.1 JB04 (M047JHB; $Ge_{22}Sb_8Se_{70}$) glass rod produced from the silica glass ampoule after melt-quenching method and annealing. The rod appeared black and shiny. The contraction cone (indicated by the red dashed box) was approximately 10 mm deep for a 50 mm long rod product of 10 mm outer diameter.**

Usually, more than one glass of the same nominal composition was fabricated, extruded and drawn to fibre. Therefore composition, glass pair, melt, extrusion and fibre drawing were each coded as follows:

- *Composition* 'JBXX' (*e.g.* JB01) was chosen to identify each of the four glass compositions. The number (01-04) is prefixed by the initials of this Author.
- *Glass pair* 'Pair X' (*e.g.* Pair I) was selected to identify the three glass pairs that were drawn to fibre in this Project. The Roman numeral (I-III) is used to distinguish between the three pairs.
- *Melt number* 'MXXXJHB' (*e.g.* M047JHB) was used to reference each glass melt. The number is prefixed by 'M' which stands for 'melt', followed by three numbers which were assigned chronologically within the University of Nottingham, UK, MIR Photonics Research Group. JHB are the initials of this Author, who fabricated the glass. A list of all glasses synthesised during this work is given in Table 4.1.
- *Extrusion number* 'EXXJHB' (*e.g.* E014JHB) was assigned to each extrusion to correspond to the chronological order in which the glass boules (cut from the

glass melts) were extruded within the University of Nottingham, UK, MIR Photonics Research Group. All extrusions were heavily supervised by Dr. David Furniss (DF), Senior Postdoctoral Fellow, the manufacturer of the extruder. Again the initials of this Author are given after the number. The process of extrusion was described in section 3.4.

- *Fibre number* (*e.g.* F0_JHB) was appointed to each fibre draw to represent the chronological order in which the cane or fibre drawing occurred within the University of Nottingham MIR Photonics Research Group. The initials of this Author are given after the number. Again all fibre drawing was heavily supervised by DF who had made in-house alterations to the Heathway fibre tower. The process of fibre drawing was described in section 3.5.

Four glass compositions were used in this Project selected from [1]; JB01 ($Ge_{19}Sb_{15}Se_{66}$), JB02 ($Ge_{20}Sb_{10}Se_{70}$), JB03 ($Ge_{24}Sb_{4}Se_{72}$) and JB04 ($Ge_{22}Sb_{8}Se_{70}$). The main driving forces behind selecting the glass compositions were; (1) compositions which were resistant towards devitrification and able to withstand the many thermal processes that are involved in fabricating a fibre (*e.g.* extrusion and the fibre drawing); (2) to select candidate glass pairs that could be manipulated into forming a small core-cladding SCG fibre with intended core diameters of 15 µm, 10 µm and 7 µm, as will be discussed further in section 5.3. Section 4.3 reviews the three glass pairs which were drawn to fibre, with the glass pairs as follows; Pair I (core glass JB04 and cladding glass JB03), Pair II (core glass JB01 and cladding glass JB02) and Pair III (core glass JB02 and cladding glass JB03).

**Table 4.1 Codes and compositions of the Ge-Sb-Se glasses used for characterisation studies presented in Chapter 4.**

| Glass code | Nominal batch composition / (at. %) | Glass melt codes | Rod diameter* / (mm) | End use |
|---|---|---|---|---|
| JHB01 | $Ge_{19}Sb_{15}Se_{66}$ | M068JHB | 10 | XRD |
| | | M070JHB | 10 | TEC |
| | | M078JHB | 5 | Viscosity: Re-melt of M070 |
| | | M098JHB | 10 | Core for cane drawing FTIR; EDX; DTA |
| JHB02 | $Ge_{20}Sb_{10}Se_{70}$ | M071JHB | 10 | XRD |
| | | M077JHB | 10 | TEC |
| | | M079JHB | 5 | Viscosity: Re-melt of M071 |
| | | M084JHB | 15 | Inner cladding for co-extrusion FTIR; EDX; DTA |
| | | M087JHB | 28 | Outer cladding for tube extrusion |
| | | M093JHB | 28 | Outer cladding for tube extrusion |
| | | M094JHB | 28 | Outer cladding for tube extrusion |
| | | M101JHB | 15 | Core for co-extrusion |
| JHB03 | $Ge_{24}Sb_{4}Se_{72}$ | M049JHB | 10 | FTIR; XRD |
| | | M053JHB | 15 | Inner cladding for co-extrusion EDX |
| | | M054JHB | 28 | Outer cladding for tube extrusion DTA |
| | | M060JHB | 28 | Outer cladding for tube extrusion |
| | | M061JHB | 28 | Outer cladding for tube extrusion |
| | | M080JHB | 5 | Viscosity: Re-melt of M053 |
| | | M104JHB | 15 | Inner cladding for co-extrusion TEC |
| | | M105JHB | 28 | Outer cladding for tube extrusion |
| JHB04 | $Ge_{22}Sb_{8}Se_{70}$ | M047JHB | 10 | FTIR; XRD |
| | | M052JHB | 15 | Core for co-extrusion EDX; TEC; DTA |
| | | M081JHB | 5 | Viscosity: Re-melt of M052 |
| *note that the rod lengths of the as-annealed samples varied from 40 – 50 mm. | | | | |

Table 4.1 provides a list of the chalcogenide glasses reported in this chapter, including the glass code, composition, melt code, diameter of the melted glass rod and intended glass application. To the best of this Author's knowledge Mr Q. Li, M. Phil. Student, at the University of Nottingham, UK, was the first to fabricate the Ge-Sb-Se bulk glass compositions analysed in this chapter. However, Mr Li's glasses were not drawn to fibre. Thus, initial selection of the compositions was based on the bulk glass physical properties reported in [83]. Nevertheless, it was important to verify the data independently ( as will be discussed in detail in section 4.2).

The first characterisation procedure conducted after the as-quenched glass melt was annealed, was X-ray diffraction analysis (XRD; section 4.1.1). To determine if the nominally batched Ge-Sb-Se glass composition was accurate, energy-dispersive X-ray microanalysis (EDX) was conducted (section 4.1.2). Although efforts were made to reduce impurities it was impossible to completely eradicate them. Therefore their contribution to the optical loss of the MIR transmission of the Ge-Sb-Se chalcogenide glasses was investigated using FTIR spectroscopy (section 4.1.3).

### 4.1.1. Investigation of material amorphicity using X-ray diffraction (XRD)

XRD measurements were performed on the contraction cone of the as-annealed glass rods as explained in section 3.6.1. The contraction cone was ground into fine powder in a pestle and mortar with a minimum amount of polishing oil (Bühler) added to reduce heat being generated from friction. The fine powder was poured onto an XRD holder and flattened with a microscope slide. The XRD measurements were carried out with the conditions, 2θ scan; 10 °- 70 °,0.05 ° step and 40 s per step with a total run time of 13.2 h. Figure 4.2 displays the XRD patterns of the contraction cone of the as-annealed (JHB03) $Ge_{24}Sb_4Se_{72}$ and (JHB04) $Ge_{22}Sb_8Se_{70}$ glasses.

From Figure 4.2, each XRD pattern presents amorphous behaviour as no diffraction peaks are seen. However, please note that the XRD system used herein was suggested to be capable of detecting > 3-5 volume % of crystals [185]. The atoms in an amorphous material are randomly distributed, thus the diffracted X-rays are scattered in many directions resulting in characteristic broad humps. This is in contrast to a crystalline material where the atoms are periodically distributed resulting in high intensity peaks as the X-rays are diffracted in an ordered direction. Three broad humps for both Ge-Sb-Se chalcogenide glasses can be observed in Figure 4.2, centred at 15 °, 29.5 ° and 51 ° 2θ, respectively, which are typical of the amorphous pattern of the glass matrix.

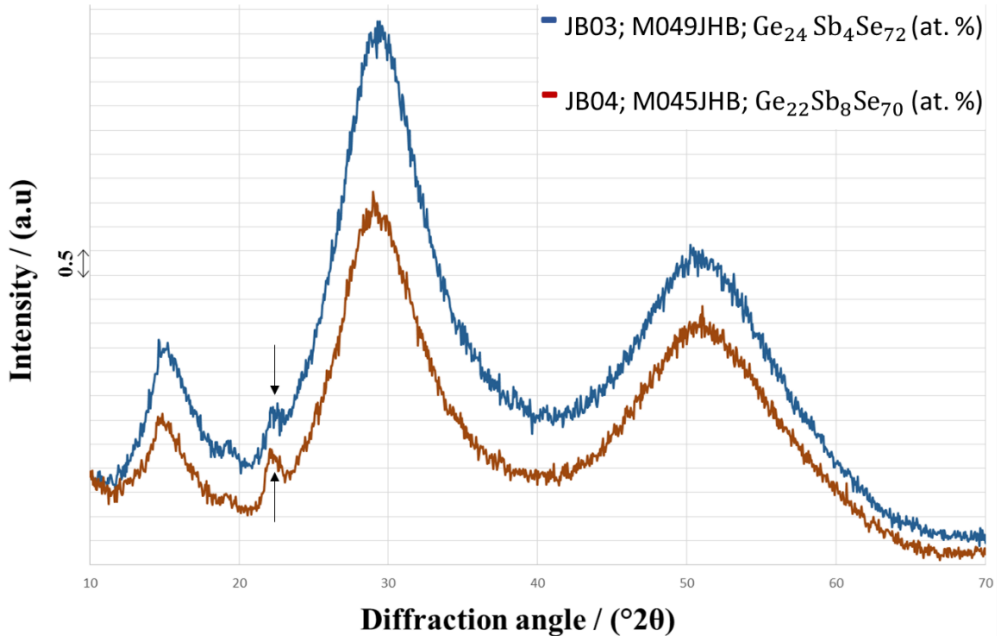



**Figure 4.2 Powder X-ray diffraction (XRD) pattern, measured from March 2013 to June 2015, as was described in section 3.6.1. The upper curve JB03 (blue; $Ge_{24}Sb_4Se_{72}$) and lower curve (red; $Ge_{22}Sb_8Se_{70}$,), both show amorphous behaviour. The curves are shifted vertically for clarity. Three broad humps for both glasses can be observed centred at 15 °, 29.5 ° and 51 ° 2θ respectively, which are typical of the amorphous state. The small peaks centred at 2θ = 22 ° and at 2θ = 19 ° (arrowed in black) were not expected. Although these peaks may have been caused by silica glass contamination, it was thought that this was unlikely as they appeared on every XRD pattern of glasses taken at the time. Further investigation was carried out to see if they could be attributed to instrument response, Figure 4.3.**

However, the small peaks centred at 2θ = 22 ° and at 2θ = 19 ° were not expected. Although these peaks could have been caused by silica glass contamination, it was thought that this was unlikely as they appeared on every XRD pattern of glasses taken at the time. Thus further investigation was conducted. The XRD machine was re-calibrated by Dr. N. Neate[7] to see if the peaks could be attributed to instrument response. This proved to be successful and after the re-calibration the peaks disappeared, as shown in Figure 4.3.

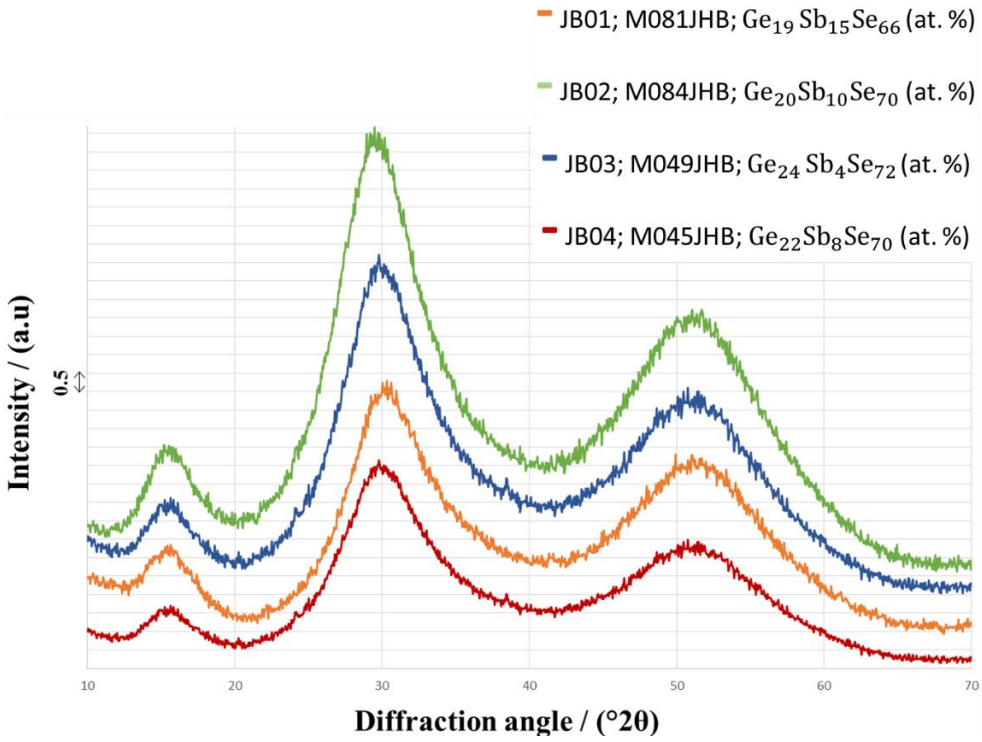



**Figure 4.3 Powder X-ray diffraction (XRD) pattern after instrument calibration. In descending order, the upper curve is JB02 (green; $Ge_{20}Sb_{10}Se_{70}$), the second curve is JB03 (blue; $Ge_{24}Sb_4Se_{72}$), the third curve is JB01 (orange; $Ge_{19}Sb_{15}Se_{66}$) and the lower curve is JB04 (red; $Ge_{22}Sb_8Se_{70}$). The curves have been vertically shifted for clarity. Similarly to Figure 4.2, three broad humps for all the Ge-Sb-Se glasses can be observed centred at 15 °, 29.5 ° and 51 ° 2θ respectively, showing amorphous behaviour. The small peaks centred at 2θ = 22 ° and at 2θ = 19 ° seen in Figure 4.2 were not observed after the instrument calibration, suggesting they were due to the instrument and not silica contamination.**

[7] Dr. N. Neate, Senior Research Technician of the Wolfson Centre for Materials, University of Nottingham, UK.

As mentioned in section 2.1, Tang *et al.* found evidence of crystallisation in a $Dy^{3+}$ selenide chalcogenide glass using transmission electron microscopy (TEM) [196]. They suggested TEM investigation was necessary after Bragg peaks appeared in the $Dy^{3+}$ selenide chalcogenide glass XRD patterns. However, as Bragg peaks were not observed in the XRD patterns for the Ge-Sb-Se chalcogenide glasses in this Project, it was not deemed necessary for further investigation and the glasses were assumed to be amorphous.

In order to determine the stability of the glasses after fibre drawing, XRD patterns were also collected of the three types of fibres drawn in this Project (which will be shown in Figure 5.23) and indicated amorphicity.

### 4.1.2. Assessment of nominal batched Ge-Sb-Se glass composition using SEM energy-dispersive X-ray microanalysis (EDX)

Compositional analysis was conducted by SEM-EDX. In EDX analysis, X-rays were generated from the Ge-Sb-Se chalcogenide glass sample when the primary electron beam (generated from the electron column gun in the SEM equipment. FEG-XL30 ESEM system) scattered an inner shell electron from a Ge-Sb-Se glass sample atom. The equipment, sample preparation and methodology of EDX were discussed in section 3.7. When an outer shell electron (which has a higher energy than the scattered inner shell electron) filled the vacancy, energy was released as an X-ray photon. The energy differences between electron shells are well defined and specific to every element. Therefore the energy of the X-rays was characteristic of the emitting atom and the composition of the Ge-Sb-Se glass could be determined.

EDX analyses were performed on a sample of the Ge-Sb-Se chalcogenide glasses to assess the nominal batch accuracy. A carbon coating (Edwards Coating System,

E306A) was applied to the Ge-Sb-Se chalcogenide glass surface, as was discussed in section 3.7, to generate a conducting surface on the Ge-Sb-Se chalcogenide glass. Carbon was selected as the conductive coating as it has a low atomic number of four [171] which is beneficial for low background electron imaging, it is inert at room temperature, it should not have been present in the sample, and carbon peaks should not have overlapped the peaks generated by the Ge-Sb-Se glass in the EDX spectrum. EDX was performed using a 15 kV electron beam, backscattered electron (BSE) mode and with a 10 mm working distance. In EDX, characteristic X-rays result from electron transitions between inner orbitals. The electron beam 'knocks out' an electron from an orbital and an electron from an outer orbital can 'fall' into the vacancy. The K and L lines indicate the shell containing the inner vacancy. The results are displayed in Table 4.2.

**Table 4.2 Typical Ge-Sb-Se chalcogenide glasses nominally batched composition, corresponding glass melts and composition determined from SEM-EDX analysis. Difference = between nominal and measured atomic (at.) %.**

| Glass code | Expected batched composition / (at. %) | Glass melt codes | Element | | | | | |
|---|---|---|---|---|---|---|---|---|
| | | | Ge K-lines / (at. %) | Difference | Sb L-lines / (at. %) | Difference | Se K-lines / (at. %) | Difference |
| JHB01 | $Ge_{19}Sb_{15}Se_{66}$ | M098JHB | 20.23 | +1.23 | 14.73 | -0.27 | 65.04 | -0.96 |
| JHB02 | $Ge_{20}Sb_{10}Se_{70}$ | M084JHB | 20.35 | +0.35 | 8.92 | -1.08 | 70.73 | +0.73 |
| JHB03 | $Ge_{24}Sb_{4}Se_{72}$ | M053JHB | 22.73 | -1.27 | 4.23 | +0.23 | 73.04 | +1.04 |
| JHB04 | $Ge_{22}Sb_{8}Se_{70}$ | M052JHB | 20.77 | -1.23 | 8.27 | +0.27 | 70.96 | +0.96 |
| Mean average batching error ± 0.8 at. % | | | | | | | | |

Given that the error margin [185] for the EDX system was estimated to be ± 0.5 at. % (and ± 0.5 wt. %), for elements heavier than oxygen, it can be deduced from Table 4.2,

that the batching technique was mostly accurate. The compositions measured were within ± 1.23 at. % of the target composition.

### 4.1.3. Determining the mid-IR transmission of (JB01) $Ge_{19}Sb_{15}Se_{66}$, (JB02) $Ge_{20}Sb_{10}Se_{70}$, (JB03) $Ge_{24}Sb_{4}Se_{72}$ and (JB04) $Ge_{22}Sb_{8}Se_{70}$ bulk chalcogenide glasses using Fourier transform infrared spectroscopy (FTIR)

When fabricating chalcogenide glasses for optical fibres, the most important consideration is to reduce factors which would contribute to optical loss wherever possible. Contamination by ppm levels of impurities like oxides would have a deleterious effect on the MIR transmission of the Ge-Sb-Se chalcogenide glass. Therefore pre-treatment of the silica glass ampoule was conducted (see section 3.1 for ampoule preparation) to further reduce carbon contamination and chemisorbed and physisorbed water. Exposure of the precursor elements to the atmosphere was minimised (*e.g.* batching in a glovebox (section 3.2.2), evacuating and sealing the silica glass melting ampoules (section 3.2.3)). Furthermore, some of the precursor elements were heat-treated for additional purification (see section 3.2.1). However, it proved to be difficult to remove all impurities, as the precursor elements were susceptible to oxidation and hydrolysis. Thus FTIR spectroscopy was conducted to assess the level of impurities within the Ge-Sb-Se chalcogenide glasses, see Figure 4.4.

To measure the optical transmission of the Ge-Sb-Se glasses, near-infrared (NIR) and MIR FTIR absorption measurements were conducted. The as-annealed glass rods were cut, measured and prepared as discussed in section 3.6.5. After grinding and polishing the opposite faces to a 1 µm finish the sample heights ranged from 1.17 mm to 1.9 mm. The impurity content (oxides, hydrogen, $CO_2$ and water) was determined by means of

absorption spectra using the known extinction coefficients from the literature shown in Appendix II.

The inset to Figure 4.4 displays an overview of the optical absorption spectrum of the Ge-Sb-Se chalcogenide glasses in the wavelength range 0 – 25 µm. Overall, the glasses show high transparency in the range 2 – 12 µm (the main image in Figure 4.4) due to the low phonon energy of the glasses. As mentioned in section 2.1.2, the limited transmission of selenide-based glasses at short wavelengths (*i.e.* JB01 < 0.76 µm, JB02 < 0.75 µm, JB03 < 0.71 µm and JB04 < 0.72 µm) is due to the characteristic electronic bandgap. On the other hand the transmission limitations at longer wavelengths (*i.e.* > 12 µm) are accountable to the material's multi-phonon absorptions due to the overtone and combination vibrations produced by the fundamental vibrational absorptions of the molecular bonds within the glass (*e.g.* [≡Ge-Se-] or [=Sb-Se-]) [59, 64, 197]. The transparency domain of the Ge-Sb-Se chalcogenide glasses is very attractive as it corresponds to the region of strong fundamental vibrational modes of biologically relevant molecules including lipids, proteins and nucleic acids, as was discussed in section 2.4.

However as shown in the main image in Figure 4.4, the glass optical absorption over the wavelength region of interest (*i.e.* 2 – 12 µm) has many unwanted vibrational absorption bands. The atmospheric vibrational absorptions were observed at 2.9 µm, 4.2 µm and ~6.28 µm accountable to O-H, $CO_2$ and $H_2O$ respectively [47, 198, 199]. Responsible for the vibrational absorption bands seen at [~3.5 µm and ~4.49 µm], 8.9 µm and 9-10 µm are Se-H, Ge-O and Si-O impurities, respectively. Even with the pre-treatment of the silica glass ampoule, it is likely that it substantially contributed to the

Se-H and O-H impurities due to the transfer of H and O-H from the silica glass ampoule walls to the Ge-Sb-Se chalcogenide glass melt at temperatures ≥ 650 °C [148, 149].

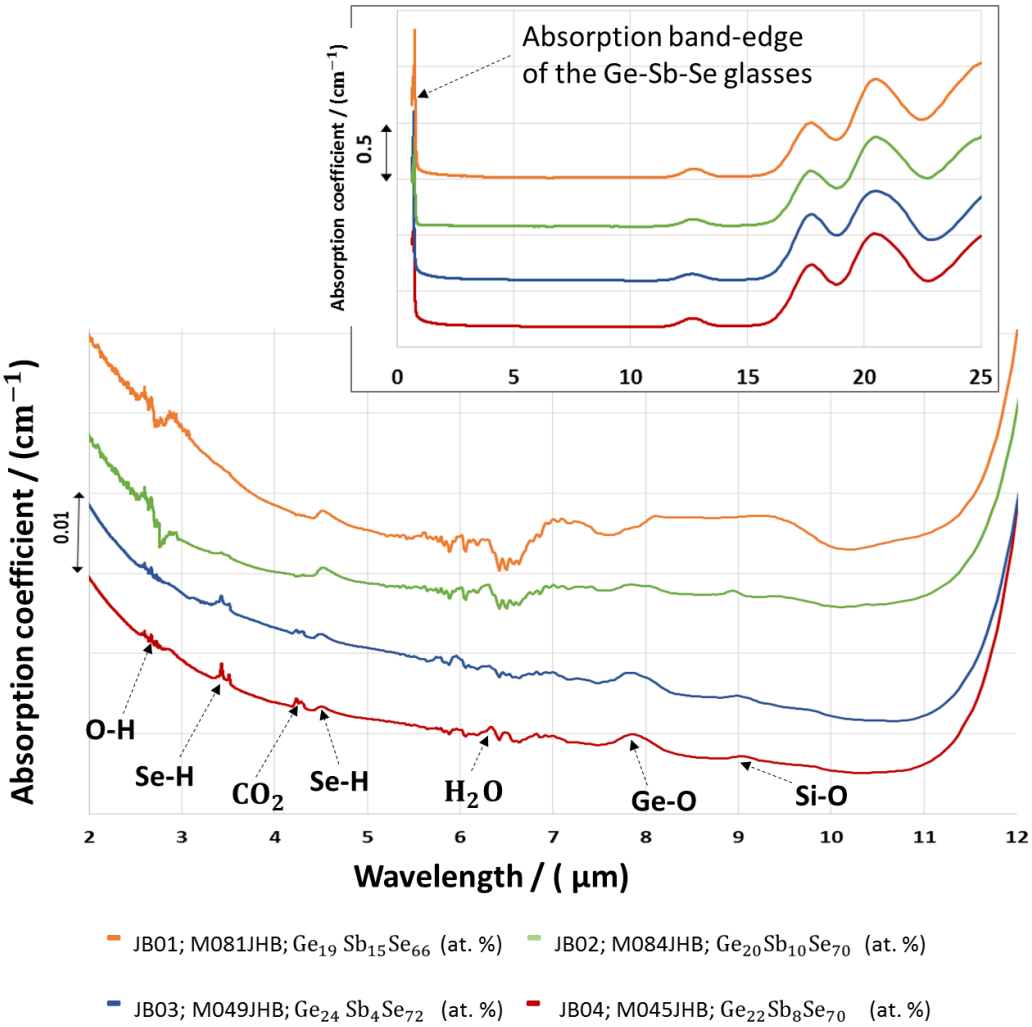



**Figure 4.4 Optical absorption of Ge-Sb-Se bulk glass samples; JB01 ( $Ge_{19}Sb_{15}Se_{66}$ ; orange), JB02 ( $Ge_{20}Sb_{10}Se_{70}$; green), JB03 ( $Ge_{24}Sb_4Se_{72}$; blue) and JB04 ($Ge_{22}Sb_8Se_{70}$; red) in the wavelength range 2 – 11 µm. The vibrational absorptions of impurities in the glass and their respective functional groups are indicated using the known extinction coefficients from the literature shown in Appendix II. Hydroxides, (*i.e.* dissolved O-H, molecular $H_2O$, and hydrides, Se-H, Ge-H and Sb-H) have fundamental absorptions over the 1-7 µm region [22]. Oxide impurities (*i.e.* Si-O, Ge-O) tend to absorb at > 7 µm. The inset shows the broad spectral region of the optical absorption for all the Ge-Sb-Se glasses in the range of 0 - 25 µm. The absorption band-edge is highlighted; JB01 at ~0.76 µm, JB02 at ~ 0.75 µm, JB03 at ~ 0.71 µm and JB04 at ~ 0.72 µm. The long-wavelength cut-off absorption edge can be seen to be punctuated with multiphoton absorptions due to overtone and combination vibrations.**

Furthermore it can also be considered that 'H' (*i.e.* hydrogen based impurities including hydrides, hydroxides and water) accompanying the as-purchased Se precursor was not

all removed during the purification heat-treatment. All the curves shown in Figure 4.4 have a moderate downwards slope between 2 – 11 μm. This may have been caused by scattering by impurity micro-inclusions (*e.g.* carbon and $SiO_2$ [200]). It is also true that the polishing finish of the glasses can lead to in advertant scattering [201].

The initial transmission measurements showed that all the glasses were suitable candidates for MIR transmission, predominantly between 3-12 μm with some extrinsic absorption bands identified.

The transmission of the glasses in fibre form was investigated in greater detail with fibre loss measurements using the 'cut-back' method (Chapter 6, section 6.3). Furthermore, novel glass purification methods were developed in this Project to reduce the extrinsic absorption bands and will be discussed in Chapter 6, section 6.4.

## 4.2. Determining the thermal properties of (JB01) $Ge_{19}Sb_{15}Se_{66}$, (JB02) $Ge_{20}Sb_{10}Se_{70}$, (JB03) $Ge_{24}Sb_4Se_{72}$ and (JB04) $Ge_{22}Sb_8Se_{70}$ chalcogenide glasses to develop the optimum glass pair for fabrication of a MIR core-cladding optical fibre

When considering a glass pair for the Ge-Sb-Se small core-cladding MIR optical fibre the thermal properties of the two glasses must be taken into consideration. An ideal glass pair would have perfectly matched $T_g$, viscosity/ temperature behaviour and a slightly higher thermal expansion of the core than the cladding. Thus upon cooling from fibre drawing the core would attempt to contract slightly more than the cladding generating residual stress, which enhances the mechanical strength of the fibre [47]. Furthermore, the core-cladding optical fibre also requires the core to have a higher refractive index than the cladding (to provide for light guiding). For fibre mid-infrared supercontinuum generation (MIR SCG), a large difference is desirable between the refractive indices of the core and cladding to generate as large a numerical aperture

(NA) as possible to control the fibre dispersion. As shown in Figure 2.15, NA characterises the range of angles over which a fibre can accept or emit light. However, to create this difference in refractive index the compositions of the core and cladding must be different. Thus compromises must be made as to which thermal properties to match when selecting a core-cladding glass pair.

Three glass pairs were drawn to fibre during this Project; Pair I (core JB04; $Ge_{22}Sb_8Se_{70}$ and cladding JB03; $Ge_{24}Sb_4Se_{72}$), Pair II (core JB01; $Ge_{19}Sb_{15}Se_{66}$ and cladding JB02; $Ge_{20}Sb_{10}Se_{70}$) and Pair III (core JB01; $Ge_{20}Sb_{10}Se_{70}$ and cladding JB03; $Ge_{24}Sb_4Se_{72}$). During the course of fabricating the fibres the following thermal characterisation experiments were made; differential scanning calorimetry (DSC; section 4.2.1), differential thermal analysis (DTA; section 4.2.2), viscosity/ temperature analysis (section 4.2.3.1) and thermal expansion coefficient (section 4.2.3.2). As discussed in section 4.3 during the course of fabricating the fibres it was discovered that particular thermal properties had greater importance than others.

### 4.2.1. Onset $T_g$ of (JB01) $Ge_{19}Sb_{15}Se_{66}$, (JB02) $Ge_{20}Sb_{10}Se_{70}$, (JB03) $Ge_{24}Sb_4Se_{72}$ and (JB04) $Ge_{22}Sb_8Se_{70}$ chalcogenide glasses

The Ge-Sb-Se chalcogenide glass rods were fabricated by quenching the glass forming melt in air and with a $N_2$ jet applied (see section 3.2.4 for glass quenching): before annealing; thus the rate of cooling was not measured and was likely to be different for each glass sample depending upon: the composition (the at. % of each element); glass transition temperature ( $T_g$); the diameter of the sample and the mass of the batch. The rate of cooling would have differed throughout the diameter of the glass rod, as the outside was quenched more quickly than the inside. $T_g$ is an event which occurs with a change in the heat capacity of a glass as the disordered material transitions from the

glass state to the super-cooled liquid state. The rate of quenching through $T_g$ defines the fictive temperature of a glass (as discussed in section 2.1), which affects measurements of $T_g$ of a glass on reheating. Therefore, as was shown in Figure 3.13, section 3.6.3, measurements of $T_g$ from the differential scanning calorimetry (DSC) procedure (section 3.6.3), were repeated three times. The first run was not deemed to be accurate due to the influence of the different thermal history of the glasses during the initial melt-quenching.

The Ge-Sb-Se chalcogenide glass rods were broken into small chunks (~2-5 mg) in a pestle and mortar and sealed in aluminium (Al) pans (Perkin Elmer). DSC provided a quantitative measure of the electrical energy (for resistance heating) which was either supplied to, or withheld from, the Ge-Sb-Se chalcogenide glass sample so that the temperature difference between the glass and the inert empty Al-pan reference was maintained at zero during isochronal heating or cooling. The temperature range of the DSC investigation was limited to $T_g$ + 50 °C as the sample Al pans were not hermetically sealed. Therefore the DSC liquidus peak ( $T_l$) of the Ge-Sb-Se glasses was not observed and DTA measurements in section 4.2.2 were conducted to investigate the $T_l$ region. The Ge-Sb-Se glasses were isochronally heated at 10 °C $min^{-1}$ and held isothermally for 1 minute up to $T_g$ + 50 °C. The DSC analyser was equipped with water circulating chillers and an argon gas flow through the head at 20 ml $min^{-1}$ allowing regulated cooling to 40 °C at 10 ° C $min^{-1}$ .

$T_g$ is an endothermic event (heat energy is required for the transition of the glass state to the super-cooled liquid state, see section 2.1). Measurements of the onset of $T_g$ taken from tangent lines of the endothermic peak were described in section 3.6.3.

Table 4.3 gives the $T_g$ values of JB01 ( $Ge_{19}Sb_{15}Se_{66}$), JB02 ( $Ge_{20}Sb_{10}Se_{70}$), JB03 ( $Ge_{24}Sb_4Se_{72}$) and JB04 ($Ge_{22}Sb_8Se_{70}$) chalcogenide glasses, obtained from DSC curves. Onset $T_g$ values are quoted using a mean average of the second and third peak generated in the DSC measurements. The results obtained from the third heating process were used to assess reproducibility and calculate error. The mean average onset $T_g$ for JB03 ($Ge_{24}Sb_4Se_{72}$; $T_g$ = 226 °C) and JB04 ($Ge_{22}Sb_8Se_{70}$; $T_g$ = 238 °C) shown in Table 4.3 are comparable to the onset $T_g$ values reported in [83]. However, it can be observed that there is a marked difference between the onset $T_g$ measured for JB01 ($Ge_{19}Sb_{15}Se_{66}$; $T_g$ = 234 °C) and JB02 ($Ge_{20}Sb_{10}Se_{70}$; $T_g$ = 211 °C) and the $T_g$ results reported in [83] (*i.e.* 240 °C and 220 °C, respectively). The difference must have been due to the compositional variation because from EDX (section 4.1.2) the batching was accurate to ± 0.8 at. %.

Onset $T_g$ values from the DTA measurements (section 4.2.2) were used for the $T_g$ measurements made in this Project, but differences were found compared with the earlier results of Li using DSC [83]. The $T_g$ values obtained from the DTA curves, Figure 4.5, shows that the $T_g$ values measured in this Project by means of DTA were 2-7 °C lower than those measured from DSC curves by Li [83].

As will be discussed in section 4.3, the conclusion was drawn that matching the $T_g$ values of the glass pairs had a greater significance for co-processing of two glasses to core/ cladding fibre than matching the viscosities at the fibre drawing temperature. A large difference in $T_g$ created problems in securing the core/cladding preform in the fibre drawing tower during cane drawing. In F029JHB the co-extrudate from E030JHB was fabricated from Pair II (the core glass was JB01; $Ge_{19}Sb_{15}Se_{66}$; $T_g$= 234 °C and

cladding glass was JB02; $Ge_{20}Sb_{10}Se_{70}$; $T_g$= 211 °C). This meant that the cladding went through $T_g$ at a temperature 23 °C lower than the core. Therefore the temperature required to heat the core to reach the $T_g$ region was not achieved, and, as the cladding became too soft, the preform could not be secured in the preform holder.

**Table 4.3 Onset $T_g$ values for the second and third runs of the four Ge-Sb-Se glass compositions studied for MIR optical fibres measured using DSC (see section 3.6.3), including the glass code, composition, melt number and standard deviation. The samples were each 20 ± 5 mg. Values reported in the literature [83] are provided for reference.**

| Glass code | Glass composition / (at. %) | Onset $T_g$ measured from second run / ( °C) | Onset $T_g$ measured from third run / ( °C) | Mean average $T_g$ / ( °C) | Standard deviation (SD) / ( °C) | Onset $T_g$ from [83] |
|---|---|---|---|---|---|---|
| JHB01 | $Ge_{19}Sb_{15}Se_{66}$ | 233.8 | 234.5 | 234 | 0.5 | 240 |
| JHB02 | $Ge_{20}Sb_{10}Se_{70}$ | 210.7 | 211.1 | 211 | 0.3 | 220 |
| JHB03 | $Ge_{24}Sb_{4}Se_{72}$ | 225.3 | 226.4 | 226 | 0.8 | 225 |
| JHB04 | $Ge_{22}Sb_{8}Se_{70}$ | 238.1 | 237.2 | 238 | 0.6 | 235 |

### 4.2.2. Differential thermal analysis (DTA)

In Figure 2.1, section 2.1, the relationship between glassy, liquid and crystalline states were discussed. It was therefore important to understand the thermal stability of the Ge-Sb-Se chalcogenide glasses in order to predict the likelihood of crystallisation during fibre drawing. DTA can be used to study the thermal behaviour (*e.g.* glass crystallisation peak temperature ($T_c$) and glass transition temperature ($T_g$)) and the phase change of a glass (liquidus temperature $T_l$). The region between $T_c$ - $T_g$ (known as the Hruby parameter [188]) is useful as a guide to evaluate the fibre drawing ability of the Ge-Sb-Se chalcogenide glasses and provides a semi-quantitative measure of glass stability to reheating. A greater Hruby parameter indicates that the glass has a more stable glass forming ability. The temperature difference ($\Delta T$) between the sample

ampoule and the reference ampoule in the DTA equipment was detected by thermocouples, as was explained in section 3.6.4.

DTA measurements were carried out in a Perkin Elmer DTA 7. As chalcogenide glass reacts with oxygen and water vapour in the atmosphere when heated above its $T_g$, the as-annealed chalcogenide glass rods were broken into chunks and sealed under vacuum in silica glass ampoules (Baumback; 3/4.7 mm ID/OD) as was described in section 3.6.4. As the samples were hermetically sealed the experiment in theory can be run to higher temperatures than the DSC procedures because sample volatilisation is curtailed. A reference sample was prepared by sealing an empty silica ampoule under vacuum which had the same mass (± 20 mg) and approximate shape as the empty sample ampoule. Only one DTA measurement was taken for each sample for two reasons. First, the DTA equipment was only equipped with air cooling facilities and therefore the cooling rate could not be regulated. Second, if the glass were to crystallise during heating it would be from the as-annealed state. Therefore, if the experiment were to be repeated the sample would have lost its annealing thermal history.

The ΔT was measured and endotherms were plotted against temperature, as shown in Figure 4.5. It was attempted to define characteristic temperatures by endothermic ($T_g$ and $T_l$ ) and the exothermic peaks ($T_c$). $T_g$ was measured by attempting to take the intersection of the tangential lines around the onset of the curve of endotherms ΔT against temperature, Figure 4.5(b), to see if it was comparable to the onset $T_g$ measured from DSC in section 4.2. The measurements were repeated several times adjusting the tangential lines as generally the gradients were difficult to depict. As discussed in section 3.6.4 it was suggested that DSC was a more sensitive technique than DTA for finding $T_g$ due to better thermal contact between the Ge-Sb-Se chalcogenide glass

sample and the thermocouple. In DSC the samples were pressure cold-sealed in aluminium pans, whereas in DTA the samples were sealed under vacuum in silica ampoules which had a wall thickness of ~ 1.7 mm. This meant that in DTA the thermal contact between the Ge-Sb-Se chalcogenide glass sample and thermocouple was quite poor. The onset $T_g$ from the DTA curves was only used as a comparison to the onset $T_g$ calculated from the DSC measurements. As can be seen from Table 4.4 which provides a summary of the results presented in Figure 4.5, $T_g$ calculated from DTA results were slightly higher (between 2-7 °C) than those calculated from DSC.

From Figure 4.5(a), it can be seen that there were no definitive peaks for $T_l$ and $T_c$. Equation 3.1 showed the calculation of $T_l$ by the '2/3 rule' [181]. It is worth noting that the $T_g$ used in performing this calculation here was taken from the DSC measurements, Table 4.3. According to the 2/3 rule [181] $T_l$ would be expected to have occurred at the following temperature for each glass composition; JB01 ($T_l \leq 504$ °C), JB02 ($T_l \leq 215$ °C), JB03 ($T_l \leq 229$ °C) and JB04 ($T_l \leq 241$ °C). However, the associated peak areas would have depended on the magnitude of the crystallisation encountered and, as the glasses did not exhibit an obvious $T_c$ peak, $T_l$ peaks could have low intensity and be spread out over a broad temperature range. $T_c$ is an exothermic event and if crystallisation occurred the baseline would shift up (in an opposite manner to the endothermic event at $T_g$). As $T_c$ could not be identified, the Hruby parameter, which helps to predict the likelihood of crystallisation during fibre drawing, could not be calculated. However as the glass compositions yielded DTA curves without crystallisation tendency, it was deemed that this was enough evidence that the glasses could be drawn to fibre successfully. The viscosity-temperature relationship is another significant property affecting fibre drawing that should not be ignored, see section

4.2.3.1. The smooth viscous flow of these samples on heating above $T_g$ in the viscosity-temperature experiments, Figure 4.8, also indicated that the glasses withstood the reheating process without devitrification. As a preliminary indication, the stability of the Ge-Sb-Se chalcogenide glasses on reheating could also be observed from their DTA curves, Figure 4.5.

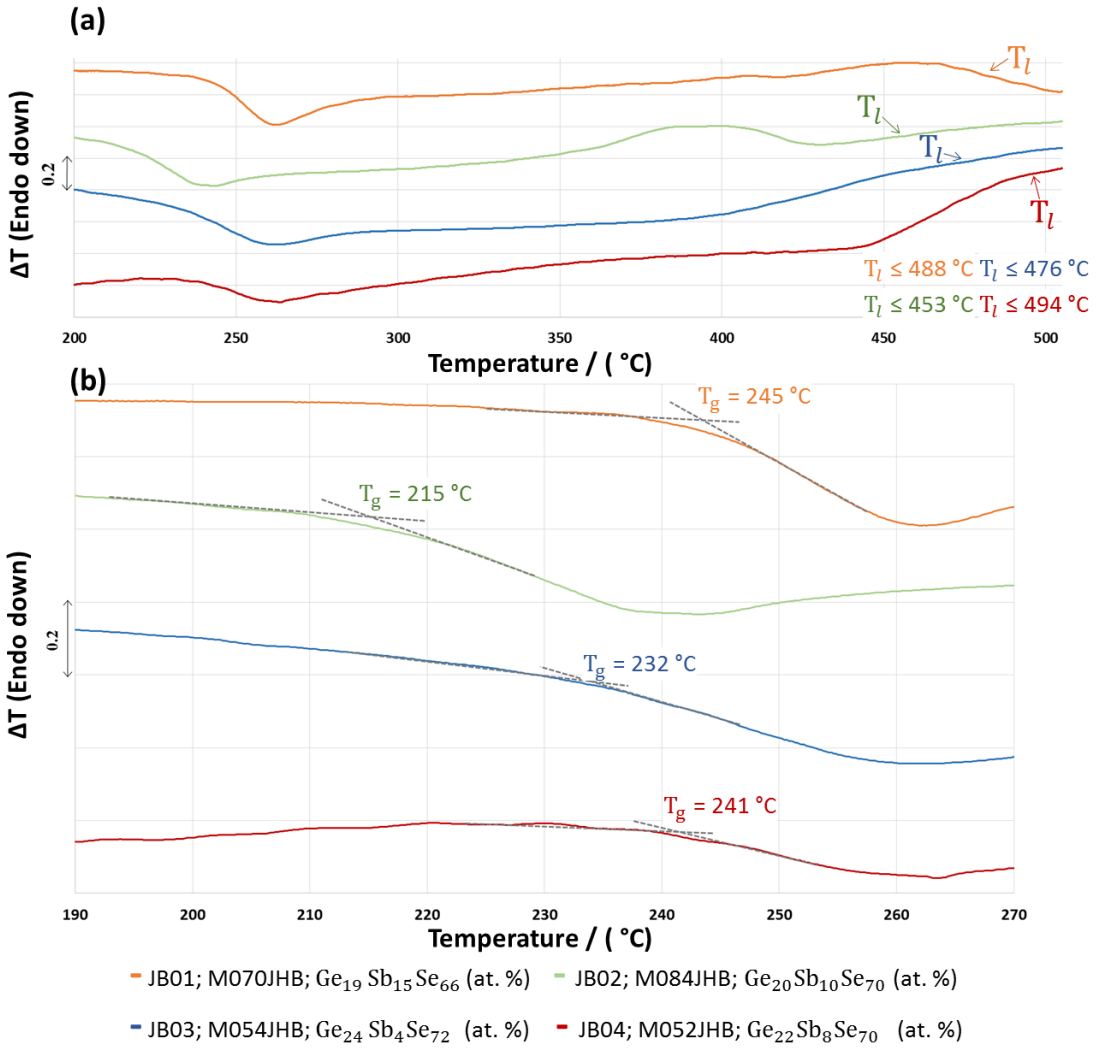



**Figure 4.5 Differential thermal analysis (DTA) curves of Ge-Sb-Se glass samples; JB01 ($Ge_{19}Sb_{15}Se_{66}$; orange), JB02 ($Ge_{20}Sb_{10}Se_{70}$; green), JB03 ($Ge_{24}Sb_4Se_{72}$; blue) and JB04 ($Ge_{22}Sb_8Se_{70}$; red). The curves are vertically shifted for clarity. Showing (a) $T_l$ values calculated from the 2/3 rule; JB01 ($T_l \leq$ 488 °C), JB02 ($T_l \leq$ 453 °C), JB03 ($T_l \leq$ 476 °C) and JB04 ($T_l \leq$ 494 °C). (b) Onset $T_g$; JB01 ($T_g$ = 245 °C), JB02 ($T_g$ = 215 °C), JB03 ($T_g$ =232 °C) and JB04 ($T_g$ = 241 °C). DTA results are summarised in Table 4.4.**

**Table 4.4 Liquidus temperature ($T_l$) (calculated from 2/3 rule [181] using onset $T_g$ measured from DSC results); onset $T_g$ measured from DTA results and onset $T_g$ measured from DSC results are included for comparison.**

| Glass number | Composition / (at %) | $T_l$ / ( °C) | Onset $T_g$ from DTA / ( °C) | Onset $T_g$ from DSC / ( °C) |
|---|---|---|---|---|
| JHB01 | $Ge_{19}Sb_{15}Se_{66}$ | 488 | 245 | 234 |
| JHB02 | $Ge_{20}Sb_{10}Se_{70}$ | 453 | 215 | 211 |
| JHB03 | $Ge_{24}Sb_{4}Se_{72}$ | 476 | 232 | 226 |
| JHB04 | $Ge_{22}Sb_{8}Se_{70}$ | 494 | 241 | 238 |

From Table 4.4, it can be seen that DSC $T_g$ is systematically lower than DTA $T_g$. DSC $T_g$ is more accurate as there is less thermal inertia associated with the sample.

### 4.2.3. Thermal mechanical analysis (TMA)

TMA measurements were used to measure the change in the Ge-Sb-Se chalcogenide glass sample height under mechanical load with changes in temperature (*e.g.* increasing the temperature or cooling down). Using this principle, TMA was used to examine the viscosity / temperature property of the Ge-Sb-Se glasses, above $T_g$, section 4.2.3.1 and the thermal expansion coefficients, below $T_g$, section 4.2.3.2. Perkin Elmer TMA7 equipment was used and the method was described in section 3.6.6. A flow of purging gas (helium, BOC) was used to minimise lag in the recorded temperature (*i.e.* between the sample temperature and the sample thermocouple) when the temperature was changed.

#### 4.2.3.1. Viscosity/ temperature analysis

As was discussed in section 2.1 a good glass former will have a greater viscosity at or above the liquidus causing the atoms within the melt to exhibit restricted motion.

Viscosity maybe be defined as a parameter to measure the resistance of a fluid to being deformed by either shear stress or extensional stress (longitudinal stress). The viscosity of a liquid is dependent upon temperature. An amorphous material can achieve viscous flow when it is heated above its $T_g$ or under ultra-high pressure when glass below $T_g$ is pressed between parallel plates [188]. After difficulties in producing a circular core with Pair I measurement of the viscosity / temperature properties of the Ge-Sb-Se chalcogenide glasses was conducted. It is suggested that the viscosity of extrusion is $10^7 - 10^8$ Pa.s and that of fibre drawing is ~ $10^{4.5}$ Pa.s [143]. We wished to understand the temperature variation of viscosity during fibre drawing to help maintain flow of the super-cooled liquid to yield a uniform core shape in the fibre. However from the resulting fibre draws (discussed in section 4.3) it would appear that this parameter was not as important to satisfy as matching other thermal properties (such as $T_g$).

To obtain samples of the required dimensions, ~2.5 g of each Ge-Sb-Se chalcogenide bulk glass composition was batched in air into a 4 / 7 (ID / OD, mm) ampoule (QB glass) and re-melted, see section 3.6.6.1 for equipment and sample preparation and Table 3.6.1 for viscosity/ temperature melting schedule. The re-melted glass rod was ~ 35 mm long and was cut orthogonal to the axial direction of the glass rod as described in section 3.3, to the required height (~1.6 mm for a load of 50 mN and ~4.1 mm for a load of 400 mN) as listed in Table 4.5. The diameter of each sample was measured with a micrometer (Mitutoyo) with the measurement repeated in four different areas to assess the degree of curvature (± 0.005 mm tolerance).

For the viscosity/ temperature measurements, the cylindrical glass samples were placed in between two stainless-steel plates (made in-house) and pressure was applied using a silica probe (made in-house) attached to the top plate inside the TMA equipment. Each Ge-Sb-Se chalcogenide glass sample was rapidly heated to 200 °C at 40 °C $min^{-1}$

(below $T_g$) and held isothermally for 1 min to ensure thermal equilibrium at the start of the experiment. Due to the sample size being much larger than that in the case of DTA or DSC measurements, care was taken to limit the temperature ramps to a rate that did not incur an appreciable temperature lag between the glass sample and the sample thermocouple. Therefore, the viscosity/ temperature measurements were proceeded by heating the Ge-Sb-Se chalcogenide glass sample to 500 °C at either 10 °C $min^{-1}$ or 5 °C $min^{-1}$ to determine whether there was a large difference in the resulting viscosity/ temperature profiles.

**Table 4.5 Composition and height of the Ge-Sb-Se chalcogenide glass samples for viscosity/ temperature measurements.**

| Glass code | Composition / (at. %) | Colour of plot on graph shown in Figure 4.8 | Sample height for 50 mN measurement for the extrusion viscosity region of $10^8$ Pa.s / (mm) | Sample height for 400 mN measurement for the fibre drawing viscosity region of $10^{4.5}$ Pa.s / (mm) |
|---|---|---|---|---|
| JHB01 | $Ge_{19}Sb_{15}Se_{66}$ | Orange | 1.598 | 4.100 |
| JHB02 | $Ge_{20}Sb_{10}Se_{70}$ | Green | 1.652 | 4.114 |
| JHB03 | $Ge_{24}Sb_{4}Se_{72}$ | Blue | 1.621 | 4.1245 |
| JHB04 | $Ge_{22}Sb_{8}Se_{70}$ | Red | 1.626 | 4.207 |

Figure 4.6 shows the viscosity/ temperature behaviour results of four different samples from the same melt M079JHB (composition: JB02; $Ge_{20}Sb_{10}Se_{70}$) when heated at both temperature rates, in the temperature range 255-280 °C, and results are summarised in Table 4.6. The difference between the measured viscosity for both heating rates was marginal with a maximum error (calculated by standard deviation) of ± $10^{0.12}$ Pa.s. This difference can be attributed to sample variation. However, for convenience, and just in case a larger sample would exhibit a lag, the viscosity results quoted throughout this Thesis are the value for the measurement with a heating rate of 10 °C $min^{-1}$.

As was discussed in section 3.6.6.1, the expansion of the sample was calculated prior to heating and the program was switched to cooling at 10 °C $min^{-1}$ once the sample had reached the lowest acceptable height, before the sample might flow enough to cause it to touch the thermocouple. Helium was used as the purge gas as it exhibits high thermal conductivity and is inert as the Ge-Sb-Se glasses are reactive to water vapour and oxygen when heated. For the Ge-Sb-Se chalcogenide glasses the lowest acceptable height was usually reached before the program got to 400 °C (although JB03 reached 440 °C). The measurements were performed with a static load of either 50 mN or 400 mN applied (depending on the intended viscosity region investigated, see Table 4.5) and the viscosity / temperature behaviour was then calculated as described in [188].

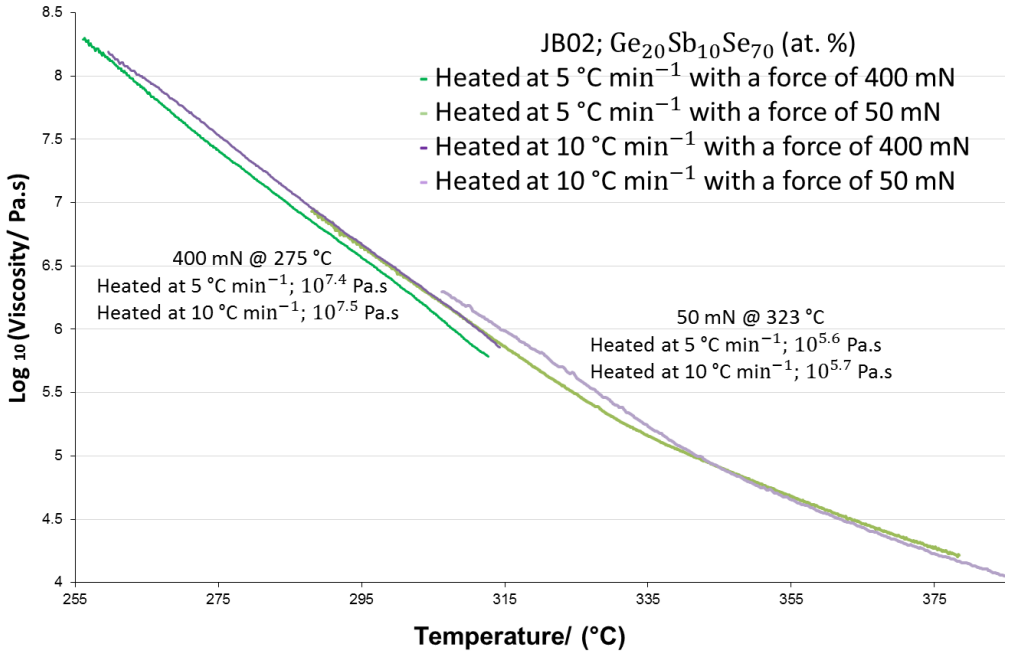



**Figure 4.6 Log viscosity versus temperature for sample M079JHB (JB02; $Ge_{20}Sb_{10}Se_{70}$). To assess whether the heating rate had a large impact on the viscosity/ temperature curves of the Ge-Sb-Se chalcogenide glasses the glasses were heated at 5 °C $min^{-1}$ and 10 °C $min^{-1}$. Differences in viscosity measurements could have occurred if there was a lag in the heating of the bulk material if the heating rate was too fast and therefore not a true temperature reading from the thermocouple. It can be seen that the results only varied slightly with a maximum difference ± $10^{0.12}$ Pa.s and there were two overlapping sections.**

**Table 4.6 Quantitative comparison between four samples from the same melt M079JHB (JB02; $Ge_{20}Sb_{10}Se_{70}$) measuring the viscosity / temperature behaviour to assess the effect of heating rate on the measurement.**

| Heating rate / (°C $min^{-1}$) | 5 | 10 | 5 | 10 | Standard deviation (SD) |
|---|---|---|---|---|---|
| Force / (mN) | 400 | 400 | 50 | 50 | |
| Temperature / (°C) | Log viscosity / (Pa.s) | | | | |
| 260 | 8.12 | 8.16 | | | 0.03 |
| 270 | 7.63 | 7.76 | | | 0.09 |
| 280 | 7.19 | 7.31 | | | 0.08 |
| 290 | 6.77 | 6.88 | 6.86 | | 0.06 |
| 300 | 6.36 | 6.47 | 6.45 | | 0.06 |
| 310 | 5.89 | 6.05 | 6.06 | 6.18 | 0.12 |
| 320 | | | 5.67 | 5.82 | 0.11 |
| 330 | | | 5.31 | 5.42 | 0.08 |
| 340 | | | 5.03 | 5.06 | 0.02 |
| 350 | | | 4.79 | 4.77 | 0.01 |
| 360 | | | 4.57 | 4.55 | 0.01 |
| | | | | | 0.06 |

To check reproducibility three samples of the Ge-Sb-Se chalcogenide glasses were cut from the same melt and the viscosity/ temperature measurements were conducted under the exact same conditions. Figure 4.7 shows the viscosity/ temperature measurements when performed on three $Ge_{19}Sb_{15}Se_{66}$ samples from the same melt M078JHB, heated at 10 °C $min^{-1}$ with a force of 50 mN. Although the greatest care was taken to ensure both flat edges of the Ge-Sb-Se sample were parallel, inevitably there were some imperfections on a nanometre scale. At the beginning of the experiment any flattening of a slight angle or a high spot would result in a lower viscosity reading. This can be seen in the inset to Figure 4.7 with Trial 3 (pink curve) having a particularly low dip at the start of the measurements. These discrepancies were removed as the applied force flattened them into the rest of the bulk sample and the measurement continued with a smooth flow (which also suggested the glass withstood the reheating process without devitrification [168]). Therefore the initial unstable values were removed before the viscosity curve settled into a smooth line. From Table 4.7, which provides a quantitative

comparison of results shown in Figure 4.7, it can be seen that the standard deviation in log (viscosity) difference of the three trials of the viscosity/ temperature measurements conducted for the $Ge_{19}Sb_{15}Se_{66}$ samples was 0.03 Pa.s.

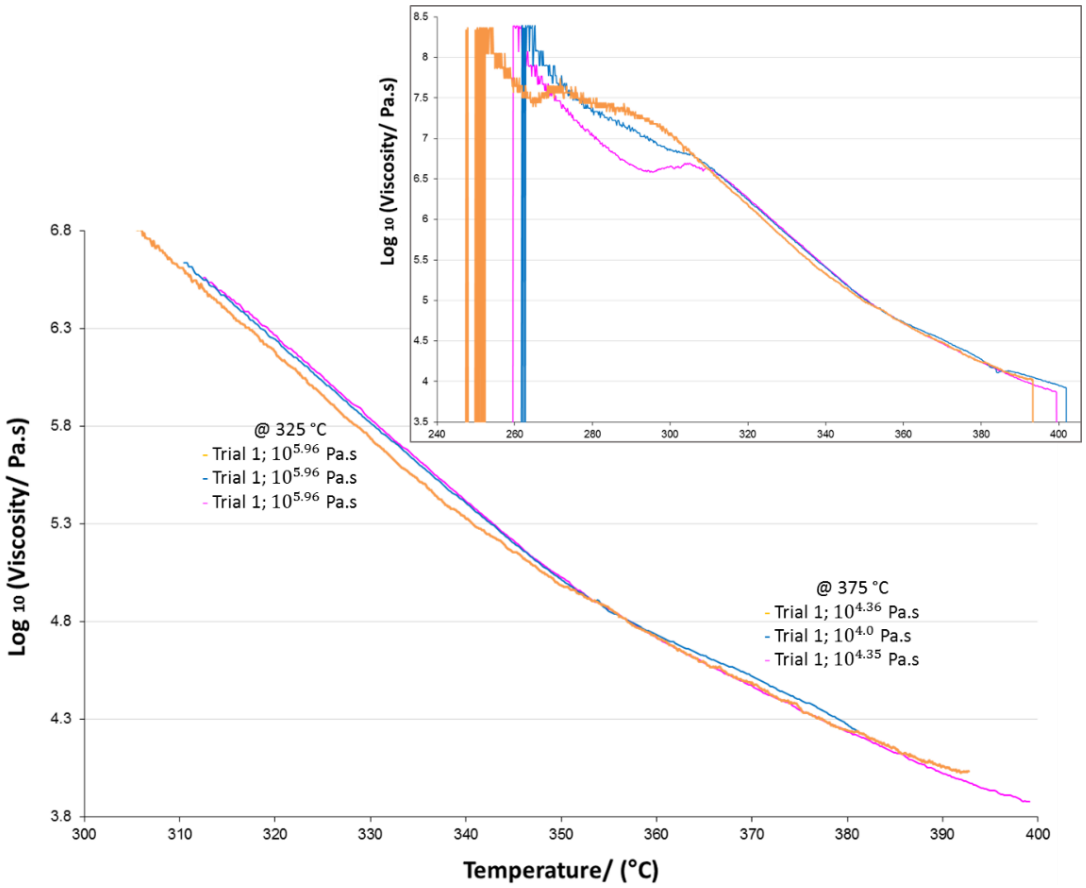



**Figure 4.7 Viscosity/ temperature measurements of three different samples taken from the same melt M078JHB (composition JB01; $Ge_{19}Sb_{15}Se_{66}$) heated at 10 °C $min^{-1}$, in the temperature range 300- 400 °C and with a force of 50 mN applied. The measurements were made to examine the reproducibility of results and it can be seen that repeatable behaviour was observed. The curves were cropped to remove the inaccurate viscosity measurements at the beginning of the experiment caused by surface defects. The inset shows the viscosity/ temperature results before values were removed. A quantitative comparison between the three trials is shown in Table 4.7**

Viscosity/ temperature measurements for all the Ge-Sb-Se chalcogenide glass compositions measured in this Project are displayed in Figure 4.8. It can be seen that the Ge-Sb-Se chalcogenide glasses exhibited smooth flow within the measured temperature range (255 – 440 °C) indicating that reheating was achieved without devitrification [168]. This suggests that all the glass compositions could be drawn to

fibre successfully without crystallisation (crystallisation would have great consequences on their transmission abilities as discussed in section 2.4). Furthermore the process of crystallisation involves the rearrangement of atoms, and therefore a high viscosity indicates a resistance to devitrification.

**Table 4.7 Quantitative comparison between three trials of measuring the viscosity/ temperature from the same glass melt M078JHB (composition JB01; $Ge_{19}Sb_{15}Se_{66}$ ) heated at 10 °C $min^{-1}$ with a force of 50 mN applied, presented in Figure 4.7, in the temperature range 300 – 400 °C.**

| Temperature / (°C) | Trial 1 | Trial 2 | Trial 3 | Standard deviation (SD) |
|---|---|---|---|---|
| | Log viscosity / (Pa.s) | | | |
| 315 | 6.37 | 6.44 | 6.46 | 0.05 |
| 325 | 5.96 | 6.02 | 6.05 | 0.05 |
| 335 | 5.52 | 5.61 | 5.62 | 0.06 |
| 345 | 5.16 | 5.20 | 5.21 | 0.03 |
| 355 | 4.87 | 4.85 | 4.86 | 0.01 |
| 365 | 4.59 | 4.62 | 4.59 | 0.02 |
| 375 | 4.36 | 4.40 | 4.35 | 0.03 |
| | | | | 0.03 |

In Figure 4.8(a) it was not possible to measure up to $10^8$ Pa.s for JB03 and JB04 as it was for JB01 and JB02. On the other hand, as the curves for both JB03 and JB04 were smooth, the graph could be extrapolated. The predicted values for JB03 and JB04 are in Table 4.8, along with the measured values for JB01 and JB02. It can be seen that measurement of the fibre drawing viscosity was possible for all compositions.

**Table 4.8 A quantitative comparison between the four Ge-Sb-Se chalcogenide glass compositions of the viscosity / temperature measurements for (JB01) $Ge_{19}Sb_{15}Se_{66}$, (JB02) $Ge_{20}Sb_{10}Se_{70}$, (JB03) $Ge_{24}Sb_{4}Se_{72}$ and (JB04) $Ge_{22}Sb_{8}Se_{70}$. The estimated error for each measurement was ± 3 °C.**

| Glass code | Composition / (at. %) | Temperature at the extrusion region ($10^8$ Pa.s) viscosity / ( °C) | Temperature at the fibre drawing region ($10^{4.5}$ Pa.s) viscosity / ( °C) |
|---|---|---|---|
| JHB01 | $Ge_{19}Sb_{15}Se_{66}$ | 278 | 369 |
| JHB02 | $Ge_{20}Sb_{10}Se_{70}$ | 264 | 362 |
| JHB03 | $Ge_{24}Sb_{4}Se_{72}$ | 292* | 409 |
| JHB04 | $Ge_{22}Sb_{8}Se_{70}$ | 282* | 389 |
| *values obtained from extrapolating the graph in Figure 4.8(a) | | | |

In section 4.3 it will be discussed that Pair II (JB01; $Ge_{19}Sb_{15}Se_{66}$ and JB02; $Ge_{20}Sb_{10}Se_{70}$) was selected to be drawn to fibre on account of the glasses being closely matched in the temperature at which they reached the fibre drawing viscosity region, $10^{4.5}$ Pa.s, ($\Delta T = 8$ °C), see Table 4.9. However, during the development of the glass pairs and the experience obtained during the fibre drawing and extrusion procedures, it was discovered that matching viscosities at the fibre drawing region (Table 4.9) was not as important as matching the $T_g$ of the glass pair (Table 4.3). Furthermore it was deemed that a close match in temperature in the extrusion viscosity region was an important value during the extrusion process. This will be discussed further in section 4.3.

**Table 4.9 A quantitative comparison of the differences in temperature at the extrusion and fibre drawing viscosity region between the glass pairs which were used to make fibre.**

| Glass codes | Glass pair | Compositions / (at. %) | Difference in temperature at the extrusion region ($10^8$ Pa.s) viscosity / ( °C) | Difference in temperature at the fibre drawing region ($10^{4.5}$ Pa.s) viscosity / ( °C) |
|---|---|---|---|---|
| JHB03<br>JHB04 | Pair I | $Ge_{24}Sb_4Se_{72}$<br>$Ge_{22}Sb_8Se_{70}$ | 10 | 20 |
| JHB01<br>JHB02 | Pair II | $Ge_{19}Sb_{15}Se_{66}$<br>$Ge_{20}Sb_{10}Se_{70}$ | 14 | 7 |
| JHB02<br>JHB03 | Pair III | $Ge_{20}Sb_{10}Se_{70}$<br>$Ge_{24}Sb_4Se_{72}$ | 28 | 47 |

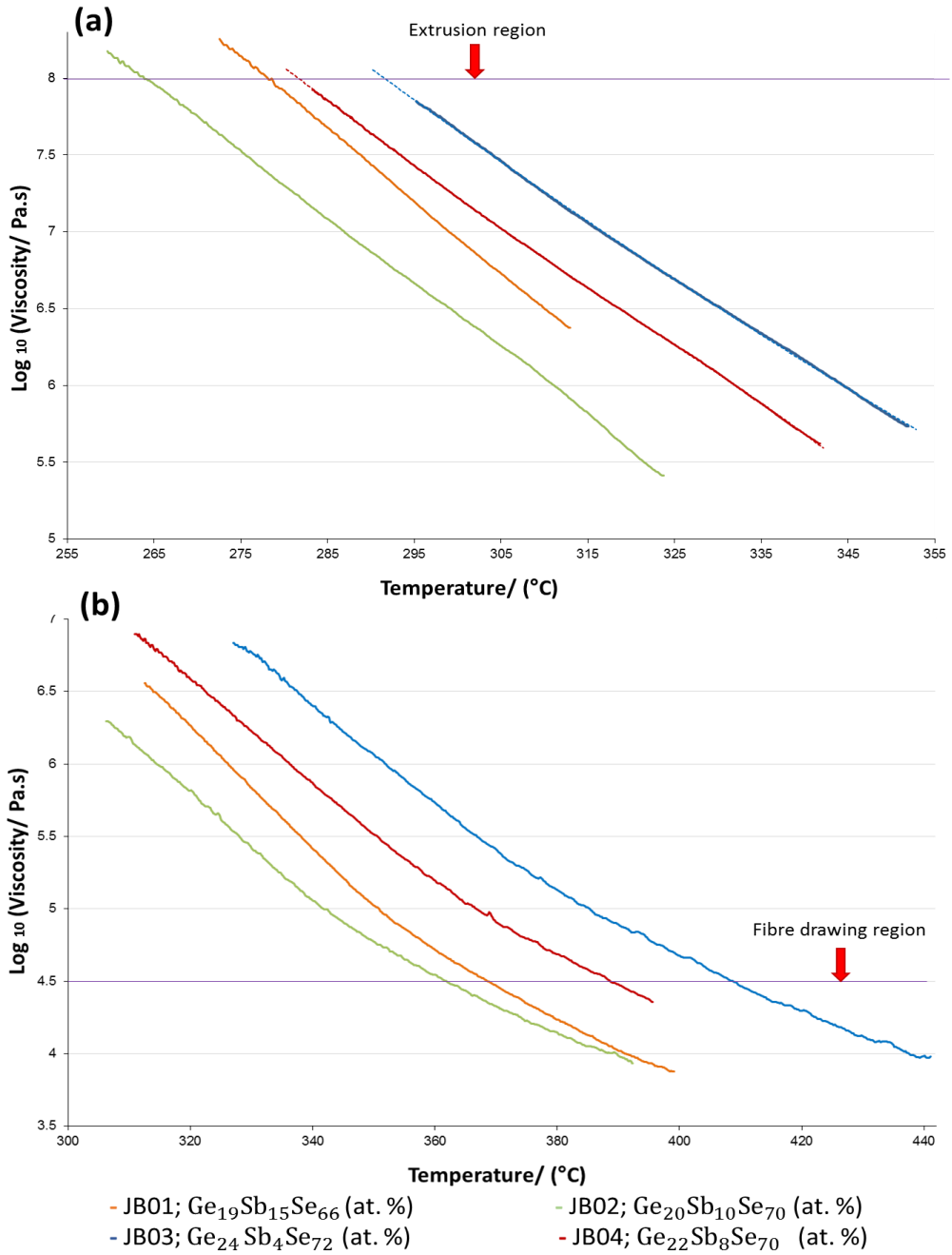



**Figure 4.8 Viscosity/ temperature graph for JB01 ($Ge_{19}Sb_{15}Se_{66}$; orange), JB02 ($Ge_{20}Sb_{10}Se_{70}$; green), JB03 ($Ge_{24}Sb_4Se_{72}$; blue) and JB04 ($Ge_{22}Sb_8Se_{70}$; red) using a heating rate of 10 °C $min^{-1}$ to show the region of (a) extrusion at $10^8$ Pa.s, a load of 400 mN and a sample height of ~ 4 mm, (b) fibre drawing at $10^{4.5}$ Pa.s, a load of 50 mN and a sample height of ~ 1.6 mm. See Table 4.5 for individual glass sample details.**

### 4.2.3.2. Thermal expansion coefficient

Chalcogenide glasses expand on heating through a particular temperature range above room temperature [202]. The thermal expansion is caused by the asymmetry of the

amplitude of thermal vibrations in the glass [203]. Furthermore, the asymmetric vibrations can be related to the chemical bonding and composition (*e.g.* the presence of the more loosely bonded chemical units increase thermal expansion [204]) and the temperature and fictive temperature (*e.g.* thermal history such as a fast cooling rate which will increase the thermal expansion or annealing which will reduce thermal expansion [188]). When fabricating a small core-cladding MIR SCG fibre it is suggested that the core should have a higher thermal expansion coefficient (TEC) than the cladding [47, 83]. This should enforce the mechanical strength of the fibre as after fibre drawing the core glass would attempt to contract more than the cladding glass, putting the cladding glass under compression. As will be discussed in section 4.3, TEC measurements were conducted after fabricating an extremely fragile fibre (F032JHB) from Pair II. It was thought that a mismatch in TEC might be the cause of fibre cracks, leading to spontaneous breakages in the fibre where the residual tension could not be released.

To measure the thermal expansion coefficient the as-annealed glass rods were cut parallel and the sample height was measured using a micrometer, as was described in section 3.6.6.2. The TEC probe was a flat silica rod of 4 mm diameter which was cleaned with isopropanol. The sample was positioned so that the silica probe was applied, with a force of 100 mN, to the whole cross-section of the sample. A conditioning cycle of heating at 5 °C $min^{-1}$ to ~ 270 °C and cooling down at 10 °C $min^{-1}$ to room temperature, was performed first to ensure any thermal history effects on the glass were standardised. This first run could produce error on account of the irregular settlement of the glass due to stress relaxation (*e.g.* from annealing effects) and change of morphology. The process was then repeated three times for each sample, as shown in Figure 4.9 for the glass melt M104JHB (composition JB03; $Ge_{24}Sb_4Se_{72}$)

and summarised in Table 4.10, with a heating schedule of 30 – 300 °C at 5 °C $min^{-1}$ and a set cooling rate of 10 °C $min^{-1}$ from 300 - 30 °C to assess reproducibility.

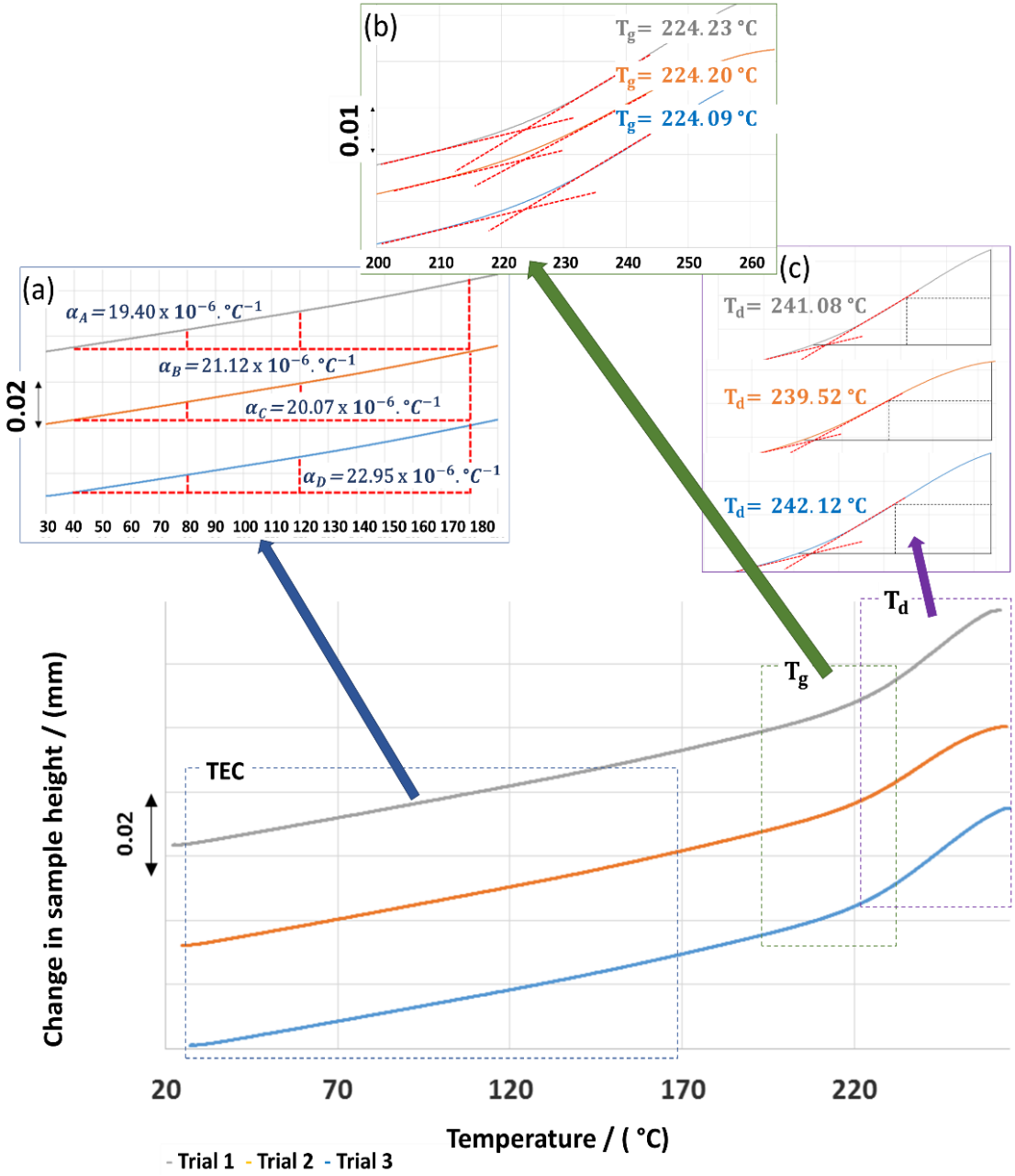



**Figure 4.9 Sample height versus change in temperature heating at 5 °C $min^{-1}$ for the glass melt M104JHB (composition JB03; $Ge_{24}Sb_4Se_{72}$). Three runs were conducted on the same sample after an initial heating at 5 °C $min^{-1}$ and cooling conditioning cycle at 10 °C $min^{-1}$, to ensure any annealing effects were removed and that all samples had the same thermal history. The graphs are shifted vertically for clarity. Trial 1 (grey), Trial 2 (orange) and Trial 3 (blue). Depicted in the insets are: (a) linear thermal expansion coefficients ($\alpha_L$) in the temperature ranges $\alpha_A$= 40-80 °C, $\alpha_B$= 40-180 °C, $\alpha_C$= 80-120 °C and $\alpha_D$= 120-180 °C, (b) the onset $T_g$ and (c) $T_d$. The results are also summarised in Table 4.10.**

Please note that the temperature never reached 300 °C as testing was halted manually before the chalcogenide glass became deformed.

**Table 4.10 A quantitative comparison of the linear thermal expansion coefficients ($\alpha_L$) for JB03 ($Ge_{24}Sb_4Se_{72}$), in the temperature ranges 40-80 ºC, 40-180 ºC, 80-120 ºC, 120-180 ºC. The onset $T_g$ and onset $T_d$ calculated from Figure 4.9 are shown. Three runs were conducted after an initial heating at 5 °C $min^{-1}$ and cooling conditioning cycle at 10 °C $min^{-1}$, to ensure any annealing effects were removed and that all samples had the same thermal history.**

| Run | Thermal history | Linear thermal expansion coefficient (TEC) / ($10^{-6}$.°$C^{-1}$) | | | | Onset $T_g$ / ( °C) | $T_d$ / ( °C) |
|---|---|---|---|---|---|---|---|
| | | $\propto_A$ 40-80 °C | $\propto_B$ 40-180 °C | $\propto_C$ 80-120 °C | $\propto_D$ 120-180 °C | | |
| 1 | Cooled at 10 °C $min^{-1}$ | 19.21 | 20.96 | 20.09 | 22.7 | 224.23 | 241.08 |
| 2 | Cooled at 10 °C $min^{-1}$ | 19.76 | 21.39 | 20.34 | 23.18 | 224.20 | 239.52 |
| 3 | Cooled at 10 °C $min^{-1}$ | 19.23 | 21 | 19.79 | 22.97 | 224.09 | 242.12 |
| Mean | | 19.40 | 21.12 | 20.07 | 22.95 | 224.17 | 240.91 |
| Standard deviation | | 0.31 | 0.24 | 0.28 | 0.24 | 0.07 | 1.31 |

The thermal expansion curve can provide details of three important glass properties: linear thermal expansion coefficient ($\alpha_L$) (inset (a) to Figure 4.9), glass transition temperature ($T_g$) (inset (b) to Figure 4.9), and dilatometric softening temperature ($T_d$) (inset (c) to Figure 4.9).

The $\alpha_L$ can be defined using Equation 4.1 [205];

$$\alpha_L\ (°C^{-1}) = \frac{\Delta h}{h_i.\Delta T} \qquad \textbf{Equation 4.1}$$

where Δh is the change in sample height, $h_i$ is the initial height of the sample and ΔT is the change in temperature.

From Figure 4.9 it can be seen that the curve of the thermal expansion gradually increased in gradient with increasing temperature. A rapid increase in gradient was observed corresponding to $T_g$ (inset b) of the Ge-Sb-Se glass sample (onset $T_g$ was calculated using the intersection of two tangents fitted on to the baseline using a similar method to that used for DSC $T_g$ calculations, see section 3.6.3). Deriving $T_g$ from the

change in gradient of the slope of a thermal expansion curve, and how the linear sections should be found, has not been clearly defined. $T_g$ values were used as a comparison for results obtained from DSC (section 4.2) and DTA (section 4.2.2).

The thermal expansion curve continued through the $T_g$ region until it started to plateau. Here contraction occurred as the super-cooled glass-forming liquid started to flow under the force applied by the silica glass probe, $T_d$. $T_d$ can be defined as the temperature of maximum expansion and is where the onset of a flow under a modest load is initiated [47, 205]. Seddon *et al*. suggest a viscosity of $10^{12.5}$ Pa.s at $T_d$ [188]. Conventionally, $T_d$ is taken as the midway point between the sharp increase in expansion and the onset of contraction, as was shown in inset (c) to Figure 4.9.

The linear thermal expansion coefficient between 40 - 80 °C, 40 – 180 °C, 80 – 120 °C and 120-180 °C for each glass composition: (JB01) $Ge_{19}Sb_{15}Se_{66}$ from the glass melt M070JHB; (JB02) $Ge_{20}Sb_{10}Se_{70}$ from the glass melt M077JHB; (JB03) $Ge_{24}Sb_4Se_{72}$ from the glass melt M104JHB and (JB04) $Ge_{22}Sb_8Se_{70}$ from the glass melt M052JHB, are summarised in Table 4.11, along with onset $T_g$ and $T_d$ calculated from each composition's thermal expansion curve. The onset $T_g$ obtained from DSC measurements as was stated in Table 4.3 are also included for comparison.

The instantaneous thermal expansion coefficient is derived from the gradient of the thermal expansion curve. Figure 4.10 shows both the linear thermal expansion coefficient ($\alpha_L$) and the instantaneous thermal expansion coefficient for Trial 1 of the glass melt M104JHB (composition JB03; $Ge_{24}Sb_4Se_{72}$) from Figure 4.9.

Instantaneous thermal expansion coefficient curves for the four glass compositions will be shown in Figure 4.11. The importance of the instantaneous expansion coefficient will be discussed further in section 4.3.

**Table 4.11 The composition, corresponding melt number and initial height of each sample JB01 ($Ge_{19}Sb_{15}Se_{66}$), JB02 ($Ge_{20}Sb_{10}Se_{70}$), JB03 ($Ge_{24}Sb_4Se_{72}$) and JB04 ($Ge_{22}Sb_8Se_{70}$) used for thermal expansion (TEC) analysis and the mean linear thermal expansion value over a temperature range of 40-80 °C, 40-180 °C, 80-120 °C and 120-180 °C.**

| Glass code | Height / (mm) | Linear thermal expansion coefficient* (TEC) / ($10^{-6}$.°$C^{-1}$) | | | | Onset $T_g$* / ( °C) | $T_d$* / ( °C) | Onset $T_g$ from DSC / ( °C) |
|---|---|---|---|---|---|---|---|---|
| | | 40-80 °C | 40-180 °C | 80-120 °C | 120-180 °C | | | |
| JHB01 | 10.21 | 17.19 | 18.01 | 17.57 | 18.81 | 225 | 242 | 234 |
| JHB02 | 9.99 | 19.13 | 20.86 | 19.91 | 22.64 | 202 | 219 | 211 |
| JHB03 | 9.99 | 19.40 | 21.12 | 20.07 | 22.95 | 224 | 241 | 226 |
| JHB04 | 9.85 | 18.29 | 19.60 | 18.70 | 21.08 | 222 | 240 | 238 |
| Standard deviation | | 0.39 | 0.26 | 0.34 | 0.28 | 3 | 5 | 0.8 |
| *Mean value taken from three experiments | | | | | | | | |

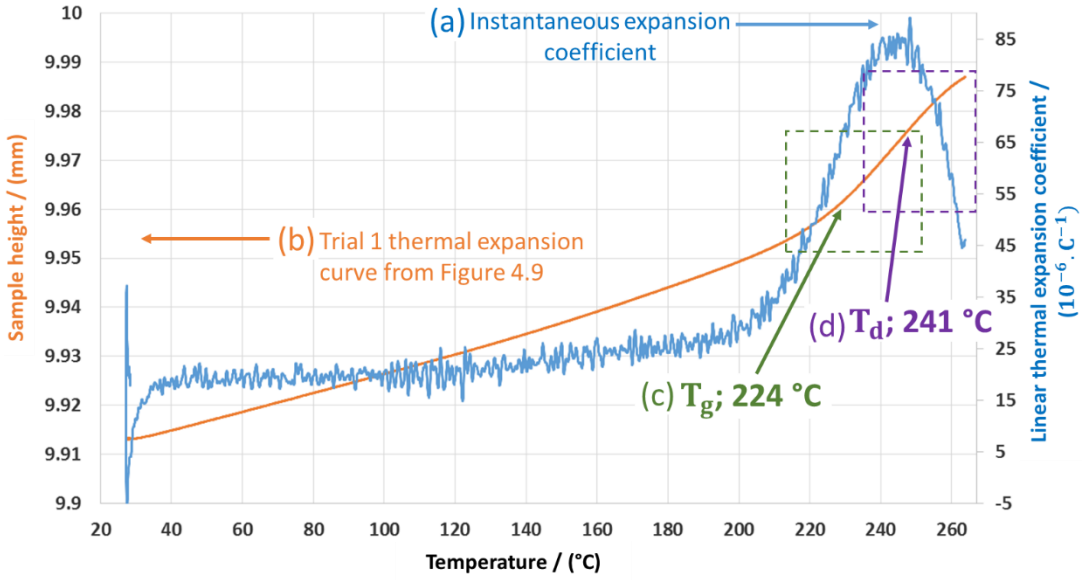



**Figure 4.10 Sample height versus temperature for the glass melt M104JHB composition (JB03; $Ge_{24}Sb_4Se_{72}$) (orange curve, as was shown in Figure 4.9) and the change in instantaneous expansion coefficient versus temperature (blue curve). From Table 4.10, the mean average $T_g$= 224 °C and $T_d$ = 241 °C have been highlighted.**

## 4.3. Development of selecting Ge-Sb-Se chalcogenide glass pairs from extrusion and fibre drawing experience

When choosing a glass pair for the Ge-Sb-Se small core/cladding MIR SCG optical fibre, compromises are sought after optical and physical properties had to be made.

Although it was desirable to have a high NA, with the core having a higher refractive index than the cladding, whether the fibre could actually be fabricated needed to be carefully considered. Evidently the ideal glass candidates would have perfectly matched physical properties, however in practice this is not possible. From the XRD patterns (section 4.1.1) it was established that all the Ge-Sb-Se compositions fabricated amorphous materials, had been batched accurately assessed by EDX analysis (section 4.1.2) and were suitable candidates for MIR transmission, predominantly between 3-12 µm, observed via FTIR spectra (section 4.1.3).

The first small core/cladding glass to be drawn to fibre in this Project was Pair I (core JB04; $Ge_{22}Sb_8Se_{70}$, and cladding JB03; $Ge_{24}Sb_4Se_{72}$). The selection of the core and cladding candidate glass pair for a small core/cladding fibre was based on suggestions by Li [83]. Two co-extrusions (E015JHB and E018JHB) and two fibres (F019JHB and F023JHB) were fabricated from this glass pair, (see section 5.4) yet difficulties arose in producing a circular core in the fibre, as will be shown in Figure 5.9 and Figure 5.12. Nevertheless, fibre loss measurements were obtained from the 242 x 253 µm cane F018JHB drawn from the core/cladding co-extrusion (Figure 6.3) and near-field imaging was accomplished at 1436 nm, in the small core fibres F019JHB (Figure 6.1(a-b)).

Another glass pair, Pair II (core JB01; $Ge_{19}Sb_{15}Se_{66}$ and cladding JB02; $Ge_{20}Sb_{10}Se_{70}$) was investigated, again based on early experimental bulk glass findings in [83]. This pair was selected based on the suggestion that the refractive index of a Ge-Sb-Se glass increases with a higher concentration of Sb and a lower concentration of Ge. From [83], it was reported that the compositions JB01 and JB02 had a refractive index at 1460 nm of 2.67 and 2.58 respectively generating a NA of 0.72 (Pair I had a

NA of 0.54). Furthermore it was considered that a circular core did not form in F019JHB and F023JHB due to a difference in viscosity at the fibre drawing region causing the glasses to not uniformly coalesce during the collapse down. Viscosity/ temperature measurements were conducted, shown in section 4.2.3.1, and further supported the selection of Pair II as the viscosity at the fibre drawing region $10^{4.5}$ Pa.s was only 7 °C different, complementing the 8 °C reported in [83]. Pair II was successfully co-extruded (E030JHB) however the extruded preform was very brittle and broke easily, as will be shown in Figure 5.14. Problems also arose in securing the preform in the fibre tower during cane drawing, as the cladding (JB02; $Ge_{20}Sb_{10}Se_{70}$; $T_g$ = 211 °C) softened before the core (JB01; $Ge_{19}Sb_{15}Se_{66}$; $T_g$ = 234 °C). The hot zone of the fibre furnace was fitted with a graphite ring which was heated by a RF coil, as was shown in Figure 3.11. The temperature of the graphite ring was controlled by varying the RF power, expressed as a percentage of its maximum. At a RF power of 23 % the preform started to neck down but would then suddenly drop from the holder. Another attempt was made using a different section of the preform and the lowest RF power (and therefore temperature) was used to soften the glass for the neck down. On the subsequent heating attempt ~ 30-40 mm neck down was achieved, however the preform failed at a heating RF power setting of 31 %.

Nevertheless JB02 ( $Ge_{20}Sb_{10}Se_{70}$) was successfully extruded into a tube, thus JB01 ( $Ge_{19}Sb_{15}Se_{66}$) was drawn to cane directly from a propylamine etched glass melt in an 8/12 ID/ OD, mm ampoule (see section 5.5.2). This unstructured cane was suspended in the outer cladding tube and it was possible to draw the preform to fibre (F032JHB). However, it was noted that once on the fibre drum the drawn fibre would spontaneously break during the ensuing days and characterisation procedures. Thermal expansion

coefficient measurements were conducted on the Ge-Sb-Se bulk glasses (see section 4.2.3.2) and it was found that Pair II had the greatest difference in thermal expansion of all the glass pairs (*e.g.* between 40-180 °C Pair II had a difference of Δ TEC = 3 x $10^{-6}.°C^{-1}$ compared to Pair I which had a difference of Δ TEC = 1 x $10^{-6}.°C^{-1}$). It was also established that the cladding glass JB02 ($Ge_{20}Sb_{10}Se_{70}$) had a higher expansion coefficient than the core glass JB01 ($Ge_{19}Sb_{15}Se_{66}$). As mentioned in section 4.2, a slightly higher thermal expansion coefficient of the core can be beneficial to produce a stronger fibre, as residual compression in the cladding will be generated when the core expands more than the cladding upon heating, and then attempts to contract to a higher degree than the cladding during cooling below the $T_g$ region. Furthermore the phenomenon of TEC was also applied to the difficulty in producing a circular core with Pair I in fibres F019JHB and F023JHB. Again from the TEC results discussed in section 4.2.3.2 it was found that the core had a lower TEC than the cladding. Therefore it was suggested that a higher TEC of the core should encourage the core to expand further into the cladding during fibre drawing, maintaining its circular geometry and aiding a more uniformed collapse-down.

Figure 4.11 displays the instantaneous expansion coefficients for each glass pair. For the glass pair, Pair II, Figure 4.11(b), it can be seen that there is approximately a 6-fold increase in the instantaneous expansion coefficient for both glasses. However, the region where this occurs for each glass differs greatly with temperature (JB02 initiates at ~ 180 °C, whereas JB01 starts its rapid increase at ~ 210 °C). This could create large internal stresses in the fibre upon cooling from fibre drawing, as the glass is cooled from above its $T_g$ to room temperature within seconds.

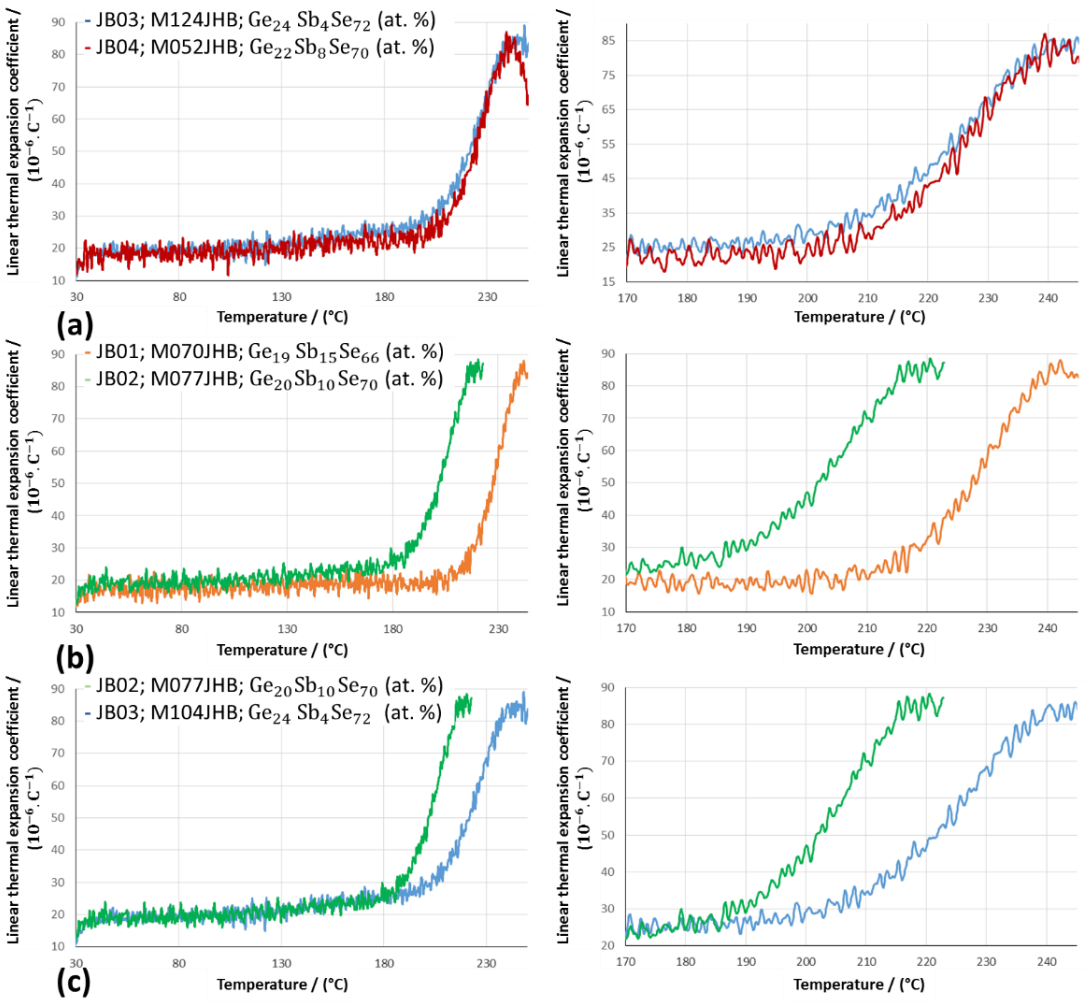



**Figure 4.11 Instantaneous expansion coefficient for each glass pair. (a) Pair I with glass composition JB04 as the core ($Ge_{22}Sb_8Se_{70}$; red) and JB03 as the cladding ($Ge_{24}Sb_4Se_{72}$; blue). (b) Pair II with glass composition JB01 as the core ($Ge_{19}Sb_{15}Se_{66}$; orange) and JB02 as the cladding ($Ge_{20}Sb_{10}Se_{70}$; green). (c) Pair III with glass composition JB02 as the core ($Ge_{20}Sb_{10}Se_{70}$; green) and JB03 as the cladding ($Ge_{24}Sb_4Se_{72}$; blue).**

Each curve in Figure 4.11 appears to reach a maximum where apparently the glass is no longer expanding upon heating. This can be misinterpreted as expansion of the glass has not stopped. The sample is still expanding, however, as $T_g$ is exceeded the now viscoelastic sample becomes deformed under the load and it is compressed. If the glass was contained in a vessel that did not allow room for deformation, the expansion would continue beyond this point.

A third glass pair, Pair III, was selected to be drawn to fibre with JB02 ($Ge_{20}Sb_{10}Se_{70}$)

as the core and JB03 ($Ge_{24}Sb_4Se_{72}$) as the cladding. Due to the problems experienced with the Pair II producing such a fragile and brittle fibre (F032JHB), the linear thermal expansion coefficient results, section 4.2.3.2, were evaluated and Pair III was selected as the linear thermal expansion coefficient was the same between 40 – 180 °C for both glasses. Although it has been discussed that it is more desirable to have a slightly higher TEC in the core than in the cladding, this amount has not been quantified before too much internal stress is generated. Therefore it was suggested that matching the TEC value was acceptable. However it was later queried if the temperature at which the onset of the large increase in the instantaneous expansion coefficient occurred was of greater importance to match. Figure 4.11(c) shows that although the temperature difference between the regions of the rapid increase was not as great as it was for Pair II ($\Delta T$ = ~ 30 °C) there was still a significant difference for Pair III ($\Delta T$ = ~ 16 °C). As will be discussed in section 5.6 the mechanical stability of the fibre F035JHB was low and the fibre spontaneously broke from the fibre drum during storage.

From [83] the refractive index of JB02 and JB03 at a wavelength of 1460 nm were 2.58 and 2.50 respectively, giving a NA of 0.65. Furthermore, due to the difficulties in glass handling with Pair II, the previous experience with tube extrusions of the glass JB03 (E014JHB, E017JHB and E019JHB) was valuable and the tube extrusion was fabricated straightforwardly. As mentioned in section 4.2.1, it was reflected that there was a difference in $T_g$ values measured for JB02 in this Thesis ($T_g$ = 211 °C) and those reported in [83] also measured using DSC ($T_g$ = 220 °C). This discrepancy would mean that the difference in $T_g$ of the glass pair would either be 5 °C from [83] or 15 °C as-measured in this Thesis. The $T_g$ values measured for JB02 from DTA (215 °C) and TEC (202 °C) in this work are a closer match to the lower $T_g$ value measured from DSC in

this Project, indicating that the $T_g$ value measured using DSC in this work can be taken over the value reported in [83]. However, as Pair I successfully drew to fibre and had a $T_g$ difference of 12 °C, by basing the decision on the $T_g$ values reported in this Thesis it was still expected that a successful fibre could be drawn. It is worth remembering that a difference in viscosity at the fibre drawing region was thought to be accountable for the difficulties in producing a circular core with Pair I.

However, it was found to be not possible to co-extrude Pair III. During the extrusion the extrudate bent towards the inside of the guide tube as the core glass was pushed through the cladding. It is suggested that a difference in the super-cooled melt flow velocity across the extrudate caused the curvature and once contact of the super-cooled melt with the guide tube was made, the increased drag caused the extrudate to become swollen filling the guide tube, see section 5.6.1. In hindsight, from the viscosity/ temperature results shown in section 4.2.3.1, it could have been expected with a difference in 28 °C between the core and the cladding glass at $10^8$ Pa.s (approximate viscosity in the extrusion region). Therefore, the glass JB02 (with composition $Ge_{20}Sb_{10}Se_{70}$) was singly extruded from the remainder of the boule and drawn to cane. The un-structured cane was inserted in the tube extruded from JB03 and the core-cladding preform was drawn to fibre. Problems arose in fibre drawing when the fibre preform unfortunately made contact with the carbon graphite receptor, leading to vaporisation of the chalcogenide melt, as will be shown in Figure 5.19. Nevertheless enough preform survived, and after vigorous cleaning of the fibre preform small core-cladding optical fibres were produced. As will be seen from Figure 5.21 for the anticipated 15 µm core, although the core did not form a perfect circle it was more circular than the fibres formed from Pair I.

**Table 4.12 Physical properties of the fabricated glass pair fibres made in this Project, collated from the experiments conducted in this chapter.**

| Glass pair | Core | Cladding | Δ $T_g$ ( °C) | Δ viscosity ( °C) | | Δ TEC ($10^{-6}.°C^{-1}$) ( 40- 180 °C) | NA* |
|---|---|---|---|---|---|---|---|
| | | | | At $10^8$ Pa.s (extrusion viscosity) | At $10^{4.5}$ Pa.s (fibre drawing viscosity) | | |
| Pair I | JB04 | JB03 | 12 | 10 | 20 | 1 | 0.54 |
| Pair II | JB01 | JB02 | 23 | 14 | 7 | 3 | 0.72 |
| Pair III | JB02 | JB03 | 15 | 28 | 47 | 0 | 0.65 |
| *NA calculated from refractive index values at 1463 nm wavelength reported in [83]. | | | | | | | |

## 4.4. Discussion

From observations made in this Project when selecting candidate glass pairs for small core/cladding MIR SCG optical fibres, a hierarchy of the order of selection of physical properties is suggested. Firstly with any new glass composition it is important to establish that in fact the material is amorphous (by means of XRD, section 4.1.1) and that the composition batched is correct (through EDX section 4.1.2). Furthermore, MIR transmission needs to be determined (using FTIR, section 4.1.3). Once the glass compositions have been confirmed the following order of matching thermal properties is suggested as vital in achieving a glass pair that can be drawn to fibre.

1) It was established that to match $T_g$ first was most important. $T_g$ could be determined by means of DSC (section 4.2.1), DTA (section 4.2.2) or TEC (section 4.2.3.2). However, it is considered that DSC is the most accurate method. It was not possible to cane draw glasses from a co-extruded preform due to a large difference in $T_g$ (*e.g.* Pair II; Δ $T_g$ = 23 °C). In this Project great consideration was given to matching the viscosities in the fibre drawing region of the Ge-Sb-Se chalcogenide glass pairs with the ambition of producing a circular core. Unfortunately this was chosen over the importance of matching values of $T_g$. However, it was found that a large difference (23 °C) in $T_g$ meant that the glasses could not reach the viscosity of the fibre drawing region ($10^{4.5}$ Pa.s) at the same time, thus making the nominal

matching of the viscosities redundant. Moreover it was found that even with a large difference in temperature (*e.g.* Pair III; 47 °C) at the fibre drawing viscosity region ($10^{4.5}$ Pa.s) the glass pair could still be drawn to fibre and produced the most near-circular core.

2) It is proposed that the second property to match is the viscosity at the extrusion region ($10^{8}$ Pa.s). It was not possible to co-extrude glasses with large differences in viscosity at $10^{8}$ Pa.s (*e.g.* Pair III; 28 °C) due to the glasses swelling and becoming locked in the die. It is worth mentioning that glasses with a larger difference in $T_g$ could be co-extruded (*e.g.* Pair II; $\Delta T_g$ = 23 °C); however this is inconsequential if the glasses could not subsequently be drawn to cane, on account of their difference in $T_g$.

3) It is suggested that the temperature at which the large increase in the instantaneous expansion coefficient occurs for the each glass should be the third property to be matched. Although having a mismatch in the instantaneous expansion coefficient did not appear to have an immediate impact on extrusion or fibre drawing procedures, it was thought that a large difference in temperature of this rapid thermal expansion region caused stresses during cooling of the fibre. This resulted in the fragility and spontaneous breaks in the fibre, *e.g.* F032JHB from Pair II (ΔT of the onset of the instantaneous expansion coefficient was ~ 25 °C. This glass pair also had the greatest difference in TEC between 40 – 180 °C of 3 x $10^{-6}$. $°C^{-1}$). From Figure 4.11 it can be seen that only Pair I had a closely matched region of the rapid increase in the instantaneous thermal expansion coefficient.

   Pair III was selected as there was zero difference in TEC (between 40-180 °C), whereas Pair II was selected as the difference in temperature when the glasses reached the fibre drawing viscosity ($10^{4.5}$ Pa.s) was 7 °C. It is worth noting that the

failed core/cladding co-extrusion occurred (for Pair III) when the TEC values (between 40 – 180 °C) were deliberately matched. The cause of this failure was deemed to be a result of the large difference in viscosity at the extrusion region $10^{4.5}$ Pa.s (for Pair III; Δ 28 °C). The Pair I properties were not as closely matched for either of these parameters (ΔTEC = 1, ΔT at the fibre viscosity = 20 °C). However, if a fibre is too fragile to handle or to complete its application, it is irrelevant that these other material properties are matched. By chance the instantaneous expansion coefficient was the most closely matched.

Furthermore it is preferable that the thermal expansion coefficient of the cladding glass is lower than that of the core glass. Upon cooling from either extrusion or fibre fabrication, the core glass will attempt to contract to a larger degree than the cladding, putting the cladding glass under compression, resulting in enhanced mechanical fibre stability.

4) It could be thought that achieving the highest NA of a small core-cladding MIR SCG optical fibre should be the first priority when selecting candidate glass pairs. Although important, as was described in this chapter, if a stable fibre cannot be fabricated the benefits of a high NA are futile. Therefore it is suggested that only when points 1-3 are satisfied should the selection based on high NA be considered.

As a result of the characterisation of the glasses for the three glass pairs; Pair I, Pair II and Pair III the properties of three un-fabricated glass pairs has evolved, as summarised in Table 4.13. The refractive index obtained from [83] has been used to establish which glass would form the core. From the impact of the thermal properties of the Ge-Sb-Se glasses, and abiding by the suggestions given in 1-4 above, it is worth considering the fabrication of Pair V (JB01 and JB04) as a core-cladding glass pair (Table 4.13).

**Table 4.13 Physical properties of the un-fabricated glass pair fibres, collated from the experiments conducted in this chapter.**

| Glass pair | Core | Cladding | Δ $T_g$ / ( °C) | Δ / ( °C) | | Δ TEC / ($10^{-6}$. °$C^{-1}$) ( 40- 180 °C) | Δ $T_d$ /( °C) | NA* |
|---|---|---|---|---|---|---|---|---|
| | | | | At $10^8$ Pa.s (extrusion viscosity) | At $10^{4.5}$ Pa.s (fibre drawing viscosity) | | | |
| Pair IV | JB01 | JB03 | 8 | 14 | 40 | 3 | 0.66 | 0.98 |
| Pair V | JB01 | JB04 | 4 | 4 | 20 | 2 | 1.98 | 0.81 |
| Pair VI | JB02 | JB04 | 27 | 18 | 27 | 1 | 20.55 | 0.37 |
| *NA calculated from refractive index values at 1463 nm wavelength reported in [83] | | | | | | | | |

Many of the properties measured for JB01 and JB04 are closely matched, most significantly the Δ $T_g$ = 4 °C. From the investigation in candidate glass pairs discussed in this chapter, a close match in $T_g$ is crucial for a successful cane draw and benefits both extrusion and fibre drawing procedures. Furthermore the small difference in temperature at the extrusion region viscosity (~ $10^8$ Pa.s) of 4 °C would indicate a co-extrusion would be possible. The instantaneous expansion coefficient for Pair V is shown in Figure 4.12. Similarly to Pair I, it would appear that there is minimal temperature difference between the onset of the large increase in the instantaneous expansion coefficient between the glasses. Using the refractive index values reported in [83] at 1460 nm (JB01 2.68 and JB04 2.55) the NA of the fibre can be calculated as 0.81, the highest of any of the glass pairs.

However, the suggestion of JB01 and JB04 as a glass pair does not come without anticipated difficulties. From the refractive index results reported in [83] JB01 should be the core and JB04 the cladding to assist in light guiding. JB01 has a lower TEC (18 x $10^{-6}$.°$C^{-1}$ between 40 - 180 °C) than JB04 (20 x $10^{-6}$.°$C^{-1}$ between 40 - 180 °C). This could cause potential problems with the mechanical strength of the fibre as it is recommended that the core should have a higher TEC than the cladding. Nevertheless it is suggested that JB01 and JB04 would be good candidates as a glass pair for a small core-cladding MIR SCG optical fibre.

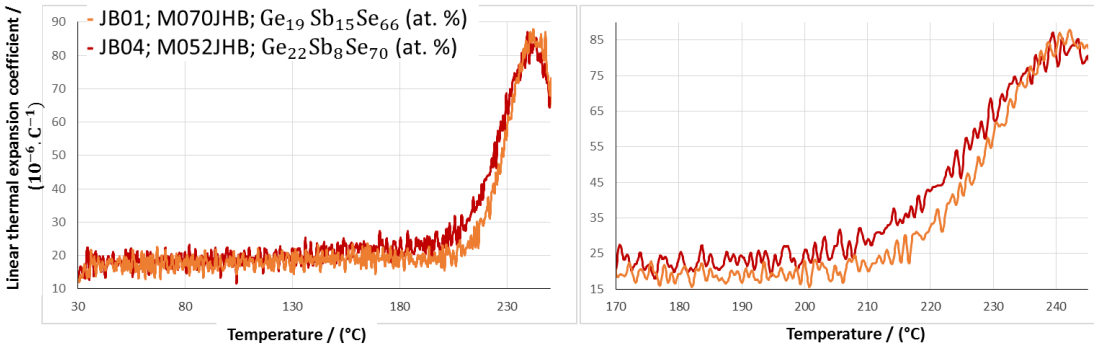



**Figure 4.12 Instantaneous expansion coefficient for the un-fabricated Pair V (core JB01; $Ge_{19}Sb_{15}Se_{66}$ and cladding JB04; $Ge_{22}Sb_8Se_{70}$), collated from the experiments conducted in this chapter.**

## 4.5. Summary

In this chapter the physical and optical properties of the bulk Ge-Sb-Se glasses were analysed. The Ge-Sb-Se bulk glass samples were characterised by a low tendency to crystallise (section 4.1.1) and good transparency in the MIR (section 4.1.3). The thermal properties of the bulk Ge-Sb-Se glasses were characterised by: DSC (section 4.2.1) to determine the onset $T_g$ values; viscosity/ temperature behaviour (section 4.2.3.1) to predict the temperature of the glasses when at the extrusion viscosity ($10^8$ Pa.s) and fibre drawing viscosity ($10^{4.5}$ Pa. s) and TEC (section 4.2.3.2) over a temperature range. It was not possible to obtain the crystallisation temperature from DTA (section 4.2.2). The development of how the Ge-Sb-Se compositions were selected to draw to fibre was explained (section 4.3) and conclusions as to the importance of selecting the right thermal properties of the core and cladding glasses were given (section 4.4). Chapter 5 reports the fabrication of the glass pairs into fibres via extrusion and fibre drawing techniques.

# 5. Fabrication of Ge-Sb-Se chalcogenide glass fibres

In this Chapter the three glass pairs (Pair I, II and III) discussed in Chapter 4, section 4.3 and their development into fibres is described in greater detail. Extrusions and fibre drawing conducted in this Project were assisted by Senior Research Fellow Dr Furniss[8]. Furthermore much knowledge resulting in adaptations and improvements of the extrusion and fibre drawing process have been achieved within the Mid-Infrared (MIR) Photonics Group at the University of Nottingham, UK, reported in [45, 47, 161] which have ultimately benefitted the fibre fabrication conducted for this Project. Nevertheless, the Ge-Sb-Se glass system studied in the present work was a new glass system to extrude and the behaviour was different from the glass system encountered before.

Here, in Chapter 5, a brief explanation of the super-cooled melt velocity in extrusions is provided in section 5.1 and where the core super-cooled melt enters the cladding super-cooled melt during a co-extrusion is suggested. Design changes were made to the tube extrusion die and pin components during the course of this Project and are discussed in section 5.2. The method of achieving different fibre dimensions is explained in section 5.3 and the specification of the small core fibres is discussed. The extrusion and fibre drawing of selected Ge-Sb-Se chalcogenide glass pairs is reported including: Pair I (core composition JB04; $Ge_{22}Sb_8Se_{70}$ and cladding composition JB03; $Ge_{24}Sb_4Se_{72}$) in section 5.4 where two trials were conducted before and after the alterations in the die and pin design; Pair II (core composition JB01; $Ge_{19}Sb_{15}Se_{66}$ and cladding composition JB02; $Ge_{20}Sb_{10}Se_{70}$) in section 5.4 and Pair III (core composition JB02; $Ge_{20}Sb_{10}Se_{70}$ and cladding composition JB03; $Ge_{24}Sb_4Se_{72}$) in

[8] Dr. David Furniss. Senior Researcher in the MIR Photonics Research Group, George Green Institute for Electromagnetics Research, Faculty of Engineering, University of Nottingham, UK.

section 5.6. X-ray diffraction (XRD) results for all the fibres fabricated in this Project are given in section 5.7. Concluding remarks are made about the complications encountered during extrusion and fibre drawing in section 5.8. This chapter is summarised in section 5.9. The extrusion parameters for all the tube and co-extrusions are given in Appendix III, Table A and Table B, respectively.

## 5.1. Understanding velocity during extrusion and optimising core/ cladding ratios in co-extrusions for optical fibre applications

It was important to understand the core/ cladding ratio of an extrudate produced from a co-extrusion to help determine which section should be drawn to cane. The extrusion process and the loading of the glass charge boules into the extruder (the end furthest from the contraction cone was positioned against the die, thus the saw-cut end was situated under the bobbin) was described in section 3.4. For cane drawing, ~ 80 mm (plus an additional 20 mm for securing to the preform holder) of the extrudate was required where the core was thought to be ~ 60 % of the cladding. Roeder [206] showed that the flow behaviour of an extruded glass had ~ 0 fluid flow of the super-cooled melt at the barrel wall boundaries and the outer layers of the glass was left behind during extrusion, see Figure 5.1.

This is beneficial for extruded glasses which are to be drawn to high purity optical fibres, as it means that the glass surface which was in contact with the silica ampoule wall is removed, providing higher optical purity. Furthermore, it was suggested that the charge glass closest to the die (in the case of this Project the cladding) holds in the lower corners of the barrel, remaining static until pulled through the die by the glasses stacked on top of it (in this Project, the core). Better understanding of this flow pattern would enable a more accurate prediction of the best section of extrudate to use for cane drawing.

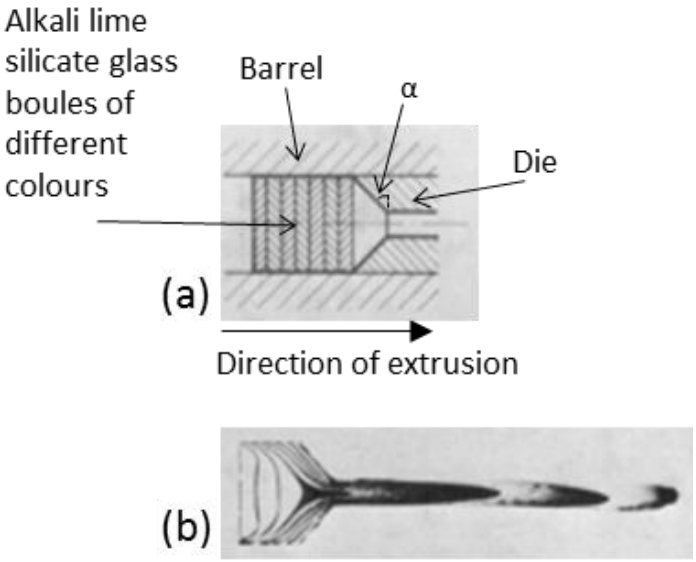



**Figure 5.1 Roeder** *[206]* **used different coloured alkali lime silicate glasses to show the flow pattern of the glasses during an extrusion. (a) Extrusion set up. Die angle $2\alpha = 90°$. (b) Flow patterns during the extrusion (at 750 °C, a viscosity of $10^{7.2}$ Pa.s and a force of 100 kg $cm^{-2}$). It can be seen that at the walls of the barrel the velocity of the glass is near 0, thus the surface of the glass boules remains in the barrel. The majority of the extrudate (particularly the central section) consists of the internal region of the glass boules (where the flow rate was highest). The lower glass charges can be seen to hold in the corners of the barrel until pulled through the die by the final core charge. Figure reproduced from** *[206]*.

Analysis of the core/ cladding ratio from co-extruded glasses was conducted for a 4th year Undergraduate Master's Project [207] run by Mr T. Arnold, under the partial supervision of this Author. Due to the high cost of Ge, Sb and Se precursors, and the time intensive process to melt the glass and extrude it, borosilicate glass ($5Na_2O - 75B_2O_3.20SiO_2$) was extruded in Arnold's project as an exemplar. The same borosilicate glass melt was used to prepare two 10 mm glass charge boules (14 mm ø), with 0.5 wt. % cobalt oxide added to one of the two melts to allow visual distinction between the two glasses, colourless versus blue.

For the co-extrusion, the minimum load was applied when the die temperature was 405 °C (the borosilicate glass $T_g$ = 332 °C). The temperature was then further increased to 535 °C and a 200 kg load was applied. The extrusion progressed at a rate of 0.5 mm $min^{-1}$. The extrudate is shown in Figure 5.2(a).

The extrudate was cut into 15 pieces along its length, Figure 5.2(b), to investigate the introduction of the core glass into the cladding glass. It was found that within approximately the first 30 mm of extrusion the core came through as ~ 30 % of the extrudate. This increased with the core coming through as 87 % of the extrudate by ~ 110 mm.

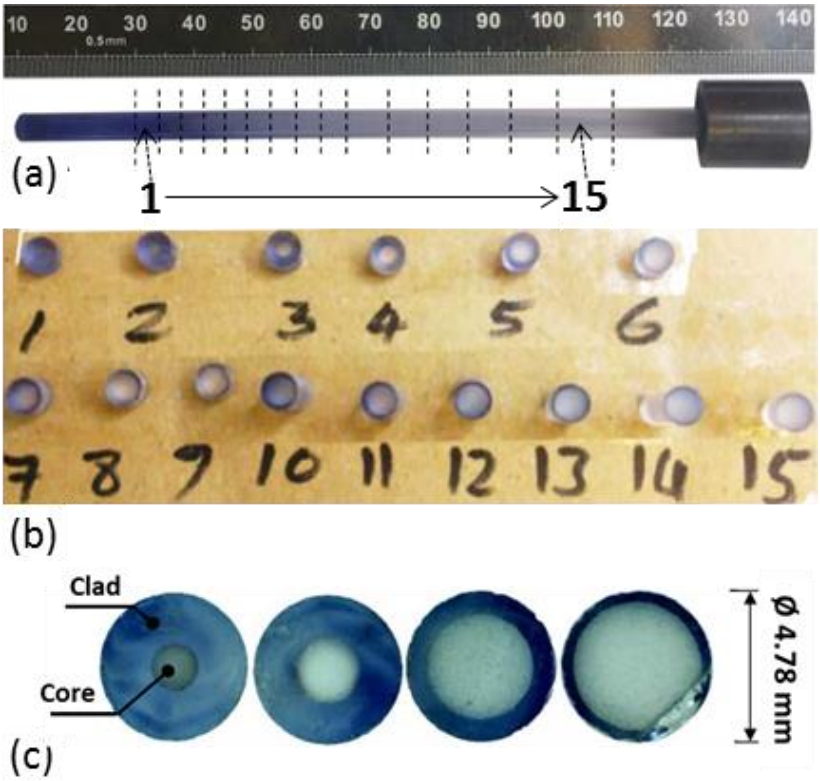



**Figure 5.2 Extrudate resulting from borosilicate co-extrusion of core glass ($5Na_2O - 75B_2O_3.20SiO_2$) and cladding glass ($5Na_2O - 75B_2O_3.20SiO_2$ + CoO). (a) Extrudate directly after co-extrusion. The dotted lines correspond to where the extrudate was cut for the sections displayed in (b). Section 1 represents the section on the far left, increasing in number to section 15 on the far right. (b) The preform was cut into sections ranging from 5-10 mm in length to assess the core/ cladding ratio. (c) A magnified view of sections 1 (far left, with ~ 30 % core), 3, 7 and 15 (far right, with ~ 87 % core). Figure adapted from [207].**

The remaining Ge-Sb-Se glass extrudate produced from co-extrusion (E018JHB, core composition JB04; $Ge_{22}Sb_8Se_{70}$ and cladding composition JB03; $Ge_{24}Sb_4Se_{72}$ section 5.4) was used as a comparison to the borosilicate glass. It is worth mentioning that the extrudate was 197 mm in length and the section between ~ 65 – 110 mm was used for cane drawing F021JHB, see Figure 5.11. Therefore only the first section (up to ~ 65

mm) could be used for comparison. The SEM images of the Ge-Sb-Se extrudate at 57.5 mm, 54.4 mm, 41.9 mm and 38.8 mm lengths are shown in Figure 5.3.

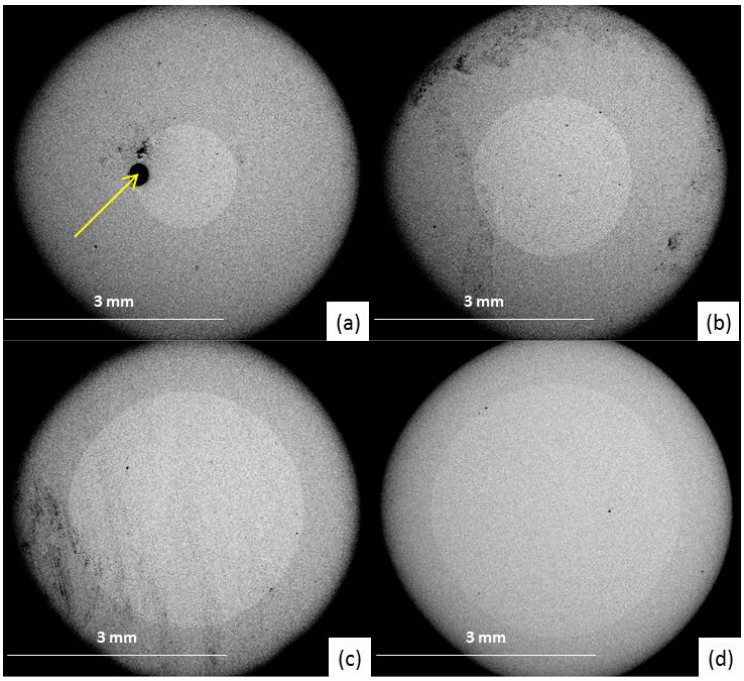



**Figure 5.3 The remaining Ge-Sb-Se glass preform produced from co-extrusion (E018JHB, core composition JB04; $Ge_{22}Sb_8Se_{70}$ and cladding composition JB03; $Ge_{24}Sb_4Se_{72}$) which was not involved in the cane drawing (F021JHB) was investigated to assess where the core glass entered the cladding glass. Cross-sections along the extrudate are shown at lengths: (a) 57.5 mm; (b) 54.4 mm; (c) 41.9 mm and (d) 38.8 mm. The dark mark (yellow arrow) in (a) was suggested to be an external artefact (*e.g.* dust or oil used in glass cutting). It can be seen that the core is practically central in all the images and it is assumed that the images from this co-extrusion are a good representation of all co-extrusions in this Project.**

Choong [208] and Savage [143] conducted similar studies with arsenic containing glasses. Their core/ cladding ratios, the results found for the borosilicate glass extrudate and those for the Ge-Sb-Se extrudate, are plotted on an absolute scale for comparison in Figure 5.4. Glass compositions and boule geometry are stated in Figure 5.4. From Figure 5.4 it was suggested that the slightly steeper gradient of the core/ cladding ratio against length curve of the borosilicate glass was accountable to the matched viscosity/ temperature and $T_g$ of the core and cladding glasses, which promoted coherent flow. Thus, the borosilicate glass represented an ideal preform extrusion. However, in

practice, due to the desired optical properties of a fibre to have a high NA to control the fibre dispersion (see section 2.6), the core and cladding glasses cannot be the same composition and therefore their physical properties will differ.

**Table 5.1 Comparison of oxide and chalcogenide extrusion. Glass compositions and boule dimensions of glasses for core/ cladding ratio analysis after extrusion. The core/ cladding ratios are plotted against length along the preform in Figure 5.4.**

| | Savage [143] | Choong [208] | E018JHB [This work] | Borosilicate glass [207] |
|---|---|---|---|---|
| **Core composition** | $Ge_{17}As_{18}Se_{65}$ | $As_{40}Se_{60}$ | $Ge_{22}Sb_8Se_{70}$ | $5Na_2O - 75B_2O_3.20SiO_2$ |
| **Cladding composition** | $Ge_{17}As_{18}Se_{62}S_3$ | $Ge_{10}As_{21}Se_{66.6}$ | $Ge_{24}Sb_4Se_{72}$ | $5Na_2O - 75B_2O_3.20SiO_2$ + CoO |
| **Core boule height / mm** | ~15 | ~15 | 10.59 | 10.04 |
| **Cladding boule height / mm** | ~15 | ~15 | 10.47 | 9.98 |
| **Initial boule diameter of core and cladding / mm** | ~29 | ~29 | 15* | 13.80-13.85 |
| **Extrudate diameter / mm** | ~10 | ~10 | 4.74-4.76 | 4.88-4.91 |
| *Boules were slightly over-sized (~15.05-15.06 mm ø) thus the sides were ground to fit barrel. | | | | |

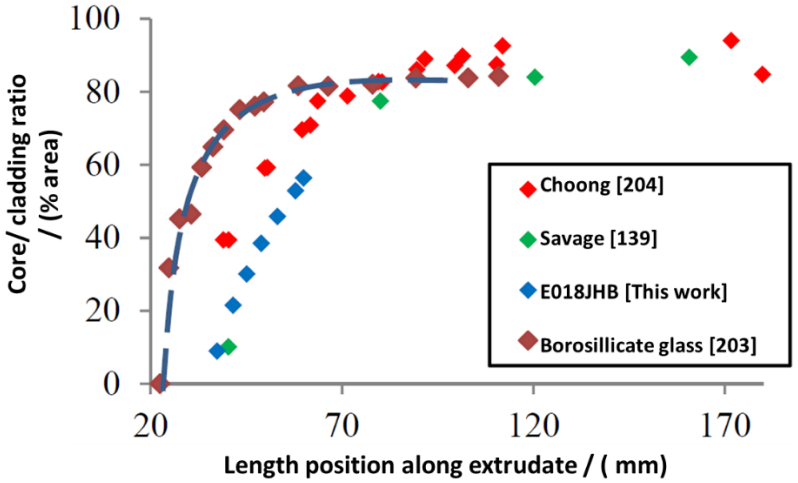



**Figure 5.4 Comparison of core/cladding ratios of oxide and chalcogenide glass co-extruded preforms after co-extrusion. A steeper gradient was observed for the borosilicate extrudate (indicated by the blue line). It was thought that this was due to the matched viscosities at the extrusion temperature of the core/ cladding super-cooled liquid boules. It was calculated that after an extruded length of ~ 60 mm a stable core/ cladding ratio was achieved of ~ 87 %. Graph adapted from [207].**

As discussed in section 4.4, it is this Author's proposal that there should be a hierarchy when choosing glass pairs based on their physical properties (*e.g.* matching $T_g$ has greater importance than matched viscosities at the processing temperatures).

Nevertheless the results displayed in Figure 5.4 confirm that the correct section of preform (~ 70-110 mm) from the Ge-Sb-Se co-extrusion E018JHB (which will be described in section 5.4.4) was selected to use in cane drawing, where a 60 % core/ cladding ratio was achieved.

## 5.2. Optimising the bore diameter in Ge-Sb-Se chalcogenide glass tube extrusions

The pin and die construction for the outer cladding tube extrusions (fabricated in-house by Furniss) is depicted in Figure 5.5. The pin, Figure 5.5(a), consisted of a pin head (polished NIMONIC) inserted into a 3-spoked 'spider' support body (316 stainless steel), Figure 5.5(b). This was then assembled within the 10 mm inner diameter (ID) graphite lined extruder die (bulk material 316 stainless steel), Figure 5.5(c). Graphite appears to exhibit a low coefficient of friction with chalcogenide glasses which permitted the extruded super-cooled melt to flow smoothly along the inner surface of the die. Graphite apparently also is chemically inert towards chalcogenide glasses, which is critical at the high extrusion temperatures. The 'spider' spokes of the pin created an obstacle to the super-cooled melt flow into the extruder die. They were chamfered on the lead-in edge to reduce the turbulence of the super-cooled melt flow and allow a greater hydrostatic pressure to reach the graphite lining of the die.

From Figure 5.5(a) (bottom image), it can be seen that the 1 mm pin had an angled shoulder (~ 60 °) leading onto the shaft of the pin. This tapering down was designed to encourage the three streams of super-cooled melt from the 'spider' spokes to combine around the pin and form a tube. However during extrusion E014JHB (described in section 5.4.1) although a tube was successfully fabricated, it was observed that the glass had not formed closely around the shaft of the pin. Furthermore, the glass remaining in the die body after the tube extrusion showed that the glass melt had left the pin to form

the bore 2-3 mm before the pin was reduced to 1 mm diameter (ø), see section 5.4.1. Voids were visible in the final fibre at the core/ cladding interface. It was thought that creating a smaller bore in the outer cladding tube would produce a closer fit of the cane and therefore assist in a more uniform coalescence of the preform during fibre drawing. Therefore the dimensions of the pin were changed from 1 mm to 1.5 mm, as shown in Figure 5.5(a) (top image), for all subsequent tube extrusions. It was thought that with a larger ø pin there was a higher likelihood of super-cooled melt flow onto the shaft of the pin, simply due to there being less distance for the super-cooled melt to travel. Additionally the shoulder of the pin started higher in the die. From Figure 5.5(d) it can be seen that the parallel shaft of the original pin started where the die also became parallel. Therefore the sides of the graphite die initially squeezed the glass melt to form around the pin, but when the die became parallel (thus the funnelling effect was reduced) the glass melt had not quite reached the pin ø. The re-designed pin was positioned higher in the die so that the die edges were still angled when the pin became parallel, pressing the three streams of glass melt into the annular space around the pin forming a tube, see Figure 5.5(e). The pin was also elongated to 17 mm (original pin was 10 mm). The tapering angle remained at 60 °; however due to the elongation of the pin, the angle occurred over a longer length.

The result of the pin re-design was a longer lead-in of the three super-cooled melt channels onto the shaft of the pin, which was further enhanced by a slightly greater angle of the die's graphite lining. The elongated pin also helped to reduce the risk that the change in the die's shape could cause die swell. Although the alterations to die and pin design were found to produce tubes with ~ 1.5 mm ID, it was found that the final size of the bore and the combining of the three melt streams was affected by factors such as extrusion temperature and load. This is discussed further in section 5.7.

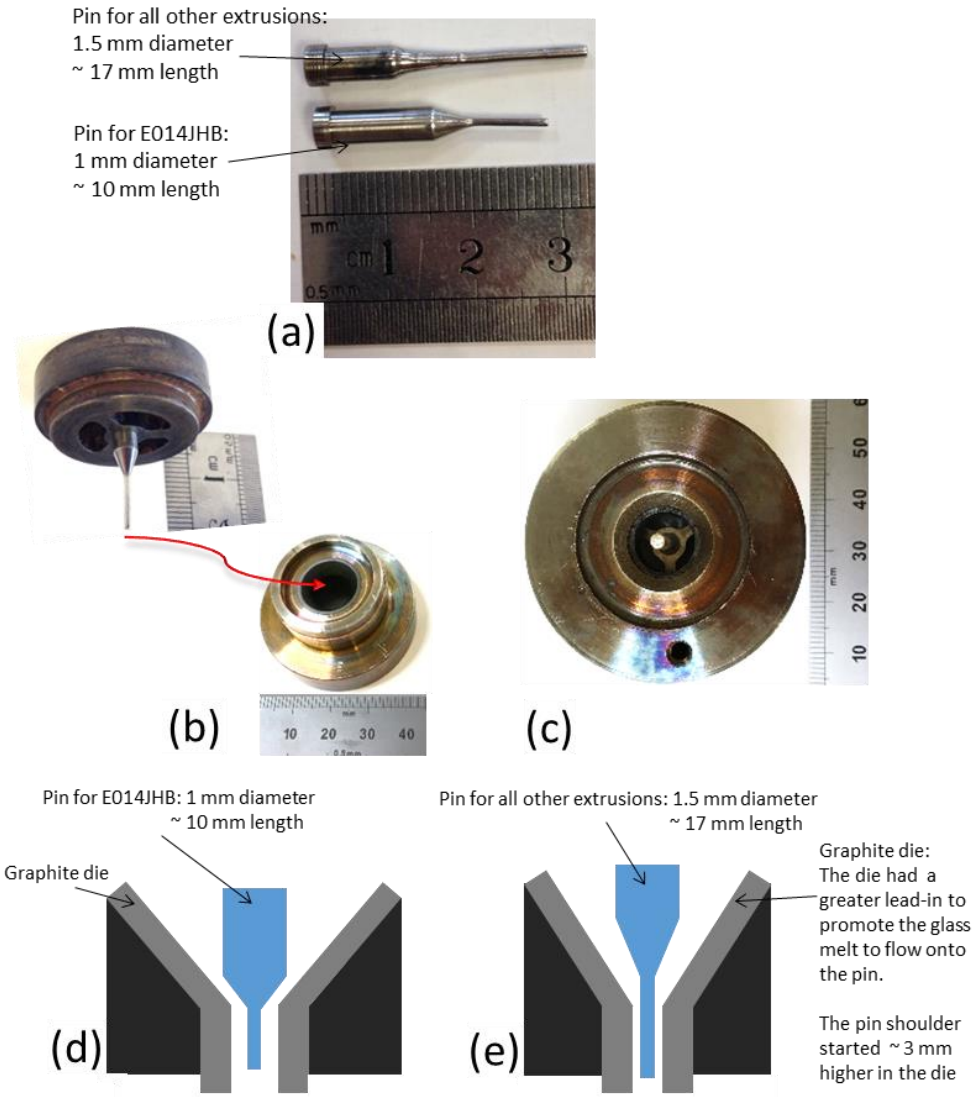



**Figure 5.5 Components used in tube extrusions. (a) Bottom: 1 mm pin head used for extrusion E014JHB. Top: 1.5 mm pin head used for all subsequent tube extrusions. The pin head (polished NIMONIC) was redesigned to reduce the ID of the outer cladding tube to assist in a more even flow of Ge-Sb-Se chalcogenide super-cooled melt around the pin. (b) The pin head was assembled with a 3 spoked 'spider' support body (left) which was inserted into the graphite lined die (bulk material 316 stainless steel) (right). (c) The constructed 3 spoked 'spider' pin with the 1 mm pin head inside the die, viewed from the bottom of the extruder looking up through the die. The 1 mm pin extended ~ 8 mm (1.5 mm pin extended ~ 15 mm) beyond the die to prevent the closure of the bore after passage through the die and pin, due to swelling. (d-e) Schematic diagrams of cross-sectional view through one of the spider spokes of pin inside die. (d) 1 mm pin and (e) 1.5 mm pin.**

## 5.3. Optical fibre dimensions

For a glass optical fibre, a centrally located core glass minimises optical loss because a too thin cladding glass would encourage leakage of the light from the fibre via the

evanescent field [143]. It has been suggested that the 'rod and tube' method (shown in Figure 3.12) produces chalcogenide fibres of acceptable quality in terms of uniformity of ø, cladding thickness and core centrality [43]. It was vital that the fibre preforms assembled for the 'rod-in-tube' method had optically smooth and chemically pure internal and external surfaces as the evanescent field would propagate in this region.

### 5.3.1. Fabricating small core fibres

The general cane and fibre drawing method which was applied to all the fibres fabricated in this Project was explained in section 3.5. Fibre and cane drawing from the extruded chalcogenide glasses were conducted on a customised Heathway drawing tower using a resistance frequency (RF) silicon carbide fibre drawing furnace of 6 mm hot-zone length (water cooled at 18 ± 0.1 °C), placed in a cleanroom (Class 10, 000). The preform was positioned with the lower end of the cladding tube 10 mm below the hot zone and the speed at which each fibre preform was lowered into the hot zone (the feed rate) for each fibre made in this Project is stated in the relevant section of this chapter. A carbon graphite receptor (made in-house) was located within this 6 mm hot-zone and the dimensions of the receptor varied with each fibre draw. It is worth noting that the inert atmosphere prevented $CO_2$ production from the receptor during heating. The height of the receptor and the RF power required to heat each preform is reported in this chapter within the relevant section.

As the fibre preform was heated gradually to the fibre drawing temperature of the glass melt, its thickness decreased as a gob (lump of molten glass) descended under the effects of gravity and drawing force from the formation of drawing the gob. This was termed as 'the neck down' of the preform. Once the preform had necked down, the gob was removed and the fibre was manually fed through the pulley system and onto the

fibre drum. The fibre drum speed (the feed-out rate) controlled the outer diameter (ø) of the cane and fibre. Control of the cane ø (at least twice the ø of the fibres) was more difficult to achieve due to the associated lower fibre drum speeds. For the later cane draw (F034JHB) a finger puller (Controls Interface Limited) had been installed for improved controllability of the cane ø (the intermediate and small core fibre ø for F035JHB were still controlled by the fibre drum speed).

### 5.3.2. Specification of Ge-Sb-Se fibre small core sizes

Small core ø of 15 µm, 10 µm and 7 µm were chosen based on modelling proposed by Bang[9] and demonstration of a 3 – 12 µm supercontinuum (SC) generation 10 µm ø core step-index $As_2$-$Se_3$ chalcogenide fibre pumped at 4.5 µm [2].

This Project focused on generating fibres with a core size of 10 µm, one core size higher (15 µm) and one lower (7 µm), with the prospect of the fibres being sent to DTU Fotonik to test the modelled theory practically. Table 4.12 stated the calculated NA of the three fabricated glass pairs, Pair I, Pair II and Pair III: 0.54, 0.72 and 0.65, respectively.

## 5.4. Investigation of Pair I (core composition JB04; $Ge_{22}Sb_8Se_{70}$ at. % and cladding composition JB03; $Ge_{24}Sb_4Se_{72}$) SCG fibre

The first small core/ cladding glass to be drawn to fibre in this Project was Pair I (core JB04; $Ge_{22}Sb_8Se_{70}$, and cladding JB03; $Ge_{24}Sb_4Se_{72}$). Initially three small core fibres were drawn from this glass pair, however voids were observed at the core/ cladding interface, as will be discussed in section 5.4.3. As a result the re-design of the pin and die (described in section 5.2) was applied in an attempt to produce a smaller bore in the

[9] Personal communication with Ole Bang, DTU Fotonik, Department of Photonics Engineering, Technical University of Denmark. This work was part of the integrated Project MINERVA (www.minerva-Project.eu) supported through the EC Seventh Framework Programme (FP7).

outer cladding tube. The carbon graphite receptor used to heat the assembled cane/ outer cladding tube preform was also changed to have a greater height to provide a large heating region of the preform, see section 5.4.5. No voids were seen in the resulting three small core fibres (section 5.4.6), however a circular core was not obtained.

### 5.4.1. Trial 1: E014JHB (tube extrusion of outer cladding composition JB03) and E015JHB (co-extrusion of core composition JB04 and cladding composition JB03)

For the tube extrusion E014JHB, the bottom part of the glass melt M054JHB ($Ge_{24}Sb_4Se_{72}$, ø = ~28 mm) was saw-cut and the height (13.55 mm) and mass (38.89 g) were measured, see Figure 5.6.

The tube extrusion was conducted using a 10 mm ID graphite lined die with a 1 mm ø, three spoked spider pin, as shown in Figure 5.5. The minimum load (100 kg) was applied when the temperature at the die reached 245 °C.

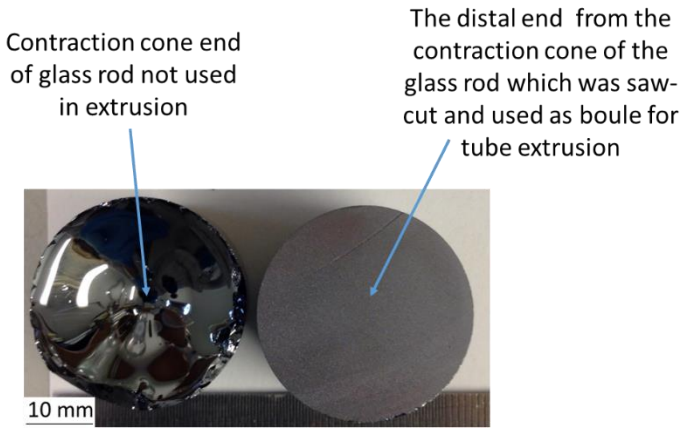



**Figure 5.6 JB03 glass boule (M054JHB, $Ge_{24}Sb_4Se_{72}$, ø = ~ 28 mm) used for Trial 1 of the outer cladding tube extrusion, E014JHB. Charge boule height varied (between ~ 13.06 – 18.86 mm) for the tube extrusions, however the image displaying the contraction cone and the saw-cut edge is a good representation of all the 28 mm ø glass boules used for this Project. The distal end from the contraction cone was used in the extrusions, with the saw-cut edge positioned against the die.**

The load was then increased to 500 kg once the temperature reached 300 °C. The extrusion was completed at 2 h 04 minutes, at a rate of 0.48 mm $min^{-1}$. During the

extrusion it could be seen that the bore was not in contact with the pin as it formed. The straight tube extrudate (E014JHB, Figure 5.7 (a)) had a length of ~ 99 mm, outer diameter (OD) of 9.47 mm and inner diameter (ID) of 2.82 mm. Three prominent folds of glass can be seen in Figure 5.7(a) at the end of the tube. This suggests that the temperature when the minimum load was applied was slightly too low as the glass melt streams did not join well. The temperatures chosen for extrusion were a compromise between having a high enough temperature to achieve low enough viscosity of the glass melt but not too high so as to cause die swell. The OD of the tube (9.47 mm) showed that the glass exhibited minimum die swell. It was suggested that this was partly due to the temperatures used and lack of closure around the pin. This 'free space' would allow the OD of the tube to reduce and there was no drag experienced due to contact of the super-cooled melt with the pin.

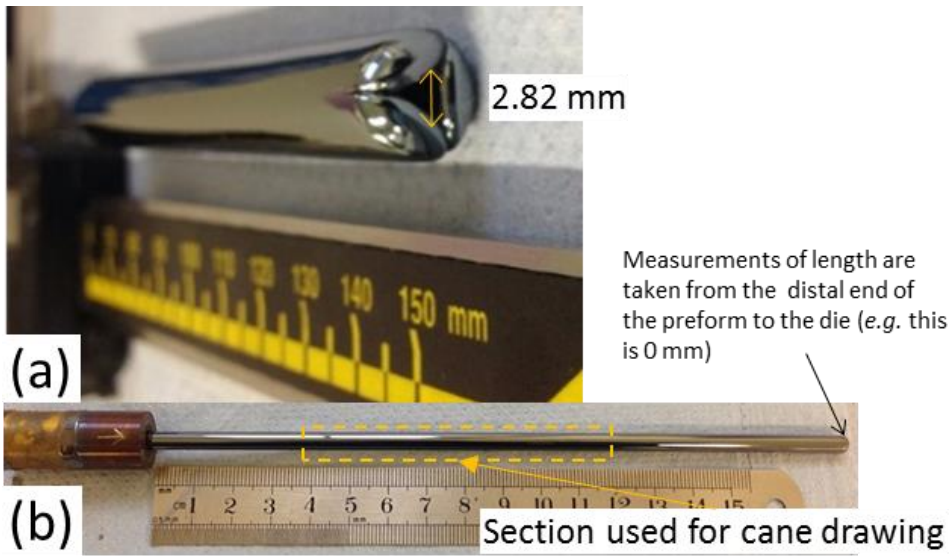



**Figure 5.7 (a) E014JHB tube extrusion. The extrudate was straight, ~ 99 mm long, 9.47 ± 0.02 mm OD and had a ~ 2.82 ± 0.01 mm ø bore. Thus the formed tube did not closely match the dimensions of the pin. Three lobes were visible at the start of the extrudate suggesting that the temperature when the minimum load was applied was slightly too low. Therefore the glass melt viscosity was too high for the glass streams to merge fully. (b) E015JHB co-extrusion. The extrudate was straight, had a diameter ~ 4.75 mm and was 202 mm long.**

To produce a core/ cladding rod glass preform, the core (8.406 g) and cladding (8.282 g) boules were 10.47 mm and 10.49 mm in height, respectively. The minimum load

was applied when the die temperature reached 240 °C. The load was increased to 200 kg at 311 °C. The extrusion was completed in ~ 2 h 13 min at a rate of 0.48 mm $min^{-1}$. The straight co-extrusion E015JHB (Figure 5.7 (b)) was ~ 202 mm long with an OD of ~ 4.75 mm.

### 5.4.2. Trial 1: F018JHB (cane and intermediate fibre produced from co-extrusion E014JHB), F019JHB (small core fibres produced from F018JHB cane and tube extrusion E014JHB)

From section 5.1, it can be determined that a fibre having 60 % core area in its cross-section was expected to have extruded through the cladding after ~ 70 mm. However, it is worth noting that this analysis was not conducted until after F019JHB was drawn to fibre and the section of the extrudate used (60 -140 mm) complements the analysis in section 5.1.

Cane drawing (F018JHB) and fibre drawing (F019JHB) were successful and the parameters of the draws are summarised in Table 5.2. The 500 µm ø cane drawn in F018JHB was uniform in cross-sectional ø and a 140 mm section was used for construction of the rod-in-tube fibre preform. Once the fibre drawing F019JHB stabilised, an initial vacuum of 10 kPa was applied to help the collapse down of the assembled preform. The vacuum was then increased to 15 kPa for the rest of the fibre draw.

Once the three fibre diameters were successfully drawn, the polymer (poly vinylidene fluoride-co-hexafluoropropylene; DSM Desotch) coating system was turned on, see Figure 3.11(c). However, the viscosity of the polymer was very high and the drag caused the fibre to break. After several attempts the fibre draw was terminated. Later it was found that the clean room temperature was 15 °C (usual room temperature 20-22 °C) which may have caused the high viscosity of the polymer.

**Table 5.2 Fibre drawing record summary for Trial 1 from Pair I (core JB04; $Ge_{22}Sb_8Se_{70}$ and cladding JB03; $Ge_{24}Sb_4Se_{72}$) of the 500 µm ø cane, 250 µm ø intermediate fibre and for small core fibres with predicted 300 µm ø, 200 µm ø and 140 µm ø. For both the cane and the fibre draws a carbon graphite receptor was used with 13.5 / 20.8 / 2.8 ID/OD mm height.**

| | Cane (structured) | Intermediate fibre (step-index) | Small core fibre F019JHB | | |
|---|---|---|---|---|---|
| | F018JHB | | | | |
| **Diameter / (µm)** | 500 | 250 | 300 | 200 | 140 |
| **Preform feed speed / (mm $min^{-1}$)** | 4 | 3 | 2 | 2 | 2 |
| **Drum speed / (m $min^{-1}$)** | 0.265 | 1.060 | 1.800 | 4.050 | 8.260 |
| **Pitch /(mm)** | n/a | 2 | 2 | 2 | 2 |
| **Total fibre length / (m)** | 1.5 | 30 | 10 | 30 | 20 |

### 5.4.3. Trial 1: Analysis of fibre F018JHB and F019JHB geometry via scanning electron microscopy (SEM)

Firstly, the intermediate fibre F018JHB of anticipated 250 µm ø was examined under a scanning electron microscope (SEM) to ensure that the higher Sb content of the core could be distinguished from the cladding, as shown in Figure 5.8. The SEM image, Figure 5.8(a), shows a typical cross-section of the intermediate fibre, 243 x 253 µm ø, with a clear contrast between the core and cladding. The central ~ 95 % by ø of the fibre was the core (~ 239 µm ø) and the outer ~ 5 % was the cladding (~13.7 µm radial width). Thus, the area of the cladding was slightly lower than expected, as the ratio of 90 % core area to 10 % cladding area was intended. Figure 5.8(b-h) displays compositional germanium (Ge), antinomy (Sb) and selenium (Se) mapping, using backscattered electrons and energy dispersive X-ray analysis (EDX) (see section 3.7 for method). The Sb content in the central core region was higher than that in the cladding, with the remaining chemical elemental concentrations (Se and Ge) at similar levels. This difference in Sb content is what produces the required difference in refractive index [83].

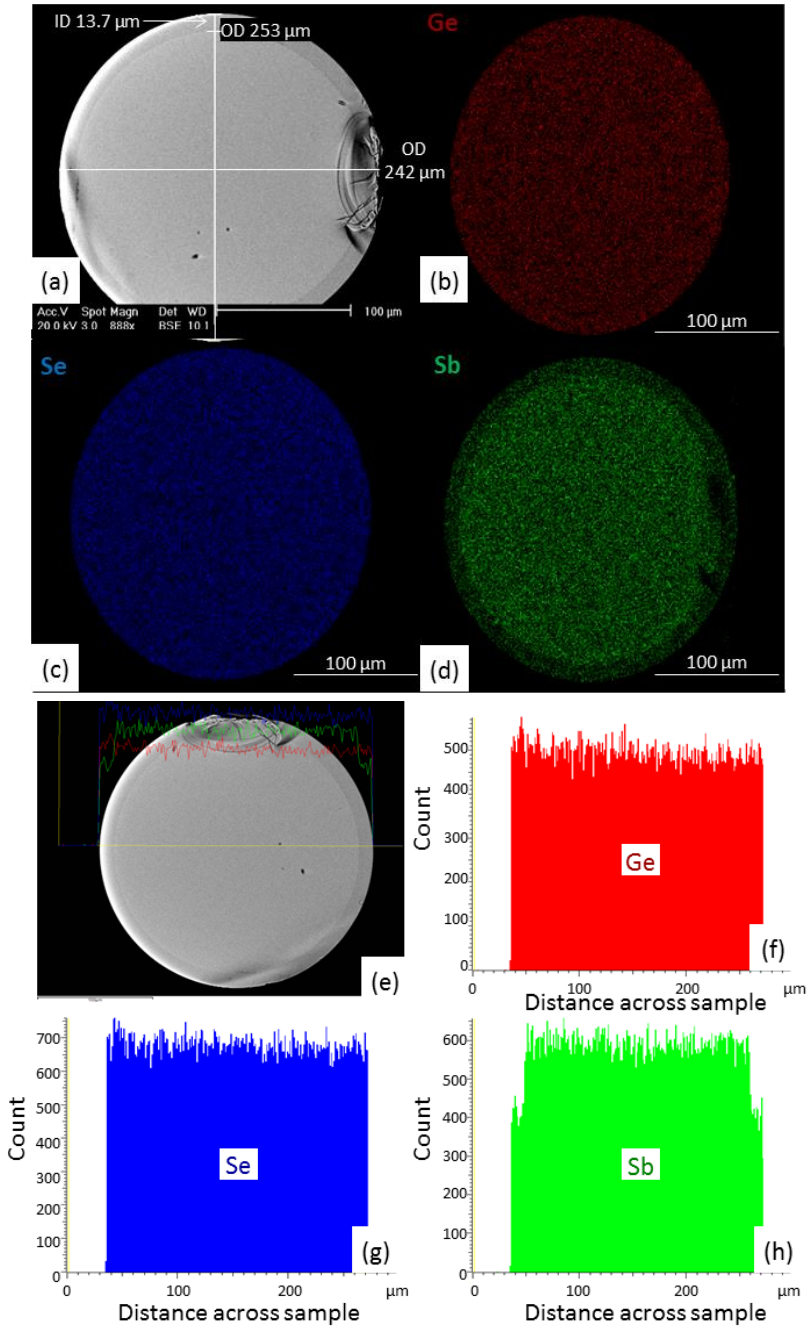



**Figure 5.8 Typical cross-section of Pair I (core JB04; $Ge_{22}Sb_8Se_{70}$ and cladding JB03; $Ge_{24}Sb_4Se_{72}$) for Trial 1 intermediate fibre (F018JHB), 242 x 253 µm OD. (a) Backscattered electron image showing contrast between the core (composition JB04; $Ge_{22}Sb_8Se_{70}$ at. %) and cladding (composition JB03; $Ge_{24}Sb_4Se_{72}$ at. %). (b)-(d) Energy dispersive X-ray analysis (EDX) elemental mapping for Ge (red), Sb (green) and Se (blue). A higher concentration of Sb was observed in the core than the surrounding cladding fibre. Due to similar concentrations of both Ge and Sb in the core and cladding, a contrast in the EDX map could not be distinguished. (e-h) EDX elemental line scan for Ge, Sb and Se across the horizontal yellow scan line in (e).**

Upon closer investigation of the small core fibres via SEM images (F019JHB; Figure 5.9) it was discovered that the geometry of the fibres was not as anticipated. EDX

analysis was conducted to confirm the identification of the core, Figure 5.9(c), (f) and (i). The intended 15 µm ø small core final fibre, had a smaller than expected OD of 208 µm, with an elongated, rather than circular as required, core.

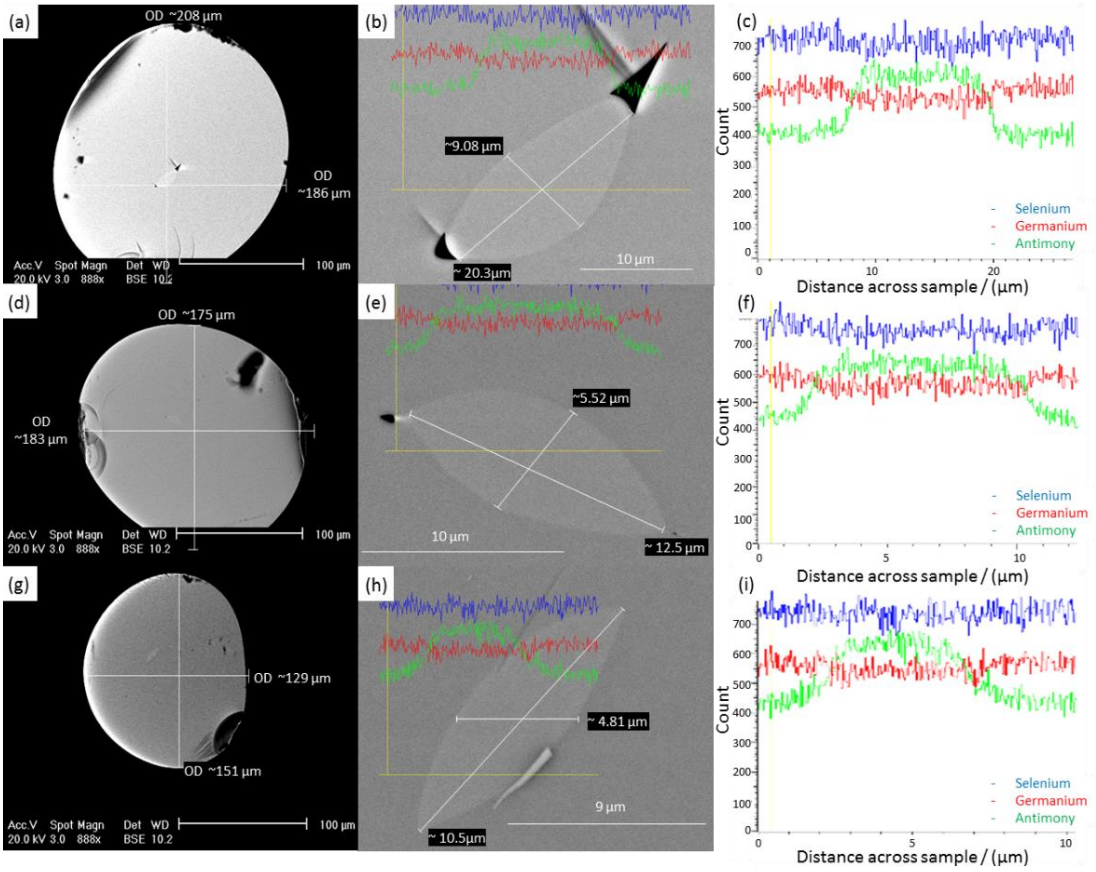



**Figure 5.9 Typical cross-sections of Pair I (core JB04; $Ge_{22}Sb_8Se_{70}$ and cladding JB03; $Ge_{24}Sb_4Se_{72}$) for Trial 1 small core fibres (F019JHB). (a-b) Backscattered electron images showing contrast between the core and cladding. Expected 15 µm diameter circular core: actual was an elongated core, 20.3 x 9.08 µm, with unwanted voids at the core interface. (c) Energy dispersive X-ray analysis (EDX) elemental line scan for Ge (red), Sb (green) and Se (blue) across the horizontal yellow scan line shown in (b). Sb was at a higher concentration in the core, than the surrounding cladding fibre. (d-e) Backscattered electron images showing contrast between the core and cladding. Expected 10 µm diameter circular core: actual was 12.7 x 5.52 µm with voids at the interface. (f) Energy dispersive X-ray analysis (EDX) elemental line scan for Ge, Sb and Se across the horizontal yellow scan line in (e). Sb was at a higher concentration in the core than in the surrounding cladding fibre. (g-h) Backscattered electron image showing contrast between the core and cladding. Expected 7 µm diameter circular core: actual was 10.5 x 4.81 µm but no voids were observed at the interface. A defect can be seen on the surface of the sample but it is thought to be an exterior inclusion based on EDX anlaysis. (i) Energy dispersive X-ray analysis (EDX) elemental line scan for Ge, Sb and Se across the horizontal yellow scan line in (h). Sb is at a higher concentration in the core than in the surrounding cladding fibre.**

Two small voids, ~5 x 3 µm in size, were visible from Figure 5.9(b) at the core/cladding interface. Similarly, the intended 10 µm ø small-core final fibre, also had voids visible, ~1 x 2 µm in size, at the core/ cladding interface, Figure 5.9(d-e). Voids were not detected in the anticipated 10 µm ø small core final fibre, Figure 5.9(g-h). A defect can be observed on this fibre surface, Figure 5.9(h), but this was assumed from the analysis to be from an external interference, such as dust.

The SEM images, Figure 5.9(a-b), (d-e) and (g-h), suggested that the ID of the preform outer cladding was too large for the assembled preform to collapse down uniformly during the fibre drawing procedure. The result of an uneven collapse caused a distortion of the core and was likely to have created the observed voids at the interface, seen in Figure 5.9(b) and (e). It was thought that a closer fit between the cane and tube bore would have allowed for a more symmetrical coalescence.

Glass remaining in the die body after the tube extrusion E014JHB showed that the glass melt left the pin to form the bore 2-3 mm before the pin was reduced to 1 mm ø. It was also noticed from visual observations made during the extrusion that the bore was not in contact with the pin as the extrusion progressed. This suggested that the pin shoulder should start ~ 3 mm earlier. Thus adaptions of the graphite-lined die and NIMONIC pin were made and applied to the outer cladding tube extrusion process, as described in section 5.2.

### 5.4.4. Trial 2: E017JHB and E019JHB (tube extrusion of outer cladding composition JB03, with redesign of pin and die) and E018JHB (co-extrusion of core composition JB04 and cladding composition JB03)

A second trial of producing small core fibres of Pair I was conducted with efforts made to produce a closer fit of the cane (from the co-extruded core and cladding) into the

outer cladding tube. The pin and die design changes described in section 5.2 were applied.

For the tube extrusion E017JHB the bottom part of the glass melt M060JHB (glass composition JB03; $Ge_{24}Sb_4Se_{72}$, 28 mm ø) was saw-cut and the height was 13.06 mm and mass = 35.81 g. Although the pin and die had been re-shaped, as the same glass composition (JB03) was used it was expected that the glass would behave similarly to the extrusion E014JHB.

From Figure 5.7 it can be seen that the glass melt did not fully merge at the start of the extrusion. Therefore the temperature at the die was next raised slightly to 267 °C (255 °C was used in Trial 1) before the minimum load was applied. The maximum load was also increased to 750 kg (500 kg was used in Trial 1) and was applied when the temperature at the die reached 303 °C, contributing to a steady extrusion rate of 0.15 mm $min^{-1}$. The extrusion was completed within 2 h 23 min.

During this extrusion it was observed that the extrudate made contact with the guide tube, however it was guided back to a straight tube and had a length of ~ 79 mm and 1.81/ 9.68 mm ID/ OD (Figure 5.10(a)). Unfortunately, due to confusion during fibre drawing, E017JHB was used with the wrong cane. Therefore the extrusion was repeated with the same glass composition (JB03; $Ge_{24}Sb_4Se_{72}$) but with the new melt M061JHB. The glass boule for E019JHB was saw-cut and had a height of 13.80 mm and mass = 41.85 g. As the extrusion conditions selected were exactly the same as E017JHB, the extrusion E019JHB also proceeded easily with an initial temperature of the die set at 267 °C and the minimum load applied. At 298 °C, a 750 kg load was applied and the extrusion proceeded at a rate of 0.18 mm $min^{-1}$. The extrusion

E019JHB was completed within 2 h 33 mins. The tube, Figure 10.5(b) and (c), was 99 mm long, 1.59/ 9.82 mm ID/OD.

For the co-extrusion E018JHB (core JB04 and cladding JB03) the extrusion parameters were kept the same as for E015JHB (see section 5.4.1). The core (8.396 g) and cladding (8.200 g) boules were 10.59 mm and 10.47 mm in height, respectively. The minimum load was applied when the die temperature reached 260 °C. At 314 °C the load was increased to 200 kg. The extrusion was completed in ~ 1 h 56 min at a rate of 0.5 mm $min^{-1}$.

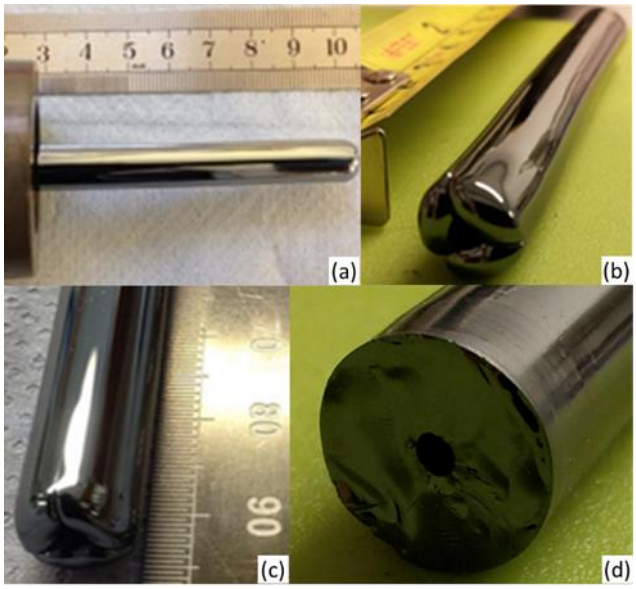



**Figure 5.10 Outer cladding tube extrusions of glass JB03 ($Ge_{24}Sb_4Se_{72}$): (a-b) E017JHB tube extrusion. The extrudate was straight, with little die swell, ~ 80 mm long and had an OD of 9.50 mm and a ~ 1.81 mm hole. It was observed that the extrudate made contact with the guide tube early in the extrusion but was guided back on track. An error in fibre drawing meant that this extrudate was not used; (c) E019JHB tube extrusion showing the distal end to the die ~ 1.59 mm ID, close to pin and (d) E019JHB tube extrusion showing proximal end to the die.**

The straight co-extrusion (E018JHB) shown in Figure 5.11 was 197 mm long with an OD of 4.74-4.76 mm.

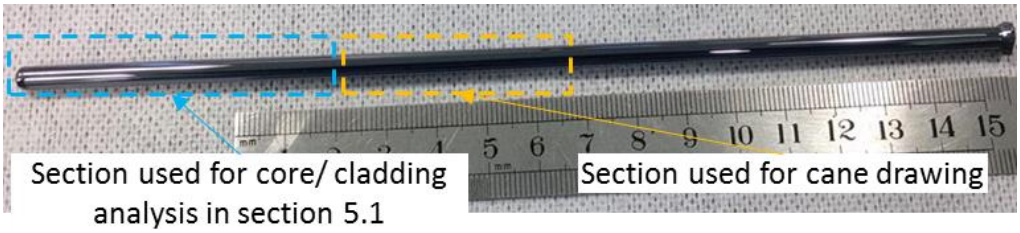



**Figure 5.11 Co-extrusion E018JHB. The preform was straight, and the total length of extrusion was 197 mm with an OD between 4.75 – 4.76 mm. The section between ~ 65 - 110 mm was used for the cane draw F021JHB. The first section (0 ~ 61 mm) of the preform was used for the core/ cladding ratio analysis discussed in section 5.1.**

### 5.4.5. Trial 2: F021JHB (cane and intermediate fibre produced from co-extrusion E019JHB) for F023JHB (small core fibres produced from F021JHB cane and tube extrusion E018JHB)

A taller carbon graphite receptor (5.6 mm height) was used than the receptor used in Trial 1 (2.8 mm height). The ID and OD remained at 13.5 and 20.8 mm respectively. It was anticipated that the greater receptor height would produce a more gradual neck down, thus achieving a slower collapse of the outer cladding tube. It was predicted that the gentler drawing would allow greater opportunity for atmospheric bubbles (the potential cause of the voids at the core/ cladding interface thought to be caused by trapped $N_2$ atmosphere from co-extrusion) to be expelled. The same receptor was used for production of both the cane and the fibre. The cane and fibre drawing details are summarised in Table 5.3.

**Table 5.3 Fibre drawing record summary for Trial 2 from Pair I (core JB04; $Ge_{22}Sb_8Se_{70}$ and cladding JB03; $Ge_{24}Sb_4Se_{72}$) of the 500 µm ø cane, 250 µm ø intermediate fibre and for small core fibres with predicted 330 µm ø, 220 µm ø and 154 µm ø. For both the cane and the fibre draws a carbon graphite receptor was used with 13.5 / 20.8 / 5.6 ID/OD mm height.**

| | Cane (structured) | Intermediate fibre (step-index) | Small core fibres F023JHB | | |
|---|---|---|---|---|---|
| | F021JHB | | | | |
| **Outside diameter / (µm)** | 500 | 250 | 330 | 220 | 154 |
| **Preform feed speed / (mm $min^{-1}$)** | 4 | 4 | 3 | 3 | 3 |
| **Drum speed / (m $min^{-1}$)** | 0.353 | 1.400 | 2.7 | 6 | 12.4 |
| **Pitch /(mm)** | n/a | 2 | 2 | 2 | 2 |
| **Total fibre length / (m)** | 2 | 23 | 6 | 9+13 | 17 |

As mentioned in section 5.4.4 the wrong cane was used with the tube extrusion E017JHB and therefore E019JHB was extruded. During this process the correct cane was stored in the glovebox for ~1 week. Once removed it was etched in propylamine for 10 minutes in the clean room (room temperature ~ 15 °C) to try to remove any oxide. During fibre drawing a vacuum of 20 kPa was achieved. As the temperature of the clean room was still 15 °C, no polymer coating was applied.

### 5.4.6. Trial 2: Analysis of fibre F023JHB geometry via SEM

In Figure 5.10 it was shown that the changes made to the die and pin successfully produced a smaller ID in the outer cladding tube preform E019JHB ~1.59 mm. Therefore there was a closer fit of the assembled preform when the F021JHB cane (~ 500 µm) was inserted. The SEM images in Figure 5.12 show promising results for all the small core drawn fibres, with no voids visible at the core/cladding interface. However, as seen from Figure 5.12, difficulties again arose with obtaining a circular core. It was suggested that this might have been due to a mismatch in temperature at the fibre drawing viscosity (~ $10^{4.5}$ kPa). The cladding glass had a lower $T_g$ (226 °C) than the core glass (238 °C). Therefore it might be expected that the cladding would have softened at a lower temperature than the core glass, depending on the heat diffusivity, during the heating up of the assembled fibre preform.

Thus the 500 µm cane should have kept its circular geometry as the cladding softened around it before they were drawn to fibre. However, from Figure 4.8 it was shown that the core glass would have reached fibre drawing viscosity 20 °C lower than the cladding glass. Therefore the core would have had a lower viscosity at the fibre-drawing temperature than the cladding. It is possible that the lower viscosity core adhered to one side of the outer cladding and the greater fluidity of the core allowed the outer cladding to compress around it, resulting in core distortion. The misshaped semi-circular core

from the SEM images (Figure 5.12) imply that the cladding had impacted on the core's geometry, compressing one side.

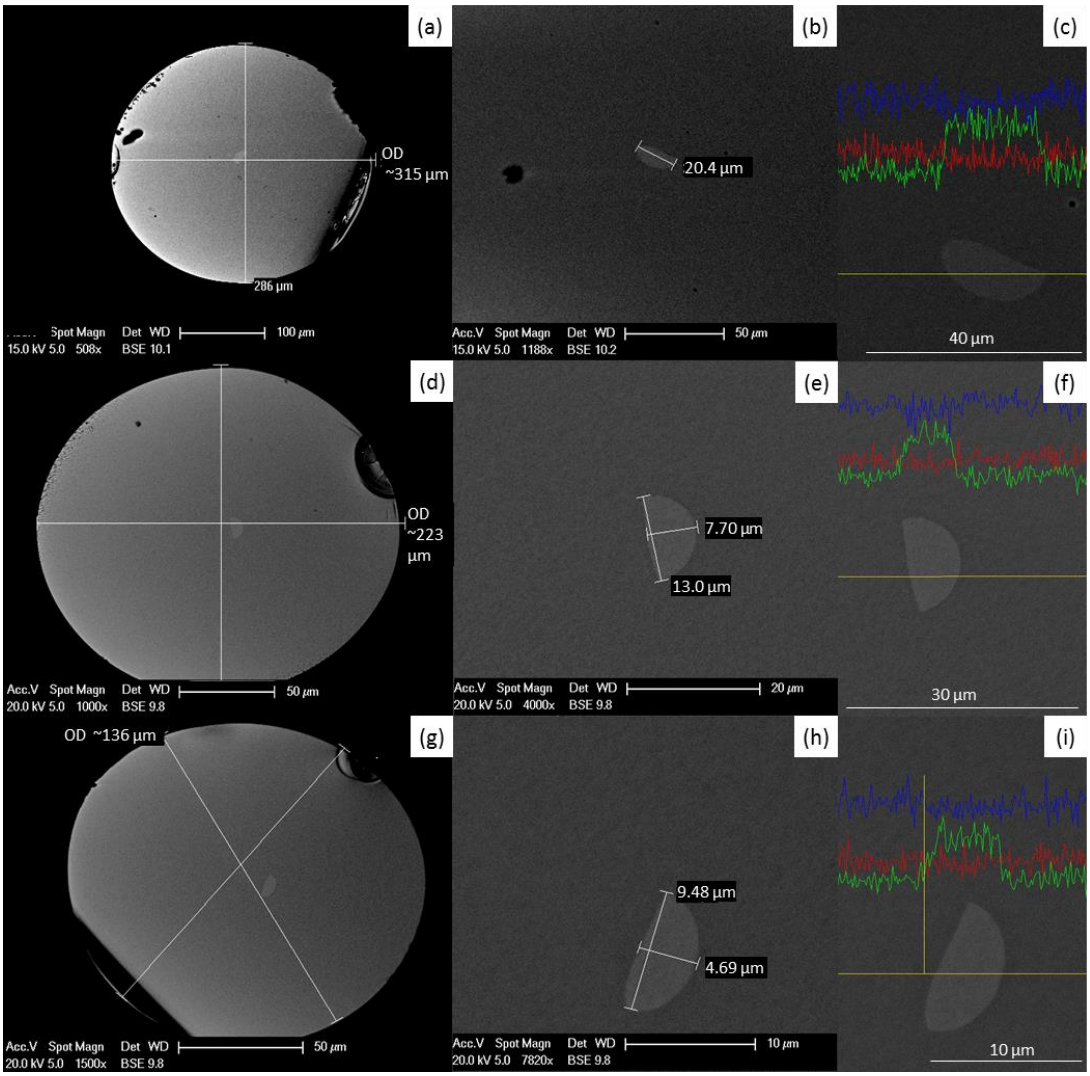



**Figure 5.12 Backscattered electron images of Pair I (core JB04; $Ge_{22}Sb_8Se_{70}$ and cladding JB03; $Ge_{24}Sb_4Se_{72}$) for Trial 2 small core fibres F023JHB. (a-b) Expected 15 µm diameter circular core in a 330 µm diameter fibre: actual was 20.4 x 10.1 µm, with no voids at the interface. A defect can be seen but it is believed to be an exterior inclusion; (c) EDX analysis to confirm presence of the core, Ge (red), Sb (green) and Se (blue); (d-e) Expected 10 µm diameter circular core in a 220 µm diameter fibre: actual was a semi-circular core, 7.70 x 13.0 µm, again with no voids at the interface; (f) EDX analysis to confirm presence of the core; (g-h) Expected 7 µm diameter circular core in a 154 µm diameter fibre: actual was 9.48 x 4.69 µm with no visible voids at the interface; (i) EDX analysis to confirm presence of the core.**

## 5.5. Investigation of Pair II (core composition JB01; $Ge_{19}Sb_{15}Se_{66}$ and cladding composition JB02; $Ge_{20}Sb_{10}Se_{70}$ ) SCG fibre

A new glass pair, Pair II (core glass JB01; $Ge_{19}Sb_{15}Se_{66}$ and cladding glass JB02; $Ge_{20}Sb_{10}Se_{70}$) was drawn to fibre based on their closely matched temperatures (T) at the fibre drawing viscosity region, $10^{4.5}$ Pa.s ($\Delta T$= 7 °C), see section 4.3. It was hoped that this close match would produce a more circular fibre core. Furthermore, from [83] it was reported that the glass compositions JB01 and JB02 had a refractive index of 2.67 and 2.58, respectively, measured at a wavelength of 1460 nm. Thus the NA can be calculated at 0.72 (Pair I calculated NA was 0.54).

### 5.5.1. E025JHB, E026JHB, E029JHB (tube extrusions of outer cladding composition JB02) and E030JHB (co-extrusion of core composition JB01 and cladding composition JB02)

As discussed in section 5.2, the more streamlined three spoked "spider" pin and die design was applied to all the subsequent outer tube extrusions after Pair I in Trial 1 (section 5.4.1). The first two tube extrusion attempts of the glass composition JB02 (E025JHB and E026JHB, from the glass melts M087JHB and M093JHB respectively) were unsuccessful due to die swell, see Figure 5.13(a-b). Die swell is caused by a difference in velocity across the glass melt cross-section during extrusion on emerging from the die. Usually an extruded glass will experience a small amount of die swell upon exiting the die orifice, as the velocity of the super-cooled melt extruding through the centre of the die is greater than at the edges. It is worth noting that the final tube extrudates had an OD < 10 mm due to contraction during cooling. For glass melt extrusion E025JHB (Figure 5.13(a)) the minimum load was applied at 227 °C and a maximum load of 750 kg was used. During the extrusion E025JHB the glass melt filled the exit part of the die before reaching the guide tube. Evidence of this can be seen by

the flattened rim at the top (Figure 5.13(a)) where a small amount of glass filled the guide tube. No bore was produced as the glass flooded the space between the end of pin head and the guide tube.

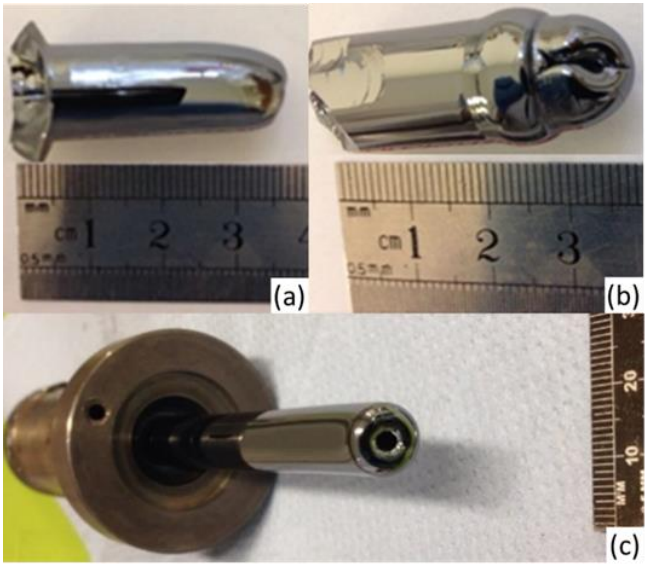



**Figure 5.13 Tube extrusions of outer cladding JB02 ($Ge_{20}Sb_{10}Se_{70}$): (a-b) Ge-Sb-Se glasses were subjected to die swell; (a) E025JHB. When the extrudate was removed from the die it was observed that the drag on the pin was so great the tube bore swelled shut; (b) E026JHB extrusions failed due to over-heating. (c) E029JHB was successfully extruded after ~5 h 35 mins with very careful control of the temperature of the die. The tube was straight, 79 mm long, with a 9.899 mm OD and a ~ 2 mm bore at the distil end, ~ 1.5 mm bore at the end closest to die.**

It was suggested that due to a too high temperature and load, the viscosity of the glass melt was too low so that the glass melt flowed through the die without any structure.

Therefore the temperature and load were reduced for the extrusion E026JHB. The minimum load was applied at 220 °C and the maximum load was reduced to 500 kg. It was suggested that during this extrusion the extrudate made contact with the guide tube. Inevitably due to the complicated geometry of the die and pin, when the super-cooled melt was pushed through the three spoked 'spider' more friction would have occurred on one side or the other. Therefore, the flow velocity of each of the three super-cooled melt streams would have varied, thus the super-cooled melt flow onto the shaft of the pin would not have been completely even. This would have promoted the super-cooled

melt to flow in a particular direction and unavoidably curve towards one side of the guide tube. However, rather than be guided back on track (as in the case of E017JHB, Figure 5.10(b)), the low viscosity of the glass melt in E026JHB due to too high a temperature, resulted in drag. This caused more back pressure leading to the extrudate becoming oversized (~ 14 mm) as the glass melt quickly filled the guide tube. In Figure 5.13(b) the bore can be seen on the side of the tube showing the bend of the glass melt as contact was made. The drag resulting from the contact of the viscous Ge-Sb-Se chalcogenide super-cooled melt is evident in the increased ø observed just after the bore. Visual checks were made throughout the extrusion process and once it had been realised that contact with the guide tube was made, the guide tube was quickly removed in the hope that the oversized extrudate could continue to form in just the shield tube. The extrusion temperature was also reduced. Unfortunately the damage from the guide-tube contact was irreversible and it was concluded that the temperature for the extrusion was still too high.

For the tube extrusion E029JHB the temperature at the die was tightly regulated in an attempt to use the lowest temperature possible for the extrusion. A lower temperature would have caused a higher viscosity of the Ge-Sb-Se chalcogenide super-cooled melt resulting in less friction and therefore reducing die swell. It is worth noting that a too low a temperature increases the risk of nucleation of the glass melt. Control of the temperature during the extrusion was difficult to achieve as there was a lag between the temperature value set at the furnace and the temperature reading at the die, the extrusion setup was described in section 3.4.

The glass boule charge for E029JHB was cut from M094JHB leading to a height of 15.75 mm (45.49 g). The minimum load was applied, after heating the charge for 2 h (~ heating rate of 1.6 °C $min^{-1}$), at a die temperature of 219 °C. The temperature at the

furnace was then successively increased by 5 °C at 30 minute intervals. The extrusion progressed slowly, with little entry of the glass melt into the die. When the die temperature reached 229 °C (after 2 h 52 min) the load was increased to 500 kg. This achieved an extrusion rate of 0.008 mm $min^{-1}$. The temperature at the die was further raised to 255 °C which increased the extrusion rate to 0.017 mm $min^{-1}$, until the end of the process. As the extrudate entered the guide tube a perimeter gap was observed between the glass and the walls of the tube indicating no contact was made. The tube extrusion was 79 mm long, straight, with a smooth and shiny surface (thus no or minimal surface oxidation), as shown in Figure 5.13(c). The OD of the tube was 9.90 mm. The bore was ~ 1.5 mm and the three streams of glass melt had combined well at the end of the tube. The extrusion took 6 h 30 min.

Due to the problems encountered with the tube extrusion, great care was taken with controlling the temperature for the core/ cladding co-extrusion E030JHB from Pair II, Figure 5.14.

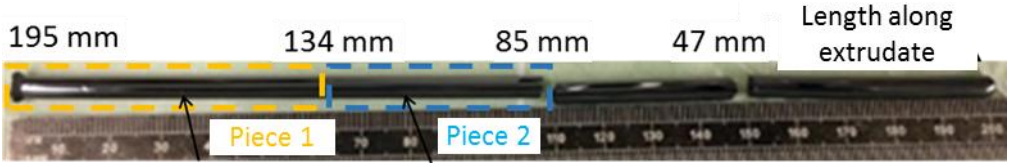



**Figure 5.14 Co-extrusion E030JHB of core and cladding Pair II (core JB01; $Ge_{19}Sb_{15}Se_{66}$ and cladding JB02; $Ge_{20}Sb_{10}Se_{70}$). The total length of the extrudate was 195 mm, however the extrudate fractured into three sections easily upon handling. The yellow and blue dashed lines indicate the lengths which were used for cane drawing. The diameter of the extrudate was 4.76-4.78 mm.**

The core glass JB01 ($Ge_{19}Sb_{15}Se_{66}$, 10.34 mm height, 8.5678 g, and 15.05-15.14 mm ø) was cut from the glass melt M081JHB and the cladding glass JB02 ($Ge_{20}Sb_{10}Se_{70}$, 10.293 mm height, 8.32019 g and 15.01-15.06 mm ø) was cut from the glass melt M084JHB. The minimum load was applied when the die temperature was 230 °C. The temperature was then increased by 5 °C every 30 min until the die temperature reached 291 °C and a 200 kg load was applied. The extrusion proceeded well at a rate of 0.16

mm $min^{-1}$and was completed in 5 h 35 min. The extrudate was 195 mm in length with a slight curve at the distal end of the glass to the die. Although the extrudate was retrieved from the extrusion whole, it broke easily into three places during subsequent handling as shown in Figure 5.14.

### 5.5.2. F029JHB (cane produced from co-extrusion E030JHB), F031JHB (cane produced directly from melt M098JHB) for F032JHB (small core fibres produced from F031JHB cane and E028JHB tube extrusion)

Although the co-extruded preform E030JHB had broken into pieces at 47 mm and 85 mm (distances measured from distal end of preform to the die), the sections were still large enough to draw to cane. The section measured from 195 mm to 134 mm was cleaved (Figure 5.14, piece 1) and used in the extrusion. A 13.5/ 20.8 mm ID/ OD carbon graphite receptor 2.8 mm of height was used. It was suggested that although the 5.6 mm high receptor contributed to the successful removal of the voids in F019JHB, the receptor produced much more heat than the 2.8 mm receptor and only required a RF power at the very bottom range of adjustment of the fibre drawing tower furnace. It was considered that having better control over the fibre drawing temperature of a new glass pair was of greater importance than the larger heating zone (proposed to help a more uniformed collapse the fibre preform). Due to the fragile nature of the preform it was decided that a step-index intermediate fibre of ~ 250 µm OD would not be drawn for fibre loss experimentation as establishing three small core fibres with a central, circular core was a higher priority.

For the cane drawing of the extrudate E030JHB, the fibre preform feed rate was set at 3 mm $min^{-1}$ and an initial RF power setting of 6 % was used. This was gradually increased at 2 % $min^{-1}$ to a 23 % power setting. Here the preform started to neck down by ~ 5-10 mm. However, within seconds the entire preform dropped from the preform

holder. It was noted that the difference in $T_g$ of the core (JB01; $T_g$ = 234 °C) and the cladding (JB02; $T_g$ = 211 °C) was 23 °C. As the cladding had a lower $T_g$ than the core, it was suggested that the cladding softened first resulting in the preform holder losing its grip, before the core had reached fibre drawing temperature.

Nevertheless, cane drawing was attempted again using piece 2 (see Figure 5.14). The preform was positioned higher in chamber so that only the end 2-3 mm were in the central zone of the resistance heater. RF heating was initiated at a power setting of 5 % and was increased at 1 % $min^{-1}$. The draw looked promising and neck down occurred at 25 % power. The power was increased to 31 % and the neck-down reached ~ 30-40 mm. However, again the preform suddenly failed and dropped from the holder.

Due to the failed cane drawing of the co-extrusion E030JHB, the core glass JB01 was batched and melted in an 8/12 mm ID/OD ampoule (M098JHB). As was discussed in section 5.1, it was suggested that drawing directly from a melt could impact a fibre's transmission properties due to the glass having had direct contact with a silica glass ampoule's wall. When a glass boule is extruded the outer surface layers of the boule tended to remain in the extruder, see Figure 5.1, thus the extrudate is fabricated from the untouched inner glass. Every effort was made to reduce the impurity content of the silica glass ampoule used for glass melting. The ampoules (Baumbach) were received as-annealed and HF-etched. They were then further treated to air baking (to remove any carbon deposits) and vacuum baking (to remove any physisorbed or chemisorbed water) as was detailed in section 3.1.2. However, it is thought that the silica ampoule still contributed to the Se-H and O-H impurity absorption bands observed in FTIR transmission spectrum of the as-prepared Ge-Sb-Se bulk glasses and fibres, on account of the transfer of H and O-H at temperatures > 650 °C [148], see section 4.1.3 for bulk glass transmission and section 6.3.3 for fibre transmission.

The melt-quench preform was 45 mm in length with 8.01-8.03 mm ø. It was etched in propylamine for 10 minutes to reduce surface contamination from the silica glass ampoule. The contraction cone end was clamped in the preform holder.

The cane (F031JHB) and fibre (F032JHB) details are summarised in Table 5.4. A 20 kPa vacuum was established in fibre drawing. A fibre with an intended 7 µm ø core was not achieved. When the fibre drum speed was increased to 12.8 m $min^{-1}$, the resulting thin fibre (expected 124 µm OD) was very fragile and continuously broke. Several attempts were made to guide the thin fibre through the pulley system and onto the fibre drum, however it was found that even if a length was wound on to the drum it would spontaneously break and spring off.

**Table 5.4 Fibre drawing record summary from Pair II (core JB01; $Ge_{19}Sb_{15}Se_{66}$ and cladding JB02; $Ge_{20}Sb_{10}Se_{70}$) of the 500 µm ø cane and for small core fibres with predicted 265 µm ø, 177 µm ø and 124 µm ø. A carbon graphite receptor was used with 13.5 / 20.8 / 2.8 mm ID/OD/ height for both the cane and fibre draws.**

| | Cane F031JHB (unstructured) | Small core fibres F032JHB | | |
|---|---|---|---|---|
| **Intended outer diameter / (µm)** | 500 | 265 | 177 | 124 |
| **Preform feed speed / (mm $min^{-1}$)** | 4 | 2 | 2 | 2 |
| **Drum speed / (m $min^{-1}$)** | 0.27 | 2.70 | 6.20 | 12.80 |
| **Pitch /(mm)** | n/a | 2 | 2 | n/a |
| **Total fibre length / (m)** | 1+1 | 8 | 15 | 0 |

During cane drawing, it was observed that the cane (F031JHB) was noticeably distorted in the first 1 m, thus another metre was also drawn. SEM images were taken of the first metre of cane, Figure 5.15(a-b). The most round 90 mm section of cane was selected, however the ø was slightly bigger than the 500 µm ø intended at ~ 560 ± 0.8 µm ø, Figure 5.15(c).

### 5.5.3. Analysis of fibre F031JHB and F032JHB geometry via SEM analysis

Figure 5.15(a-b) shows the ‘m’ shaped tapered cane F031JHB within the first 40 and 60 cm of drawing. It was suggested that the shape could have been formed by a trapped

gas bubble during the quenching process, which was elongated during cane drawing. The quenching process was described in section 3.2.4(ii). For the 8/12 mm ID/OD ampoule melt M098JHB, initially the glass melt was suspended in air for 30 s before being placed in a quenching furnace. The glass melt was then quenched, via a $N_2$ jet focused onto the outside of the ampoule, perpendicular to the melt and just above the contraction cone. This meant that the melt solidified at the top first, which prevented any trapped gases from escaping, which was not necessarily ideal.

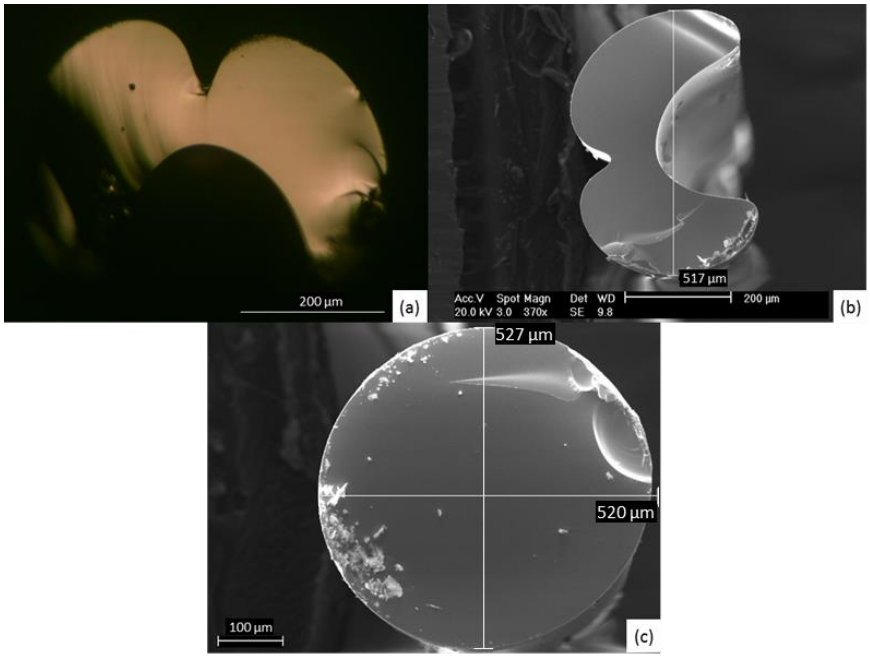



**Figure 5.15 Sample of cleaved sections from the unstructured cane drawing F031JHB (composition JB01; $Ge_{19}Sb_{15}Se_{66}$). It was observed that the initial metre of the cane was tapered and drawn flat. (a) Optical microscope image of sample 1 taken at ~ 40 cm. (b) SEM image of sample 2 taken at ~ 60 cm. (c) SEM image of the cane taken at 1.3 m (35 cm before the 90 mm section of cane used for fibre drawing where the diameter was found to be most stable at 560 ± 0.8 µm).**

During extrusion the glass was re-heated to a super-cooled liquid which allowed any residual stresses from quenching or annealing to relax and any trapped gasses to be released. However, as the cane was drawn directly from the melt, this could not occur. It is suggested that a better method of quenching would be to release the ampoule from the bottom of the quenching furnace and apply the $N_2$ jet to the base of the ampoule.

This would mean that the lower section would solidify first permitting any gases to be guided up through the glass melt and released from the top.

Figure 5.15(c) displays the cane at ~ 1.3 m with ~ 520- 528 µm ø showing that the cane had become more circular. The piece used for the fibre drawing preform was drawn ~ 35 cm later, with an increased ø of ~ 560 µm. It was selected as the 90 mm piece of unstructured cane was found to have the most stable ø over the length.

Figure 5.16 shows the SEM images of the small core fibre F032JHB. In Figure 5.16(a) a large crack is visible across the fibre. It was found that the fibre was very difficult to cleave without breaking and Figure 5.17(a) was the only image achieved without such a break. As was discussed in section 4.3 it was thought that the stability of the fibre was greatly affected by the large temperature difference ($\Delta T$ ~ 25 °C) between where the onset of the rapid increase in linear thermal expansion occurred for each glass, Figure 4.11. Once a fibre was drawn it was quenched in the atmosphere from above its $T_g$ to room temperature within seconds on account of the fibre's small ø and comparatively large surface area. This did not allow time for any internal stresses to relax (unlike when a glass was annealed, see section 3.2.4). The core glass (JB01) went through its rapid change in thermal expansion coefficient before the cladding glass (JB02). As the cladding glass was still above its $T_g$ generated stresses could be relaxed. However, as the core glass had a higher $T_g$ (234 °C) than the cladding glass (211 °C), when the cladding glass went through its region of large change in thermal expansion coefficient the core glass had become more solid as it reached $T_g$ first. This meant that the core glass was in a relatively low region of thermal expansion coefficient when the cladding glass was contracting through its large region of thermal expansion: thus internal stresses were generated.

The fibre ø ~ 268 x 262 µm (Figure 5.16 (a)), and ~ 180 x 189 µm (Figure 5.17 (a)) were very close to their anticipated ø 265 µm and 177 µm respectively.

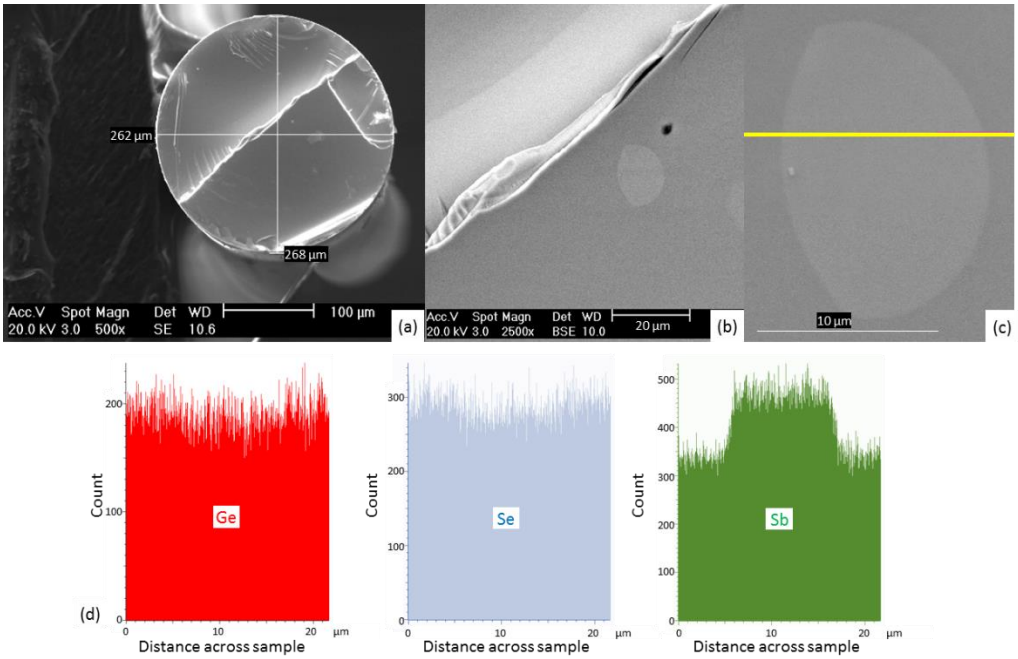



**Figure 5.16 SEM images of F032JHB (Pair II: core JB01; $Ge_{19}Sb_{15}Se_{66}$ and cladding JB02; $Ge_{20}Sb_{10}Se_{70}$) of expected 15 µm diameter core in a 265 µm diameter fibre, showing contrast between the core and cladding: (a) Secondary electron image with a measured diameter of ~ 268 x 262 µm. The core was measured at 16.4 x 12.1 µm (not shown); (b) Backscattered electron image of the core measured at ~ 16.4 x 12.1 µm. It can be seen that the core was located close to the fracture in the fibre, however it did not impact the core; (c) EDX analysis was taken across the yellow line to confirm the presence of the core and (d) EDX results showed a higher level of Sb in the core.**

Subsequently their core sizes, ~16.4 x 12.1 µm (Figure 5.16 (b-c)), and ~ 11.9 x 9.9 µm (Figure 5.17 (b-c)) were also a close match to the desired core sizes of 15 and 10 µm respectively. It is suggested that this was due to the close match in temperature ($\Delta T$ = 7 °C) at the fibre drawing viscosity region ($10^{4.5}$ Pa.s), see Figure 4.8. In Figure 5.16(b) it can be seen that the fracture in the fibre did not pass through the core.

In Figure 5.17, a small void, ~ 500 x 500 nm, was observed at the core/ cladding interface along with either contamination particles or defects. Therefore an EDX map of the area was taken to see if these defects could be detected (Figure 5.17(c-d)), however, they did not appear in the map. The decrease in Sb levels towards the edge of

the sample is suggested to have been caused by the angling of the fibre towards the edge, indicated in (a) created during cleaving. The Sb Lα line (3.60 keV) is more easily absorbed than the Kα lines for Ge (9.88 keV) and Se (11.21 keV) thus, will be more effected by topography.

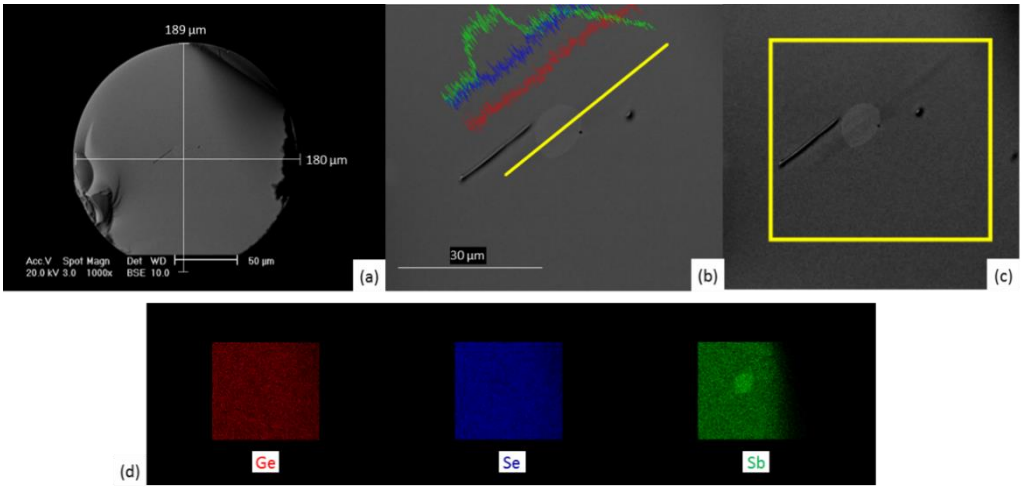



**Figure 5.17 SEM images of F032JHB (Pair II: core JB01; $Ge_{19}Sb_{15}Se_{66}$ and cladding JB02; $Ge_{20}Sb_{10}Se_{70}$) of expected 177 µm diameter fibre with a 10 µm diameter core, showing contrast between the core and cladding: (a) Secondary electron image showing the measured 180 x 189 µm OD. The core was measured to be 9.47 x 7.11 µm; (b) Backscattered electron image of the core measuring ~ 11.1 x 9.9 µm. An EDX line scan was taken across the yellow line, with the results displayed on the image above the core. It can be seen that the core has a higher Sb content than the cladding. However rather than staying stable the Sb content appears to decrease further into the cladding; (c) An EDX map was taken of the area highlighted by the yellow box to see if the defects visible in (b) were compositional changes, surface contamination or scratches and to assess the apparent reduction of Sb and (d) the EDX maps of Ge (red), Se (blue) and Sb (green). There were no apparent compositional changes and it was assumed that the line visible in (b) and (c) was a scratch. It is proposed that the black circle at the core/ cladding interface was a void, similar to the ones which were shown in Figure 5.9. The decrease in Sb was recorded again and it was suggested that this could be caused by the angling of the fibre towards the edge, indicated in (a), created during cleaving. The Sb Lα line (3.60 keV) is more easily absorbed than the Kα lines for Ge (9.88 keV) and Se (11.21 keV) thus, will be more effected by topography.**

## 5.6. Investigation of Pair III (core composition JB02; $Ge_{20}Sb_{10}Se_{70}$ and cladding composition JB03; $Ge_{24}Sb_{4}Se_{72}$ ) SCG fibre.

A third glass pair, Pair III, was selected to be drawn to fibre, consisting of JB02 ($Ge_{20}Sb_{10}Se_{70}$) as the core and JB03 ($Ge_{24}Sb_{4}Se_{72}$) as the cladding. On account of the

fragile and brittle nature of the fibre (F032JHB) the thermal expansion coefficient results, section 4.2.3.2, were evaluated and Pair III was selected as there was no difference in thermal expansion coefficient over the region 40-180 °C (the region often quoted in the literature [47, 83]). It is considered beneficial to have a slightly higher TEC in the core than the cladding, however this value has not been quantified before too much internal stress is generated. It is worth noting that since drawing the fibre it has been suggested that where the sharp increase in the instantaneous expansion coefficient occurred had great impact on the resulting fibre, see Figure 4.11. The temperature region of this rapid increase in the instantaneous expansion coefficient was not matched for Pair III ($\Delta T \sim 20$ °C). As will be discussed in section 5.7, the fabricated fibre experienced similar fragility problems during storage as Pair II (the onset of the instantaneous thermal expansion coefficient $\Delta T \sim 25$ °C). From [83] the refractive indices of JB02 and JB03 at 1460 nm were 2.58 and 2.50 respectively, corresponding to a NA of 0.65. Furthermore, due to the difficulties in the tube extrusion of the glass composition JB02 (E025JHB and E026JHB) the previous successful experience with tube extrusions of the glass composition JB03 (E014JHB, E017JHB and E019JHB), as was reported in section 5.4, was considered valuable.

### 5.6.1. E039JHB (tube extrusion of outer cladding composition JB03), E040JHB (co-extrusion of core composition JB02 and cladding composition JB03) and E042JHB (single unstructured extrusion of core composition JB02)

For the tube extrusion E039JHB the bottom part of the glass melt M105JHB (glass composition JB03; $Ge_{24}Sb_4Se_{72}$, 28.77 – 28.66 mm ø) was saw-cut to a height of 18.86 mm (53.65 g).

This was the fourth time this glass had been tube extruded (third time with the new pin and die set-up), thus valuable experience had been gained with the temperature range

and times required for a successful extrusion. The minimum load was applied when the die temperature reached 274 °C. The extrusion progressed well and the load was increased to 500 kg when the temperature reached 285 °C in the die. The temperature stabilised around ~ 300 °C and was maintained, producing a steady rate of extrusion of 0.098 mm $min^{-1}$. The extrusion was completed in 4 h 01 min. This was the longest of all the tube extrusions for the glass composition JB03 on account of using a lower load and temperature. Furthermore, the initial boule height was larger than the previous extrusions, thus there was also more material to extrude. The lower load and temperature were used to try and further reduce die swell in an attempt to achieve an exact 1.5 mm ø bore. However, it would appear that these parameters were slightly too low as the three lobes did not merge as well as for the tube extrudate (E019JHB), producing a slightly larger bore of ~1.68 mm ø (E019JHB bore was 1.59 mm ø), suggesting a slightly higher extrusion temperature would be desirable. The straight extrudate shown in Figure 5.18(a-b) was ~ 118 mm long and had a 9.48 mm OD.

For the co-extrusion of Pair III (E040JHB), the core (JB02 from glass melt M101JHB; 8.5217 g) and cladding (JB03 from glass melt M104JHB; 82548 g) boules were 10.47 mm and 10.58 mm in height, respectively. The minimum load was applied when the die reached 315 °C. During the extrusion, it was noticed that although the co-extrusion had initially gone well the glass then became swollen, filling the guide tube. A maximum temperature of 329 °C was reached with only the minimum load applied, when the probe position had reached its end. This indicated that all the material from the glass charge boules had been pushed through the die. As can be seen from Figure 5.18(c), the first ~ 21 mm of the co-extrusion appeared to proceed well before a bend in the extrudate was observed and the OD increased.

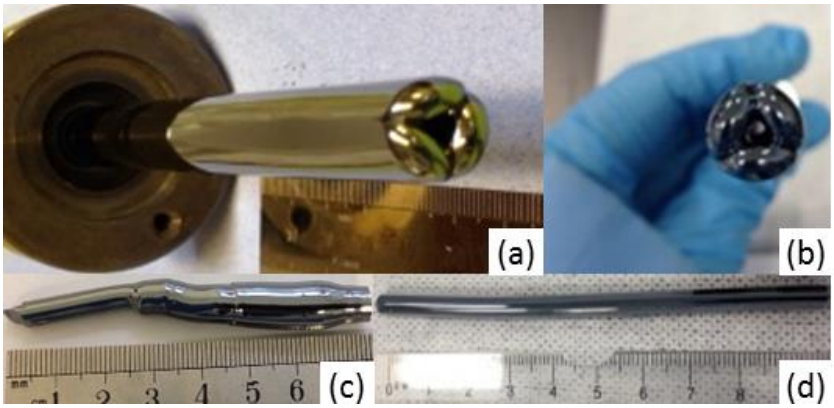



**Figure 5.18 Images of extrudates. (a-b) Tube extrusion E039JHB, of glass composition JB03 ($Ge_{24}Sb_4Se_{72}$). The tube was straight, ~ 118 mm long, with an OD of 9.48 mm and an ID of ~1.6 mm. (c) Co-extrusion E040JHB, of glass composition JB02 and JB03. The first ~21 mm of the glasses appeared to extrude well, however the extrudate then became swollen and the extrusion failed. (d) Single extrusion E042JHB, of glass composition JB02, which was slightly curved along the longitudinal axis. However, the outer surface was bright and shiny thus showing no obvious signs of turbulent flow (*e.g.* lesions or scratches in the surface as a result of the curve).The extrudate was ~ 103 mm long with an OD of 4.24-4.26 mm.**

Similarly to the failed tube extrusion E026JHB (reported in section 5.5.1) contact with the guide tube had caused a backlog of material filling the tube. However, in E040JHB it was thought that the bend in the extrudate was caused by the core super-cooled melt coming through the cladding at a higher velocity than the cladding super-cooled melt was being extruded. From Figure 4.8 it can be seen that there was a large difference in temperatures ($\Delta T$ = 28 °C) at the extrusion viscosity region ($10^8$ Pa.s) between the glass composition JB02 (core) and JB03 (cladding). Therefore, it is suggested that the core had a lower viscosity than the cladding as it was extruded through the cladding, causing a difference in velocity across the glass melt. This would have resulted in the curvature of the extrudate and once contact was made with the guide tube wall causing drag, the glass melt backed-up inside the tube.

A single unstructured extrusion E042JHB was conducted with the core glass JB02 ($Ge_{20}Sb_{10}Se_{70}$) from the same glass rod produced from melt M101JHB. The contraction cone was removed leaving a glass boule ~ 14.34 mm high. The minimum

load was applied when the temperature at the die reached 277 °C and was increased to 200 kg when the temperature reached 280 °C. The extrusion was completed in ~ 2 h 59 min at a rate of 0.08 mm $min^{-1}$. The single unstructured extrudate (E042JHB) had a slight curve to the end as can be seen in Figure 5.18(d). It was 103 mm long with an OD of 4.24-4.26 mm.

### 5.6.2. F034JHB (produced cane and intermediate fibre from single extrusion E042JHB) and F035JHB (small core fibres from F034JHB cane and tube extrusion E039JHB)

The previous fibre draw (F023JHB) with the glass composition JB03 ($Ge_{24}Sb_4Se_{72}$) for the outer cladding tube used a large receptor (13.2/ 20.7/ 5.6 mm ID/ OD/ H) to encourage a uniformed coalesce of the fibre preform. Therefore cane and fibre drawing was initially conducted using a 13.2/ 20.7/ 6.8 mm ID/ OD/ H receptor (sizes varied slightly as receptors were made in-house). Since the cane drawing of F031JHB a finger puller (Contacts Interface Limited) had been installed on the fibre tower for greater control over cane ø. Once the cane had been drawn the fibre was manually guided through the pulley system onto the fibre drum and the intermediate fibre was drawn as usual. As the extrudate from E042JHB was from a single melt, the section of preform used was not dependent on the core/ cladding ratio. Therefore the bottom 10 mm was removed to prevent any initial extrusion irregularities and the rest of the extrudate was used for cane drawing.

The cane (F034JHB) and fibre drawing (F035JHB) details can be found in Table 5.5. On account of the failed co-extrusion E040JHB the outer cladding tube was stored in a glovebox for eight days. Therefore, it was etched in propylamine for 30 minutes before fibre preform assembly. Due to the accuracy of the finger puller the cane was 500 ± 1 µm ø along the entire drawn length and a section of 130 mm was suspended in the outer

cladding tube E039JHB. The fibre drawing commenced with a RF power setting of 6 % and the temperature was raised at 2 % $min^{-1}$ to 9 % where the fibre preform started to neck down. However, red fumes engulfed the tube furnace and the heating power was shut down. It appeared that the fibre preform had touched the side of the receptor becoming immediately vaporised. It was suggested that a small unnoticed crack at the top of the preform shifted the preform slightly during the initial heating stage, causing the contact with the receptor. The remaining fibre preform with the condensed Ge-Sb-Se chalcogenide vapour is shown in Figure 5.19.

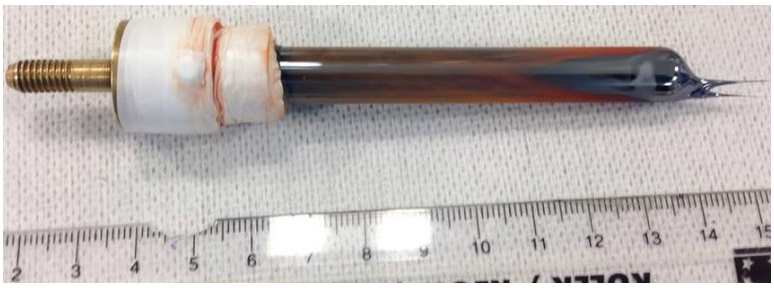


**Figure 5.19 The fibre preform from Pair III (core JB02; $Ge_{20}Sb_{10}Se_{70}$ and cladding JB03; $Ge_{24}Sb_4Se_{72}$) during fibre draw F035JHB after contact with the carbon graphite receptor. Condensed Ge-Sb-Se chalcogenide fumes (red) can been seen on the preform.**

The preform was cleaned by wiping down with acetone (> 99.5%, Sigma Aldrich) and isopropanol (> 99.5%, Sigma Aldrich). It was then etched in propylamine for 5 minutes and the preform holder was repositioned. The receptor was replaced with a 13.2/ 20.7/ 2.9 mm ID/ OD/ H receptor. Fibre drawing was attempted again starting at a RF heating power setting of 6 % and the temperature was raised at 2 % $\mathbf{min^{-1}}$ to a power setting of 17 %. The fibre preform feed rate was set at 2 mm $\mathbf{min^{-1}}$. It was observed that the glass was very brittle and several attempts were made to guide it through the pulley system and to wind it onto the fibre drum. At a 20 % power setting the fibre was drawing stably and a 10 kPa vacuum was initiated. The drum speed was set at 5 m $\mathbf{min^{-1}}$ and the power was increased to a setting of 29 %, drawing 8 m of fibre. The drum speed was then changed to 2.22 m $\mathbf{min^{-1}}$ and the power setting was increased to 32 %. 6 m

of fibre was collected. The drum speed was then further reduced to 10.20 m $\mathbf{min^{-1}}$. However the fibre broke somewhere in the pulley system. There was still preform remaining so the fibre drawing commenced again. At a power setting of 29 % the fibre was drawing stably (*e.g.* the fibre tension was good with no observable fluctuation in diameter), 10 kPa vacuum was applied and the drum speed was set at 10.20 m $\mathbf{min^{-1}}$ drawing a further 5 m of 10 µm core fibre. The polymer coating system, see section 3.5.2, was turned on and a further ~1.5 m of fibre was drawn. However, the fibre failed again as the coating created too much drag. Once again fibre drawing was re-started and neck down was achieved at a power setting of 20 %. It was noticed that there were bumps on the fibre surface, although the fibre tension was stable. The drum speed was set at 2.22 m $\mathbf{min^{-1}}$ and the power setting was increased to 32 - 35 %. A further 3 m of fibre was drawn until there was no remaining preform.

**Table 5.5 Fibre drawing record summary from Pair III (core JB02; $Ge_{20}Sb_{10}Se_{70}$ and cladding JB03; $Ge_{24}Sb_4Se_{72}$ ) of the 500 µm ø cane, 250 µm ø intermediate fibre and for small core fibres with predicted 297 µm ø, 198 µm ø and 139 µm ø. Initially a 13.2/ 20.7 mm ID/ OD, 6.08 mm height (H) carbon graphite receptor was used, however after contact of the fibre preform the receptor had to be changed to a 13.2/ 20.7/ 2.9 mm ID/ OD/H. The preform and drum speeds were kept the same.**

| | Cane (unstructured) | Intermediate fibre (unstructured) | Small core fibres F035JHB | | |
|---|---|---|---|---|---|
| | F034JHB | | | | |
| **Intended outer diameter / (µm)** | 500 | 250 | 297 | 198 | 139 |
| **Intended core diameter / (µm)** | n/a | n/a | 15 | 10 | 7 |
| **Preform feed speed / (mm $\mathbf{min^{-1}}$)** | 4 | 3 | 2 | 2 | 2 |
| **Drum speed/ (m $\mathbf{min^{-1}}$)** | Feed out speed 61.3 mm $min^{-1}$ | 0.87 | 2.22 | 5.00 | 10.20 |
| **Pitch /(mm)** | n/a | 2 | 2 | 2 | n/a |
| **Total fibre length / (m)** | 1.5 | 12 | 6+3 | 8+5+1.5 | n/a |

As the fibre preform was being used the metal mounting holding the top of the preform was lowered closer to the tubular furnace. As the metal became closer to the hot zone it was noticed that more RF power was required to heat the preform as heat was

conducted through the metal clamp. The increase in power to compensate for the heat loss through the clamping system caused difficulties in temperature control towards the end of fibre drawing.

### 5.6.3. Analysis of fibre F034JHB and F035JHB geometry via SEM analysis

Firstly, the intermediate fibre of anticipated 250 µm ø (F034JHB) was examined to measure the actual ø of the fibre as it was to be used for fibre loss measurements (shown in Figure 6.3). The slightly oval shaped fibre was ~ 248 x 238 µm ø.

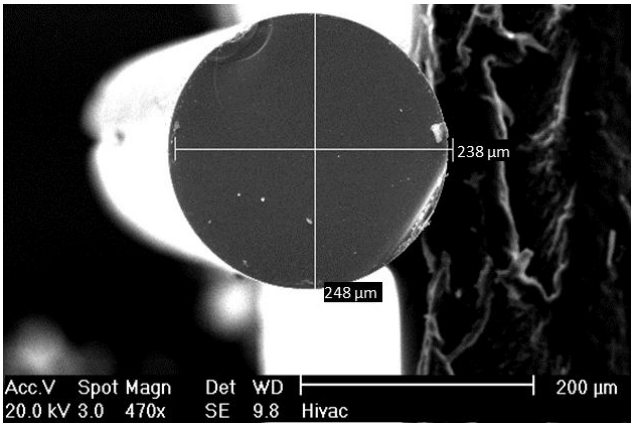



**Figure 5.20 Secondary electron image of the typical cross-section of the intermediate fibre F034JHB, drawn from the single unstructured extrusion E042JHB of core composition JB02 ($Ge_{20}Sb_{10}Se_{70}$). OD measured 248 x 238 µm. The fibre loss measurements for this fibre are shown in Figure 6.3.**

Once the vacuum was applied and the RF heating power setting had reached 20 % a few metres of fibre of unknown ø were collected whilst the fibre tension was allowed to stabilise (before the fibre drum speed was set at 5 m $min^{-1}$). A section of this fibre was analysed to see how the fibre preform initially collapsed-down. As was discussed in section 5.4.6, rather than the core maintaining its central position as the cladding collapsed evenly around it, the core adhered to one side of the cladding tube. It was suggested that this was on account of the core glass reaching the fibre drawing viscosity ($10^{4.5}$ Pa.s) at a lower temperature than the cladding glass (which was the case for both Pair I and Pair III). Evidence of the adherence of the core to the side of the cladding

tube can be seen in Figure 5.21, during the first few metres of fibre drawing.

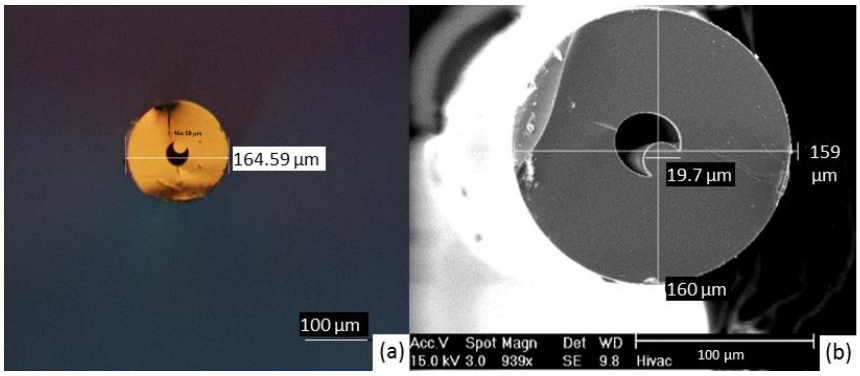



**Figure 5.21 Section of the fibre (F035JHB) from Pair III (core JB02; $Ge_{20}Sb_{10}Se_{70}$ and cladding JB03; $Ge_{24}Sb_4Se_{72}$ ) during the first few metres of drawing. It can be seen that the core adhered to one side of the cladding tube. This compressed one side of the core causing the core geometry in the subsequent fibres to not be circular. However, it is worth noting that this fibre still achieved the most near-circular and near-axis cores of all the fibres drawn in this Project. (a) Optical light microscope image showing a measured fibre diameter of ~ 164.59 µm. (b) Secondary electron image with a measured diameter of ~ 159 x 160 µm. The core diameter was ~ 19.7 µm.**

Unlike in Pair I, where the $T_g$ of the core glass (238 °C) was higher than the cladding (226 °C), the Pair III core $T_g$ (211 °C) was lower than that of the cladding (226 °C). Thus the core would also soften before the cladding. It is suggested that this, along with the lower viscosity of the core, benefitted the core's geometry as its higher fluidity meant it could adapt to the changes in the cladding tube's shape without being compressed, thus producing a more circular shape than the semi-circle produced in F023JHB. From Figure 5.21, it appears that in the fibre F035JHB, after the core adhered to one side of the cladding tube, the core kept its circular shape during the collapse-down into fibre, apart from a slight deformation at the adjoining interface.

Figure 5.22 shows a typical backscattered electron images of F035JHB of the entire diameter of the fibre and of the fibre core. From the figure it can be seen that the intended 15 µm ø small core fibre, had a smaller than anticipated OD of 279 µm: the predicted OD was 297 µm.

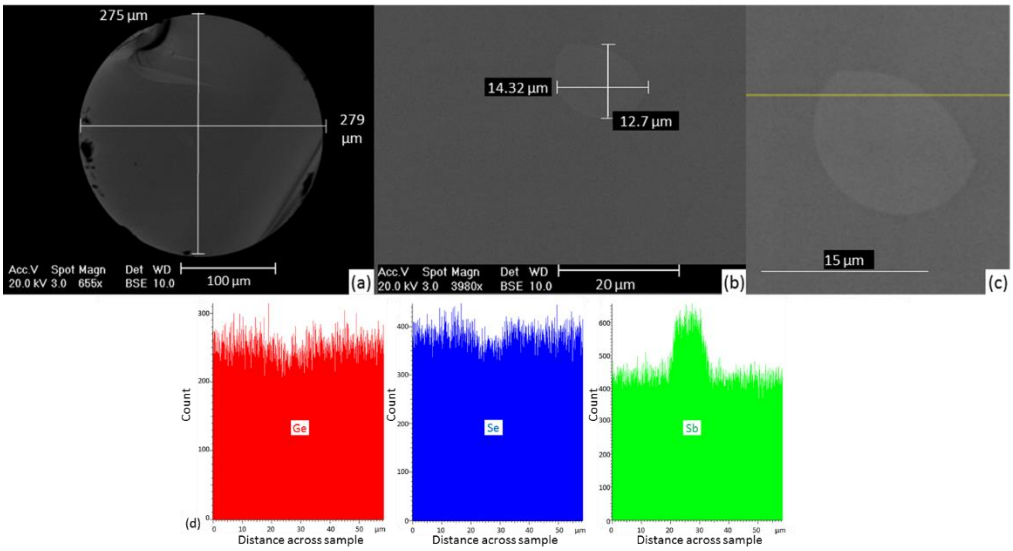



**Figure 5.22 Typical backscattered electron images of F035JHB from Pair III (core JB02; $Ge_{20}Sb_{10}Se_{70}$ and cladding JB03; $Ge_{24}Sb_4Se_{72}$). (a-b) Expected 15 µm diameter circular core in a 297 µm diameter fibre: actual was a "partially circular" 12.7 x 14.32 µm ø core in a 275 x 279 µm OD fibre. (c) EDX analysis was conducted across the yellow line to confirm presence of the core. (d) EDX analysis showed a higher Sb content in the core and a slightly reduced content in Se.**

The fibre was concentric with a "partially circular" 12.7 µm ø core. Figure 5.23 shows the small-core step index fibre with intended 10 µm ø core and anticipated 198 µm OD.

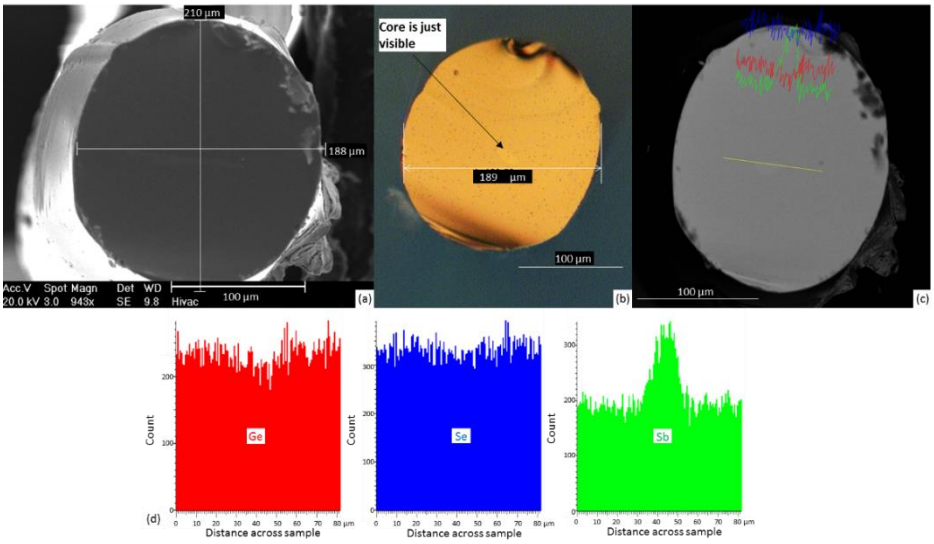



**Figure 5.23 (a) Secondary electron image of F035JHB from Pair III (core JB02; $Ge_{20}Sb_{10}Se_{70}$ and cladding JB03; $Ge_{24}Sb_4Se_{72}$) of the expected 10 µm diameter circular core in a 198 µm outer diameter fibre. The outer fibre diameter varied between 210 and 188 µm. The core was difficult to detect in (a) and could just be seen using optical microscopy in reflection (b) and backscattered electron image (c). EDX analysis was conducted across the yellow line in (c) to confirm presence of the core. (d) EDX analysis showed a higher Sb content in the core.**

In Figure 5.23(a) it is shown that the fibre was not quite concentric and the OD varied between 188- 210 µm. The core was found difficult to detect using SEM imaging Figure 5.23(a) and could just been seen using optical microscopy in reflection Figure 5.23(b). Its presence was confirmed by EDX analysis as shown in Figure 5.23(c-d).

## 5.7. Investigation of Ge-Sb-Se fibre amorphicity using X-ray diffraction (XRD)

No crystallisation was observed in the SEM images of any fibre fabricated in this Project. However, it was important to verify this using X-ray diffraction measurements. XRD was performed on each small core fibre after fibre drawing. The sample preparation and XRD methodology was described in section 3.6.1. In Figure 5.24 the XRD pattern of each Ge-Sb-Se small core fibre is displayed.

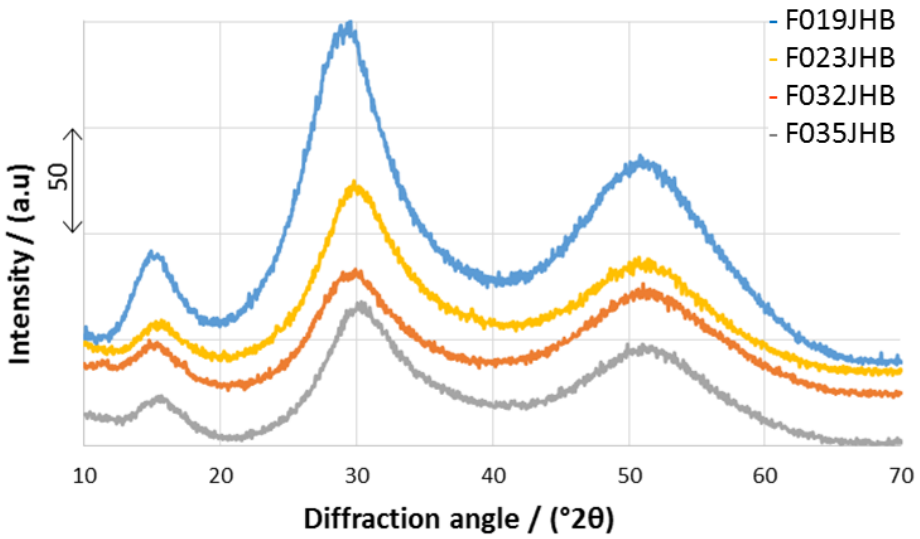



**Figure 5.24 Powder X-ray diffraction XRD patterns of all fibres made in this Project. In descending order; the upper curve (blue) is F019JHB (Pair I, analysed in section 5.4.2); the second curve (orange) is F023JHB (Pair I, analysed in section 5.4.6); the third curve (red) is F032JHB (Pair II, analysed in section 5.4) and the lower curve (grey) is F035JHB (Pair III, analysed in section 5.6). The curves have been vertically shifted for clarity. Similarly to the bulk glass XRD results (Figure 4.3), three broad humps can be observed for all the Ge-Sb-Se fibres centred at 15 °, 29.5 ° and 51 ° 2θ, respectively. This confirms the amorphicity of the fibres suggested from SEM analysis.**

Tang [45] reported that for a 1000 ppmw $Dy^{3+}$ ($DyCl_3$) − doped $Ge_{16.5}As_9Ga_{10}Se_{64.5}$ bulk glass sample no crystallisation peaks were observed in the XRD pattern. However,

after the same glass composition was fabricated into fibre crystallisation peaks were found after XRD analysis. It was suggested that the crystals grew during the reheating of the glass for fibre drawing. The results in Figure 5.24 for the Ge-Sb-Se glasses studied in this Project confirm the fibres were amorphous and this provided evidence of the glasses stability after being exposed to an extensive thermal history.

## 5.8. Conclusions

A priority of this Project was to fabricate small core fibres with core sizes of 15 µm, 10 µm and 7 µm ø. Although the 10 µm core size was suggested on account of the collaborative work with Bang at DTU Fotonik within the MINERVA Project[10] (see section 5.3), it is worth noting that the extrusions and fibre drawing carried out during this Project were exploratory with the new Ge-Sb-Se glass system and no pre-modelling of the light guiding properties of the resulting preforms had been carried out. Since the fibres have been fabricated in this work, research proposed by Agger *et al.* suggested that a core size of 10 µm would require a higher NA of 0.7 than first hypothesised, due to the step-index fibre having too long a zero-dispersion wavelength [209]. It is now proposed that a core size of 20 µm is optimal. Unfortunately, none of the fibres produced in this Project was sent to DTU Fotonik due to the likelihood of the fragile fibres not surviving transportation, especially as a polymer coating was not applied.

A concise summary of all the Ge-Sb-Se chalcogenide glass tube extrusions is given in Appendix III (Table A). There was a delicate balance in selecting the extrusion temperature and load between a high temperature and high load (promoting good super-cooled melt flow and reducing the risk of crystallisation) and a low temperature and

[10] MINERVA Project (www.minerva-Project.eu) supported through the EC Seventh Framework Programme (FP7).

low load (reducing the amount of die swell). The key to a successful extrusion is a compromise between the two, which is individual for each glass composition. A quantitative comparison of the co-extrusion parameters for all the co-extrusions conducted in this Project is provided in Appendix III (Table B).

Below are the main conclusions drawn from Chapter 5:

- It was predicted that during extrusion of the Ge-Sb-Se chalcogenide glasses, the core would enter the cladding after ~ 70 mm to achieve a 60 % core ratio of the total area of the extrudate (section 5.1) and this is the recommended section to be used for cane drawing.
- The re-design of the pin head and die for the outer cladding tube extrusions (section 5.2) reduced the bore size of the outer cladding tube for Pair I (section 5.4). It was suggested that this helped a more uniform collapse down of the fibre preform resulting in no voids at the core/ cladding interface of the subsequent drawn fibre.
- For Pair I, the reduction in bore size of the outer cladding tube, combined with using a large receptor in fibre drawing, resulted in no visible voids at the core/ cladding interface. However, a circular core was still not achieved. It was found that using a larger receptor made the control of RF heating power difficult. Thus it was decided that a greater control of the temperature was more important for new glass compositions for future fibre draws.
- The average extrusion temperature was 295 °C for the glass composition JB03 complementing the viscosity/ temperature results obtained in Figure 4.8. The glass composition JB02 was extruded at a slightly lower temperature (255 °C) than that predicted from Figure 4.8 (265 °C). It is important to note that the steady state extrusion temperature varies with load.

- Three lobes were observed at the end of the tube in E014JHB (Figure 5.7), E017JHB (Figure 5.10(b)), E019JHB (Figure 5.10(c)) and E039JHB (Figure 5.18). It was suggested that the temperature was too low to completely combine the three glass melt streams forming around the pin at the start of extrusion. The low temperature was used to reduce the risk of die swell. The glass composition JB02 produced the only tube (E029JHB, Figure 5.13) where the glass streams merged entirely. However, incomplete fusion at the end of the tube extrudates was not deemed to have had an impact on the final small core fibres themselves, since the end of the tube was not used in the final fibre as it was removed in a gob.
- Die swell was observed in E025JHB (section 5.5.1) due to the use of too high temperature and load. The problems encountered with this tube extrusion provided evidence of the importance of understanding the different thermal properties of the different glass compositions. Although previously using a 750 kg load had produced successful tubes (in section 5.4.4, for the glass composition JB03), it was a contributing factor to the die swell observed for the glass JB02. From the viscosity/ temperature measurements that were shown in Table 4.8, the temperature at the extrusion viscosity $\sim 10^8$ Pa.s should be ~ 265 °C. However, the steady state extrusion temperature for the successful tube extrusion (E029JHB) of the glass JB02 was 255 °C, suggesting that the extrusion region was higher than $10^8$ Pa.s. After tight regulation of temperature, E029JHB produced the best tube extrudate with minimal die swell and the three streams of glass combining well at the end of the tube.
- Die swell was observed in E026JHB (section 5.5.1) due to the Ge-Sb-Se chalcogenide glass tube making contact with the PTFE guide tube which impeded the super-cooled melt flow and resulted in a backing-up of material (die swell). As

a result of the work conducted in this Project, the PTFE guide tube has been replaced with a graphite lined one. PTFE was initially chosen due to its apparent low coefficient of friction with chalcogenide glasses, however it is not as low as that of graphite. Furthermore, measurements of the guide tube walls showed a decrease in the PTFE thickness suggesting it was degrading at the extrusion temperatures (PTFE melting point = 327 °C [210]). However as the surface of the extrudates were smooth and shiny it was not thought that this had contaminated the extrusions in this Project.

- It is suggested that a lower linear thermal expansion coefficient ($\alpha_L$) at onset $T_g$ should mean that despite the change in environment upon exit of the die, swell is negligible. For example, minimal die swell was encountered for tube extrusions for the glass composition JB03 ($\alpha_L$ at onset $T_g$ (226 °C) = 58 x $10^{-6}$. $°C^{-1}$) compared to JB02 ($\alpha_L$ at onset $T_g$ (211 °C) = 72 x $10^{-6}$. $°C^{-1}$).
- Co-extrusion was successful with Pair I (E015JHB and E018JHB) and Pair II (E030JHB). However, similar to the small core fibre produced from Pair II (F032JHB), the extrudate E030JHB was fragile and broke easily. From Figure 4.11(b) it can be seen that the point where there is a large increase of the instantaneous thermal expansion coefficient for the glass composition JB02 (the cladding glass, $T_g$= 211 °C) occurred ~ 25 °C earlier than it did for the glass composition JB01 (the core glass, $T_g$= 234 °C). Therefore as both glasses cooled together the core glass went through its region of large contraction first. This was above the cladding glass's $T_g$, thus both glasses were still soft and the stresses could be relaxed. However, once the core glass went through its large region of contraction it became more solid than the cladding glass as it reached $T_g$ first. Therefore when the cladding glass cooled through its $T_g$, it became solid enough

to support a load but was still in a region of high expansion coefficient. Thus, as the core glass was in a region of relatively low thermal expansion coefficient stresses were generated within the glass extrudate as the cladding glass continued to contract.

- The co-extrusion E040JHB failed as the glass composition JB02 and JB03 had a temperature difference of 47 °C at the extrusion viscosity region ($10^8$ Pa.s), see Table 4.9. As shown in Figure 5.18(c) the extrusion started well. However, it was suggested that as the core started to come through the cladding, due to its lower viscosity at the extrusion temperature, a difference in velocity of the super-cooled melt flow between the core and cladding was generated across the extrudate resulting in die swell.
- The extrudate from the co-extrusion E030JHB could not be drawn to cane due to the difference in $T_g$ (23 °C) between the core and cladding, see Table 4.12. The cladding glass JB02 ($T_g$= 211 °C) had a lower $T_g$ than the core glass JB01 ($T_g$= 234 °C). Therefore the fibre drawing temperature required for the core could not be reached as the cladding glass softened at a lower temperature than the core and could not be clamped, see section 5.5.2.
- Drawing directly from the melt resulted in a tapered cane, Figure 5.15. It was suggested that this could be the result of the quenching process, described in section 3.2.4(ii). As the glass melt was quenched from the top of the ampoule, the glass melt would have solidified at the top first preventing any trapped gases from escaping. A new approach to quenching is suggested in section 5.5.3, by lowering the silica glass ampoule from the bottom of the quenching furnace so that the ampoule can be quenched from the bottom first.

- As the fibre preform was used during fibre drawing it was lowered into the hot zone of the furnace. This meant that the metal mounting holding the top of the preform was also getting lowered. As the metal became closer to the hot zone it was noticed that more RF power was required to heat the preform as heat was conducted through the metal clamp. The increase in power to compensate for the heat loss through the clamping system caused difficulties in temperature control towards the end of fibre drawing.
- It was suggested that if the viscosity of the core and cladding glasses were not matched at the fibre drawing region (viscosity of $10^{4.5}$ Pa.s) this could result in a mis-shaped core, such as the semi-circular core observed in F023JHB. It was thought that the geometry of the more fluid core could be influenced by the higher viscosity cladding, compressing on the core's structure.
- The importance of the temperature difference between where the sharp rise in the instantaneous expansion coefficient occurs between the core glass and the cladding glass has been significantly better understood, on account of the fibres drawn in this Project. Chalcogenide glasses have lower fracture stress than silica glass [211, 212]. However, the fibres produced in this Project were quite brittle. The fibre F032JHB (from Pair II) spontaneously broke from the fibre drum and only one image was achieved where there was not a crack across the cleaved surface (Figure 5.17). Although initially more stable, the fibre F035JHB (produced from Pair III) experienced similar independent fractures from the fibre drum after a few days of storage. The only mechanically stable fibres were F019JHB and F023JHB (from Pair I) which continued to remain tightly wound to the fibre drum. Therefore it is suggested that the only glass pair that is stable enough to produce 20 µm core MIR SCG fibres is Pair I.

Suggestions for future work are;

- Graphite was chosen to line the die due to its low coefficient of friction with chalcogenide glass and because it does not chemically react with the glass. It would be beneficial to have a similar lining / coating on the extrude pin head to reduce drag. However, the die was lined with graphite by heating the die body with graphite, so that when the components were cooled the graphite was put under compression. It would not be possible to apply the same graphite hot fitting method to the pin head as the graphite could not be put under compression. Therefore this Author suggests future work should investigate sputtered coatings that have a low coefficient of friction with chalcogenide glasses, are chemically inert to the glasses, and which could withstand the extrusion temperatures, such as titanium nitride or boron nitride.
- Greater understanding of the Ge-Sb-Se glass behaviour has been gained as a result of the work in this Project. From section 5.1 it was suggested that for a co-extrusion of equal height (10 mm) boules a 60 % ratio of core to cladding area after an extrusion length of 70 mm is achieved. However, from Figure 4.8 it is shown that the temperature at which the Ge-Sb-Se glasses reach the extrusion viscosity ($10^8$ Pa.s) varies with composition. This was further evident in the co-extrusion E040JHB (Pair III core JB02; $Ge_{20}Sb_{10}Se_{70}$ and cladding JB03;$Ge_{24}Sb_4Se_{72}$) as the core had a lower viscosity than the cladding causing die swell. It is suggested that a difference in viscosity for each glass pair would cause the core to enter the cladding at a different point. Therefore it would be beneficial to conduct core/cladding analysis for each glass pair extrudate to assess where a target cross-sectional area ratio of 60 % core: cladding is achieved.

- Investigation of polymer coatings to enhance the mechanical strength of fibres. Unfortunately equipment malfunctions impacted the application of a polymer coating in this Project. However, it is suggested that a polymer coating would have dramatically improved the mechanical strength of the fibres. It would be important to assess whether the fragile fibres from Pair II and Pair III would break internally within a polymer coating.

### 5.9. Summary

A brief explanation of the glass velocity in extrusions was provided and the impact it had on where the core glass entered the cladding glass during a co-extrusion was discussed (section 5.1). The design changes to the tube extrusion die and pin components were described and as a direct result of this PhD Project the developments made to the extrusion process (section 5.2) have benefitted the research conducted in the MIR Photonics Group. The method of achieving different fibre dimensions during fibre drawing was explained and the specification of the small core fibres were given (section 5.3). The extrusion and fibre drawing processes of three Ge-Sb-Se glass compositions were described: Pair I (core composition JB04; $Ge_{22}Sb_8Se_{70}$ and cladding composition JB03; $Ge_{24}Sb_4Se_{72}$) (section 5.4); Pair II (core composition JB01; $Ge_{19}Sb_{15}Se_{66}$ and cladding composition JB02; $Ge_{20}Sb_{10}Se_{70}$) (section 1.1) and Pair III (core composition JB02; $Ge_{20}Sb_{10}Se_{70}$ and cladding composition JB03; $Ge_{24}Sb_4Se_{72}$) (section 5.6). Greater understanding of the importance of the Ge-Sb-Se glass properties was established and concluding remarks were made about the complications that were encountered during extrusion and fibre drawing (section 5.7). In Chapter 6 the optical properties of the fabricated Ge-Sb-Se glass optical fibres discussed here, are characterised.

# 6. Light guiding and fibre loss measurements of Ge-Sb-Se chalcogenide glass fibres and a new purification method to fabricate high purity SCG MIR glass fibres

## 6.1. Overview

The physical and optical characteristics of the germanium, antinomy and selenium (Ge-Sb-Se) chalcogenide bulk glasses were addressed in Chapter 4. The extrusion and fibre drawing of selected Ge-Sb-Se chalcogenide glass pairs were reported in Chapter 5. Here, in Chapter 6, the optical properties of the fabricated Ge-Sb-Se chalcogenide glass optical fibres are described including; near-field transmission at 1463 nm wavelength in section 6.2 and the MIR optical loss in section 6.3. The benefits for fibre optical performance of glass distillation are discussed in section 6.4 and the trial of a large quantity of Se was conducted, see section 6.4.1. During the course of the Se distillation work this Author and Tang[11] designed and trialled a new distillation glass rig, see section 6.4.2 and section 6.4.3, respectively. Conclusions drawn for the optical fibre characterisation and the distillation work are discussed in section 6.5 and this chapter is summarised in section 6.6.

## 6.2. Near-field Ge-Sb-Se fibre performance

The fabricated small core fibres discussed in Chapter 5; F019JHB (section 5.4.2), F023JHB (section 5.4.5), F032JHB (section 5.5.2) and F035JHB (section 5.6.2) were examined for near-field light guiding at 1.463 µm wavelength.

[11] Dr. Zhuoqi Tang, Mid-Infrared Photonics Glasses Research Group at the University of Nottingham.

**Table 6.1 Summary of the Ge-Sb-Se fibres checked for near-field imaging at 1463 nm and their properties. The refractive indices were obtained from *[83]*. Key: - means it did not light guide.**

| Fibre code | Glass pair | Core composition / (at. %) | Cladding composition / (at. %) | Predicted core ø / (µm) | Measured core dimensions from SEM images in Chapter 5 / (µm) | Refractive index of core at 1463 nm | Refractive index of cladding at 1463 nm | Near-field light guiding image in Figure 6.1 |
|---|---|---|---|---|---|---|---|---|
| F019JHB | Pair I | $Ge_{22}Sb_8Se_{70}$ | $Ge_{24}Sb_4Se_{72}$ | 15 | 20.30 x 9.08 | 2.549 ± 0.002 | 2.491 ± 0.003 | (a) |
| | | | | 10 | 12.70 x 5.52 | | | (b) |
| | | | | 7 | 10.50 x 4.81 | | | (c) |
| F023JHB | Pair I | $Ge_{22}Sb_8Se_{70}$ | $Ge_{24}Sb_4Se_{72}$ | 15 | 20.40 x 10.10 | 2.549 ± 0.002 | 2.491 ± 0.003 | (d) |
| | | | | 10 | 13.0 x 7.70 | | | (e) |
| | | | | 7 | 9.48 x 4.69 | | | (f) |
| F032JHB | Pair II | $Ge_{19}Sb_{15}Se_{66}$ | $Ge_{20}Sb_{10}Se_{70}$ | 15 | 16.40 x 12.10 | 2.676 ± 0.003 | 2.576 ± 0.003 | - |
| | | | | 10 | 9.47 x 7.11 | | | - |
| F035JHB | Pair III | $Ge_{20}Sb_{10}Se_{70}$ | $Ge_{24}Sb_4Se_{72}$ | 15 | 14.32 x 12.70 | 2.576 ± 0.003 | 2.491 ± 0.003 | (e) |
| | | | | 10 | ~ 16* | | | (f) |
| *the core was difficult to distinguish from SEM images but was detected from EDX analysis. | | | | | | | | |

As was discussed in section 3.4, it was imperative that the mating surfaces of the core and cladding boules during extrusion to make core/ cladding fibre optic preforms, were highly polished and clean prior to the extrusion. This was to ensure an inclusion free, light guiding, core/ cladding interface, in both the core/ cladding fibreoptic preform and subsequent step-index fibre. Furthermore, fibre drawing was conducted in a cleanroom (Class 10,000) (see section 3.5) to reduce exposure to dust and contamination, which could have resulted in scattering losses, crack propagation centres and low fracture stress. A summary of the Ge-Sb-Se fibres which were characterised using near-field imaging at 1463 nm and their properties are given in Table 6.1.

### 6.2.1. Sample preparation, equipment and methodology

The small core fibres were characterised using an optical bench system, built in-house. A B1980A tuneable semiconductor laser (Agilent 81980A) operating at 1463 nm with a power of 5 mW was coupled into the core of each of the test fibre samples using a commercial, standard tapered silica-glass optical fibre (core ~ 9 μm ø). The transmitted light was then collected using x10 microscope objective lens and focused onto a NIR sensitive camera (Siemens XQ1112). A television monitor was connected to the NIR camera to image the fibre output and a computer was connected to the camera to capture the displayed images.

### 6.2.2. Near-field imaging at 1463 nm: results

Near-field imaging at 1463 nm results for the fibres F019JHB (from Pair I), F023JHB (from Pair I) and F035JHB (from Pair III) are shown in Figure 6.1(a-c), (e-f) and (g-h), respectively. These images confirm that, despite their different geometries and core sizes, all of the fibres fabricated from Pair I and Pair III were capable of NIR light transmission and light confinement in the central core at the 1463 nm test wavelength.

Furthermore, voids were seen in fibre F019JHB at the interface between the core and cladding (shown in Figure 5.9) yet it was found that light guiding was still possible.

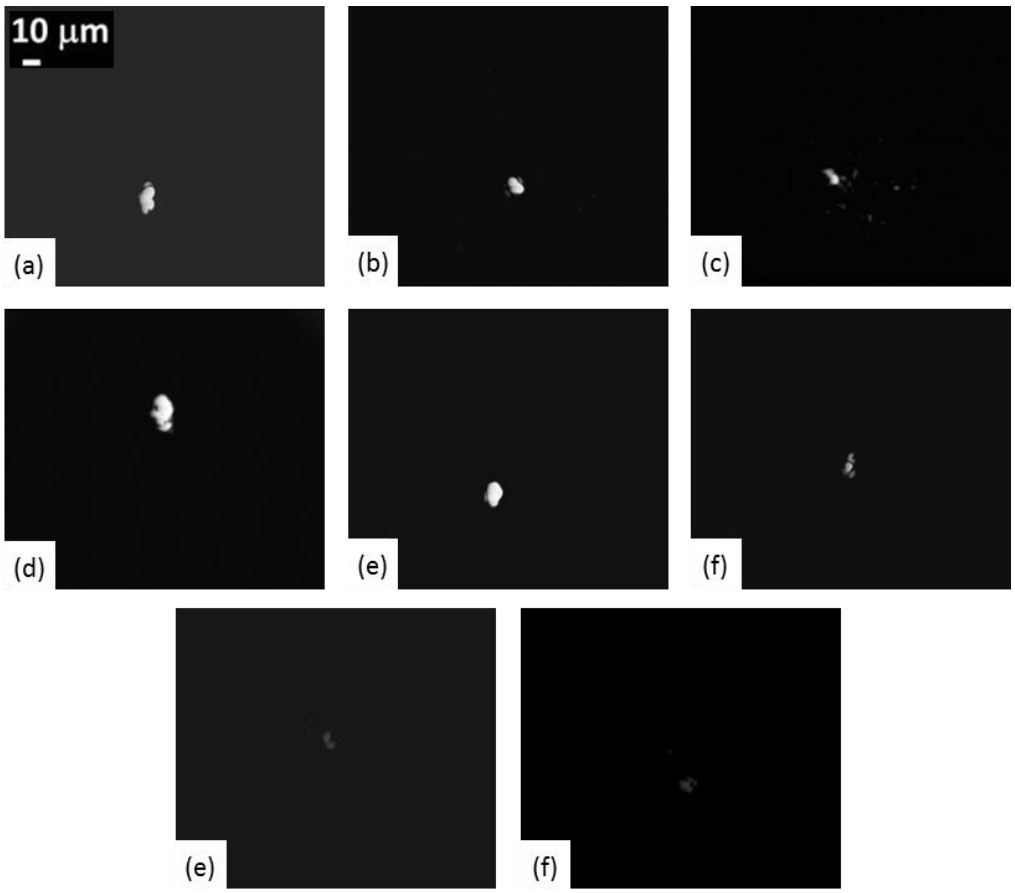



**Figure 6.1 Near-field images of light at 1463 nm wavelength, using a B1980A tunable laser. 15 mW power was used, with an objective lens 10 and a sample length of 500 ± 1.5 mm of small core fibre. Fibre F019JHB (Pair I) with intended core sizes: (a) 15 µm, (b) 10 µm and (c) 7 µm. Fibre F023JHB (Pair I) with intended core sizes: (d) 15 µm, (e) 10 µm and (f) 7 µm. Fibre F035JHB (Pair III) with intended core sizes: (e) 15 µm and (f) 10 µm. The results confirm light confinement within the central core region. Scale bar given in (a) applies to all images. See Table 6.1 for core/ cladding glass composition and measured core dimensions. Fibre F032JHB did not light guide.**

However, Fibre F032JHB from Pair II did not achieve light guiding. Fractures could be observed across the cleaved-ends of the fibre surface (as was shown in Figure 5.16). Thus, it is suggested that light guiding was not achieved in these fibres due to micro-cracks throughout the fibre length. As was discussed in section 2.1.1 the Young's modulus of chalcogenide glasses varies from 17 to 18.5 GPa compared to that of silica glass with a Young's modulus of 72.1 GPa [21]. It is worth repeating that any micro-

crystal growth would potentially scatter the radiation transmitted through the optical fibre also causing the fibre to not achieve light guiding. However, the XRD analysis of the fibres Figure 5.24 confirmed F032JHB amorphicity.

FTIR loss spectra may be used to gain an understanding of the light guiding properties of a glass in terms of extrinsic and intrinsic, absorption and scattering, see section 6.3.

## 6.3. Fibre optical loss

### 6.3.1. Introduction to fibre optical loss

As was discussed in section 2.6.1, it was suggested that the three main sources of impurities in the Ge-Sb-Se chalcogenide glasses synthesised in this Project were: (i) the silica- glass containment utilised for the synthesis of the glass-forming melt, as was discussed in section 3.1.1; (ii) the local environment and residual gases after evacuation during synthesis and treatment of the glass (note, every effort was made to ensure the precursor elements and glass melt were not exposed to the ambient atmosphere (*e.g.* batching was conducted in a glovebox (< 0.1 ppm $H_2O$, < 0.1 ppm $O_2$; MBraun), see section 3.2.2, and melting was achieved in an evacuated silica glass ampoule ($10^{-5}$ Pa), see section 3.2)). At the elevated temperatures of the extrusion and fibre drawing processes, the Ge-Sb-Se glass were at greater risk of contamination from further exposure to impurities and (iii) the precursor elements used for Ge-Sb-Se chalcogenide glass synthesis (the heat-treatment precursor purification processes used in this Project were detailed in section 3.2.1 and purification processes are further discussed in section 6.4).

It was reported in section 4.1.3, that the Ge-Sb-Se bulk chalcogenide glasses were observed to be sensitive to impurities such as [O] and [H]. These impurities were manifested in the transmission spectra of Ge-Sb-Se bulk glasses (Figure 4.4) as

absorption bands, the positions of which were determined by the nature of the impurities, see Appendix II. The impurities contributed to extrinsic absorption, punctuating the 2 - 12 µm transmission window of the Ge-Sb-Se bulk glasses and caused wavelength dependent and wavelength independent scattering losses.

After extrusion and fibre drawing, the Ge-Sb-Se glass matrices had been subjected to an extensive thermal history, increasing the risk of nucleation of the glass melt. As was discussed in section 2.6.2 crystallisation usually results in an increase in optical scattering. However, as previously mentioned from XRD analysis (Figure 5.24) the amorphicity of all the Ge-Sb-Se fibres fabricated in this Project was confirmed.

The optical loss of the step-index core/cladding fibre F018JHB from Pair I (core composition; JB04; $Ge_{22}Sb_8Se_{70}$ at. % and cladding composition JB03; $Ge_{24}Sb_4Se_{72}$ at. %) and the core-only fibre F034JHB from glass composition JB02 ($Ge_{20}Sb_{10}Se_{70}$ at. %) were measured using the widely reported 'cut-back' method [164] with the aid of a FTIR spectrometer (Fourier transform IR; IFS 66/S, Bruker FT), as was described in section 3.6.5.2. Furthermore, another fibre F020DJJHB also from Pair I was fabricated by Mr D. Jayasuriya as part of a 4$^{th}$ year Undergraduate Master's Project, partly supervised by this Author [213]. The precursor elements (Se and Sb) were not subjected to any heat-treatment processes so that the 'unpurified' fibre could be used as a direct comparison to F018JHB. It is worth noting that the silica-glass ampoule containment to hold the chalcogenide glass melt preparation cleaning procedure, was conducted the same for all glass melting (see section 3.1.1) and the same precautions were made to reduce the precursor element's exposure to the ambient atmosphere (such as batching inside a MBraun glovebox, section 3.2.2, and melting in an evacuated ampoule, section 3.2.3).

### 6.3.2. Fibre optical loss: methodology

The fibre loss spectra, spanning the range 1 -10 µm, were collected as two spectral regions: (i) 1 - ~ 2.5 µm wavelength, using a liquid nitrogen cooled InSb detector (Judson; 0.9 – 5.4 µm), tungsten (W) light source (Bruker; for NIR, 0.6 – 3.3 µm) and $CaF_2$ broadband beam (BB) splitter '$CaF_2$-BB' (Bruker; for NIR) and (ii) ~ 2.5 – 10 µm wavelength using a liquid nitrogen cooled MCT detector (Bruker; 2-11.7 µm), a Globar light source (Bruker; for MIR, 3.3 – 100 µm), and a KBr beam-splitter (Bruker; for MIR).

The initial light alignment of the optical components used during the measurements was conducted with a fibre sample piece of ~ 1 ± 0.01 m taken from the fibre stored on the drum just before the piece used for the loss measurement. This ensured that the highest light intensity was launched into the Ge-Sb-Se chalcogenide glass fibres and that the loss measurements were obtained under the best collection conditions. It also helped the prediction of the optimal length for the Ge-Sb-Se chalcogenide fibre to be used for the measurements. Thus, the initial length of the chalcogenide fibre used for the loss measurements was chosen to be as long as possible (*e.g.* 3 ± 0.8 m for losses of 2-16 dB/ m in the range 2.5 – 10 µm). The longest possible piece of fibre ensured that the light intensity difference was dominated by the fibre loss and not the cleave quality. The maximum length was defined by the measured intensity output.

As was described in section 3.6.6.3 after making the initial measurement of intensity through as long a piece of fibre as possible, the 'cut-back' method [164] was applied. Figure 3.17 displayed the 'cut-back method' schematically, showing the removal of a length of fibre (section *B* ~1.5 m) followed by a group of measurements from different fibre cleaves, "Group 2" (each cleaved fibre piece ~ 10-15 mm).

Due to the nature of the cleaving process, it was expected that there would be defects on the cleaved end faces of the fibre causing end-face modal reflectivity. On cleaving a fibre, two pieces of fibre were obtained. One was the main length of the fibre which was measured using the FTIR system, the 'actual-face' of the fibre, and the other cleaved facet was the 'mirror-face'. Each cleaved mirror-face of the Ge-Sb-Se chalcogenide fibre was checked using a reflection optical microscope (Nikon Optiphot/ Vickers RT2112 with GXoptical detection camera GXCAM-5) before each light intensity measurement was collected. If the cleaving quality of the cleaved mirror-face was deemed to be satisfactory (see Figure 3.17(a) for an example of a good cleave and Figure 3.17(b) for an example of a bad cleave), the light intensity exiting the Ge-Sb-Se chalcogenide fibre cleaved actual-face was collected using FTIR. After the measurements, the mirror-face and the actual-face, were checked using a reflection visible optical microscope (Nikon Eclipse LV100ND) (Figure 6.2(a-b)) and also SEM imaging. It is worth noting that the cleaved actual-face SEM images of the intermediate fibres F018JHB and F034JHB were shown in Figure 5.8 and 5.20, respectively. As can be seen from Figure 6.2 the mirror-end cleave was in general a good representative of the actual-face cleave of the fibre, shown here for the F034JHB fibre.

When the intensity measurements were completed (*i.e.* the light intensity spectra had been collected for all the "good" cleaves in both Group 1 and Group 2), the best cleave in each group was selected mathematically, as follows:

(i) The result of a cleave in Group 1 (any cleave) was used as a reference to calculate the fibre loss for each of the cleaves in Group 2 (*i.e.* the spectrum with the highest loss was considered to be on account of the best cleave in Group 2).

(ii) The best cleave in Group 2 was used as a reference to calculate the fibre loss of cleaves in Group 1 (*i.e.* the spectrum with the lowest loss was considered to be the best cleave in Group 1).

(iii) Thus the results corresponding to the best cleaves in Group 1 and 2 were used in the calculation of the final fibre loss spectrum using Equation 3.7.

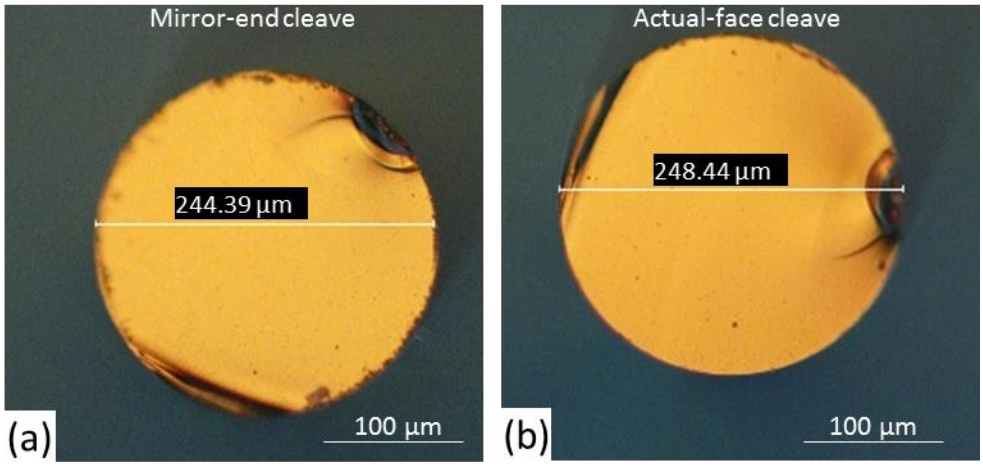



**Figure 6.2 Typical examples of fibre cleaves of the ~ 248 x 238 µm core-only intermediate fibre F034JHB in reflection under visible optical microscopy (Nikon Eclipse LV100ND). (a) The mirror-end of the Ge-Sb-Se chalcogenide fibre before the intensity measurement of the actual-face and (b) after the measurement was taken the actual-face cleave of the Ge-Sb-Se chalcogenide fibre was assessed.**

As can be seen in Figure 6.3, there are gaps in the spectra where the detectors did not receive enough light to register a reading, thus a true reading could not be recorded. Once section *B* had been removed the measurements recorded from the Group 2 cleaves did not experience such a great total optical loss, on account of the shorter fibre. Therefore, in some cases, the Group 2 cleaves could be used usefully to predict the height of the large absorption bands. Using a similar method to the calculations to obtain the fibre loss spectra and Equation 3.7, the result of the first cleave in Group 2 (*e.g.* 2a) was used as a reference to calculate the fibre loss for each of the remaining cleaves in Group 2. If the absorption was not too high, the height of the large absorption bands could be found.

### 6.3.3. Fibre optical loss: results

Figure 6.3 shows the optical loss spectra of the step-index core/cladding fibres, F018JHB and F020DJJHB from Pair I (core JB04; $Ge_{22}Sb_8Se_{70}$, and cladding JB03; $Ge_{24}Sb_4Se_{72}$), and the core-only fibre F034JHB (JB02; $Ge_{20}Sb_{10}Se_{70}$). Similarly to the optical absorption of the Ge-Sb-Se bulk glass samples in Figure 4.4, the vibrational absorption bands of the impurities in the glass fibre, and their respective functional groups, are indicated on Figure 6.3 using the known extinction coefficients from the literature given in Appendix II. Vibrational absorption bands associated with hydroxide (*i.e.* dissolved O-H at 2.86 µm [214], molecular $H_2O$ at 6.31 µm [21]), hydride (*i.e.* Se-H at 3.50 µm and 4.5 µm) [22]) and oxide impurities (*e.g.* $CO_2$ at 4.31 µm [25], Ge-O at 7.8 µm [21] and Si-O at 9 – 10 µm [149]), were found. Se-O is reported to have vibrational absorptions at 10.67 µm, 11.06 µm and 15.3 µm wavelength and so these were not observed here [21, 193]. Furthermore, Lezel proposed that Sb-O absorptions occur at 13.55 µm, 14.53 µm and 17.60 µm [58], thus they also do not appear within the wavelength range amenable to detection here.

From Figure 6.3, the step-index core/ cladding fibre (F018JHB) (minimum loss 2.62 dB/m at 6.08 µm) exhibited higher loss than the core-only fibre (F03JHB) (minimum loss 2.47 dB/m at 6.04 µm wavelength). Both fibres had been subjected to the same glass melting procedure and heat-treatment purifications of the precursor elements, Sb and Se. It is also worth noting that the core-only fibre F034JHB was produced from a singly extruded preform and not directly from a glass melt. Therefore like the co-extruded core/cladding glasses used in fibre F018JHB, F034JHB also benefitted from the removal of the glass surface that had been in contact with the silica ampoule walls on account of the extrusion process, see section 5.1.

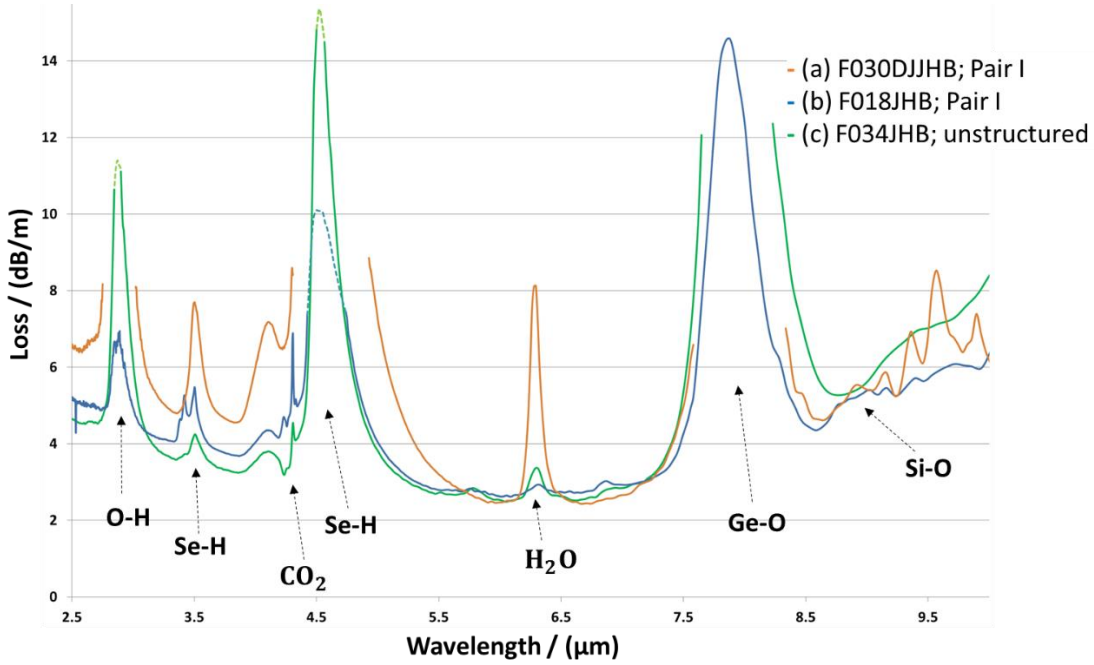



**Figure 6.3 Mid-infrared (MIR) spectra optical loss spectra for intermediate fibres; (a) F030DJJHB (orange) ~ 247 OD step-index core/cladding fibre, without pre-purified precursor elements. Minimum loss was 2.42 dB/m at 6.66 µm wavelength. (b) F018JHB (blue) ~ 242 x 253 OD step-index core/ cladding fibre with pre-purified precursor elements (selenium (Se) and antinomy (Sb). Minimum loss was 2.62 dB/m at 6.08 µm wavelength. (c) F034JHB (green) ~ 248 x 238 µm core-only fibre with pre-purified precursor elements (Se and Sb). The minimum loss was 2.47 dB/m at 6.04 µm wavelength. The vibrational absorption bands of impurities in the glass fibres and their respective functional groups are indicated using the known extinction coefficients from the literature shown in Appendix II [215]. Extrinsic absorption bands related to hydride and hydroxide impurities punctuate the 0.8-6.5 µm wavelength window. Oxide impurities are seen to absorb at >7 µm wavelength. The gaps in the spectra at the tops of the absorption bands are due to large absorption. It was possible to predict the heights of some of the peaks (indicated using dotted lines) using Group 2 measurements. However, this could not be achieved if the absorption was exceptionally high.**

The higher minimum loss exhibited by the step-index core/ cladding fibre (F018JHB) than the core-only fibre (F034JHB), suggests that additional loss mechanisms could have been introduced during the core/cladding fabrication process. Fibre F018JHB was fabricated from a co-extruded core/ cladding preform which was drawn to a cane of ~ 500 µm ø. The cane was then suspended in an outer cladding tube 2.82/ 9.47 mm ID/OD and drawn to fibre (see section 5.4.2 for fibre drawing details). Great efforts were made to ensure the abutting polished surfaces of the core and cladding glass charge boules

used in the fabrication of fibre F018JHB were pristine. However, the higher minimum loss of the fibre F018JHB compared to the core-only fibre F034JHB, suggests the incorporation of impurities potentially at the core/cladding interface. No voids were detected at the core/cladding interface in the ten cross-sections studied for fibre F018JHB and an example of the cross-section was shown in Figure 5.8. On the other hand, the intensity of the impurity absorption peaks was much lower for fibre F018JHB than for F034JHB. It is unlikely that this was related to the different compositions of the fibre cores (F018JHB; core composition JB04; $Ge_{22}Sb_8Se_{70}$ and F034JHB; core composition JB02; $Ge_{20}Sb_{10}Se_{70}$) as there was minimal composition change. It is suggested that the precursor materials used to fabricate the step-index fibre had received a better purification process. The fibres were fabricated at different times, thus different as-received batches of the precursor materials from the manufacturer were used. It is possible that the purification varied between batches.

In Figure 6.3, spectra (a) and (b), the fibre loss measurements were conducted from structured core/ cladding intermediate fibres of the same core (JB04; $Ge_{22}Sb_8Se_{70}$) and cladding (JB03; $Ge_{24}Sb_4Se_{72}$) composition, but with the precursor heat-treatment process to purify Sb and Se only applicable in spectrum (b). Therefore a direct comparison can be made about the impact of the heat-treatment process to purify these precursor elements. It was surprising to note that the minimum loss was lower for the fibre F030DJJHB with no prior purification (2.42 dB/m at 6.66 µm) compared to the fibre F018JHB which had been fabricated from glasses using pre-purified Sb and Se by heat-treatment (2.62 dB/m at 6.09 µm). However, all of the Se-H, O-H, $H_2O$ and Ge-O absorption bands were more intense for the former (Figure 6.3 spectrum (a)) than the latter (Figure 6.3 spectrum (b)). The most striking observation was the near removal of the $H_2O$ absorption band upon the precursor purification. Therefore showing that the

prior purification of the Sb and Se elemental precursors was of great benefit in reducing extrinsic absorption in the subsequent fibre. It is also suggested that the prior purification of the precursor elements had little impact on the extrinsic scattering processes in the fibre assumed to be responsible for the main part in the baseline loss of these fibres. Of course, scattering caused by species such as silica fume particulates would not have been reduced by purification of the precursor elements and may be responsible for most of the background scattering loss.

It is worth noting that it was not possible to calculate the height of any of the large absorption bands for F030DJJHB due to the high intensity absorption levels preventing enough light getting to the detector.

During the Sb and Se precursor element purification great care was taken to reduce exposure to the atmosphere: by batching in a MBraun glovebox and ensuring that the silica glass ampoules, used as the vessel for Ge-Sb-Se glass melting, underwent a vigorous pre-treatment process (*i.e.* annealing, HF-etching, air baking and vacuum baking) to reduce contamination at the silica glass ampoule walls. Nevertheless, it was still likely that the silica glass not only added silica fume particulates but also contributed to the Se-H and O-H impurities due to the transfer of H and O-H to the Ge-Sb-Se chalcogenide glass melt at temperatures ≥ 650 °C [148, 149].

Furthermore it can also be considered that ‘H’, ‘O’ and ‘$H_2O$’ accompanying the as-purchased Se and Sb precursor were not completely removed during heat-treatment.

The silica glass insert used in the Se heat-treatment purification did not undergo the same preparation process as the silica glass ampoule. Although the insert was not in direct contact with the Ge-Sb-Se chalcogenide glass melt, any chemisorbed or physisorbed impurities (removed from the silica glass ampoule in the air and vacuum

baking process, see section 3.1.1) could have been released during the Se heat-treatment and reacted with the Se, impeding the effect of the heat-treatment process. Therefore it is suggested that for future Se heat-treatment conducted in the MIR Photonics Research Group, the silica glass inserts should also be subjected to the same preparation processes as the silica glass ampoule.

The MIR Photonics Group at the University of Nottingham, UK, has developed chalcogenide glass fibres achieving the lowest reported loss figures to date propagating MIR light through 52 m of a germanium, arsenic and selenium (Ge-As-Se) fibre of 83 ± 2 dB/km at 6.60 μm wavelength [164]. It is clear that greater purification of the precursor elements with respect to hydroxide and oxide impurities is required to help extend the transmission window of the Ge-Sb-Se chalcogenide glass fibres. This is discussed further in section 6.4.

### 6.4. Distillation

The melting and fabrication of the Ge-Sb-Se chalcogendie glasses in this Project comprised heat-treatment to purify the Se and Sb precursor elements (section 3.2.1), batching them along with as-received Ge into a pre-treated silica glass ampoule within a MBraun glovebox (section 3.2.2).

As was discussed in section 3.2.1, currently high purity precursor elements can be commercially sourced as 5 x 9 – 7 x 9 but only with regards to cationic impurities (*i.e.* metal ions). Anionic impurity content (*i.e.* $H_2O$) is not considered by the manufacturers [168]. Comparing spectra in Figure 6.3(a) and (b), it is apparent that impurity bands such as Se-H, O-H, $H_2O$ and Ge-O were significantly reduced after the heat-treatment purification of the precursor materials Sb and Se. However, despite the heat-treatment purification process, the fibres did not achieve ultra-low loss, such as the 83 ± 2 dB/km

at 6.60 μm wavelength achieved by Tang *et al.* for a Ge-As-Se fibre [164]. Snopatin [22] and Churbanov [145] have suggested that to achieve optical losses at the level of intrinsic losses, the acceptable content of impurity elements (*e.g.* O, C and Si) should not exceed 1-100 ppb wt. and the tolerable content of heterophase inclusions is $10^3 - 10^4$ $cm^{-3}$. However, it is worth noting that currently it is not economical to fabricate ultra-low loss fibres if the length of fibre required for the device is < 1 m.

As was discussed in section 2.6.2, there are three different chalcogenide glass purification techniques reported in the literature; (i) removal of surface oxide and hydride from raw precursor elements (as conducted in this Project (section 3.2.1); (ii) distillation and gettering of the raw precursor elements and (iii) the distillation and gettering of homogenised glass. Here, the methods of obtaining high purity chalcogenide glasses from the distillation of the precursor elements were investigated further. Techniques developed from a collaboration with Shiryaev[12], conducting a preliminary Se distillation experiment, were used to see if a large quanity of Se could be distilled by this Author and Tang[13] (section 6.4.1). During the distillation work a simplified distillation rig design was developed by this Author and Tang with the intention of its future application to distill other precursor elements. The design of this rig is given in section 6.4.2 and an initial trial using gallium iodide ($GaI_3$) is described in section 6.4.3, the merits of using an iodide precursor matieral are also explained.

### 6.4.1. Trial of Se distillation with in-house built rig (code D011JHBZQT)

#### 6.4.1.1. Introduction

A trial Se distillation (code D011JHBZQT) was conducted. The aim of this distillation was to investigate whether a large amount of Se could be distilled, for later use in

[12] Professor Vladamir Shiryaev, Russian Academy of Science, Moscow, Russia.
[13] Dr. Zhuoqi Tang, Mid-Infrared Photonics Glasses Research Group at the University of Nottingham.

generating high purity chalcogenide optical fibres. Prior to the experiment reported in this Project (conducted by this Author and Tang), a Se distillation trial had been performed with in-house silica glass apparatus built by Shiryaev, based on the "Sangerha rig" [156].

The Se distillation apparatus used in this Project was built by Baumbach, UK. The apparatus was hydrogen fluoride (HF)-etched (40 % concentration for 5 min) and annealed by Baumbach (6 h at 1000 °C). The apparatus was not air or vacuum baked due to its size. The apparatus was used once only. Later, this Author and Tang developed a more simple design of distillation rig with potential for use with other glass precursors (section 6.4.2).

#### 6.4.1.2. Se distillation method (code D011JHBZQT)

For the Se distillation (code D011JHBZQT), batching was carried out in the glovebox (MBraun, ≤0.1 ppm $O_2$, ≤0.1 ppm $H_2O$). 115 g ± 0.0005 g of commercial Se (Materion, Table 3.4) was weighed using a balance (Sartorious, model BP221S accurate to ± 0.1 mg), and batched into the charge end of the distillation ampoule, Chamber 1 (Figure 6.4(a)). The open end of Chamber 1 was then sealed in air (completed within 4 minutes), using an ignited oxy-propane (a mixture of $O_2$; BOC and $C_3H_2$; Calor gas) torch (Jenson, Junior Jet 7).

It was not possible to place the entire apparatus within one clamshell furnace nor to place two clamshell furnaces directly next to each other because they were not heated along the entire internal length and so the outer edges inside the furnace tube were not wound; it was expected that this was a safety feature of the manufacturers but it was inconvenient when using them. To overcome this, the distillation rig was placed across two clamshell furnaces (3508 Carbolite), positioned so that the Chamber 1 and

Chamber 2 (the Se collection chamber, Figure 6.4(c)), were in the centre of each clamshell (allowing the greatest temperature control of the chambers), respectively, and a small portion of the apparatus, the link tube (Figure 6.4(b)), protruded from one clamshell furnace before entering the other. To avoid condensation of Se within the link tube and the tube between Chamber 2 and the cold trap (Figure 6.4(d)), the temperature of the tubes had to be kept higher during distillation than that of the Se collection chamber. Wire (0.6 mm nickel chrome) was wrapped around the tubes using the silica glass protrusions to anchor them Figure 6.4(b). The silica glass protrusions were ~ 1 mm ø, and spaced approximately every 5 mm along the outside of the silica glass link tube. Current was supplied to the wire and adjusted accordingly (after temperature feedback from thermocouples positioned within each clamshell and at the two link tubes, indicated in Figure 6.4(i)) to maintain a constant temperature profile.

The vacuum system (rotary pump VRC 200-7 and diffusion pump Edwards B30207240) was connected via an Edwards Saunders valve to the end of the cold trap. An O-ring (Imperial nitrile O-ring, RS Ltd.) was attached to the end of the cold-trap to reduce glass-metal contact with the valve. Liquid nitrogen ($N_2$, BOC) was used in the cold trap to freeze any volatiles to protect the pump. The distillation rig was kept under an open vacuum of $10^{-5}$ Pa for 3 h to remove any water within the distillation rig. Furnace blanket (Superwool™ 607™ Blanket; classification temperature: 1300 °C) was used to pack each clamshell and wrapped around the entire apparatus to provide good thermal insulation. Vacuum baking of the distillation rig was implemented by turning the furnaces for the clamshell chambers on (Chamber 1; 150 °C, Chamber 2; 350 °C) and the current was supplied to the wire (link tube; 300 °C, tube between Chamber 2 and cold trap; 300 °C) for 2 h. It is worth noting that the current supplied was dependent on several factors (*e.g.* the resistance of the wire and how many wire

turns were used) thus the parameter measured was the temperature which was recorded by the thermocouple. Distillation did not occur as the temperature of Chamber 1 was only 150 °C. The wire heating was then turned off (the furnaces for the clamshells remained on) and the Se distillation rig was then left under vacuum overnight.

The set temperature values using the clamshell furnace controllers were slightly different from the actual temperatures read by the external thermocouples (*e.g.* thermocouples read 20 - 50 °C lower than the furnace pre-set temperature, dependent upon how high the temperature was set). A detailed temperature/ time schedule recorded from the thermocouples during the distillation process is shown in Table 6.2.

Before distillation commenced, the temperature of Chamber 1 was raised to 240 °C and maintained at this temperature for 1.5 h. Chamber 2, was kept at 350 °C so that it had a higher temperature than Chamber 1. This was to promote the removal of oxygen and hydrogen from the elemental Se, without activating Se distillation, similar to the heat-treatment purification process which was described in section 3.2.1.

The temperature profile was then reversed to promote Se distillation. The temperature of Chamber 1 was increased to 400 °C and the temperature of Chamber 2 was reduced to 200 °C, to allow the vapour pressure of the Se to underpin the movement from Chamber 1 to Chamber 2. The link tube was maintained at 425 ± 5 °C to ensure the distilled Se condensed in Chamber 2 and not in the tube. The tube between Chamber 2 and the cold trap was maintained at 335 ± 2 °C to prevent Se from entering the cold trap. The Se was collected in the four fingers of Chamber 2. It was expected that the distillation should have taken 2 h based on the preliminary trial by Shiryaev and Tang, however after 2.5 h only a very little of the Se had distilled. Therefore the temperature of Chamber 1 was increased to 435 ± 10 °C and the distillation completed within a

further 2 h. The furnace heating the clamshell encasing Chamber 1 was turned off and once the temperature had reduced to 350 °C, the heating current in the wires on the link tubes was also switched off.

**Table 6.2 Detailed temperature/ time schedule of the Se distillation (code D011JHBZQT). The temperature of each clamshell was monitored by the external thermocouples (see Figure 6.4 (i) for position). The temperature of the link tube between Chamber 1 and Chamber 2 and the tube between Chamber 2 and the cold trap was maintained at 425 ± 5 °C and 335 ± 2 °C, respectively, throughout the course of the distillation. The total time for the Se distillation was 4.5 h. Key; RT – ramp temperatures.**

<table>
<tr><th>Total Time / (h)</th><th>Chamber 1</th><th>Chamber 2</th><th>Notes</th></tr>
<tr><td>0.5</td><td>RT from 150 °C to 240 °C in 0.5 h</td><td rowspan="2">Dwell at 350 °C for 1 h</td><td>Temperature raised of link tube and tube between Chamber 2 and cold trap at 425 ± 5 °C and 335 ± 2 °C, respectively. This was maintained throughout the distillation.</td></tr>
<tr><td>1</td><td rowspan="2">Dwell at 240 °C for 1.5 h</td><td rowspan="2">Se melted in Chamber 1 for 1.5 h, as in section 3.2.1 to remove $H_2O$ and [O].</td></tr>
<tr><td>1.5</td><td>RT from 350 °C to 200 °C in 0.5 h</td></tr>
<tr><td>2</td><td>RT from 240 °C to 400 °C at 400 °C/ h</td><td rowspan="3">Dwell at 200 ± 30 °C for 5.5 h</td><td rowspan="3">All Se distilled from Chamber 1 to Chamber 2 in 4.5 h , Chamber 1 at 400 ± 45 °C.</td></tr>
<tr><td>2.5</td><td>Dwell at 400 ± 45 °C for 4.5 h</td></tr>
<tr><td>7</td><td>Furnace switched off</td></tr>
<tr><td rowspan="7">Steps after distillation was complete</td><td colspan="3">When Chamber 1 at 350 °C, switched off the heating of the link tube wire, the wire between Chamber 2 and the cold trap.</td></tr>
<tr><td colspan="3">When the wires were cold sealing between Chambers 1 and 2 was conducted. Once sealed, sealing between Chamber 2 and the cold trap was conducted.</td></tr>
<tr><td colspan="3">RT Chamber 2 from 200 °C to 300 °C in 0.2 h.</td></tr>
<tr><td colspan="3">Dwell Chamber 2 at 300 °C for 0.5 h.</td></tr>
<tr><td colspan="3">Chamber 2 removed and immediately placed in pre-heated vertical furnace at 300 °C for 0.5 h.</td></tr>
<tr><td colspan="3">Quenched in air for 4 minutes.</td></tr>
<tr><td colspan="3">Annealed in vertical furnace pre-heated at 100 °C. Switched furnace off to cool as soon as Chamber 2 placed inside.</td></tr>
</table>

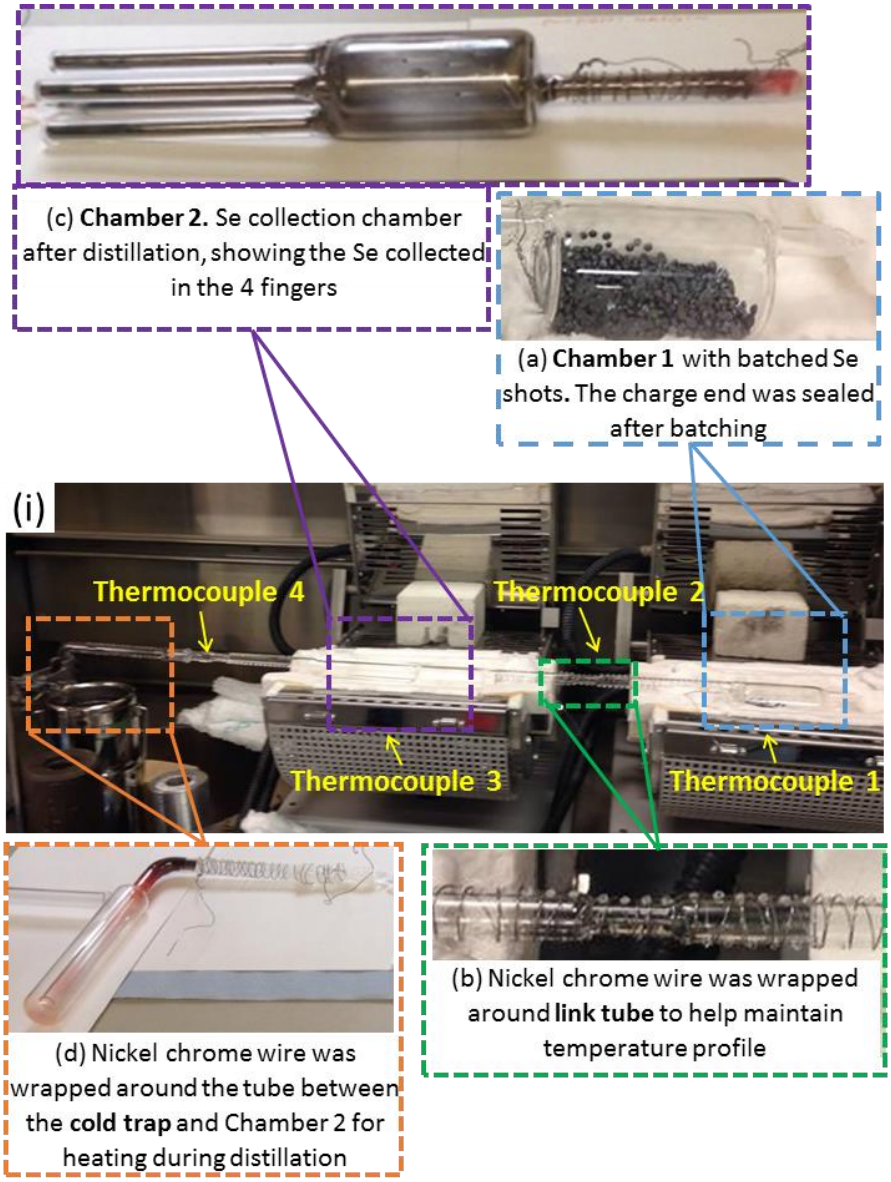



**Figure 6.4 (i) Distillation apparatus using clamshell furnaces. The positions of four external thermocouples are highlighted and these were used to monitor accurately the temperature profile of each section during the distillation. The apparatus could be divided into four sections; (a) Chamber 1 (51 / 55 mm ID/ OD, L=80 mm); the Se was batched into this chamber and sealed before distillation; (b) 0.6 mm nickel chrome wire was wrapped along the link tube, the wire was used to maintain the temperature along the tube in the gap between the two clamshell furnaces; (c) Chamber 2 (51/ 55 mm ID/OD, L=120 mm) with four fingers (10/ 14 mm ID/ OD, L=140 mm) collected the distilled Se and (d) a cold trap was used to freeze any volatiles to protect the pump (dynamic high vacuum pump consisting of Rotary pump (to $10^{-2}$ Pa, VRC 200-7.0) and then a diffusion pump (to $10^{-5}$ Pa, Edwards B30207240)).**

Once the wire had cooled around the link tube, the link tube was sealed using an ignited oxy-propane torch. Although sealing was conducted horizontally rather than vertically, the process was the same as that described in section 3.2.3, as the distillation rig was

under vacuum. The tube between Chamber 2 and the cold trap was then sealed to isolate Chamber 2 from the rest of the apparatus, shown in Figure 6.5.

#### 6.4.1.3. Results

The Se distillation was apparently successful, as shown in Figure 6.5. A large quantity (estimated at ~ 98 %) of Se was distilled and may be seen in the four fingers of Chamber 2 of the apparatus in Figure 6.4(c) and in Figure 6.5. As described in section 6.4.1.2, Chamber 2 was sealed at the link tube and at the tube between the chamber and the cold trap, to prevent contamination from the ambient atmosphere. The distilled Se was kept in the sealed silica glass chamber and stored in the glovebox for protection, in order to be used in future high-purity chalcogenide glass melts. On this occasion the distilled Se was not characterised using (E)SEM-EDX as in order to do so the ampoule would have had to be opened. This would have caused a risk of exposing the highly purified Se to silica glass and other particle contamination, before it was needed for chalcogenide glass melting.

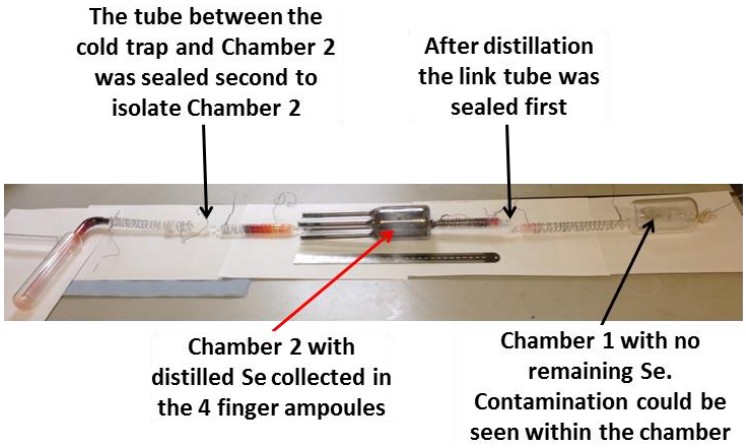



**Figure 6.5 Image of distillation apparatus after the process was completed and compartments sealed. The distilled Se can be seen in the four 'finger' ampoules, highlighted by the red arrow.**

This work was conducted towards the end of this Author's research and therefore time constraints precluded glasses from being made from the purified Se. However, the MIR

Photonics Research Group has benefitted immensely from this work [189]. The experience gained was used to design a new distillation rig, section 6.4.2, where the construction could be outsourced to facilitate future distillations conducted by the MIR Photonics Group, University of Nottingham, UK.

### 6.4.2. Developing the distillation rig design

From the success of the Se distillation (section 6.4.1), it was established that a simplified distillation process and rig was needed for other precursor elements. Under close supervision and guidance from Tang, the work was completed by this Author. A new rig was designed from the ideas built and developed from the Se distillation apparatus (section 6.4.1). The total length of the rig was designed to be 450 mm. This was to ensure that it could fit into the same furnace (Instron, TF105/4.5/1ZF, 86 mm ID, 450 mm height) used for vacuum and air-baking the silica ampoule, as was described in section 3.1.1.

The ‘S’ bend in the rig was designed to restrict the flow of refractory particles from the charge to the distillate end of the ampoule. Rowe [47] found evidence that fine, atmosphere-born particles originating from the impure charge were reaching the distillate side when using a simple ‘V’ bend in distillation apparatus.

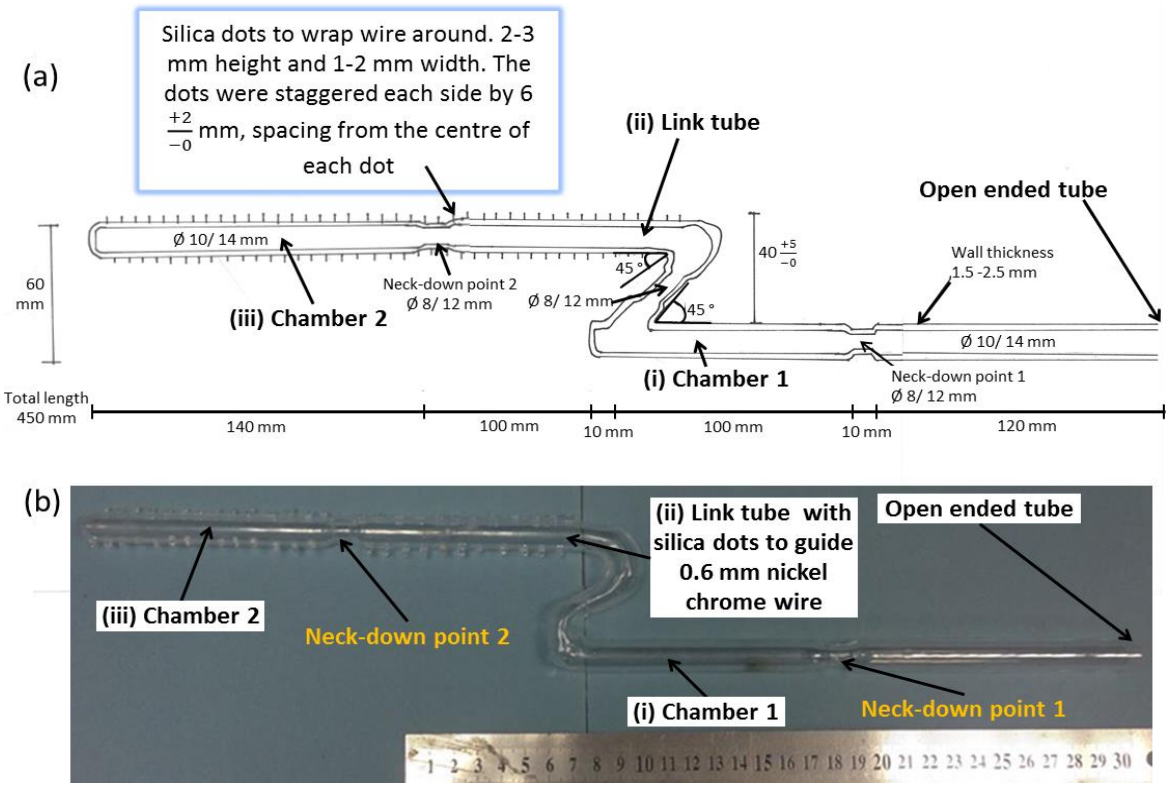



**Figure 6.6 Distillation rig designed in this Project. The rig was composed of three sections: (i) Chamber 1 where the precursor element was batched into; (ii) link tube where 0.6 mm nickel chrome wire was wrapped around to maintain the temperature profile during distillation and (iii) Chamber 2 where the distilled product was condensed, the rig had an open ended tube for batching the precursor material, but was then sealed at the neck-down point 1 before distillation started. After distillation Chamber 2 was isolated by sealing at the neck-down point 2.**

### 6.4.3. Trial of distillation rig with distillation of $GaI_3$ (code D018MINJHBZQT)

The first use of the newly designed distillation rig from section 6.4.2, was conducted by this Author and Tang.

#### 6.4.3.1. Rationale behind distilling $GaI_3$

Although the majority of this Project was focussed on fabricating supercontinuum generation (SCG) fibres and passive transmitting fibres, active rare earth (RE)-doped fibres were another important focus of the MIR Photonics Group at The University of Nottingham, UK, in association with the MINERVA[14] Project. As was shown in Figure 2.10 it was suggested by Seddon [3] that a (RE)-doped chalcogenide glass active fibre is required alongside the SCG fibre for the proposed MIR spectral imaging system. RE-ions can be introduced to a chalcogenide glass to create 'active' fibres for MIR photoluminescence and direct emission fibre lasers. Small additions of gallium (Ga) are known to improve RE-ions solubility [216-218].

It is practically impossible to distil Ga in a high vacuum system due to its extremely low volatility (Ga: 0.078 Pa (0.0058 mmHg) at 1000 °C [219] and 1 torr (~$10^2$ Pa) at 1350 °C [21]). Furthermore, the majority of Ga in a Ga -chalcogenide glass, when being distilled under vacuum, is suggested to remain un-distilled. The thermal decomposition between Ga and the other elements occurs which results in the distillation of the other elements and not Ga [167].

A new method of generating high purity Ga was proposed by Shiryaev *et al.* [21] by a chemical transport reaction route for a Ga-Ge-As-Se glass. Metallic Ga was transferred

[14] The MINERVA Project (www.minerva-project.eu) supported through the EU Seventh Framework Programme (FP7).

in a gallium (III) iodide ($GaI_3$) vapour flow, dependent on the forwards and backwards reaction [21]:

$$\mathbf{Ga^{[III]}I_3 + 2Ga^{[0]} = 3Ga^{[I]}I} \qquad \textbf{Equation 6.1}$$

Shiryaev *et al.* reported that the purified Ga lowered the content of impurities of oxide, hydroxide and molecular water. Therefore the new distillation rig from section 6.4.2 was trialled for the distillation of $GaI_3$, see section 6.4.3.2 for method and section 6.4.3.3 for results.

### 6.4.3.2. $GaI_3$ distillation method (code D018MINJHBZQT)

The silica glass rig was manufactured by Clive Dixon[15]. After glass blowing, the rig was cleaned with acetone (> 99.5 %, Sigma Aldrich) three times. The rig was then HF-etched (48 %, Sigma) for 1 h, before being air and vacuum baked using the same process as was described in section 3.1.2, for silica glass ampoule preparation. The $GaI_3$ (Alfa Aesar, 99.999 % purity) arrived in a sealed ampoule shown in Figure 6.7. Score marks (using a diamond blade) were made on the neck down section of the ampoule prior to being placed inside the glovebox (< 0.1 ppm $H_2O$, < 0.1 ppm $O_2$; MBraun). The ampoule was broken open inside the glovebox and the contents was poured into a plastic boat (Fisher, 100 ml, anti-static), ensuring there was no silica glass fragments. In a fresh plastic boat, 4.9016 g of $GaI_3$ was weighed using a balance (Sartorious, model BP221S accurate to ± 0.1 mg).

The batch was then transferred into the first chamber of the silica glass rig, see Figure 6.8, using a long handled spoon (stainless steel, Fischer). To the best of this Author's ability only unavoidable contact was made between the $GaI_3$ powder and the walls of

[15] Clive Dixon. School of Chemistry Glass Blower. University of Nottingham, UK.

the silica glass rig to minimise the transfer of the powder before it reached the bottom of Chamber 1.

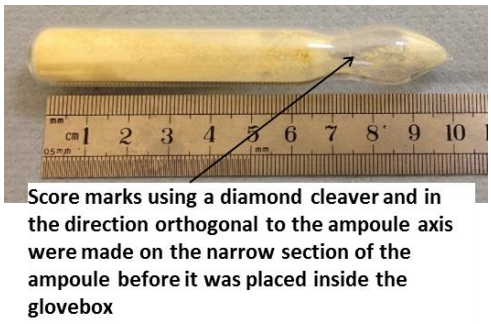



**Figure 6.7 The as-received gallium iodide ($GaI_3$) inside its transportation ampoule. The ampoule was scored using a diamond pen before it was placed inside the glovebox. Once opened inside the glovebox, the $GaI_3$ was poured into a plastic boat (Fisher, 100 ml, anti-static) before being batched into the distillation rig (see Figure 6.8) to ensure any fragments of silica would not be transferred into the distillation rig.**

An O-ring (Imperial nitrile O-ring, RS Ltd.) was attached to the top of the ampoule to reduce glass-metal contact with the valve and to help make a hermetic seal (Edward Saunders). Once the valve had been fitted and closed the silica glass distillation rig was transferred from the glovebox and connected to the vacuum rig. The rig was then sealed using the process that was described in section 3.2.3 and aluminium foil was wrapped around Chamber 1 to protect the $GaI_3$ powder from the light of the flame.

From [21], it was reported that the optimum temperature of the evaporation of $GaI_3$ (at $10^{-5}$ Pa.s) was experimentally established to be in the range of 220-230 °C. It is worth noting that as the apparatus was of shorter length than the apparatus used for the Se distillation (code D011JHBZQT described in section 6.4.1.2) only one clamshell furnace was required. Similarly to the Se distillation (code D011JHBZQT), nickel chrome wire was wrapped around the link tube (Figure 6.8(b)) and a current was supplied to help maintain a constant temperature profile. Temperatures were recorded from thermocouples placed at Chamber 1, the link tube and Chamber 2, see Figure 6.8.

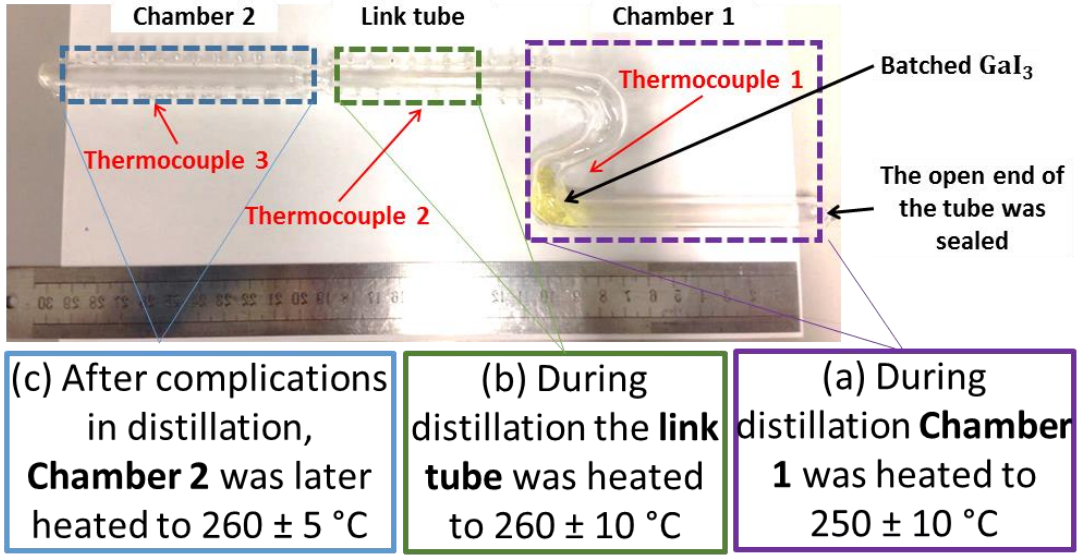



**Figure 6.8 The gallium iodide ($GaI_3$) was batched into Chamber 1 inside a glovebox (< 0.1 ppm $H_2O$, < 0.1 ppm $O_2$; MBraun). It was then sealed under vacuum ($10^{-5}$ Pa). For the distillation D018MINJHBZQT: (a) Chamber 1 was heated in a clamshell furnace to 250 ± 10 °C; (b) at the same time the link tube was heated using 0.6 mm nickel chrome wire to 260 °C; (c) initially the clamshell encasing Chamber 2 was not heated in the anticipation that the distilled material would condense at the end of the Chamber 2. However, as can be seen in Figure 6.9, the distillate condensed in the link tube just after the bend, at the end of the nickel chrome wire. Once this was realised the wire around the link tube was extended to Chamber 2 and Chamber 2 was heated to 260 ± 5 °C.**

Furnace blanket was used to pack the clamshell and wrapped around the entire rig (especially the link tube and Chamber 2) to provide good thermal insulation. Unlike the Se distillation (code D011JHBZQT, see section 6.4.1) the silica glass distillation rig had been vacuumed and air baked, so the distillation process could commence as soon as all the components were in place.

Initially the clamshell encasing Chamber 1 was heated to 230 °C and the link tube was heated to 240 °C and held isothermally, see Figure 6.8. However after ~ 1 h, no visual sign of distillation was observed; the receiving end (Chamber 2) was empty. Therefore the temperature was gradually increased at ~ 5 °C every 10 minutes until Chamber 1 was at 250 °C and the link tube was at 260 °C, then the rig was held isothermally at these temperatures. The distillation continued at these temperatures ± 10 °C. After 3 h

no remaining $GaI_3$ could be observed in Chamber 1.

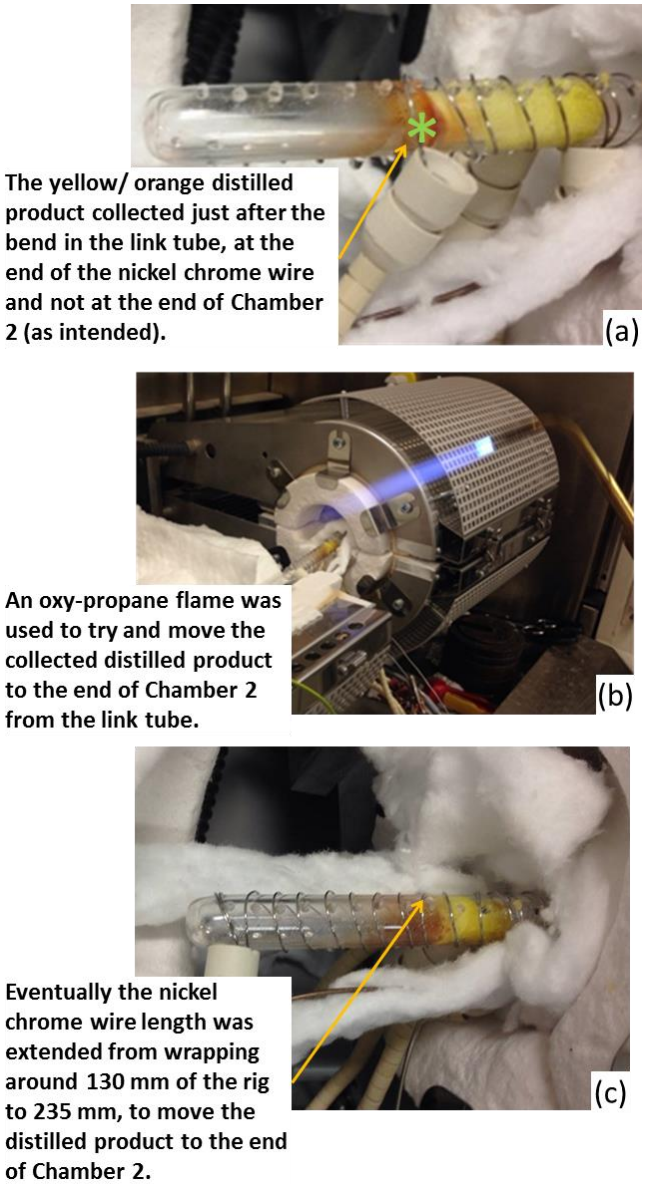



**Figure 6.9 (a) At the end of the $GaI_3$ distillation (code D018MINJHBZQT) the distilled product condensed in the link tube (see Figure 6.8 for the position of the link tube in the rig) at the end of the nickel chrome wire, indicated by the green *; (b) an oxy-propane (a mixture of $O_2$; BOC and $C_3H_2$; Calor gas) torch (Jensons, Junior Jet 7) was ignited and used to try and encourage the distilled product along; (c) after no effects were seen from using the torch, the wire section was increased (from 130 mm to 235 mm) to the end of the ampoule and was isothermally held at 260 °C for 30 mins until the distilled product was successfully transferred to the end of Chamber 2, shown in Figure 6.10.**

However, it was realised that the distillation product had collected just after the bend at the end section of the nickel chrome wire shown in Figure 6.9(a) as a green *. An oxy-propane (a mixture of $O_2$; BOC and $C_3H_2$; Calor gas) torch (Jensons, Junior Jet 7) was

ignited and it was attempted to heat the distilled product to the end of Chamber 2, shown in Figure 6.9(b).

Concerns were raised at exposing the distilled product to an intense source of light (it was stated in the MSDS form to store the $GaI_3$ in the dark) and after ~ 3 minutes of heating with the torch no effects were observed. Therefore the wire section was extended from 130 mm to 235 mm, by connecting additional wire to the original piece of wire and wrapping it round the rig to the end of Chamber 2. The rig was designed for the wire to go to the end of Chamber 2: it had silica glass protrusions to secure the wire along the length of the link tube and Chamber 2 (section 6.4.2). Therefore, the length of tube heated at 260 °C was increased, from the original section of wire around the link tube, to the end of Chamber 2.

After a further 30 minutes the distilled product had successfully transferred to the end of Chamber 2, as shown in Figure 6.10. Chamber 2 was isolated from the rest of the rig by sealing off at the link tube. As the rig was under vacuum ($10^{-5}$ Pa) and the distilled product had solidified at the end of Chamber 2, sealing was completed in the vertical position, as was described in section 3.2.3.

#### 6.4.3.3. Results of distillation of $GaI_3$ (code D018MINJHBZQT)

The distilled product sealed in Chamber 2 is shown in Figure 6.10(a). The distilled product was kept in the sealed chamber and stored in the glovebox for future high purity chalcogenide glass melts. A black ‘soot’ was observed in Chamber 1 (Figure 6.10(b)).

To further investigate the black ‘soot’ in Chamber 1, the silica glass rig was cut using a diamond coated, circular saw (Isomet saw, Buehler Ltd. With diamond-impregnated blade, LECO Instruments Ltd. 15HC ø = 100 mm, thickness = 0.35 mm). First a small slit was made to relieve the internal vacuum pressure before the sample section was cut.

~ 1 mm of the outer silica glass wall was cut to create a flat bottom of the sample to mount onto a SEM aluminium specimen-stub (Agar). A double-sided sticky carbon tab (Agar) was used to secure the sample in position. The SEM equipment and methodology were described in section 3.7.3. However, on this occasion the environmental low vacuum mode was used (*i.e.* wet-mode). Therefore the sample did not need to have a conductive coating.

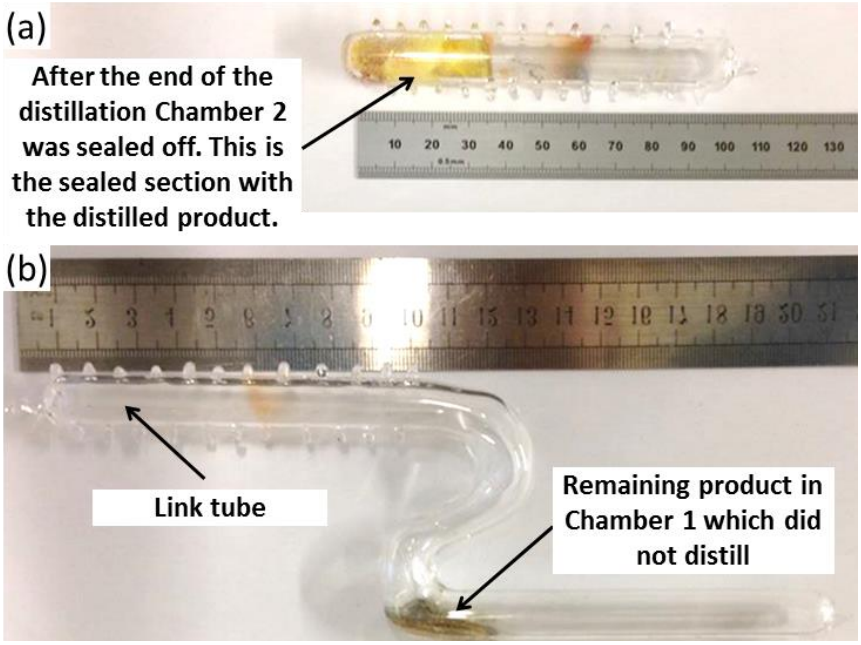



**Figure 6.10 (a) The distilled product was isolated in Chamber 2 by sealing using an oxy-propane (a mixture of $O_2$; BOC and $C_3H_2$; Calor gas) torch (Jensons, Junior Jet 7). (b) A black 'soot' remained in Chamber 1 after the distillation and was analysed using ESEM-EDX, see Figure 6.11.**

The ESEM-EDX of the examined product remaining in Chamber 1 of the silica glass distillation rig are presented in Figure 6.11. The approximate location of the EDX analysis is marked by a red 'x' with spectra 1 - 4 measured from the top in descending order, (*e.g.* spectrum 4 was the top layer of the remaining product in Chamber 1), Figure 6.11(a). The morphology of the product changed from a crack formation observed in spectra 4 to dark circles seen in spectra 1. This was in correlation with the relative greater amounts of Ga and I being detected in spectra 4 and decreasing through to spectra 1. It is suggested that due to the geometry of the 'S' bend in the distillation rig,

more material remained either trapped or condensed on the sides of the ampoule than in the middle of the tube.

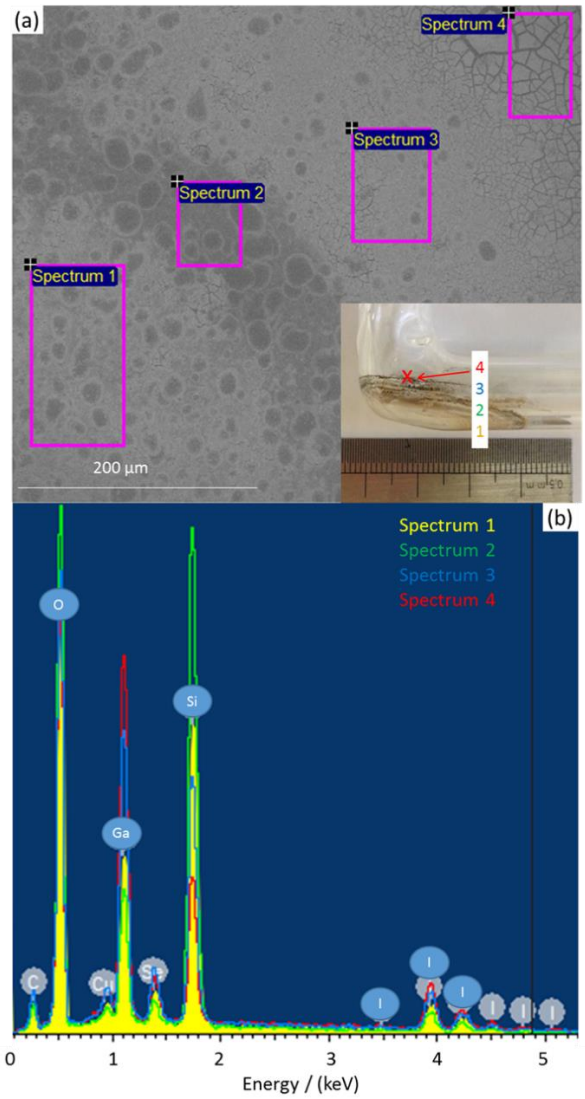



**Figure 6.11 ESEM-EDX analysis of a section of the un-distilled residue which remained on the silica glass wall in Chamber 1 of the distillation rig after the $GaI_3$ distillation (code D018JHBZQT). The silica glass rig was cut and a sample of the residue on the silica glass wall was mounted on a SEM stub and analysed in 'wet-mode'; (a) the red 'x' on the inset indicates the approximate location of where the spectra were taken of the un-distilled residue. Four spectra (shown in the main image of (a)) were taken from the top of the residue (with the rig was in a vertical position), in descending order from 4 to 1 and (b) the EDX results showing the intensity of the elements gallium (Ga), iodine (I), silica (Si) and oxygen (O) for the four spectrums. From spectrum 1 to 4 it can be seen that the relative level of Ga and I increased. This correlated to the different morphologies from the areas of where the spectra were taken.**

When the distilled product is used within the MIR Photonics Research Group at the University of Nottingham, UK to synthesise high purity chalcogenide glasses, it would

be interesting to compare the optical transmission of the glass or glass fibre with the purified Ga to one of the same composition using as-purchased Ga.

Jiang *et al.* [67] reported greatly reduced optical loss of a $Ge_{20}Sb_5Se_{55}I_{20}$ glass fibre (3.5 dB/ m at 3.3 µm wavelength) compared to a $Ge_{20}Sb_5Se_{75}$ glass fibre (48 dB/ m at 3.3 µm wavelength) after distillation under vacuum (2 x $10^{-3}$ Pa) of the melted precursor materials (batched into the same chamber and melted at 950 °C) using a magnesium powder getter. The as-received precursor elements for both fibres were of high purity (*i.e.* Ge, 5N %; Sb, 5N %; Se, 5N % and I, 4N %). The distilled Ge-Sb-Se-I glass was then homogenised in a rocking furnace for 20 h, quenched in water at room temperature and annealed. Jiang *et al.* reported loss for the Ge-Sb-Se fibre without any purification steps was exceptionally high (48 dB/ m at 3.3 µm wavelength). It is worth noting that the minimum loss obtained for the Ge-Sb-Se fibre F030DJJHB fabricated in this Project (Figure 6.3) which was not subjected to any precursor purification heat-treatment processes was much lower (the minimum loss was 2.42 dB/m at 6.66 µm wavelength). Furthermore, the minimum losses for fibres F018JHB and F034JHB with precursor purification using heat-treatment, were also lower than Jiang's reported loss for the $Ge_{20}Sb_5Se_{55}I_{20}$ glass fibre (F018JHB lowest loss was 2.62 dB/m at 6.08 µm wavelength and F034JHB lowest loss was 2.47 dB/m at 6.04 µm). This suggests that the glass synthesis process and fibre fabrication technique used in this Project were more efficient at reducing impurity inclusions. However, in this Project the spectra at 3.3 µm wavelength were increased due to the tail of the Se-H absorption (at 3.51 µm wavelength) resulting in higher losses than the Ge-Sb-Se-I fibre at 3.3 µm wavelength (viz.: F030DJJHB was 4.89 dB/m, F018JHB was 4.07 dB/m and F034JHB was 3.65 dB/m).

Using a precursor element of iodine or an iodide is an attractive method as it has the potential for lowing the glass-melting temperature (≤ 650 °C [220]). Thus, reducing the chalcogenide's glass reaction with the silica ampoule wall, as a result of the iodide's high volatility and substantially lower temperatures of melting. Therefore it is suggested that future work should focus on distilling precursor elements (Se, germanium (IV) iodide ($GeI_4$; $T_m$= 146 °C, boiling point (b.p.) unavailable [221] and antimony (III) iodide ($SbI_3$; m.p. = 170 °C, b.p. = 401 °C [222])) individually using the new distillation rig designed in this Project (section 6.4.2). If the distillations are successful it is this Author's suggestion that two glass synthesis routes should then be trialled. First the as-distilled precursors elements should be batched and homogenised in a rocking furnace, as conducted for all the Ge-Sb-Se glasses in this Project as was described in section 3.2.4. The second route should include another distillation step, before melting, by batching the as-distilled precursor elements into a distillation rig along with an oxygen getter. Then once distilled, the melt should be homogenised in a rocking furnace. It is proposed that optical fibres should be fabricated from both of these glasses and the optical loss spectra compared to the spectra in Figure 6.3, to see if the methods improve the loss spectrum and if one method is more successful than the other.

## 6.5. Conclusions

The optical properties of the Ge-Sb-Se glass fibres fabricated in this Project were assessed and led to the ability to identify impurities; methods to remove these were trialled. Below are the main conclusions summarised from Chapter 6, put into context with the conclusions from the earlier chapters:

(i) Near-field imaging of the Ge-Sb-Se fibres

- From Chapter 5 it was found that the core of each small core Ge-Sb-Se fibre, with anticipated core sized of 15 µm, 10 µm and 7 µm diameter, fabricated in this Project was not circular. On the other hand near-field imaging at 1463 nm wavelength was achieved in all of these fibres F019JHB, F023JHB and F034JHB (section 6.2). Light guiding was not possible in fibre F032JHB and it was suggested that this was on account of the fragile and brittle nature of the fibre, with suspected micro-cracks throughout the length. In Chapter 4, section 4.3, it was suggested that the low mechanical strength of the fibre was on account of a large mismatch between where the sharp increase in the onset of the instantaneous thermal expansion coefficient occurred between the core and cladding glasses.

(ii) Purification of precursors versus no purification: effect on fibre optical loss for core/ cladding fibres

- The effect of heat-treating to purify the precursor elements Sb and Se on subsequent fibre loss was observed (section 6.3). Core/ cladding fibres of $Ge_{22}Sb_8Se_{70}$/ $Ge_{24}Sb_4Se_{72}$ composition, F030DJJHB (un-purified) and F018JHB (with precursor purification of Sb and Se by heat-treatment) were compared. It was clear that the purification of the precursor elements lowered the absorption bands of the hydroxide and oxide impurities. However, the minimum losses were lower for F030DJJHB (2.42 dB/m at 6.66 µm wavelength) than for fibre F018JHB (2.62 dB/m at 6.09 µm wavelength).

(iii) Influence of processing on fibre optical loss: silica glass inserts

- In Chapter 3, section 3.2.1.2 the Se purification processes using heat-treatment was described. A sacrificial silica glass insert was used to collect volatilised contaminants. In section 6.3, it was suggested that any chemisorbed or physisorbed impurities in the silica glass insert could have been released during the Se heat-

treatment and reacted with the Se, inhibiting the effect of the heat-treatment process. Therefore it was proposed that any future Se heat-treatment processes conducted by the MIR Photonics Group should subject the silica glass inserts to the same pre-treatment at the silica glass ampoule (*e.g.* HF-etched, annealed, air and vacuumed baked).

(iv) New precursor purification technique: large Se mass distillation

- Currently precursor elements of high purity with respect to anionic impurities cannot be sourced, thus a preliminary experiment was conducted to distil a large quantity of Se (section 6.4.1). The distillation was successful and the distilled Se will be used to make high purity chalcogenide glasses within the MIR Photonics Research Group at the University of Nottingham.

(v) Development of new distillation apparatus

- Greater understanding of the distillation technique obtained during the large Se mass distillation led to the development of a new simplified distillation apparatus for other precursor material distillation (section 6.4.2). The distillation rig was trialled with a $GaI_3$ distillation (section 6.4.3). The successful operation of the new distillation rig led to the suggestion of the precursor elements (Sb and Se) of the Ge-Sb-Se glass system to be individually distilled before glass melting.

(vi) Influence of precursor purity using iodine or iodide inclusions

- In the literature it was suggested that the inclusion of iodide in a chalcogenide glass composition has the potential to lower the glass-melting temperature (≤ 650 °C [220]), thus reducing the chalcogenide's glass reaction with the silica ampoule wall. Therefore, it was suggested that future work should focus on distilling precursor elements (Se, germanium (IV) iodide ($GeI_4$) and antimony (III) iodide ($SbI_3$) individually using the new distillation rig designed in this Project (section 6.4.2). It

was proposed to investigate the effects of $SbI_3$ and $GeI_4$ on the optical loss spectra of the resulting Ge-Sb-Se-I fabricated fibres. Furthermore, it was proposed to compare these Ge-Sb-Se-I fibres to ones which had further been distilled as a glass melt with an oxygen getter and the optical loss spectra from the fibres measured in this Project (section 6.3).

### 6.6. Summary

In this chapter the optical properties were analysed of the Ge-Sb-Se chalcogenide glass fibres whose fabrication was reported in Chapter 5. Near-field imaging at 1463 nm wavelength was reported in all the fabricated fibres of F019JHB, F023JHB and F035JHB, light guiding in the core was observed. However, light guiding was not possible in the fibres from F032JHB (core JB02; $Ge_{20}Sb_{10}Se_{70}$ and cladding JB03; $Ge_{24}Sb_4Se_{72}$ section 6.2.2). The refined 'cut-back' method was used for fibre loss measurements in this Project (section 6.3) and from the fibre loss spectra obtained it was shown that glass purity was a critical factor affecting the intensity of hydride and oxide impurity absorption bands punctuating the 2.5 – 10 μm wavelength transmission region. Therefore distillation methods were explored as a means of generating high purity chalcogenide glasses (section 6.4). For the first time in the MIR Photonics Research Group at the University of Nottingham, a large quantity of Se was successfully distilled by this Author and Tang (section 6.4.1). Techniques and understanding obtained by this Author during the Se distillation trial, led to the development of a new distillation rig, transferring the method to other precursor elements (section 6.4.2). The new distillation rig was trialled using $GaI_3$ (section 6.4.3). Conclusions from the Ge-Sb-Se optical fibre characterisation and the distillation techniques were drawn (section 6.5) and the potential for using iodide for generating high purity Ge-Sb-Se supercontinuum generation fibres was suggested.

# 7. Preliminary cytotoxic evaluation of fibre F018JHB

## 7.1. Overview

Chalcogenide glass fibres containing antimony (Sb) have been extensively researched for photonic applications [69, 223]; however, their toxicity and stability in conditions during biomedical imaging remains nearly unknown. As was highlighted in section 2.4.2, before chalcogenide glasses are used for clinical application it is vital to assess the glass cytotoxicity (the degree to which these glasses are toxic to cells). *In vitro* (in glass) cytotoxicity assays are primary screening tests for materials which have the potential to be used in medical devices.

The step-index fibre F018JHB (core JB04; $Ge_{22}Sb_8Se_{70}$ and cladding JB03; $Ge_{24}Sb_4Se_{72}$) was investigated using cytotoxicity tests. The fabrication of F018JHB was described in section 5.4.2 with SEM images shown in section 5.4.3. Optical analysis via near-field imaging and optical loss measurements were discussed in section 6.2 and section 6.3, respectively. The preliminary cytotoxicity assessment was conducted by the 4$^{th}$ year Undergraduate Master's student Miss C. Podesta (2012-2013) [224]. Her Project was conducted under the close supervision of this Author. This was the first time that chalcogenide glasses made in the MIR Photonics Group had undergone cytotoxicity investigation. The aim of this preliminary work was to gain cell laboratory experience and to pass this knowledge onto the MIR Photonics Group, University of Nottingham, UK, so that more focused research could be conducted in the future.

The cells used throughout this study were standard mammalian fibroblast cells known as 3T3 (The Culture Collections, UK). The 3T3 cell line, abbreviation for '3-day transfer, inoculum 3 x $10^5$ cells', was developed by Todaro and Green in 1962 and are

capable of growing indefinitely [225]. Cell lines (cells harvested from culture) were chosen over primary cells (cells directly from a living organism) due to their better reproducibility *in vitro* and to reduce variation between experiments by allowing comparisons with the same cell line. The preparation of the cell culture medium, defrosting the cell lines, cell concentration and cell counting are described in section 7.2. Alamar Blue assays, which use Alamar Blue as an indicator, that yield a colorimetric change and a fluorescent signal in response to cell metabolic activity (section 7.3.4) were combined with scanning electron microscopy (SEM) images together with energy-dispersive X-ray spectroscopy (SEM-EDX). SEM allowed imaging of the cell growth on the F018JHB fibres (SEM and SEM-EDX methodology was described in section 3.7). The preparation of the F018JHB fibres for the Alamar Blue assays and subsequent SEM analysis, cell seeding and the methodology of the Alamar Blue assays are described in section 7.3. The Alamar Blue results of Trial 1 and Trial 2 are discussed further in section 7.4. The SEM images characterised the extent of cell attachment to the fibre surface and the results of Trial 1 and Trial 2 are discussed in section 7.5. Final conclusions made from the preliminary cytotoxicity work are given in section 7.6. This chapter is summarised in section 7.7.

## 7.2. Cell preparation

Cell culture conditions and passage chosen to test the chalcogenide glasses followed The University of Nottingham, UK, Wolfson Building's Cell Culture Laboratory Protocol. This protocol had previously produced consistent results over a period of 5 years and was closely monitored by the cell laboratory technician: Mrs Julie Thompson. 3T3 mammalian fibroblast cells were used in this Project. Fibroblast cells have a vital role in tissue repair and are responsible for making extracellular matrix and collagen, the structural framework of animal tissue [226]. Fibroblast's ability to proliferate,

together with their solitary lifestyle, strong attachment to surfaces and rapid replication, accounts for why they are easy to grow in culture. Thus, fibroblasts were deemed an appropriate choice to assess the cytotoxicity of the F018JHB fibres.

The following sections comprise: preparation of the culture medium (section 7.2.1); defrosting frozen cell lines (section 7.2.2); cell preparation and obtaining the required cell concentration (section 7.2.3) and cell counting (section 7.2.4), provide a general outline of the cell preparation stages that were required before the Alamar Blue assay was conducted. The culture medium was used throughout the cell preparation stages and Alamar Blue assays, to sustain cell growth and to ensure the cells received the same nutrition.

### 7.2.1. Preparation of the culture medium

First 500 ml of Dulbecco's Modified Eagle's Medium (DMEM, Low Glucose with Pyruvate, Gibco, Life Technologies), 10 ml of 4-(2-hydroxyethyl)-1-piperazineethanesulfonic acid (HEPES, Sigma Aldrich) and 5 ml of non-essential amino acids (NEAA, Sigma Aldrich) were pre-warmed to 37 °C. Simultaneously 75 mg of ascorbic acid (Sigma Aldrich) and 5 ml of L-Glutamine (Sigma Aldrich) were added to 50 ml of foetal bovine serum (FBS, Gibco Life Technologies) at room temperature. The resulting solutions were then added to DMEM and mixed with 10 ml of antibiotics-antimycotics solution (AA/AM, 100x, Sigma Aldrich).

### 7.2.2. Defrosting frozen cell lines

Cells were frozen at 1.5 – 2 x $10^6$/ 1 ml vial of Recovery Cell Culture Freezing Medium (10 % dimethyl sulfoxide (DMSO) in foetal bovine serum, Gibco Life Technologies). The cell passages were; Trial 1: passage 13 and Trial 2: passage 23. To thaw the cell freezer mix, cell ampoules (polystyrene universal container with a polyethylene screw-

cap, Fischer Scientific) were extracted from the liquid nitrogen cell store and left at room temperature for 1 minute. The frozen medium was removed by gently heating the cell ampoule to 37 °C in a water bath and allowing it to thaw until 90 % of cells were defrosted. The outside of the ampoule was cleaned with 70 % industrial methylated spirit (IMS, Fisher Scientific) and the contents of the ampoule were transferred to a 20 ml universal via a polystyrene serological pipette (Fischer Scientific) to ensure no bubbles were formed. 10 ml of culture medium (see section 7.2.1 for preparation) (maintained at 37 °C) was added to the universal dropwise to avoid osmotic shock of the as-defrosted cells. The contents of the universal was then mixed by withdrawing approximately half of the contents into the pipette and then releasing it five times. Thawed cells were then centrifuged (Jouan CR4.22, Labequip) at 300 x g (gravitational force) for 3 minutes at 37 °C.

The cell pellets were then re-suspended in 10 ml of fresh culture medium in a cell culture flask (polystyrene, surface area 75 $cm^2$, Corning®) and incubated horizontally to allow growth to a sought after 80 % confluency at 37 °C and 5 % $CO_2$. The cell culture medium was changed after 24 h to remove dead cells. The culture medium was removed by tilting the flask to vertical, so that the culture medium and any dead cells dropped to the bottom of the flask. The viable cells (a viable cell can be defined as a cell that is capable of actively growing or dividing and therefore surviving successfully [227]) stayed adhered to the large surface area of the side of the flask. The medium was aspirated using a 10 ml pipette and great care was taken not to touch the side of the flask where the viable cells were. 5 ml of phosphate buffered saline (37 °C) was used to rinse the flask and was aspirated again. This process was then repeated.

### 7.2.3. Cell preparation and obtaining the required cell concentration

Cell seeding is a term given to the process of calculating and distributing the required concentration of cells for the experiment. Once the cell lines had been defrosted they could be kept incubated until needed (a maximum of two weeks), if the culture medium was regularly replaced. Once the cells were removed from the incubator, the first stage was to check that they were at least 80 % confluent using an optical microscope (Nikon Eclipse TS100). Figure 7.1(a) shows cells that are > 80 % confluency.

To obtain the required concentration of cells, first the cell culture flask was aspirated with a sterile 10 ml pipette and the cells were gently rinsed with 5 ml of phosphate-buffered saline (PBS, prepared from PBS tablets Oxoid). This helped to remove any remaining serum, which might have inhibited the action of the trypsin. The PBS was then aspirated from the cell culture and replaced with 1.5 ml of 0.2 % trypsin (Sigma Aldrich) with HEPES at the 37 °C. Trypsin was used to lift the cells off the surface of the flask in order for them to be transferred. HEPES was used to maintain the pH between 7.2 and 7.4. The contents of the flask were swirled to ensure the trypsin-HEPES solution covered the cells. The flask and its contents were then incubated at 37 °C for 3 + 2 minutes. The flask was checked at regular intervals to observe any cell detachment, see Figure 7.1(b).

The flask was lightly tapped to detach the cells and 4.5 ml of culture medium at 37 °C was added. The contents of the flask were transferred to a cell ampoule (polystyrene universal container with a polyethylene cap, Fischer Scientific). The flask was then rinsed using 4 ml of culture medium and transferred to the cell ampoule making the total volume 10 ml. The trypsinised cells were centrifuged at 250 x g (gravitational force) for 4 minutes at 37 °C to separate the cells from the trypsin and the media solution. The centrifuging generated a supernatant (the liquid lying above the solid

residue) which was aspirated and the cell pellet (the solid residue under the supernatant), which was re-suspended in 4.5 ml of culture medium. The cell suspension was then transferred evenly into three flasks together with 7 ml of culture medium. The flasks were then incubated at 37 °C and 5 % $CO_2$. The cell culture medium was changed after 24 h to remove any dead cells.

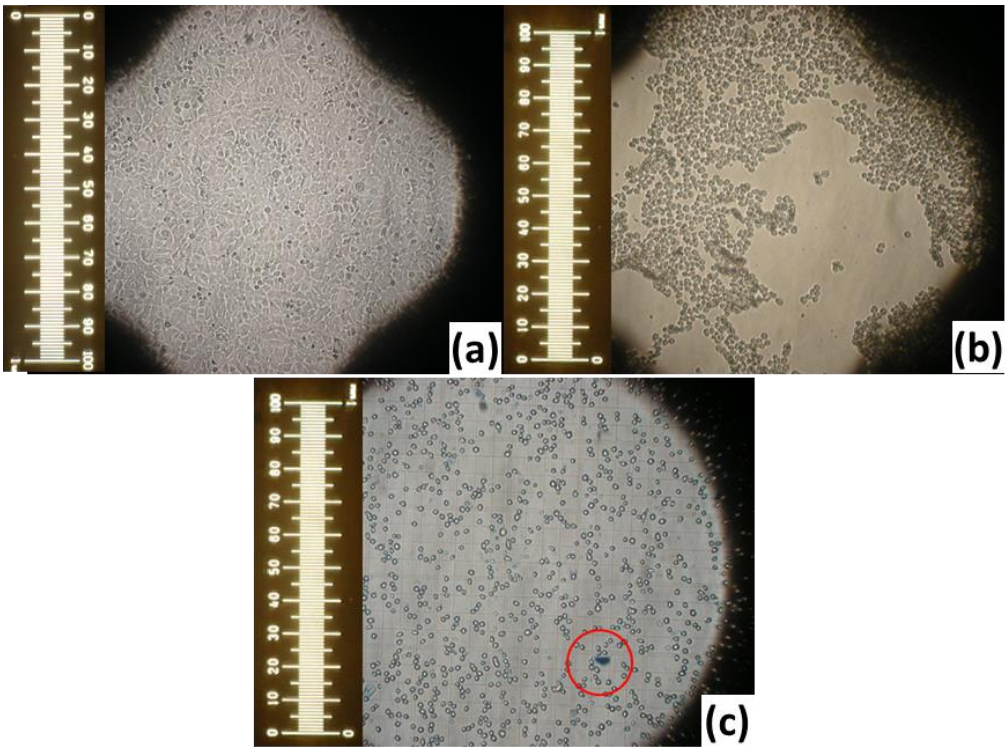



**Figure 7.1 Optical micrograph images showing the typical stages of 3T3 mammalian fibroblast cell seeding with 1 mm scale bar. (a) A layer of confluent cells (> 80%). It is worth noting that cell growth to 80 % confluency was recommended. (b) Detached cells floating in trypsin. (c) Cells containing Trypan Blue solution; red circle identifies dead cells from visual assessment (stained blue).**

### 7.2.4. Cell counting

A sample of the cell suspension obtained from the cell line was counted to help predict the total number of cells, using a haemacytometer (Marienfeld-superior). The cell viability was checked to have counts between 100 and 300 cells per $mm^2$ using the Trypan Blue exclusion method [228]. The viable cells were counted first and then the dead (blue stained) cells were counted separately afterwards, Figure 7.1(c).

The viable cell count per ml is defined as in Equation 7.1.

$$\textbf{Viable cell count per ml} = \frac{\textbf{average viable cells}}{\textbf{suspension volume}} \times \textbf{dilution factor} \times 0.95 \times 10^4 \quad \textbf{Equation 7.1}$$

Equation 7.2 was used to calculate the dilution, to obtain the cell suspension at the desired seeding rate.

$$\textbf{Volume of media to add to 1 ml suspension} = \frac{\textbf{average viable cell count}}{\textbf{cells required per sample}} \quad \textbf{Equation 7.2}$$

### 7.3. Sample preparation and Alamar Blue assay methodology

The methodology of the Alamar Blue assay used in this Project adhered to the strict control measures of The University of Nottingham, UK, Wolfson Building's Alamar Blue Protocol which was based on the Alamar Blue manufacturer's (BIORAD) guidelines. As with any biological or chemical assay, severe changes in pH and temperature can have serious consequences on the assay and great care was taken to maintain these. Similar to the cell culture preparation described in section 7.2, all sample preparation and Alamar Blue assay work was conducted in The University of Nottingham, UK, Wolfson Building's Cell Laboratory.

The F018JHB fibres were placed directly in the culture medium with cells seeded directly onto it (see section 7.3.1 for F018JHB fibre sample preparation and section 7.3.3 for cell seeding and incubation). During this cytotoxicity test great care had to be taken to avoid physical trauma to the cells from either movement of the F018JHB fibre or crushing. However, it was considered that having the cells in direct contact with the Ge-Sb-Se chalcogenide glass fibres, where the extent of cell attachment to the glass fibres could also be characterised via SEM would provide more illuminating results for the purpose of this preliminary project.

### 7.3.1. Step-index fibre F018JHB (core JB04; $Ge_{22}Sb_8Se_{70}$ and cladding JB03; $Ge_{24}Sb_4Se_{72}$) preparation

The Ge-Sb-Se chalcogenide glass fibres were obtained from the step-index, 242 x 253 µm ø, fibre F018JHB (core JB04; $Ge_{22}Sb_8Se_{70}$ and cladding JB03; $Ge_{24}Sb_4Se_{72}$). The F018JHB fibres were manually broken to lengths of 6.4 ± 0.1 mm using tweezers and were divided into two categories (shown schematically in Stage 1 in Figure 7.2) of either etched in propylamine (Sigma Aldrich) for 18 minutes or not etched. It is known that chalcogenide glasses tend to form a nm layer of oxide in air [58]. Wilhelm *et al.* [121] suggested that for the observed toxicity towards A549 immortalised human lung cells for tellurium, arsenic and selenium ($Te_2As_3Se_5$) fibres, there was a soluble toxic surface layer likely to be composed of $As_2O_3$, resulting from a slow reaction with atmospheric oxygen. They reported that, while the oxidised fibres released arsenate ions, which result in toxic effects to cells, fresh or washed fibres showed no toxic effects. The oxide layer was 5 nm thick after three years of exposure to atmospheric oxygen at room temperature [121]. As was discussed in section 2.1.2, As is a well-known toxic element and along with its inorganic compounds has been classified in Group 1 as carcinogenic to humans, by the International Agency for Research on Cancer (IARC 1987) [89]. As is a protoplasmic (protoplasm is the fluid found inside a cell) poison due to its effect on sulfhydryl group in the protoplasm of cells interfering with cell enzymes, cell respiration, metabolic function and mitosis (usual method of cell division) [229]. Unlike As, to date Sb itself has not been listed by the IARC [20]. However, the IARC has concluded that animal carcinogenicity data were sufficient for antimony trioxide ($Sb_2O_3$) to be classified in Group 2B, possibly carcinogenic to humans via inhalation and ingestion [20]. Therefore it would be desirable to remove a $Sb_2O_3$ layer without damage to the Ge-Sb-Se fibre. Propylamine is a weak base and

has often been used to remove surface contaminants in the preparation of chalcogenide glasses [230]. From the work conducted in the MIR Photonics Group at the University of Nottingham, UK, it is proposed that as propylamine removes the surface layers of chalcogenide glasses, it concurrently removes any oxide layer. Thus propylamine etching was also used to prepare some of the fibre drawing preforms in Chapter 5.

Etching was conducted by immersing the 6.4 ± 0.1 mm F018JHB fibres individually in a petri dish (Soda-lime, 100 mm ø, Fisher Scientific, UK), containing 100 ml of propylamine (99+ N, Fluka) and held at 18 °C in a water bath (Ultrawave). Each petri dish was gently shaken three times at ~ 6 minute intervals to roll the fibre, helping all surfaces to be exposed to the propylamine.

Four F018JHB fibres for each time interval shown at Stage 3 in Figure 7.2 (a total of 12 fibres) were either etched or non-etched. Immediately following, a vigorous cleaning process was then applied to both sets of fibres with acetone (99.5 N, Fisher Scientific) and wiped down to remove any residue with optical lens tissue (Agar Scientific). Lens tissue was non-shedding and was used rather than standard-issue blue paper towel as it was discovered that the Ge-Sb-Se fibres could catch on the towel, either breaking or becoming contaminated. In addition the blue dye from the towels was leachable, thus could have contaminated the fibres.

It was expected that the anticipated oxide layer would regrow in-time on re-exposure of the etched F018JHB fibre surface to air. Thus UV sterilisation, cell seeding (section 7.3.3) and the Alamar Blue assay (section 7.3.4), were conducted immediately after the washing and drying procedures.

### 7.3.2. Material control preparation, sample sterilisation and sample preparation in the tissue culture plastic (TCP) well plate

Controls were included in the experiments to ensure the operation of the Alamar Blue assay method and for results' comparison. In Trial 1, a 3 µm pore size polycarbonate membrane permeable support (Corning ©,Transwell®) which was used to help anchor the F018JHB fibres (shown schematically in Figure 7.3) was also used as an internal control.

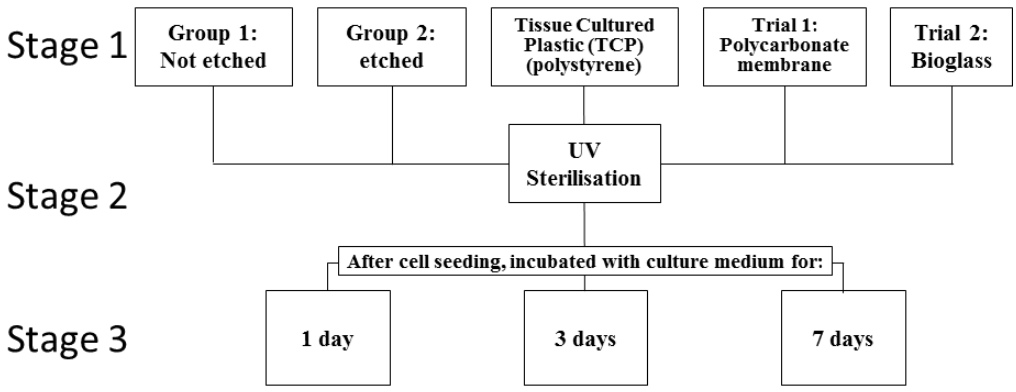



**Figure 7.2 The three different stages of the preparation for the Alamar Blue assay, displayed as a hierarchy. The testing materials used for each trial are shown in Stage 1. 9 samples of tissue cultured plastic (TCP), polycarbonate membranes and bioactive glass fibres were required for each Trial. 12 samples of the F018JHB fibres both etched in propylamine and non-etched were needed. Two Trials were conducted. The only difference between the two Trials were the controls. For Trial 1 a polycarbonate membrane (Corning©) was used as an internal control and for Trial 2 bioactive glass fibre (phosphate based glass, $45\ P_2O_5$- 16CaO- $10Na_2O - 24MgO - 5B_2O_3$ (mol %) [231] made 'in-house') was used as a negative control. For both Trials the tissue cultured plastic was used as a blank and 6.4 ± 0.1 mm samples of F018JHB were divided into group 1 and group 2. Group 2 of the fibre samples were pre-treated by etching in propylamine for 18 minutes. All the testing materials were subjected to ultraviolet (UV) sterilisation in Stage 2. Cells were seeded into nine well plates of each testing material of Stage 1. Three of each material samples, which had been exposed to cells, were extracted at each time slot shown in Stage 3. A F018JHB fibre etched in propylamine and non-etched was included at each time-point in Stage 3 which had not been exposed to cells. This was to assess the medium alone on the fibres.**

This was to assess the cell behaviour after exposure to the polycarbonate insert alone. In Trial 2, bioactive glass fibres (phosphate-based glass, $45\ P_2O_5$- 16CaO- $10Na_2O - 24MgO - 5B_2O_3$ (mol %) [231] made 'in-house' by the Research Group of Dr Ifty

Ahmed, University of Nottingham, UK) were used as a negative control. In a cytotoxic test the negative control is a known material that does not elicit a cytotoxic response. Prior to cell seeding, all the testing material samples (see Stage 1 in Figure 7.2) were subjected to initial sterilisation via ultraviolet (UV) radiation for 15 minutes using a mercury arc lamp.

The polycarbonate permeable support (also used as the internal control in Trial 1) was used to help anchor the F018JHB fibres in both Trials 1 and 2, and the bioactive glass fibre in Trial 2, longitudinally to the base of each individual well in a 24 tissue culture plastic (TCP) well plate (polystyrene, Thermo Scientific, Nunclon Delta Surface), see Figure 7.3.

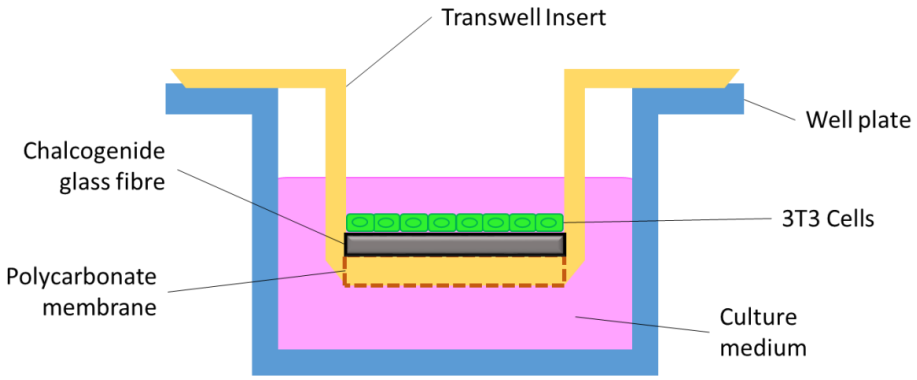



**Figure 7.3 Schematic showing the anticipated cross-sectional set-up of a well of a 24 tissue cultured plastic (TCP) well plate with a 3 µm pore size polycarbonate membrane permeable support (Corning ©, Transwell®), chalcogenide fibre and 3T3 fibroblast cells in place. It is worth noting in the experiment there was an unavoidable gap between the fibre and the edges of the polycarbonate support. Thus, some cells were also seeded onto the polycarbonate membrane.**

### 7.3.3. Cell seeding into tissue culture plastic (TCP) wells and incubation

Prior to cell seeding, 0.6 ml of culture medium was pipetted below the insert and 0.1 ml of the medium above the insert, see Figure 7.3 for the position of the insert. The well plates were then placed in an incubator (Nuaire AutoFlow Nu-5500) at 37 °C and 5 %

$CO_2$. The samples in their wells were kept in the incubator for 2 h to allow for equilibrium prior to cell seeding, for enhanced cell attachment.

Cells were then seeded at a rate of 30,000 ± 1000 into the individual wells containing the sample material and the empty TCP wells used as a control, the process of cell seeding was described in section 7.2(c). The well plates were then returned to the incubator at 37 °C and 5 % $CO_2$ for each time point (either 1, 3 or 7 days, see Figure 7.2). Note that the medium in the wells was aspirated using a sterile micropipette and fresh medium of the same quantity was placed in the wells using a sterile micropipette every 48 ± 2 h. As a control measure, both etched and non-etched 6.4 ± 0.1 mm F018JHB fibre samples were incubated in the culture medium, but without cells, to assess the effects of the medium alone on the fibre samples.

### 7.3.4. Alamar Blue assay

Alamar Blue was selected as an indicator as it is a sensitive, non-radioactive homogeneous assay, has a robust performance and is highly referenced for studies of cell viability and cytotoxicity [232-235]. The low cytotoxicity of the Alamar Blue dye at low concentrations, and the non-toxicity to the user, meant that it did not require any special handling or disposal methods.

Alamar Blue is a fluorogenic redox indicator. Resazurin, the oxidised form of Alamar Blue is blue and non-fluorescent, whereas resorufin the reduced form, is red and highly fluorescent. O'Brien *et al.* [236] suggest that the reduction of Alamar Blue is mediated by mitochondrial enzymes. Whereas Gonzalez *et al.* [237] propose that both the microsomal cytosolic and the enzymes contribute. After considering this dispute combined with their own findings, Bonnier *et al.* [232] suggest that Alamar Blue reduction is the result of multiple metabolic reactions and does not necessarily

specifically indicate a mitochondrial dysfunction. Nonetheless, unanimously they [232, 236, 237] agree that analysis of cell proliferation and cytotoxicity is a vital step in evaluating cellular health and Alamar Blue is a suitable indicator. When a cytotoxic compound interacts with a fibroblast cell, the cell may alter its metabolism. The extent of the Alamar Blue conversion, blue to red, can be quantified by both optical density and fluorescence. Fluorescence measurements were used for the analysis in this work.

#### 7.3.4.1. Alamar Blue assay: method

The Alamar Blue (BIORAD) was stored in a fridge at 4 °C. On the day of testing, the Alamar Blue was diluted to a 1:10 ratio with Hanks Balanced Salt Solution (ThermoFisher) in a 50 ml universal and kept in a water bath at 37 °C wrapped in aluminium foil (Terinex) until testing. Great care was taken to prevent the premixed Alamar Blue solution from being exposed to ambient light as the solution is sensitive to UV radiation.

At each time point (either day 1, 3 or 7, see Figure 7.2) one well plate containing three of each of the sample materials that has been seeded with cells (*i.e.* F018JHB fibres etched, non-etched, the controls and blank cells) was removed from the incubator. The culture medium was aspirated using a fresh sterile 1000 µl micropipette and the cells adhering to the samples were gently rinsed with an equal quantity of fresh PBS. The PBS was then aspirated after 5 ± 1 minutes. This process was repeated three times, using a fresh pipette tip each time to guarantee all media had been removed from the cells and the well plate. 1.15 ml of Alamar Blue was pipetted below the polycarbonate membrane insert and 0.3 ml above the insert. The same total volume was added rigorously to three further TCP wells without cells. These wells were used to help eradicate any background effects by subtracting their recordings from the other

readings. The same total volume was also added to the F018JHB fibres which had not been seeded with cells. The plates were then incubated at 37 °C and 5 % $CO_2$ for 80 minutes. After removal from the incubator to ensure even distribution and complete dissolution of the Alamar Blue indicator, the well plate was wrapped in aluminium foil and placed on a plate-shaking instrument (Heidolph Titramax 100) for 8 minutes at 150 rpm. Each experiment was conducted in triplicate, three aliquots of 100 µl of the now dissolved Alamar Blue indicator in the culture medium, were taken from each well using a sterile micropipette and transferred to a 96 TCP well plate for fluorescence analysis of the metabolic activity. The TCP plates were then returned to the incubator for parallel SEM preparation, see section 7.3.5.

Since fluorescence intensity is sensitive to temperature, the 96 well plates were allowed to equilibrate to room temperature for approximately 30 minutes prior to reading. Using a fluorescence reader (Biotek, FLx800 with KC junior software), the plates were exposed to an excitation wavelength of 560 nm ($\lambda_{ex}$= 560 nm) and the emission at 590 nm ($\lambda_{ex/em}$= 590 nm) was recorded (excitation and emission wavelengths were stated by the Alamar Blue manufacturer protocol).

The fluorescence values for each well plate were determined by subtracting the mean average background reading (provided by the TCP well plates containing solely the Alamar Blue indicator and no cells) from each of the triplicate well plate conditions.

### 7.3.5. Scanning electron microscopy (SEM) preparation of the cytotoxicity test sample materials after Alamar Blue testing

To complement the Alamar Blue results and to help further understanding of the cell behaviour, a cell coverage analysis was performed via SEM on the sample materials (*i.e.* F018JHB fibres etched in propylamine and non-etched, the polycarbonate

membrane in Trial 1 and the bioactive glass fibres in Trial 2) to characterise the morphology and the extent of the cell layer. As discussed in section 7.3.4, Alamar Blue is non-toxic to cells and does not affect the cells' morphology, thus the cells (and the material samples) can be recovered after the assay for further analysis [238].

Succeeding fluorescence measurements, the remaining Alamar Blue was removed with a sterilised micropipette and each well was washed with an equal quantity of PBS to remove any solution residue. This process was repeated three times. The control Ge-Sb-Se fibres etched in propylamine and non-etched were mounted on SEM stubs using a carbon tab directly after this stage.

To preserve the cell's structure and to help maintain their attachment to the sample, the cells were then covered in 3 % Glutaraldehyde fixative (Sigma Aldrich) in 0.1 M cacodylate buffer (Acros Organics) for 30 minutes at room temperature. The fixative was then removed with a micropipette and the cells were washed with 7 % sucrose in 0.1 M cacodylate buffer. This was repeated three times, removing the buffer solution after 5 minutes of contact. To help stabilise the cell lipids and proteins during SEM preparation, 1 % osmium tetroxide (in aqueous solution) was administered by just covering the fibres and left at room temperature for 45 minutes. The osmium tetroxide was then aspirated off and the cells were dehydrated by fully immersing them in a series of aqueous solution of increasing ethanol concentration at room temperature. Initially 20 vol. % ethanol (80 vol. % distilled water) was applied using a micropipette for 2 minutes and then aspirated using the same micropipette. Then 40 vol. % ethanol was applied with 5 minutes immersion time, followed by 60 vol. %, 70 vol. %, 80 vol. %, 90 vol. % and 100 vol. % using the same process. The 100 vol. % ethanol washing was done twice overall. Finally hexamethyldisilazane (HMDS) was used as a drying agent. First the entire well containing the sample materials and cells was submerged in HMDS

for 5 minutes. Once aspirated a smaller quantity of HMDS was applied to cover just the cells and sample material. The wells were left in a sterile fume hood to dry at room temperature for 24 h, to allow the complete evaporation of HMDS. As the samples were placed in an insert, the insert could be removed from the well plate without contact being made to the fibre or moving the fibre's position within the insert. Great care was taken with this step to insure the insert remained flat to prevent the fibre from rolling. The insert was removed from the well plate using two pairs of tweezers, one on each side, and gently placed on a carbon sticky tab mounted onto a SEM stub. Once mounted the sides of the insert were carefully cut and removed. The SEM stub holding the sample was then platinum coated.

Images were captured using a Philips XL30 ESEM-FEG, equipped with an energy dispersive spectroscopy (EDX) system, Oxford instruments with INCA system. Magnification calculations were accurate to within 5 % error.

SEM images were captured at each time point (either day 1, 3 or 7, see Stage 3, Figure 7.2) for each of the sample materials (*i.e.* F018JHB fibres etched in propylamine and non-etched, the polycarbonate membrane in Trial 1 and the bioactive glass fibres in Trial 2). The TCP wells were not analysed with SEM imaging as preparing them for SEM would be very difficult without causing damage to the cells.

### 7.4. Analysis of cell metabolic activity after exposure to fibre F018JHB (core JB04; $Ge_{22}Sb_8Se_{70}$ and cladding JB03; $Ge_{24}Sb_4Se_{72}$) after either being etched in propylamine or non-etched and controls (bioactive glass fibre and polycarbonate membrane) using Alamar Blue assays

The results of the Alamar Blue assays from Trial 1 and Trial 2 are shown in Figure 7.4. Triplicates were taken for each sample, and three samples of each material were tested. The mean value of these values is given for each material with standard deviation error

bars. Statistical analysis was performed using the Prism software package (version 3.02, GraphPad Software). A two-way analysis of variance (ANOVA) was calculated with the Tukey multiple comparison post-test ($P < 0.05$) to compare the significance of change across the samples.

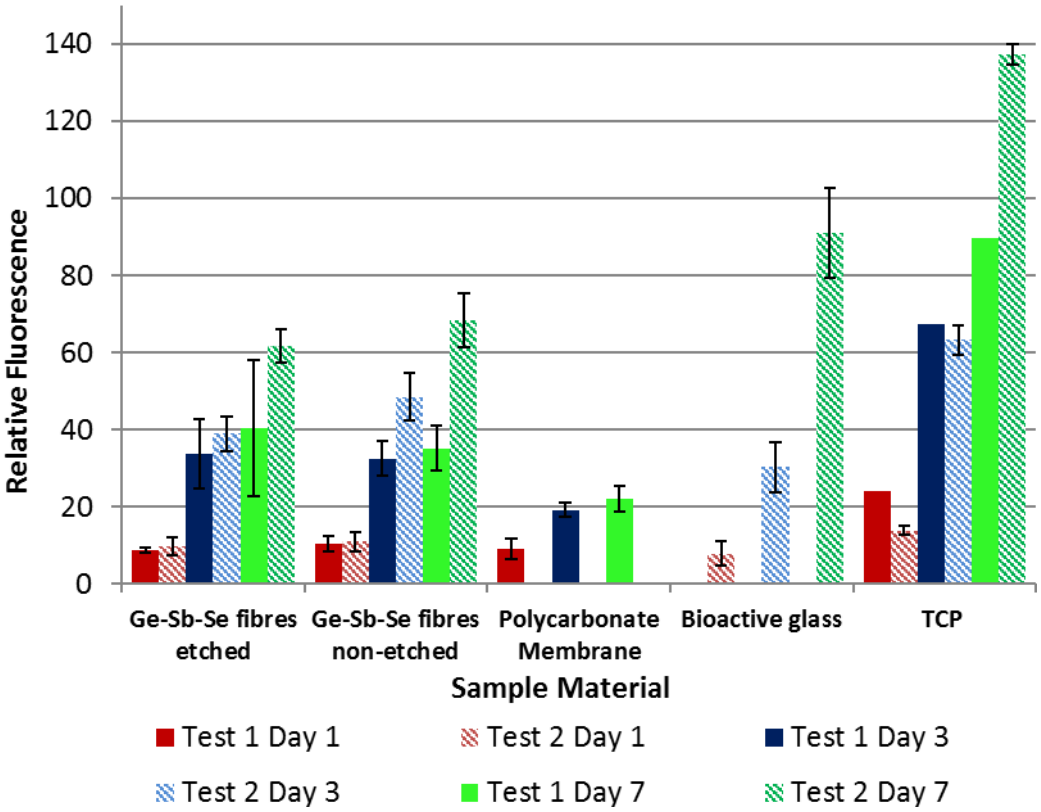



**Figure 7.4 Results for the Alamar Blue assays conducted in Trial 1 and Trial 2 using 3T3 mammalian fibroblast cells. The sample materials used in Trial 1 were, F018JHB fibres (taken from fibre drawn after ~ 3 m in the fibre draw) etched in propylamine and non-etched, polycarbonate membranes and the tissue cultured plastic cell well plate (TCP, polystyrene). The sample materials used in Trial 2 were, F018JHB fibres (taken from fibre drawn after ~ 10 m in the fibre draw) etched in propylamine and non-etched, bioactive glass fibres (phosphate based glass, 45 $P_2O_5$- 16CaO- 10$Na_2O$ – 24MgO – 5$B_2O_3$ (mol %) [231] made 'in-house') and the TCP cell well plate. The level of relative fluorescence (vertical axis) corresponds to the cell metabolic activity. Triplicates were taken for each sample, and three samples of each material were tested. The mean of these values is shown. The error bars indicate the standard deviation of the experiments9o.**

From visual observations made after the Alamar Blue assays in Figure 7.4 of both the F018JHB fibres etched in propylamine and non-etched fibres, it was discovered that on day 3 > 50 % of both sets of fibres had disintegrated in Trial 1. This was not observed

in any of the control F018JHB fibres which were not exposed to cells. In Trial 2 the disintegration had reduced < 20 % for both sets of F018JHB fibres. An example of the damaged F018JHB fibres is illustrated in Figure 7.8.

### 7.4.1. Trial 1

The Alamar Blue assay was conducted using the method detailed in section 7.3.4. The F018JHB fibre (core JB04; $Ge_{22}Sb_8Se_{70}$ and cladding JB03; $Ge_{24}Sb_4Se_{72}$) was taken after approximately 3 m of drawing. The fibres were cut to 6.4 ± 0.1 mm and half of the fibres were etched for ~ 18 minutes in propylamine, the rest remaining non-etched. The polycarbonate membrane (also used as the anchor to hold the F018JHB fibres in place, see Figure 7.3) was selected as an internal control. The TCP well plate without any testing materials was also included.

For Trial 1, the results in Figure 7.4, show that there had been a gradual increase in cell metabolic activity from day 1 to day 7 for all well plate conditions. In contrast to expectations, the polycarbonate membrane, produced the lowest fluorescence readings throughout the duration of the experiment. Polycarbonate is used in the food industry and for medical applications and has been found to comply with ISO 10993-1 (Biological evaluation of medical devices - evaluation and testing within a risk management process) [120, 239]. However its use is controversial, based on its hydrolysis to release bisphenol A (a controversial chemical with concerns about its safety) [240]. Nevertheless, this usually only occurs at high temperatures and it seems unlikely to have occurred at 37 °C, as here.

In Figure 7.4, there was no statistical significant difference (defined as a P value > 0.05) between the average Alamar Blue fluorescence reading for the etched and the non-etched F018JHB fibres.

### 7.4.2. Trial 2

The Alamar Blue assay was repeated using the same method detailed in section 7.3.4. The F018JHB fibre (core JB04; $Ge_{22}Sb_8Se_{70}$ and cladding JB03; $Ge_{24}Sb_4Se_{72}$) was taken after approximately 10 m of drawing. The fibres were cut to 6.4 ± 0.1 mm and half of the fibres were etched for ~ 18 minutes in propylamine, the rest remaining non-etched. Bioactive glass fibres (phosphate based glass, 45 $P_2O_5$- 16CaO- 10$Na_2O$ – 24MgO – 5$B_2O_3$ (mol %) [231] made 'in-house') were selected as a negative control. Phosphate-based bioactive glasses and silica-containing bioglasses, have been recognised to not elicit a cytotoxic response [241-242]. For example, using human ostrosarcoma (MG63) cells, Hasan *et al.* found that a family of bioactive glasses in the glass system $P_2O_5$- CaO- $Na_2O$– MgO– $Fe_2O_3$, gave a good response for cytocompatability in terms of cell viability, proliferation and differentiation when the glasses did not degrade [244]. Bioglass is a commercially available family of bioactive glasses and Bioglass 45S5 (46.1$SiO_2$- 2.6$P_2O_5$- 26.9CaO- 24.4$Na_2O$ (mol %)) has been shown to promote the proliferation of rat fibroblast cells *in-vitro* [243] and to promote *in-situ* tissue regeneration stimulating local tissue repair [244].

Furthermore, the bioactive glass fibres used in this study were initially deemed to be a representation of the Ge-Sb-Se chalcogenide fibres both in geometry and surface properties, allowing comparison between the results. However, after SEM analysis (section 7.5) the validity of this assumption is questioned. It was suggested that due to the smaller fibre diameter (ø) of the bioactive glass fibre, ~ 66 µm ø compared to 242 x 253 µm ø of the F018JHB fibres, several bioactive glass fibres were used in one well. Therefore, a greater surface area was available for cell proliferation. The TCP well plate without any testing materials was also included.

The results for Trial 2 are shown in Figure 7.4. The non-etched F018JHB fibres had no statistically significant difference in fluorescence than the F018JHB fibres etched in propylamine. This was consistent with the results from Trial 1. The metabolic activity of the cells grown on the bioactive glass fibres started more slowly than both sets of F018JHB fibres, although by day 7 it had greatly surpassed them.

### 7.4.3. Discussion

From Figure 7.4, the standard deviation (S.D.) for both Group 1 and Group 2 of the F018JHB fibres (*i.e.* etched in propylamine and non-etched), and the TCP well plate was lower in Trial 2 than in Trial 1 (*e.g.* the maximum S.D. recorded for Trial 1 was for the F018JHB fibres etched in propylamine at day 7 = 17.61, and in Trial 2 the non-etched F018JHB fibres at day 7 = 6.96). However, the standard deviation for the bioactive glass fibres was quite large (11.65) which was pipetted in Trial 2. It is suggested that the higher S.D. for the bioactive glass fibres was on account of an unknown number of bioactive glass fibres being placed in each polycarbonate membrane, thus the surface area exposed to the cells would have varied. The reduction in the S.D. between Trial 1 and Trial 2 could be due to improved pipetting technique. Furthermore, it is suggested that the reduction of the S.D. for the F018JHB fibres is also accounted for by the fact that < 20 % of the fibres disintegrated in Trial 2, compared to > 50 % in Trial 1. Evidence of fibre disintegration was discovered by visual examination after the Alamar Blue assays. SEM images of the damaged fibres are shown in Figure 7.8.

It is suggested that the cells seeded in the TCP well plates exhibited the characteristic cell behaviour of the testing conditions, if the cells had not been exposed to an external influence. In Trial 1, the cells grown on the TCP well plate exhibited significantly

greater fluorescence, > 50 %, after incubation for each time frame (1, 3 and 7 days) than the other testing materials (*i.e.* F018JHB fibres etched in propylamine and non-etched, and the polycarbonate membrane). In Trial 2 > 50 % fluorescence observed by comparing the TCP well plate to the other testing materials (*i.e.* F018JHB fibres etched in propylamine and non-etched, and the bioactive glass fibres) was also obtained. This indicated that exposure to the testing sample materials (*i.e.* the F018JHB fibres both etched in propylamine and non-etched, the polycarbonate membrane and the bioactive glass fibre) had a negative impact on cell metabolism compared to the TCP well plate. However, as was shown in Figure 7.3, it is worth noting that the polycarbonate membrane support reduced the surface area that the cells were seeded onto, to ~ 80 % of the surface area of the TCP well plate. The cells were seeded at the same rate of 30,000 ± 1000 into both the TCP wells and the TCP wells containing the polycarbonate supports. Therefore there was a greater area for cell proliferation and it is proposed that this was also accountable to the greater fluorescence readings of the TCP wells.

It is important to note that there are several other factors that could have contributed to the greater fluorescence readings of the TCP wells. Leachable cytotoxic compounds from the testing materials (*i.e.* both sets of the F018JHB fibres, the polycarbonate membrane and the bioactive glass fibre) could have changed the fibroblast cell's metabolism resulting in a reduction of the fluorescence reading. Furthermore, a material's surface properties such as: surface chemistry, surface energy, surface area and its topography (the deviation of a surface from a perfectly flat plane) have been shown to influence cell behaviour such as adhesion, growth and differentiation [125, 245-252]. The nano- and microstructure of surfaces has been established as a significant factor affecting cell morphology and adhesion [248, 249]. Cousins *et al.* [250] reported that nano-rough surfaces created with silica nanoparticles influenced the fibroblast cell

morphology, reduced cell adhesion and inhibiting cell spreading and thus cell proliferation. It is also considered that the surface properties of a material such as wettability, surface charge and surface structure affects the interaction of fibroblast cells with the material surface [251]. Grinnell *et al.* [252] reported that fibroblast cells show better adhesion and proliferation on wettable surfaces in comparison to non-wettable surfaces. This is further supported by Lucas *et al.* [125] who suggested that the organic liquid/ glass interaction strength of $Te_2As_3Se_5$ chalcogenide glasses was on account of the chalcogenide glass' hydrophobic surface. Thus before conclusion can be drawn as to the cause of the reduction in fluorescence for the testing materials (*i.e.* both sets of the F018JHB fibres, the polycarbonate membrane and the bioactive glass fibre) compared to the TCP well plate, it is suggested that future work should include other cytotoxicity assays, such as the minimum essential media (MEM) elution assay [253, 254], which are independent of the testing material surface properties. Furthermore this would eliminate any physical trauma to the cells from possible movement of the testing materials.

A fairer comparison of the Alamar Blue assay results can be made between the F018JHB fibres etched in propylamine and non-etched. However, no statistical significant difference was observed in Trial 1 between the Alamar Blue fluorescence readings and the S.D. for the etched fibres was large, see Figure 7.4. Additionally, the fluorescence results obtained from Trial 2 also had no difference in statistical significance. Therefore, it is difficult to draw conclusions from the Alamar Blue results alone.

To truly understand the lower bound of the assay, in order to assess whether cells are non-viable, future work should include a positive control (a material that is known to induce a cytotoxic response). This would allow the generation of a rating scale of no,

slight, moderate and severe response grades. Furthermore, it is suggested that the Alamar Blue assays are conducted for a longer time period, > than 7 days. None of the control F018JHB fibres (both etched and non-etched and not seeded with cells) showed any signs of disintegration after incubation in the medium during both Trial 1 and Trial 2. It is suggested that increasing the duration of the experiment would help to confirm that the F018JHB fibres remain stable in aqueous solution and would not become damaged after 7 days. Although establishing whether the F018JHB fibres could be maintained in aqueous solution would not be beneficial for the medical diagnostic system proposed by Seddon [3, 28] in section 2.4.1 (as the system is primarily designed for skin cancer detection), the information would be useful for any further development of the diagnostic system, such as internal diagnosis (*e.g.* endoscopy).

Due to the difficulties highlighted to draw firm conclusions from the Alamar Blue results in Figure 7.4 alone, cell coverage analysis was performed via SEM to characterise the morphology and the extent of the cell layer, see section 7.5.

## 7.5. Cell coverage analysis of fibre F018JHB (core JB04; $Ge_{22}Sb_8Se_{70}$ and cladding JB03; $Ge_{24}Sb_4Se_{72}$) and controls (bioactive glass fibre and polycarbonate membrane) using Scanning Electron Microscopy (SEM)

Fibroblast are morphologically heterogeneous with diverse appearances depending on their location and activity [255]. Usual fibroblast morphology is a large, flat elongated (spindle-shaped) cell with a branched cytoplasm extending out from the cell body [256]. The cell nucleus is flat and oval. Unhealthy (non-viable) cells can often be distinguished as a clump of cells attached to one another with a rounded, swollen morphological appearance, whereas viable cells can be seen as cell spreading (a process where the cells flatten as they adhere to a surface). It was anticipated that the fibroblast cells would

form a confluent layer on the testing materials, if the material did not induce a cytotoxic response.

### 7.5.1. Trial 1

For Trial 1 the Ge-Sb-Se fibre samples (6.4 ± 0.1 mm) etched in propylamine and non-etched were taken from fibre draw F018JHB at ~ 3 m. In Figure 7.5(a-d), the greatest fibroblast cell coverage is shown (of the three samples of each material) for both Group 1 and Group 2 F018JHB fibres, etched in propylamine and non-etched and the polycarbonate membrane after 7 days of incubation.

A nearly confluent layer of cells was seen on the surfaces of the F018JHB fibres etched in propylamine (an example is given in Figure 7.5(a-b)) and on the surfaces of the polycarbonate membranes (an example is given in Figure 7.5(e-f)), whereas only a few cells grew on the non-etched F018JHB fibres (the greatest cell growth for the non-etched F018JHB fibres is shown in Figure 7.5(c-d)).

For the F018JHB fibre etched in propylamine and the non-etched fibre, the SEM images obtained were in agreement with the Alamar Blue assay for Trial 1 (Figure 7.4). After 7 days of incubation the F018JHB fibres etched in propylamine exhibited higher fluorescence in the Alamar Blue assays than the non-etched Ge-Sb-Se fibres. However, the confluent layer on the polycarbonate membrane in Figure 7.5(e-f), is not consistent with the Alamar Blue assay for Trial 1 as the fluorescence readings for the polycarbonate membrane were the lowest for any of the samples in Trial 1 (Figure 7.4).

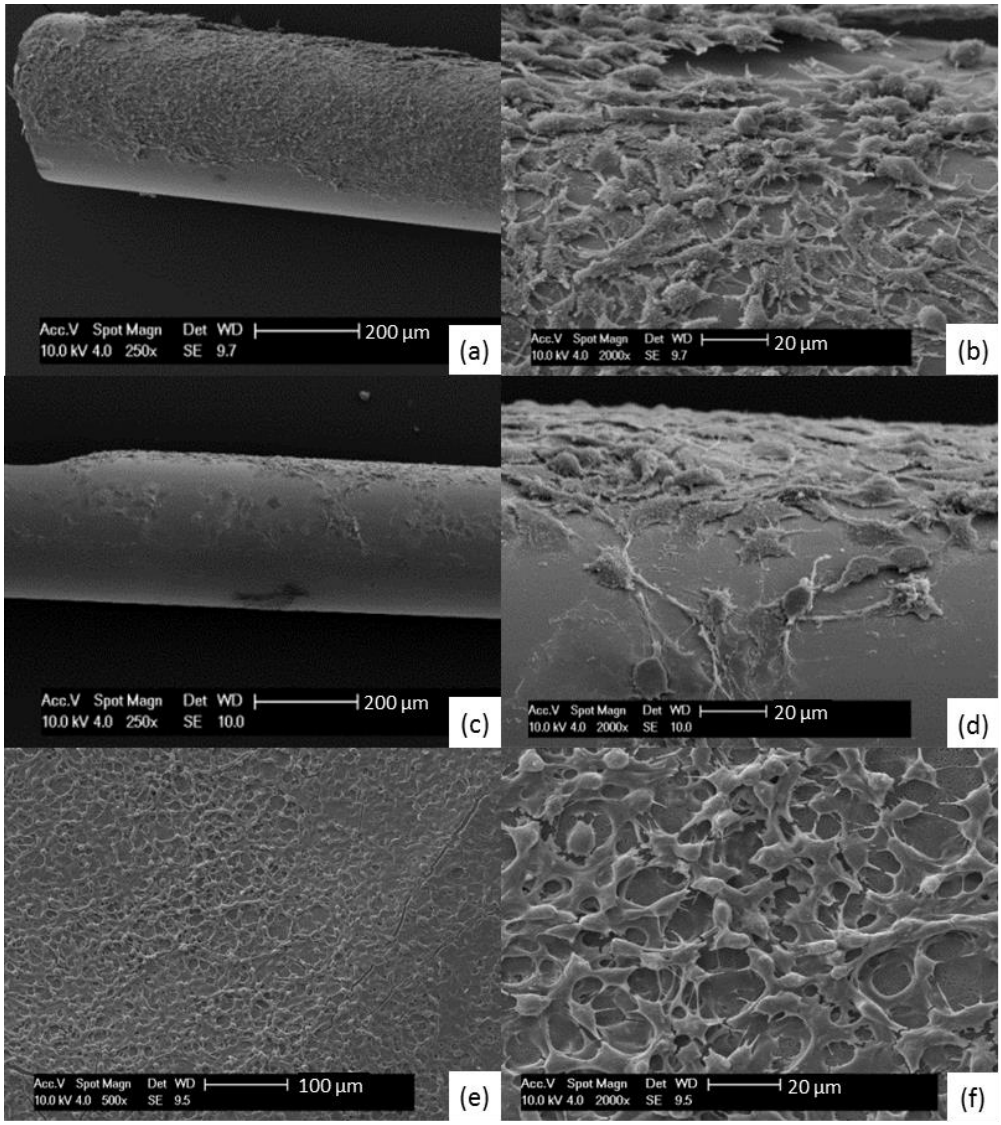



**Figure 7.5 After the Alamar Blue assays conducted on fibre F018JHB (core JB04; $Ge_{22}Sb_8Se_{70}$ and cladding JB03; $Ge_{24}Sb_4Se_{72}$) in Trial 1, SEM observations were made to aid analysis of cellular toxicity. The images (a-f) show the greatest of the cell coverage observed from the three test samples of each material, after 7 day's incubation. (a-b) Group 2, etched F018JHB fibre. It is worth noting that a nearly confluent layer similar to the example shown was observed all the Group 2 fibres. (c-d) Group 1, non-etched F018JHB fibre with best of cell growth. (e-f) Polycarbonate membrane with a confluent layer of cells. It is worth noting that a confluent layer similar to the example shown was observed all the polycarbonate membrane samples. Note (b), (d) and (f) are high magnification images of (a), (c) and (e), respectively.**

### 7.5.2. Trial 2

For the second set of testing, the samples were taken from the same fibre draw F018MINJHB, but from a later stage in the fibre drawing procedure, after ~ 10 m.

Bioactive glass fibres were used as the negative control in the Alamar Blue assay. Figure 7.6 shows the greatest cell growth (of the three samples of each material) after 7 days of incubation with the fibroblast cells, for the F018JHB fibres both etched in propylamine, non-etched and the bioactive glass fibres.

A nearly confluent coverage was observed for two of the three F018JHB fibres etched in propylamine and all of the bioactive glass fibres after 7 days incubation. This is in agreement with the Alamar Blue assay results (Figure 7.4) where the cells grown on the bioactive glass fibres exhibited the highest fluorescence readings after 7 days of incubation, of both Group 1 (non-etched) and Group 2 (etched) of the F018JHB fibres. For example the relative fluorescence of the bioactive glass fibres were 91.17 ± 11.65 and the F018JHB fibres which were etched in propylamine and non-etched were, 61.71 ± 4.44 and 68.38 ± 6.96, respectively.

From comparing the F018JHB fibres etched in propylamine to the non-etched F018JHB fibres, the SEM images are inconsistent with the Alamar Blue assay results from Trial 2 (Figure 7.4). The Alamar Blue results indicated that there was no significant difference in the cells grown on the non-etched F018JHB fibres than the F018JHB fibres etched in propylamine. Whereas, the SEM images showed a confluent layer on two of the three F018JHB fibres etched in propylamine and only a sparse covering of cells on all non-etched F018JHB fibres after 7 days of incubation. It is worth noting that one of the F018JHB fibres etched in propylamine did not have any cell growth (not shown). It is suggested that this would have reduced the Alamar Blue assay fluorescent readings, as the mean of all the three F018JHB fibres etched in propylamine samples was taken. It is therefore recommended that future analysis should disregard large outliers.

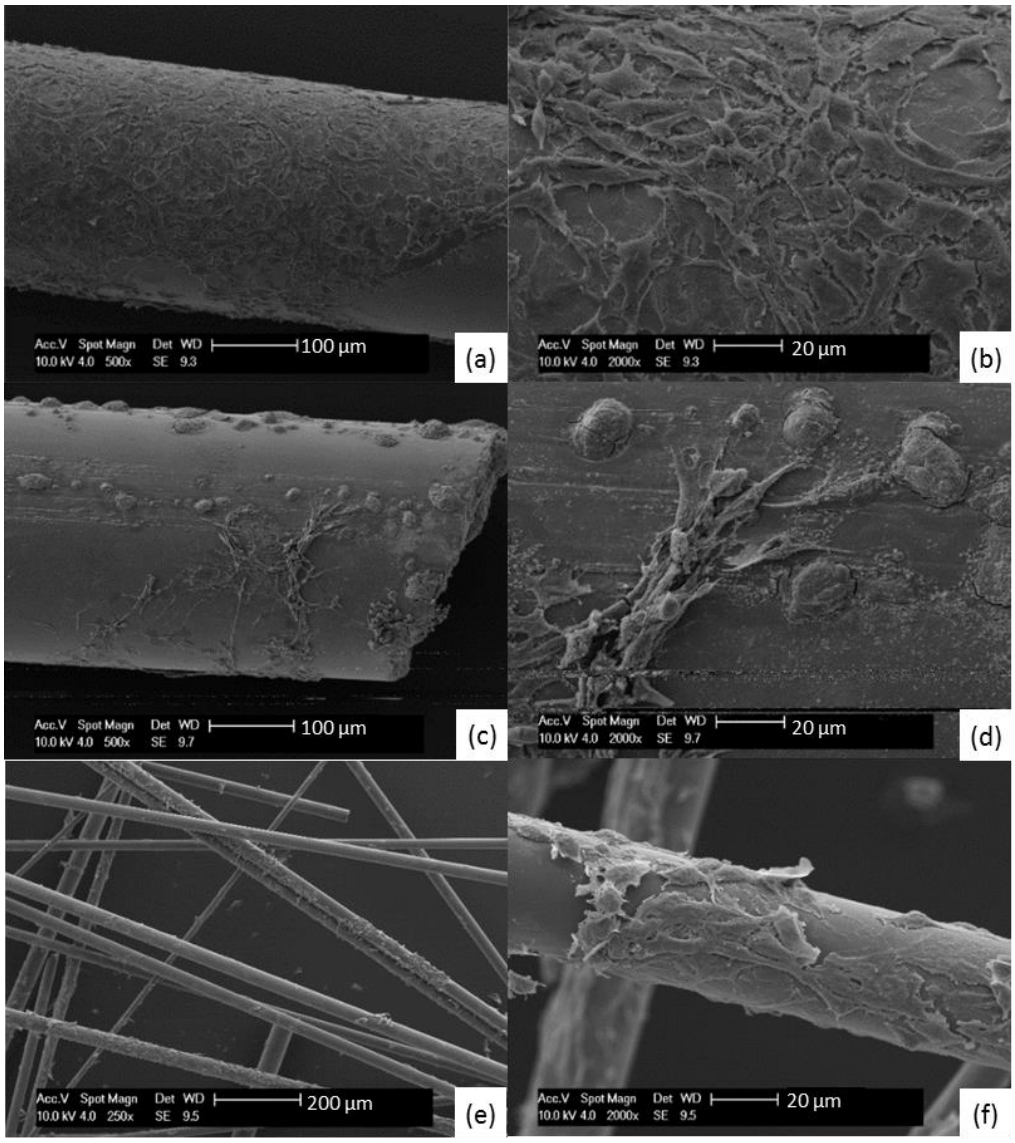



**Figure 7.6. After the Alamar Blue assays conducted on fibre F018JHB (core JB04; $Ge_{22}Sb_8Se_{70}$ and cladding JB03; $Ge_{24}Sb_4Se_{72}$) in Trial 2, SEM observations were made to aid analysis of cellular toxicity. The images (a-f) show the greatest cell coverage observed for each material from the three test samples of each material, after 7 days incubation. (a-b) Group 2, etched F018JHB fibre. It is worth noting that a nearly confluent layer similar to the example shown was observed on two of the Group 2 fibres. (c-d) Group 1, non-etched F018JHB fibre. (e-f) Bioactive glass fibre (phosphate-based glass, $45\ P_2O_5$- $16CaO$- $10Na_2O$ – $24MgO$ – $5B_2O_3$ (mol %) [231] made 'in-house'). It is worth noting that a nearly confluent layer similar to the example shown was observed all the bioactive glass fibres. Note (b), (d) and (f) are high magnification images of (a), (c) and (e), respectively.**

The non-etched F018JHB fibres were not only sparsely covered by cells, but the cells also appeared to be unhealthy, Figure 7.6(c-d). The cells had a substantial difference in morphology from the F018JHB fibres etched in propylamine and the bioactive glass

fibres. The nearly confluent layer of fibroblast cells observed on the F018JHB fibres etched in propylamine and the bioactive glass fibres were flat and elongated. However, the fibroblast cells on the non-etched F018JHB fibres appeared to lose their tight packing and were round. Enlarged images of some of the cells observed on different samples of the non-etched F018JHB fibres are shown in Figure 7.7. Figure 7.7(a-b) are images of the same non-etched F018JHB fibre after 3 days incubation but of different areas of the same fibre and Figure 7.7(c) is a different non-etched F018JHB fibre again after 3 days of incubation. This cell morphology was observed for approximately 70 % of the cells on all the non-etched F018JHB fibres in Trial 2 for every time point (*i.e.* 1, 3 and 7 days).

To confirm that the rounded artefacts seen on the surface of the non-etched F018JHB fibres were fibroblast cells SEM-EDX analysis was conducted. SEM-EDX spectra were taken of several of the artefacts and an example of the SEM-EDX analysis collected from the area shown in Figure 7.7(c) is shown in Figure 7.7(d).

All the SEM-EDX spectra collected identified osmium and oxygen. This suggested that the cell staining agent, osmium tetroxide, used in the SEM preparation (see section 7.3.5), was present. Thus, it is likely that the rounded, porous artefacts were cells. It is suggested that the cells were either unhealthy cells as a result of the potential cytotoxicity of the non-etched F018JHB fibres or from leachable cytotoxic compounds released from the fibres, or poorly preserved cells subjected to damage during the fixing stage of the SEM cell preparation process.

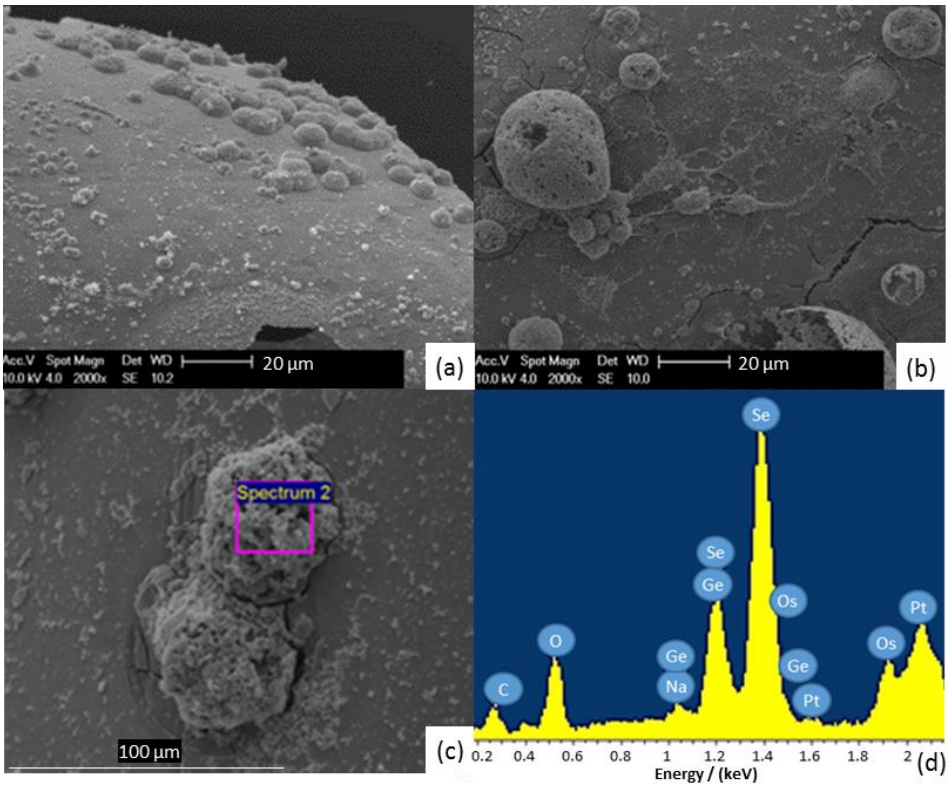



**Figure 7.7. SEM images and SEM-EDX analysis was carried out in Trial 2 to identify swollen artefacts only observed on the non-etched F018JHB fibre surfaces (core JB04; $Ge_{22}Sb_8Se_{70}$ and cladding JB03; $Ge_{24}Sb_4Se_{72}$). Approximately 70 % of the artefacts observed on the non-etched Ge-Sb-Se fibres exhibited this morphology on all of the non-etched Ge-Sb-Se fibres in Trial 2. (a-b) SEM images of different areas of the surface of the same non-etched F018JHB fibre after incubation for 3 days. (c) SEM image of the surface of a different non-etched F018JHB fibre after incubation for 3 days. (d) EDX point scan spectrum using INCA software with a 10 kV electron beam. The spectrum shows the composition includes osmium, as well as organic species and components of the chalcogenide glass (Ge and Se). Osmium tetroxide was used to stain the fibroblast cells during SEM sample preparation, see section 7.3.5.**

### 7.5.3. Discussion

The SEM images of the fibroblast cells grown on the polycarbonate membranes (an example was given in Figure 7.5(e-f) did not corroborate the Alamar Blue assay results. As was shown in Figure 7.4, the fluorescence readings for the polycarbonate membranes were lower than both the F018JHB fibres etched in propylamine and non-etched. As viable cells were observed on the polycarbonate membrane and the cells had proliferated across the surface forming a confluent layer, it was therefore suggested that

the observed lower metabolic activity of the cells on the polycarbonate membrane was not on account of a cytotoxic environment. As was described in section 7.3.4, the Alamar Blue assays were conducted in triplicate and three samples of each material were tested. The S.D. for the polycarbonate membranes fluorescence results were reasonably small (a maximum S.D. of 19.25 relative fluorescence) compared to the F018JHB fibres (a maximum S.D. of 40.33 relative fluorescence for the F018JHB fibre etched in propylamine). Therefore it is suggested that the low fluorescence readings were not on account of poor conduction of the methodology of the Alamar Blue assay or that the Alamar Blue indicator was not performing. A possible reason for the low fluorescence could have been due to the Alamar Blue indicator migrating through the polycarbonate membrane, from the lower compartment of the well plate where the cells had not been seeded. Therefore, the Alamar Blue indicator would have still been in its oxidised resazurin state. This could have diluted the concentration of resorufin and decreased the fluorescence measurement. However, it is worth noting that as was described in section 7.3.4, the plates were incubated for 80 minutes and shaken on a plate-shaker for 8 minutes to help an even distribution of the Alamar Blue indicator. Furthermore, both the etched in propylamine and non-etched F018JHB fibres and bioactive glass fibres were anchored with the polycarbonate membrane, see Figure 7.3. Thus, the cells were also not seeded on the bottom of the TCP well plate.

As was discussed in section 7.3.1, etching of the F018JHB (core JB04; $Ge_{22}Sb_8Se_{70}$ and cladding JB03; $Ge_{24}Sb_4Se_{72}$) glass fibres in propylamine was conducted in an attempt to remove a potentially toxic $Sb_2O_3$ oxide layer on the surface of the fibre. The SEM images provided a clear distinction of the cell proliferation between the etched and non-etched F018JHB fibres. In Trial 1 (Figure 7.5(a-b)) and Trial 2 (Figure 7.6(a-b)), a nearly confluent layer of cells were observed on the majority of fibres which had

been etched in propylamine, similar to the nearly confluent layer of cells observed on the bioactive glass fibres (Figure 7.6(e-f)), a known non-toxic material. For the non-etched F018JHB fibres in Trial 1 only a sparse cell layer was observed (Figure 7.5(c-d)) and in Trial 2 not only was there a sparse cell layer but there was potential evidence of cell swelling and rounding (Figure 7.6(c-d)). It is worth noting that only 5-10 % of the cells on the non-etched F018JHB fibres in Trial 1 exhibited the rounded cell appearance. A possible reason for this could be on account of Trial 2 being conducted approximate six months after Trial 1, thus the F018JHB fibre had been exposed to the atmosphere for longer and the anticipated $Sb_2O_3$ layer could have become denser. Thus, the observed greater proliferation of the fibroblast cells on the F018JHB fibres etched in propylamine than the non-etched F018JHB, could complement the theory that propylamine etching removes the $Sb_2O_3$ toxic layer.

As was discussed in section 7.4.3, a material's surface properties have been shown to influence cell behaviour and morphology. Therefore, it should be considered that the morphology of the cells grown on the non-etched F018JHB fibres, although suggested to be caused by a cytotoxic environment, could also have been on account of the different surface properties of the non-etched Ge-Sb-Se fibre surface compared to the surface properties of the Ge-Sb-Se fibre surface after etching. The fibroblast cells may not have liked the non-etched fibre surface resulting in them not spreading initially, thus the cells could have stayed in their rounded form.

In both trials, no fibroblast cells were observed in SEM images (not shown) on several of the F018JHB fibres both etched and non-etched. This could account for the large S.D. range in the Alamar Blue assay (Figure 7.4). As with any biological assay, reproducibility can be difficult. The absence of cells for both types of fibres: etched and non-etched, could have been due to the seeding rate, contamination, physical

disturbance or the cells may have fragmented or become detached from the fibre during SEM preparation. However, there was always some level of fluorescence in the Alamar Blue assays for all the etched and non-etched Ge-Sb-Se fibres tested at all time points (*i.e.* 1, 3 and 7 days). Therefore, it was expected that even a small number of cells should have been metabolically active at all times in the experiment. It is suggested that as the F018JHB fibres did not completely fill the bottom of the polycarbonate membrane cells could have also proliferated on the polycarbonate surface contributing to the Alamar Blue fluoresce reading.

Dalby *et al.* reported observations of fibroblast cell alignment on grooved quartz slides (12.5 µm wide, 2 µm deep) compared to cells on flat quartz slides [255]. The aligned cell's minor axis (cell width) was narrower for the aligned cells than the cells on the flat surface and the major axis (cell length) was longer for the aligned cells. There is an indication of similar cell behaviour in this Project from comparison of the evenly distributed network of cells on the flat polycarbonate membrane, (Figure 7.5(e-f)) and the potentially aligned fibroblast cells observed on the bioactive glass fibres (ø~ 60 µm) (Figure 7.6(e-f)). However, caution should be taken with making a direct comparison of the cell morphology solely based on the geometry of the samples, as the materials (and therefore the material surface properties) are different.

Chalcogenide glasses are brittle and difficult to handle. As was discussed in section 2.1.1 the Young's modulus of chalcogenide glasses varies from 17 to 18.5 GPa compared to that of silica glass with a Young's modulus of 72.1 GPa [21]. It was stated in section 7.4, that from visual inspection of the F018JHB fibres both etched and non-etched after cell seeding and the Alamar Blue assay, a reduction in fibre disintegration was observed from Trial 1 from > 50 %, to < 20 % in Trial 2. An example of some of the F018JHB fibres which disintegrated in Trial 1 are shown in Figure 7.8. The

damaged F018JHB fibres were mounted on carbon tabs with the disintegrated fragments either reconstructed or the fibre further disintegrated during mounting. It was suggested in section 7.4.3 that the reduction in the disintegration of the fibres between the trials contributed to the decrease in the S.D. from Trial 1 to Trial 2.

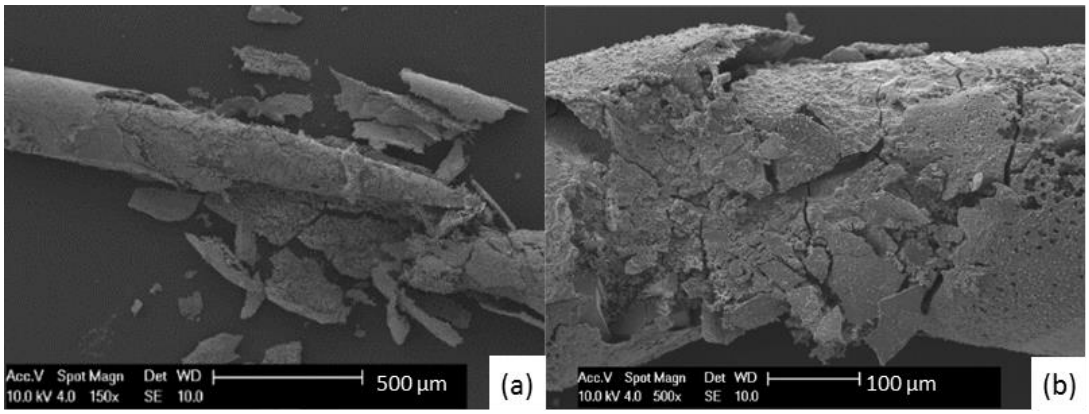



**Figure 7.8 An example of the F018JHB fibre (core JB04; $Ge_{22}Sb_8Se_{70}$ and cladding JB03; $Ge_{24}Sb_4Se_{72}$) disintegration in Trial 1 where over 50 % of both sets of F018JHB fibres were found to disintegrate after three days of incubation. The damaged F018JHB fibres were mounted on carbon tabs with the disintegrated fragments either reconstructed or the fibre further disintegrated during mounting. (a) Non-etched F018JHB fibre. (b) F018JHB fibre etched in propylamine. In Trial 2 less than 20 % of the F018JHB fibres which were etched in propylamine and the non-etched fibres disintegrated (not shown).**

The reduction of the disintegration in Trial 2, was proposed to have been due to reduced human error on account of an improvement in manual handling of the fibres from the experience gained by the student operator in Trial 1. It is suggested that this would have limited micro-cracks and damage to the fibre. Furthermore, for Trial 2 the Ge-Sb-Se fibres came from a later stage in the F018JHB (core JB04; $Ge_{22}Sb_8Se_{70}$ and cladding JB03; $Ge_{24}Sb_4Se_{72}$) fibre drawing, at ~ 10 m (the F018JHB fibres used in Trial 1 were taken at ~ 2 m). Thus, it is proposed that the F018JHB fibres used in Trial 2 might have been in a more stabilised state during fibre drawing, reducing intrinsic stress. It is suggested that further improvements to the preparation of the Ge-Sb-Se chalcogenide fibre samples is to cleave each fibre end using a diamond pen, applying the same

method of fibre cleaving as was used for the fibre loss measurements described in section 3.6.6.3.

However, several of the F018JHB chalcogenide fibres, both etched in propylamine and non-etched, still disintegrated in Trial 2. It is suggested that although the F018JHB fibre was taken from a later stage of the fibre draw in Trial 2, the fibre fabrication procedures would still have created intrinsic residual permanent stress within the fibre, see Chapter 5. It is worth noting that out of all the fibres fabricated in Chapter 5, fibre F018JHB from Pair I (core JB04; $Ge_{22}Sb_8Se_{70}$ and cladding JB03; $Ge_{24}Sb_4Se_{72}$) was deemed to be the most mechanically stable. As was discussed in Chapter 4, section 4.3, the greater mechanical stability was suggested to be on account of the closest match in the region of the sharp increase in instantaneous thermal expansion coefficient of both glass composition, see Figure 4.11. However, this is not to suggest that there were no residual stresses within fibre F018JHB, which may have been exacerbated during cell proliferation. Nonetheless to draw a conclusion of cell viability comparing the F018JHB chalcogenide glass fibres etched in propylamine or non-etched based on the Alamar Blue results in light of the damage to the fibres would be difficult. The fibroblast cells could have experienced physical trauma when the fibres broke impacting their metabolic activity. On the other hand, the resulting many shards of the fibre provided a larger surface area to promote subsequent cell proliferation. Therefore, there would have been other factors affecting the cell viability rather than a direct comparison of the two fibres.

The atomic structure of any glass can be potentially altered when exposed to photonic energy near the optical band gap [257]. It is worth noting that it is standard practice in hospitals to sterilise equipment. Sterilisation of hospital equipment can range from wiping down with an alcoholic infused cloth to Gamma and UV sterilisation [258].

As was shown in Figure 2.4 for a $Ge_xSb_{10}Se_{90}$-x glass system [68], the optical band gap rose with an increase in Ge content up to 25 at.%. This was confirmed in the optical absorption of the Ge-Sb-Se bulk glasses from FTIR analysis in section 4.1.3. The absorption band-edge was highlighted in the inset to Figure 4.4, as follows; $Ge_{24}Sb_4Se_{72}$ at ~ 0.71 µm, $Ge_{22}Sb_8Se_{70}$ at ~ 0.72 µm, $Ge_{20}Sb_{10}Se_{70}$ at ~ 0.75 µm and $Ge_{19}Sb_{15}Se_{66}$ at ~ 0.76 µm. As was discussed in section 4.1.3, it is worth noting that this is not a direct comparison with the $Ge_xSb_{10}Se_{90}$-x glass system reported in [68] as the content of Sb was not kept the same. The emission spectra of an UV mercury arc lamp is shown in Figure 7.9.

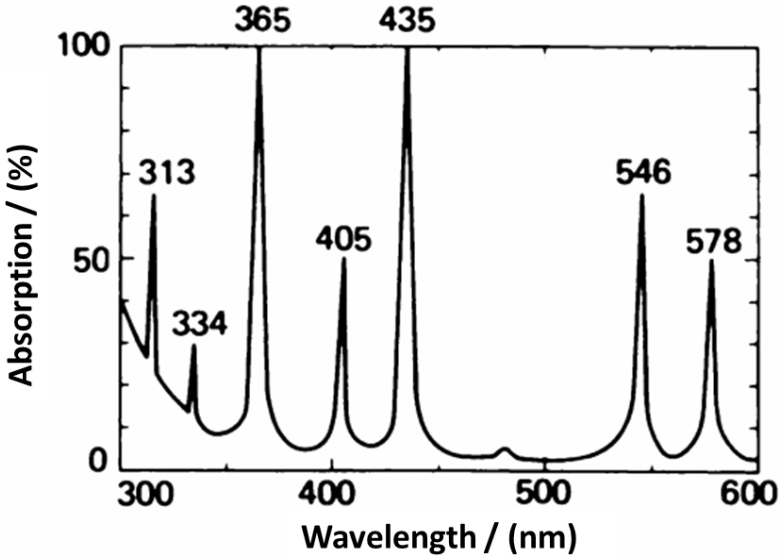



**Figure 7.9 Emission spectra of an ultra-violet (UV) mercury arc lamp. Figure adapted from [259].**

Thus UV radiation is at a higher energy than the band gap of the Ge-Sb-Se chalcogenide glasses and therefore the UV photons would have been absorbed by the glasses. Therefore it is possible that the glasses would have been susceptible to photo-damage which could have contributed to the surface deterioration seen in Figure 7.8. Photo-damage can manifest as photodarkening, photo-crystallisation or photo-chemical effects [260]. The effect of photodarkening was not further investigated in this Project.

## 7.6. Conclusions

The *in vitro* cytotoxicity Alamar Blue assays and subsequent SEM analysis conducted in this Project were part of early discovery efforts to provide important cytotoxicity understanding about the Ge-Sb-Se glass fibres fabricated in this Project. However, if these Ge-Sb-Se fibres were to be used for the medical diagnostic system proposed by Seddon [3, 146] in section 2.4.1, much greater investigation is required to fulfil the standard ISO 10993-5 [120]. Nevertheless, this work has provided some insight into the cell behaviour upon interaction with the F018JHB fibres (core JB04; $Ge_{22}Sb_8Se_{70}$ and cladding JB03; $Ge_{24}Sb_4Se_{72}$) and has provided the foundations for further investigation of the MIR Photonics Group. The general conclusions from this work were:

- The Alamar Blue assay results obtained for the F018JHB fibres etched in propylamine and non-etched were difficult to distinguish and to draw sufficient conclusions from to differentiate between the two surface conditions. Statistical analysis found that there was no significant difference between the two samples. It was suggested that a minimum essential media (MEM) elution assay should be conducted to acquire results independent of material surface properties and compare them to the Alamar Blue results from this Project. The MEM elution assays are designed to demonstrate the cytotoxic effects of potential leachables from a material.

- A reduction in disintegration of both the F018JHB fibres: etched and non-etched, was observed from Trial 1 from > 50 %, to < 20 % in Trial 2. It was suggested that this was on account of better manual handling of the fibres and that the fibre used in Trial 2 was drawn from a later stage of fibre drawing. It was also considered that the UV sterilisation stage might have caused photo-damage of the fibres. An

improvement to the preparation of the Ge-Sb-Se chalcogenide fibre samples was recommended to cleave each fibre end using a diamond pen, applying the same method of fibre cleaving as was used for the fibre loss measurements, described in section 3.6.6.3.

- It was recommended that future work should include a positive control (a material that is known to induce a cytotoxic response) in the Alamar Blue assays to help understanding of the lower bound of the assay. It was suggested that this would allow the generation of a rating scale of no, slight, moderate and severe response grades. Furthermore, it was suggested that the Alamar Blue assays should be conducted for a longer time period, > than 7 days, as increasing the duration of the experiment would help to confirm that the F018JHB fibres remain stable in aqueous solution and would not become damaged after 7 days.

- Cell coverage analysis conducted via SEM was performed to complement the Alamar Blue assays. It was shown that 3T3 mammalian fibroblast cells can be maintained viable in contact with F018JHB fibres etched in propylamine up until 7 days of incubation and a confluent layer of cells grew on most of these etched fibres.
- A confluent cell layer did not form on the non-etched F018JHB fibres and the cell morphology of ~70 % of the cells that were observed differed from the cell morphology on the etched F018JHB fibres and the bioactive glass fibres. Although different surface properties were considered to have contributed to the change in morphology, it was suggested that the cell morphology was likely to be on account of the cells exhibiting phobicity for the non-etched Ge-Sb-Se fibre surface.

### 7.6.1. Final remarks

From the confluent cell layers observed on the F018JHB fibres (core JB04; $Ge_{22}Sb_8Se_{70}$ and cladding JB03; $Ge_{24}Sb_4Se_{72}$) after etching in propylamine and the sparse layer of the potentially non-viable cells observed on the non-etched F018JHB fibres, it is suggested that similar to the $Te_2As_3Se_5$ fibres discussed in section 7.3.1, these initial data demonstrated the potential of the etching technique to reduce any cytotoxic response caused by the Ge-Sb-Se fibres. However, the existence of this anticipated $Sb_2O_3$ layer has not been confirmed and it is suggested for future work that the presence of this oxide layer is established via X-ray Photoelectron Spectroscopy (XPS). For the $Te_2As_3Se_5$ fibres discussed in section 7.3.1, Wilhelm *et al.* showed that the $As_2O_3$ layer dissolved in saline solution and therefore the diffusion of the highly toxic and mobile arsenate ions within the cells was prevented [121]. They also noted that the elemental As within the glass network was stable and insoluble.

Once the $Sb_2O_3$ layer presence is confirmed on the Ge-Sb-Se glasses, with the prospect of clinical application it is important to assess how quickly the oxide layer forms after fibre drawing. If the oxide layer was discovered to grow slowly, fresh Ge-Sb-Se fibres could be used to lower cytotoxicity, however this is impractical and not economical. Encapsulating the fibre in a polymer coating would help to protect the fibre, however currently it is believed that the probe end will have to be bare. Therefore a simple cleaning process would need to be designed. It is suggested that other Ge-Sb-Se glass etching solutions, such as saline, are investigated.

## 7.7. Summary

Cytotoxicity tests are a primary evaluation technique to identify the presence of toxins or other potentially harmful effects caused by cell interaction with materials. This

chapter conducted *in vitro* preliminary cytotoxicity assessment of the F018JHB fibres (core JB04; $Ge_{22}Sb_8Se_{70}$ and cladding JB03; $Ge_{24}Sb_4Se_{72}$) characterised in Chapters 4-6. The preparation of the cell culture medium, defrosting the cell lines, cell concentration and cell counting were described in section 7.2. The preparation of the F018JHB fibres for the Alamar Blue assays and subsequent SEM analysis, cell seeding and the methodology of the Alamar Blue assays were described in section 7.3. It was suggested that potential cytotoxicity of the Ge-Sb-Se fibres could be on account of a cytotoxic $Sb_2O_3$ surface layer. Therefore, half of the F018JHB fibres were etched in propylamine with the anticipation that the oxide layer was removed. The Alamar Blue assays were conducted in two trials discussed in section 7.4. However, drawing comparisons between the etched in propylamine F018JHB fibres and the non-etched F018JHB fibres were inconclusive. Nevertheless, the subsequent SEM images shown in section 7.5 provided characterisation of the extent of cell attachment to the F018JHB fibre surfaces. There was a distinct difference in the cell spreading and the cell morphology between the cells on the F018JHB fibres etched in propylamine and the non-etched F018JHB fibres. Final conclusions made from the preliminary cytotoxicity work were given in section 7.6.

# 8. Structure-property relationship of Ge-Sb-Se glasses along the stoichiometric tie-line x($GeSe_2$)-(1-x)( $Sb_2Se_3$)

## 8.1 Overview

This chapter presents an initial study of the structure of a series of stoichiometric germanium-antinomy-selenium (Ge-Sb-Se) glasses. Six glass compositions along the stoichiometric tie-line, x($GeSe_2$)-(1-x)( $Sb_2Se_3$) (shown in Figure 2.5) where x = 0.4, 0.5, 0.6, 0.7, 0.8 and 0.9, are investigated using neutron diffraction. The basic structural units expected, [$GeSe_4$] and [$SbSe_3$], were shown in Figure 2.3.

The Ge-Sb-Se glasses characterised in Chapters 4-7 had Se rich compositions. Therefore, it is suggested these glasses would contain Se-Se chains in between the [$GeSe_4$] and [$SbSe_3$] units. As was discussed in section 2.2, the total correlation function T($r$) measures the frequency of the occurrence of interatomic distances in the sample. However, the Se-Se peak is at the same interatomic distance in T($r$) as the Ge-Se peak [261], making it difficult to differentiate between the two peaks. The stoichiometric tie-line within the Ge-Sb-Se glass series was selected for this initial neutron diffraction study to minimise the number of different potential bonds present. Therefore, the assumption has been made in this work that there was no Se-Se bonding within the x($GeSe_2$)-(1-x)( $Sb_2Se_3$) glass series and the glasses solely consisted of [$GeSe_4$] and [$SbSe_3$] units. Due to the non-periodic nature of glass it is necessary to specify the co-ordinates of each atom in order to define the structure. However, this is not practical and, in reality, glasses are described using

statistical averaging. To extract the average Ge-Se and Sb-Se bond lengths and co-ordination numbers here, peak fitting was used.

As was discussed in section 2.2 the neutron diffraction patterns were collected using the GEM diffractometer [74] at the ISIS Neutron and Muon source, Rutherford Appleton Laboratory, UK. The preparation of the Ge-Sb-Se chalcogenide glass rod samples and the methodology of the data analysis from the neutron diffraction experiments are described in section 8.2. The results of density, glass transition temperature ($T_g$) and neutron diffraction measurements are presented in section 8.3 and the results are further discussed in section 8.4. Final conclusions are given in section 8.5 and this chapter is summarised in section 8.6.

## 8.2 Preparation and methodology

### 8.2.1 Ge-Sb-Se glass melting and characterisation

The compositions of the Ge-Sb-Se chalcogenide glasses for structural analysis are stated in Table 8.1. The glasses were fabricated using the melting-quenching method which was described in section 3.2.4. The contraction cone was removed from the as-annealed Ge-Sb-Se glass rods, using the method which was described in section 3.3.1. This generated glass rods of lengths ranging from 30 – 46 mm. The specific dimensions of the Ge-Sb-Se glass rods are given in Table 8.1.

Density and glass transition temperature ($T_g$) measurements were conducted on the glass rods prior to neutron diffraction experimentation, as the properties were required for the neutron diffraction analysis. The entire length of the rod, as

stated in Table 8.1, was used for the density measurements using a helium gas pycnometer (Micromeritics, AccuPyc 1330), the method was described in section 3.6.3. The removed contraction cone was used for the onset $T_g$ measurements, using differential scanning calorimetry (DSC) equipment (Perkin Elmer DSC7 and Pyris 1 DSC analyser) as was described in section 3.6.4.

### 8.2.2 Ge-Sb-Se glass rod preparation for neutron diffraction experiments

The Ge-Sb-Se glass rods were placed in either 8.3 mm or 10.3 mm diameter (ø) vanadium cans, depending upon the rod's outer diameter (OD) (the OD was determined by the size of the silica glass ampoule that it was melted in, see section 3.1.1 for ampoule selection). The neutron beam size was 40 x 15 mm, the size of the rods was such that the height of the beam was filled, where possible. The individual dimensions of each Ge-Sb-Se glass rod are stated in Table 8.1. Data were also collected from empty 8.3 mm ø and 10.3 mm ø vanadium cans, the empty diffractometer and a vanadium rod (8 mm ø, 70 mm length). The vanadium cans had thin walls (25 μm) to minimise the amount of scattering from the can, which reduced the magnitude of the experimental corrections required. The incident neutron beam on the GEM diffractometer, with flux $I_0$, had a range of different energies which gave rise to a flux profile which needed to be removed to obtain the scattering pattern for the sample. Vanadium scatters neutrons incoherently (the scatter occurs in all directions). Thus the scattering is independent of Q (the magnitude for the scattering vector for elastic scattering) and contains negligible structural information. Therefore, the scattering from a vanadium rod enabled the neutron flux profile to be measured. This neutron flux profile and the scattering from the vanadium cans,

could then be mathematically removed from the Ge-Sb-Se glass rod experimental data to leave the total scattering pattern for the sample, I(Q), which was a sum of $I^s(Q)$ (the self-scattering data) and i(Q) (the distinct scattering data). The corrections to the data for background scattering are further discussed in section 8.2.3.1 The GEM diffractometer was comprised of eight detector banks, as was shown in Figure 2.7, covering an angular range of 1-171 ° [74]. The collection time was between 6-8 hours, depending on the individual sample (*e.g.* diameter and composition), to gather 750 – 1000 µamps. GEM had an automatic sample holder, which changed the sample after each measurement.

**Table 8.1 Melt number, compositions, vanadium can size used and sample size for the Ge-Sb-Se chalcogenide glass samples along the stoichiometric tie-line x($GeSe_2$)-(1-x)($Sb_2Se_3$) analysed in the neutron diffraction experiments at the ISIS Neutron and Muon source, Rutherford Appleton Laboratory, UK.**

| Melt number | Composition / (at. %) | Value of x | Vanadium can diameter / (mm) | Height of the Ge-Sb-Se glass rod / (mm) |
|---|---|---|---|---|
| M044JHB | $Ge_{10}Sb_{29}Se_{61}$ | 0.4 | 8.3 | 46 |
| M033JHB | $Ge_{13}Sb_{25}Se_{62}$ | 0.5 | 8.3 | 46 |
| M032JHB | $Ge_{16}Sb_{21}Se_{63}$ | 0.6 | 8.3 | 30 |
| M031JHB | $Ge_{19}Sb_{17}Se_{64}$ | 0.7 | 8.3 | 37 |
| M047JHB | $Ge_{23}Sb_{12}Se_{65}$ | 0.8 | 10.3 | 37 |
| M048JHB | $Ge_{28}Sb_{6}Se_{66}$ | 0.9 | 10.3 | 37 |

Additional to the Ge-Sb-Se glass series stated in Table 8.1 the glass composition $GeSe_2$ was also used for the structural analysis in this Project. Neutron diffraction data for $GeSe_2$ were obtained from [261]. The data were obtained from the SANDALS (Small Angle Neutron Diffractometer for Amorphous and Liquids Samples) instrument at the ISIS Neutron and Muon source, Rutherford Appleton Laboratory, UK. It is worth bearing in mind that, due to the different instrument set-ups and data processing, as well as variations between the

instrumentation, small discrepancies between data gathered by SANDALS and GEM could be introduced.

### 8.2.3 Neutron scattering diffraction: analysis of data to extract T(*r*)

A brief theory of how neutron diffraction can give rise to structural information was given in section 2.2. The definitions and equations were stated for the differential cross-section, $\frac{d\sigma}{d\Omega}$ (Equation 2.1), the magnitude of the scattering vector for elastic scattering, Q (Equation 2.2) and the total scattering of neutrons from the sample, I(Q) (Equation 2.3). The term distinct scattering, i(Q), was defined as the interference between scattered waves from different nuclei and it was stated that i(Q) contained the structural information for the scattering system. The term self-scattering, $I^S(Q)$, was defined as the interference between scattered waves from the same nucleus in an atom within a sample. The processing involved in the extraction of i(Q) data is given in section 8.2.3.1 and the calculations to obtain the total correlation function T(*r*) from i(Q) are described in section 8.2.3.2. The calculations performed to obtain the co-ordination number for the Ge-Sb-Se glasses are given in section 8.2.3.3.

#### 8.2.3.1 Extracting distinct scattering data, i(Q)

Before i(Q) could be obtained, a series of corrections were applied to the neutron diffraction data. These were conducted using GUDRUN (including Xsect) [262] and the ATLAS [263] suite of programs (This software was run in Open Genie, and correction levels to match i(Q) to $I^S(Q)$ were carried out using Excel [264]). Figure 8.2 schematically shows the order of these corrections and calculations.

The GUDRUN software, which was used to help analyse the neutron scattering data employed here, was implemented in five stages to correct the data. These stages shall only briefly be discussed, but are described in detail in the GUDRUN manual [262]. As highlighted in section 8.2.2, it was necessary to remove the instrument background from the I(Q) scattering data collected for the samples and the empty vanadium cans. Firstly, I(Q) data were collected with an empty diffractometer (*i.e.* no vanadium cans or samples). Secondly, the I(Q) data for the Ge-Sb-Se glass rod samples and the vanadium cans were normalised to remove the neutron flux profile using the scattering for the vanadium rod. The sample I(Q) data were then further amended to remove the scattering from the vanadium can, corrected for attenuation effects (attenuation = $e^{-\mu t}$ where μ is the linear attenuation coefficient and t is the sample thickness) and for inelastic effects (*i.e.* neutrons can gain or lose energy in the scattering process as they scatter inelastically) by applying the inelasticity correction, first calculated by Placzek [265]. Finally, the I(Q) sample data was normalised to the number of atoms in the sample using the effective density (*i.e.* the number of atoms that are in the path of the neutron beam) which was calculated from the mass and the volume of the sample in the vanadium can.

I(Q) extracted from the raw data only covered a finite range in Q due to it being limited by the I(Q) oscillations, which provide the structural information, becoming weaker at higher Q as they are masked by instrument noise. For the experiments described here the high Q ($Q_{max}$) limit of useable data was 35 $Å^{-1}$, and the low Q limit (determined by the λ and θ range of the experiment) was ~ 0.3 $Å^{-1}$.

PLATOM, part of the ATLAS suite of software, was used to calculate $I^S(Q)$. To calculate the $I^S(Q)$ for a particular Ge-Sb-Se composition, it was necessary to know the relative molar amounts and scattering lengths of the Ge, Sb and Se elements present. The scattering lengths of the elements are shown in Figure 8.1. Any slight difference (*e.g.* such as compositional difference in nominal composition and as-batched composition) in scattering levels between the I(Q) data and the calculated $I^S(Q)$, were corrected and removed in Excel and the INTERFERE program [264]. $I^S(Q)$ was then subtracted from the normalised I(Q) data to give the distinct scattering data, i(Q). Finally, the MERGE program [264] was used to combine the normalised I(Q) data from different banks to produce a single merged i(Q) data set.

#### 8.2.3.2 Calculating total correlation function, T(*r*), from i(Q)

As was mentioned in section 2.2 the i(Q) term from the total scattering can be interpreted in terms of correlation functions. The total correlation function, T(*r*), is a measure of the frequency of the occurrence of a particular interatomic distance in a sample in real space.

To obtain T(*r*), i(Q) was Fourier transformed in Open Genie. As mentioned in section 8.2.3.1 i(Q) data does not cover an infinite range and was capped at a finite maximum value, $Q_{max}$. After Fourier transformation, this finite Q range caused termination ripples in the real space data (i(Q) data was measured in reciprocal space). A Lorch modification function [266], $M(Q)$, was used to reduce the termination ripples, however applying $M(Q)$ also caused the broadening of peaks in T(*r*) in real space. The Lorch modification function in

Equation 8.1, is a sine function which dampened i(Q) at values near Q = 0 and $= Q_{max}$. For the calculations in this Project $Q_{max}$ = 35 $Å^{-1}$.

$$M(Q) = \frac{\sin \Delta rQ}{\Delta rQ} \quad Q \leq Q_{max} \qquad \textbf{Equation 8.1}$$

$$M(Q) = 0 \qquad Q > Q_{max}$$

where $\Delta r$ (the resolution in r space, as was shown in Figure 2.6) $= 2\pi / Q_{max}$. Equation 8.2 was used to calculate T($r$):

$$T(r) = T^0(r) + \frac{2}{\pi}\int_0^\infty Qi(Q)M(Q)\sin(rQ)\,dQ \qquad \textbf{Equation 8.2}$$

where r is the distance between atoms in the glass and $T^0(r)$ is the average density contribution to the correlation function. $T^0(r)$ is calculated from Equation 8.3.

$$T^0(r) = 4\pi r n^0 \left(\sum_j c_j \bar{b}_j\right)^2 \qquad \textbf{Equation 8.3}$$

where $n^o$ is the average atomic number density, $c_j$ the atomic fraction for element $j$ and $\bar{b}_j$ is the coherent neutron scattering length (the correlated motions of the atoms) for element $j$. When $j$ = Ge, Se and Sb, b = 8.185, 7.97 and 5.57, respectively, see Figure 8.1.

Gaussian peaks were used to fit the peaks in T($r$) within the real space resolution (section 8.3.2.4). From these fits the coordination number, $n$ , and bond lengths of the Ge-Sb-Se glasses were extracted (section 8.3.2.4).

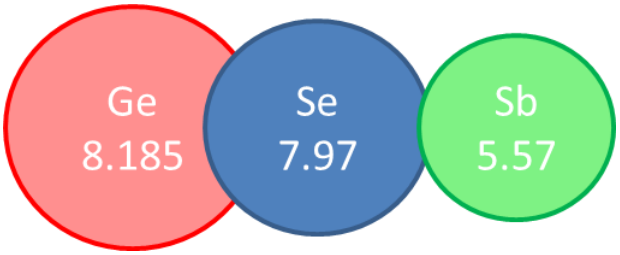



**Figure 8.1 The neutron scattering length (*b*) of germanium (Ge), antimony (Sb) and selenium (Se). The radius of each circle is scaled with *b* [267].**

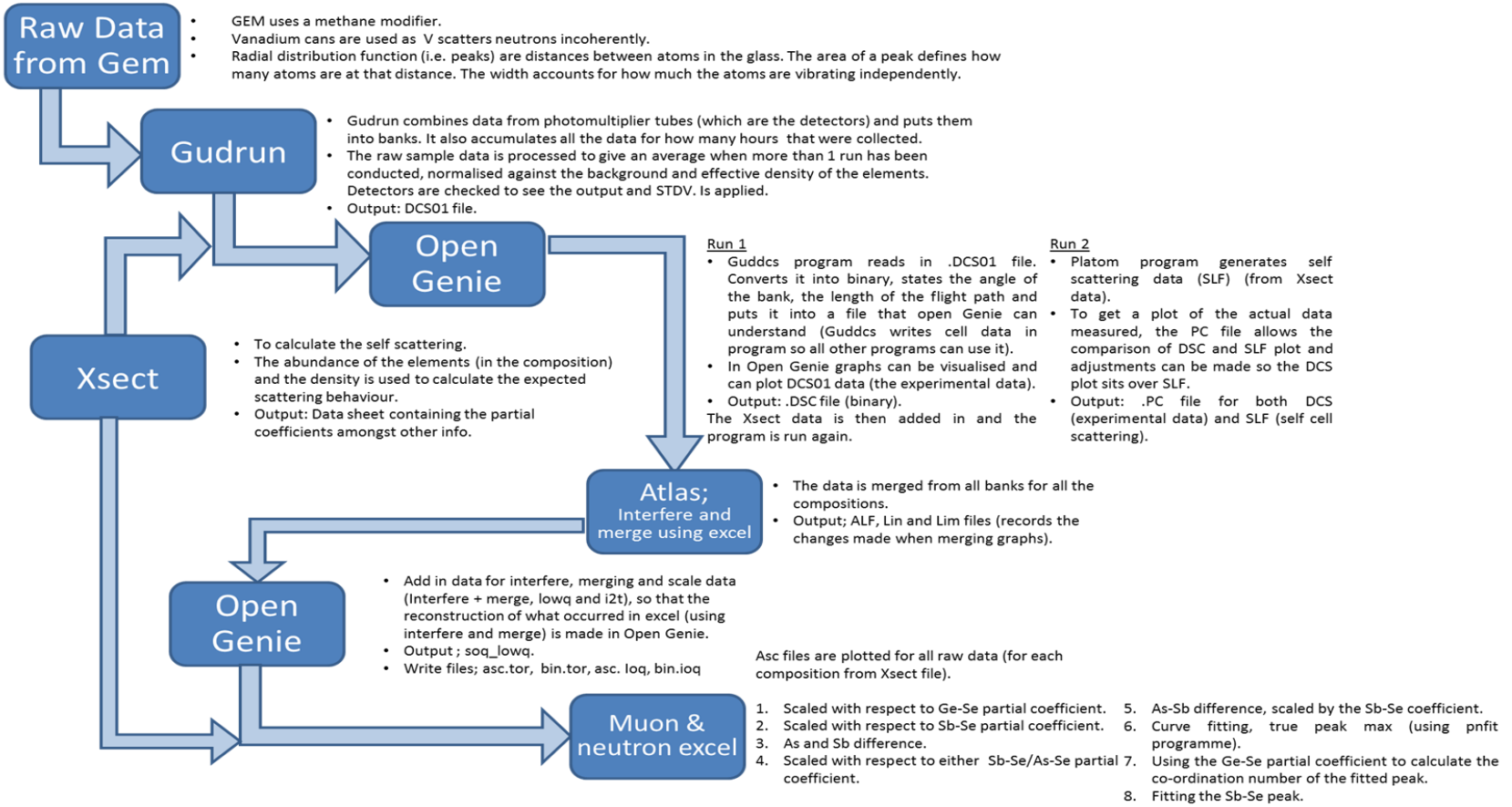



**Figure 8.2 Flow chart to show the stages of the analysis applied in this Project in order to obtain glass structural information from the neutron diffraction data. Distinct scattering, i(Q), and self-scattering, $I^s(Q)$, were extracted from the total scattering of neutrons from the Ge-Sb-Se chalcogenide glass rods, I(Q), obtained from the GEM diffractometer at the ISIS Neutron and Muon Source, Rutherford Appleton Laboratory Didcot, UK.**

#### 8.2.3.3 Calculating the co-ordination number, $n$, of the Ge-Sb-Se glasses from the total correlation function T($r$)

Once T($r$) had been calculated, the coordination numbers, $n$, for Ge-Se and Sb-Se were extracted. T($r$) is the sum of all the partial correlation coefficients functions of each element within a sample. Every peak in T($r$) arises from a particular pair of elements (*e.g.* Ge and Se). $n$ can be calculated from peak area (*e.g.* $A_{Ge-Se}$ ) and the interatomic distance between the elements (*e.g.* $r_{Ge-Se}$) is given by the position of the peak, Equation 8.4.

$$\boldsymbol{n_{jk}} = \frac{\boldsymbol{r_{jk}A_{jk}}}{\boldsymbol{(2-\delta_{jk})c_j\bar{b}_j\bar{b}_k}} \qquad \textbf{Equation 8.4}$$

where $j$ and $k$ are a pair of elements in the sample (*e.g.* Ge and Se), $\delta_{jk}$ is the Kronecker delta and $c_j\bar{b}_j\bar{b}_k$ is the coefficient for the partial correlation coefficients.

## 8.3 Results

### 8.3.1 Onset glass transition temperature ($T_g$) and density results

No crystallisation peaks were found for any of the glasses along the tie-line x($GeSe_2$)-(1-x)( $Sb_2Se_3$) with x varying from 0.4 to 0.9, in the DSC curves (in the measured temperature region up to 350 ºC) as shown in Figure 8.3.

As was mentioned in section 8.2.2 the glass composition $GeSe_2$ was also included in the Ge-Sb-Se chalcogenide glass structural analysis. $T_g$ and density data for $GeSe_2$ were obtained from [268]. The change in onset $T_g$ and density for the six Ge-Sb-Se glasses along the stoichiometric tie-line x($GeSe_2$)-(1-x)( $Sb_2Se_3$) with x varying from 0.4 to 1, are shown in Figure 8.4 and summarised in Table 8.2.

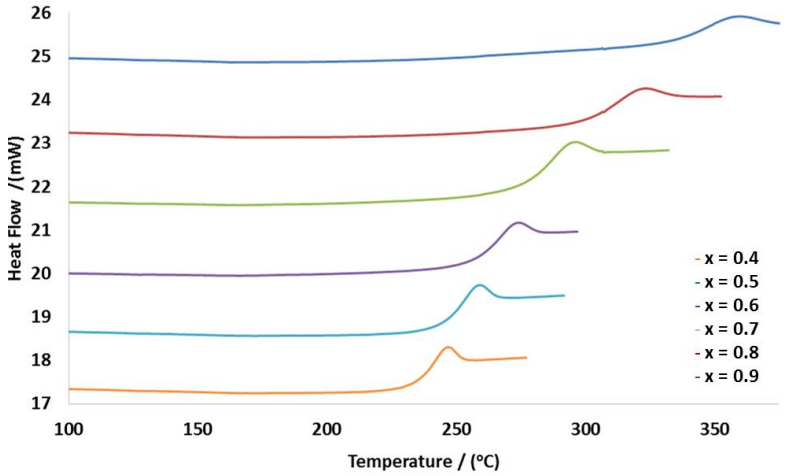



**Figure 8.3 The compositional dependences of onset $T_g$ (calculated from a DSC curve) for the stoichiometric tie-line x($GeSe_2$)-(1-x)($Sb_2Se_3$) where x = 0.9 (dark blue), 0.8 (red), 0.7 (green), 0.6 (purple), 0.5 (light blue) and 0.4 (orange). The graphs are vertically shifted for clarity.**

In Figure 8.4 it can be seen that the onset $T_g$ values were found to decrease when the Sb concentration increased. It was considered that two linear trend lines could be fitted for the $T_g$ data. The linear fit for values between x = 0.4 - 0.7 had a correlation coefficient ($R^2$) = 0.987 and for values between x = 0.7 - 1and $R^2$ = 0.974.

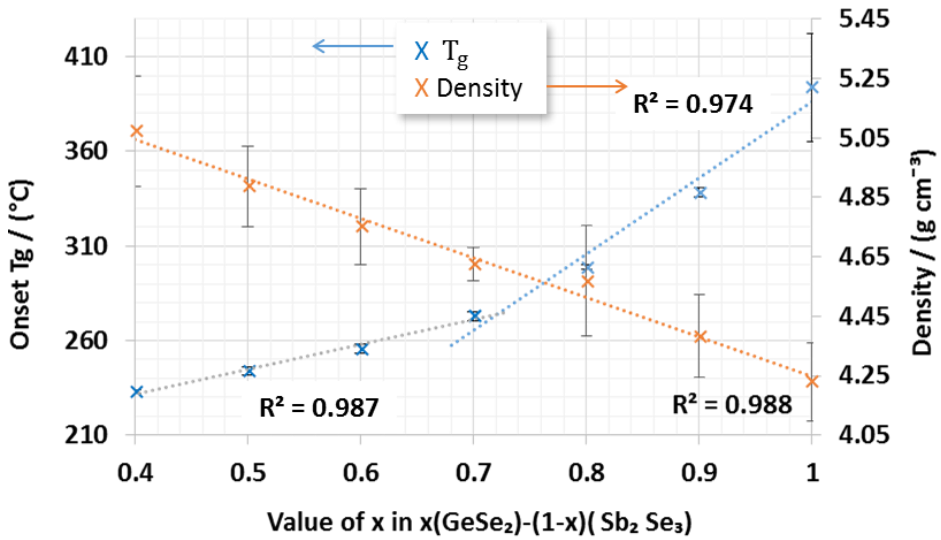



**Figure 8.4 The compositional dependences of onset $T_g$ in blue (calculated from a DSC curve) and density in orange (using helium pycnometers) for the stoichiometric tie-line x($GeSe_2$)-(1-x)($Sb_2Se_3$) where x = 0.9, 0.8, 0.7, 0.6, 0.5 and 0.4. The values for x= 1 were obtained from [268].**

Densities for the x($GeSe_2$)-(1-x)($Sb_2Se_3$) glass system ranged from 4.23 to 5.07 ± 0.19 g $cm^{-3}$, increasing linearly as Ge was substituted for Sb. In Figure 8.4 it can be seen that a single line of best fit to the data had a $R^2$ = 0.988.

**Table 8.2 Compositions and properties (density and onset $T_g$) listed for the Ge-Sb-Se glass samples used in the neutron diffraction experiments at ISIS Neutron and Muon source, Rutherford Appleton Laboratory, UK.**

| Value of x | Theoretical composition / (at. %) | Density / (gm/$cm^3$) | Onset Tg / (°C) |
|---|---|---|---|
| 0.4 | $Ge_{10}Sb_{29}Se_{61}$ | 5.07 ± 0.19 | 233 ± 1 |
| 0.5 | $Ge_{13}Sb_{25}Se_{62}$ | 4.89 ± 0.14 | 244 ± 2 |
| 0.6 | $Ge_{16}Sb_{21}Se_{63}$ | 4.75 ±0.13 | 256 ± 2 |
| 0.7 | $Ge_{19}Sb_{17}Se_{64}$ | 4.62 ± 0.06 | 273± 2 |
| 0.8 | $Ge_{23}Sb_{12}Se_{65}$ | 4.57 ± 0.19 | 299 ± 2 |
| 0.9 | $Ge_{28}Sb_6Se_{66}$ | 4.38± 0.13 | 338 ± 2 |
| 1 | $GeSe_2$ | 4.23 ± 0.13 | 394 ± 28 |

### 8.3.2 Neutron scattering diffraction results

The structure of the x($GeSe_2$)-(1-x)($Sb_2Se_3$) glass series where x = 0.4, 0.5, 0.6, 0.7, 0.8 and 0.9, were studied using pulsed-neutron diffraction techniques. The generation of i(Q) for each glass sample was explained in section 8.2.3.1. For the analysis in this section i(Q) was obtained via an amalgamation of data from detector banks 3, 4 and 5. These banks covered a range of mean scattering angles from 24 ° to 114 ° and the results are shown in section 8.3.2.1. The calculations to obtain T(*r*) from i(Q) were described in section 8.2.3.2. The T(*r*) results are given in section 8.3.2.2 and results of the T(*r*) scaled by the partial correlation coefficients (*e.g.* $t_{GeSe}$ and $t_{SbSe}$) are given in section 8.3.2.3. To extract the bond lengths and the coordination number of the [$GeSe_4$] and [$SbSe_3$] units, the first two peaks in the correlation function were fitted, discussed in section 8.3.2.4.

#### 8.3.2.1 Neutron distinct scattering, *i*(*Q*)

The distinct scattering, i(Q) , for each of the samples is shown in Figure 8.5.

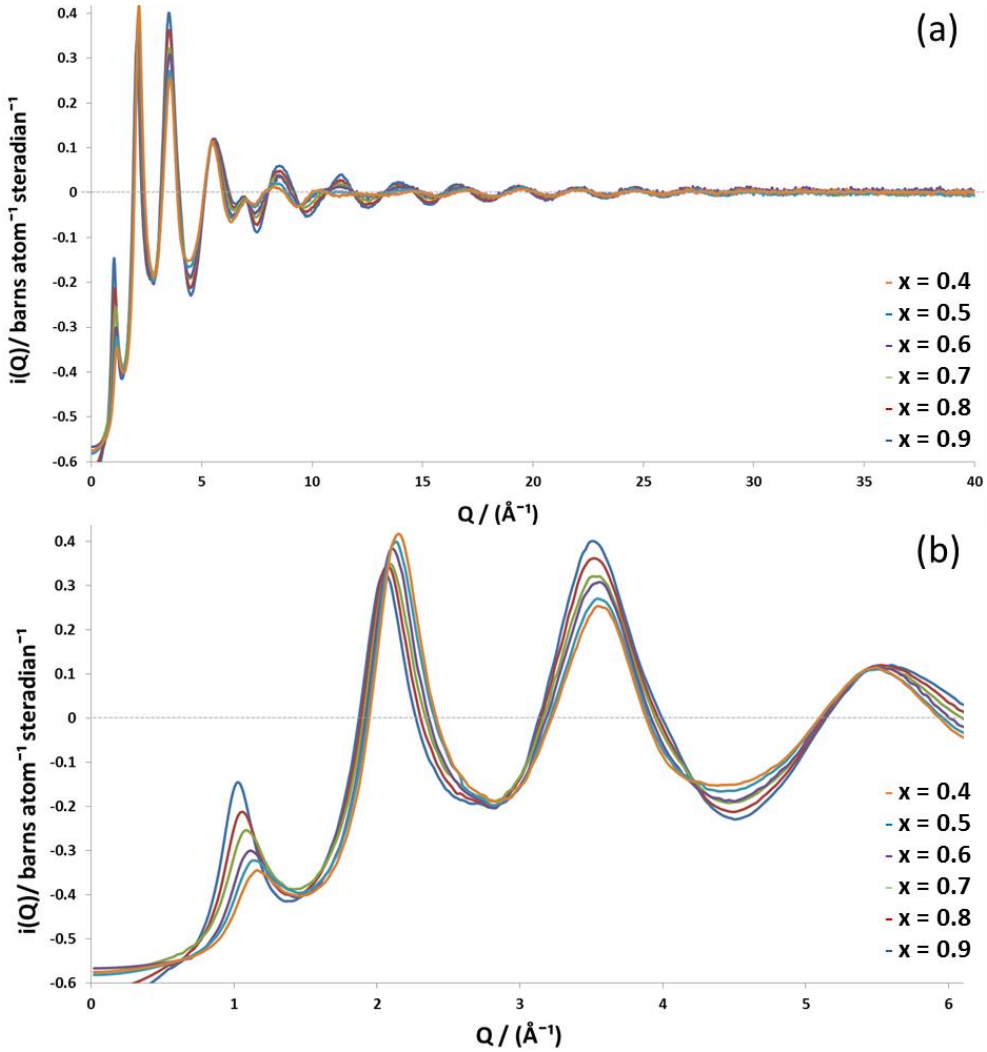



**Figure 8.5 i(Q) data collected for the Ge-Sb-Se glass series: x($GeSe_2$)-(1-x)( $Sb_2Se_3$) where x = 0.4, 0.5, 0.6, 0.7, 0.8 and 0.9, after correction of the raw experimental data. (a) Full scale of i(Q). (b) Enlarged i(Q) from 0 to 6 Q (Å$^{-1}$). The peak position of Q shifted from 1.02 to 1.16 Å$^{-1}$, as $Sb_2Se_3$ was incorporated in the glass.**

From Figure 8.5 it can be seen that the Ge-Sb-Se glasses were amorphous as no Bragg diffraction peaks were detected in the i(Q) data. In i(Q), the first sharp diffraction peak (FSDP) is a low Q feature in the structure factor of chalcogenide network glasses [261]. From Figure 8.5 it can be seen that the position of the FSDP shifted to higher Q (from 1.02 to 1.16 Å$^{-1}$) and decreased in intensity as the $Sb_2Se_3$ concentration was increased in the glass.

### 8.3.2.2 The total correlation function, $T(r)$

T($r$) measures the frequency of the occurrence of interatomic distances in the sample. Figure 8.6 displays the correlation functions measured for the six glasses studied here (x($GeSe_2$)-(1-x)($Sb_2Se_3$) where x = 0.4, 0.5, 0.6, 0.7, 0.8 and 0.9) and $GeSe_2$ (T($r$) data were obtained from [261]).

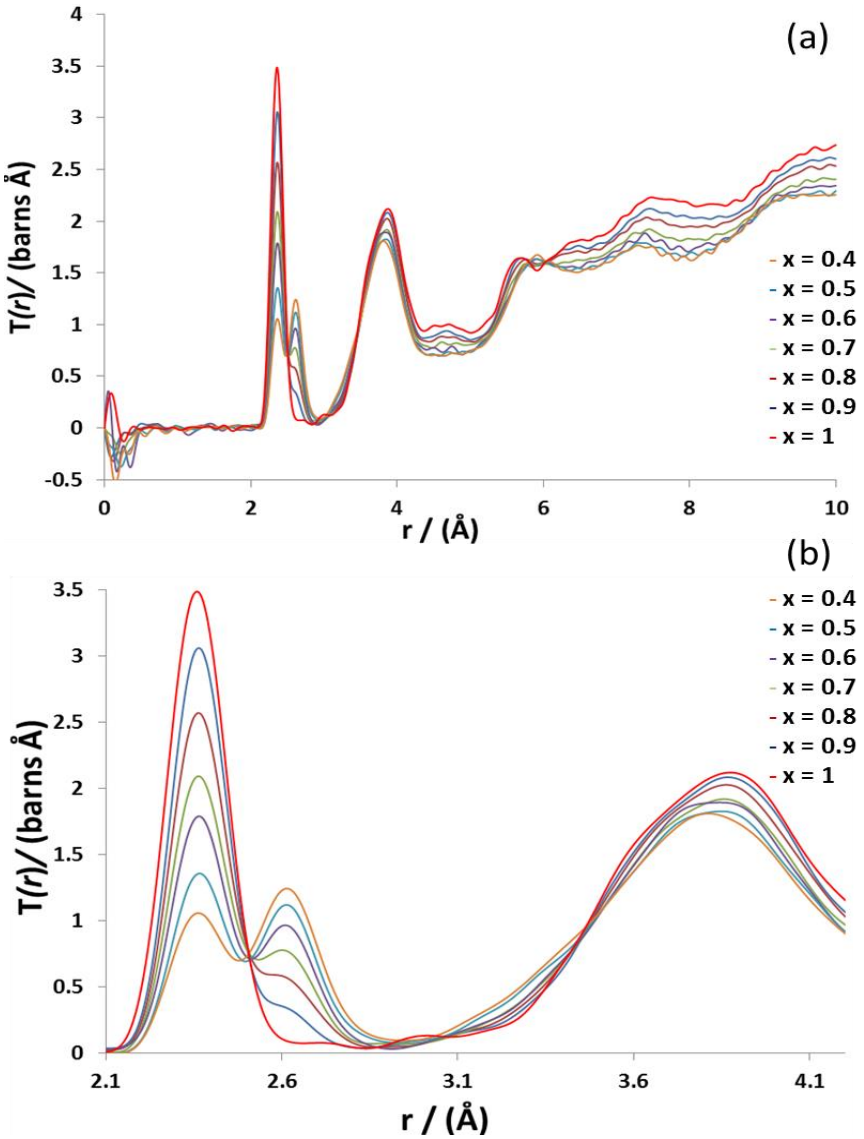



**Figure 8.6 T($r$) extracted from i(Q) data for the Ge-Sb-Se glass series: x($GeSe_2$)-(1-x)($Sb_2Se_3$) where x = 0.4, 0.5, 0.6, 0.7, 0.8, 0.9 and x= 1 , obtained from [261], after Fourier transform and the Lorch modification function M(Q). (a) Full scale of T($r$) from 0-10 Å. (b) Enlarged T($r$) from 2.1 – 4.1 Å. The peak manifold at ~ 2.35 Å can be assigned as the Ge-Se bond length [261, 269]. The shoulder attached to this peak (at a position of ~ 2.63 Å) can be assigned to the Sb-Se bond length [261].**

In Figure 8.6 it can be seen T($r$) exhibits well defined peaks between approximately 2.1 - 4.1 Å. From the literature, the peak at ~ 2.35 Å can be assigned as the Ge-Se bond length [261]. As would be expected, this peak decreased in intensity from, ~ 3.46 to 1.04 barns Å, as the concentration of $Sb_2Se_3$ in the Ge-Sb-Se glass samples was increased.

For the T($r$) data in Figure 8.6 the shoulder attached to this peak (at a position of ~ 2.63 Å) can be assigned to the Sb-Se bond length [261]. Accordingly, the area of this peak increased as the $Sb_2Se_3$ concentration was increased. The final distinct broad peak (at a peak position ranging from ~ 3.80 – 3.88 Å) is suggested to be a collection of different atomic correlations [65, 66]. It is expected to have arisen from the next nearest neighbours in the glass structure and could comprise of a mix of X…X distances (where … denotes a non-bonding distance between two atoms), for example: Se...Se distances within both [$GeSe_4$] unit and [$SbSe_3$]unit; Ge...Ge distances arising from edge sharing [$GeSe_4$] units and two structural units corner sharing a Se atom of either Sb...Ge, Ge...Ge and Sb...Sb [261].

#### 8.3.2.3 $T(r)$ scaled by the partial correlation functions $t_{GeSe}$ and $t_{SbSe}$

As was mentioned in section 8.2.3.2, T($r$) is a weighted sum of the partial correlation functions. The first peak in T($r$), at approximately at 2.35 Å (see Figure 8.6), was at a distance at which all contributions, other than $t_{Ge-Se}$, were considered to be equal to zero. Therefore, dividing T($r$) by the weighting factor for the partial correlation function, $2c_{Ge}\bar{b}_{Ge}\bar{b}_{Se}$ (see Equation 8.4), yielded the Ge-Se partial correlation function over the limited region of its first peak. Figure

8.7(a), shows the result of dividing the measured T(*r*) by the Ge-Se weighting factors for each Ge-Sb-Se composition.

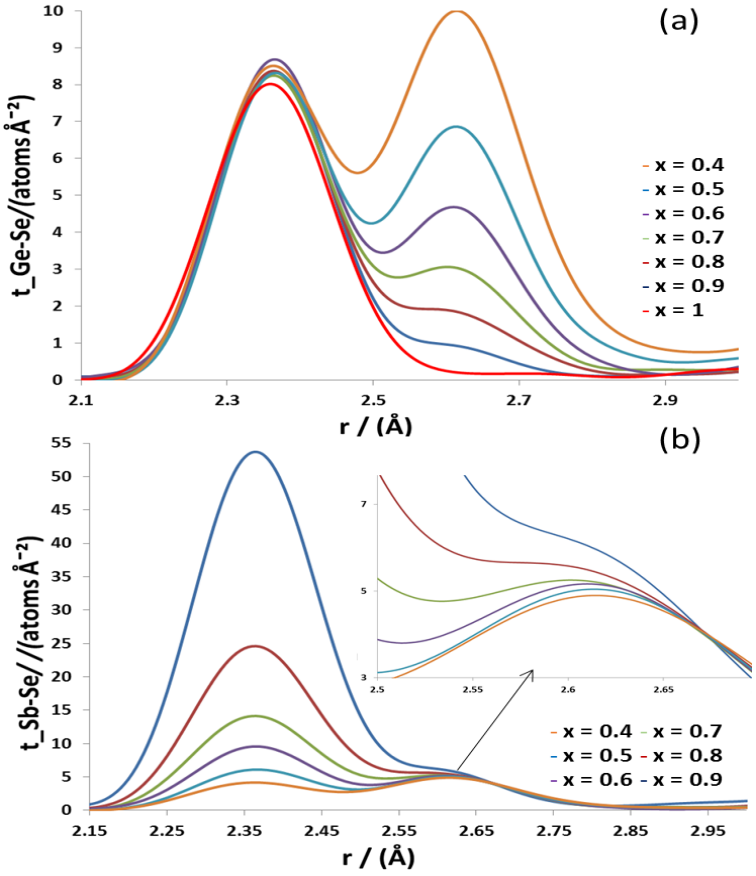



**Figure 8.7 T($r$) data scaled by the partial correlation function coefficient ($c_j\bar{b}_j\bar{b}_k$) for (a) Ge-Se correlations, $t_{Ge-Se}(r)$. The leading edge of the Ge-Se peak for each glass coincided well for all the Ge-Sb-Se glasses and there was little area change of the first peak between compositions. (b) Sb-Se correlations, $t_{Sb-Se}(r)$ and enlarged inset to the Sb-Se peak. The trailing edge of the Sb-Se peak for each Ge-Sb-Se glass coincided well, however, it was difficult to compare the area change as there was a strong overlap with Ge-Se peak. Therefore more accurate fitting was applied to the peak, see section 8.3.2.4.**

The position of Q for the Ge-Se peak only shifted marginally (a maximum of 0.01 Å) for all the Ge-Sb-Se glass composition. Furthermore there was little area change of the peak between compositions. Consequently, this similarity of the Ge-Se peak for the x($GeSe_2$)-(1-x)( $Sb_2Se_3$) glass series is strong evidence that the Ge coordination number should be unchanged with composition.

Furthermore, the leading edge of the Ge-Se peaks, at ~ 2.1- 2.35 Å, for each Ge-Sb-Se glass coincided well with each other. Thus, it can be determined that there was minimal change in Ge-Se bond length and coordination number,$n_{GeSe}$, with the compositions studied in this Project.

For the shoulder attached to the first peak in T($r$) at a peak position of ~ 2.63 Å, see Figure 8.6, the same assumption was made that all contributions other than $t_{Sb-Se}$ were equal to zero. Thus, T($r$) was divided by the weighting factor, $2c_{Sb}\bar{b}_{Sb}\bar{b}_{Se}$, to yield the Sb-Se partial correlation function. Figure 8.7(b), shows the results of dividing the measured T($r$) by Sb-Se weighting factors for each Ge-Sb-Se composition. The trailing edges of the Sb-Se peak, from ~ 2.63 - 2.7 Å, for each Ge-Sb-Se glass coincided well with each other.

The position of the Sb-Se peak did not appear to shift for x = 0.4 - 0.7 in the x($GeSe_2$)-(1-x)( $Sb_2Se_3$) glass series. However, there was a strong overlap with the Ge-Se peak for all the Ge-Sb-Se glasses, which was particularly apparent for values of x > 0.7. Thus, the leading edge of the Sb-Se peaks could not be distinguished making it difficult to draw conclusions about the coordination number from the Sb-Se peak area. Therefore, it was necessary to more accurately fit the Sb-Se peaks to obtain $n_{SbSe}$ as will be explained in section 8.3.2.4. The Ge-Se peaks were also fitted.

#### 8.3.2.4 Peak fitting the Ge-Se and Sb-Se peaks to obtain the coordination number

To quantitatively confirm the qualitative analysis of the peaks scaled by $t_{Ge-Se}(r)$ and $t_{Sb-Se}(r)$, the first two peaks in T($r$) for each Ge-Sb-Se glass composition were analysed individually. Gaussian peaks (convoluted with the

resolution of the instrument) were fitted to extract the bond information for Ge and Sb. Peak fitting was conducted using the Pnfit software, for more information see [270].

The Ge-Se peak was fitted first using lower and upper r values (over a fitting range of 2.1 – 2.45 or 2.5 Å) manually selected from the graph in Figure 8.7(a). The Ge-Se coordination number ($n_{GeSe}$) and the bond lengths were extracted from the direct fitting of T($r$) shown in Figure 8.8, for the Ge environment. The values obtained are summarised in Table 8.3.

**Table 8.3 The lower and upper bond length values (r) used for fitting, average r value, the Ge-Se coordination number (n), the peak width (σ) and the error for x = 0.9 to 0.4 in the x($GeSe_2$)-(1-x)($Sb_2Se_3$) glass series.**

| x value | Lower r limit / (Å) | Upper r limit / (Å) | r / (Å) | n | σ / (Å) |
|---|---|---|---|---|---|
| 0.9 | 2.1 | 2.5 | 2.37 ± 0.001 | 3.86 ± 0.07 | 0.062 ± 0.001 |
| 0.8 | 2.1 | 2.5 | 2.37 ± 0.001 | 3.87 ± 0.07 | 0.064 ± 0.001 |
| 0.7 | 2.1 | 2.5 | 2.37 ± 0.001 | 4.02 ± 0.07 | 0.066 ± 0.001 |
| 0.6 | 2.1 | 2.45 | 2.37 ± 0.001 | 3.99 ± 0.07 | 0.061 ± 0.001 |
| 0.5 | 2.1 | 2.45 | 2.37 ± 0.001 | 3.95 ± 0.07 | 0.061 ± 0.001 |
| 0.4 | 2.1 | 2.4 | 2.36 ± 0.001 | 3.87 ± 0.07 | 0.058 ± 0.001 |

As was seen from T($r$) in Figure 8.7, the peak arising from Ge-Se bonds were symmetric, which allowed the peak fitting to T($r$) to be carried out in one fit. During the peak fitting it was observed that the coordination number was very sensitive to the fitting range, which provided evidence of the difficulty in deconvoluting the Ge-Se peak from the Sb-Se peak. The residual calculated from fitting the Ge-Se peak (shown as the green curve in Figure 8.8) was used to fit a second peak to determine the Sb-Se bond length and the coordination number. The fit was carried out using a range of r = 2.35 – 2.5 to yield the Sb-Se coordination number ($n_{SbSe}$) and the bond lengths for each sample. The values obtained are summarised in Table 8.4.

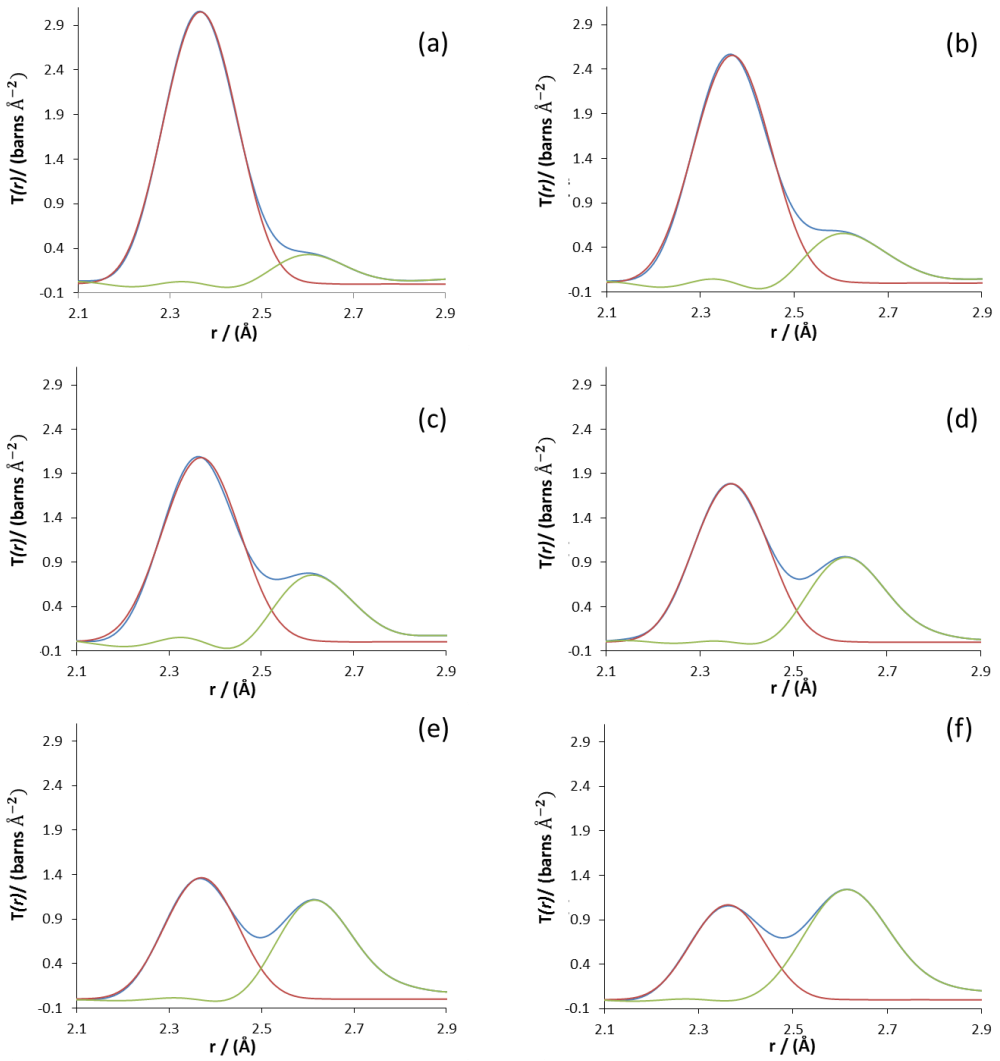



**Figure 8.8 The T($r$) data for the x($GeSe_2$)-(1-x)($Sb_2Se_3$) glass series (shown in blue) and with the fits to the Ge-Sb peak (shown in red). The upper and lower r values used to fit the peak are given in Table 8.3. The residual (shown in green) shows the leading edge of the Sb-Se peak. (a) x = 0.9. (b) x = 0.8. (c) x = 0.7. (d) x = 0.6. (e) x = 0.5. (f) x = 0.4.**

**Table 8.4 The lower and upper bond length values (r) used for fitting, average r value, the Sb-Se coordination number (n), the peak width (σ) and the error for x = 0.9 to 0.4 in the x($GeSe_2$)-(1-x)($Sb_2Se_3$) glass series.**

| x value | Lower r limit / (Å) | Upper r limit / (Å) | r / (Å) | n | σ / (Å) |
|---|---|---|---|---|---|
| 0.9 | 2.5 | 2.8 | 2.61 ± 0.001 | 2.75 ± 0.07 | 0.043 ± 0.001 |
| 0.8 | 2.5 | 2.8 | 2.62 ± 0.001 | 2.73 ± 0.07 | 0.051 ± 0.001 |
| 0.7 | 2.5 | 2.8 | 2.62 ± 0.001 | 2.54 ± 0.07 | 0.048 ± 0.001 |
| 0.6 | 2.5 | 2.8 | 2.62 ± 0.001 | 2.67 ± 0.07 | 0.056 ± 0.001 |
| 0.5 | 2.5 | 2.8 | 2.62 ± 0.001 | 2.70 ± 0.07 | 0.063 ± 0.001 |
| 0.4 | 2.5 | 2.8 | 2.62 ± 0.001 | 2.90 ± 0.07 | 0.073 ± 0.001 |

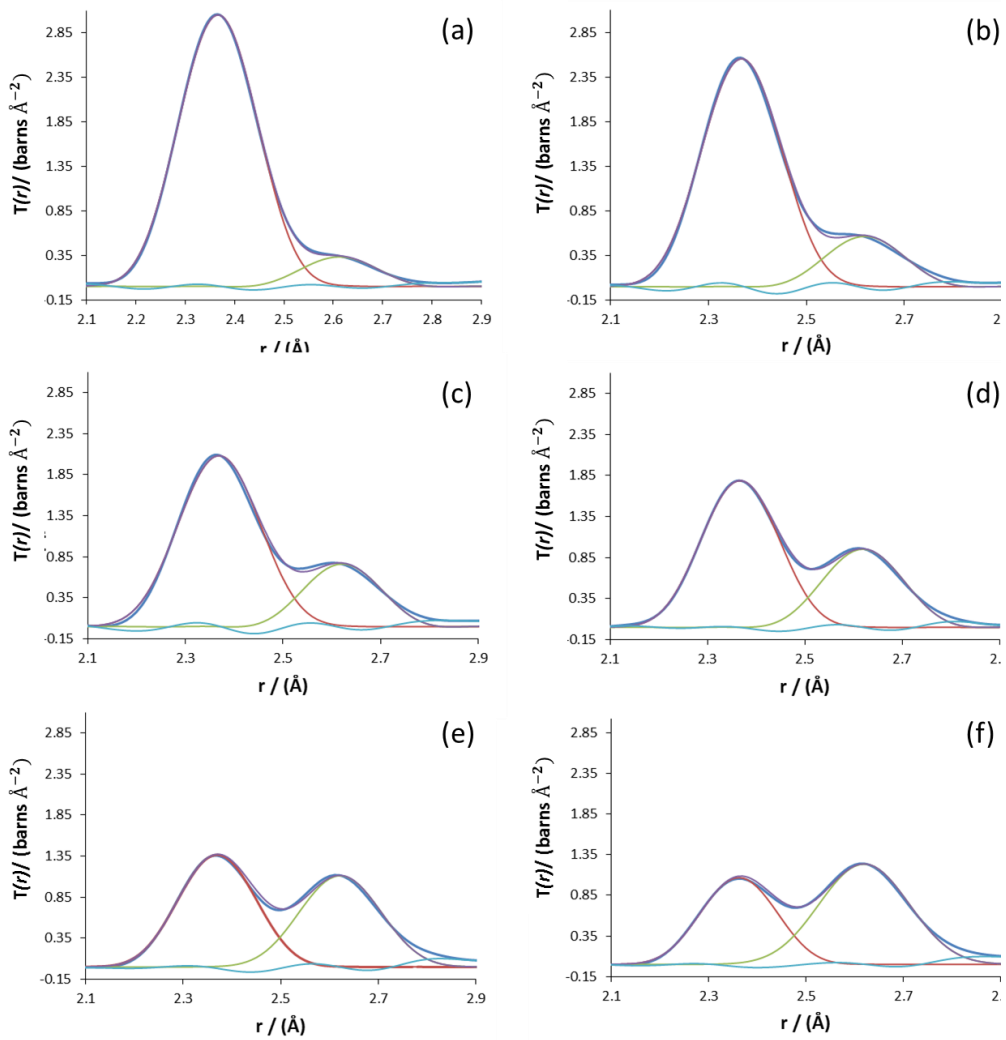



**Figure 8.9 The $T(r)$ data for the x($GeSe_2$)-(1-x)($Sb_2Se_3$) glass series a) x = 0.9 b) x = 0.8 c) x = 0.7 d) x = 0.6 e) x = 0.5 f) x = 0.4. The upper and lower r values used to fit the peak are given in Table 8.4. The original T($r$) data is in dark blue, the Ge-Se peak (from previous fitting of Ge-Se peak) is in red, the Sb-Se peak after the fit is in green, the sum of the two peaks is in purple and the residual is in light blue.**

## 8.4 Discussion

### 8.4.1 Onset glass transition temperature ($T_g$) and density

The chemical bonding in the Ge-Sb-Se glass system is relatively weak, as was discussed in section 2.1.2, due to the elements being neighbours in the Periodic Table. The elements exhibit similar electronegativities (Se= 2.55, Sb = 2.05 and Ge= 2.01 [41]). However, Se is slightly more electronegative and therefore can be considered as the anion, with Sb and Ge as the cations. Sb is a lone pair

electron element ($1s^2 2s^2 2p^6 3s^2 3p^6 3d^{10} 4s^2 4p^6 4d^{10} 5s^2 5p^3$) that can form three bonds to anions forming [$SbSe_3$] pseudotrigonal units. Ge ($1s^2 2s^2 2p^6 3s^2 3p^6 3d^{10} 4s^2 4p^6$) can form four bonds to anions and forms tetrahedral units with Se, [$GeSe_4$]. A representation of these basic structural units was shown in Figure 2.3.

From the $T_g$ results shown in Figure 8.4, it is suggested that the $T_g$ of the glass is lowered as a result of a change from a network composed of tetrahedral [$GeSe_4$] units to one containing an increasing number of pseudotrigonal [$SbSe_3$] units. In Table 2.2 it was shown that the bond energy of a Sb-Se bond (183.93 kJ/ mol [42]) is weaker than the bond energy of a Ge-Se bond (206.77 kJ/ mol [42]). Therefore, the Sb-Se bonds were more easily broken than Ge-Se bonds and thus an increasing number of Sb-Se bonds in the Ge-Sb-Se glass structure lowers the Ge-Sb-Se glass's $T_g$. As was discussed in section 3.2.4 a lower $T_g$ is beneficial as melting temperatures can be decreased, reducing the likelihood of chemical interactions with impurities in the silica glass ampoule walls. Furthermore, glass melting and fibre drawing at a lower temperature would reduce glass synthesis and fabrication costs.

The observed decrease in $T_g$ as $Sb_2Se_3$ was incorporated into the Ge-Sb-Se chalcogenide glass structure is consistent with the literature [59, 70, 71]. In Figure 2.4(a) it was shown for a $Ge_x Sb_{10} Se_{90-x}$ glass system, with the Ge content increasing from 7.5 to 32.5 at. %, that the $T_g$ rose with a reduction of Sb at. % content. Furthermore Olivier *et al.* [70] studied a $(GeSe_2)_{100-x}(Sb_2Se_3)_x$ glass system varying x from 5 to 70, and it was reported that the $T_g$ decreased when the $Sb_2Se_3$ content increased, shown in Figure 8.10. Apart from x = 10 in

Figure 8.10 (which was ~ 18 °C lower than the $T_g$ reported in this Thesis) the reported $T_g$ values were slightly higher (a maximum of 10 °C) than the $T_g$ values measured in this Project. However, Olivier *et al.* did not state the method of calculating the $T_g$ from the DSC curve and whether the onset $T_g$ value was used, as here.

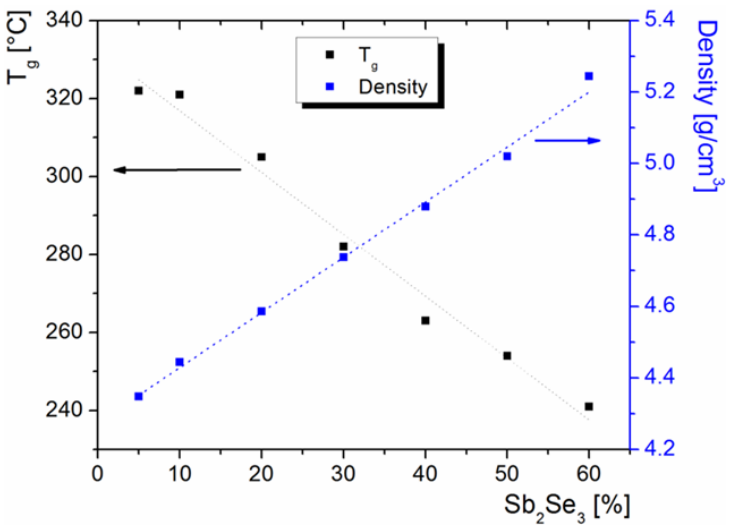



**Figure 8.10 Reported $T_g$ and density value for a $(GeSe_2)_{100-x}(Sb_2Se_3)_x$ glass system where x ranged from 5 – 60 *[70]*. The density values complimented the values obtained in this Project within the calculated error. The $T_g$ values were slightly higher (a maximum of 10 °C) than the values measured in this Project, however it was not stated how the $T_g$ values were obtained from the DSC curves and if it was the onset $T_g$ reported, as here.**

Nevertheless, the trend of a decrease in $T_g$ as $Sb_2Se_3$ was incorporated into the Ge-Sb-Se chalcogenide glass structure is in support of the findings in this Project. Furthermore, in Figure 8.10, it is suggested that two linear trend lines could be fitted for the $T_g$ data rather than the one line shown, similar to the ones fitted in Figure 8.4, for $Sb_2Se_3$ between 10 – 30 % and for 30 – 60 %. The change in gradient is observed when more than ~ 70 % of the glass network consists of [$GeSe_2$] structural units. Therefore, it is suggested that the change in gradient might due to homopolar Se-Se bonds (184.10 kJ/ mol [42]) starting to form in

the Ge-Sb-Se glass network further increasing the strength in bonding. $GeSe_2$ is reported to have as much as 16 % of Se bonds being homopolar [271, 272].

From the results shown in Figure 8.4, it is suggested that the glass density is increased as a result of a change from a network composed of tetrahedral [$GeSe_4$] units to one containing an increasing number of pseudotrigonal [$SbSe_3$] units. When taking into account the relative atomic masses of the elements (Sb = 121.76 [273] Ge = 72.63 [273]) it is expected that the density of the Ge-Sb-Se glasses should increase with increasing $Sb_2Se_3$ concentration. The density values shown in Figure 8.10 compliment the results found in this Project, within the error.

### 8.4.2 Neutron diffraction data

In the i(Q) data shown in Figure 8.5, the position of the FSDP peak was shifted to higher Q as $Sb_2Se_3$ was incorporated into the Ge-Sb-Se glass network. The position in Q for the FSDP for each Ge-Sb-Se glass composition was plotted and is shown in Figure 8.11. The position of the FSDP for $GeSe_2$ was also included from [261]. It was considered that two linear trend lines could be fitted for the i(Q) data. The linear fit for values between x = 0.4 - 0.8 had a $R^2$ = 0.975 and the linear fit for values between x = 0.8 - 1 had a $R^2$ = 1.000. This non-linear shift in the position of the peak is suggested to arise from changes in the longer scale ordering of the Ge-Sb-Se network structure. For future work it is proposed that a greater number of glasses along the x($GeSe_2$)-(1-x)( $Sb_2Se_3$) tie line are investigated (*e.g.* where x = 0.45, 0.55, 0.65, 0.75, 0.85 and 0.95) to confirm these suggested linear correlations.

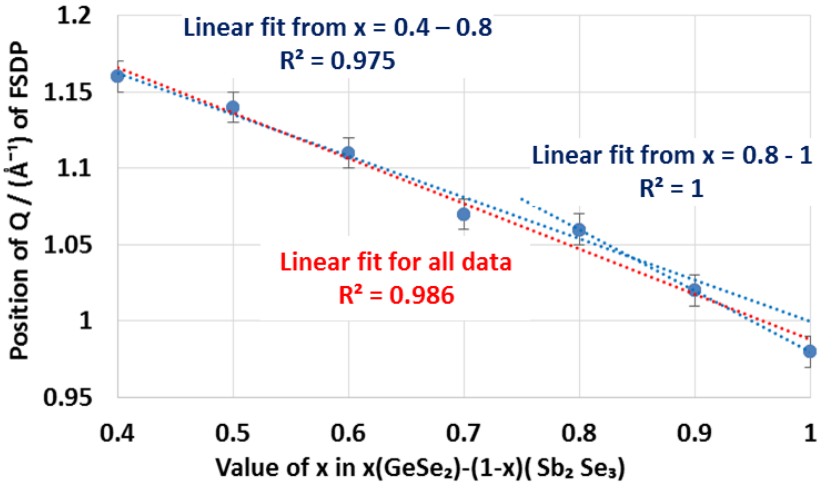



**Figure 8.11 Position of the first sharp diffraction peak (FSDP) from the i(Q) data displayed in Figure 8.5 for the x($GeSe_2$)-(1-x)($Sb_2Se_3$) glass series where x = 0.4, 0.5, 0.6, 0.7, 0.8 and 0.9. $GeSe_2$ data for FSDP obtained from** [261] **was also included. It can be seen that the position of the FSDP was shifted to lower Q with the reduction of $Sb_2Se_3$ in the Ge-Sb-Se glass network.**

The shift in Q for the FSDP peak position can be related to the distance between planes of atoms where there are repeating units in the glass structure (*d*), as shown in Equation 8.5.

$$Q = \frac{2\pi}{d} \qquad \textbf{Equation 8.5}$$

Equation 8.5 combines Equation 2.2 with the Bragg scattering equation [274] $d = \frac{\lambda}{2\sin\theta}$ and relates the position of the peaks in Q with the distances of the bonds within the glass. The higher FSDP shifts observed therefore correspond to a contraction of the Ge-Sb-Se glass network as [$SbSe_3$] is added. At first, this may be considered counter intuitive if the relative sizes of Sb (atomic radius 2.06 Å [273]) and Ge (atomic radius 2.11 Å [273]) are considered. The second diffraction peak (from 2.06 to 2.16 $Å^{-1}$) and third diffraction peak (from 3.52-3.56 $Å^{-1}$) in the i(Q) data also shifted to higher Q as the concentration of $Sb_2Se_3$ increased. Bychkov *et al.* studied a series of binary selenide glasses of composition $A_xSe_{x-1}$, where x = 0.4 to 0.7 and A = an element in Group 14, 15

or 16 of the Periodic Table [261]. They reported in a glass containing cations with a lower co-ordination number, the FSDP peak shifted to higher Q. For example, the FSDP for $GeSe_2$, comprised of four-coordinated units, was reported to be at 0.98 $Å^{-1}$, while that for $As_2Se_3$, comprised of [$AsSe_3$] units, the FSDP was at 1.32 $Å^{-1}$. In TeSe, where Te and Se form chains where Te and Se are two-coordinated, the FSDP was at 1.42 $Å^{-1}$. This compliments the shift from Q = 1.02 to 1.16 $Å^{-1}$ found for the x($GeSe_2$)-(1-x)( $Sb_2Se_3$) glass system in this Project, as 3 co-ordinated [$SbSe_3$] units are replaced with 4 coordinated [$GeSe_4$] units.

Upon taking a closer look at the FSDP (Figure 8.5), the intensity of the peak reduced (from -0.148 to -0.345 barns $atom^{-1}$ $steradian^{-1}$) as the concentration of $Sb_2Se_3$ increased. As this peak is a dominant feature in $GeSe_2$, it is suggested that the reduction in intensity is due to fewer [$GeSe_4$] units being bonded together. As was shown in Figure 8.1, Ge (*b* = 8.185) has a greater neutron scattering length than Sb (*b* = 5.57) thus, as $Sb_2Se_3$ was added into the Ge-Sb-Se glass matrix the characteristic feature in the [$GeSe_4$] units that gave rise to the greater intensity of the FSPD were broken up.

In the T(*r*) data shown in Figure 8.6, a systematic change can be seen in the third peak manifold (at a peak position ranging from ~ 3.80 – 3.88 Å) over the concentration range from x = 0.4 to 1 in x($GeSe_2$)-(1-x)( $Sb_2Se_3$). As the overall intensity of the peak was increased, the peak broadened and shifted to higher Q. This could be partly accounted for by Sb (*b* = 5.57) scattering more weakly than Ge (*b* = 8.185), see Figure 8.1 [267]. Thus with Sb addition in the glass Ge...Ge

correlations were replaced with Ge...Sb and Sb...Sb correlations, which scattered neutrons less strongly and are at longer distances.

The neutron diffraction data for the Ge-Se peak (Table 8.3) and Sb-Se peak (Table 8.4), suggest that for short range order there are no structural changes within the x($GeSe_2$)-(1-x)($Sb_2Se_3$) glass system. The Ge ions in the Ge-Sb-Se glass were found to have a coordination number between 3.87-4.02 ± 0.07, suggesting that the Ge ions were four coordinated, independent of sample composition. The Ge-Se bond lengths (between 2.36-2.37 ± 0.001 Å) were consistent with the bond length predictions (~ 2.36 Å) shown in Figure 2.3 [66]. The coordination numbers for the Sb-Se bond (between 2.54 – 2.90 ± 0.07) were slightly lower than the anticipated three. There was a greater variation found with the coordination number for the Sb environment, which was inconsistent with Ge-Sb-Se sample composition. The Sb-Se bond length (between 2.61- 2.62 ± 0.001 Å) was found to be slightly lower than the bond length predictions (~ 2.66 Å) shown in Figure 2.3 [66]. It is suggested that the lower values obtained for the Sb-Se environment were likely to be on account of the difficulties that arose with peak fitting due to the overlap with the Ge-Se peak. From the direct fitting of T($r$) shown in Figure 8.8, $n_{GeSe}$ and the bond lengths were extracted (Table 8.3). Similarly, $n_{SbSe}$ and the bond lengths were extracted by fitting as was shown in Figure 8.9 (Table 8.4). It can be seen that when the $n_{SbSe}$ is low, $n_{GeSe}$ is higher (*e.g.* for x = 0.7 $n_{SbSe}$ = 2.54 ± 0.07 and $n_{GeSe}$ = 4.02 ± 0.07). This is due to the peaks being sufficiently close so that the fits were highly interrelated.

It should be noted that there were large errors associated with the coordination numbers for both the Ge and Sb environment obtained in this work. The underlying reasons for the difficulty in analysing the neutron diffraction data to achieve the $[GeSe_4]$ and $[SbSe_3]$ coordination numbers of 4 and 3, respectively, are not fully understood at this time. However, it is suggested that the initial assumption that there were no Se-Se homopolar bonds in the stoichiometric glass compositions was incorrect. The assumption was based from the analysis of $As_2Ch_3$ (where Ch = chalcogenide) glasses by Barney *et al.* [275]. In the case of the $As_2Ch_3$ glasses the assumption of no Ch-Ch homopolar bonds was more accurate as the $[AsCh_3]$ could be easily fitted and it was supported by evidence for $Se^{77}$ magic angle spinning (MAS), nuclear magnetic resonance (NMR) and Raman Spectroscopy. It should also be noted that the binary $As_2Ch_3$ is a significantly different glass composition to the ternary Ge-Sb-Se glasses studied here. Gjersing *et al.* and Petri *et al.* both reported that as much as 16 % of Se bonds in $GeSe_2$ were homopolar [271, 272]. Therefore, it may be expected that in the Ge-Sb-Se glasses along the x$(GeSe_2)$-(1-x)( $Sb_2Se_3$) stoichiometric tie-line, from $GeSe_2$ to $Sb_2Se_3$ (a compound that does not form a glass by itself), a small fraction of Se-Se homopolar bond may be present.

The strength of neutrons scattering upon interaction with an element depends on the precise structure of the nucleus of that element and so varies haphazardly across the periodic table. As was shown in Figure 8.1 Sb had the lowest neutron scattering length of the elements in the Ge-Sb-Se glass system. X-rays scatter from the electrons, thus the strength of scattering is proportional to the atomic mass. Therefore in the Ge-Sb-Se glass system, Sb scatters X-rays the strongest,

as shown in Figure 8.12. It is suggested that future investigations should involve X-ray scattering data to provide greater information to deconvolute the first three peaks in T(*r*).

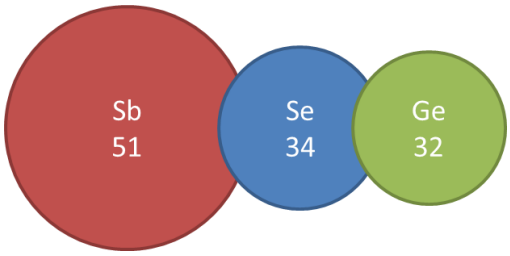



**Figure 8.12 The variation in X-ray scattering length of form factor F(Q)=0 of each element in the Ge-Sb-Se glass system. The radius of each circle is scaled with F(Q) [276].**

As was mentioned, Barney *et al*. proposed assumption that there were no Ch-Ch homopolar bonds in the $As_2Ch_3$ glass network was supported by MAS NMR work. Therefore, the x($GeSe_2$)-(1-x)( $Sb_2Se_3$) glasses synthesised in this work were subsequently analysed using $^{77}$Se MAS NMR by Dr Barney[16] and Dr Jeremy Titman[17] to further characterise the Se environment. Details of the methodology used for this experiment can be found in [275]. Figure 8.13 shows the data collected for the x = 0.8 Ge-Sb-Se glass, along with two possible fits to the data. In Figure 8.13(a) the fit uses only a single peak at a chemical shift of 405 ppm, at a position associated with Ge-Se-Ge bridges between corner sharing [$GeSe_4$] units in germanium-selenide glasses [271]. Figure 8.13(b) shows the same data fitted with two peaks at 405 and 580 ppm, with the latter peak being characteristic of Se-Se-Ge bridges (*i.e.* Se - Se homopolar bonds) [271]. Both fits are equally good, but the second suggests that ~ 4 % of Se atoms are in homopolar bonds.

[16] Dr Emma Barney. MIR Photonics Research Group. University of Nottingham, UK.
[17] Dr Jeremy Titman. School of Chemistry. University of Nottingham, UK.

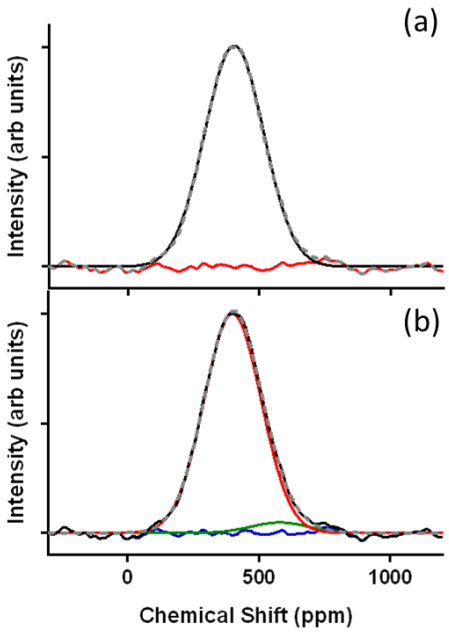



**Figure 8.13 $Se^{77}$ MAS NMR spectrum (black) collected for the x($GeSe_2$)-(1-x)( $Sb_2Se_3$) glass system where x = 0.8. Two fits have been carried out assuming the presence of (a) only Ge-Se-Ge bridges (red) in the glass and (b) a mixed of Ge-Se-Ge bridges (red) and Se-Se dimers (green). For both fits the total fit to the data is shown as a the grey dashed line. The quality of the fit in (b) can be seen in the residual (blue).**

A further systematic $^{77}$Se MAS NMR study to determine the role of Se in all the stoichiometric glasses would show whether homopolar bonds are more likely to form in the $GeSe_2$ rich glasses, as suggested.

To extend this work further, a combined neutron/ X-ray/ MAS NMR study of Se rich glasses would provide an understanding of the role of the Se-Se bonds in determining the structure and properties of glasses with compositions more similar to those investigated in this Project for optical applications. It is suggested that future work should include tie lines that run from a stoichiometric composition to pure Se glass, passing through the compositions reported in Chapters 4-7 (*e.g.* (JB01) $Ge_{19}Sb_{15}Se_{66}$, (JB02) $Ge_{20}Sb_{10}Se_{70}$, (JB03) $Ge_{24}Sb_4Se_{72}$ and (JB04) $Ge_{22}Sb_8Se_{70}$). This would provide structural information on how small changes in the composition would affect the glass

properties. It is anticipated that this could yield important insights into structure-property relationships that would inform future selection of glass composition.

## 8.5 Conclusions

From the density, $T_g$ and neutron diffraction results analysed in this chapter the following conclusions were drawn.

- This preliminary work has shown that the stoichiometric glasses were predominantly made up of [$GeSe_4$] and [$SbSe_3$] units. From decreasing the Sb content along the x($GeSe_2$)-(1-x)($Sb_2Se_3$) stoichiometric tie line the vitreous structure changed from higher levels of Sb, where Se was in a pseudotrigonal environment [$SbSe_3$] to Se being in a tetrahedral environment [$GeSe_4$]. It was shown that this change in structure increased the $T_g$ of the glass (when x = 0.4 the $T_g$ = 240 ± 4 °C and when x = 0.9 the $T_g$ = 330 ± 3 °C) and decreased the density of the glass (when x = 0.4 the density was 5.07 ± 0.19 g $cm^{-3}$ and when x = 0.9 the density was 4.38± 0.13 g $cm^{-3}$). This change in thermal property of the Ge-Sb-Se glasses was explained on account of the change of bond energy (Ge-Se 206.77 kJ/ mol [42] and Sb-Se 183.93 kJ/ mol [42]) increasing the thermal stability of the Ge-Sb-Se glass. The change in the density was suggested to be due to the increased relative atomic masses of the elements (Sb = 121.76 [273] Ge = 72.63 [273]).
- In the i(Q) data shown (Figure 8.5), the position of the FSDP peak was shifted to higher Q as $Sb_2Se_3$ was incorporated into the Ge-Sb-Se glass network. It was considered that two linear trend lines could be fitted for the i(Q) data. The linear fit for values between x = 0.4 - 0.8 had a $R^2$= 0.975 and the linear fit for values between x = 0.8 - 1 had a $R^2$ = 1.000. This non-linear shift in the position of the peak was suggested to arise from changes in the

longer scale ordering of the Ge-Sb-Se network structure and it was suggested that the FSDP shifts observed corresponded to a contraction of the Ge-Sb-Se glass network. For future work it is proposed that a greater number of glasses along the x($GeSe_2$)-(1-x)( $Sb_2Se_3$) tie line are investigated (*e.g.* where x = 0.45, 0.55, 0.65, 0.75, 0.85 and 0.95) to confirm these suggested linear correlations.

- The intensity of the FSDP peak reduced (from -0.148 to -0.345 barns $atom^{-1}$ $steradian^{-1}$) as the concentration of $Sb_2Se_3$ increased. As this peak is a dominant feature in $GeSe_2$, it is suggested that the reduction in intensity is due to fewer [$GeSe_4$] units being bonded together. As was shown in Figure 8.1, Ge ($b$ = 8.185) has a greater neutron scattering length than Sb ($b$ = 5.57) thus, as $Sb_2Se_3$ was added into the Ge-Sb-Se glass matrix the characteristic feature in the [$GeSe_4$] units that gave rise to the greater intensity of the FSPD were broken up.
- It was suggested that the average bond length of Sb-Se was 2.62 ± 0.001 Å and the average bond length of Ge-Se was 2.37 ± 0.001 Å. It was explained that it was difficult to extract the coordination of the Ge and Sb elements on account of an overlap of the Ge-Se and Sb-Se peaks. However, it was suggested that the Ge in [$GeSe_4$] units were 3.86 – 4.02 ± 0.07 coordinated and that Sb in [$SbSe_3$] were 2.54 – 2.90 ± 0.07 coordinated. However, it was highlighted that homopolar Se bonds may be present in the stoichiometric glass compositions. Therefore further analysis using XRD and NMR was suggested.

## 8.6 Summary

Neutron diffraction data for a x($GeSe_2$)-(1-x)( $Sb_2Se_3$) glass series where x = 0.4, 0.5, 0.6, 0.7, 0.8 and 0.9 were obtained using the GEM diffractometer at ISIS. The Ge-Sb-Se glass series was also characterised by density and $T_g$ measurement in section 8.2.1. The preparation of the Ge-Sb-Se glass rod samples for the neutron scattering diffraction experiments was explained in section 8.2.2. The extraction of the raw neutron data and the subsequent corrections which were applied were described in section 8.2.3. The results of the density and $T_g$ measurements for the Ge-Sb-Se glass series were given in section 8.3.1. The onset $T_g$ values were found to decrease linearly when the Sb concentration increased and the density values were found to increase when the Sb concentration increased. The bond lengths and the coordination number of the Se atoms were proposed from the neutron scattering diffraction results in section 8.3.2. It was suggested that the average bond length of Sb-Se was 2.62 ± 0.001 $Å^{-1}$ and the average bond length of Ge-Se was 2.37 ± 0.001 $Å^{-1}$. In section 8.4 it was discussed that the change in density coincided with an increased relative atomic masses of the elements and the increased bond length. It was also explained that the structural change of Se being in a pseudotrigonal environment [$SbSe_3$] to Se being in a tetrahedral environment [$GeSe_4$] increased the thermal stability of the glass. The difficulties in extracting accurate values for the coordination number of the Ge and Sb elements were explained. However, it was suggested that the Ge in [$GeSe_4$] units were 3.86 – 4.02 ± 0.07 coordinated and that Sb in [$SbSe_3$] were 2.54 – 2.90 ± 0.07 coordinated. Future work including MAS NMR and XRD studies are suggested.

# 9. Conclusions and suggestions for future work

The work reported in this Thesis was divided into three main sections: (i) a study of four Ge-Sb-Se glass compositions (atomic %): ($Ge_{19}Sb_{15}Se_{66}$), ($Ge_{20}Sb_{10}Se_{70}$), ($Ge_{24}Sb_{4}Se_{72}$) and ($Ge_{22}Sb_{8}Se_{70}$), in terms of their physical properties, optical properties and cytotoxicity to match potential glass pairs for small core-cladding MIR SCG fibres, (ii) development and optimisation of methods of achieving high-purity chalcogenide glasses, and (iii) a preliminary study of the structure of Ge-Sb-Se glasses along the stoichiometric tie-line x($GeSe_2$)-(1-x)( $Sb_2Se_3$) to guide future selection of candidate glass pairs to draw to step-index fibre. The major conclusions drawn from the work undertaken in the three main sections stated above are presented in section 9.1. Suggestions for future work are discussed in section 9.2

## 9.1. Conclusions

### 9.1.1. A study of physical, optical and cytotoxic properties of Ge-Sb-Se glass compositions (atomic %): ($Ge_{19}Sb_{15}Se_{66}$), ($Ge_{20}Sb_{10}Se_{70}$), ($Ge_{24}Sb_{4}Se_{72}$) and ($Ge_{22}Sb_{8}Se_{70}$) to match potential glass pairs for small-core step-index MIR SCG fibres.

- **Physical and optical properties**
  - It was established that all the Ge-Sb-Se compositions studied (in atomic %, viz.: $Ge_{19}Sb_{15}Se_{66}$, $Ge_{20}Sb_{10}Se_{70}$, $Ge_{24}Sb_{4}Se_{72}$ and $Ge_{22}Sb_{8}Se_{70}$) could be fabricated as amorphous bulk glasses (section 4.1.1) and fibres (section 5.7). The Ge-Sb-Se bulk glasses and fibres were found to be suitable candidates for MIR transmission, predominantly between 3-12 µm, observed via FTIR spectra (section 4.1.3 and section 6.3, respectively).

- After characterisation of the physical and optical properties of the Ge-Sb-Se bulk glasses intended for small-core step-index fibres, the following order of matching thermal properties for candidate glass pairs was suggested (section 4.3): It was established that a matched $T_g$ is the first is crucial requirement for a successful fibre draw and benefits both extrusion and fibre drawing procedures. It was discussed that the most accurate way to measure onset $T_g$ was with DSC. The second requirement, it was proposed, was to match the viscosity at the extrusion region ($\sim 10^8$ Pa.s) to encourage core/ cladding co-extrusions. Furthermore, it was then suggested to match the temperature where the onset of the large increase in the instantaneous expansion coefficient occurs, to reduce internal stresses within the fibre, resulting in greater mechanical stability of the fibre. Finally, only when the previous properties discussed have been satisfied, it was suggested to consider a glass pair with a high NA. It was understood that a high NA is important for a small-core step-index MIR SCG optical fibre. However, it was proposed that if a stable fibre cannot be fabricated the benefits of a high NA are futile.

- **Extrusion procedure**
  - From analysis of co-extruded oxide and chalcogenide glasses (section 5.1), it was predicted that, under the particular geometry of the extrudate-feed and out-die during extrusion of the Ge-Sb-Se chalcogenide glasses here, the core would enter the cladding after ~ 70 mm to achieve a 60 % core ratio of the total area of the extrudate. It was recommended that this extrudate-section should be used for subsequent cane or fibre drawing.
  - To reduce the bore size of the Ge-Sb-Se outer cladding extruded tube, the pin head and die extrusion components were re-designed (section 5.2). The result

of the pin re-design was a longer lead-in of the three super-cooled melt channels onto the shaft of the pin, which was further enhanced by a slightly greater angle of the die's graphite lining. From comparison of small-core step-index fibres produced from Pair I (core composition JB04; $Ge_{22}Sb_8Se_{70}$ and cladding composition JB03; $Ge_{24}Sb_4Se_{72}$), it was suggested that a smaller bore to the extruded tube (1.59 mm ø from the original 2.82 mm ø), together with close-fitting cane diameter, helped a more uniform collapse down of the "rod-in-tube" fibre preform resulting in no voids at the core/ cladding interface of the subsequent drawn fibre (F023JHB).

- Die swell was observed in the tube extrusion E026JHB (JB02; $Ge_{20}Sb_{10}Se_{70}$, section 5.5.1) due to the extruded tube making contact with the PTFE guide tube, which was located just beyond the die-exit. This impeded the super-cooled melt flow and resulted in a backing-up of material (die swell). As a result of the work conducted in this Project, the PTFE guide tube has been replaced with a graphite-lined one for future extrusions. PTFE was initially chosen due to its apparent low coefficient of friction with chalcogenide glasses, however it is not as low as that of graphite.
- It was discussed that extrusion operating temperatures are a compromise between having a high-enough temperature to achieve low-enough viscosity of the glass melt but not too high so as to cause die swell. It was suggested that a lower linear thermal expansion coefficient ($\alpha_L$), of the glass to be extruded, at onset $T_g$ tends to reduce die swell. Thus, minimal die swell was encountered for tube extrusions for the glass composition JB03 ($\alpha_L$ at onset $T_g$ (226 °C) = 58 x $10^{-6}$. $°C^{-1}$) compared to JB02 ($\alpha_L$ at onset $T_g$ (211 °C) = 72 x $10^{-6}$. $°C^{-1}$).

- Pair III (core JB02; $Ge_{20}Sb_{10}Se_{70}$ and cladding JB03; $Ge_{24}Sb_{4}Se_{72}$) could not be co-extruded (section 5.6.1). It was suggested that a difference in the super-cooled melt flow velocity across the extrudate (orthogonal to the direction of extrusion) tended to cause instability of the extruding melt and tended to allow curvature of the extrudate, which then resulted in contact with the guide tube wall. Once contact of the super-cooled melt with the guide tube was made, the increased drag caused the extrudate to become swollen filling the guide tube. It was suggested that this was caused due to a difference of 28 °C between the core and the cladding glass at $10^8$ Pa.s (approximate viscosity in the extrusion region).

- **Fabricated Ge-Sb-Se chalcogenide glass fibres**
  - Pair I (core JB04; $Ge_{22}Sb_{8}Se_{70}$, and cladding JB03; $Ge_{24}Sb_{4}Se_{72}$) was selected to be drawn to fibre based on suggestions by Li [83]. Two trials to produce fibre were conducted for this composition (section 5.4). Voids were observed at the core/ cladding interface after Trial 1. After the extrusion components were re-designed to reduce the bore size of the outer cladding tube in Trial 2, while maintaining the core-rod diameter, no voids were visible at the core/ cladding interface in Trial 2. Pair I produced the only co-extruded core/ cladding extrudates which were successfully drawn to cane and subsequently fibre. Two step-index core/ cladding fibres (F018JHB and F021JHB) and small core fibres (F019JHB and F023JHB) were fabricated from this glass pair. Near-field imaging was accomplished at 1463 nm in the small core fibres F019JHB and F023JHB (section 6.2). Optical loss measurements with minimum loss 2.62 dB/m at 6.08 µm wavelength, was achieved in the intermediate fibre (~ 242 x 253 µm ø) F018JHB (section 6.3). The fibres fabricated from this glass pair

were the most robust in this Project. It was suggested that this was on account of the closest match of the glass pairs in the region where the sharp rise in the instantaneous expansion coefficient occurred. However, the fibre-core was still elliptical rather than the desired round shape and thus the better match of thermal properties of the core and cladding glasses is still desirable.

- Pair II (core JB01; $Ge_{19}Sb_{15}Se_{66}$ and cladding JB02; $Ge_{20}Sb_{10}Se_{70}$) were selected for two reasons: (i) from the reported refractive index at 1460 nm in [83] (JB01 = 2.67, JB02 = 2.58) generating a NA for the glass pair of 0.72, and (ii) a close match in temperature (only 7 °C difference) at the predicted viscosity at the fibre drawing region ($10^{4.5}$ Pa.s). It was hoped that this close match would produce a circular fibre core. Pair II was co-extruded (E030JHB) but produced a brittle extrudate which broke easily upon handling (section 5.5.1). Additionally, the extrudate could not be secured in the fibre tower at operating temperatures. It was suggested that the cladding softened before the core as the $T_g$ of the cladding was ~ 23 °C lower than the core. Therefore, small core fibres (F032JHB) fabricated from Pair II were from an unstructured cane (F031JHB) produced directly from the glass melt M098JHB (section 5.5.2). The F032JHB fibres had the lowest mechanical stability of all the fibres fabricated in this Project and would spontaneously break from the fibre drum. Near-field imaging was not achieved in any of the fibres. It was suggested that this was on account of many internal micro-cracks and fractures within the fragile fibre. It was suggested that high residual stresses were generated in this fibre due to a great difference (~ 25 °C) between where the onset of the large increase in the instantaneous expansion coefficient occurred for each glass.

- Pair III (core JB02; $Ge_{20}Sb_{10}Se_{70}$ and cladding JB03; $Ge_{24}Sb_{4}Se_{72}$) were selected as the linear thermal expansion coefficient ($\alpha_L$) was the same between 40 – 180 °C for both glasses, with the initial prediction that this would improve mechanical stability of the fibre. Co-extrusion of the core and cladding was not achieved. Therefore, the core (JB02) was singly extruded. An unstructured intermediate fibre F034JHB (~ 248 x 238 µm ø) and small-core step-index fibres (F035JHB) were fabricated. Optical loss measurements of F034JHB achieved minimum loss 2.47 dB/m at 6.04 µm wavelength (section 6.3). Near-field imaging was accomplished at 1463 nm in all the small core fibres F035JHB (section 6.2). However, although not as fragile as the fibres produced from Pair II, after several days of storage the fibres produced from Pair III would also spontaneously break from the fibre drum. Although this glass pair was selected due to their matched $\alpha_L$ between 40 – 180 °C, it was suggested that residual stresses were generated in this fibre due to a difference (~ 16 °C) between where the onset of the large increase in the instantaneous expansion coefficient occurred for each glass.

- **Preliminary cytotoxicity evaluation of F018JHB ($\mathbf{Ge_{22}Sb_{8}Se_{70}/Ge_{24}Sb_{4}Se_{72}}$)**
  - A procedure to evaluate the cytotoxicity of chalcogenide glass fibres was established (section 7.3). More than 50 % of both Ge-Sb-Se fibres: etched in propylamine and non-etched, was observed to disintegrate in Trial 1. This was reduced to < 20 % in Trial 2 and it was suggested that this was on account of better manual handling of the fibres. Furthermore, the fibre used in Trial 2 was drawn from a later stage of fibre drawing and it was proposed that the fibre would have therefore had greater mechanical strength. It was also proposed and

considered that the UV sterilisation stage might have caused photo-damage of the fibres.

- The Alamar Blue assay results obtained for the Ge-Sb-Se fibres etched in propylamine and non-etched were found difficult to distinguish and to draw conclusions from, to differentiate sufficiently between the two surface conditions (section 7.4). Cell coverage analysis conducted via SEM was performed to complement the Alamar Blue assays (section 7.5). It was shown that 3T3 mammalian fibroblast cells could be maintained viable in contact with Ge-Sb-Se glasses etched in propylamine up until seven days of incubation. A confluent layer of cells was observed to grow on > 90 % of the Ge-Sb-Se propylamine etched fibres. A confluent cell layer did not form on any of the non-etched Ge-Sb-Se chalcogenide fibres and the cell morphology of ~ 70 % of the cells that were observed differed from the cell morphology on the etched Ge-Sb-Se fibres. Although different surface properties were considered to have contributed to the change in cell morphology, it was suggested that the cell morphology was likely to be on account of the cells exhibiting phobicity for the non-etched Ge-Sb-Se fibre surface, which was suggested to have a potentially cytotoxic $Sb_2O_3$ layer present.

### 9.1.2. The development of methods to achieve high-purity chalcogenide glasses.

It was reported that the Ge-Sb-Se chalcogenide bulk glasses and fibres were observed to be sensitive to oxidation, hydration and hydrolysis, resulting in impurities such as oxide, hydride and hydroxide. These impurities manifested in the transmission spectra (~ 2 – 12 µm wavelength) of Ge-Sb-Se bulk glasses (section 4.1.3) and fibre (section 6.3) as absorption bands, the positions of which were determined by the nature of the impurities. It was suggested that the three main sources of impurities in the Ge-Sb-Se

chalcogenide glasses synthesised in this Project were: the silica- glass containment utilised for the synthesis of the glass-forming melt, the local environment and residual gases after evacuation during synthesis and treatment of the glass and the precursor elements used for Ge-Sb-Se chalcogenide glass synthesis.

- **The silica- glass containment utilised for the synthesis of the glass-forming melt**
    - The silica glass ampoules, used as the vessel for Ge-Sb-Se glass melting, underwent a vigorous pre-treatment process (*i.e*. annealing, HF-etching, air baking and vacuum baking) to reduce contamination at the silica glass ampoule walls. However, it was suggested that the silica glass not only added silica fume particulates but also contributed to the Se-H and O-H impurities due to the transfer of H and O-H from the silica glass into the Ge-Sb-Se chalcogenide glass melt at temperatures ≥ 650 °C [148, 149].
- **The local environment and residual gases after evacuation during synthesis and treatment of the glass**
    - It was discussed that impurities and glass defects were reduced by the careful fabrication methods conducted in this Project to limit exposure of the precursor elements and glass melt to the atmosphere (section 3.2.2).
- **The precursor elements used for Ge-Sb-Se chalcogenide glass synthesis**
    - The effect of heat-treating to purify the precursor elements Sb and Se on subsequent fibre loss was observed by comparing two step-index fibres fabricated from Pair I (core JB04; $Ge_{22}Sb_8Se_{70}$ and cladding JB03; $Ge_{24}Sb_4Se_{72}$ ) (section 6.3). Fibre F030DJJHB was considered as un-purified and fibre F018JHB was fabricated from a glass melt with precursor purification of Sb and Se by heat-treatment. It was clear that the purification of the precursor elements lowered the absorption bands of the hydroxide, hydride and oxide impurities. However, the minimum losses were lower for F030DJJHB (2.42

dB/m at 6.66 µm wavelength) than for fibre F018JHB (2.62 dB/m at 6.09 µm wavelength). It was also suggested that the prior purification of the precursor elements had little impact on the extrinsic scattering processes (*e.g.* silica particulate fume) in the fibre which was proposed to be responsible for the main part in the baseline loss.

- Currently precursor elements of high purity with respect to anionic impurities cannot be sourced, thus a preliminary experiment was conducted to distil a large quantity of Se (section 6.4.1). The distillation was successful and the distilled Se was to be used to make high purity chalcogenide glasses beyond the lifetime of this PhD work, within the MIR Photonics Research Group at the University of Nottingham.
- Greater understanding of the distillation technique obtained during the large Se mass distillation led to the development of a new simplified distillation apparatus for other precursor material distillation (section 6.4.2). The distillation rig was trialled with a $GaI_3$ distillation (section 6.4.3). The successful operation of the new distillation rig led to the suggestion of the precursor elements of the Ge-Sb-Se glass system to be individually distilled before glass melting.

### 9.1.3. A preliminary study of the structure-property relationship of Ge-Sb-Se glasses along the stoichiometric tie-line x($GeSe_2$)-(1-x)( $Sb_2Se_3$) to guide future selection of candidate glass pairs to draw to fibre.

- **Structure**
  - The stoichiometric glasses were predominantly made up of tetrahedral [$GeSe_4$] and pseudotrigonal [$SbSe_3$] units.
  - From the fitted T($r$) peaks (section 8.3.2.4) for the Ge-Se peak and Sb-Se peak, it was suggested that for short range order there was no structural changes within the x($GeSe_2$)-(1-x)( $Sb_2Se_3$) glass system. The Ge ions in the Ge-Sb-Se glass

were found to have a coordination number between 3.87 - 4.02 ± 0.07, suggesting that the Ge ions were four coordinated, and independent of sample composition. The Ge-Se bond lengths were between 2.36-2.37 ± 0.001 Å. The coordination numbers for the Sb-Se bond were between 2.54 – 2.90 ± 0.07. There was a greater variation found with the coordination number for the Sb environment, which was inconsistent with Ge-Sb-Se sample composition. The Sb-Se bond lengths were between 2.61- 2.62 ± 0.001 Å. It was highlighted that there were large errors associated with the coordination numbers for both the Ge and Sb environment obtained in this work. The underlying reasons for the difficulty in analysing the neutron diffraction data to achieve the [$GeSe_4$] and [$SbSe_3$] coordination numbers of 4 and 3, respectively, were not fully understood at this time. However, it was suggested that the large errors were likely to be on account of the difficulties that arose with peak fitting due to the overlap of the Sb-Se peak with the Ge-Se peak. Furthermore, it was also suggested that the initial assumption that there were no Se-Se homopolar bonds in the stoichiometric glass compositions was incorrect. From further characterisation of the Se environment of the x($GeSe_2$)-(1-x)( $Sb_2Se_3$) glasses synthesised in this work by Barney and Titman using $^{77}$Se magic-angle spinning nuclear magnetic resonance (MAS NMR) it was suggested that ~ 4 % of Se atoms were in homopolar bonds.

- It was shown that the position of the first sharp diffraction peak (FSDP) in the i(Q) data (section 8.3.2.1) was shifted to higher Q as $Sb_2Se_3$ was incorporated into the Ge-Sb-Se glass network. It was considered that two linear trend lines could be fitted for the i(Q) data. The linear fit for values between x = 0.4 - 0.8 had a correlation coefficient of 0.975 and the linear fit for values between x =

0.8 - 1 had a correlation coefficient of 1.000. This non-linear shift in the position of the peak was suggested to arise from changes in the longer scale ordering of the Ge-Sb-Se network structure and it was suggested that the FSDP shifts observed corresponded to a contraction of the Ge-Sb-Se glass network.

- It was observed that the intensity of the FSDP in the i(Q) data (section 8.3.2.1) reduced from -0.148 to -0.345 barns $\text{atom}^{-1}$ $\text{steradian}^{-1}$, as the concentration of $Sb_2Se_3$ was increased. It was suggested that the reduction in intensity was due to fewer $[GeSe_4]$ units being bonded together. Ge has a greater neutron scattering length ($b$) ($b$= 8.185) than Sb ($b$ = 5.57). Thus, it was suggested as $Sb_2Se_3$ was added into the Ge-Sb-Se glass matrix the characteristic feature in the $[GeSe_4]$ units that gave rise to the greater intensity of the FSPD were broken up, resulting in a reduction of intensity of the FSDP.
- In the T($r$) data (section 8.3.2.2), a systematic change was seen in the third peak manifold (at a peak position ranging from ~ 3.80 – 3.88 Å) over the concentration range from x = 0.4 to 1. It was observed that as the overall intensity of the peak was increased, the peak broadened and shifted to higher Q. It was suggested that this could have been partly accounted for by the Sb ($b$ = 5.57) scattering more weakly than Ge ($b$ = 8.185). Thus it was proposed that with Sb addition in the glass Ge...Ge correlations were replaced with Ge...Sb and Sb...Sb correlations, which scattered neutrons less strongly

- **Structure-property relationship of Ge-Sb-Se stoichiometric glasses**
  - From decreasing the Sb content along the $x(GeSe_2)$-$(1-x)(Sb_2Se_3)$ stoichiometric tie line (from x = 0.4 to 0.9), it was shown that the change in structure of Se from a pseudotrigonal environment [$SbSe_3$] to a tetrahedral environment [$GeSe_4$], increased the $T_g$ of the glass (when x = 0.4 the $T_g$ = 240 ± 4 °C and when x = 0.9 the $T_g$ = 330 ± 3 °C). It was also found that the density of the glass decreased (when x = 0.4 the density was 5.07 ± 0.19 g $cm^{-3}$ and when x = 0.9 the density was 4.38 ± 0.13 g $cm^{-3}$). This change in thermal property of the Ge-Sb-Se glasses was explained on account of the change of bond energy (Ge-Se 206.77 kJ/ mol [42] and Sb-Se 183.93 kJ/ mol [42]) increasing the thermal stability of the Ge-Sb-Se glass. The change in the density was suggested to be due to the increased relative atomic masses of the elements (Sb = 121.76 [273] Ge = 72.63 [273]).

## 9.2. Suggestions for future work

As has been concluded in section 9.1, the Ge-Sb-Se chalcogenide glass fibres are potential materials for MIR SCG. Although difficulties were encountered in the extrusion and fibre drawing procedures, from the characterisation of thermal properties a greater understanding of the cause of these problems was achieved. Nevertheless, several ideas to aid the fabrication techniques can be followed to further improve the techniques, as suggested in section 9.2.1. Several suggestions are also made in section 9.2.2 to further reduce impurity absorption losses across the 2 - 12 µm range and improve glass purity. Future analysis proposed to help better understanding of the role of Se within the Ge-Sb-Se

glasses for greater investigation into the structure-property relationship is given in section 9.2.3.

### 9.2.1. Further investigation of physical, optical and cytotoxic properties and cytotoxicity of Ge-Sb-Se glass compositions to match potential glass pairs for small core-cladding MIR SCG fibres.

- As a result of the characterisation of the Ge-Sb-Se glasses in this Project the properties of three un-fabricated glass pairs evolved. Abiding by the suggested order of matching thermal properties (section 4.4), the fabrication of another glass pair, Pair V (core JB01; $Ge_{19}Sb_{15}Se_{66}$ and cladding JB04; $Ge_{22}Sb_{8}Se_{70}$) was recommended. Collated from the measurements conducted in this Project the properties of the fibre are suggested to be: Δ onset $T_g$ = 4 °C, ΔT (temperature at the extrusion region viscosity (~ $10^8$ Pa.s)) = 4 °C and a closely matched region of the rapid increase in the instantaneous thermal expansion coefficient (Figure 4.12). Furthermore, using the refractive index values reported in [83] at 1460 nm (JB01 2.68 and JB04 2.55) the NA of the fibre can be calculated as 0.81, the highest of any of the glass pairs.
- It was suggested that a difference in viscosity for each glass pair caused the core to enter the cladding at a different point during co-extrusion (section 5.1). It was shown that the temperature at which the Ge-Sb-Se glasses reach the extrusion viscosity ($\sim 10^8$ Pa.s) varied with composition (section 4.2.31). This was further evident in the co-extrusion E040JHB as the core had a lower viscosity than the cladding causing die swell (section 5.6.1). Therefore it is recommended to conduct

core/cladding analysis for each glass pair extrudate to assess where a target cross-sectional area ratio of 60 % core: cladding is achieved.

- For all extrusions in this Project, graphite was chosen to line the die due to its apparent low coefficient of friction with chalcogenide glass and because it did not appear to chemically react with the glass. It was suggested to be beneficial to have a similar lining / coating on the extrude pin head to reduce super-cooled melt drag. However, it was discussed that the die was lined with graphite by heating the die body with graphite, so that when the components were cooled the graphite was put under compression. Therefore, it was assumed that it would not be possible to apply the same graphite hot fitting method to the pin head as the graphite would not be able to be put under compression. Therefore the investigation into sputtered coatings that have a low coefficient of friction with chalcogenide glasses, are chemically inert to the glasses, and which could withstand the extrusion temperatures, such as titanium nitride or boron nitride, is proposed.
- It was found that cane drawing directly from the melt resulted in a tapered cane (section 5.5.3). It was suggested that this could be the result of the quenching process. As the glass melt was quenched from the top of the ampoule, the glass melt would have solidified at the top first preventing any trapped gases from escaping. A new approach to quenching is suggested which releases the ampoule from the bottom of the quenching furnace and applies the $N_2$ jet to the base of the ampoule. This would mean that the lower section would solidify first permitting any gases to be guided up through the glass melt and released from the top.

- Unfortunately equipment malfunctions impacted the application of a polymer coating in this Project (section 5.4 – 5.6). However, the investigation of polymer coatings to enhance the mechanical strength of fibres is suggested. It would be important to assess whether the fragile fibres from Pair II and Pair III would break internally within a polymer coating.
- The Alamar Blue assay results obtained for the Ge-Sb-Se fibres etched in propylamine and non-etched were difficult to distinguish and draw conclusions to sufficiently differentiate between the two surface conditions (section 7.4). It is suggested that a minimum essential media (MEM) elution assay should be conducted to acquire results independent of material surface properties and compare them to the Alamar Blue results from this Project. The MEM elution assays are designed to demonstrate the cytotoxic effects of potential leachables from a material.
- Cell coverage analysis conducted via SEM (section 7.5) showed that mammalian 3T3 fibroblast cells proliferated better on Ge-Sb-Se fibres which had been etched in propylamine than non-etched Ge-Sb-Se fibres. It is suggested that this was on account of the existence of an anticipated $Sb_2O_3$ layer formed on the surface of the fibres, which was removed with propylamine etching. It is recommended that the presence of this potential $Sb_2O_3$ layer should be established via X-ray Photoelectron Spectroscopy (XPS).
- With the prospect of the Ge-Sb-Se fibres to be used in clinical application, it is suggested to be important to assess how quickly the potential $Sb_2O_3$ layer formed (once its presence was established) after

fibre drawing. It is recommended that a simple cleaning process would need to be designed and suggested that other Ge-Sb-Se glass etching solutions, such as saline, are investigated.

### 9.2.2. The development of methods to achieve high-purity chalcogenide glasses.

- The Se purification processes using heat-treatment was described (section 3.2.1.2) to use a sacrificial silica glass insert to collect volatilised contaminants. It was suggested that any chemisorbed or physisorbed impurities in the silica glass insert could have been released during the Se heat-treatment and reacted with the Se, inhibiting the effect of the heat-treatment process. Therefore it is proposed that any future Se heat-treatment processes conducted by the MIR Photonics Group should subject the silica glass inserts to the same pre-treatment at the silica glass ampoule (*e.g.* HF-etched, annealed, air and vacuumed baked).
- In the literature it was suggested that the inclusion of iodide in a chalcogenide glass composition has the potential to lower the glass-melting temperature (≤ 650 °C [220]), thus, reducing the chalcogenide's glass reaction with the silica ampoule wall. Therefore, it is suggested that future work should focus on distilling precursor elements (Se, germanium (IV) iodide ($GeI_4$) and antimony (III) iodide ($SbI_3$) individually using the new distillation rig designed in this Project (section 6.4.2). It is proposed to investigate the effects of $SbI_3$ and $GeI_4$ on the optical loss spectra of the resulting Ge-Sb-Se-I fabricated fibres. Furthermore, it is proposed to compare these Ge-Sb-Se-I fibres to ones which had further been distilled as a glass melt with an oxygen getter and

the optical loss spectra from the fibres measured in this Project (section 6.3).

### 9.2.3. Future analysis proposed to help better understanding of the role of Se within the Ge-Sb-Se glasses for greater investigation into the structure-property relationship

- A further study combining Neutron, X-ray and NMR investigation of Se rich glasses is suggested. It was considered that this would provide an understanding of the role of the Se-Se bonds in determining the structure and properties of Ge-Sb-Se glasses with compositions more similar to those investigated in this Project for optical applications. It is suggested that future work should include tie lines that run from a stoichiometric composition to pure Se glass, passing through the compositions reported in Chapters 4-7 (*e.g.* JB01; $Ge_{19}Sb_{15}Se_{66}$, JB02, $Ge_{20}Sb_{10}Se_{70}$, JB03, $Ge_{24}Sb_{4}Se_{72}$ and JB04; $Ge_{22}Sb_{8}Se_{70}$). It is suggested that this would provide structural information on how small changes in the composition would affect the glass properties. It is anticipated that this could yield important insights into structure-property relationships that would inform future selection of glass composition for step-index Ge-Sb-Se chalcogenide glass fibre.

# References


1. BS ISO 20473:2007 Bristish Standards Institution. Optics and Photonics. Spectral Bands.: BSI.(2007).
2. C. R. Petersen, U. Møller, I. Kubat, B. Zhou, S. Dupont, J. Ramsay, T. Benson, S. Sujecki, N. Abdel-Moneim, Z. Tang, D. Furniss, A. Seddon and O. Bang. Mid-Infrared Supercontinuum Covering the 1.4–13.3 µm Molecular Fingerprint Region Using Ultra-High NA Chalcogenide Step-Index Fibre. Nature Photonics. 8, p.830-834, (2014).
3. A. B. Seddon. A Prospective for New Mid-Infrared Medical Endoscopy using Chalcogenide Glasses. International Journal of Applied Glass Science. 2, p.177-191, (2011).
4. M. Diem, S. Boydston-White and L. Chirboya. Infrared Spectroscopy of Cells and Tissues: Shining Light onto a Novel Subject. Applied Spectroscopy. 153, p.148-161, (1999).
5. C. Boussard-Pledel, S. Hocde, G. Fonteneau, H.L. Ma, X.-H Zhang, K. Le Foulgoc, J. Lucas, B. Perio and J. Hamelin. Infrared Glass Fibers for Evanescent Wave Spectroscopy. in Specialty Fiber Optics for Medical Applications: San Jose. p. 91-98.(1999).
6. O. Humbach, H. Fabian, U. Grzesik, U. Haken and W. Heitmann. Analysis of OH Absorption Bands in Synthetic Silica. Journal of Non-Crystalline Solids. 203, p.19-26, (1996).
7. P. M. Moselund, C. Petersen, S. Dupont, C. Agger, O. Bang and S. R. Keiding. Supercontinuum: Broad as a Lamp, Bright as a Laser, Now in the Mid-Infrared. in Proc. SPIE 8381, Laser Technology for Defense and Security VIII. Baltimore.(2012).
8. P. Domachuk, N. A. Wolchover, M. Cronin-Golomb, A. Wang, A. K. George, C. M. B. Cordeiro, J. C. Knight and F. G. Omenetto. Over 4000 nm Bandwidth of Mid-IR Supercontinuum Generation in Sub-Centimeter Segments of Highly Nonlinear Tellurite PCFs. Optics Express. 16, p.7161-7168, (2008).
9. R. Thapa, D. Rhonehouse, D. Nguyen, K. Wiersma, C. Smith, J. Zong and A. Chavez-Pirson. Mid-Infrared Supercontinuum Generation in Ultra-Low Loss, Dispersion-Zero Shifted Tellurite Glass Fiber with Extended Coverage Beyond 4.5 µm. in Proc. SPIE 8898, Technologies for Optical Countermeasures X and High-Power Lasers Dresden.(2013).
10. G. Steinmeyer and J. S. Skibina. Supercontinua: Entering the Mid-Infrared. Nature Photonics. 8, p.814-815, (2014).
11. R. R. Gattass, Brandon S. L., V. Q. Nguyen, P. C. Pureza, I. D. Aggarwal and J. S. Sanghera. All-Fiber Chalcogenide-Based Mid-Infrared Supercontinuum Source. Optical Fiber Technology. 18, p.345-348, (2012).
12. L. B. Shaw, V. Q. Nguyen, J. S. Sanghera, I. D. Aggarwal, P. A. Thielen and F. H. Kung. IR Supercontinuum Generation in As-Se Photonic Crystal Fiber. in Advanced Solid-State Photonics (TOPS). Vienna: Optical Society of America.(2005).
13. Y. Yu, X. Gai, T. Wang, P. Ma, R. Wang, Z. Yang, D.-Y. Choi, S. Madden and B. Luther-Davies. Mid-Infrared Supercontinuum Generation in Chalcogenides. Optical Materials Express. 3, p.1075-1086, (2013).
14. Z. Zhao, X. Wang, S. Dai, Z. Pan, S. Liu, L. Sun, P. Zhang, Z. Liu, Q. Nie, X. Shen and R. Wang. 1.5–14 µm Mid-Infrared Supercontinuum Generation in a Low-

Loss Te-Based Chalcogenide Step-Index Fiber. Optics Letters. 41, p.5222-5225, (2016).
15. T. Cheng, K. Nagasaka, T. H. Tuan, X. Xue, M. Matsumoto, H. Tezuka, T. Suzuki and Y. Ohishi. Mid-Infrared Supercontinuum Generation Spanning 2.0 to 15.1 um in a Chalcogenide Step-Index Fiber. Optics Letters. 41, p.2117-2120, (2016).
16. H. Ou, S. Dai, P. Zhang, Z. Liu, X. Wang, F. Chen, H. Xu, B. Luo, Y. Huang and R. Wang. Ultrabroad Supercontinuum Generated from a Highly Nonlinear Ge–Sb–Se Fiber. Optics Letters. 41, p.3201-3204, (2016).
17. J. A. Savage. Chapter 23 - Chalcogenide Glasses for Optical Applications. Glass - Current Issues Springer Netherlands. p. 281-306.(1985).
18. D. Lezal, J. Pedlikova and J. Zavadil. Chalcogenide Glasses for Optical and Photonics Applications. Journal of Optoelectronics and Advanced Materials. 6, p.133-137, (2004).
19. S. Cui, R. Chahal, C. Boussard-Plédel, V. Nazabal, J.-L. Doualan, J. Troles, J. Lucas and B. Bureau. From Selenium- to Tellurium-Based Glass Optical Fibers for Infrared Spectroscopies. Molecules. 18, p.5373, (2013).
20. International Agency For Research On Cancer (IARC). Agents Classified by the IARC Monographs, Volumes 1–112. [ Access Date 07/05/ 2015]; Available from: http://monographs.iarc.fr/ENG/Classification/ClassificationsAlphaOrder.pdf.
21. V. S. Shiryaev and M. F. Churbanov. Chapter 1 - Preparation of High-Purity Chalcogenide Glasses. Chalcogenide Glasses. Preparation, Properties and Applications Woodhead Publishing. Oxford. p. 3-35.(2014).
22. G. E. Snopatin, V. S. Shiryaev, V. G. Plotnichenko, Dianov E.M. and M.F. Churbanov. High Purity Chalcogenide Glass for Fibre Optics. Inorganic Materials. 45, p.1439-1460, (2009).
23. R. C. Schimmel, A. J. Faber, H. de Waardt, R. G. C. Beerkens and G. D. Khoe. Development of Germanium Gallium Sulphide Glass Fibres for the 1.31 µm Praseodymium-Doped Fibre Amplifier. Journal of Non-Crystalline Solids. 284, p.188-192, (2001).
24. P. McNamara, D. G. Lancaster, R. Bailey, A. Hemming, P. Henry and R. H. Mair. A Large Core Microstructured Fluoride Glass Optical Fibre for Mid-Infrared Single-Mode Transmission. Journal of Non-Crystalline Solids. 355, p.1461-1467, (2009).
25. J. S. Sanghera, L. B. Shaw, L. E. Busse, V. Q. Nguyen, P. C. Pureza, B. C. Cole, B. B. Harrison, I. D. Aggarwal, R. Mossadegh, F. Kung, D. Talley, D. Roselle and R. Miklos. Development and Infrared Applications of Chalcogenide Glass Optical Fibers. Fiber and Integrated Optics. 19, p.251-274, (2000).
26. J. Nishii, S. Morimoto, I. Inagawa, R. Iizuka, T. Yamashita and T. Yamagishi. Proceedings of the Seventh International Symposium on Halide Glasses. Recent Advances and Trends in Chalcogenide Glass Fiber Technology: A Review. Journal of Non-Crystalline Solids. 140, p.199-208, (1992).
27. J. Nishii, T. Yamashita and T. Yamagishi. Low-Loss Chalcogenide Glass Fiber with Core-Cladding Structure. Applied Physics Letters. 53, p.553-554, (1988).
28. A. B. Seddon, B. Napier, I. Lindsay, S. Lamrini, P. M. Moselund, N. Stone and O. Bang. Mid-infrared Spectroscopy/ Bioimaging: Moving Towards MIR Optical Biopsy. Bio Optics World. (2016).
29. H. Elkadi. Cultures of Glass Architecture. Abingdon. Ashgate Publishing Group.(2006).
30. R. H. Doremus. Glass Science. Canada. John Wiley and Sons.(1973).

31. J. E. Shelby. Introduction to Glass Science and Technology. 2nd Edition. Cambridge. The Royal Society of Chemistry.(2005).
32. W. Vogel. Glass Chemistry. Heidelberg. Springer-Verlag.(1994).
33. J. Kawamura, R. Asayama, N. Kuwata and O. Kamishima. Ionic Transport in Glass and Polymer: Hierarchical Structure and Dynamics Physics of Solid State Ionics. p.193-246, (2006).
34. J. Wong and C. A. Angell. Glass: Structure by Spectroscopy. Vol. 10. New York. Dekker.(1976).
35. W. H. Zachariasen. The Atomic Arrangement in Glass. Journal of the American Chemical Society. 54, p.3841-3851, (1932).
36. K. Ross, S. Arntfield and S. Cenkowski. A Polymer Science Approach to Physico-Chemical Characterization and Processing of Pulse Seeds. Polymer Science.(2013)
37. P. G. Debenedetti and F. H. Stillinger. Supercooled Liquids and the Glass Transition. Nature. 410, p.259-267, (2001).
38. W. H. Beamer and C. R. Maxwell. Physical Properties of Polonium. II. X-Ray Studies and Crystal Structure. The Journal of Chemical Physics. 17, p.1293-1298, (1949).
39. A. K. Varshneya, A. N. Sreeram and D. R Swiler. A Review of the Average Coordination-Number Concept in Multicomponent Chalcogenide Glass Systems. Physics and Chemistry of Glasses. 34, p.179-193, (1993).
40. Z. Yang, G. Tang, L. Luo and W. Chen. Visible Transparent GeSe2-Ga2Se3-KX (X=I,Br or Cl) Glasses for Infrared Optics. Journal of American Ceramics Society. 80, (2007).
41. N. Hasanzadeh and D. Nori-Shargh. Correlations Between Hardness, Electronegativity, Anomeric Effect Associated with Electron Delocalizations and Electrostatic Interactions in 1,4,5,8-tetraoxadecalin and its Analogs Containing S and Se Atoms. Computational and Theoretical Chemistry. 1051, p.1-9, (2015).
42. N. Sharma, S. Sharda, V. Sharma and P. Sharma. Far-Infrared Investigation of Ternary Ge–Se–Sb and Quaternary Ge–Se–Sb–Te Chalcogenide Glasses. Journal of Non-Crystalline Solids. 375, p.114-118, (2013).
43. S. Savage. Development of Low Optical Loss Chalcogenide Glass Fibres for Mid-Infared Transmission. Doctor of Philosophy Thesis. The University of Nottingham: UK. p. 9-53.(2006).
44. A. B. Seddon. Chalcogenide Glasses: A Review of Their Preparation, Properties and Applications. Journal of Non-Crystalline Solids. 184, p.44-50, (1995).
45. Z. Tang. Rare Earth Ion Doped Selenide-Based Chalcogenide Glasses and Fibres Towards Mid-infrared Fibre Lasers. Doctor of Philosophy Thesis. The University of Nottingham: UK.(2010).
46. H. Sakr. Towards Mid-Infrared Fibre Lasers: Rare Earth Ion Doped Chalcogenide Glasses and Fibres. Doctor of Philosophy Thesis. The University of Nottingham: UK.(2016).
47. H.L. Rowe. Infrared Transmitting Optical Fibres with Potential Use in Medical Diagnosis and Treatment. Doctor of Philosophy Thesis. The University of Nottingham: UK.(2008).
48. A. B. Seddon. Chalcohalides: Glass-Forming Systems and Progress in Application of Percolation Theory. Journal of Non-Crystalline Solids. 213–214, p.22-29, (1997).

49. M. Lasocka. The Effect of Scanning Rate on Glass Transition Temperature of Splat-Cooled Te85Ge15. Materials Science and Engineering. 23, p.173-177, (1976).
50. A. A. Piarristeguy, E. Barthélémy, M. Krbal, J. Frayret, C. Vigreux and A. Pradel. Glass Formation in the GexTe100−x Binary System: Synthesis by Twin Roller Quenching and Co-Thermal Evaporation Techniques. Journal of Non-Crystalline Solids. 355, p.2088-2091, (2009).
51. V. Dimitrov and T. Komatsu. Correlation Among Electronegativity, Cation Polarizability, Optical Basicity and Single Bond Strength of Simple Oxides. Journal of Solid State Chemistry. 196, p.574-578, (2012).
52. D. N. Talwar, M. Vandevyver, K. Kunc and M. Zigone. Lattice Dynamics of Zinc Chalcogenides Under Compression: Phonon Dispersion, Mode Gruneisen and Thermal Expansion. PHYSICAL REVIEW B. 24, p.741-753, (1981).
53. I. Moreels, K. Lambert, D. De Muynck, F. Vanhaecke, D. Poelman, J. C. Martins, G. Allan and Z. Hens. Composition and Size-Dependent Extinction Coefficient of Colloidal PbSe Quantum Dots. Chemistry of Materials. 19, p.6101-6106, (2007).
54. K. Palanjyan, S. H. Messaddeq, Y. Messaddeq, R. Vallée, E. Knystautas and T. Galstian. Study of Photoinduced Birefringence vs As Content in Thin Ge-As-S Films. Optical Materials Express. 3, p.671-683, (2013).
55. E. R. Scerri. The Periodic Table: Its Story and its Significance. New York. Oxford University Press.(2007).
56. S. Tanabe, T. Hanada, M. Watanabe, T. Hayashi and N. Soga. Optical Properties of Dysprosium-Doped Low-Phonon-Energy Glasses for a Potential 1.3 µm Optical Amplifier. Journal of the American Ceramic Society. 78, p.2917-2922, (1995).
57. B. Cole, L. B. Shaw, P. C. Pureza, R. Mossadegh, J. S. Sanghera and I. D. Aggarwal. Rare-Earth Doped Selenide Glasses and Fibers for Active Applications in the Near and Mid-IR. Journal of Non-Crystalline Solids. 256–257, p.253-259, (1999).
58. D. Lezal. Chalcogenide Glasses-Survey and Progress. Journal of Optoelectronics and Advanced Materials. 5, p.23-34, (2003).
59. D. I. Bletskan. Glass Formation in Binary and Ternary Chalcogenide Systems. Chalcogenide Letters. 3, p.81-119, (2006).
60. L. G. Aio, A. M. Efimov and V. F. Kokorina. Refractive Index of Chalcogenide Glasses Over a Wide Range of Compositions. Journal of Non-Crystalline Solids. 27, p.299 - 307, (1978).
61. Y. Sharma and P. Srivastava. First Principles Investigation of Electronic, Optical and Transport Properties of α- And β-Phase of Arsenic Telluride. Optical Materials. 33, p.899-904, (2011).
62. M. Dongol, T. Gerber, M. Hafiz, M. Abou-Zied and A. F. Elhady. On the Structure of As2 Te3 Glass. Journal of Physics: Condensed Matter. 18, p.6213, (2006).
63. V. Trappe, V. Prasad, L. Cipelletti, P. N. Segre and D. A. Weitz. Jamming Phase Diagram for Attractive Particles. Nature. 411, p.772-775, (2001).
64. N. Mehta, R. S. Tiwari and A. Kumar. Glass Forming Ability and Thermal Stability of Some Se–Sb Glassy Alloys. Materials Research Bulletin. 41, p.1664-1672, (2006).
65. N. W. Tideswell, F. H. Kruse and J. D. McCullough. The Crystal Structure of Antimony Selenide, Sb2Se3. Acta Crystallographica. 10, p.99-102, (1957).

66. G. Dittmar and H. Schäfer. Die Kristallstruktur Von Germaniumdiselenid. Acta Crystallographica Section B. 32, p.2726-2728, (1976).
67. C. Jiang, C. Cheng, Q. Zhu, X. Wang, Q. Nie, S. Dai, G. Tao, M. Zhu, F. Liao, P. Zhang, X. Shen, T. Xu, P. Zhang, Z. Liu and X. Zhang. Fabrication and Characterization of Ge–Sb–Se–I Glasses and Fibers. Applied Physics A. 120, p.127-135, (2015).
68. W.-H. Wei, L. Fang, X. Shen and R.-P. Wang. Transition Threshold in GexSb10Se90− x Glasses. Journal of Applied Physics. 115, p.113510, (2014).
69. S. Sharda, N. Sharma, P. Sharma and V. Sharma. Thermal Stability and Crystallization Kinetics of Quaternary Sb–Se–Ge–In Chalcogenide Glasses. Journal of Alloys and Compounds. 611, p.96-99, (2014).
70. M. Olivier, J. C. Tchahame, P. Němec, M. Chauvet, V. Besse, C. Cassagne, G. Boudebs, G. Renversez, R. Boidin, E. Baudet and V. Nazabal. Structure, Nonlinear Properties and Photosensitivity of (GeSe2)100-x(Sb2Se3)x Glasses. Optical Materials Express. 4, p.525-540, (2014).
71. J. A. Savage, P. J. Webber and A. M. Pitt. An Assessment of Ge-Sb-Se Glasses as 8 to 12 μm Infrared Optical Materials. Journal of Materials Science. 13, p.859-864, (1978).
72. F. Xia, S. Baccaro, W. Wang, L. Pilloni, X. Zhang, H. Zeng and G. Chen. Nanophase Separation and Effects on Properties of Ge–As–Se Chalcogenide Glasses. Journal of Non-Crystalline Solids. 354, p.1137-1141, (2008).
73. B. T. M. Willis and C. J. Carlile. Experimental Neutron Scattering. Oxford, UK. Oxford University Press.(2009).
74. A. C. Hannon. Results on Disordered Materials from the General Materials Diffractometer, GEM, at ISIS. Nuclear Instruments and Methods in Physics Research A. 551, p.88-107, (2005).
75. A. C. Hannon. Neutron Diffraction, Instrumentation. High Energy Spectroscopy. Methods and Instrumentation. 2, p.1479-1492, (1999).
76. G. L. Squires. Introduction to the Theory of Thermal Neutron Scattering. New York. Dover Publications.(1996).
77. D. L. Price and K. Skold. Chapter 1 - Introduction to Neutron Scattering. Methods in Experimental Physics. Academic Press. p. 1-97.(1986).
78. A.C. Wright, C. J. Simmons and O. H. El-Bayoumi. Experimental Techniques of Glass Science. American Ceramic Society,. 205, (1993).
79. B. G. Yerozolimsky. Free Neutron Decay: A Review of the Contemporary Situation. Nuclear Instruments and Methods in Physics Research Section A: Accelerators, Spectrometers, Detectors and Associated Equipment. 440, p.491-498, (2000).
80. B.T.M. Willis and C.J. Carlie. Experimental Neutron Scattering. Oxford UK. Oxford University Press.2009.
81. A. C. Wright. Neutron and X-ray Amorphography. Journal of Non-Crystalline Solids. 106, p.1-16, (1988).
82. G. Herzberg. Molecular Spectra and Molecular Structure. Princeton. D.Van Nostrand Company Inc.(1950).
83. L. Quingquan. Microstructured Optical Fibres in Chalcogenide Glass. Master of Philosophy Thesis. The University of Nottingham: UK.(2013).
84. P. W. France, M. G. Drexhage, J. M. Parker, M. W. Moore, S. F. Carter and J. V. Wright. Fluoride Glass Optical Fibres. Glasgow & London. Blackie and Son Ltd.(1990).
85. F. L. Pedrotti, L. M. Pedrotti and L. S. Pedrotti. Introduction to Optics. Third Edition. Pearson. Pearson International Edition.(2007).

86. P. R. Griffiths and J. A. De Haseth. Fourier Transform Infrared Spectrometry. Oxford. John Wiley & Sons.(2007).
87. Cancer Research UK. A Leading Cancer Research Charity. [ Access Date: 03/02/2016]; Available from: http://www.cancerresearchuk.org/.
88. J. Maddams, M. Utley and H. Moller. Projections of Cancer Prevalence in the United Kingdom. British Journal Of Cancer. 107, p.1195-1202, (2012).
89. World Health Organization. Ultraviolet Radiation and the Intersun Programme – Skin Cancers. [Access Date 30/11/2015]; Available from: http://www.who.int/uv/intersunprogramme/en/.
90. J. Orazio, S. Jarrett, A. Amaro-Ortiz and T. Scott. UV Radiation and the Skin. International Journal of Molecular Sciences. 14, p.12222, (2013).
91. H. W. Rogers, M. A. Weinstock, A. R. Harris, M. R. Hinckley, S. R. Feldman, A. B. Fleischer and B. M. Coldiron. Incidence Estimate of Nonmelanoma Skin Cancer in the United States in 2006. Archives of Dermatology. 146, p.283-287, (2010).
92. A. C. Geller and G. D. Annas. Epidemiology of Melanoma and Nonmelanoma Skin Cancer. Seminars in Oncology Nursing. 19, p.2-11, (2003).
93. B. Suarez, G. Lopez-Abente, C. Martinez, C. Navarro, M. Tormo, S. Rosso, S. Schraub, L. Gafa, H. Sancho-Garnier, J. Wechsler and R. Zanetti. Occupation and Skin Cancer: The Results of the HELIOS-I Multicenter Case-Control Study. BMC Public Health. 7, p.180, (2007).
94. D. L. Narayanan, R. N. Saladi and J. L. Fox. Review: Ultraviolet Radiation and Skin Cancer. International Journal of Dermatology. 49, p.978-986, (2010).
95. R. Gordon. Skin Cancer: An Overview of Epidemiology and Risk Factors. Seminars in Oncology Nursing. 29, p.160-169, (2013).
96. V. Nikolaou and A. J. Stratigos. Emerging Trends in the Epidemiology of Melanoma. British Journal of Dermatology. 170, p.11-19, (2014).
97. R. Soffieti, P. Cornu, J. Y. Delattre, R. Gaunt, F. Graus, W. Grisold, J. Heimans, J. Hildebrand, P. Hoskin, M. Kallijo, P. Krauseneck, C. Marosi, T. Siegal and C. Vecht. Brain Metastases. European Handbook of Neurological Managements: Oxford.(2011).
98. B.G. Aitken, C.W. Ponader and R.S. Quimby. Clustering of Rare Earths in GeAsS Glass. Comptes Rendus Chimie. 5, p.865-872, (2002).
99. R. Salzer and H. W. Siesler. Infrared and Raman Spectroscopic Imaging. Wiley-VCH: Weinheim.(2014).
100. H. J. Butler, L. Ashton, B. Bird, G. Cinque, K. Curtis, J. Dorney, K. Esmonde-White, N. J. Fullwood, B. Gardner, P. L. Martin-Hirsch, M. J. Walsh, M. R. McAinsh, N. Stone and F. L. Martin. Using Raman Spectroscopy to Characterize Biological Materials. Nature Protocols. 11, p.664-687, (2016).
101. H. Barr, O. Old, M. Almond, C. Kendall, G. Rhys-Lloyd, G. Shetty, J. Hutchings and N. Stone. Vibrational Spectroscopy: The Solution for Immediate Medical Diagnosis. Materials Today: Proceedings. 2, p.890-893, (2015).
102. L. M. McIntosh, M. Jackson, H. H. Mantsch, J. R. Mansfield, A. N. Crowson and J. W. P. Toole. Non-Invasive Screening of Skin Diseases by Visible/ Near-IR Spectroscopy. Journal of Investigative Dermatology. 116, p.175-181, (2001).
103. L. M. McIntosh, M. Jackson, H. H. Mantsch, A. N. Crowson, A. Neil and J. W. P. Toole. Non-Invasive Screening of Skin Disease by Visible/ Near-Infrared Spectroscopy. Patent 7280866. US, Editor.(2007).
104. L. M. McIntosh, M. Jackson, H. H. Mantsch, M. F. Stranc, D. Pilavdzic and A. N. Crowson. Infrared Spectra of Basal Cell Carcinomas are Distinct from Non-

Tumor-Bearing Skin Compnent. Journal of Investigative Dermatology. 112, p.951-956, (1999).
105. E. Ly, O. Piot, A. Durlach, P. Bernard and M. Manfait. Differential Diagnosis of Cutaneous Carcinomas by Infrared Spectral Micro-imaging Combined with Pattern Recognition. Analyst. 134, p.1208-1214, (2009).
106. Cancer Research UK. Incisive Health. Saving Lives, Averting Costs. An Analysis of the Financial Implications of Achieving Earlier Diagnosis of Colorectal, Lung and Ovarian Cancer.(2014). [Access Date 02/12/ 2015]; Available from: w.w.w.incisivehealth.com/uploads /Saving lives averting costs.pdf ].
107. M. Diem, S. Boydston-White and L. Chiriboga. Infrared Spectroscopy of Cells and Tissues: Shining Light onto a Novel Subject. Applied Spectroscopy. 53, p.148-161, (1999).
108. S. Clancy. DNA Damage and Repair: Mechanisms for Maintaining DNA Integrity. Nature Education. 1, p.103, (2008).
109. C. A. Horswill. Hydration and Health. AMERICAN JOURNAL OF LIFESTYLE MEDICINE. 5, p.304-315, (2001).
110. I. Kaplan. The CO2 Surgical Laser. Photomedicine and Laser Surgery. 28, p.847-848, (2010).
111. O. Tokuya and N. Kayoko. The Role of the CO2 Laser and Fractional CO2 Laser in Dermatology. Laser Therapy. 23, p.49-60, (2014).
112. A. Breslow. Thickness, Cross-Sectional Areas and Depth of Invasion in the Prognosis of Cutaneous Melanoma. Annals of Surgery. 172, p.902-908, (1970).
113. M. T. Sun, N. H. Andrew, B. O'Donnell, A. McNab, S. C. Huilgol and D. Selva. Periocular Squamous Cell Carcinoma: TNM Staging and Recurrence. Ophthalmology. 122, p.1512-1516, (2015).
114. R. K. Freinkel and D. T. Woodley. The Biology of the Skin. New York. Parthenon Publishing Group.(2001).
115. J. R. Mourant, J. P. Freyer, A. H. Hielscher, A. A. Eick, D. Shen and T. M. Johnson. Mechanisms of Light Scattering from Biological Cells Relevant to Non-invasive Optical-Tissue Diagnostics. Applied Optics. 37, p.3586-3593, (1998).
116. G. J. Tearney, M. E. Brezinski, B. E. Bouma, M. R. Hee, J. F. Southern and J. G. Fujimoto. Determination of the Refractive Index of Highly Scattering Human Tissue by Optical Coherence Tomography. Optics Letters. 20, p.2258-2260, (1995).
117. D. Huafeng, Q. L. Jun, A. W. William, J. K. Peter and H. Xin-Hua. Refractive Indices of Human Skin Tissues at Eight Wavelengths and Estimated Dispersion Relations Between 300 and 1600 nm. Physics in Medicine and Biology. 51, p.1479, (2006).
118. T. Lister, P. A. Wright and P. H. Chappell. Optical Properties of Human Skin. Journal of Biomedical Optics. 17, p.11-15, (2012).
119. A. P. M. Michel, S. Liakat, K. Bors and C. F. Gmachl. In Vivo Measurement of Mid-Infrared Light Scattering from Human Skin. Biomedical Optics Express. 4, p.520-530, (2013).
120. International Standard ISO. Biological Evaluation of Medical Devices. [ Access Date 06/01/2016]; Available from: http://www.iso.org/iso/catalogue_detail.htm?csnumber=36406.

121. A. A. Wilhelm, P. Lucas, D. L. DeRosa and M. R. Riley. Biocompatibility of Te–As–Se Glass Fibers for Cell-Based Bio-Optic Infrared Sensors. Journal of Materials Research. 22, p.1098-1104, (2007).
122. P. Lucas, M. A. Solis, D. Le Coq, C. Juncker, M. R. Riley, J. Collier, D. E. Boesewetter, C. Boussard-Plédel and B. Bureau. Infrared Biosensors Using Hydrophobic Chalcogenide Fibers Sensitized With Live Cells. Sensors and Actuators B: Chemical. 119, p.355-362, (2006).
123. J. Keirsse, C. Boussard-Plédel, O. Loréal, O. Sire, B. Bureau, P. Leroyer, B. Turlin and J Lucas. Optical Fibre Sensor for Biomedical Applications. Vibrational Spectroscopy. 32, p.23-32, (2003).
124. K Taga, R Kellner, U Kainz and UB Sleytr. In Situ Attenuated Total Reflectance FT-IR Analysis of an Enzyme-Modified Mid-Infrared Fiber Surface Using Crystalline Bacterial Surface Proteins. Analytical Chemistry. 66, p.35-39, (1994).
125. P. Lucas, M. A. Solis, D. Le Coq, C. Juncker, M. R. Riley, J. Collier, D. E. Boesewetter, C. Boussard-Plédel and B. Bureau. Infrared Biosensors using Hyrdrophobic Chalcogenide Fibers Sensitized with Live Cells. Sensors and Actuators B. 119, p.355-362, (2006).
126. J. Swiderski. High-Power Mid-Infrared Supercontinuum Sources: Current Status and Future Perspectives. Progress in Quantum Electronics. 38, p.189-235, (2014).
127. R. R. Alfano and S. L. Shapiro. Observation of Self-Phase Modulation and Small-Scale Filaments in Crystals and Glasses. Physical Review Letters. 24, p.592-594, (1970).
128. G. Geloni, V. Kocharyan and E. Saldin. Brightness of Synchrotron Radiation from Wigglers. Nuclear Instruments and Methods in Physics Research Section A: Accelerators, Spectrometers, Detectors and Associated Equipment. 807, p.13-29, (2016).
129. S. Dai, F. Chen, Y. Xu, Z. Xu, X. Shen, T. Xu, R. Wang and W. Ji. Mid-Infrared Optical Nonlinearities of Chalcogenide Glasses in Ge-Sb-Se Ternary System. Optics Express. 23, p.1300-1307, (2015).
130. Q. Coulombier, L. Brilland, P. Houizot, T. Chartier, T. N. N'Guyen, F. Smektala, G. Remversez and J. Troles. Casting Methods for Producing Low-Loss Chalcogenide Microstructured Optical Fibres. Optics Express. 18, p.9107-9112, (2010).
131. J. H. V. Price, T. M. Monro, H. Ebendorff-Heidepriem, F. Poletti, P. Horak, V. Finazzi, J. Y. Y. Leong, P. Petropoulos, J. C. Flanagan, G. Brambilla, X. Feng and D. J. Richardson. Mid-IR Supercontinuum Generation from Nonsilica Microstructured Optical Fibers. Institute of Electrical and Electronics Engineers. 13, p.738-749, (2007).
132. R. E. Slusher, G. Lenz, J. Hodelin, J. Sanghera, L. B. Shaw and I. D. Aggarwal. Large Raman Gain and Nonlinear Phase Shifts in High-Purity As2Se3 Chalcogenide Fibers. Journal of the Optical Society of America B. 21, p.1146-1155, (2004).
133. J. W. Nicholson, A. D. Yablon, P. S. Westbrook, K. S. Feder and M. F. Yan. High Power, Single Mode, All-Fiber Source of Femtosecond Pulses at 1550 nm and its Use in Supercontinuum Generation. Optics Express. 12, p.3025-3034, (2004).
134. A. K. Abeeluck and C. Headley. Continuous-Wave Pumping in the Anomalous- and Normal-Dispersion Regimes of Nonlinear Fibers for Supercontinuum Generation. Optics Letters. 30, p.61-63, (2005).

135. J. Świderski, A. Zając and M. Skórczakowski. Pulsed Ytterbium-Doped Large Mode Area Double-Clad Fiber Amplifier in MOFPA Configuration. Opto-Electronics Review. 15, p.98-101, (2007).
136. A. Chong, W.H. Renninger and F.W. Wise. All-Normal-Dispersion Femtosecond Fiber Laser with Pulse Energy Above 20nJ. Optical Letter. 32, p.2408-2410, (2007).
137. L. Sojka, Z. Tang, H. Zhu, E. Beres-Pawlik, D. Furniss, A.B. Seddon, T.M. Benson and S. Sujecki. Study of Mid-Infrared Laser Action in Chalcogenide Rare Earth Doped Glass with Dy3+, Pr3+ and Tb3+. Optical Materials Express. 2, p.1580-1587, (2012).
138. R. Frerichs. New Optical Glasses with Good Transparency in the Infrared. Journal of the Optical Society of America. 43, p.1153-1157, (1953).
139. N. S. Kapany and R. J. Simms. Recent Developments in Infrared Fiber Optics. Infrared Physics. 5, p.69-80, (1965).
140. D. L. Andrews. Photonics, Volume 1 : Fundamentals of Photonics and Physics. ed. A Wiley-Science Wise Co-Publication Somerset, US. Wiley.(2015).
141. A. C. S. Van Heel. A New Method of Transporting Optical Images without Aberrations. Nature. 173, p.39-39, (1954).
142. G. F. Smith and T. A. King. Optics and Photonics: An Introduction. Chichester. John Wiley & Sons, Ltd.(2001).
143. S. D. Savage, C. A. Miller, D. Furniss and A. B. Seddon. Extrusion of Chalcogenide Glass Preforms and Drawing to Multimode Optical Fibers. Journal of Non-Crystalline Solids. 354, p.3418-3427, (2008).
144. M. F. Churbanov, V. S. Shiryaev, V. V. Gerasimenko, A. A. Pushkin, I. V. Skripachev, G. E. Snopatin and V. G. Plotnichenko. Stability of the Optical and Mechanical Properties of Chalcogenide Fibers. Inorganic Materials. 38, p.1063-1068, (2002).
145. M. F. Churbanov, V. S. Shiryaev, A. I. Suchkov, A. A. Pushkin, V. V. Gerasimenko, R. M. Shaposhnikov, E. M. Dianov, V. G. Plotnichenko, V. V. Koltashev, Yu N. Pyrkov, J. Lucas and J. L. Adam. High-Purity As-S-Se and As-Se-Te Glasses and Optical Fibers. Inorganic Materials. 43, p.441-447, (2007).
146. Personal communication with Professor A.B. Seddon. Latest Result of the MIR Photonic Glasses Research Group. University of Nottingham, UK.(2016).
147. X. Chen, G. Zhang and H. Zeng. Advances in Nonlinear Optics. Berlin. De Gruyter.(2015).
148. J. Troles, V. Shiryaev, M. Churbanov, P. Houizot, L. Brilland, F. Desevedavy, F. Charpentier, T. Pain, G. Snopatin and J. L. Adam. GeSe4 Glass Fibres with Low Optical Losses in the Mid-Infrared. Optical Materials. 32, p.212-215, (2009).
149. M. F. Churbanov. High-Purity Chalcogenide Glasses as Materials for Fiber Optics. Journal of Non-Crystalline Solids. 184, p.25-29, (1995).
150. G.G. Devyatykh, E.M. Dianov, V.G. Plotnichenko, I.V. Skripachev and M.F. Churbanov. Fiber Waveguides Based on High-Purity Chalcogenide Glasses. High-Purity Substances. 5, p.1-27, (1991).
151. R.-D. Sun and T. Tsuji. Preparation of Antimony Sulfide Semiconductor Nanoparticles by Pulsed Laser Ablation in Liquid. Applied Surface Science. 348, p.38-44, (2015).
152. Q. Looker, M. Amman and K. Vetter. Inter-Electrode Charge Collection in High-Purity Germanium Detectors with Amorphous Semiconductor Contacts. Nuclear Instruments and Methods in Physics Research Section A: Accelerators, Spectrometers, Detectors and Associated Equipment. 781, p.20-25, (2015).

153. A. I. Isayev, S. I. Mekhtiyeva, N. Z. Jalilov, R. I. Alekperov and G. K. Akberov. Localised States in the Band Gap of Chalcogenide Glass-Like Semiconductors of Se–As System with Sm Impurity. Solid State Communications. 149, p.45-48, (2009).
154. A. M. Reitter, A. N. Sreeram, A. K. Varshneya and D. R. Swiler. Modified Preparation Procedure for Laboratory Melting of Multicomponent Chalcogenide Glasses. Journal of Non-Crystalline Solids. 139, p.121-128, (1992).
155. C. T. Moynihan, P. B. Macedo, M. S. Maklad, R. K. Mohr and R. E. Howard. Intrinsic and Impurity Infrared Absorption in As2Se3 Glass. Journal of Non-Crystalline Solids. 17, p.369-385, (1975).
156. J. Sanghera and I. D. Aggarwal. Infrared Fiber Optics. Patent. CRC Press LLC: Washington D.C.(1998).
157. S. A. Adamchik, A. Yu Malyshev, A. D. Bulanov and E. N. Bab'eva. Fine Purification of Sulfur from Carbon by High-Temperature Oxidation. Inorganic Materials. 37, p.469-472, (2001).
158. T. M. Monro and H. Ebendorff-Heidepriem. Progress In Microstructured Optical Fibres. Annual Review of Materials Research. 36, p.467-495, (2006).
159. T. Kanamori, Y. Terunuma, S. Takahashi and T. Miyashita. Chalcogenide Glass Fibers for Mid-Infrared Transmission. Lightwave Technology. 2, p.607-613, (1984).
160. P. Houizot, C. Boussard-Plédel, A. J. Faber, L. K. Cheng, B. Bureau, P. A. Van Nijnatten, W. L. M. Gielesen, J. Pereira do Carmo and J. Lucas. Infrared Single Mode Chalcogenide Glass Fiber for Space. Optics Express. 15, p.12529-12538, (2007).
161. D. Furniss and A. B. Seddon. Towards Monomode Proportioned Fibreoptic Preforms by Extrusion. Journal of Non-Crystalline Solids. 256–257, p.232-236, (1999).
162. D. Hewak. Next Generation Chalcogenide Glass for Active and Passive Applications. in The Future Photonics Hub Industry Day and Exhibition. University of Southampton, Optoelectronics Research Centre.(2016).
163. M. Saito, M. Takizawa, S. Sakuragi and F. Tanei. Infrared Image Guide with Bundled As–S Glass Fibers. Applied Optics. 24, p.2304-2308, (1985).
164. Z. Tang, V. S. Shiryaev, D. Furniss, L. Sojka, S. Sujecki, T. M. Benson, A. B. Seddon and M. F. Churbanov. Low Loss Ge-As-Se Chalcogenide Glass Fiber, Fabricated using Extruded Preform, for Mid-Infrared Photonics. Optical Materials Express. 5, p.1722-1737, (2015).
165. V. S. Shiryaev, M. F. Churbanov, G. E. Snopatin and F. Chenard. Preparation of Low-Loss Core–Clad As–Se Glass Fibers. Optical Materials. 48, p.222-225, (2015).
166. G. Boudebs, S. Cherukulappurath, M. Guignard, J. Troles, F. Smektala and F. Sanchez. Linear Optical Characterization of Chalcogenide Glasses. Optics Communications. 230, p.331-336, (2004).
167. V. S. Shiryaev, A. P. Velmuzhov, Z. Q. Tang, M. F. Churbanov and A. B. Seddon. Preparation of High Purity Glasses in the Ga–Ge–As–Se System. Optical Materials. 37, p.18-23, (2014).
168. A. B. Seddon, Z. Tang, D. Furniss, S. Sujecki and T. Benson. Progress in Rare-Earth-Doped Mid-Infrared Fiber Lasers. Optics Express. 18, p.26704-26719, (2010).
169. L. S. Brooks. The Vapor Pressures of Tellurium and Selenium. Journal of the American Chemical Society. 74, p.227-229, (1952).

170. W. Armarego and C. Chai. Purification of Laboratory Chemicals (7th Edition). London. Elsevier.(2013).
171. D. R. Lide. Handbook of Chemistry and Physics. Florida. CRC Press LLC.(2001).
172. J. A. Savage. Optical Properties of Chalcogenide Glasses. Journal of Non-Crystalline Solids. 47, p.101-115, (1982).
173. G. M. Rosenblatt and C. E. Birchenall. Vapor Pressure of Antimony by the Torsion-Effusion Method. The Journal of Chemical Physics. 35, p.788-794, (1961).
174. G. P. Ustyugov, E. N. Vigdorovich, B. M. Kuadzhe and I. A. Timoshin. Saturated Vapour Pressure of the Antimony Chalcogenides. Izvestiya Akademii Nauk. 5, p.589-590, (1969).
175. D. Ferro, B. Nappi and V. Piacente. Vapour Pressure of Antimony Triiodide. The Journal of Chemical Thermodynamics. 11, p.193-201, (1979).
176. T. Zeng, A. F. Sarofim and C. L. Senior. Vaporization of Arsenic, Selenium and Antimony During Coal Combustion. Combustion and Flame. 126, p.1714-1724, (2001).
177. T.C. Anderson. The Heat Capacities at Low Temperatures of Antimony, Antimony Trioxide, Antimony Tetroxide and Antimony Pentoxide Journal of the American Chemical Society. 52, p.2712-2720, (1930).
178. D. Lezal, A. Pedlı, J. Ková, J. Zavadil, P. Kostka and M. Poulain. Preparation and Characterization of Sulfide, Selenide and Telluride Glasses. Journal of Non-Crystalline Solids. 326–327, p.47-52, (2003).
179. O. Kubaschewski, E. L. I. Evans and C. B. Alcock. Metallurgical Thermochemistry. 4th edition ed Oxford. Pergamon Press.(1967).
180. T. Katsuyama, S. Satoh and H. Matsumura. Scattering Loss Characteristics of Selenide-Based Chalcogenide Glass Optical Fibers. Journal of Applied Physics. 71, p.4132-4135, (1992).
181. S. Sakka and J. D. Mackenzie. Relation Between Apparent Glass Transition Temperature and Liquids Temperature for Inorganic Glasses. Journal of Non-Crystalline Solids. 6, p.145-162, (1971).
182. National Physical Laboratory. Vapour Pressures from 0.2 to 101.325 kPa. [Access Date 03/02/2016]; Available from: http://www.kayelaby.npl.co.uk/chemistry/3_4/3_4_4.html.
183. Y. Tsuchiya. The Velocity of Sound in Liquid Arsenic: Evidence for Rapid Structural Changes with Temperature. Journal of Physics: Condensed Matter. 9, p.10087, (1997).
184. M. Eckert. Max Von Laue and the Discovery of X-ray Diffraction in 1912. Annalen der Physik. 524, p.A83-A85, (2012).
185. Personal communications with Dr. N. Neate Senior Research Technician. Wolfson Centre for Materials Research Department of Mechanical, Materials and Manufacturing Engineering, Faculty of Engineering, University of Nottingham, UK.(2014-2015).
186. S. J. Fomon, R. L. Jensen and G. M. Owen. Determination of Body Volume of Infants by a Method of Helium Displacement. Annals of the New York Academy of Sciences. 110, p.80-90, (1963).
187. E. Freire. Differential Scanning Calorimetry. Protein Stability and Folding: Theory and Practice. Bret A. Shirley. Editor Humana Press. Totowa, New Jersey. p. 191-218.(1995).
188. D. Furniss and A. B. Seddon. Chapter 10: Thermal Analysis of Inorganic Compound Glasses and Glass-Ceramics. Principles and Applications of Thermal Analysis. ed. P. Gabbot. Oxford, UK. Blackwell Publishing Ltd.(2008).

189. Personal communications with Professor A.B. Seddon and Professor T. M. Benson. MIR Photonics Research Group, The University of Nottingham.(2015-2016).
190. B Stuart. Infrared Spectroscopy : Fundamentals and Applications. Hoboken. Wiley.(2004).
191. G. C Righini and M. Ferrari. Photoluminescence of Rare-Earth-Doped Glasses. Rivista del Nuovo Cimento. 28, p.1-53, (2005).
192. L. Petit, N. Carlie, H. Chen, S. Gaylord, J. Massera, G. Boudebs, J. Hu, A. Agarwal, L. Kimerling and K. Richardson. Compositional Dependence of the Nonlinear Refractive Index of New Germanium-Based Chalcogenide Glasses. Journal of Solid State Chemistry. 182, p.2756-2761, (2009).
193. X. Jiang and A. Jha. Engineering of a Ge–Te–Se Glass Fibre Evanescent Wave Spectroscopic (FEWS) Mid-Infrared Chemical Sensor for the Analysis of Food and Pharmaceutical Products. Sensors and Actuators B: Chemical. 206, p.159-169, (2015).
194. A.J. Schwartz, M. Kumar, B.L. Adams and D. P. Field. Electron Backscatter Diffraction in Materials Science. New York. Springer.(2010).
195. C. W. Oatley, W. C. Nixon and R. F. W. Pease. Chapter 2: Scanning Electron Microscopy. Advances in Electronics and Electron Physics Academic Press. p. 181-247.(1966).
196. Z. Tang, D. Furniss, M. Fay, N. C. Neate, S. Sujeeki, T. M. Benson and A. B. Seddon. Crystallization and Optical Loss Studies of Dy3+ Doped, Low Ga Content, Selenide Chalcogenide Bulk Glasses and Optical Fibers. Processing, Properties, and Applications of Glass and Optical Materials. John Wiley & Sons, Inc.: Oxford. p. 193-199.(2012).
197. W. A. King, A. G. Clare and W. C. LaCourse. Laboratory Preparation of Highly Pure As2Se3 Glass. Journal of Non-Crystalline Solids. 181, p.231-237, (1995).
198. T. Katsuyama, K. Ishida, S. Satoh and H. Matsumura. Low Loss Ge-Se Chalcogenide Glass Optical Fibers. Applied Physics Letters. 45, p.925-927, (1984).
199. M. F. Churbanov. Purification Of Chalcogenide Glasses. in Properties, Processing and Applications of Glass and Rare Earth Doped Glasses for Optical Fibres. D. Hewak, Editor EMIS Date-reviews Series No. 22: London. p. 340-343.(1998).
200. G. G. Devyatykh, M. F. Churbanov, V. S. Shiryaev, G. E. Snopatin and V. V. Gerasimenko. Impurity Inclusions in Extra-Pure Arsenic and Chalcogens. Inorganic Materials. 34, p.902-906, (1998).
201. Personal communications with Dr. Z. Tang. Research in MIR Photonics Group. Wolfson Centre for Materials Research Department of Mechanical, Materials and Manufacturing Engineering, Faculty of Engineering, University of Nottingham, UK.(2015-2016).
202. J. E. Shelby. Thermal Expansion of Amorphous Metals. Journal of Non-Crystalline Solids. 34, p.111-119, (1979).
203. W. L. Konijnendijk and J. M. Stevels. Linear Thermal Expansion of Borosilicate Glasses in Relation to Their Structure. Verres et Refractaires. 30, p.371-77, (1976).
204. S. English and W. E. S. Turner. The Heat Expansion of Soda-Lime Glasses. Society of Glass Technology. 3, p.238, (1919).
205. J.E. Shelby. Introduction to Glass Science and Technology. First Edit. Cambridge. The Royal Society of Chemistry.(1997).

206. E. Roeder. Extrusion of Glass. Journal of Non-Crystalline Solids. 5, p.377-388, (1971).
207. T. Arnold, D. Furniss, J. H. Butterworth and E. Barney. Optimsing Core-Clad Ratios in Glass Extrusions for Optical Fibre Applications. M.Eng. MM4MPR Indiviual Research Paper. in Mechanical, Materials and Manufacturing Engineering. The University of Nottingham: UK.(2014).
208. W. Choong and A.B. Seddon. Monomode Mid-Infrared Fibre Optics.M.Eng. MM4MPR. Indiviual Research Paper. in Mechnanical, Materials and Manufacturing Engineering. The University of Nottingham: UK.(2013).
209. C. Agger, I. Kubat, U. Møller, P. M. Moselund, C. Petersen, B. Napier, A. Seddon, S. Sujecki, T. Benson, M. Farries, J. Ward, S. Lamrini, K. Scholle, P. Fuhrberg, O. Bang, B. Boulanger, S. Cundiff, M. Kauranen and W. Knox. Numerical Demonstration of 3-12 µm Supercontinuum Generation in Large-Core Step-Index Chalcogenide Fibers Pumped at 4.5 µm. in Nonlinear Optics Conference. Hawaii: Optical Society of America.(2013).
210. H. W. Starkweather. The Effect of Heating Rate On the Melting of Polytetrafluoroethylene. Journal of Polymer Science: Polymer Physics Edition. 23, p.1177-1185, (1985).
211. A. K. Varshneya and D. J. Mauro. Microhardness, Indentation Toughness, Elasticity, Plasticity, and Brittleness of Ge–Sb–Se Chalcogenide Glasses. Journal of Non-Crystalline Solids. 353, p.1291-1297, (2007).
212. J.-P. Guin, T. Rouxel, J.-C. Sanglebœuf, I. Melscoët and J. Lucas. Hardness, Toughness, and Scratchability of Germanium–Selenium Chalcogenide Glasses. Journal of the American Ceramic Society. 85, p.1545-1552, (2002).
213. D. Jayasuriya, J. Butterworth, D. Furniss and A. B. Seddon. Towards Ge-Sb-Se IR Step Index Monomode Optical Fibre for Mid-Infrared Supercontinuum Generation. MM4MPR Indiviual Research Paper. in Mechanical, Materials and Manufacturing Engineering. The University of Nottingham: UK.(2013).
214. V. S. Shiryaev and M. F. Churbanov. Trends and Prospects for Development of Chalcogenide Fibers for Mid-Infrared Transmission. Journal of Non-Crystalline Solids. 377, p.225-230, (2013).
215. G. E. Snopatin, V. S. Shiryaev, V. G. Plotnichenko, E. M. Dianov and M. F. Churbanov. High-purity chalcogenide glasses for fiber optics. Inorganic Materials. 45, p.1439-1460, 2009.
216. B. J. Park, H. S. Seo, J. T. Ahn, Y. G. Choi, D. Y. Jeon and W. J. Chung. Mid-Infrared (3.5–5.5 microns) Spectroscopic Properties of Pr3+-Doped Ge–Ga–Sb–Se Glasses and Optical Fibers. Journal of Luminescence. 128, p.1617-1622, (2008).
217. J. K. Kim, B. Kyou Jin, W. J. Chung, B. J. Park, J. Heo and Y. G. Choi. Influence of the Ga Addition on Optical Properties of Pr in Ge–Sb–Se Glasses. Journal of Physics and Chemistry of Solids. 72, p.1386-1389, (2011).
218. E. V. Karaksina, V. S. Shiryaev, T. V. Kotereva and M. F. Churbanov. Preparation of High-Purity Pr(3+) Doped Ge–Ga–Sb–Se Glasses with Intensive Middle Infrared Luminescence. Journal of Luminescence. 170, p.37-41, (2016).
219. R. Speiser and H. L. Johnston. Vapor Pressures of Inorganic Substances. I X. Gallium 1. Journal of the American Chemical Society. 75, p.1469-1470, (1953).
220. A P. Velmuzhov, A. A. Sibirkin, V. S. Shiryaev, M. F. Churbanov, A. I. Suchkov, A. M. Potapov, M. V. Sukhanov, V. G. Plotnichenko, V. V. Koltashev and A. D.

Plekhovich. Preparation of Glasses in the Ge–Sb–Se–I System via Volatile Iodides. Journal of Non-Crystalline Solids. 405, p.100-103, (2014).
221. Sigma-Aldrich Safety Data Sheet. Germanium (I V) iodide. 383252 Aldrich.(2016).
222. Sigma-Aldrich Safety Data Sheet. Antimony (I I I) iodide. 401188 Aldrich.(2016).
223. Y. Chen, T. Xu, X. Shen, R. Wang, S. Zong, S. Dai and Q. Nie. Optical and Structure Properties of Amorphous Ge–Sb–Se Films for Ultrafast All-Optical Signal Processing. Journal of Alloys and Compounds. 580, p.578-583, (2013).
224. C. E. Podesta, J. Butterworth and A. B. Seddon. Mid-Infrared Optical Fibres For Cancer Detection: Biocompatibility Of Sb-Se-Ge Chalcogenide Glass. M.Eng. MM4MPR Indiviual Research Paper. in Mechanical, Materials and Manufacturing Engineering. The University of Nottingham: UK.(2014).
225. G. J. Todaro and H. Green. Quantitative Studies of the Growth of Mouse Embryo Cells in Culture and Their Development into Established Lines. The Journal of Cell Biology. 17, p.299-313, (1963).
226. B. Alberts, A. Johnson and Lewis. J. Fibroblasts and Their Transformations: The Connective-Tissue Cell Family. Molecular Biology of the Cell. 4th edition. New York. Garland Science.(2002).
227. L. Zhang, H. Yu, A. Badzio, T. A. Boyle, H.-U. Schildhaus, X. Lu, R. Dziadziuszko, J. Jassem, M. Varella-Garcia, L. E. Heasley, A. A. Kowalewski, K. Ellison, G. Chen, C. Zhou and F. R. Hirsch. Fibroblast Growth Factor Receptor 1 and Related Ligands in Small-Cell Lung Cancer. Journal of Thoracic Oncology. 10, p.1083-1090, (2015).
228. W. Strober. Trypan Blue Exclusion Test of Cell Viability. Current Protocols in Immunology John Wiley & Sons. Oxford.(2001).
229. D. Beyersmann. Effects of Carcinogenic Metals on Gene Expression. Toxicology Letters. 127, p.63-68, (2002).
230. V. Matějec, J. Pedliková, I. Barton, J. Zavadil and P. Kostka. Optical Properties of As2S3 Layers Deposited from Solutions. Journal of Non-Crystalline Solids. 431, p.47-51, (2016).
231. N. Sharmin, A. J. Parsons, C. D. Rudd and I. Ahmed. Effect of Boron Oxide Addition on Fibre Drawing, Mechanical Properties and Dissolution Behaviour of Phosphate-Based Glass Fibres with Fixed 40, 45 and 50 mol% P(2)O(5). Journal of Biomaterials Applications. 29, p.639-653, (2014).
232. F. Bonnier, M. E. Keating, T. P. Wróbel, K. Majzner, M. Baranska, A. Garcia-Munoz, A. Blanco and H. J. Byrne. Cell Viability Assessment using the Alamar Blue Assay: A Comparison of 2D and 3D Cell Culture Models. Toxicology in Vitro. 29, p.124-131, (2015).
233. G. R. Nakayama, M. C. Caton, M. P. Nova and Z. Parandoosh. Assessment of the Alamar Blue Assay for Cellular Growth and Viability in Vitro. Journal of Immunological Methods. 204, p.205-208, (1997).
234. R. Hamid, Y. Rotshteyn, L. Rabadi, R. Parikh and P. Bullock. Comparison of Alamar Blue and MTT Assays for High Through-Put Screening. Toxicology in Vitro. 18, p.703-710, (2004).
235. J. Mikus and D. Steverding. A Simple Colorimetric Method to Screen Drug Cytotoxicity Against Leishmania Using the Dye Alamar Blue®. Parasitology International. 48, p.265-269, (2000).
236. J. O'Brien, I. Wilson, T. Orton and F. Pognan. Investigation of the Alamar Blue (Resazurin) Fluorescent Dye for the Assessment of Mammalian Cell Cytotoxicity. European Journal of Biochemistry. 267, p.5421-5426, (2000).

237. R. J. Gonzalez and J. B. Tarloff. Evaluation of Hepatic Subcellular Fractions for Alamar Blue and MTT Reductase Activity. Toxicology in Vitro. 15, p.257-259, (2001).
238. M. M. Nociari, A. Shalev, P. Benias and C. Russo. A Novel One-Step, Highly Sensitive Fluorometric Assay to Evaluate Cell-Mediated Cytotoxicity. Journal of Immunological Methods. 213, p.157-167, (1998).
239. L. A. Poole-Warren and A. J. Patton. Chapter 1 - Introduction to Biomedical Polymers and Biocompatibility. Biosynthetic Polymers for Medical Applications Woodhead Publishing. Oxford. p. 3-31.(2016).
240. E. J. Hoekstra and C. Simoneau. Release of Bisphenol A from Polycarbonate—A Review. Critical Reviews in Food Science and Nutrition. 53, p.386-402, (2013).
241. L. L. Hench. Bioceramics. Journal of the American Ceramic Society. 81, p.1705-1728, (1998).
242. M. S. Hasan, I. Ahmed, A. J. Parsons, G. S. Walker and C. A. Scotchford. Material Characterisation and Cytocompatibility Assessment of Quinternary Phosphate Glasses. Journal of Materials Science: Materials in Medicine. 23, p.2531-2541, (2012).
243. J. Wilson, G. H. Pigott, F. J. Schoen and L. L. Hench. Toxicology and Biocompatibility of Bioglasses. Journal of Biomedical Materials Research. 15, p.805-817, (1981).
244. L. L. Hench. The Story of Bioglass®. Journal of Materials Science: Materials in Medicine. 17, p.967-978, (2006).
245. F. J. O'Brien, B. A. Harley, I. V. Yannas and L. J. Gibson. The Effect of Pore Size on Cell Adhesion in Collagen-GAG Scaffolds. Biomaterials. 26, p.433-441, (2005).
246. A. J. Engler, S. Sen, H. L. Sweeney and D. E. Discher. Matrix Elasticity Directs Stem Cell Lineage Specification. Cell. 126, p.677-689, (2006).
247. S. R. Peyton and A. J. Putnam. Extracellular Matrix Rigidity Governs Smooth Muscle Cell Motility in a Biphasic Fashion. Journal of Cellular Physiology. 204, p.198-209, (2005).
248. S. Mitragotri and J. Lahann. Physical Approaches to Biomaterial Design. Nature Materials. 8, p.15-23, (2009).
249. C. S. Chen, M. Mrksich, S. Huang, G. M. Whitesides and D. E. Ingber. Geometric Control of Cell Life and Death. Science. 276, p.1425-1428, (1997).
250. B. G. Cousins, P. J. Doherty, R. L. Williams, J. Fink and M. J. Garvey. The Effect of Silica Nanoparticulate Coatings on Cellular Response. Journal of Materials Science: Materials in Medicine. 15, p.355-359, (2004).
251. G. Altankov, F. Grinnell and T. Groth. Studies on the Biocompatibility of Materials: Fibroblast Reorganization of Substratum-Bound Fibronectin on Surfaces Varying in Wettability. Journal of Biomedical Materials Research. 30, p.385-391, (1996).
252. F. Grinnell, M. Milam and P. A. Srere. Studies On Cell Adhesion. Archives of Biochemistry and Biophysics. 153, p.193-198, (1972).
253. B. D. Ratner, A. S. Hoffman, F. J. Schoen and J. E. Lemons. Biomaterials Science: An Introduction to Materials in Medicine. San Diego. Academic press.(2004).
254. B. Hexig, R. Nakaoka and T. Tsuchiya. Safety Evaluation of Surgical Materials by Cytotoxicity Testing. Journal of Artificial Organs. 11, p.204-211, (2008).

255. M.J. Dalby, M. O. Riehle, S. J. Yarwood, C. D. W. Wilkinson and A. S. G. Curtis. Nucleus Alignment and Cell Signaling in Fibroblasts: Response to a Micro-Grooved Topography. Experimental Cell Research. 284, p.272-280, (2003).
256. S. P. Allen, L. M. Duffy, P. J. Shaw and A. J. Grierson. Altered Age-Related Changes in Bioenergetic Properties and Mitochondrial Morphology in Fibroblasts from Sporadic Amyotrophic Lateral Sclerosis Patients. Neurobiology of Aging. 36, p.2893-2903, (2015).
257. F. S. Al-Hazmi. Effect of Annealing on Optical Constants of Se75S25−xCdx Chalcogenide Thin Films. Physica B: Condensed Matter. 404, p.1354-1358, (2009).
258. A. Simmons. Chapter 11 - Future Trends for the Sterilisation of Biomaterials and Medical Devices. Sterilisation of Biomaterials and Medical Devices Woodhead Publishing. Oxford. p. 310-320.(2012).
259. D. C. Peters. A Comparison of Mercury Arc Lamp and Laser Illumination for Flow Cytometers. Journal of Histochemistry & Cytochemistry. 27, p.241-5, (1979).
260. M. Cable and J. M. Parker. High-Performance Glasses. Glasgow. Blackie.(1992).
261. E. Bychkov, C. J. Benmore and D. L. Price. Compositional Changes of the First Sharp Diffraction Peak in Binary Selenide Glasses. Physical Review B. 72, p.71-74, (2005).
262. S.E. McLain, D. T. Bowron, A.C. Hannon and A.K. Soper. Gudrun. A Computer Program Developed for Analysis of Neutron Diffraction Data. (2006).
263. A.C. Hannon, W.S. Howells and A.K. Soper. ATLAS : A Suite of Programs for the Analysis of Time-of-flight Neutron Diffraction Data From Liquid and Amorphous Samples. Institute of Physics Conference Series. 107, p.193-211, (1990).
264. A. C. Hannon. INTERFERE and MERGE -using Microsoft Excel to Choose Parameters for LAD Data.(2013) [Access Date 12/08/2015]; Available from: http://www.isis.stfc.ac.uk/instruments/gem/software/intmer-manual6151.pdf.
265. G. Placzek. The Scattering of Neutrons by Systems of Heavy Nuclei. Physical Review. 86, p.377-388, (1952).
266. E. Lorch. Neutron Diffraction by Germania, Silica and Radiation-Damaged Silica Glasses. Journal of Physics C: Solid State Physics. 2, p.229, (1969).
267. C. Quemard, F. Smektala, V. Couderc, A. Barthelemy and J. Lucas. Chalcogenide Glasses with High Nonlinear Optical Properties for Telecommunications. Journal of Physical Chemistry Solids. 62, p.1435-1440, (2001).
268. MDL Information Systems. SciGlass-6.0. San Leandro, Editor.(2003).
269. E. Bychkov, C. J. Benmore and D. L. Price. Compositional Changes of the First Sharp Diffraction Peak in Binary Selenide Glasses. PHYSICAL REVIEW B. 72, p.107-172, (2005).
270. A.C. Hannon. Neutron Diffraction Techniques for Structural Studies of Glasses. Modern Glass Characterisation. M. Alffatigato. Editor.Wiley. New York. p. 158.(2015).
271. E. L. Gjersing, S. Sen and B. G. Aitken. Structure, Connectivity, and Configurational Entropy of GexSe100−x Glasses: Results from 77Se MAS NMR Spectroscopy. The Journal of Physical Chemistry C. 114, p.8601-8608, (2010).

272. I. Petri, P. S. Salmon and H. E. Fischer. Defects in a Disordered World: The Structure of Glassy GeSe2. Physical Review Letters. 84, p.2413-2416, (2000).
273. J. G. Speight. Lange's Handbook of Chemistry. Vol. 1. New York. McGraw-Hill (2005).
274. W. H. Bragg and W. L. Bragg. The Reflection of X-rays by Crystals. Proceedings of the Royal Society of London. Series A, Containing Papers of a Mathematical and Physical Character. 88, p.428-438, (1913).
275. E. Barney, N. Abdel-Moneim, J.J. Towey, J. Titman, J. E. McCarthy, H. T. Bookey, A. Kar, D. Furniss and A. Seddon. Correlating Structure with Non-Linear Optical Properties in xAs40Se60·(1 − x)As40S60 Glasses. Physical Chemistry Chemical Physics. 17, p.6314-6327, (2015).
276. P. J. Brown, A. G. Fox, E. N. Maslen, M. A. O'Keefe and B. T. M. Willis. Chapter 6.1 - Intensity of Diffracted Intensities. International Tables for Crystallography. Volume C. Springer. The Netherlands.(2006).

# Appendix I

**Table A Position of absorption impurity bands in Ge-Sb-Se glasses. Collated from [58][141][161][210-211]**

| Functional group causing absorption | Position of absorption band / (μm) |
|---|---|
| $CO/CO_2$ | 4.31; 4.33; 15.0 |
| Free $H_2O$ | 2.77, 2.79, 2.83, 2.86, 6.31, 6.32 |
| Ge-H | 4.95 |
| Ge–O | 7.8, 7.9, 12.8 |
| O–H/OH- | 1.44, 2.20, 2.86, 2.90, 2.92, 4.40 |
| Sb-O | 13.55, 14.53; 17.60 |
| Se–H | 2.32, 3.50, 3.52, 3.55, 4.12, 4.15, 4.57, 5.00, 7.80 |
| Se–O | 10.67; 11.06, 11.10, 15.30 |
| Si-O | 9.1-10 |

# Appendix II

**Table A. A quantitative comparison of the outer cladding tube extrusion parameters conducted in this Project. Outer cladding tubes were extruded from either glass composition JB03 ($Ge_{24}Sb_4Se_{72}$) or JB02 ($Ge_{20}Sb_{10}Se_{70}$). Each glass boule was melted in a 28/ 32 mm ID/OD ampoule and general extrusion conditions which were subjected to all tube extrusions were; 0.5 L $min^{-1}$ of $N_2$ supplied to the die shield tube; extraction; minimum load of 100 kg. A new glass was batched for every extrusion, thus the boules were cut to size with the end furthest from the contraction cone extruded. Each boule was placed in the extruder with the saw cut edge closest to the bobbin.**

| Extrusion number | | E014JHB | E017JHB | E019JHB | E025JHB | E026JHB | E029JHB | E039JHB |
|---|---|---|---|---|---|---|---|---|
| Composition | | JB03 | JB03 | JB03 | JB02 | JB02 | JB02 | JB03 |
| Melt number | | M054JHB | M060JHB | M061JHB | M087JHB | M093JHB | M094JHB | M105JHB |
| Boule | Height / mm | 13.55 | 13.06 | 13.8 | 15.74 | 15.81 | 15.75 | 18.86 |
| | Weight | 38.88 | 35.81 | 41.85 | 45.48 | 45.52 | 45.49 | 53.65 |
| 316 S.S graphite lined die | Dimensions ID / mm | 10 | 10 | 10 | 10 | 10 | 10 | 10 |
| Nimonic pin | Dimensions OD/ mm | 1 | 1.5 | 1.5 | 1.5 | 1.5 | 1.5 | 1.5 |
| Extruder parameters | Temperature when minimum load was applied* / °C | 255 | 267 | 267 | 227 | 222 | 219 | 274 |
| | Steady-state extrusion temperature* / °C | 300 | 303 | 298 | n/a | n/a | 255 | 285 |
| | Extrusion rate /mm $min^{-1}$ | 0.090 | 0.150 | 0.180 | n/a | n/a | 0.017 | 0.098 |
| | Completion time | 4 h 45 min | 2 h 23 min | 2 h 33 min | n/a | n/a | 6h 30 min | 4 h 01 min |
| | Max load / kg | 500 | 750 | 750 | 750 | 500 | 500 | 500 |
| Dimensions of extrudate | Length / mm | 99 | 79 | 99 | n/a | n/a | 79 | 118 |
| | OD / mm | 9.47 | 9.68 | 9.82 | n/a | n/a | 9.9 | 9.48 |
| | ID / mm | 2.82 | 1.81 | 1.59 | n/a | n/a | 1.5 | 1.68 |
| Temperature at the extrusion viscosity region $10^8$ Pa.s ** / °C | | 292 | 292 | 292 | 264 | 264 | 264 | 292 |

* as-measured by a thermocouple inside the extruder die

** from table 4.8

# Appendix III

**Table B. A quantitative comparison of the co-extrusion parameters conducted in this Project. The glass compositions were: JB01- $Ge_{19}Sb_{15}Se_{66}$; JB02- $Ge_{20}Sb_{10}Se_{70}$; JB03 - $Ge_{24}Sb_4Se_{72}$ and JB04- $Ge_{22}Sb_8Se_{70}$. Each glass boule was melted in a 15/ 18 mm ID/OD ampoule and general extrusion conditions which were subjected to all tube extrusions were; $10^{-2}$ mbar vacuum; 0.5 L $min^{-1}$ of $N_2$ was supplied to the die shield tube one extrusion was complete; extraction; minimum load of 100 kg. One side of a glass boule was polished to a 1 µm finish and the boules were loaded into the extruder so that the core was on top of the cladding in the vertical position.**

| Extrusion number | | | E015JHB | E018JHB | E030JHB | E040JHB | E042JHB |
|---|---|---|---|---|---|---|---|
| Glass Pair | | | Pair I | Pair I | Pair II | Pair III | n/a |
| Composition | | Core | JB04 | JB04 | JB01 | JB02 | JB02 |
| | | Cladding | JB03 | JB03 | JB02 | JB03 | n/a |
| Melt number | | Core | M052JHB | M052JHB | M081JHB | M101JHB | M101JHB |
| | | Cladding | M053JHB | M054JHB | M084JHB | M104JHB | n/a |
| Boule | Height / mm | Core | 10.47 | 10.59 | 10.34 | 10.47 | 14.34 |
| | | Cladding | 10.49 | 10.47 | 10.29 | 10.58 | n/a |
| | Weight | Core | 8.39 | 8.41 | 8.57 | 8.52 | 10.91 |
| | | Cladding | 8.28 | 8.20 | 8.32 | 8.25 | n/a |
| Extruder parameters | Temperature when minimum load was applied* / °C | | 240 | 260 | 230 | 315 | 277 |
| | Steady-state extrusion temperature* / °C | | 311 | 314 | 291 | n/a | 280 |
| | Extrusion rate /mm $min^{-1}$ | | 0.48 | 0.5 | 0.16 | n/a | 0.08 |
| | Completion time | | 2 h 13 min | 1 h 56 min | 5 h 35 min | n/a | 2 h 59 min |
| | Max load / kg | | 200 | 200 | 200 | n/a | 200 |
| Dimensions of extrudate | Length / mm | | 202 | 197 | 195 | n/a | 103 |
| | OD / mm | | 4.75 | 4.74-4.76 | 4.76 | n/a | 4.24-4.26 |
| Temperature at the extrusion viscosity region $10^8$ Pa.s ** / °C | | Core | 292 | 292 | 278 | 264 | 264 |
| | | Cladding | 282 | 282 | 264 | 292 | n/a |

* as -measured by a thermocouple inside the extruder die

** from Table 4.8